University of Napoli Federico II

Doctorate in
STRUCTURAL, GEOTECHNICAL
ENGINEERING AND SEISMIC RISK
XXXII CYCLE

Experimental and numerical investigation of the effectiveness of some innovative techniques to mitigate liquefaction risk

Gianluca Fasano

Supervisors

Prof. Alessandro Flora
Prof. Emilio Bilotta
Prof. Vincenzo Fioravante

PhD Coordinator

Prof. Luciano Rosati

Abstract

Many urban areas in the world have been strongly damaged by soil liquefaction during strong earthquakes. This phenomenon is caused by a progressive increment of the excess pore pressure that leads to a significant drop of the shear stiffness and strength, resulting into large settlements and a reduction of the safety margins in terms of bearing capacity of existing structures. As a consequence, when liquefaction occurs damages are more critical than those induced by inertial seismic actions.

Large economic losses induced by this phenomenon encouraged in the last decades the scientific community to spend strong efforts in the study of some techniques to reduce liquefaction risk. Conventional mitigation techniques have been used to reduce settlements and bearing capacity loss, but they require massive and expensive retrofitting interventions. So, the development of some innovative mitigation techniques characterised by lower cost and by the possibility to be used in the urban area is becoming more and more a necessity.

The project called LIQUEFACT (H2020-DRS-2015), financed by the European Committee, moved in this direction. Dynamic geotechnical centrifuge experiments were performed in this project to evaluate the effectiveness of two innovative techniques: horizontal drains (HD), which are innovative mostly for their installation procedure, that allows to place them directly under existing structures, and induced partial saturation (IPS), which is innovative for the process, never used in the past to tackle liquefaction risk.

Horizontal drains were studied to define their capability to dissipate the excess pore pressures that rise during the earthquake, while the induced partial saturation was adopted to reduce the bulk stiffness of the equivalent pore fluid, reducing the attitude to increase the excess pore pressure induced by distorsional deformations of the soil.

Each centrifuge model, realised with a loose liquefiable sand (Ticino sand), was equipped in order to measure accelerations, pore pressures and displacements. Moreover, a simplified SDOF structure was used in some tests to evaluate the interaction between the liquefiable soil and the structure, with and without the adoption of one of the mitigation techniques.

The reliability of numerical modelling of the mitigation techniques was checked by the comparison between numerical and experimental results. The presence of horizontal drains was modelled by tubes with a finite permeability, estimated on the bases of experimental tests, with an inside hydrostatic fluid pressure.

Some centrifuge tests with free-field configuration were reproduced by numerical analyses, using PLAXIS 2D, to check the possibility to calibrate two constitutive models used to study soil liquefaction (UBC3D-PLM and PM4SAND) with the aim of catching the experimental results in terms of pore pressure increments and settlements of the ground surface. The induced partial saturation was implemented by a reduction of the fluid bulk stiffness with a function of degree saturation.

The results indicate that the numerical analyses underestimate the settlements of the ground surface in free-field conditions but capture reasonably well liquefaction-induced building settlement in the centrifuge experiments.

Some parametrical analyses of the mitigation techniques were also performed, changing the HD geometrical layouts and soil mechanical properties. Moreover, an evaluation of an optimised horizontal extension of the mitigation techniques was performed for a reference building.

A simplified design method for the horizontal drains was finally proposed, for the case of three horizontal rows of drains disposed with a staggered arrangement. A simplified design method for the induced partial saturation based on the analytical procedure was proposed as well.

Summary

Acknowledgments

I want to be honest, I started my doctorate as a new experience whose I did not know who effort It required me. The difficulties arrived soon, but I knew that I could count on the help of my tutors, great persons with great ability and kindness. I thank them for the ideas and constructive discussions that improved significantly the quality of my research work. A great thank goes to Emilio for his tips with almost daily frequency.

I would like to thank my parents, in particular my father for his leniency, he has been waiting my master's degree for a help in his building business, but he realised that I would start this new experience extending his wait.

I thank Antonella, my love, for her support in my very hard times. She respected always my spaces and listened to me in my crazy moods on when all went bad. I'm sorry for the strongly cuts to the time to spent together.

I thank my friend, Domenico De Sarno, with whom stand by a great friendship and I had many constructive discussions.

Finally, I would express my gratitude to all my colleagues with whom I spent many funny moments that I will remember forever.

1 INTRODUCTION

Complex phenomena are always studied by researchers aiming to predict and manage their effects to solve uncommon application problems.

Soil liquefaction phenomenon is one of these and in the last years it received increasing attention. This phenomenon may affect saturated loose sands subjected to cyclic shear stress usually due to strong earthquakes. In this case cyclic loading may occur in undrained or partially undrained conditions and coupling threshold between shear and volumetric strains may be achieved in the soil, producing an excess pore water pressure build-up and, consequently, a reduction of the effective stresses. Liquefaction is then triggered when the effective stress reaches the zero-value and the soil strength and stiffness drop. However, even large excess pore pressures, that do not induce the soil liquefaction, may lead to a significant reduction of soil strength and stiffness, producing instability and large deformations in the soil, in turn affecting the stability and the performance of the structure there founded.

The potential of modelling soil liquefaction in boundary value problems was boosted in the last decades by, the strong computer power increase. It has permitted very complex numerical problems to be solved in short time and encouraged researchers to develop some refined constitutive soil models that are able to reproduce the excess pore pressure build-up arising when the soil is subjected to cyclic deviatoric stresses. Suitable constitutive soil models were developed, to take into account the progressive reduction of shear stiffness and strength during pore pressure build-up up to liquefaction. Therefore, nowadays numerical methods are able to investigate:

- the susceptibility of a certain site to soil liquefaction;
- the changing of soil-structure interaction in liquefying soil;
- the possibility to validate and optimize liquefaction mitigation techniques.

The thesis is focused on the analysis of horizontal drains and induced partial saturation as liquefaction mitigation technique and it is divided in two macro-parts: analysis of the experimental results of the tests carried out within the LIQUEFACT project in the geotechnical centrifuge of ISMGEO and numerical investigations with advanced constitutive models.

The experimental activities at ISMGEO aimed:

- to study the liquefaction triggering in simple centrifuge models made of Ticino sand (Italian standard sand);
- to determine the effects of some innovative liquefaction mitigation techniques like horizontal drains (HS) and induced partial saturation (IPS);
- to study the effect of previous mitigation techniques in presence of a simple structure.

Hence, starting from the experimental evidences several considerations on the behaviour of soil liquefaction phenomenon were made. The numerical analyses allowed to understand how the soil liquefaction phenomenon was triggered and what was the effect of the

mitigation technique on the liquefiable soil during shaking. Particular attention was paid on the effects of different horizontal drains spacing and of different induced values of the saturation degree.

In details, the organization of this thesis can be summarized as follows:

- Chapter 2 deals with the fundamental understanding and concepts of soil liquefaction and some cases history have been described. This is followed by a review of the behaviour of sandy soils under monotonic and cyclic loading. The main mitigation techniques against soil liquefaction and their in-situ applicability have been described in the last part of the chapter;
- Chapter 3 describes the setup of centrifuge tests carried out at ISMGEO for the LIQUEFACT project. The chapter gives details on the customised equivalent shear box used for all centrifuge tests, on the design of the simple structure used in some tests focusing on soil-structure interaction, on the input motions applied at the bottom of the box during the tests and the characteristics of the soil employed (Ticino sand). Moreover, an interpretation of the results in terms of accelerations, excess pore pressure and ground surface settlements was attempted.
- Chapter 4 presents the numerical analyses of the centrifuge test performed with two different constitutive soil models that are able to reproduce the volumetric distortional soil behaviour. When observed, the discrepancies between the numerical results and the experimental data were discussed.
- Chapter 5 presents the results of some parametric analyses performed on the mitigation schemes horizontal drains (HD) and induced partial saturation (IPS). The parametric analyses with horizontal drains were made by changing the depth of the first row and spacing among drains, whereas the extension of the treated soil region and saturation degree were changed for the case of induced partial saturation;
- In the Chapter 6 design methods for both mitigation techniques are proposed;
- Finally, in Chapter 7 a useful summary of the main findings of this research work and conclusions are provided. Possible future research on the topic is discussed.

This thesis was partly funded within the LIQUEFACT (H2020-DRS-2015) project by the EU in the framework of Horizon2020 – DRS 2015 Research Innovation Action. The project addresses the mitigation of risks to EILD events in European communities with a holistic approach (www.liquefact.eu). It involves eleven partners, including University of Napoli Federico II (Figure 1.1).

Figure 1.1. Main Partners of LIQUEFACT project.

2 SOIL LIQUEFACTION

2.1 Historical events

In the 20th century the phenomenon of soil liquefaction leaded to large economic losses in many parts of the world. Several researcher payed attentions to this phenomenon after two significative historical earthquake events happened in 1964: Prince William Sound region (M_w=9.2) in Alaska and in Niigata (M_s=7.5) in Japan. A brief explanation of historical damages induced by soil liquefaction is shown in the following.

Figure 2.1. Lateral spreading phenomena during Alaska earthquake (1964).

A moment magnitude equal to 9.2 earthquake occurred in 1964 in Prince William Sound region (Alaska, USA) and caused many effects on the natural and anthropic environmental. Important lateral spreading phenomena (Figure 2.1) and around 2.5 billion dollars of damages were registered.

Figure 2.2. Bearing capacity failures during Niigata earthquake (1964).

Several buildings shown failures of bearing capacity during the magnitude 7.6 earthquake in 1964 in Niigata in Japan. In Figure 2.2 are shown buildings in reclamation area affected by large tilt due to the liquefaction of foundation soil. It is worth noting that all the buildings tilted had the water tanks on the roofs. Probably, the tilting occurred toward the centre of gravity due to the weight of the water tanks (Ishihara and Koga, 1981).

The city of Kobe (Japan) in the year 1995 was interested by a 6.9 magnitude moment earthquake. A large part of the metropolitan area was subjected to several damages. A reclamation area called Port Island showed many evidences of liquefaction as 0.7 m of ground level settlements (Bardet et al., 1995), port quays were subjected to large lateral spreading, with 2-3 m of horizontal displacement (Figure 2.3) and sand ejecta (O'Rourke, 1995; Youd, 1995). The functionality of port was severely compromised entailed a stop of the commercial activities and delays in the reconstruction of the area.

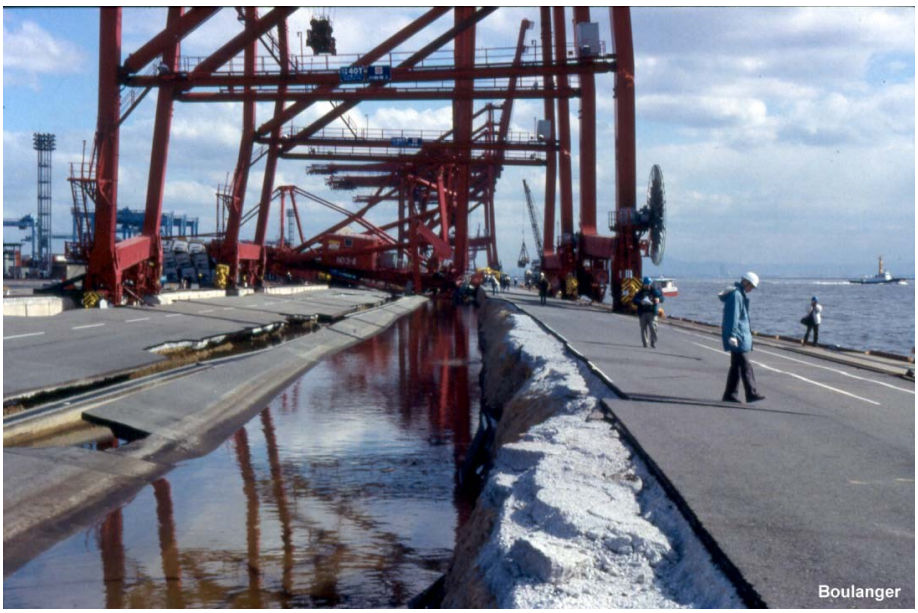

Figure 2.3. Lateral spreading during Kobe earthquake (1995) Japan (Boulanger's photo).

Four districts Kocaeli, Sakarya, Bolu and Yalova (Turkey) that represented 7 per cent of the country's GDP were strongly damaged in the year 1999 after a 7.4 magnitude moment earthquake. Communication and transports were interrupted by several damages to lifelines. The surrounding districts had indirect large economic losses due to the interruption of economic linkages. Several urban settlements were recorded, this phenomenon created a new 4 km-long coast submerged a large area to 3m of depth below the sea. Some landslides occurred on natural slope. Adapazarı city, located on young riverbed loose sediments, showed damages due to the liquefaction. Several buildings sank in the soil for about 1.5m and showed tilts (Figure 2.4). Sand boils and lateral spreading were observed in large part of the land. Buildings showed less damages due to the shaking thanks to the isolation effect provides by soil liquefaction (Erdik, 2000).

Figure 2.4. Tilting due to liquefaction in Adapazari during Kocaeli earthquake (1999) (Turkey).

The last great liquefaction events were recorded in the year 2011 in the Canterbury district (New Zealand) following a 6.3 magnitude moment earthquake. This earthquake was preceded, in the year 2010, by a stronger 7.1 magnitude moment earthquake but larger damages were recorded in following to the second event. Several buildings which presented structural damage from the first event collapsed during the second one for an accumulation of damages (event timing). The earthquake of year 2011 led to larger ground motion than earthquake of year 2010. The distribution of the motion in the second event highlighted a directionality of the fault and site effects that accentuated the amplitude of the ground shaking (Bradley and Cubrinovski, 2011; Kaiser et al., 2012).

Christchurch, the second larger city of country, was subjected to both events. This city is placed on a level ground originated by numerous rivers. The stratigraphy is composed by gravel interlayered by silt, clay and peat. The water table is placed at depth less than 5m, in many areas it is at 1m depth. Several residential, commercial and industrial areas were subjected to liquefaction phenomena during the earthquake of the 2011. Central business district and eastern suburbs were totally destroyed by liquefaction. Almost one thousand commercial buildings were unable to be used and were later demolished (Taylor et al., 2012). Sand boils, subsidence (Figure 2.5), lateral spreading and landslides were recorded during this event.

a) subsidence

b) landslide

c) sand ejecta, bearing capacity failure

d) lateral spreading

Figure 2.5. Liquefaction phenomena in Christchurch during earthquake of the year 2011 (New Zealand).

Soil liquefaction phenomenon happened also in Italy in the last years during an earthquake occurred on May 20, 2012 with a magnitude moment equal to 6.1. Effects of the liquefaction were observed in the Emilia Romagna region where many buildings collapsed, 26 fatalities, hundreds of injured and 15000 homeless were recorded. Many several damages struck some historical centres causing about 2 billion euros losses (Alessio et al., 2013).

The epicentre of the earthquake (44.89°N latitude and 11.23°E longitude) was located between the provinces of Modena and Ferrara with a hypocentre was at a depth of 6.3 km, hence it is considered a shallow earthquake (Lai et al., 2015).

The area of San Carlo and Mirabello councils was subjected to many liquefaction phenomena, indeed the subsoil in this area was composed by alluvial deposit with an alternance of silty-clayey and sandy soils deposed by an ancient river (Reno river) (Chiaradonna et al., 2018b).

To better understand the observed scenarios, an extensive investigation program, including geophysical surveys and geotechnical testing (soundings, cone penetration tests, seismic cone penetration tests, cross-hole and down-hole tests as well as many cyclic laboratory tests), was planned (Vannucchi et al., 2012).

The effects of liquefaction, followed by the 2012 earthquake in Northern Italy, have been immortalized and reported in several research works (Alessio et al., 2013; Lai et al., 2015; Lombardi and Bhattacharya, 2014; Sciarra et al., 2012; Vannucchi et al., 2012). As an example, some photos have been reported in Figure 2.6 (Alessio et al., 2013).

a) sand boils

b) soil cracking

c) sand ejecta

d) bearing capacity failure

Figure 2.6. Sand ejecta due to the soil liquefaction in Emilia Romagna region during the earthquake of the year 2012 (Italy).

Important information regarding the subsoil of the areas subjected to 2012 May earthquake has been reported by Vannucchi et al. (2012). The geological stratigraphy in the area of San Carlo and Mirabello is composed by deep alluvial deposits of the Po Valley, a large basin of Quaternary sedimentation. Pleistocene sediments are beneath characterized by sandy clays of marine origin while superior Pleistocene alternates marine clay facies with continental sands. Alternations of sandy clays, sands, silty sands and peats belong to Holocene deposits of continental origin. The shallowest soil part was deposed by recent alluvial events and it is composed by heterogeneous fine graded cohesionless soils (sands and silts).

The water table is shallow in this area and fluctuates between 80 and 130 cm depth form the ground surface during the year (Severi and Staffilani, 2012). During the May 20, 2012 earthquake the water table was near the shallowest position.

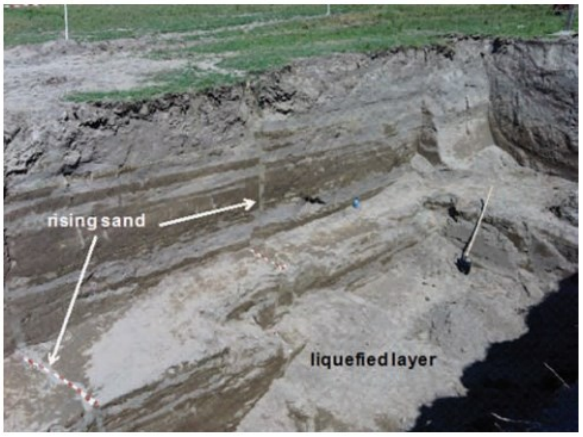

Figure 2.7. Trench in San Carlo council with the identification of soil layers (Vannucchi et al., 2012).

A trench was made in San Carlo council to investigate the soil stratigraphy and individuate the liquefiable soil layers (Figure 2.7). A shallower non liquefiable layer is followed by the liquefiable sand stratum. During the earthquake the deeper liquefied sand cracked the shallowest soil layer and it reached the ground surface forming sand boils and volcanoes (Vannucchi et al., 2012). Lombardi and Bhattacharya (2014) confirmed that the ejecta material was composed by the grey silty sand with a significant amount of fine content.

2.2 Liquefaction phenomenon

The term liquefaction was coined by Mogami, (1953) and includes several phenomena associated to soil deformation under disturbances in undrained condition. However, liquefaction phenomena can be divided in two main groups: *flow liquefaction* and *cyclic mobility* (Kramer, 1996):

- *flow liquefaction* happens when static shear stress which guarantees the equilibrium is higher than the shear strength of the liquefied soil. In this case, deformations are governed by the static stress while cyclic stress holds the shear strength of the liquefied soil low;
- in the case of *cyclic mobility,* the static shear stress is lower than the shear strength of the liquefied soil, the deformations are driven by cyclic and static shear stress. In this case the deformations grow up in incremental way during earthquake. Landslide activation in weakly slope field or in lateral unconfined field (riverbank, quay, etc.) belongs to cyclic mobility and it is called Lateral spreading (Figure 2.8). Level-ground liquefaction also belongs to cyclic mobility. This phenomenon happens in field where the static stress for lateral deformation of soil does not exist. In this case lateral displacements are negligible. Ground oscillations are the results of an upward flow of the water due to excess pore water pressure induced by earthquake. This phenomenon causes significant and differential vertical settlements.

In order for liquefaction to occur, some soil characteristics are very important. Fine grained soils are not susceptible to liquefaction, especially when they have plastic behaviour. In this case the mechanical behaviour of the soil is governed by the electrical interaction between particles due to the water bound to the particles. The electrical interaction leads to a nonzero shear strength at zero effective stress which is called cohesion. Furthermore, the presence of the bound water reduces the quantity of free water with a consequent reduction of excess pore water pressure build-up during a cyclic shear stress. In broad terms, only cohesionless soils are susceptible to liquefaction.

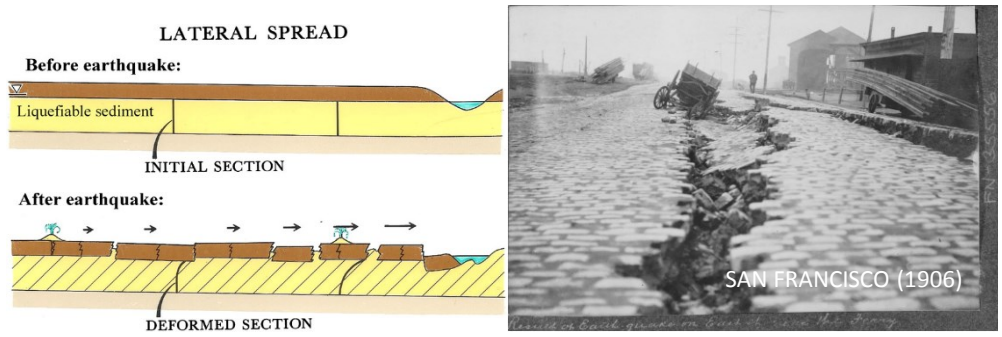

Figure 2.8. Lateral spreading (Youd, 2018).

Soils have elastoplastic mechanical behaviour. Indeed, when a shear stress is applied, the soil shows a volumetric-distortional behaviour which leads to a contraction or expansion of its volume. Loose soil upon shearing tend to reduce their volume, but if voids are saturated by water an excess water pressure may arise in fully or partially undrained conditions, that induce a reduction of effective stresses. This may lead to loss of contact between soil particles. The consequence of pore pressure build-up is a progressive decrease of the effective stress with a consequent strong and sudden drop of shear stiffness and strength of the soil (Figure 2.9) when excess pore water pressure reach the value of the initial effective stress, $\sigma'_{v,0}$ (triggering of liquefaction).

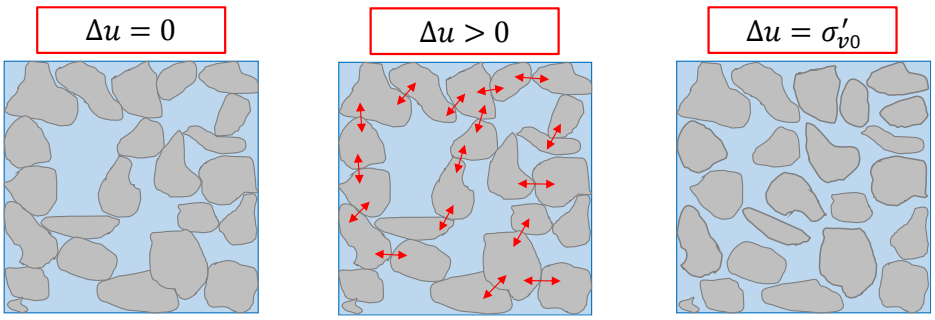

Figure 2.9. Excess pore water pressure build-up.

The amount of the excess pore water pressure is a function of the amplitude, frequency and duration of the cyclic load. Indeed, in coarse soil a large part of the water is free and the high permeability of this soil type leads to a fast dissipation of excess pore water pressure unless it is hydraulically confined, thus avoiding liquefaction. Therefore, equilibrium between the build-up and the dissipation of excess pore water pressure during cyclic shearing has an important role in the development of liquefaction phenomenon.

2.2.1 Liquefaction susceptibility

The susceptibility of a site to the occurrence of liquefaction phenomena can be assessed by different approaches and at different level of detail. Several criteria can be used to this aim, as summarised in the following.

A straightforward evaluation is possible using *Historical criteria* (Youd, 1984a) that is by investigating the field and individuating areas where the liquefaction occurred after strong earthquakes.

Geologic Criteria are based on the study of geological asset of the ground. The presence of water is an essential aspect in the evaluation of liquefaction susceptibility. A superficial water table increase the likelihood that the liquefaction may occur. The hydrological and depositional environment and the age of the soil deposit influence the liquefaction susceptibility (Youd and Hoose, 1977). Uniform grain size distribution deposits as fluvial, colluvial and aeolian are high susceptible to liquefaction. Older soil deposits are less liquefiable than newer ones.

Compositional Criteria consist in the evaluation of physical characteristics of the soil. Particles size, shape and gradation have a significant role in the liquefaction susceptibility (Ishihara, 1985, 1984). It is worth noting that liquefaction does not affect only sand but also non-plastic silts. Indeed, a range of grain size distribution for potentially liquefiable soils was defined by experimental test and natural observation of liquefaction phenomenon. When the grain size distribution curve is included in this range shown in Figure 2.10, the liquefaction susceptibility is high. The grain size range depends on the uniformity coefficient (U_C). A well-graded soil has voids partially filled by smaller grains that reduce volume change, hence the excess pore pressure build-up is reduced as compared to a uniform graded soil.

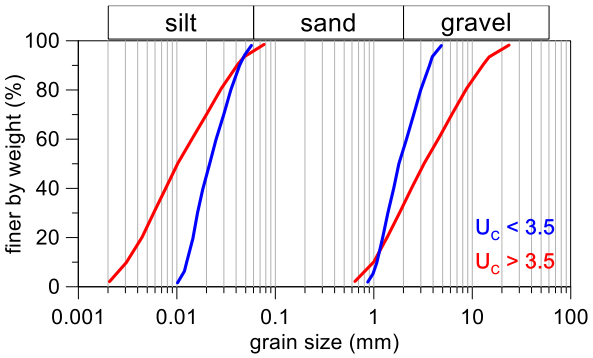

Figure 2.10. Grain size ranges for liquefiable soils.

The liquefaction susceptibility is also strongly dependent by the state of the soil and relevant state parameters such as the initial void ratio and the effective confining stress. The defining of these characteristics is required in the approach based on *State Criteria*.

It is well known from experimental evidence in drained triaxial laboratory tests (Casagrande, 1936) that a soil, subjected to an initial effective confining stress, does not change its volume at large shear strain. Furthermore, two specimens with different initial void ratio, subjected to the same effective confining stress, can reach the same void ratio at large deviatoric strains (Figure 2.11).

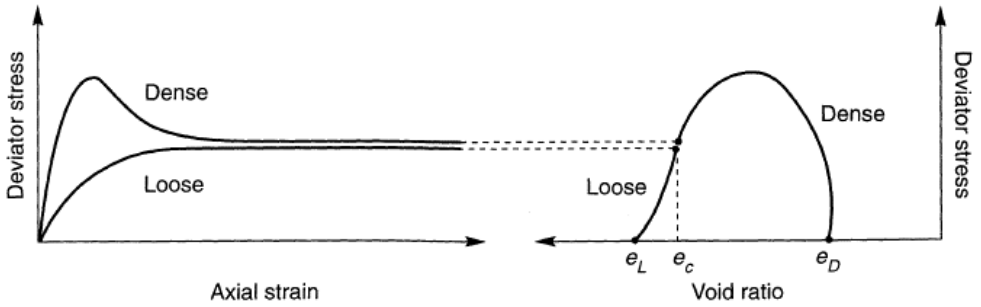

Figure 2.11. Deviatoric behaviour of dense and loose soil specimens (Kramer, 1996).

This result is due to different volumetric strain behaviour. The void ratio corresponding to stationary conditions, that is when the volume of the specimen does not change anymore upon shearing, is called critical void ratio (e_c). A critic void ratio (CVR) line can be define that separates soil specimens that exhibit contractive behaviour upon shearing (loose) from those that have a dilative behaviour (dense) (Figure 2.12).

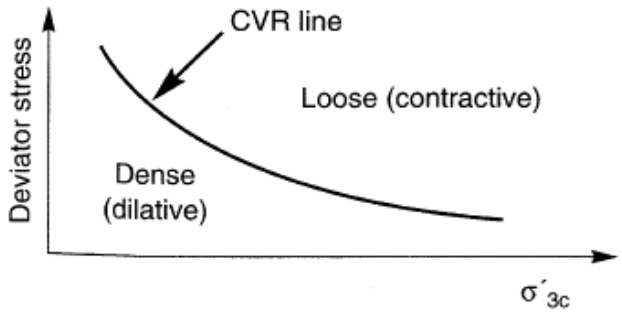

Figure 2.12. Critic void ratio curve (CVR) (Kramer, 1996).

In undrained condition, a contractive soil generates positive excess water pressures upon shearing, whereas a dilative soil shows negative excess water pressure. Therefore, the CVR line divides soil states subjected to flow liquefaction from soil states not subjected to flow

liquefaction (Figure 2.12). However, some historical events proved that also soils with an initial void ratio below the CVR line can be subjected to flow liquefaction. A better understanding of the phenomenon was achieved by (Castro, 1969) carrying out undrained triaxial tests after anisotropic consolidation. The behaviour of the soil is influenced by the initial void ratio. Very loose specimen (curve A in Figure 2.13) shows a peak strength at small strain and a low large-strain strength. In this case the initial deviatoric stress is higher than final strength, so the soil undergoes flow liquefaction. Dense specimen (curve B in Figure 2.13) initially keep a constant value of effective mean stress and later a progressive dilation occurs that increases the soil strength. In this case the soil does not liquefy. Intermediate states (curve C in Figure 2.13) show a peak higher than loose specimen and followed by a drop of the strength up to a upswing at the end the strength exceeds the initial deviatoric stress. In this case the soil is subjected to a limited flow liquefaction. The point of the strength trend inversion is called *phase transformation point*. In these tests, the void ratios achieved at large strains shape a curve in the plane e-σ'_{3c} that is below and almost parallel to the CVR line. This curve is called *steady state line (SSL)* (Castro and Poulos, 1977; Poulos, 1981). In this state the soil shows a constant volume, effective confining pressure and deformation velocity. Flow of soil structure and the orientation of the soil particles during stress-controlled conditions maybe the causes of the difference between the curves CVR and SSL. The soils with an initial void ratio below the SSL do not show flow liquefaction whereas the soils with a void ratio above the SSL show flow liquefaction.

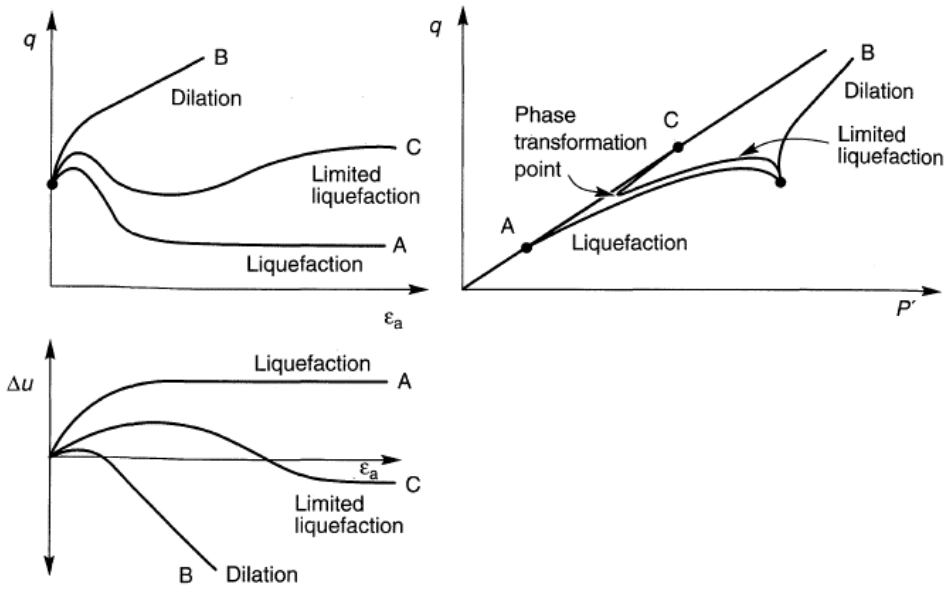

Figure 2.13. Undrained behaviour of specimens with different initial void ratio (Kramer, 1996).

The distance of the actual state of the soil from the SSL influences significantly the mechanical behaviour of the soil (Figure 2.14). it is noteworthy that soil specimens with the

same state parameter ψ (Eq. (2-1) show a similar behaviour. A soil with a positive value of this state parameter shows a contractive behaviour, while a negative value of ψ implies a dilative behaviour.

$$\psi = e - e_{ss} \qquad (2\text{-}1)$$

However, the parameter ψ referred to SSL is not able to describe the mechanical behaviour for very loose sand subjected to low effective confining stresses.

The substitution of SSL with a *quasi-steady state line* can solve this problem (Ishihara, 1993). This new line is represented by the transformation points in the limited liquefaction.

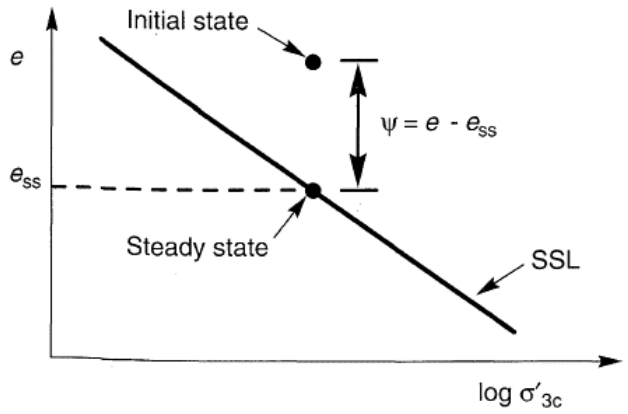

Figure 2.14. Mechanical behaviour state parameter (ψ) (Kramer, 1996).

On the other hand, cyclic mobility can occur in soils that are lied above or below the SSL. Anyway, the determination of the SSL is very difficult in practice. Its position in the plane e-log σ'_{3c} is a function of the particles shape and gradation. The former defines the slope of the line and the latter influences the vertical position of line.

As seen before, specimens susceptible to static flow liquefaction have an unstable behaviour with a peak strength at small strains and a following strength drop up to a residual liquefaction one. This behaviour is strongly dependent by the effective confining stress as shown in Figure 2.15 where different specimen with the same void ratio are tested at different effective confining stresses, noteworthy that for the same initial void ratio larger initial confining stresses imply larger drop. Generally, stress-controlled conditions occur in the field (e.g.: change of stress below a building foundation). Therefore, the point in correspondence of the peak has a great relevance. Indeed, beyond this point the soil is not able to resist at the static deviatoric stress. In these conditions a large and unacceptable displacement happens (the shear strain can reach values between 5 to 20%) (Ishihara, 1993). The strength peaks are roughly aligned on a straight line in the plane q-p'. these points constitute the *flow liquefaction surface* (FLS) in the three dimensions space e-p'-q (Vaid and Chern, 1985). The FLS divided stable states from unstable ones in undrained conditions.

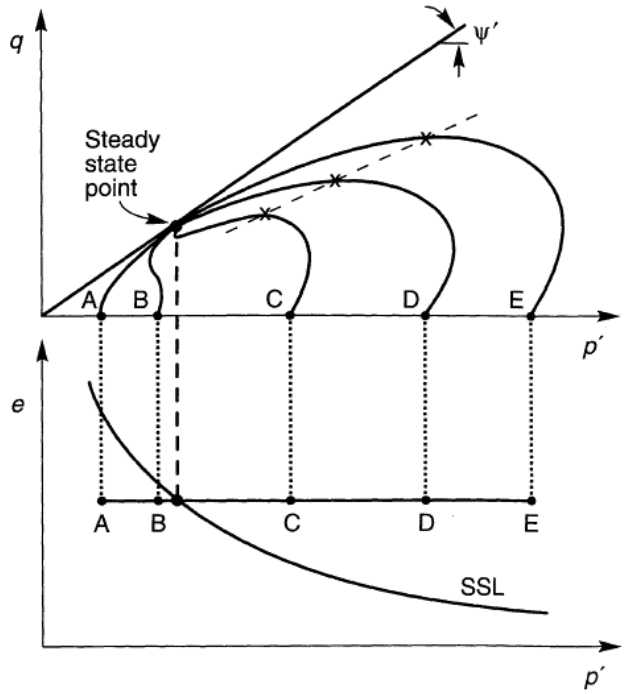

Figure 2.15. Undrained triaxial tests with the same void ratio (Kramer, 1996).

The slope of the FLS in q-p' plane, for isotropic consolidation specimens, is about two-thirds of the drained tests failure surface for clean sands. The slope of FLS line increases increasing of the initial deviatoric stress (Figure 2.16). In this case the initial state could be very close to the FLS so the flow liquefaction strength for disturbance is very low (Kramer and Seed, 1988).

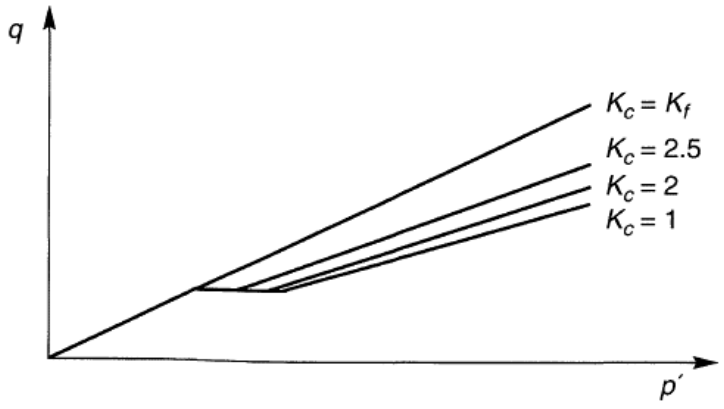

Figure 2.16. Dependency of FLS on the anisotropic initial stress conditions (Kramer, 1996).

Indeed, the excess pore pressure ratio ($\Delta u/\sigma_{3c}$) that leads to flow liquefaction is a function of the ratio between two initial principal effective stresses (Figure 2.17).

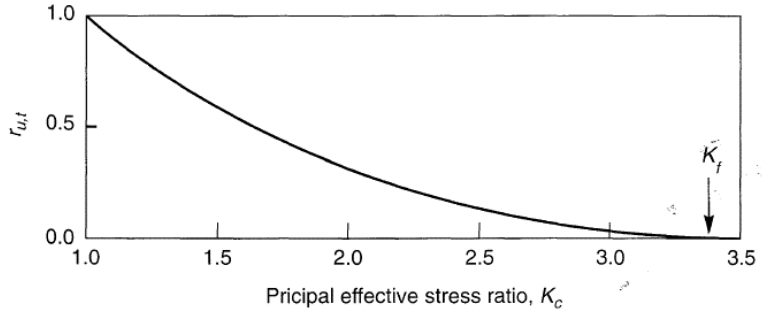

Figure 2.17. Excess water pressure ratio for flow liquefaction in function of initial deviatoric stress (Kramer, 1996).

Now in the plane q-p' is possible to identify two regions: one where the soil achieves flow liquefaction (Figure 2.18a) and another one where the soil shows the cyclic mobility (Figure 2.18b).

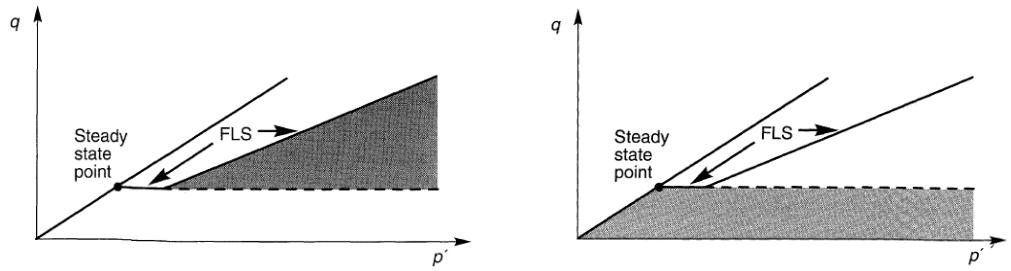

Figure 2.18. a) Flow liquefaction region; b) cyclic mobility region (Kramer, 1996).

2.2.2 Liquefaction triggering

Evaluation of liquefaction susceptibility requires the study of the type and the initial state of the soil. However, an important aspect of the problem is represented by the earthquake load. Several approaches to assess such a load were proposed in the years by different researchers. They can be broadly divided into *cyclic stress approach and cyclic strain approach.*

2.2.2.1 Cyclic stress approach

Cyclic stress approach is based on the comparison between the liquefaction strength of the soil and the earthquake load, both characterised by amplitude and number of cycles of shear load. However, a direct comparison between irregular shear load of earthquake and

regular shear load of laboratory tests is not possible. Therefore, a conversion of irregular earthquake shear load to regular one is required. Seed et al. (1975a) proposed to determine an equivalent cyclic number (N_{eq}) of a sinusoidal shear load with an equivalent amplitude equal to $\tau_{cyc} = 0.65\ \tau_{max}$ that produces the same excess water pressure of the irregular shear load due to the earthquake. Equivalent cyclic number increases with the earthquake magnitude (Figure 2.19).

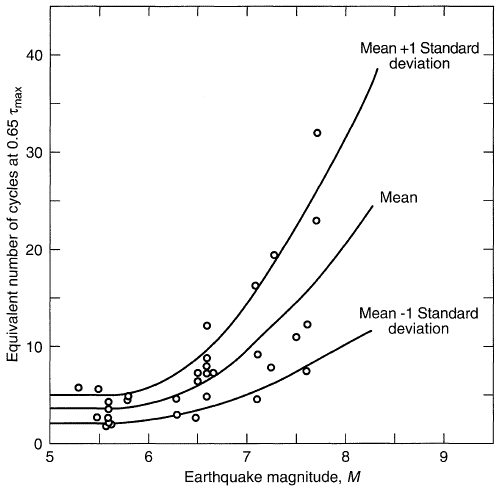

Figure 2.19. Equivalent number of cycles (N_{eq}) in function of earthquake magnitude (Seed et al., 1975a).

Maximum shear stress $(\tau_{max})$with the depth can be evaluate by a simplified procedure. Seed and Idriss (1971) proposed to calculate τ_{max} through the following relationship:

$$\tau_{max} = \frac{a_{max}}{\mathrm{g}}\ \sigma_v\ r_d \qquad (2\text{-}2)$$

where r_d is the reduction factor of the maximum acceleration with depth that considers the effects of the deformability of soil profile. Therefore, the equivalent cyclic shear stress is equal to:

$$\tau_{cyc} = 0.65\frac{a_{max}}{\mathrm{g}}\ \sigma_v\ r_d \qquad (2\text{-}3)$$

Cyclic stress approach considers that the excess water pressure build-up is due to the cyclic shear stress and the liquefaction is defined as the reaching of zero effective stress, $(u_{excess} = \sigma_{3c})$. This type of liquefaction belongs to the cyclic mobility group.

Soil liquefaction strength to compare with seismic action can be determine in two principal ways: laboratory tests and field tests. The liquefaction in laboratory tests is defined as the achievement either of a certain level of excess water pressure ratio (commonly r_u=0.9) or a cyclic deviatoric strain amplitude (commonly 5% for shear strain). The results from laboratory tests allow liquefaction strength curves for a specific soil to be defined. These curves are plotted in in function of number of cycles and cyclic shear ratio (CSR) (Figure

2.20), defined as the ratio between the amplitude of shear load and initial effective consolidation stress ($CSR = \tau/\sigma_{3c}$).

CSR depends on the stress path of the test. Indeed, CSR for the simple shear test and for triaxial test are different:

$$CSR_{ss} = c_r \, CSR_{tx} \qquad (2\text{-}4)$$

where c_r is a correction factor that can be calculated by different approaches, one of these is due to (Castro, 1975) who defined this factor as:

$$c_r = \frac{2(1 + 2K_0)}{3\sqrt{3}} \qquad (2\text{-}5)$$

As previously mentioned, liquefaction strength is a function of the initial state of the soil. Denser specimens show higher liquefaction strength (Figure 2.20).

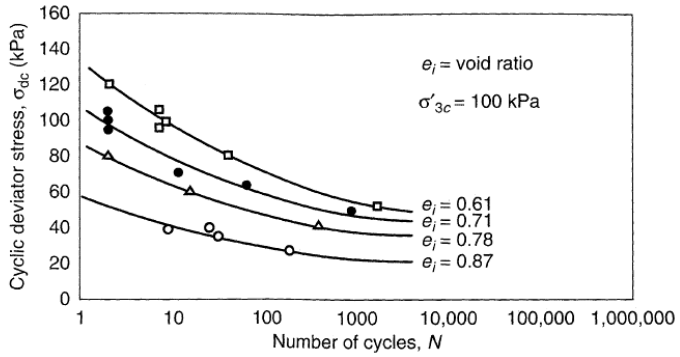

Figure 2.20. Liquefaction strength curves (Kramer, 1996).

Generally, earthquake leads to a motion in different direction that increase the pore water pressure build-up. Therefore, laboratory results lead to an overestimation of liquefaction strength and the results have to be corrected. Seed et al. (1975) proposed to consider the CSR strength in field condition equal to 90% of CSR strength in laboratory condition (Eq. (2-6).

$$CSR_{ff} = 0.9 \, CSR_{ss} \qquad (2\text{-}6)$$

Liquefaction strength can be defined also through field tests. A method with the standard penetration test (SPT) was developed by Seed et al. (1983). The corrected number of blows $(N_{1,60})$ has been correlated to historical liquefaction cases for earthquakes with 7.5 magnitude moment. In this method the value of CSR, to compare with laboratory one, is corrected by different factors that takes into account the effects of fine content, effective confining stress and earthquake magnitude moment.

Furthermore, an estimate of liquefaction strength can be performed by cone penetration test (CPT). Indeed, tip resistance can be correlated to the liquefaction strength using historical liquefaction cases. To reach a good calibration of the method, liquefaction cases database is increased by SPT investigations applying the correlations between tip resistance

of CPT and number of blows of SPT. An exhaustive approach with CPT results was developed by Boulanger and Idriss, (2016).

The evaluation of the liquefaction potential in the cyclic stress approach consists in the comparison between the liquefaction strength of the soil deposit and the action due to earthquake (2-7).

$$FS_L = \frac{\tau_{cyc,L}}{\tau_{cyc}} = \frac{cyclic\ shear\ stress\ that\ leads\ to\ liquefaction}{equivalent\ cyclic\ shear\ stress\ induced\ by\ earthquake} = \frac{CSR_L}{CSR} \qquad (2\text{-}7)$$

The value of FS_L is calculated at each depth below the water table and when it is lower than 1 the liquefaction happens. Graphical representation of FS_L values allows to individuate the soil layers susceptible to liquefaction (Figure 2.21)

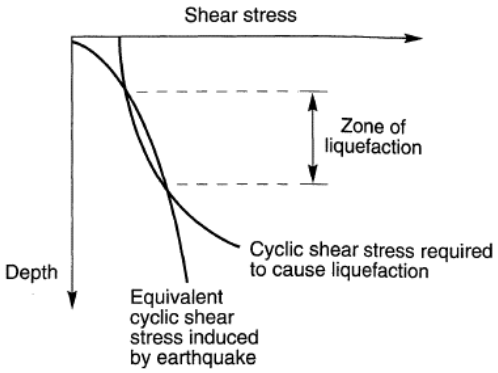

Figure 2.21. Liquefaction potential with depth (Kramer, 1996).

Since the liquefaction is defined as the reaching of unitary excess water pressure ratio, a FS_L greater than one does not indicate necessary a low value of excess water pressure ratio. This aspect is very important in the evaluation of a possible flow liquefaction induced by static deviatoric stress (Figure 2.22).

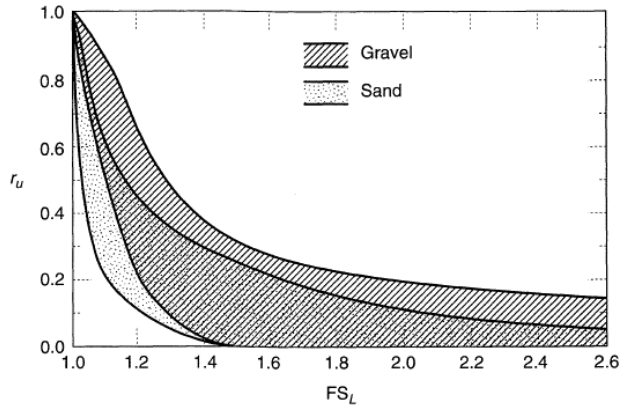

Figure 2.22. Value of excess water pressure ratio in function of liquefaction potential (Marcuson et al., 1990).

2.2.2.2 Cyclic strain approach

The cyclic strain approach is based on the evidence that the densification of the soil is controlled by cyclic strains (Youd, 1972). Indeed, the existence of a shear strain threshold below that the densification is not occur indicates the role of shear strain on the excess water pressure build-up in saturated condition. As done for cyclic shear stress approach, the irregular shear strains time history is transformed in regular one to compare this action with the laboratory results.

An estimate of the amplitude of cyclic shear strain is more difficult than shear stress. A simplified approach was proposed by Dobry et al. (1982) who used the equation (2-3 to estimate the equivalent cyclic shear strain (Eq. (2-8).

$$\gamma_{cyc} = 0.65 \frac{a_{max}}{g} \frac{\sigma_v \, r_d}{G(\gamma_{cyc})} \qquad (2\text{-}8)$$

However, the amplitude of cyclic shear strain depending on shear modulus that is a function of shear strain level achieved. Then, an iterative procedure is necessary.

In this method liquefaction potential is evaluated by the comparison between γ_{cyc} and γ_t (threshold beyond which excess water pressure rises). If $\gamma_{cyc} < \gamma_t$ the soil is not able to accumulate excess water pressure and the liquefaction does not occur. If $\gamma_{cyc} > \gamma_t$ the liquefaction can occur and its effect must be evaluate.

Dobry et al. (1982) proved that cyclic strain approach is more reliable than cyclic stress method. They performed a set of cyclic laboratory tests and verified that the state parameters changing does not influence the amount of excess pore pressure ratio in function of cyclic shear strain (Figure 2.23). Indeed, τ_{cyc} and G are both strongly dependent by cyclic shear strain but their ratio is lower influenced by γ_{cyc}.

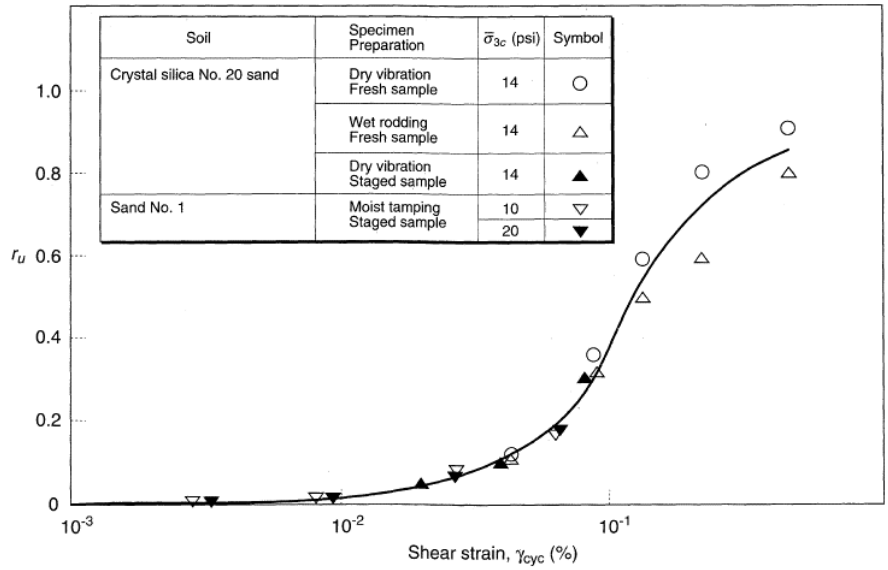

Figure 2.23. Evolution of excess water pressure ratio with cyclic shear strain (Kramer, 1996).

Furthermore, Vasquez-Herrera et al., (1988) found that an initial higher static deviatoric stress reduces flow liquefaction strength (Figure 2.24). Indeed, the static deviatoric stress moves the initial stress condition closer to the FLS.

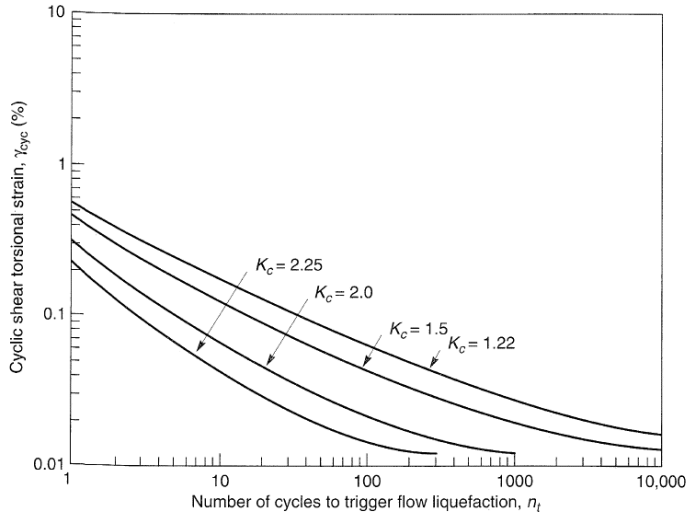

Figure 2.24. Effect of the initial deviatoric stress on the flow liquefaction strength (Kramer, 1996).

Cyclic strain approach does not allow to calculate a safety factor for liquefaction potential. Liquefaction potential is evaluated by the comparison between amplitude of equivalent cyclic shear strain induced by earthquake at equivalent number of cycles and the amplitude of cyclic shear strain of soil liquefaction strength (Figure 2.24) at the same number of cycles. The strong relationship between cyclic strains and excess water pressure build-up permits to estimate the amount of the excess water pressure ratio for events that do not achieve liquefaction.

2.3 Liquefaction effects

As previously mentioned, in historical liquefaction events several types of damage and collapse mechanisms due to the liquefaction phenomenon were recorded. Flow liquefaction and cyclic mobility generate different type of damage depending on the structure affected by ground liquefaction. Flow liquefaction can induce massive landslides, large settlements and tilting for heavy structures, the floating of underground structures and the collapse of retaining structures. Cyclic mobility can cause incremental settlements of structures, lateral spreading, retaining wall incremental rotation, ground oscillations, settlements and sand boils.

2.3.1 Ground motion modification

The propagation of waves through the soil is governed by density and stiffness of each single layer. Large strains achieved during strong motion lead to a significant changing of

the soil stiffness. This effect is amplified in soils that show excess water pressure build-up during the motion. Indeed, excess water pressure reduces progressively the shear stiffness of the soil modifying the waves propagation.

In the case of soil liquefaction lower shear stiffness leads to a decreasing of the signal frequency and amplitude of acceleration recorded at ground surface. An example of acceleration signal record is shown in Figure 2.25, the time interval where liquefaction happens can be easily identify (red brace). However, this effect increases the amplitude of displacement which can lead to large damages on structures characterised by significant cinematic interaction (piles, underground structures, etc).

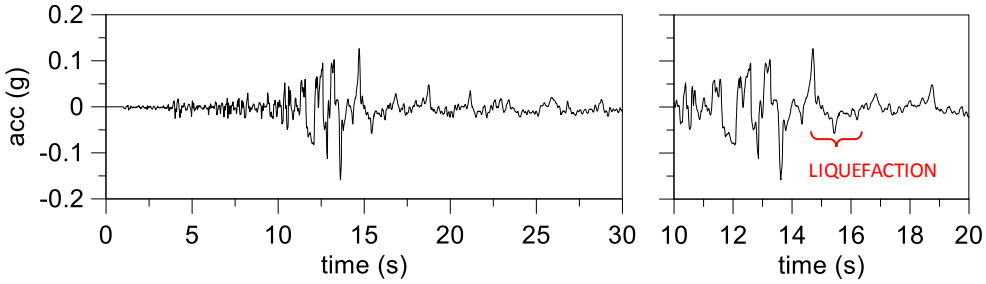

Figure 2.25. Earthquake signal modified by liquefaction.

In presence of a crust, large displacements can break ground surface and high pore pressure in liquefied soil can lead to a flow of water-soil mixture to ground surface (sand boils). This phenomenon does not occur when the liquefiable soil is at large depth and when the liquefiable soil has low permeability. Sand boils may lead to differential settlement of the ground surface that can produce significant damage on structure with discrete shallow foundations.

2.3.2 Settlements

Generally, a stratigraphy with presence of some layers of sand show a settlement during an earthquake. In free field condition settlements are due to:

- Contraction and consolidation of loose cohesionless soils;
- Ejection of waterborne sediment after liquefaction (sand boils);
- Lateral spreading;
- Anisotropic soil behaviour;
- Tectonic subsidence.

In dry condition settlements are a consequent of a volumetric strains induced by cyclic shear strains. The magnitude of settlements is a function of induced action so number of cycles and amplitude of shear strain (Silver and Seed, 1971) and soil characteristic as relative density. A simplified method to estimate settlements in dry sand was developed by Tokimatsu and Seed, (1987). They found a relationship between the maximum amplitude of volumetric strain and cyclic shear strain evaluated by the equation (2-8).

In saturated sands in addition to relative density and cyclic shear strain, the excess water pressure dissipation, during and after earthquake, has an important influence on the magnitude of final settlements. Generally, liquefied sands show large volumetric strain after excess water pressure dissipation that can reach up to 10%. Volumetric strain can be evaluated by in-situ test like SPT (Tokimatsu and Seed, 1987) and CPT (Ishihara and Yoshimine, 1992). However, the earthquake could be unable to liquefy the soil. In this case Lee and Albaisa (1974) proved that the volumetric strain is strongly dependent on the amount of the excess water pressure ratio. Indeed, when the ratio between the CSR induced by earthquake and CSR that leads to liquefaction (CSR/CSR_L) is lower than 70% the volumetric strain is very small.

In presence of a building, the deviatoric stress beneath the foundation modifies the nature of the settlements. Inertial and cinematic interaction between the soil and structure generates some mechanisms that produce higher settlements than in free field condition. Bray and Dashti (2014) identified three different mechanisms (Figure 2.26):

a. Volumetric strains due to partial drained cyclic loading that leads to sedimentation and consolidation settlements;
b. Settlements induced by punching and drop of bearing capacity consequent to the soil softening due to the excess water pressure build-up. This mechanism could cause tilt of building;
c. Cumulative ratcheting settlement due to the dynamic interaction between soil and building.

However, the uncertainties on the estimate of settlements in simplified ways are very high and sophisticated numerical analyses are required to achieve more reliable results.

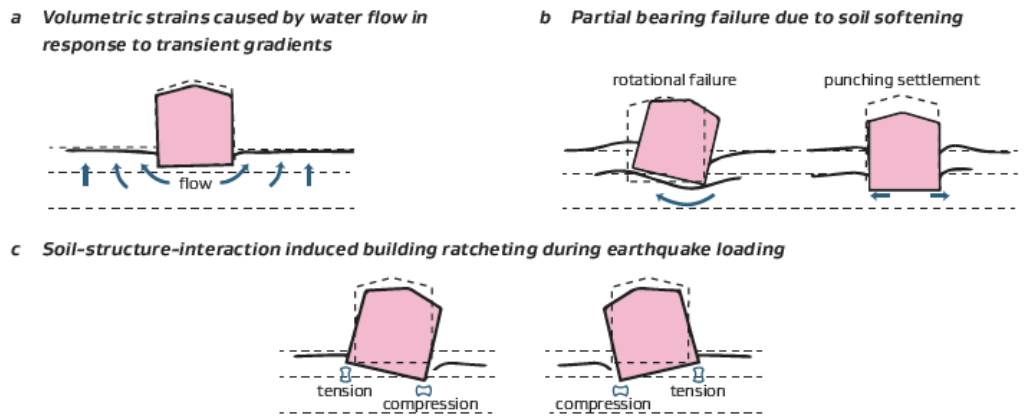

Figure 2.26. Mechanisms for settlements under building (Bray and Dashti, 2014).

2.3.3 Shear strength of liquefied soil

The excess pore pressure build-up can lead to a strong reduction of the shear strength of soil. Collapse of the soil could be achieved if the shear strength is lower than an applied

deviatoric stress. Collapse is represented by large deformations whose magnitude is influenced by the difference between the applied stress and strength of liquefied soil.

For this reason, it is important to know the amount of the shear strength of liquefied soil. An estimate can be achieved by laboratory tests, in this case the strength is determined by using the steady-state strength line that is a function of relative density. The uncertainties of this approach are related to the sampling operations that induce some disturbances to the specimen. Poulos et al., (1985) proposed a procedure to reduce these uncertainties that is composed of 4 steps:

1. Determine the in-situ relative density;
2. Determine the slope of the steady state line by reconstituted specimens, the slope is only function of the particles shape;
3. Determine the steady state strength of undisturbed specimen;
4. Correct the measured steady state strength for the in-situ void ratio.

The shear strength of the liquefied soil can be estimated also through in-situ tests. Seed and Harder Jr (1990) developed a method using SPT test for sand with a fine content higher than 10% introducing the equivalent clear-sand SPT resistance as:

$$(N_1)_{60-cs} = (N_1)_{60} + N_{corr} \qquad (2\text{-}9)$$

where N_{corr} is the correction of blows number in function of fine content. This approach has a large number of uncertainties.

Like for cohesive soils, for liquefiable soils a residual strength ratio (S_r/σ'_{v0}) approach can be used. In this case the residual strength is evaluated by effective vertical stress that is easier to determine in the field than the void ratio. However, different types of soils show different residual strength ratio that vary over a considerable range. A directly measurement can be made by field vane shear tests and through SPT resistance as proposed by Stark and Mesri (1992):

$$\frac{S_r}{\sigma'_{v0}} = 0.0055(N_1)_{60-cs} \qquad (2\text{-}10)$$

2.4 Liquefaction mitigation with ground improvement

The damages recorded on natural and urban environmental can reach different severity in function of the external actions. In the performance base design, the damage level is identified as the achieving of a limit states (LS). In the European codes four limit states are defined:

- LS of Near Collapse (NC). The structure is heavily damaged. Although vertical load bearing capacity is retained, large permanent drifts are present. Most non-structural components, where present, have collapsed;
- LS of Significant Damage (SD). The structure is significantly damaged. Although vertical load bearing capacity is retained, moderate permanent drifts may be present. Non-structural components, where present, are damaged (e.g., partitions and infills

have not yet failed out-of-plane). Thus, the structure is expected to be repairable; in some cases, it may be uneconomic to repair.

- LS of Damage Limitation (DL). The structure is only slightly damaged and economic to repair. Structural members retain their full strength with a limited decrease of stiffness. Permanent drifts are negligible. The structure retains undiminished ability to withstand future earthquakes. Non-structural components, where present, exhibit only minor damage that can be economically repaired (e.g. partitions and infills may show distributed cracking).
- LS of Fully Operational (OP). The structure is only slightly damaged and economic to repair. Systems hosted by the structure remain in continuous operation.

The level of damage depends on the intensity of the action. In the case of earthquake, the actions are represented by ground acceleration that causes inertial forces on all masses connected to the ground. Buildings are connected to the ground by either shallow foundations or deep ones, so they are subjected to inertial forces. Earthquake could have different effect that are divided in primary effects and secondary ones. The inertial forces represent the principal primary effects while secondary effects could be: subsidence, tsunami, landslide, soil liquefaction, fire, contamination of water supplies, gas leak, power outage. Secondary effects can generate higher damage level than primary ones.

As previous mentioned, soil liquefaction, which represents a secondary effect, can lead to large economic and human losses. Therefore, the respect of limit states is important and a mitigation of this phenomenon is necessary. Some liquefaction mitigation techniques will be presented in the following, focussing the attention on their effect during the earthquake. It is worth noting that all liquefaction mitigation techniques have the aim of reducing ground deformations either preventing, limiting, or slowing-down the development of excess pore water pressure or limiting the development of shear strains and vertical strains in the ground. Generally, a single mitigation technique works on different aspects (NZ guidelines). Liquefaction mitigation techniques can be implemented also through appropriate structural elements as: stiff raft, rigid foundation beams or walls and deep pile foundations.

2.4.1 Replacement

This is the simplest mitigation technique and consists in the removal of the in-situ liquefiable soil and replacement with non-liquefiable one. Replacement technique is applicable only for new buildings and for shallow liquefiable layers. Indeed, a replacing of deep layers would require large and expensive excavation. Well compacted, well graded gravel or soil mixed with cement or other additives are commonly used for replacement in liquefaction remediation. Cement stabilised soils are brittle and have low strength in tension. The replacement dimensions and modulus should be designed to avoid concentration of strains at large widely spaced cracks that could cause abrupt differential settlement of the structure. This is important where only partial depth of soils prone to liquefaction are treated. A granular layer placed over the cemented fill can smooth out abrupt changes in level or grade beneath shallow foundations. A partial replacement of deep liquefiable soils is possible using stone columns (Asgari et al., 2013).

2.4.2 Densification

Densification techniques aim to reduce the porosity of the liquefiable soil by a rearranging of soil particles. As previously mentioned, the relative density has a great effect on soil liquefaction susceptibility. Higher relative densities increase shear strength and stiffness of the soil and reduce volumetric deformability decreasing the pore water pressure build-up during the earthquake by encouraging dilative behaviour. Generally, densification is performed by vibration machines, so noises and vibrations are produced during construction. Therefore, this technique is not suitable for treatment very close to existing structures.

A variety of means exists to perform densification of liquefiable soils:

- Compaction by lateral compression of the surrounding material (e.g. stone columns or pile);
- Compaction by vibration in loose sandy deposits;
- Compaction by surface impact energy.

The effectiveness of treatment is easily verified by field tests and in the case of liquefaction the induced displacement is reduced.

Lateral compression can be achieved using compaction grouting. In this case, a volume of cement is realised aiming to displace the liquefiable soils increasing its relative density.

Densification techniques are more efficient in the treating soils with less than 15% fines content with a corresponding CPT soil behaviour index lower than 1.8. The efficiency decreases in presence of silty soil, in this case the introduction of vertical drains in the area subjected to densification treatment can increase the efficiency (Sondermann and Wehr, 2004; Thevanayagam et al., 2006).

The design of the densification technique is based on the individuation of either target relative density or cyclic resistance ratio (CRR). A check of the effectiveness of the treatment can be done by some empirical methods based on the interpretation of the CTP results (e.g. Boulanger and Idriss, 2016). Stone columns leads to an increment of the relative density of the liquefiable soil, at the same time the columns represent a soil reinforcement that reduce the seismic action increasing the safety factor. This effect can be evaluated using the method by Rayamajhi et al. (2013).

2.4.2.1 Dynamic compaction

This technique consists in the dropping of a large weight from significant height onto the ground. The energy propagation after the impact generates a rearrange of the soil in denser disposition. The mechanism for the rearrangement of the particles is strongly dependent on the degree of saturation of liquefiable soil. Indeed, the impact onto saturated soils generates excess water pressure whose dissipation leads to the rearrangement, whereas the rearrangement is instantaneous in dry condition (Idriss and Boulanger, 2008). Necessary impact energy and the spacing between the drop points are function of the ground and groundwater conditions. The level of energy allows to treat soil layers to different depth. High energy levels reach larger deep than lower energy levels.

Dynamic compaction is fast and economic but produces noise and vibration, so it cannot be employed in urban environmental. The applicability of the dynamic compaction is governed especially by grains size distribution, plasticity index and permeability of the soil. Lukas (1995) identified three regions of soil grain distribution that determine the suitable of the dynamic compaction on a datum soil (Figure 2.27).

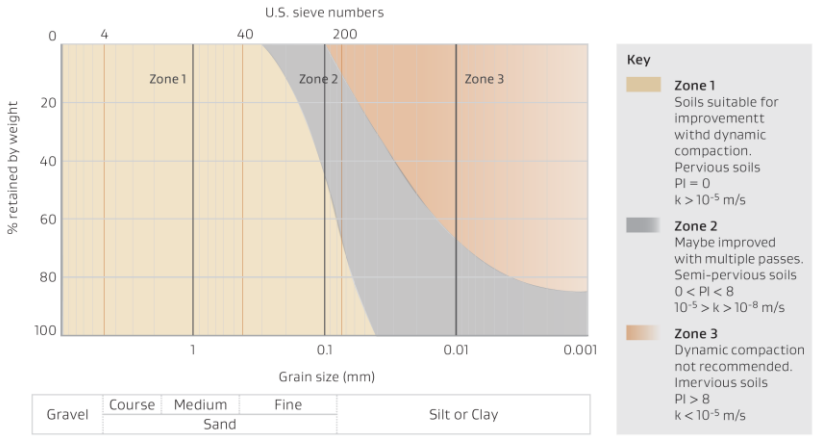

Figure 2.27. Soils suitable for dynamic compaction (Lukas, 1995).

As possible to see from Figure 2.27, dynamic consolidation has limited effects on soils that have fine content higher den 15% and no effects on soils with fine content higher than 25%. For dynamic compaction, measurement of the energy being delivered to the ground, the sequence and timing of drops, as well as ground response in the form of crater depth and heave of the surrounding ground are important quality control parameters.

2.4.2.2 Vibro-compaction

A probe vibro-compaction is inserted into the ground to treat deep liquefiable soils. The vibratory energy reduces the intergranular forces rearranging soil particles in denser disposition. Through this technique relative densities from 70 to 85% can be achieved. The probe is made of a cylindrical steel tube containing an eccentric mass that is rotated by a motor. The probe length and mass vary between 3 to 4.5 meters and 1.5 and 4.5 tons respectively. The probe penetration is aided by water jets and the verticality is guaranteed by probe weight. During the pilling a conical depression is recorded on the ground surface and the liquefaction soil is densified by filling material that is added around the probe from ground surface. Vibro-compaction is most suited for sands with low fine content (lower than 12%). In Figure 2.28 are shown the range of applicability in function of grains size distributions.

The degree of compaction decreases with increasing distance from the probe. Spacing of treatment grid can be estimated by empirical observations due to Barksdale and Bachus (1983). The cavity created by probe penetration should be filled by a soil with a specific grains size distribution to increase the compaction degree, some recommendations on particle size recommendations are given by Elias et al. (2006).

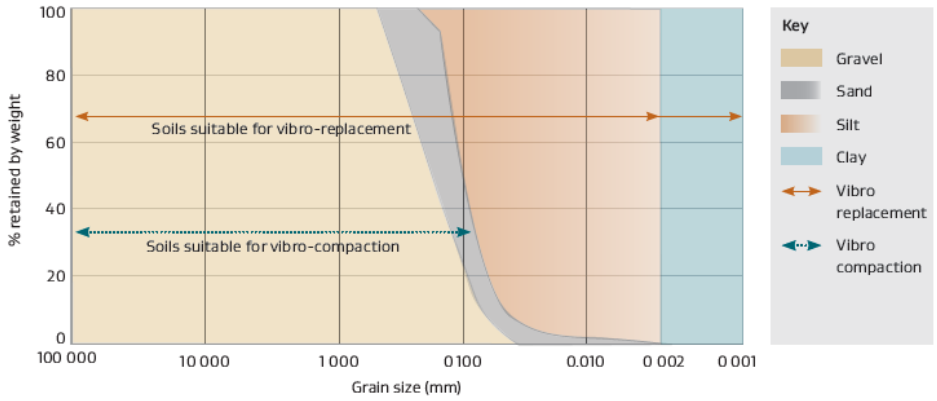

Figure 2.28. Soils suitable for vibro-compaction (Elias et al., 2008).

2.4.2.3 Stone columns

This technique consists in the introduction of columns in the soil generally filled by crushed coarse material with prescribed particle size distribution. Moreover, recycled materials can be use like crushed concrete. Stone columns are very efficient in sands with fine content lower than 20%, but silty soils can be treated with the introduction of drains. (Rollins et al., 2009). The primary effect of this technique is the densification but an contribute to the liquefaction strength is due also to: increasing of lateral stress that reduces the initial deviatoric stress; partial replacing of liquefiable soil with no liquefiable one; reinforcing due to the introduction of stiffer material; drainage given to high permeability of the columns filling material (Sondermann and Wehr, 2004).

The effects of these other mechanisms are negligible compared to densification. An estimate of the benefits of reinforcement can be evaluate by Rayamajhi et al. (2014).

The spacing of the treatment is determine preferably by pilot studies, but an estimation of spacing can be performed by Barksdale and Bachus (1983).

2.4.2.4 Compaction piles

Installation of driven piles leads to densification of the soil through displacement and vibration. Prestressed concrete or timber piles are employed in this technique installed using water jetting to aid the insert that may reduce the densification of the soil around the piles but is useful for penetrating in dense or hard layers. Piles can reach depths up to 16 meters. Furthermore, the presence of piles increases the stiffness of the soil reducing shear strains during earthquake. This effect leads to lower excess water pressure and the settlements.

2.4.2.5 Compaction grouting

Densification of the liquefiable soils can be achieved through the expansion of a volume in the ground. This volume can be realised by very stiff grout of soil-cement-water mixture is injected at high pressure. During the injection the permeation should be avoided. Consequent displacement of surrounding soil leads to a densification that increase the stiffness and strength of liquefiable soil giving a dilative behaviour. Compaction grouting

can be realised under existing structures monitoring potential surface and foundation lifting. This technique is ineffective near ground surface where it produces a lifting of the surface reducing drastically the densification effect.

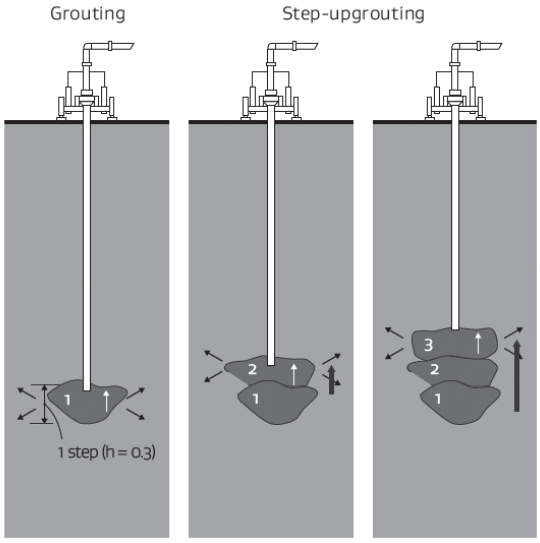

Figure 2.29. Compaction grouting process.

Compaction grouting requires a small equipment but the use of grout casing with an internal diameter lower than 50mm is not suggest avoiding high pressure to reach a sufficient grout. Monitoring of grout volumes, injection pressures and grout movement at surface or near structures are required.

Compaction grouting is realised by step and the process begins from the bottom up avoiding to load upper grouts with low initial stiffness and strength than could lead a lifting of ground surface (Figure 2.29).

2.4.2.6 Resin injection

Polyurethane resins can be used to densify liquefiable soil. They application is made by injection tubes deployed in regular grid through which a low viscosity resin is pumped at controlled pressure. The resin penetrates into the soil matrix along pre-existing planes and fractures, in high permeable soil the resin permeates in soil voids. A chemical reaction leads to a strong expansion of the resin that becomes solid. The expansion increases the horizontal stress, stiffness, strength and the density of liquefiable soil (Traylen, 2017).

A check of the resin injection results can be performed by field test like CPT. The treatment allows to reach increases of CPT tip resistance between 25-100% depending on the soil type. This technique is easily to apply in clean sands, but also silty sand can be treated.

2.4.3 Drainage

Liquefaction mitigation can be reach adopting drainage systems. This technique introduces in the liquefiable soil new seepage surfaces that accelerate the dissipation of induced excess water pressures during earthquake. Generally, Vertical drains are employed to realise drainage system and they typically are installed at 1–2 m spacing intervals. Commonly, vertical drains are composed by artificial drains in geosynthetic composites, piles with drainage functions or plastic perforated pipe wrapped in geofabric to prevent clogging from soil particles. These can be easily installed with relatively low vibration and noise compared to compaction methods and are typically cheaper than solidification. However, the required drain spacing is sensitive to the soil permeability, their effectiveness is hard to verify. Drains do not constrain ground movement, so they do not reduce excess pore pressure build-up in the surrounding liquefiable soil but allow for quicker dissipation.

Drainage system can be used also as permanent dewatering if the water can easily be disposed of. If continuous pumping is necessary, there can be substantial ongoing running and maintenance costs and there is a risk of failure in aftershocks if the dewatering system is damaged in the initial earthquake. Liquefaction can be prevented if the ground water level is reduced below the liquefiable soil layer (Cox and Griffiths, 2010). High maintenance costs make dewatering not applicable to common buildings. This technique could be used for strategical buildings. Noteworthy that dewatering leads to an increasing of the effective stresses in the soil producing settlements that can damage adjacent existing buildings. Guidelines on this remediation concept was proposed by (Yasuda, 2007).

Bouckovalas et al. (2009) proposed some solutions to design spacing and diameter of vertical drains in liquefaction mitigation. These solutions are for indefinite distribution of vertical drains, so the problem was been solved in axial-symmetric condition.

In the design of drains, it is necessary select a suitable drain material that has a permeability coefficient substantially larger than surrounding liquefiable soil.

Vertical drains can be hardly placed below existing structures. In this case, horizontal drains can represent a suitable solution, which can be placed below existing structures thanks to directional drilling technology (Allouche et al., 2000) which allows to perform bores in built environment. They are made of microperforated cylindrical tubes with at least one end accessing to atmosphere (to ensure hydrostatic condition); maximum diameter is limited by technology to about 0.3 m. However, differently from vertical drains, no design approach is available in the literature for the application of this technique in dynamic conditions.

2.4.4 Induced partial saturation

Small decreasing of saturation degree in liquefiable soil can lead to double the liquefaction resistance. Potential volumetric strains determine the compression of pore fluid that has a dominant role in excess water pressure built-up (Okamura and Soga, 2006). An estimate of the liquefaction resistance of partially saturated sand can be done by a unique relationship that was found between liquefaction resistance ratios and the potential volumetric strain. Induced partial saturation can be made by air injection into ground (Okamura et al., 2003; Tokimatsu et al., 1990), and the unsaturated condition of the desaturated soil lasted for a long time, typically more than ten years (Okamura and Soga,

2006). This effect strongly suggests that desaturation of soil could be an effective and chip technique to increase the liquefaction resistance of the soil (Yegian et al., 2007).

Similar to the air-injection technique, in situ air sparging has been well developed to modify soil pore fluid. Design of this technique requires the determination of influence zone of airflow that is strongly influenced by soil type, soil stratifications, and air-injection pressure and depth (Yasuhara et al., 2008). A prediction of airflow path can be performed by numerical simulations with a gas-liquid two phase flow simulator (Lundegard and Andersen, 1996; McCray, 2000). However, in situ monitoring of the air-flow pattern and remediation processes is also significant to examine the validity of the predictions. An attempt was made to detect the area of desaturation around the air-injection point by using the three-dimensional (3D) electric resistivity tomography technique (Daily and Ramirez, 1995; Schima et al., 1996). Indeed, electric resistivity is dependent on the volumetric water content and it allows to identify the influence area and the relevant degree of saturation. When air injection is stopped, the residual degree of saturation can be determined. The degree of saturation after air injection can be measured by laboratory tests sampling undisturbed specimens (freezing technique).

The effectiveness of induced partial saturation in liquefaction mitigation is due to the fact that the fluid bulk stiffness is very sensitive to the presence of gas, and a small volume of bubbles modify significantly the pore pressure response to loading including the value of Skempton's B parameter, P-wave velocity, and liquefaction resistance (Fourie et al., 2001; Tsukamoto et al., 2002; Yegian et al., 2007). Generally, a low homogeneous treated area is obtained by air injection, indeed the air bubbles move along preferential paths formed by interconnected large pore throats. Some methods, which generate a more homogeneous distribution of air bubbles in the soil, use electrolysis (Yegian et al., 2007), gas dissolution and air trapping during infiltration and/or rapid water table rise (Constantz et al., 1988; Fayer and Hillel, 1986) or in situ anaerobic microbial respiration (Butler and Mason, 1997). This study reviews known bacterial metabolisms that generate gas as a by-product, conduct an experimental study to improve the understanding of the process of biogenic gas generation in soils, and analyse the data using numerical models that introduce pore fluid bulk stiffness.

2.4.5 Reinforcement

During an earthquake sand deposits are subjected to shear strain that leads to an excess water pressure build-up in saturated condition. This effect reduces the stiffness and strength of soil generating large deformation of ground. The introduction of reinforcement into the soil increase the stiffness and strength of ground and mitigates the excess pore pressure build-up and settlements if liquefaction occurs.

Reinforcement typically involves the construction of underground walls which usually intersect to form a lattice. The subterranean walls can be formed using ground solidification techniques or contiguous concrete piles. Grids of stiff isolated piles have been used to improve liquefiable soils by reinforcement (Figure 2.30). Open grid systems are relatively flexible and do not offer the same degree of confinement as a lattice. Generally, the last shape of reinforcement is placed below the perimeter of the building.

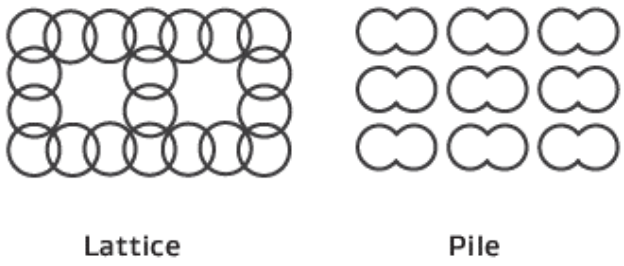

Figure 2.30. Reinforcement grid shapes.

They are less reliable than other methods of improvement and generally only applicable for lightweight structures and where the piles extend to a competent non-liquefiable stratum. The typically depth achieving by soil reinforcement is up to 20 meters.

The reinforcement can be used in wide any soil types as silty and variable soils. However, this technique is more expensive than densification and drainage ones. Lattice can be formed by different technologies that allow to realise columnar treatment using overlapping. This shape reduces shear strain and mitigates excess water pressure build-up in the soil contained into the cells dividing this soil from adjacent liquefied soils.

The design is based on the determination of spacing and sizing of the reinforcement (Bradley et al., 2013). Generally, numerical and centrifuge analyses should be performed on simplified soil profiles (Rayamajhi et al., 2013). A simplified method for reinforcement sizing and spacing was proposed by Nguyen et al. (2012). He performed some parametrical analyses adopting simplified models with fully liquefiable soil penetration and neglecting external loads.

The degree of strain relief and liquefaction mitigation is a function of:

- Columns spacing
- Stiffness and strength of columns
- Rotation constraints of columns in correspondence of liquefiable soils
- Columns-soil interface friction.

Lattice can be used also in lateral spreading mitigation, where a grid of stiff columns could be not suitable. In this case piles are designed as cantilever beam with an end fixed in underlying non-liquefiable soil.

2.4.6 Solidification

Solidification (deep mixing, jet grouting and permeation grouting) through cementation of soils. Containment of liquefied soils and limitation of ground deformation by reinforcement and soil mixing walls. Solidification involves either in-situ mixing of cementitious or other additives into the soil or filling the voids with a reagent resulting in the soil particles being bound together. This will prevent the development of excess pore water pressure, preventing the occurrence of liquefaction. Solidification techniques are typically expensive compared to other methods. Solidification techniques can be used to treat the full range of soils susceptible to liquefaction, including low plasticity silts to depths

of 30 m or more although there are some limitations with specific techniques. The advantages are: high confidence in the end product when the entire depth of liquefiable soil is treated, low vibration and noise during construction and the ability to treat beneath existing structures. Solidification techniques can be used to treat a wide range of soil types (Figure 2.31).

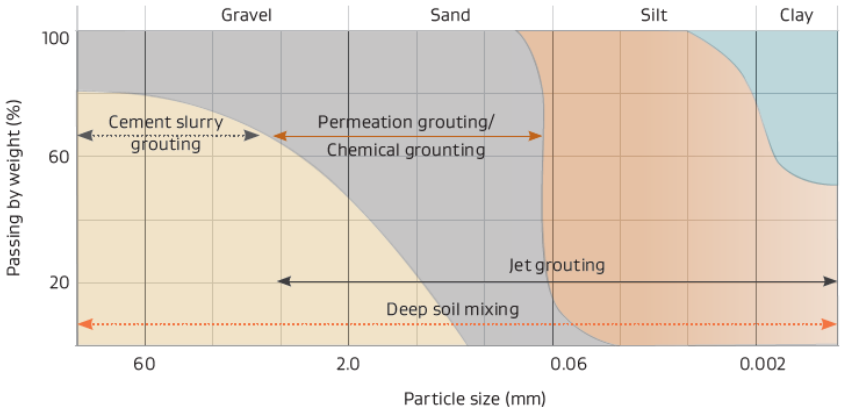

Figure 2.31. Range of applicability of solidification soil (New Zealand guidelines).

Solidification technique provides to a wide range of unconfined compressive strengths to the soil that depends on homogeneity of process, degree of compaction, the amount of cementation and characteristics of in-situ soil (Kitazume and Terashi, 2013). Unconfined compressive strength of the soil can be evaluated by field and laboratory tests. The last tests ascertain for soil mixing and jet grouting the range of binder, dosages, reactivity of mix and strength of treated soil.

Moreover, column diameter, tolerance of drilling position, verticality, timing of installation and strength gain between installations have to consider in the selection of column spacing. Cement stabilised soils show a brittle behaviour. Therefore, concentration of strains should be avoided to reduce potential differential settlement on above structures.

2.4.6.1 Soil mixing

This technology consists in the mixing of the soil with a binder in mechanical way. Several varieties of equipment are developed in the years; however, the mixing procedure is the same all of them. A rotating drum cutter attached to an excavator arm mixes the soil with a stabilising agent in massive stabilisation. In this case maximum depth reached is about 6 meters.

Deep soil mixing is employed for deeper treatment, this technique can reach depths up to 30 meters. Rotating augers or blades attached to roads are used to mix the soil with binder. The treatment consists in the realization of vertical columns generally disposed in squared or triangular grid.

Furthermore, sub horizontal beams can be realised with soil mixing below existing structures using directional drilling with cutting head.

2.4.6.2 Jet grouting

The treatment of soil with several binder can be performed by jet grouting. A drilling into the soil is realised by a beam that has up to three nozzles on the lateral surface near the tip. The number of nuzzles marks the technology of jet grouting: single fluid system (slurry grout jet), double fluid system (slurry grout jet surrounded by an air jet) and triple fluid system (water jet surrounded by an air jet, with a lower grout jet). The using of plus one fluid leads to higher efficiency of the system. The different jets break up and mix surrounding soil with binder, realising grout panels, full columns or sections with intermediate shapes. Double and triple fluid system can produce larger diameter up to 8 meters in dispersive soils.

2.4.6.3 Permeation grouting

This technique is suitable in the homogeneous ground with a moderate permeability. It is possible to treat silty soils using expensive silicate grouts. Permeation grouting requires an accurate study of vertical and horizontal permeability of liquefiable soil to reach a better treatment. Either pumping tests or laboratory tests on undisturbed specimens can be used to determine liquefiable soil permeability. Grouting material permeates into the liquefiable soil filling the pore space. The hardened grout links the soil particles by cementation reducing the tendency to contraction during shearing. Moreover, this effect leads to a stiffer soil with a higher strength. However, the control of the spread of the grout is non easily to control and there is high risk of contamination groundwater. The cost of permeation grouting is strongly dependent on the type of grouting material employed. Grouting material for soils with low permeability generally are more expensive.

3 CENTRIFUGE TESTS

3.1 Introduction

The observation and reproduction of physical phenomena have a crucial role in engineering, as in physics, to understand natural processes. Several aspects of a natural phenomenon can be caught through experiments in monitored environment that can be represented by laboratory. The measurement of physical quantities allows to define mathematical model to interpret natural phenomena. Generally, macroscopic scale is adopted in engineering to simplify the mathematical interpretation allowing to use simplify theory as continuous media. This theory requires to determine mechanical characteristics of a material on a homogeneous volume called *elementary representative volume*. Generally, this volume has centimetric sizes. However, full-scale models are required to study some complex physical phenomena where boundary condition and heterogeneity of the soil have a significant effect, these models require great economical resources and long realisation time. Some researchers proposed to use scaled models. However, many problems are strongly influenced by geometrical dimensions and by stress conditions. A better solution alternative to the simple scaled models was proposed in the first part of XIX century by Édouard Phillips. He was professor in mechanical engineering at École des Mines (1852-54), after at École Centrale (1864-75) and at École Polytechnique (1866-79). Phillips studied the behaviour of elastic springs and dashpots under static and dynamic loads. Moreover, he perfected the Stephenson joint applied to trains (Craig, 1989).

He highlighted the effect of centrifugal force on the accuracy of mechanisms (Phillips, 1868) and conceived the opportunity to apply centrifugal acceleration in the study of some engineering problems. An accelerated field could be applied by a centrifugal system and allows to scale models by appropriate scaling laws to reproduce a prototype in real size. Phillips summarised his ideas in a technical paper published on Comptes Rendus (Phillips, 1869a) where he reported some scale laws and studies on problems where density of material has an important role on the physics phenomena. In the same year Phillips proposed also the study of dynamic problems in centrifuge models (Phillips, 1869b) proving that the scale factor for inertial time is the same for geometrical sizes. These characteristics made centrifuge useful in the study of geotechnical problems where the weight of material and stress conditions have a relevant role on the mechanical behaviour of the soil.

Phillips's discoveries were applied in practice in the following years by researchers in USSR and America but without cooperation and great results. Only in '30 the first technical paper on a work in geotechnical centrifuge was published by Pokrovsky e Fedorov in the First International Conference on Soils and Mechanics and Foundation engineering (ICSMFE) in the year 1936. Starting of the first world war the geotechnical centrifuge was abandoned until '60 years. Roscoe and Schofield resumed the developing and using of this instrument realising a new geotechnical centrifuge in Cambridge University.

Nowadays several geotechnical centrifuges have been realised in the world and these represent a very sophisticated and important tool in the studies of geotechnical engineering.

The centrifuge tests considered in this work were carried out in the framework of the H2020 LIQUEFACT project (no. 700748) and were aimed at assessing the effectiveness of ground treatments against soil liquefaction, with and without the presence of a simplified structure. The basic concept of the experiments was to analyse the seismic behaviour of loose, saturated, about 15 m deep sandy deposits, either homogeneous or stratified, subjected to increasing seismic excitations up to liquefaction and to verify the effectiveness of different liquefaction mitigation techniques against liquefaction.

Thirty-seven centrifuge tests were carried out to this aim, organized in three series: the first one aimed at investigating the liquefaction triggering conditions, the second and third ones devoted at analysing the effectiveness of three selected liquefaction remediation techniques. The final scope was to produce a consistent set of experimental data to be used as a benchmark for seismic response studies, numerical simulations, and for in situ trial tests. More in details, during the first test series, geotechnical model without liquefaction mitigation were tested to define under which conditions liquefaction occurred. Some tests were carried out under free field condition, in some other a simple structure based on shallow foundations was modelled as well, in order to study the effects of soil-structure interaction in liquefaction condition. During the second test series, vertical and horizontal drains were installed in the models, in order to analyse their effectiveness in reducing the pore pressure build-up as a function of their spacing. In the third series of tests the effectiveness of the "Induced Partial Saturation" (IPS) technique on the soil liquefaction resistance was tested. The soil models were partially desaturated by air injection from the model bottom, varying the number and position of the injectors. In this work some of these centrifuge tests are analysed and numerical reproduced to study the behaviour and effectiveness of mitigation technique and their optimization.

3.2 Previous researches

As previously mentioned, liquefaction phenomenon has been studied since 1964 after strong earthquakes occurred in Alaska and Japan where large damages in urban environment were produced by liquefaction. Since the beginning the liquefaction susceptibility was studied by simplified procedures (Seed and Idriss, 1971) as well as by using more complex numerical methods (Lee and Finn, 1975; Siddharthan and Finn, 1982).

The reliability of numerical methods is affected by the procedure of calibration of the constitutive model that is adopted on the results of laboratory testing. However, depending on the constitutive model, a validation of the numerical results against the measurements recorded during real events may improve the ability of prediction of the model. In some cases, constitutive parameters may be tuned to match measurements (back-calculation) thus taking into account the model performance along stress-paths that cannot investigated through laboratory tests only. Expensive on-site instruments in necessary in this case to record pore pressure build-up and strong acceleration at various depths in a liquefiable site. However, this is hard to achieve for several reasons, among them the uncertainty of earthquake occurrence at the instrumented site. As a matter of fact, only few time histories of acceleration and pore pressure build-up in site are available in the literature for real cases

of liquefaction (e.g.: Ishihara et al., 1981). Even more difficult is to access data concerning ground displacements.

Aa an alternative, physical modelling can be very helpful and very effective to validate numerical models. They are carried out by generating seismic shaking through shaking table tests, both at 1g (Finn et al., 1971) and at increased g-level by means of a geotechnical centrifuge.

Shaking tables tests at 1g allow to measure time histories of acceleration, displacements and pore pressure build-up in the model ground and possibly identify liquefaction triggering. However, some concern may arise about the significance of the prototype behaviour. Indeed, due to the limitation in size of the model facilities, 1-g tests are carried out on ground layer approximately 1 m deep, where lower stress levels are achieved than in the field, precluding the study of stress effect on the liquefaction triggering. This affects the validity of the experimental results when dealing with the assessment of liquefaction susceptibility in real site conditions.

Geotechnical centrifuge represents a solution to these limitations since it allows the stresses field in a reduced scale model to be increased by intensifying the centrifugal acceleration. This ensures a correct reproduction of the soil mechanical behaviour in the field, provided that suitable scale laws are adopted. The first liquefaction test series were performed at Cambridge University (Lambe, 1981) in a circular cross-section laminar box allowing for a shear-type deformation of the ground layer. An upgrade of box was later made by Hushmand et al. (1988): they created a rectangular section laminar box, thus decreasing the boundary effects. Since then, centrifuge modelling has been extensively used to study the liquefaction triggering, also with the specific purpose of validating numerical procedures, sometimes involving large groups of researchers in experimental and predictive exercise such as VELACS, Verification of Liquefaction Analyses by Centrifuge Studies (1992) or LEAP, Liquefaction Experiments and Analysis Project (2015, 2017).

Moreover, in the last years centrifuge tests were used to study the effects of mitigation technique against soil liquefaction, aiming at

1. fastening the excess pore pressure dissipation during shaking;
2. reducing the excess pore pressure build-up.

The first goal can be achieved by the introduction of new seepage surfaces in the ground, thus reducing the drainage distance. Vertical drains represent a usual mitigation technique and their effectiveness has been studied in centrifuge models by several researchers (e.g. Brennan and Madabhushi, 2006, 2002; Dashti et al., 2009; Howell et al., 2012).

The mitigation pursuing the second goal can be produced in different ways, as seen in section 2.4. Among others, the induced partial saturation (IPS) is a very promising mitigation technique since it allows for a large effectiveness at a relatively low cost(Bian et al., 2008). The effects of induced partial saturation as liquefaction countermeasure were studied only in the last years.

Partial saturation can be implemented in different ways, for instance by air injection (Ishihara et al., 2003; Okamura et al., 2011; Yasuhara et al., 2008) , or by chemical reaction producing gas, or even by biogas produced by bacteria metabolism (He et al., 2013; Rebata-

Landa and Santamarina, 2012a). Some of them have been recently adopted in centrifuge modelling (e.g. Zeybek and Madabhushi, 2017).

3.3 Centrifuge tests overview

Geotechnical centrifuge has a simple structural scheme. It is composed by a rotational beam with a vertical central axis that is moved by a series of pullies linked to an electrical engine. The whole system is located in an underground stiff structure made of reinforced concrete (Figure 3.1). Two swinging baskets are attached on both ends of a rotational beam, the geotechnical model is placed in one of these and in the other one there is a counterweight that balances the centrifugal forces induced by rotation (Figure 3.2).

The phase of rotation acceleration is called *spin-up phase*. During the spin-up the model located on the basket is subjected at a centrifugal acceleration and it rotates until its base is vertical. This effect allows to assume acceleration field almost perpendicular to the ground level during whole spin-up phase avoiding the rotation of principal stresses in the soil. The acceleration field in the model can be intensified by increasing the angular velocity.

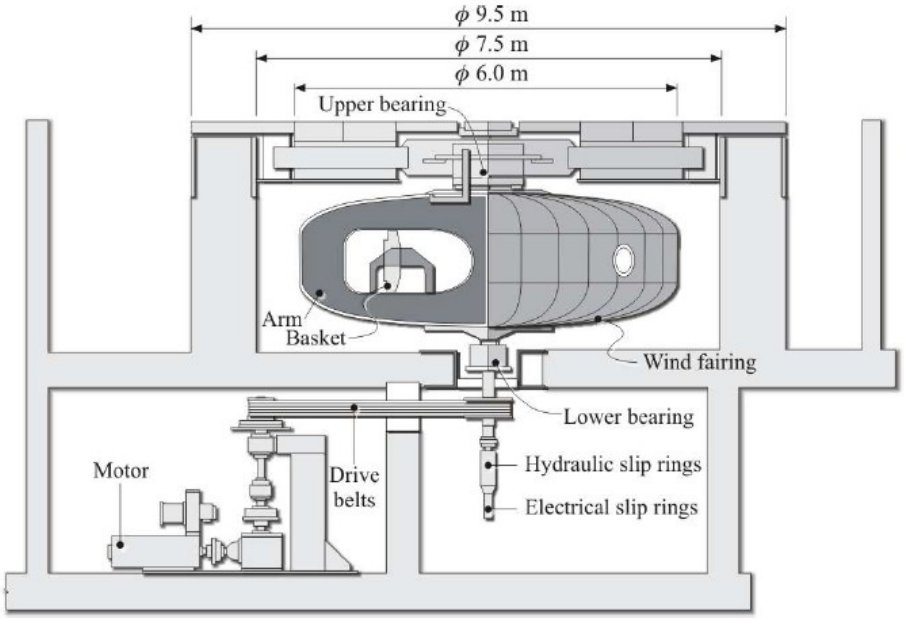

Figure 3.1. Geotechnical centrifuge structural scheme (ISMGEO geotechnical centrifuge).

Maintaining consistency in the stress field of the physical model is certainly one of the key factors to achieve accurate modelling. Multi-g physical modelling is based on the principle that, if a model, in which each linear dimension is reduced by a factor N, is subjected to a centrifuge acceleration of a = Ng (where g is the gravity field), the self-weight of any material used for the model is N times larger than in a 1g gravity field.

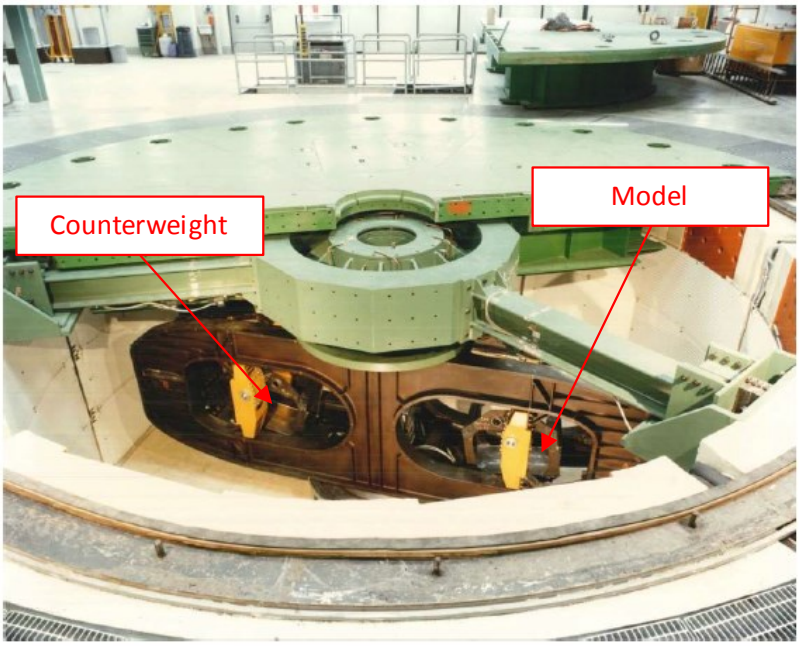

Figure 3.2. Geotechnical centrifuge (ISMGEO geotechnical centrifuge).

Therefore, a 1/N model at the centrifuge acceleration of a = Ng achieves the equivalent vertical stress of the full-scale prototype, assuming that a material with the same mass density is used in the model. If the stress–strain characteristic of the model material is the same as in the prototype, for example if the same soil is used in the model, similarity of strains is also achieved. If the scaling factor for a generic quantity is defined as:

$$x^* = \frac{\mathrm{x_{prot}}}{\mathrm{x_{mod}}} \qquad (3\text{-}1)$$

where $\mathrm{x_{prot}}$ is the quantity in prototype scale, $\mathrm{x_{mod}}$ is the quantity in the model scale.

In a geotechnical model prepared by the same prototype material the scaling factor for the density mass is unity, in this case the geometrically model is scaled down N times with respect to the prototype:

$$L^* = \frac{L_{\mathrm{prot}}}{L_{\mathrm{mod}}} = N \qquad (3\text{-}2)$$

where N is the multiplier of the acceleration field defined as:

$$g^* = \frac{g_{\mathrm{prot}}}{g_{\mathrm{mod}}} = \frac{1}{N} \qquad (3\text{-}3)$$

In this case the centrifuge acceleration reproduces the same stresses and strains as in the prototype with size N times greater than accelerated model, so that the model soil exhibits identical mechanical behaviour as the prototype soil (Schofield, 1980).

For the other parameters the model can be related to the prototype using appropriate scale laws (Table 3.1) valid within continuum mechanics (Garnier et al., 2007).

Table 3.1. Principal scaling ratio for different geotechnical parameters.

	PARAMETER	SCALE FACTOR $(x^* = x_{prot}/x_{mod})$	MODEL (Ng acceleration)
L	Length	L^*	N
ρ	Soil density	ρ^*	1
ε	Strain	ε^*	1
σ	Stresses (effective and total)	$\sigma^* = x^*\,\rho^*\,g^*$	1
G	Stiffness	$G^* = x^*\,\rho^*\,g^*/\varepsilon^*$	1
ρ_f	Fluid density	ρ_f^*	1
p	Fluid pressure	$p^* = x^*\,\rho_f^*\,g^*$	1
u	Soil displacement (continuum)	$u^* = x^*\,\varepsilon^*$	N
v	Velocity	$v^* = (x^*\,\varepsilon^*\,g^*)^{0.5}$	1
$\ddot{u}$	Acceleration	g^*	N^{-1}
t	Time (diffusion phenomena)	$t^* = \mu^*\,L^{*2}/G^*$	N^{-2}
t	Time (creep)	t^*	1
t	Time (dynamic)	$t^* = (x^*\,\varepsilon^*/g^*)^{0.5}$	N
μ	Dynamic viscosity of fluid	$\mu^* = \rho_f^*\,(g^*/x^*\,\varepsilon^*)^{0.5}$	N^{-1}

The intensity of centrifugal acceleration field is dependent on the distance from the rotational axis. Thus, a variable acceleration is applied to different depth of the geotechnical model that produces a slightly parabolic distribution of the overburden stresses. This effect is reduced extending the length of the beam of the geotechnical centrifuge.

Centrifugal acceleration can be calculated as:

$$Ng = \omega^2 \cdot R \tag{3-4}$$

where ω is the centrifuge angular velocity and R is the distance from the rotational axis.

The vertical stress field in the centrifuge model has to be computed according to the following equations:

$$d\sigma_v = \rho\, g\, N\, dR \tag{3-5}$$

$$\sigma_v(R) = \int_{R_s}^{R} \rho\, \omega^2\, R\, dR = \frac{1}{2}\rho\, \omega^2\, [R^2 - R_s^2] \tag{3-6}$$

where R_s is the radius at the model ground surface.

In the acceleration of the geotechnical model some aspects could be a significant influence on the test results. First of all, an important aspect is represented by non-level ground surface and free water surface due to the dependency of the acceleration field on the distance from the rotation axis.

The seepage processes in the accelerated model have a velocity N times larger than in prototype scale if the same soil and pore fluid are used and identical gradient is applied. This leads to an inconsistency on velocity in coupled dynamic and diffusion tests, where pore pressure build-up scales down by N while pore pressure dissipation scales down by N^2. This can be avoided using an appropriate interstitial fluid, that is by adopting in the geotechnical model a fluid with a dynamic viscosity N time larger than in prototype but with similar density (Allard and Schenkeveld, 1994).

Another important aspect is represented by rigid base and lateral containing walls that represent the boundary conditions for the model. Hydraulic and mechanical behaviour of the containing walls have to be designed in function of the problem to be studied. In the following a briefly discussion on the design of the box employed for centrifugal tests is reported.

3.4 Centrifuge characteristics of ISMGEO

The ISMGEO geotechnical centrifuge is a beam centrifuge made up of a symmetrical rotating arm with a diameter of 6 m, a height of 2 m and a width of 1 m, and a nominal radius to the model base of about 2.2 m (Figure 3.1 and Figure 3.2); further details can be found in Baldi (1988). A shaking table is fixed at one hand of the arm (Figure 3.3); at the other hand the arm holds a swinging platform which carries the model for static tests. An outer fairing covers the arm and they concurrently rotate to reduce air resistance and perturbation during flight. The centrifuge has a 240 g-ton capacity, this means that the machine has the potential of reaching an acceleration of 600g loading a payload of 400 kg. The unusual shape of the arm offers the following advantages:

- small distortion of the centrifugal field in the model, since its main dimension is parallel to the rotation axis;
- low deflection of the support plane of the swinging basket;
- easy location of instruments close to the rotation axis because of the absence of a central shaft across the arm.

The centrifuge houses a single degree of freedom shaking table, which is able to reproduce real strong motions at the model scale. The axis of motion of the shaker is parallel to the centrifuge rotational axis, thus problems related to Coriolis' acceleration are avoided. Unlike most centrifuge shaker solutions, where the shaker is integrated into the swinging basket (Derkx et al., 2006; Imamura, 1998; Ma et al., 2006; Matsuo, 1998; Shen, 1998; Van Laak et al., 1998), the ISMGEO shaker was designed specifically to be fixed to the symmetric double centrifuge arm. This arm is of a particularly rigid construction, which makes it suited as reaction base for the shaker (Figure 3.3).

During the centrifuge flight the model container rotates from horizontal towards the vertical position, at the centrifuge acceleration of about 5g the model is moved into contact with the table and released before the application of the dynamic excitation. The shaker excitation is transferred from the shaking table to the model container by mechanical coupling.

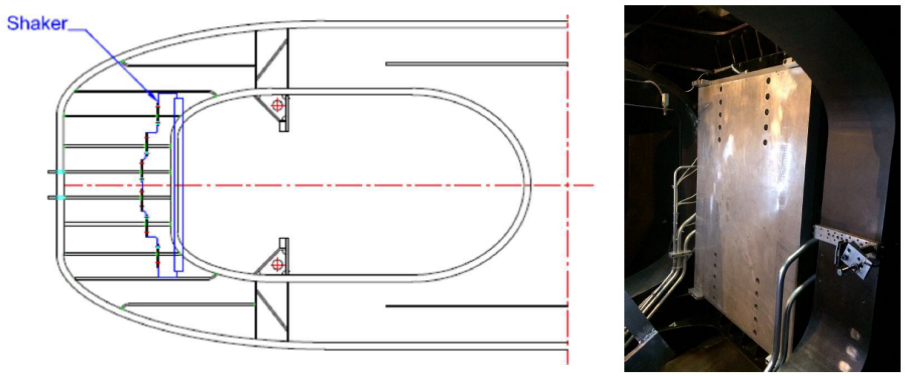

Figure 3.3. Shaking table position (ISMGEO geotechnical centrifuge).

The shaking table can work under an artificial acceleration field up to 100g, it can provide excitations at frequencies up to 700 Hz and seismic accelerations up to 50g (depending on the driving load) (Table 3.5 and Figure 3.4).The shaker is capable to reproduce single degree of freedom strong motions at the model scale (Airoldi et al., 2016).

Table 3.2. Technical characteristics of shaking table.

Peak operational centrifuge acceleration	*100 g*
Max frequency	*700 Hz*
Max payload at 100 g	*3.50 kN*
Peak velocity	*0.9 m/s*
Peak displacement	*±6.35 mm*
Max seismic acceleration	*50 g*
Full load acceleration	*16 g*

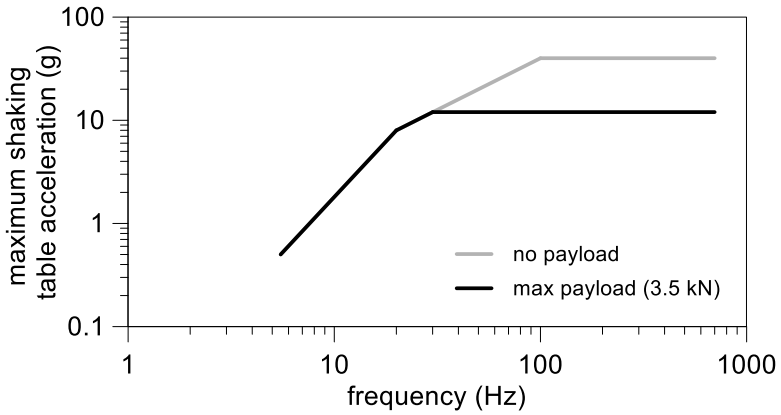

Figure 3.4. Operating map of peak acceleration vs frequency for shaking table (ISMGEO geotechnical centrifuge).

3.5 Equivalent shear beam (ESB) box

As previously mentioned, the boundary conditions imposed on the model by the presence of rigid base and containing walls have a great influence on the results of the test. These conditions are very important in dynamic tests where the deformability of the walls is required and has to calibrated on the characteristics of the soil. Indeed, the presence of deformable walls allows to reproduce an indefinite soil field achieving limited disturbances on the seismic motion. A thorough review of the main disturbances to the soil model introduced by the model container in geotechnical earthquake modelling is found in (Brennan et al., 2006; Zeng and Schofield, 1996).

The design of the box has to respect some aspects to reach a satisficing reliability of test results:

- The increasing of the acceleration field leads to a sensible increasing of horizontal stress induced by soil on the wall. A large horizontal deformability of the walls could lead the horizontal stress of the soil from K_0 conditions to K_a ones. For this reason, the walls deflection has to be lower than 0.1% of the total soil column height (Ueno, 1998);
- In spin-up phase the friction of the soil on the lateral boundaries could lead to a silo effect that decreases the vertical stresses. Then, smooth interfaces have to realised. However, in dynamic test the continuity of shear stresses on the walls is required (Brennan et al., 2006) to avoid significant rocking of the soil (Zeng and Schofield, 1996).

A strong reduction of the boundary effects can be reached by a model as bigger as possible. This possibility depends on the technical limitations of the shaking table to be used, in terms of both model dimensions and payload.

Several typologies of model containers have been developed and tested to date, however no ideal solution has been found and often the satisfaction of one boundary condition comes at the expense of a different boundary effect being generated. All the adopted solutions involve either flexible or absorbing boundaries, in order to mitigate the interaction between the soil and the container during shaking (Brennan et al., 2006). Typical containers for simulating soil liquefaction are the laminar container, composed by a high number of very thin rigid frames connected by zero friction roller bearings providing minimum lateral stiffness, and the Equivalent Shear Beam (ESB) box, composed by rigid and light frames connected by rubber inter-layers having a finite stiffness and whose functioning relies on the soil and container having similar stiffness (Brennan et al., 2006). A laminar container is ideal in reproducing the large strains occurring in fully liquefied soil and in the case of significant cumulative displacement may be generated during shaking (i.e. lateral spreading). ESB container is suitable to test dry sands, saturated soil for small earthquakes and when the triggering of liquefaction is to be investigated. This type of container has been extensively used and tested for different soil types and was studied intensively by Zeng and Schofield (1996) and (Brennan et al., 2006).

3.5.1 ISMGEO EBS box

For the centrifuge tests in LIQUEFACT project an ESB box was chosen. The using of laminar box was rejected for its incapacity to follow the response of the soil in the pre-liquefaction phase, so in the triggering path of liquefaction. Indeed, laminar box represents optimal boundary conditions for fully liquefied soil where large lateral deformations are expected. Since one of the aims of centrifuge tests was to investigate the on-set of earthquakes induced liquefaction in level ground deposits lateral deformations are to be negligible, an ESB container was preferred to a laminar one.

An ESB box was specifically designed and constructed for the tests of H2020 LIQUEFACT project (Airoldi et al., 2018b). The container was designed to match the dynamic behaviour of testing soil model constituted by loose saturated sand prior to the generation of earthquake induced excess pore pressure. Full liquefaction of the loose saturated sand during testing is anticipated. In liquefaction conditions the dynamic behaviour of the soil and lateral walls differ. Indeed, the soil loses large part of its shear stiffness whereas the walls have still the initial stiffness. Some dynamic disturbances arise from this phenomenon, but they are localized near to the walls from the large impedance between walls and liquefied soil.

The ESB container design methodology followed consisted of three phases:

- Definition of the design soil model and design earthquake parameters;
- Estimate of the soil model deformation caused by the design earthquake and soil dynamic vibration characteristics.

Iterative process for the definition of the ESB container parameters resulting in a satisfactory match between container and design soil model behaviour when subjected to the design earthquake.

The earthquake motion selected as a reference for container design resulted from a site response analysis carried out for a site in the Emilia Romagna region, near to the epicentre of the 2012 seismic sequence. Figure 3.5 reports the time history of the acceleration and the Fourier amplitude spectrum at the prototype scale. The peak ground acceleration of the ground motion is 0.287g. According to Seed and Idriss (1971), the average seismic demand on a soil column is proportional to 0.65·PHA. This acceleration was taken as reference for container design and represents the acceleration level for which the container performance is optimal and is shown in the Figure 3.5 by two red dashed lines.

Soil material for the design of ESB box is Ticino sand at 40% of relative density. A 15 meters depth soil profile was chosen since a deeper soil profile was not necessary; indeed, the full liquefaction phenomenon likely does not happen at large depth higher than 15 meters (Steedman and Sharp, 2001).

The dynamic behaviour of the ESB container is defined by the lateral stiffness of the rubber layers and by the mass of the aluminium frames. The lateral stiffness of the rubber layers depends on the layer thickness and on the shear modulus of the material (Gr). Deformable layers are constituted of Protek general purpose rubber rings supplied by Polymax. The shear modulus of this material was measured by Bertalot (2013), by testing 60mm metal-rubber-metal sandwiches in a conventional shear box. The author also

investigated the variation of the rubber shear modulus under the range of vertical confining stresses expected during centrifuge testing. The mechanical properties of Polymax Protek rubber used for the container construction are summarized in Table 3.3.

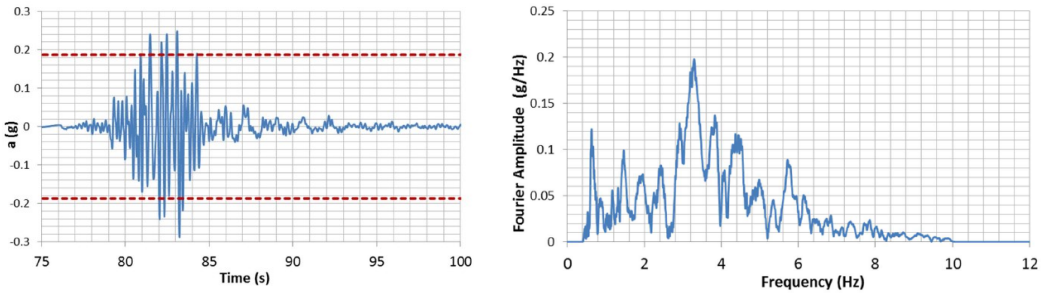

Figure 3.5. Design seismic input for the equivalent shear beam (EBS) box (Airoldi et al., 2018b).

For a given rubber type, the dynamic response of the ESB container is controlled by the following parameters:

- Mass of the aluminium frames;
- Thickness of the rubber layers;
- Number of degrees of freedom (i.e. number of rubber layers).

A trial and error iterative procedure was adopted, consisting of calculating the deflected profile of the container and its modes of vibration when subjected to the design earthquake, for different sets of the above variables, until a satisfactorily match with the soil column dynamic response was achieved.

Table 3.3. Rubber mechanical characteristics.

MATERIAL	*Protek Polymax Rubber*
Shear modulus ($G_{r,0}$)	*1300 kPa*
Stress coefficient, m	*13*
Tensile Strength	*4000 kPa*
Elongation at break	*250 %*

A final configuration consisting of twelve aluminium rectangular frames with a height of 25 mm each, and eleven 3mm thick rubber inter-layers was selected. This configuration returns a total container height of 333mm. Table 3.4 summarizes the final configuration selected for the ISMGEO ESB container, while Figure 3.6 shows the container installed in the centrifuge. In the picture is visible an upper, thin ring used to fix at the top the internal membrane, which seals the soil model; therefore, the total height of the container is 350mm.

Table 3.4. ISMGEO ESB box characteristics.

ISMGEO ESB box	
Number of rings	12
Number of rubber layers	11
Ring mass	3.4 kg
Box Height	333 mm
Internal width	250 mm
Internal length	750 mm
Ring width	40 mm
Ring length	25 mm
Rubber layer thickness	3 mm
Empty weight	110 kg

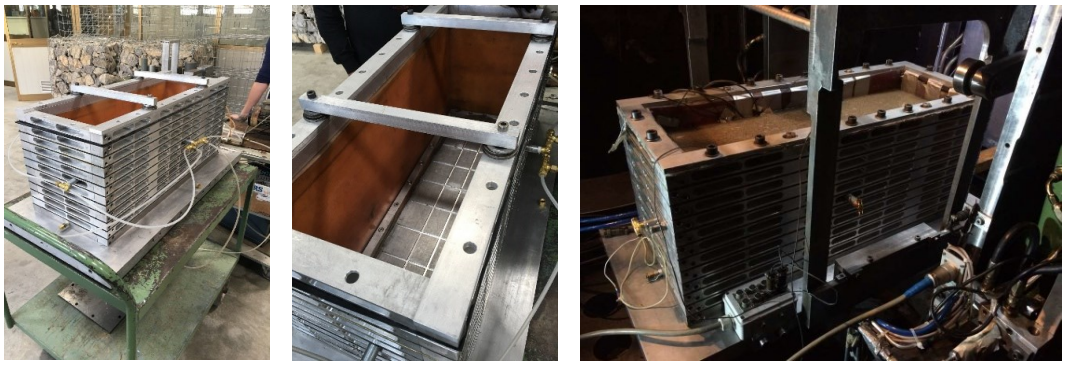

Figure 3.6. ISMGEO ESB box.

The deformation of the container under the shear stress distribution induced by the design horizontal base acceleration was calculated and the comparison between deformed wall profile and soil one is shown in Figure 3.7. It should be noted that the ESB containers deforms in a stepwise manner, as its flexibility is concentrated in the rubber inter-layers, while the soil column deforms more homogeneously.

Zeng and Schofield (1996) suggest the use of rough shear sheets securely fixed to the container base in correspondence of the end walls, in order to sustain the complementary shear stresses generated in the soil mass by base shaking. The presence of such aluminium shear sheets, together with the relatively high number of aluminium rings adopted minimizes the discrepancy between the soil column deflection profiles and the container deformed shape under the design base acceleration. However, it should be considered that the presence of this shear sheets would cause a slight distortion of the stress field in the soil during centrifuge spin-up.

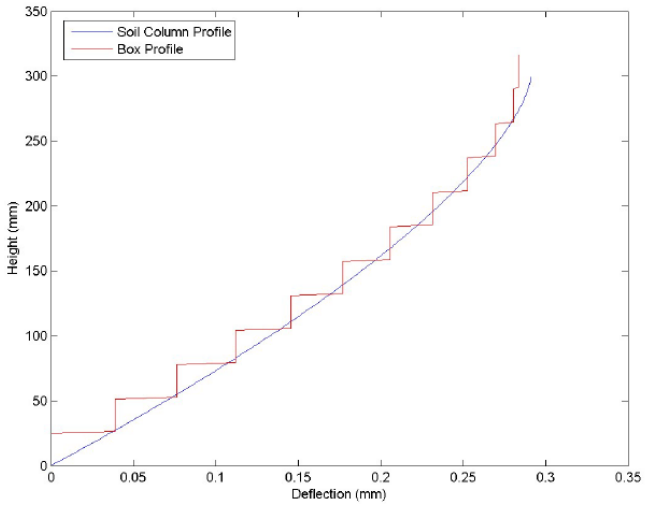

Figure 3.7. Comparison between deformed wall profile and soil one (Airoldi et al., 2018b).

A modal analysis determines the modal frequencies and modal shapes. The first five modes of the system in model scale are shown in Figure 3.8.

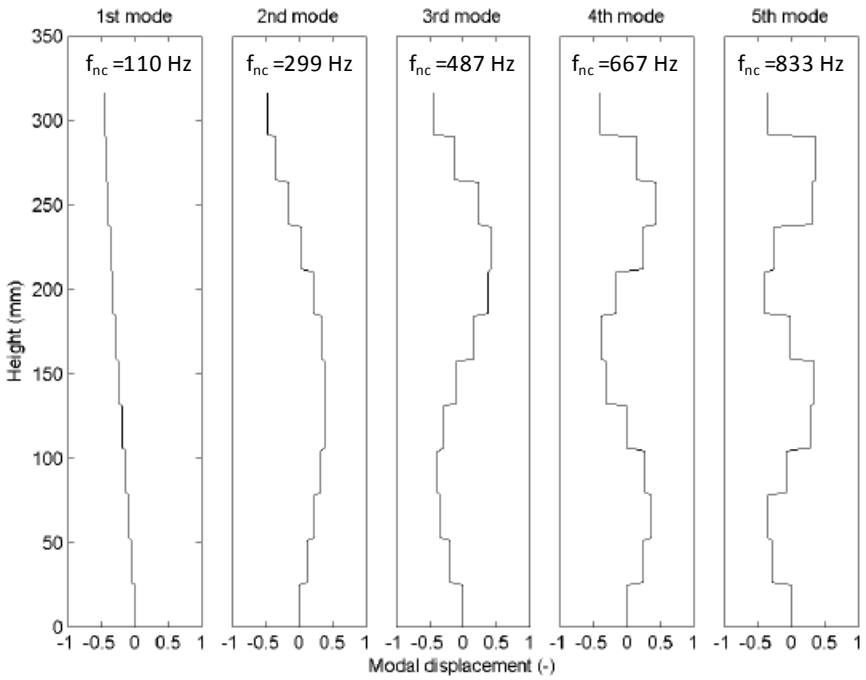

Figure 3.8. Vibration modes and relative frequencies of the lateral walls of ISMGEO ESB box (Airoldi et al., 2018b).

The ISMGEO centrifuge mounted earthquake simulator produces motions having frequency content up to 700 Hz, while the design record has energy concentrated in a

frequency range from 20 to 350 Hz. For this reason, the 3rd and higher modes of vibration of the ESB container are likely to remain unexcited during testing. On the contrary the 1st mode occurs at a frequency of 110 Hz (i.e. 2.2 Hz at prototype scale) which is likely to be associated with high excitation energy during earthquake shaking. This may result in significant amplification of the base motion, although the soil model itself, having a similar natural frequency (98-140 Hz), would also resonate when such frequency range is excited, mitigating the interaction between the container and the soil model during resonance.

The desired ring mass is obtained by matching the dynamic response of the ESB box to that of the design soil column. However, this mass differs from that of the solid aluminium rings having a rectangular section 40 by 25 mm and dimensions listed in Table 3.4.

As previously mentioned, an important effect to avoid is the bulging of the lateral walls during the increasing of the centrifugal acceleration which leads the soil to decrease horizontal stress losing the K_0 conditions. This aim can be achieved using lateral walls stiff enough and verifying the deflection of the walls as suggested by Ueno (1998).

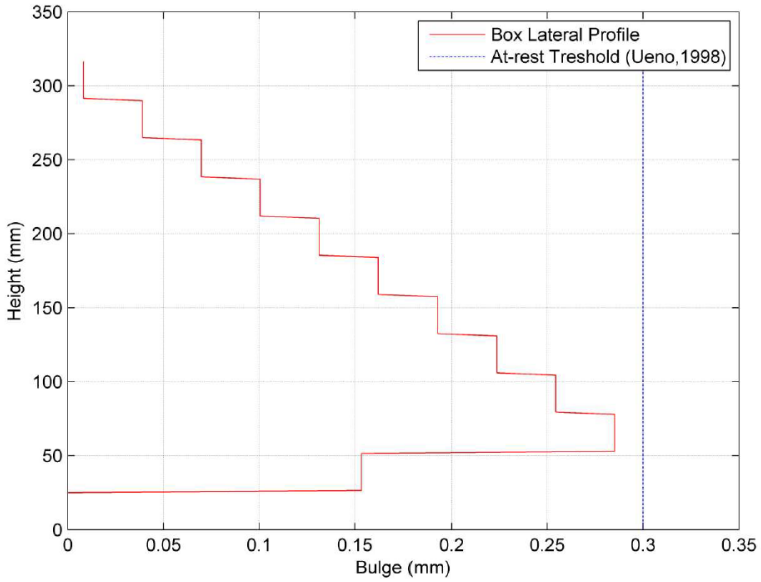

Figure 3.9. Vibration modes and relative frequencies of the lateral walls of ISMGEO ESB box (Airoldi et al., 2018b).

The static loads acting on the inside of the aluminium rings under a N-g field have been calculated by integrating the horizontal stress developing in the soil under at-rest conditions over the internal surface of each ring. The maximum static deflection will occur at the midpoint of the ring longitudinal side. Static deflection of each ring was calculated modeling the ring longitudinal side as a beam with constrained ends under a homogeneous distributed load (3-7).

$$\delta_c = \frac{\sigma_h \, h_r \, L_b^4}{384 \, EI} \qquad (3\text{-}7)$$

where h_r is the ring height, E is the Young modulus of aluminium and I the moment of inertia of the ring excavated section (U-section). The length for the calculation was equal to 84% of the internal length taking to account the presence of parts of beam with full sections. Noteworthy that the bottom ring is fixed to the container base and will not experience any lateral appreciable deformation under soil imposed stresses. At 50g acceleration the maximum ring horizontal deflection is of 0.27 mm in model scale (Figure 3.9) and respects the threshold suggested by Ueno (1998).

A test was performed to verify the effectiveness of the ISMGEO ESB box to reproduce free-field condition during a shaking (Fasano et al., 2019). A natural sand from Pieve di Cento, a town in Emilia-Romagna region in Italy, was used as model material. This sand was chosen to reproduce typical ground conditions where liquefaction occurred during the 2012 seismic sequence. The sand was retrieved from the field trial site of the LIQUEFACT project located along the Reno river. This is a silica sand (G_s = 2.69, $\gamma_{d,min}$=12.25 kN/m^3, $\gamma_{d,max}$=15.75 kN/m^3) with a coefficient of uniformity U≅1.8 (Figure 3.10). The sand has been characterised under both static and cyclic loading conditions (Mele et al., 2018).

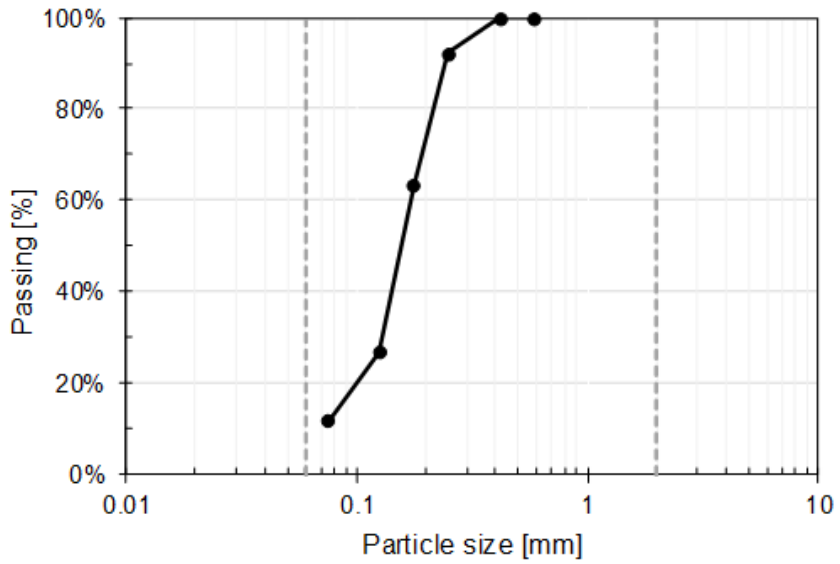

Figure 3.10. Grain size distribution of Pieve di Cento sand (Fioravante, 2000).

The soil models were reconstituted by air pluviation of dry sand at a target void ratio. A latex membrane between the soil and the container guarantees water-tightness along the vertical sides. The membrane is fixed to the bottom and the top of the frame stack.

A flexible aluminium mesh was inserted between the soil and the membrane along the short sides of the box. It was connected to the bottom of the stack to improve shear stress transmission at the side boundaries of the soil layer during shaking.

During soil pluviation the models were instrumented with miniaturised accelerometers and with pore pressure transducers deployed at several depths as shown in Figure 3.11.

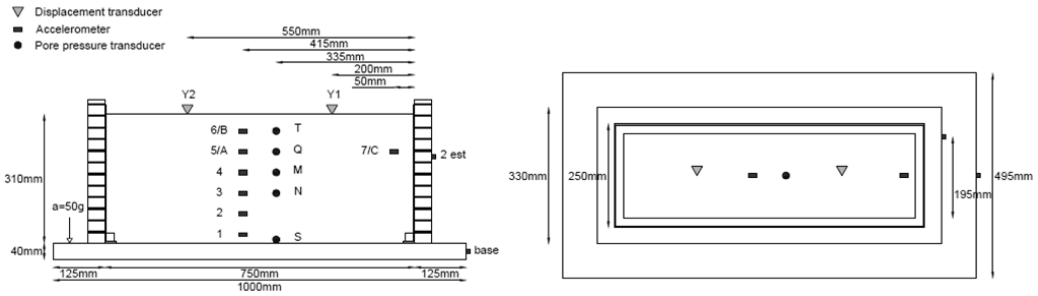

Figure 3.11. Transducers disposition in the model.

Displacement transducers (potentiometers) were located at the ground surface. In this way triggering of the liquefaction was detected and post liquefaction settlements were evaluated. After deposition, the soil layer was saturated with a pore fluid with scaled viscosity. A hydraulic gradient was imposed between the bottom and the top of the layer using a vacuum system. The achievement of complete saturation was controlled by measuring the volume of fluid accumulating in the box and comparing it with the volume of voids.

The time histories of acceleration were obtained aimed at reproducing the expected ground motion at a depth of 15 m below the ground surface at the prototype scale (Airoldi et al., 2018b). A briefly explanation on the characteristics of the input motion are reported in a following section.

A briefly explanation on the used input motions will be shown in a following section. These records were then applied at the base of the physical model after appropriate time scaling. The signals were lastly corrected to take into account the transfer function of the dynamic actuator in the centrifuge. An appropriate time interval was waited between two consecutive input motions.

A selection of results of the tests is shown in this section. However, it should be remarked that liquefaction (i.e. r_u=1) was never achieved during the tests (Figure 3.12).

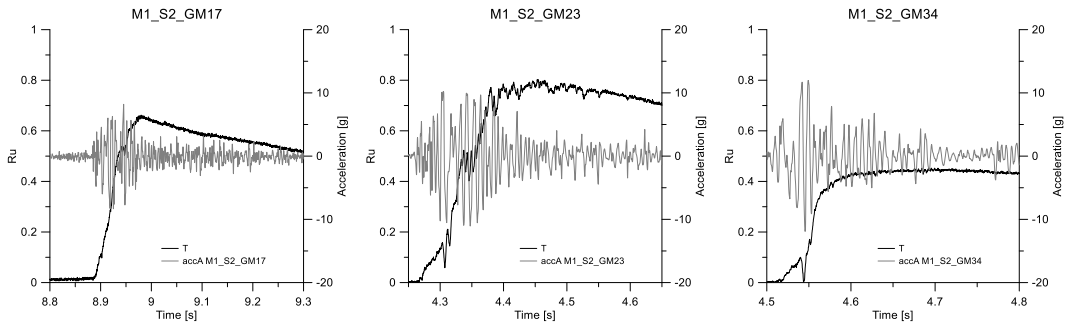

Figure 3.12. Acceleration time histories (model scale) and excess pore pressure ratio (r_u).

Figure 3.13 illustrates the accumulation of settlement at the ground surface, as measured by Y1 and Y2 potentiometers the displacements measured by the two transducers are the same at the end of the shaking showing a uniform settlement distribution along the ground surface. These results are congruent with free-field condition.

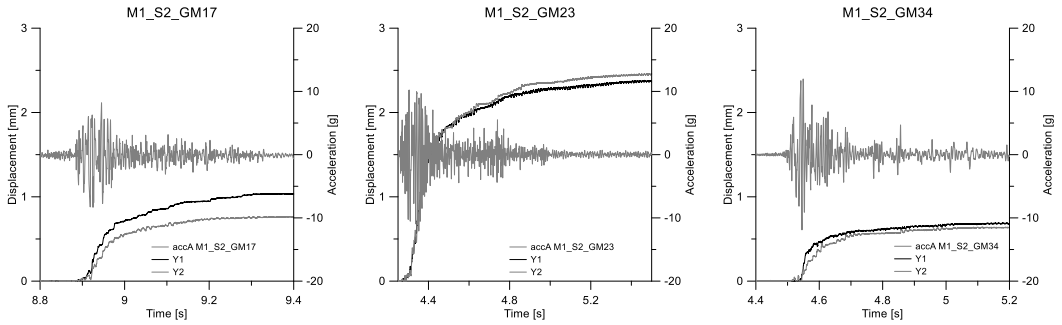

Figure 3.13. Acceleration time histories (model scale) and settlements of the ground surface.

Finally, Figure 9 shows a comparison of acceleration time histories recorded along the frame (2est) and within the sandy layer (A) during the 3 excitations (Figure 3.14). The good agreement among the time histories recorded at the same elevation along the boundary and within the domain indicates that the ESB container is performing well in mitigating the boundary effects and reproduces pretty good the free-field conditions.

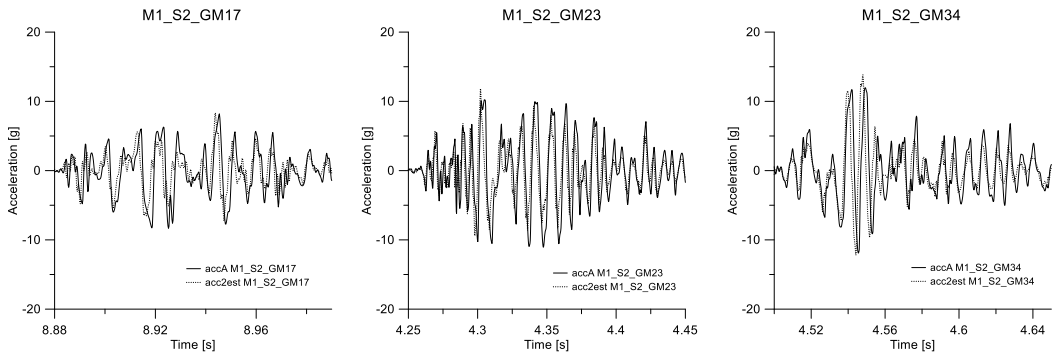

Figure 3.14. Acceleration time histories comparison (model scale) between point 2est and A.

3.6 Soil material

The basic concept of centrifuge experimentation was to analyse the seismic behaviour of loose, saturated, 15 m deep sandy deposits, homogeneous or stratified, subjected to increasing seismic excitations up to liquefaction and to verify the effectiveness of different liquefaction mitigation techniques. To this aim, a first series of tests was devoted at investigating the liquefaction triggering conditions, in order to define under which conditions liquefaction occurred and to provide a benchmark dataset to be used as

comparison to evaluate the effectiveness of the remediation techniques selected for the project (second and third series of tests). To this end, it was established to test, during the first test series, three sandy soils: a natural sands retrieved from the site of Pieve di Cento, located near to the reference localities of San Carlo and Mirabello, and tested with and without its natural fine content (natural Pieve di Cento sand and clean Pieve di Cento sand), a well-known Italian clean sand (Ticino Sand). In the following will be studied only the tests with Ticino sand considering the great reliability due to the extensively use in the last 40 years for geotechnical experimentations, so this sand results widely studied and characterised. The grain size curve of this tested soil is shown in Figure 3.16. Ticino Sand is a uniform coarse to medium sand made of angular to sub-rounded particles. It is composed by 30% quartz, 65% feldspar and 5% mica. A detailed description of its properties can be found in Fioravante and Giretti (2016). The main physical characteristics of Ticino sand used in the tests are reported in Table 3.5.

In some of the tested models, the sandy deposit was topped by a fine grain layer, reconstituted using Pontida Clay (Fioravante et al., 2008), obtained from a quarry of fine material located in Pontida, a zone northeast of Bergamo, Italy. Pontida clay is a low plasticity kaolinitic silty clay, it has a Gs of 2.77, a liquid limit of 24% and plastic limit of 11% and a compression index Cc of 0.2. Grain size analyses indicate a prevalence of silt-size particles (53% by weight) with 30% clay size particles and 17% sand.

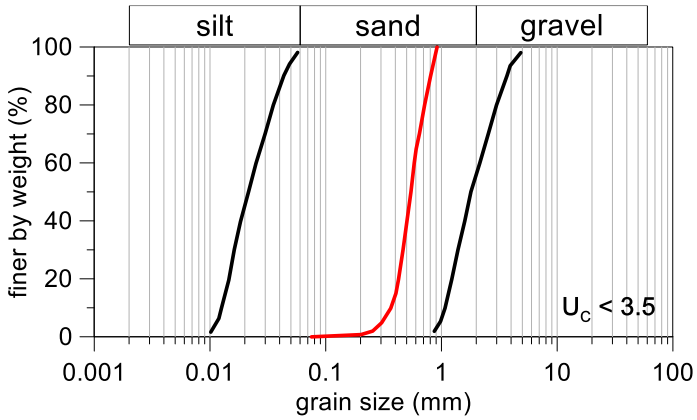

Figure 3.15. Grain distribution of Ticino Sand (red line); Grain distribution for liquefiable soils in Italian Code (black lines).

Table 3.5. Physical characteristics of Ticino Sand.

Sand	γ_{min} (kN/m^3)	γ_{max} (kN/m^3)	e_{min}	e_{max}	G_s	D_{50} (mm)
Ticino	13.64	16.67	0.574	0.923	2.68	0.53

As previously mentioned, the study of liquefaction phenomena requires defining of the dynamic and cyclic characteristics of the soil. Fioravante and Giretti (2016) made wide sets of laboratory tests defining the Ticino sand behaviour in the static and cyclic field. Static

behaviour was studied in by triaxial tests with an isotropic and anisotropic consolidation reaching the critic state conditions. the critic state line of Ticino sand is shown in Figure 3.16a. Isotropic consolidated triaxial cyclic tests were used to define the cyclic strength. As previously mentioned, the behaviour of the soil is a function of the initial state in particular it is governed by the state parameter ψ (Eq. (2-1). Different ranges of cyclic strength in function of the state parameter are shown in Figure 3.16b.

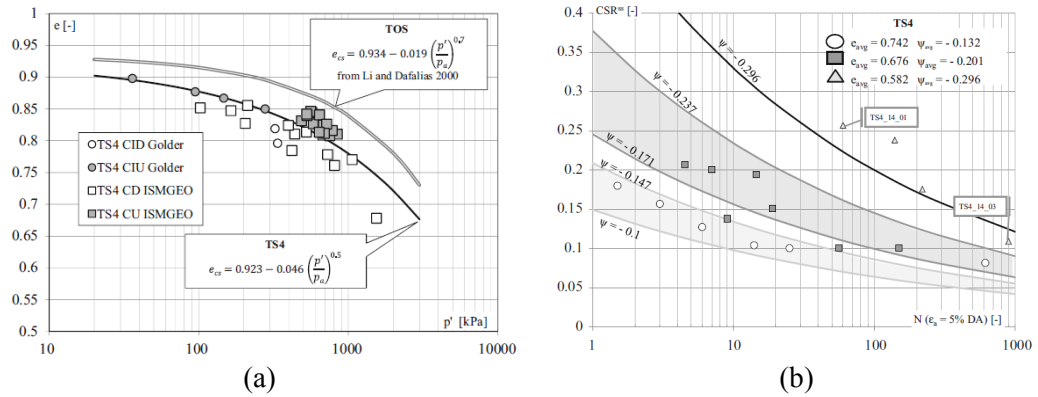

Figure 3.16. Critic state line of Ticino sand (TS4) (a) and cyclic strength of Ticino sand (b) (Fioravante and Giretti, 2016).

The dynamic behaviour of the soil was studied also in terms of shear stiffness reduction and damping generation to different shear strain levels. In the following are shown the decay law for Ticino Sand in undrained conditions at 50 kPa of mean effective stress and 45% of relative density (Figure 3.17).

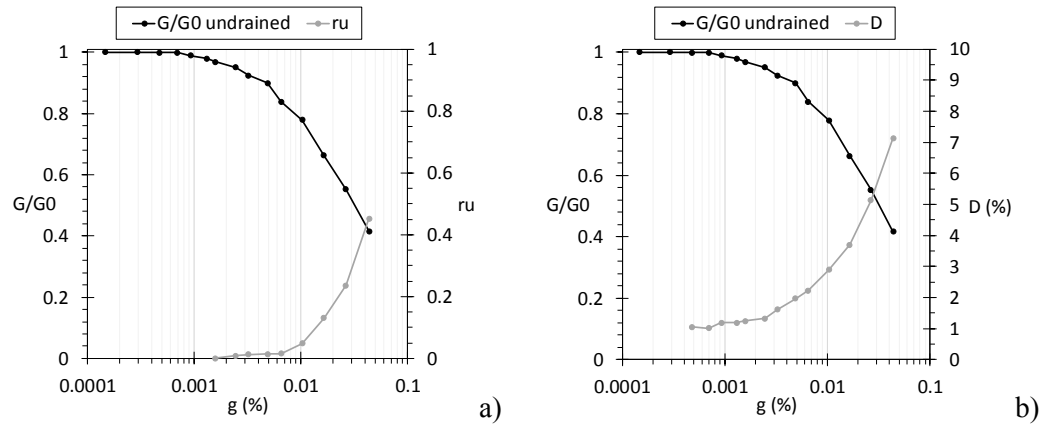

Figure 3.17. Decay law of Ticino sand in undrained condition (TS4) with excess water pressure ratio (a) and damping ratio (b) (Personal consideration).

3.7 Input motions

A specific site response analysis was carried out at University of Pavia (Italy) in order to provide a series of ground motions, corresponding to different seismic hazard levels (Return period, T_r =475, 975, and 2475 years), to be applied to the centrifuge models by the shaking table. The motions were computed referring to the Pieve di Centro deep seismic profile (Figure 3.19), largely studied during previous researches carried out after the 2012 seismic sequence.

Calculations of the centrifuge input signals were performed and verified using independent approaches. The acceleration time histories were computed at the depth of 15 meters, i.e. at the base of the sandy deposit which were simulated in centrifuge. Acceleration time histories at the depth of 15 meters are numerically computed by using the scheme presented in Figure 3.18.

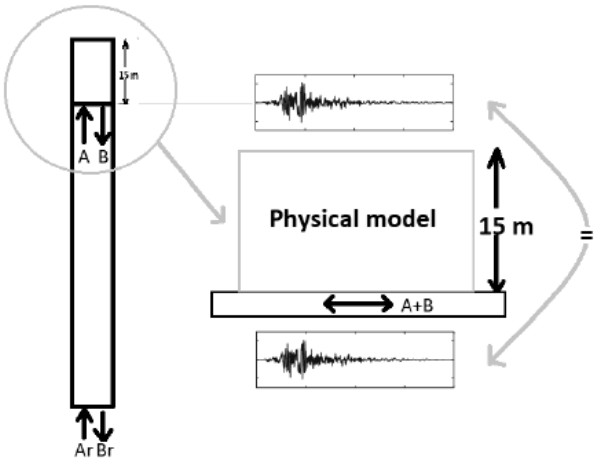

Figure 3.18. Soil system used to determine the input motions for centrifuge tests.

The Geological section provided by Minarelli et al. (2016) is presented in Figure 3.19, does not reach to engineering bedrock (V_s=800 m/s), thus in this work the bedrock level is taken as QM soil. Stratigraphy near of the test site is collected from the study of Minarelli et al. (2016) presenting the geological information (Paolucci et al., 2015) supported by also deep downhole investigations along a ~35 km-long segment in the Po Plain, starting from *Cento* and ending in Occhiobello. The closest distances from the test site to the investigation line and nearest deep downhole investigation are in the order of 2 and 5 kilometres, respectively (Özcebe et al. – unpub.).

Three sets of 7 spectrum-compatible rock outcrop motions were selected from accredited international strong-motion databases respectively for return periods of 475, 975, and 2475 years. These records were then deconvolved at the roof of seismic bedrock (in Pieve di Cento) and propagated through a soil profile in linear-equivalent ground response analyses up to a depth of 15 m below the ground surface. Finally, 4 shaking motions were chosen and

applied at the base of the centrifuge model after appropriate time scaling and after a correction that takes into account the transfer function of the dynamic actuator (Table 3.6).

Seismic motions are chosen considering the limitations due to the technical characteristics of the shaking table. In this particular case, the maximum frequency and acceleration values in flight have been limited to 500 Hz and 15g respectively. Those values correspond to 10 Hz and 0.3g at prototype scale. The computed time histories had all maximum acceleration values lower than 0.3g. On the other hand, the records contained a certain amount of information for f>10 Hz; thus, a low-pass filter was used to reduce the spectral information for higher frequencies.

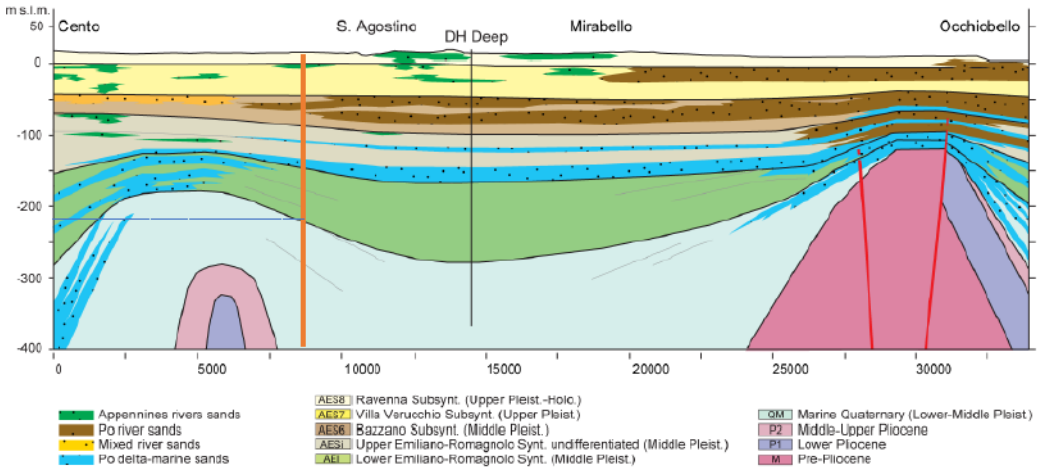

Figure 3.19. Geological stratigraphy of Po plan (after Paolucci et al., 2015; after Minarelli et al., 2016).

Full liquefaction of the models was achieved only with GM31, which was selected as reference input motion of the following test series. In some cases, to achieve liquefaction it was necessary to amplify GM31; the amplified versions of GM31 in the following are called GM31+ and GM31++.

Table 3.6. Input motions for centrifuge tests.

T_r (years)	ID (-)	M_W (-)	R_{ep} (km)	S_F (-)	Source file (-)	Model PGA (g)	f_p (Hz)
475	GM17	6.1	97.0	1.65	KiKnet EW2	5.0	500
975	GM23	5.9	10.1	2.39	ESM ACC	5.3	200
2475	GM31	6.9	62.9	1.33	ESN ACC	6.1	80
2475	GM34	6.93	28.6	0.59	NGA AT2	11.3	125

3.8 Centrifuge model configurations

Geotechnical centrifuge testing allows to analyse different geometrical configurations and soils profile with additions of some structures in depth and on the upper surface.

In this study, two soil profiles were tested in centrifuge, both simulating liquefiable sandy deposit about 15 m deep. After the positioning of the box in the centrifuge, the model saturation was realized by an application of the vacuum on the top and the injection of a viscous fluid through the bottom of the box. To observe the scale laws, a more viscous fluid was used to saturate the models. The viscosity must be N times more viscous than water where N is the ratio between the centrifugal acceleration and gravity one.

The position of ground water table was determined at the end of the spin-up phase through the data recorded by the pore pressure transducers.

Model 1 (M1) represented a homogeneous sand soil profile, *Model 2 (M2)* represented a homogeneous soil profile topped by a 1.5 m thick fine-grained layer of lower permeability (Pontida Clay). Figure 3.30 shows the basic configurations of the models with dimensions expressed for model (left) and prototype scale (right).

In some tests a simple structure founded on a shallow foundation was included in the model. This represented a single degree of freedom system (SDOF).

These three configurations without mitigation technique were tested in a first part of the testing programme aiming to evaluate the susceptibility to liquefaction, the dynamic response and the pore water pressure build-up of the system.

In the second part three different mitigation techniques were applied for each scheme aiming to evaluate their effectiveness. In the tests were used mitigation technique as: vertical drains, horizontal drains, induced partial saturation.

Vertical drains and horizontal ones were realised by silicon pipes with 6mm of external diameter and 5mm of internal one. These pipes were pierced on the lateral surface with 5mm of distance between two consecutive holes (Figure 3.20).

Figure 3.20. Silicon pipe for vertical and horizontal drains.

The permeability of the drains is equal to $1.49 \cdot 10^{-4}$ m/s and was evaluated by laboratory tests.

The arrangement of the drains in the centrifuge model was achieved using a steel needle that allowed to insert the drains in the soil, the lower end of the drains is closed (Figure 3.21).

Figure 3.21. Needle for the placement of vertical drains.

The model in centrifuge was realised installing vertical drains on a squared grid (Figure 3.22) with two different spacing-diameter ratios (s/d=5 and 10).

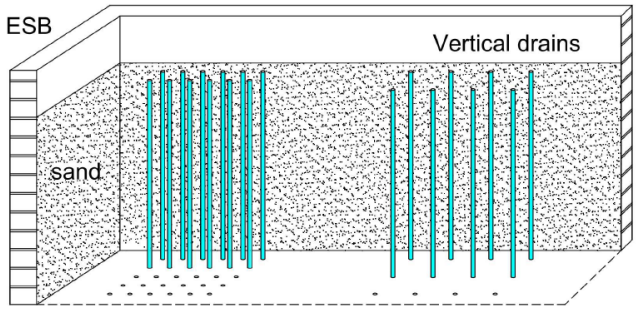

Figure 3.22. Dispositions for vertical drains

Horizontal drains were arranged in the model during the pluviation phase in subsequent layers from the bottom to the top. The length of the drains was equal to 225mm and the ends were connected to three horizontal header pipes with 12mm of diameter. These pipes ends were connected to two vertical cases filled by gravel and with the upper surface in contact with the atmosphere (Figure 3.23). This system allowed to dissipate the excess water pressure that raised in the drains during the shaking and reduced the disturbance of the vertical cases, since they were placed as far as possible from the centre of the model.

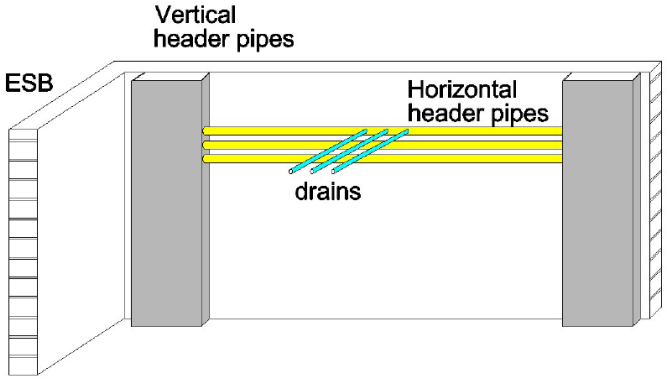

Figure 3.23. System for horizontal drains (Airoldi et al., 2018a).

Also, for the horizontal drains, two arrangement with different spacing-diameter ratios (s/d=5 and 10) were tested to study the effect of the geometry on the effectiveness of the mitigation technique.

Finally, the induced partial saturation (IPS) was implemented at the end of the spin-up phase by a system developed by ISMGEO. This procedure guaranteed the application of technique with lower disturbance of the soil due to the presence of a higher stress field similar to the in-situ one.

The IPS was applied by the injection of air in the soil model. The whole system was located in the centrifuge and was composed by two reservoirs of compressed air. A solenoidal valve allowed to control the air flow and a pressure transducer controlled the air pressure in the reservoirs (Figure 3.24).

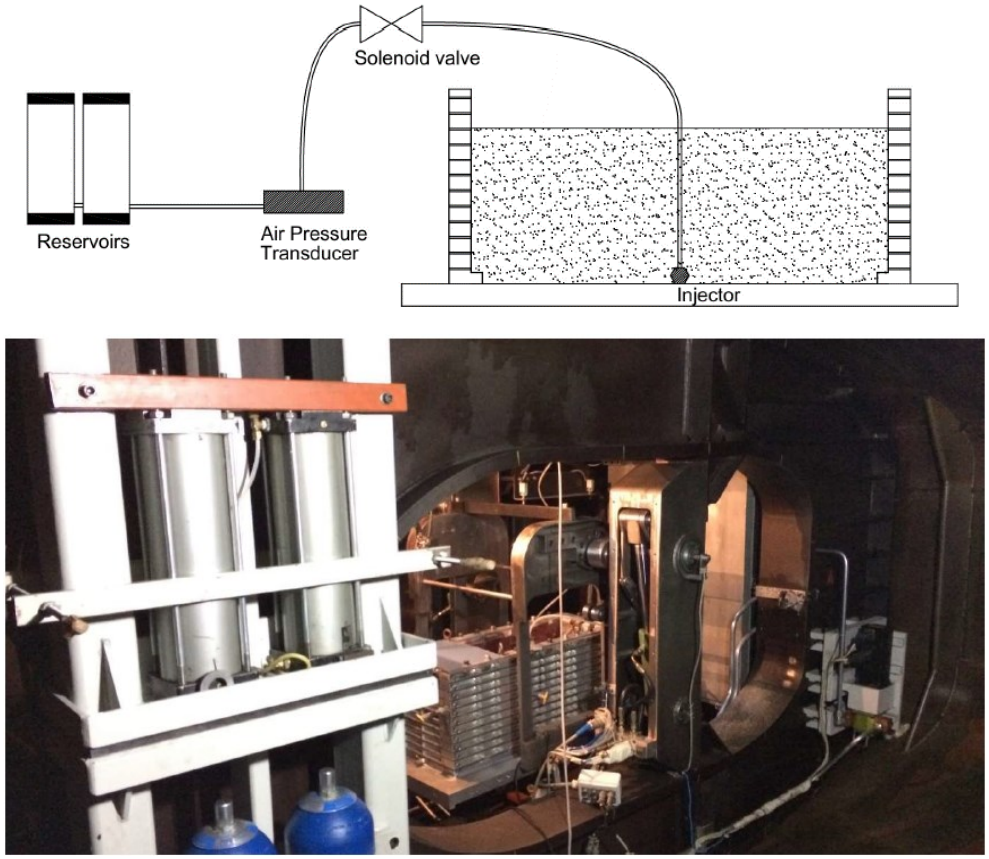

Figure 3.24. Induced partial saturation (IPS) system of ISMGEO (Airoldi et al., 2018b).

The air injection from the bottom of the model was applied by either one or four nuzzles, depending on the test layout. Each nuzzle had a diameter of 13mm with an injection surface equal to 133 mm^2. Nuzzles were deployed in the centre of the model in longitudinal direction (Figure 3.25).

Figure 3.25. Nuzzles for induced partial saturation.

3.9 Structure model for centrifuge tests

As previously mentioned, the structure is conceived as a single degree of freedom (SDOF) structure and is composed by an oscillating system on a shallow foundation composed by two aluminium beams rigidly connected by rigid bars to avoid relative rotation between beams. The foundations are embedded 3 cm (1.5 m at the prototype scale) from the ground surface. The oscillating portion is composed by two steel walls and a horizontal steel plate above these that represents a rigid beam that connects the walls and the mass of oscillating system. The oscillating portion is made by steel, the foundation is made by aluminium. The connections of the steel plates are by welding, the connections of the aluminium parts are by screws (Figure 3.26).

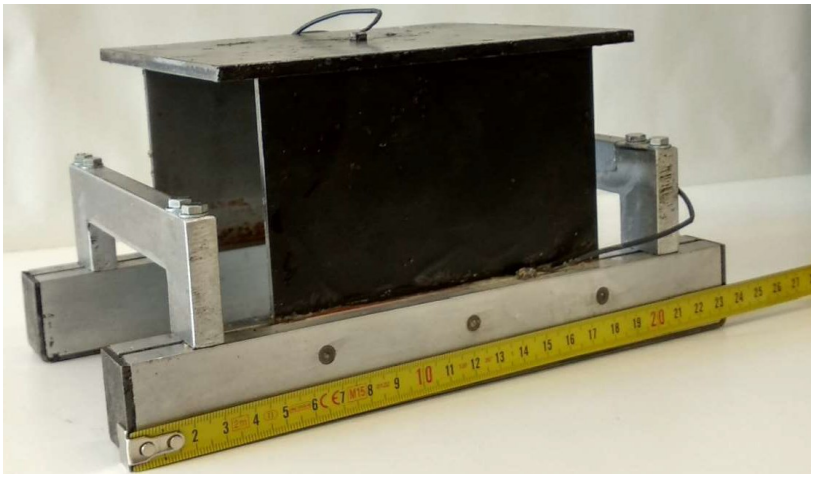

Figure 3.26. Structure used in centrifuge.

The structure is designed to reproduce the dynamic behaviour of the most common structures in towns near Reno river aiming to evaluate the soil-structure interaction on liquefiable soil. In this area, typical two stories masonry buildings are founded on shallow beams, that leaded to large differential settlements.

The dimensions of the manufactured model are reported in Figure 3.27, it has a mass of almost 2 kg and a natural frequency of 155 Hz at model scale (3.1 Hz at prototype scale). This frequency value has been measured by constraining the structure foundation on a fixed base and hitting the oscillating part. Two accelerometers installed on the oscillating part and the rigid base respectively registered the oscillation of the structure.

3.9.1 Structure design

The focalised study of liquefaction effects on the buildings near Reno river leads to design a structure for centrifuge tests that reflected the common structures that are in this region.

Table 3.7. Structure elements material.

Element	Material	E (MPa)	ρ (g/mm^3)	f_{yk} ($f_{0.2}$) (MPa)
1	Aluminium	70000	0.0027	215
2	Aluminium	70000	0.0027	215
3	Aluminium	70000	0.0027	215
4	Steel	210000	0.0078	275
5	Steel	210000	0.0078	275

As previously mentioned, the structure represents a dynamic system with single degree of freedom (SDOF) equivalent to two stories masonry building with shallow beams foundation. A sketch of the structure is shown in Figure 3.27 and Table 3.7 shows the materials and their mechanical properties adopted for each structural element whereas Table 3.8 shows the volume and mass of each element of the structure.

Table 3.8. Volume and mass of each structural element.

Element	Volume (mm^3)	m (g)
1	72220.00	195.00
2	18400.00	49.68
3	57200.00	154.44
4	85800.00	669.24
5	108000.00	842.40
	Total mass	1910.76

During an earthquake the interaction between soil and structure is governed by dynamic characteristics of the structure. A parameter that summarised the structure dynamic behaviour is the fundamental period. For a real structure, regular in plant and elevation, the fundamental period can be calculated by the empirical relationship proposed by Eurocode 8 (CEN, 2004):

$$T_{1p} = C_1 \cdot H^{3/4} \qquad (3\text{-}8)$$

where C_1 is a parameter as function of structural typology and H represents the height of the structure from the upper boundary of the foundation to the roof.

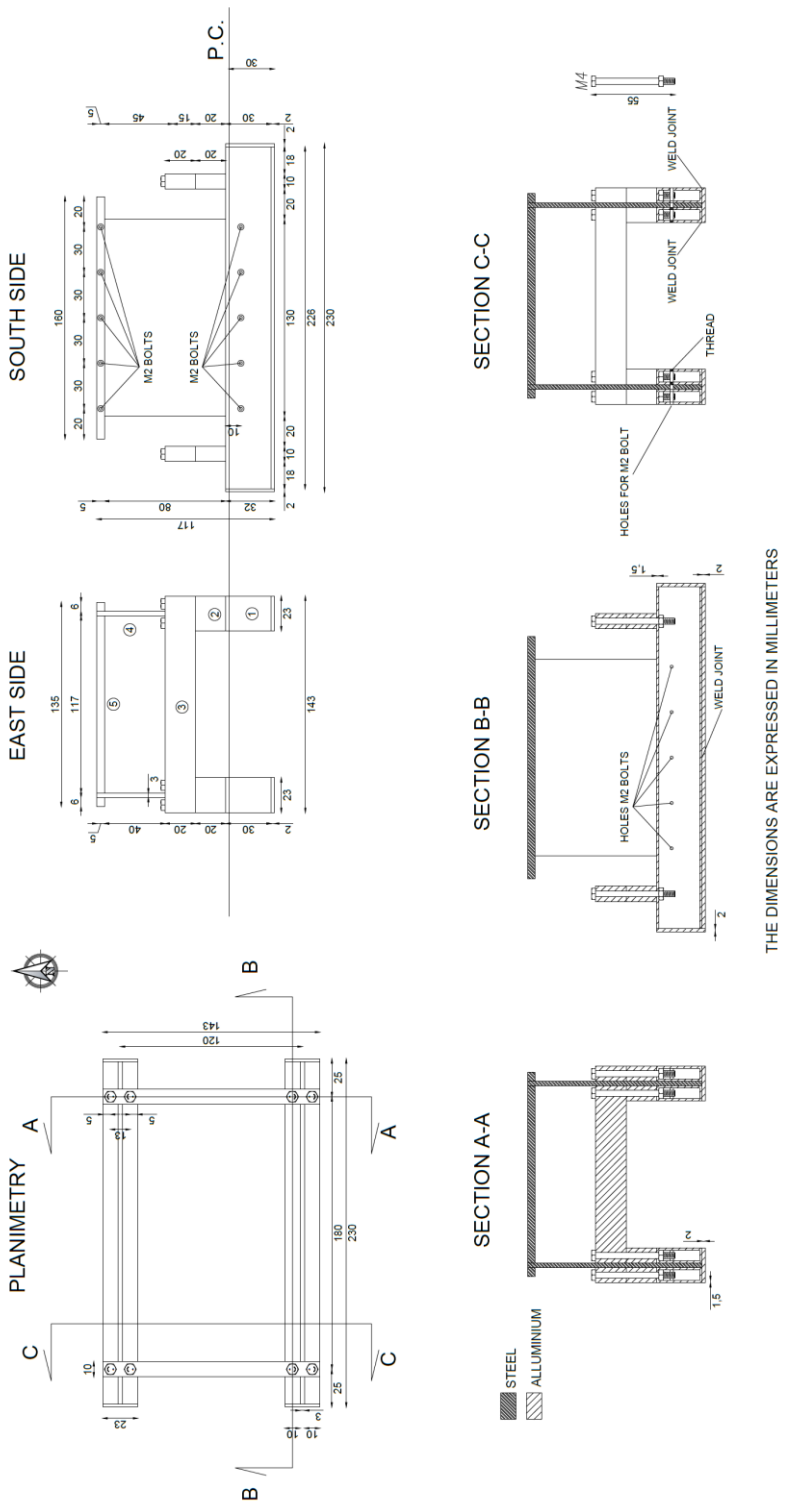

Figure 3.27. Structure dimensions.

For a two-storey masonry building, typical structure in Reno river region, these parameters are equal to:

$$C_1 = 0.05 \qquad H = 8.00\ m \tag{3-9}$$

That leads a fundamental period equal to:

$$T_{1p} = 0.238\ s \qquad f_{1p} = \frac{1}{T_{1p}} = 4.20\ Hz \tag{3-10}$$

At the model scale, with 50g centrifugal acceleration, the model period T_{1m} and the frequency f_{1m} so become:

$$n = 50g \qquad T_{1m} = \frac{T_{1p}}{n} = \frac{0.238}{50} = 0.00476\ s \tag{3-11}$$

$$f_{1m} = n{\cdot}f_{1p} = 210.22\ Hz \qquad \omega = 2\pi \cdot f_{1m} = 1320.88\ \frac{rad}{s} \tag{3-12}$$

where ω is the angular frequency.

In order to let the model structure have the frequency given by equation (3-12, it is necessary to assign proper and consistent values of the mass and of the flexural stiffness of the vertical walls of the structure.

3.9.1.1 Design of the SDOF mass

The mass was chosen consistently with the assumption of a two-storey masonry building. Assuming 10 kN/m^2 as average value of the overall unit load at each floor, and 70 square meters as a typical area of the floor at the prototype scale, it follows:

$$q = 10\ kPa \qquad area \cong 70\ m^2 \qquad no.\ of\ storeys = 2 \tag{3-13}$$

$$P_p = 1400\ kN \tag{3-14}$$

At the model scale:

$$P_m = \frac{P_p}{n^2} = \frac{1400}{50^2} = 0.56\ kN \qquad m_m = \frac{P_m}{n \cdot g} = \frac{0.56}{50 \cdot 9.81} \cdot 10^3 = 1.14\ kg \tag{3-15}$$

As usual in structural analysis, the structural mass (mass of the equivalent SDOF) is represented by the sum of the top mass and half mass of the free length of the two vertical walls:

$$m_m = \rho_{steel} \cdot \left[(L \cdot B \cdot w)_{head\ mass} + 2 \cdot \left(\frac{H_{free} \cdot B \cdot w}{2} \right)_{wall} \right] =$$
$$= 7800 \cdot \left[(0.160 \cdot 0.135 \cdot 0.005) + 2 \cdot \frac{(0.080 \cdot 0.130 \cdot 0.003)}{2} \right] = 1.09\ kg \tag{3-16}$$

In this pre-dimensioning the thickness of the walls is imposed to reach a mass as possible as nearer to the theoretical one. Noteworthy that the thickness of the walls modifies the

stiffness, so the dynamic behaviour of the system. Therefore, an iterative process is necessary to reach the design value of the fundamental period.

3.9.1.2 Design of walls stiffness

Fundamental period is a function of mass and stiffness. In this case the mass is calculated following the previously section and the stiffness of the vertical steel walls governs the dynamical behaviour of the system.

For a SDOF the angular frequency can be calculated by:

$$\omega = \sqrt{\frac{k}{m}} \tag{3-17}$$

Since the walls top and base are fixed (i.e. no relative rotation is allowed), the flexural stiffness of walls is:

$$k = 2 \cdot \frac{12EI}{H_{free}^3} \tag{3-18}$$

where E is the Young modulus of steel and I is the moment of inertia of the wall section.

The thickness of the walls is equal to 3mm and the H_{free} is 95mm, so the angular frequency of the system is:

$$\omega = \sqrt{\frac{k}{m}} = 1232.78 \frac{rad}{s} \tag{3-19}$$

this value is very close to the theoretical one reported in the equation (3-12.

Finally, the increasing of the centrifugal acceleration during the spin-up generates an increase of the static load on the structure. Therefore, a check of a buckling is necessary due the small thickness of the walls. The check was carried out following the EC7 indications:

$$N_{b,Rd} = \chi \cdot N_{pl,Rd} \tag{3-20}$$

where $N_{b,Rd}$ is the axial strength of the element to the instability, $N_{pl,Rd}$ is the axial plastic strength of the element and χ is the instability factor defined as following:

$$\chi = \frac{1}{\Phi + \sqrt{\Phi^2 - \bar{\lambda}^2}} \leq 1.0 \tag{3-21}$$

Φ is a factor that takes into account the geometrical imperfections of the element:

$$\Phi = 0.5\left[1 + \alpha\left(\bar{\lambda} - 0.2\right) + \bar{\lambda}^2\right] \tag{3-22}$$

α is a factor depending on the material and in this case is equal to 0.49 and $\bar{\lambda}$ is the dimensionless slenderness:

$$\bar{\lambda} = \sqrt{\frac{N_{pl,Rk}}{N_{cr}}} \tag{3-23}$$

N_{cr} is the critical axial force (Eulerian solution):

$$N_{cr} = \frac{\pi^2 EI}{L_0} \quad (3\text{-}24)$$

Finally, L_0 is the inflectional free length of the element, that in the case with both fixed ends, is equal to:

$$L_0 = \frac{L}{2} \quad (3\text{-}25)$$

Numerical values of the buckling check are shown in Table 3.9.

Table 3.9. Buckling check of the vertical walls of the structure.

L_0 (mm)	Area (mm^2)	I (mm^4)	N_{cr} (N)	λ (-)	Φ (-)	χ (-)	$N_{b,Rd}$ (N)	$N_{inst,Ed}$ (N)	R_d/ E_d (EC7) (-)
40	390	195.00	378900.28	0.53	0.72	0.82	80428.60	268.58	299.46

The response of the check is positive; therefore, the buckling failure is not possible for axial force.

3.9.1.3 Foundation sizing and bearing capacity

The shallow beams foundation permitted to study the same typology of the foundations in the Reno river region and allowed to study the rising of differential settlement during the liquefaction phenomenon triggering.

In order to achieve significant absolute and differential settlements during the centrifuge tests, the shape and width of the foundation beams were designed to have a low safety factor in liquefaction conditions.

Increasing of the centrifugal acceleration, the stress on the soil below the foundation beams increases and reaches the value reported in Table 3.10.

Table 3.10. Stress below the foundation beams.

P (kN)	Contact area (m^2)	q_{es} (kN/ m^2)
0.54	0.00529	123.37

The bearing capacity is a function of the soil and peak friction angle that depends on the relative density of the sand. Therefore, a range of relative density was chosen to check the bearing capacity of the structure. Ticino sand and relative densities equal to 40% and 65% were considered in the calculations.

The values of the peak friction angle and the vertical stress at depth of the lower face of the foundation plus half width of the foundation base for both relative densities to calculate the bearing capacity are shown in Table 3.10.

Table 3.11. Peak friction angle and vertical stresses for bearing capacity calculation.

D_r (-)	φ_{cs} (°)	φ_p (°)	σ_v' (kN/m^{2}°)
0.40	33.2	33.9	11.56
0.65	33.2	36.0	12.39

where φ_p is evaluated by:

$$\varphi_p = \varphi_{cv} + \frac{N_{1,60}}{10} + \max\left(0; \frac{N_{1,60} - 15}{5}\right) \quad with \quad N_{1,60} = 46\, D_r^2 \qquad (3\text{-}26)$$

During an earthquake, the pore pressure builds up and consequently the bearing capacity safety factor decreases. This effect was valued using an equivalent decrease of the friction angle, function of the excess water pressure ratio (r_u), as suggested by Cascone and Bouckovalas (1998).

Table 3.12. Bearing capacity of the structure on liquefiable soil at 40% relative density.

r_u (-)	φ_{eq} (°)	N_q (-)	N_γ (Vesic) (-)	q_{lim} (kN/m^2)	R_d/E_d (EC7) (-)	Sefety factor (-)
0.0	33.94	29.21	40.66	420.98	3.41	6.45
0.2	28.29	15.20	17.45	205.73	1.67	3.15
0.3	25.22	10.91	11.22	143.00	1.16	2.19
0.5	18.60	5.57	4.42	68.30	0.55	1.05
0.7	11.41	2.82	1.54	32.01	0.26	0.49

Table 3.13. Bearing capacity of the structure on liquefiable soil at 65% relative density.

r_u (-)	φ_{eq} (°)	N_q (-)	N_γ (Vesic) (-)	q_{lim} (kN/m^2)	R_d/E_d (EC7) (-)	Sefety factor (-)
0.0	36.03	37.90	86.59	600.25	4.87	9.20
0.2	30.19	18.81	23.06	278.52	2.26	4.27
0.3	26.98	13.17	14.43	188.44	1.53	2.89
0.5	19.99	6.39	5.38	85.12	0.69	1.30
0.7	12.31	3.06	1.77	37.67	0.31	0.58

According to EC7 (i.e. considering the partial factors introduced by the code), the calculations reported in the tables predict the attainment of bearing capacity for Ru=0.5. Without considering the partial coefficients of EC7 (i.e. considering the most likely realistic forces and resistances, in this peculiar and well controlled environment), bearing capacity failure is attained for Ru=0.7.

A partial undrained process leads to the failure for bearing capacity; therefore, a check of the punching failure is necessary (Table 3.14 and Table 3.15).

Table 3.14. Punching failure of the structure on liquefiable soil at 40% relative density.

r_u (-)	G (kN/m^2)	I_r (-)	$I_{r,max}$ (-)	ψ (-)	R_d/E_d (EC7) (-)	Safety factor (-)
0.0	412.69	33.7	225.96	0.40	1.37	2.60
0.2	330.15	33.7	116.24	0.59	0.98	1.85
0.3	288.88	33.7	84.61	0.69	0.80	1.52
0.5	206.34	33.7	46.35	0.90	0.50	0.94
0.7	123.81	33.7	26.70	1.00	0.26	0.49

Table 3.15. Punching failure of the structure on liquefiable soil at 65% relative density.

r_u (-)	G (kN/m^2)	I_r (-)	$I_{r,max}$ (-)	ψ (-)	R_d/E_d (EC7) (-)	Safety factor (-)
0.0	512.66	36.13	298.67	0.35	1.71	3.24
0.2	410.13	36.13	143.57	0.54	1.22	2.31
0.3	358.86	36.13	101.16	0.65	1.00	1.88
0.5	256.33	36.13	52.15	0.88	0.61	1.15
0.7	153.80	36.13	28.47	1.00	0.31	0.58

where the value of shear modulus (G) in function of the mean effective stress was evaluated by the following relationship:

$$G = \alpha^* \, p_{atm} \frac{(2.97 - e)^2}{1 + e} \left(\frac{p'}{p_{atm}} \right)^{0.5} \qquad (3\text{-}27)$$

where α^* is found by monotonic triaxial tests on Ticino sand at initial effective mean stress of 50 kPa taking to account the secant value at a one third of the maximum deviatoric stress. This parameter assumes the value 3.29.

The foundation design aimed to have a low safety factor during the earthquake, so in pore pressure build-up condition, to achieve significant settlements. In this way it is possible to study the consequents of liquefaction on the foundation.

3.9.1.4 Overturning of the structure

The overturning check consists in the ensuring the rotational equilibrium of the structure assumed as a rigid body. The overturning is avoided if the stabilising moment is higher than the destabilising one. This comparison can be done also between maximum lateral acceleration at the structure roof that leads to overturning (critical lateral acceleration) and the maximum lateral acceleration at the structure roof that may be applied during earthquake evaluated in free-field condition.

In the Table 3.16 is calculate the critical lateral acceleration that can be compared with the acceleration induced on a SDOF by the signals used in the centrifuge tests (Figure 3.28).

Table 3.16. Rotational equilibrium for overturning check and critical acceleration.

$d_{destab.}$ (m)	$d_{stab.}$ (m)	$M_{Rd} = M_{Ed}$ (FS=1) (N·m)	Critical acceleration (g)
0.1025	0.0715	69.78	74.89

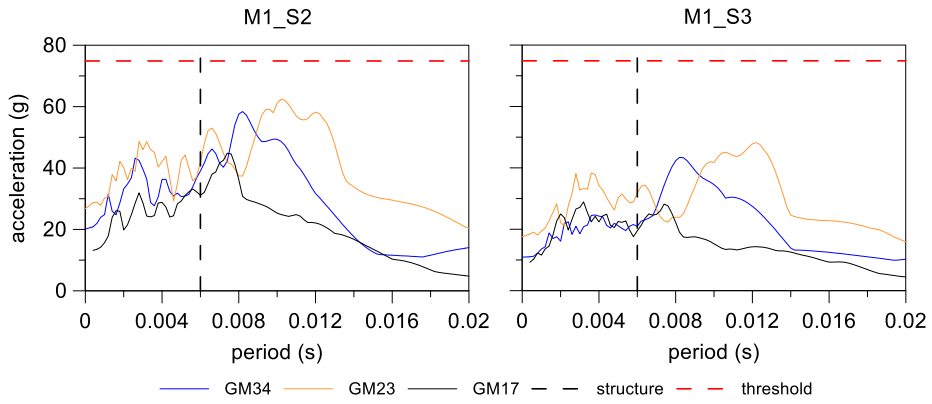

Figure 3.28. Overturning check on the fundamental period of the structure.

Observing the Figure 3.28, it is possible to see that the critical lateral acceleration is higher than the maximum lateral acceleration applied by earthquakes, so the structure are not subjected to the overturning.

3.9.2 Check of dynamic properties of structure

Assembled all parts of the structure, a check of its dynamic properties was performed. First of all, the system was weighted and the weight was almost 2 kilograms. This light difference between theoretical value (Table 3.8) and the real weight is likely due to a nominal density for the materials.

The fundamental period of the structure was determined by a free vibrational test. Foundation beams were fixed to a rigid support and the roof of the structure was hit by a hammer. Two accelerometers were applied one on the base and other one on the roof of the structure. The recordings allowed the fundamental period of the structure to be calculated by using the amplification functions. Eleven tests were carried out and 155 Hz of mean fundamental frequency is found in model scale. An example of the amplification function is shown in Figure 3.29.

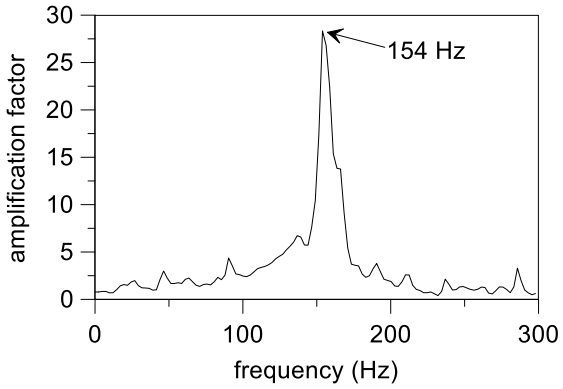

Figure 3.29. Amplification function for test n.5 on the structure.

The fundamental frequency of 155 Hz in prototype scale, in centrifuge tests at 50g, is equal to:

$$f_{structure,p} = \frac{f_{structure,m}}{n} = \frac{155}{50} = 3.1\ Hz \qquad (3\text{-}28)$$

hence the fundamental period is equal to:

$$T_{structure,p} = \frac{1}{f_{structure,p}} = \frac{1}{3.1} = 0.32\ s \qquad (3\text{-}29)$$

This value is higher than theoretical one that is equal to 0.26 s. This result may be due to a difference between the theoretical rigid constraints and the real constraints that could be more compliant.

3.10 Response without mitigation techniques

In this section the results of the centrifuge tests without mitigation techniques carried out at ISMGEO are reported and interpreted. The results in terms of acceleration, excess water pressure and displacement are presented for convenience at the prototype scale.

Dry pluviation technique was used to create the model layer with a homogeneous distribution of the sent with depth. An acceleration time history was applied on flight at the base of the ESB container through the shaking table installed in the centrifuge.

The tests intended to be carried out under the same theoretical input motion, were actually subjected to slightly different shakings due to the transfer function used for the shaking table that was modified from test to test, depending on the actual model mass. Therefore, a direct comparison between tests is not completely exhaustive and numerical analyses are necessary to better compare the results.

3.10.1 Single layer model (M1_S1_GM31)

This test was performed aiming to study the water pressure build-up in free-field conditions. Four accelerometers and six pore pressure transducers were deployed in the sand, during deposition, thus creating two vertical arrays to measure the accelerations and the pore pressures along the vertical section. The settlements of the ground surface were recorded by two displacement transducers, a plate was applied beneath their tip to avoid punching. In Figure 3.30 the dimensions of the centrifuge model are shown (a) also at the corresponding prototype scale (b). The relative density after spin-up phase was equal to 45.5%.

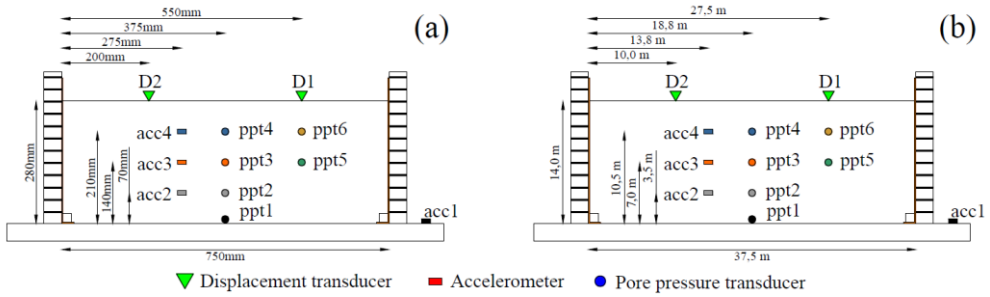

Figure 3.30. M1_S1_GM31: model scale (a) and prototype scale (b).

The acceleration time histories (Figure 3.31) and the amplification functions (Figure 3.33) show a light amplification in acc2 and a progressive deamplification toward the ground surface (acc3 and acc4). The propagation of the signal from the bottom to the top of the soil profile and the progressive increment of the excess pore pressure decrease the amplitude and frequency of the signal. This effect is due to the corresponding reduction of the effective stresses, hence of the shear stiffness of the soil. The main time interval of the signal, valuated by intensity factor in the interval 5-95% (ARIAS A, 1969), is shown on the right of the Figure 3.31.

Figure 3.32 shows that the significant frequency content of the input signal is within 10 Hz, with the largest peak at around 1 Hz.

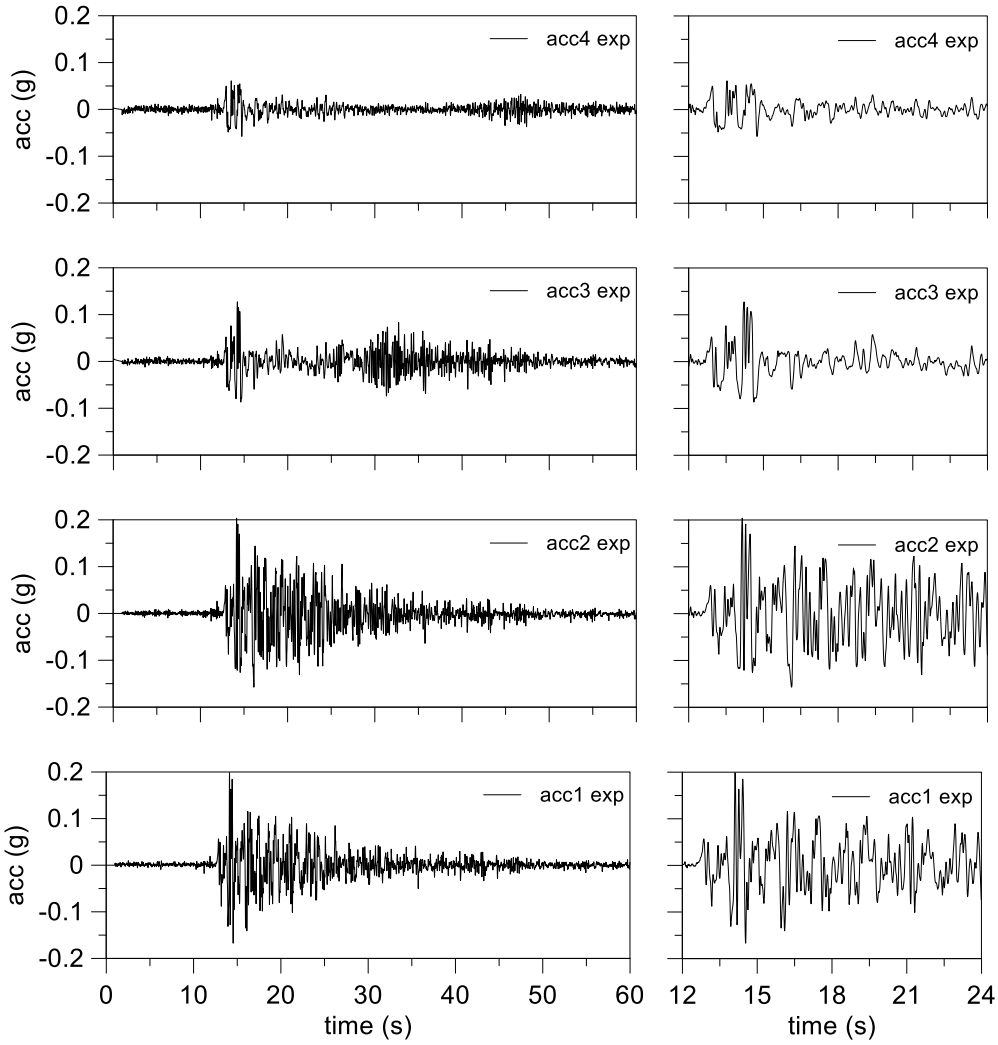

Figure 3.31. M1_S1_GM31: main time interval of acceleration time histories.

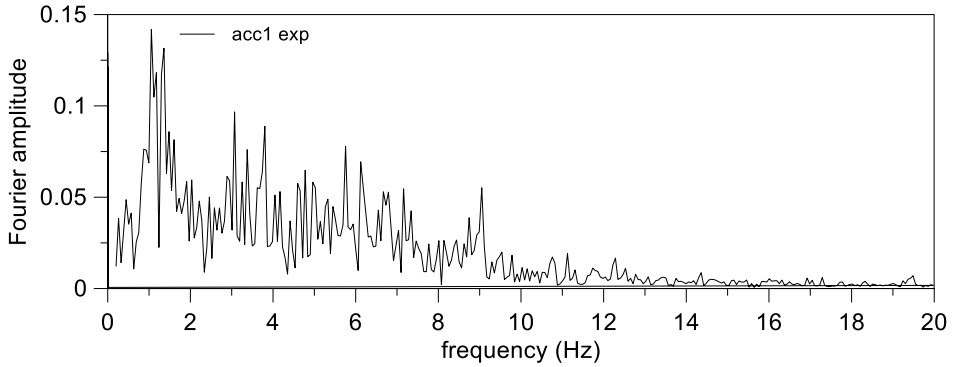

Figure 3.32. M1_S1_GM31: Fourier spectrum of the input signal.

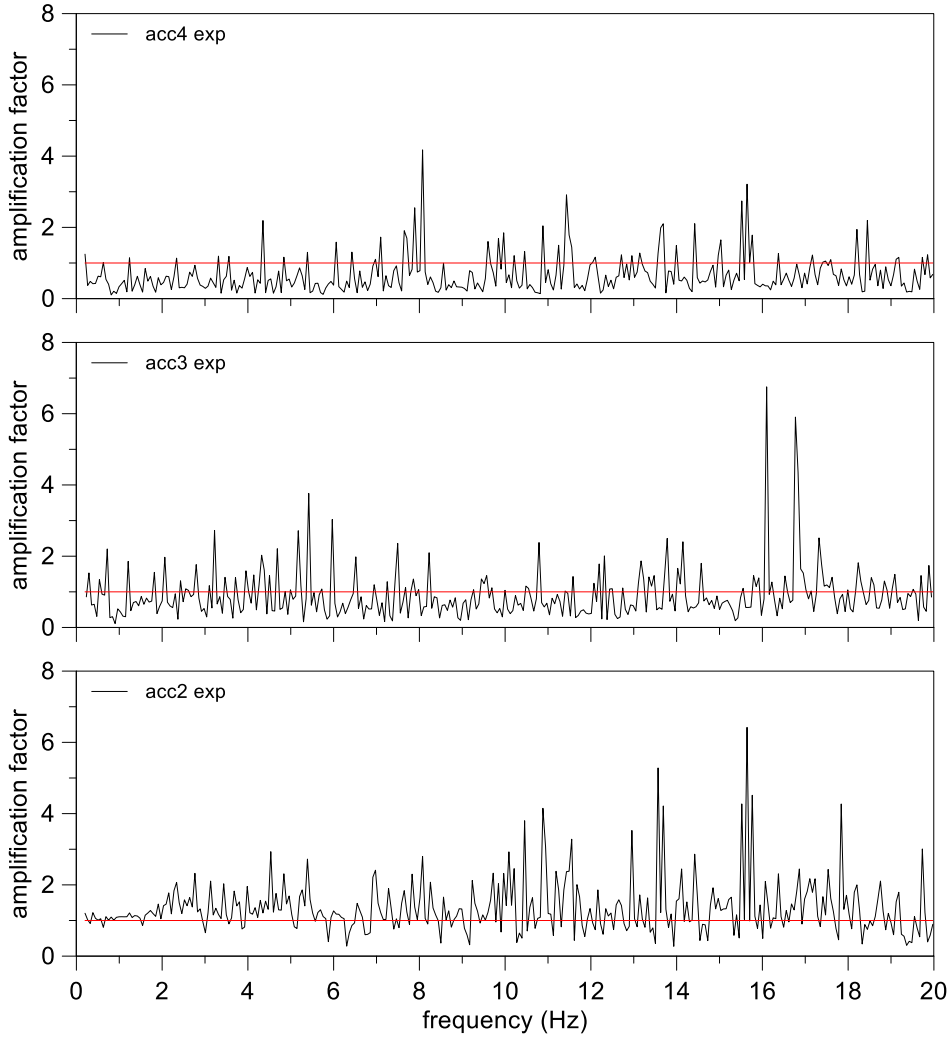

Figure 3.33. M1_S1_GM31: amplification functions.

The progressive build-up of excess pore water pressure is shown in Figure 3.34. The deeper ppt1 and ppt2 recorded the larger value of excess water pressure. The pore pressure transducers from 3 to 6 show a lower value but with a horizontal threshold that identifies the reaching of the liquefaction namely the equilibrium between total vertical stress and pore water pressure.

The liquefied status of the soil near the pore pressure transducers from 3 to 6 persists beyond the main part of the motion. Indeed, in this part of the model the excess water pressure is preserved by two mechanisms: low build-up of water pressure; significant water flow from the bottom to the upper seepage surface.

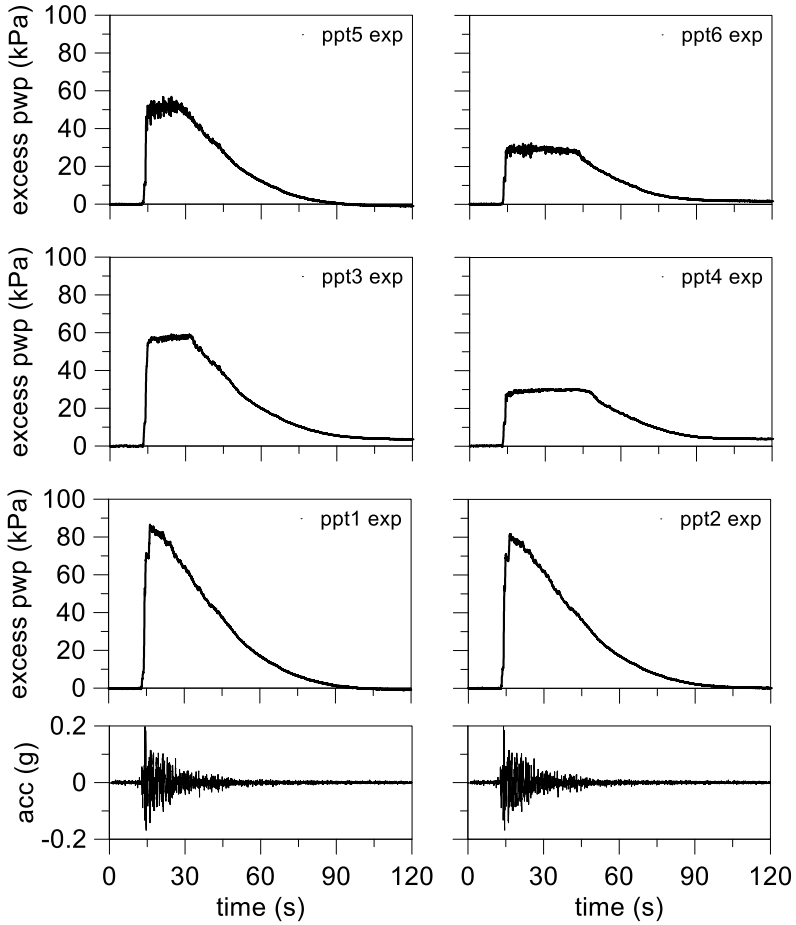

Figure 3.34. M1_S1_GM31: excess pore water pressure time histories.

In Figure 3.35 are reported the acceleration time histories at the bottom and top of the model respectively and the time history of excess pore water pressure at the top of the model. It is noteworthy that significant excess water pressure raised earlier of the acceleration peak where the maximum value of excess water pressure is recorded.

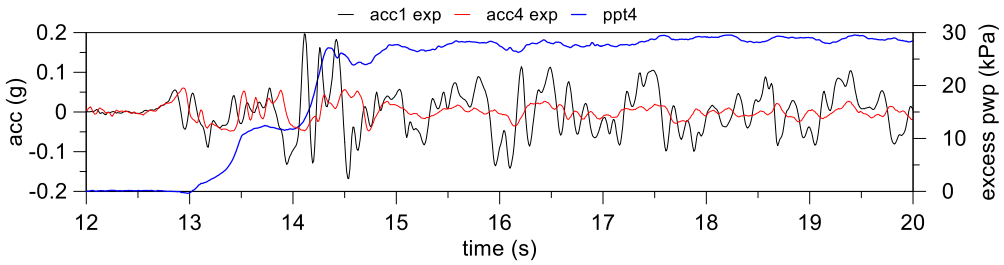

Figure 3.35. M1_S1_GM31: amplitude and frequency reduction due to excess water pressure build-up.

The amplitude of the acceleration signals is the same in the initial part of the shaking, until a reaching of a significant excess water pressure. Indeed, a large reduction of the

amplitude starting from 14 seconds. This effect reduces potential inertial forces on buildings founded on the ground surface but could lead to significant settlements.

The different distribution of the shear stress during the motion and the different liquefaction strength due to the different confining stresses along the model depth lead to a variable distribution of the excess pore pressure with depth. Vertical profiles of excess water pressure in the build-up phase and in the dissipation phase are shown on the left and right of Figure 3.36 respectively.

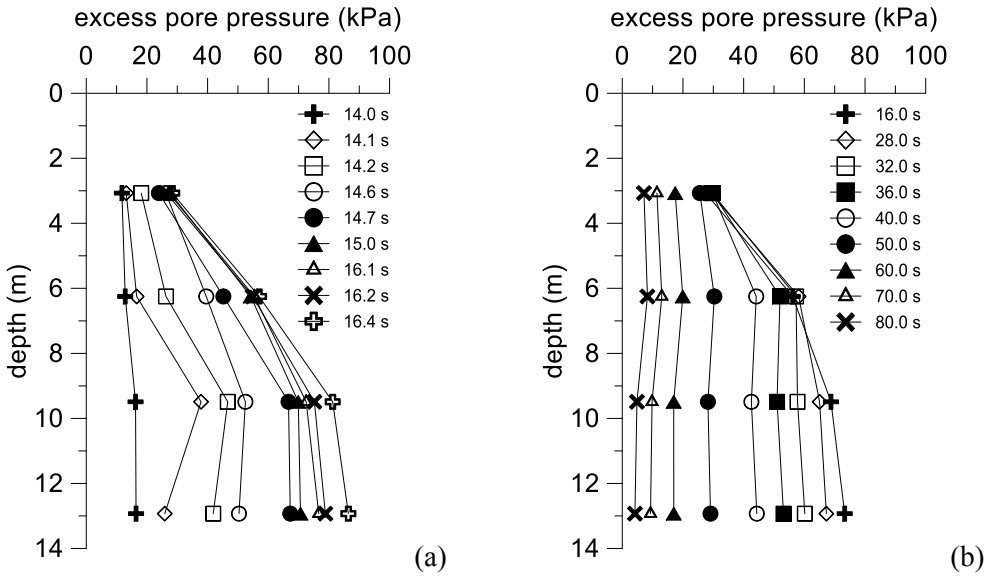

Figure 3.36. M1_S1_GM31: vertical profiles of excess pore water pressure time histories for build-up phase (a) and dissipation phase (b).

The excess water pressures increase faster in the deep part of the soil layer than in the shallow one but, as previously seen in Figure 3.34 liquefaction was achieved the in shallower part. The shape of the excess water pressure distribution suggests a flow of water from the bottom to the upper seepage surface. During the dissipation phase, this water flow preserves the maximum value of excess water pressure in the shallowest part of the soil. This phenomenon lasts until to the deeper part of the domain has the same value of excess water pressure recorded on the lower part of the liquefied soil (point at 6m depth in Figure 3.36b).

As previously mentioned, the time history of the settlement was recorded through the two displacement transducers deployed on the ground surface. The development of the settlement in time is shown in Figure 3.37. It is possible to note a slight difference between the two transducers. Large settlements were observed in the strong part of the input signal. This result could be due to two likely mechanisms: partial drainage behaviour of the soil during the strong motion; punching of the plates located on the tip of the displacement transducers.

Neglecting the punching effect, the settlement is due to the reconsolidation of the soil. Under this hypothesis, considering the thickness of liquefied soil equal around 10m, the mean volumetric strain in the soil is estimate in 2.5%. This value falls within the range of

1% - 4% suggested by Lee and Albaisa (1974). Therefore, it is likely that the punching of the plates under the displacement transducers did not occur, or it is very limited.

The amount of the displacement measured after the strong motion, in this case, is within the range from 20% to 30% of the total settlement. These results highlight that the estimates of the settlements by simplified approaches are possible, but the larger part of the settlement is developed during the strong motion, rather than afterwards.

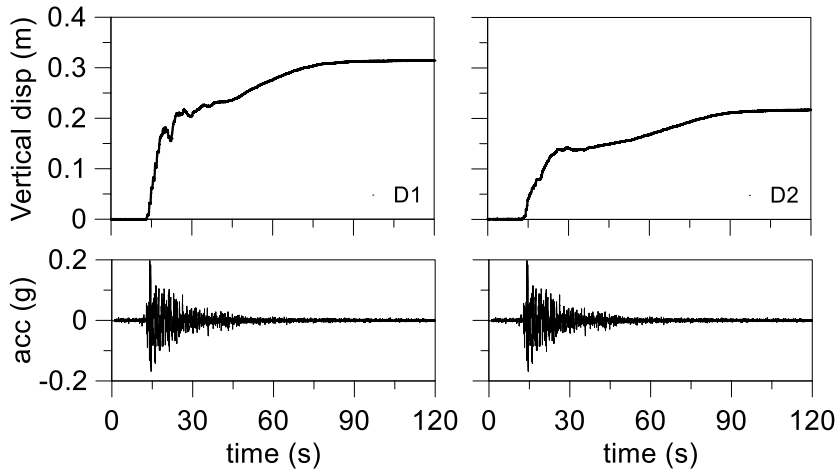

Figure 3.37. M1_S1_GM31: ground surface displacement time histories.

3.10.2 Double layer model (M2_S1_GM31)

This test was performed aiming to study the water pressure build-up in free-field conditions, in presence of an upper low-permeability crust layer. This was formed by Pontida clay with 1.5 m thickness. The clay crust was made by the 1-D consolidation of a clay mud under 10kPa vertical stress. Six accelerometers and five pore pressure transducer were deployed during the sand deposition. The sixth pore water pressure transducer was included in the clay prior to its consolidation. The accelerometers and pore pressure transducers created two vertical arrays to measure the accelerations and the pore pressures along the vertical section. The settlements of the ground surface were recorded by two displacement transducers, a plate was applied on extremity of these to avoid punching.

In Figure 3.38 the dimensions of the centrifuge model are shown (a), also at the prototype scale (b). The relative density after spin-up phase was equal to 50.5%.

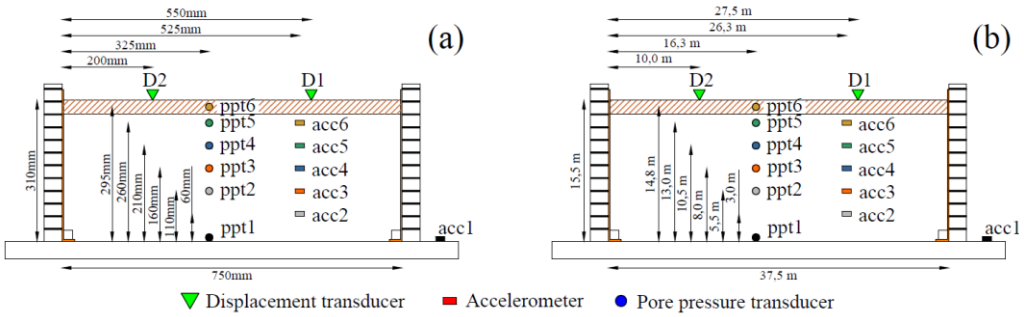

Figure 3.38. M2_S1_GM31: model scale (a) and prototype scale (b).

The acceleration time histories measured during the seismic excitation are shown in Figure 3.39. The measures from accelerometers acc3 and acc5 are not shown because they did not work. The amplification functions (Figure 3.41) show a slight amplification at acc2, a larger amplification at acc4 and a deamplification at acc6. As previously seen for the homogeneous soil profile, in this case a larger reduction of the amplitude and frequency of the signal is shown by the shallowest accelerometer (acc6). The main time interval of the signal, evaluated by an intensity factor in the interval 5-95% (ARIAS A, 1969), is shown on the right of Figure 3.39.

Figure 3.40 shows that the significant frequency content of the input signal falls within 10 Hz with largest peaks included in the interval between 1-6 Hz. It is noteworthy that this test has the same theoretical input motion of M1_S1_GM31 test, but the maximum Fourier amplitude in this case is equal to about 0.09, hence significantly lower than the amplitude reported in Figure 3.32, equal to about 0.14. Furthermore, the frequencies content is very different. Therefore, a direct comparison between the centrifuge tests results is not sufficient for the purposes of this thesis and a numerical simulation is required.

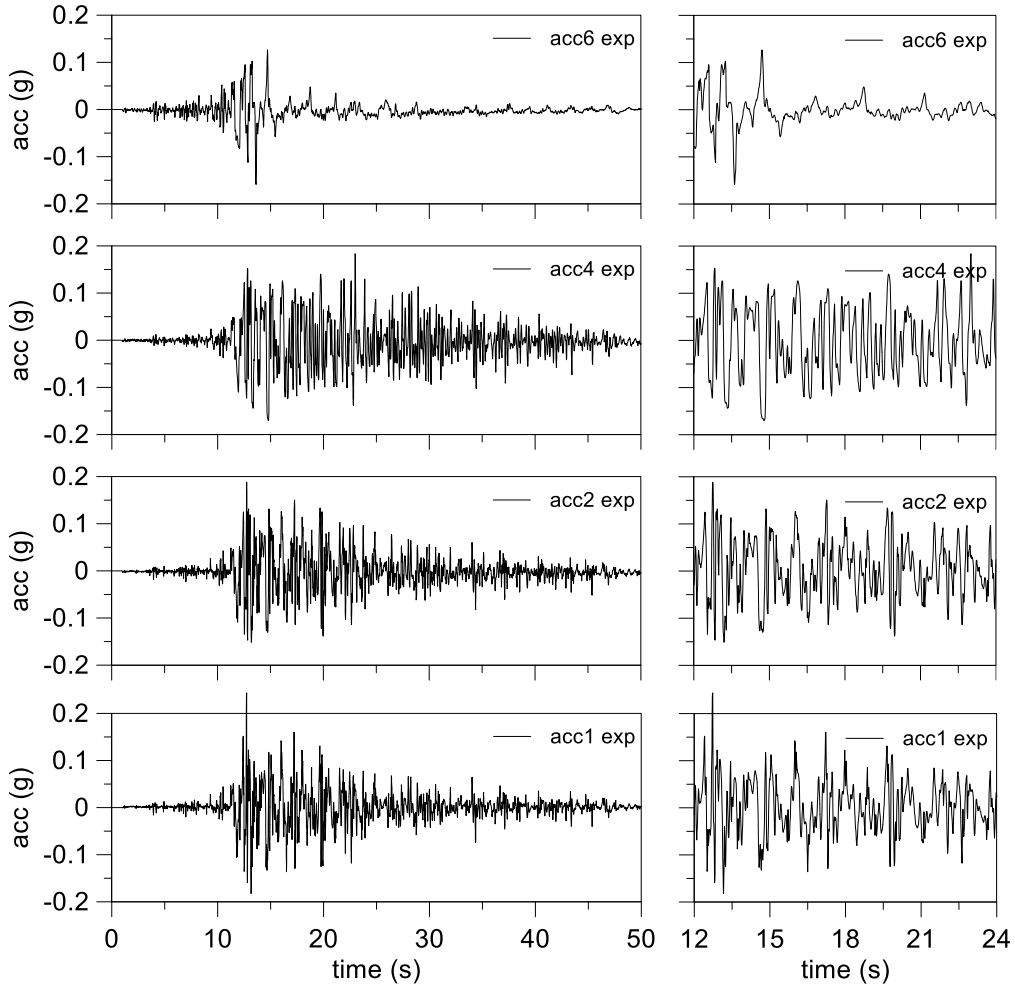

Figure 3.39. M2_S1_GM31: main time interval of acceleration time histories.

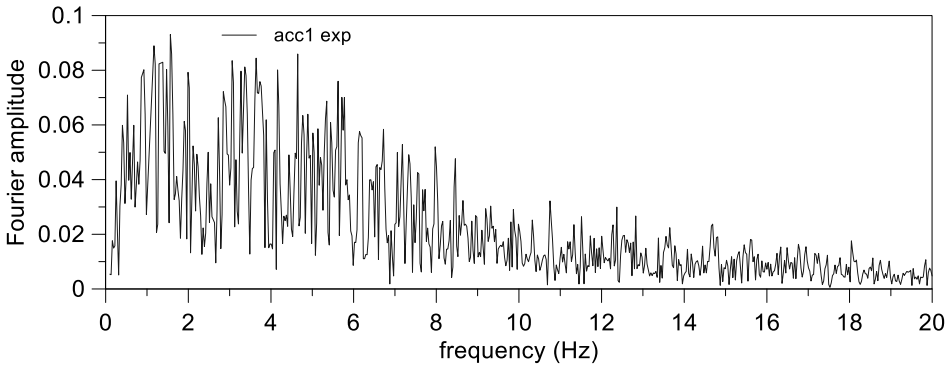

Figure 3.40. M2_S1_GM31: Fourier spectrum of the input signal.

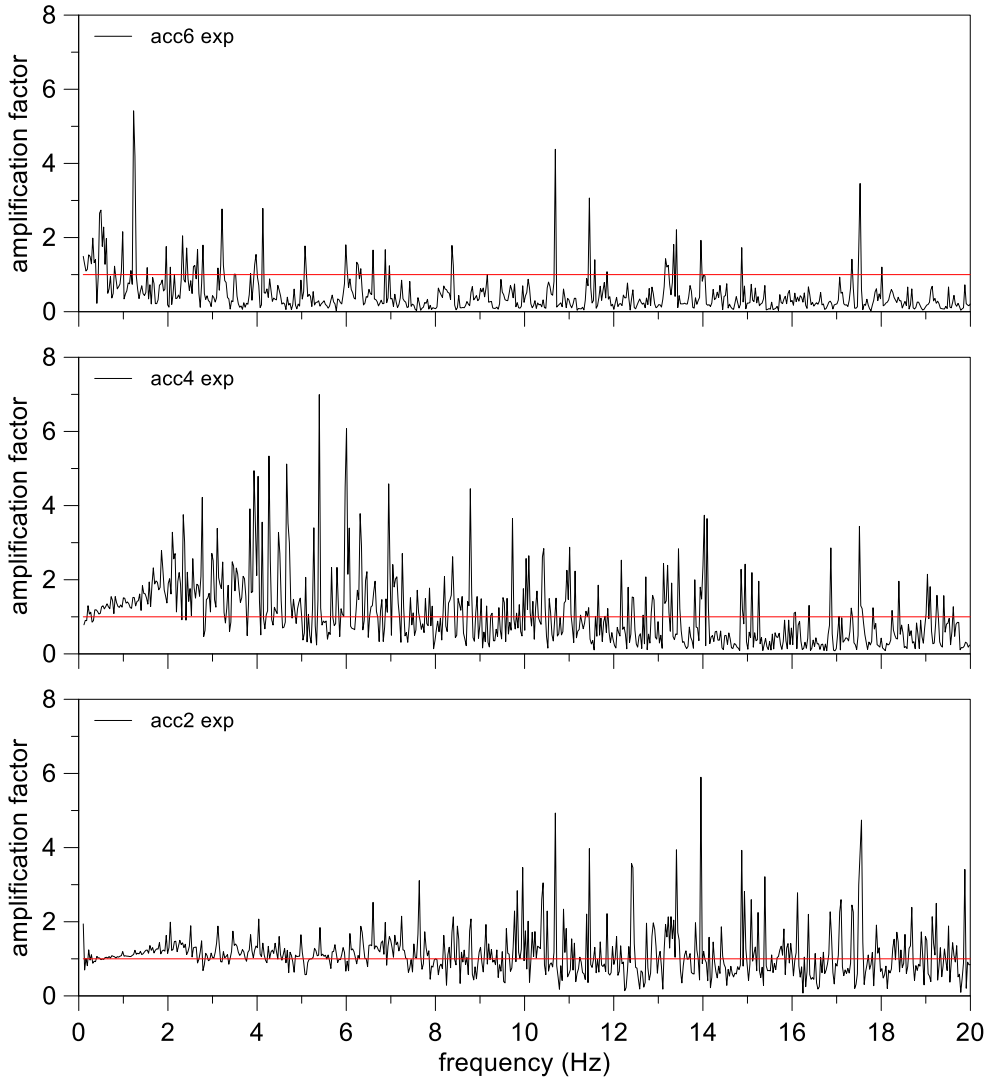

Figure 3.41. M2_S1_GM31: amplification functions.

The progressive build-up of excess pore water pressure is shown in Figure 3.42. The ppt2 was broken, ppt1 and ppt3 achieved the higher values of the excess water pressure. The ppt 4 reached a horizontal threshold, indicating soil liquefaction condition, while the ppt5 shows a strange path maybe due to the presence of the crust that could be subjected to either uplift in presence of a large water pressure on the its lower surface or cracking on top of the model. The latter event allows the seepage of the water from the sand to the ground level reducing the excess pore water pressure.

The liquefied status of the soil near the pore pressure transducers 4 and 5 persists beyond the main part of the motion. Indeed, in this part of the model the excess water pressure is preserved by two mechanisms: low build-up of water pressure; significant water flow from the bottom to the upper seepage surface.

Finally, the pore pressure transducer in the clay did not measured any excess water pressure. This result may be due either to the nature of the soil (Pontida clay), that show a low water pressure build-up for shear strains, or to a low readiness of the transducer.

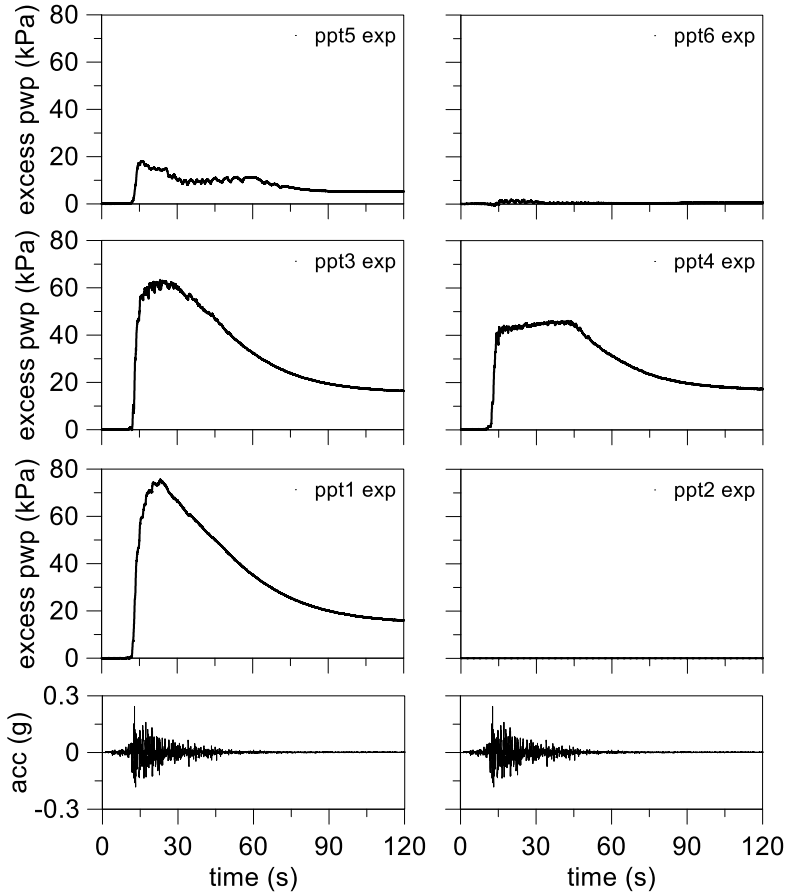

Figure 3.42. M2_S1_GM31: excess pore water pressure time histories.

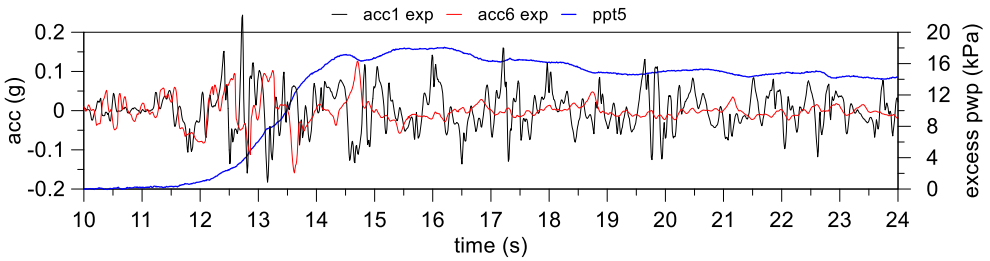

Figure 3.43. M2_S1_GM31: amplitude and frequency reduction due to excess water pressure build-up.

As previously mentioned, the signal deamplification in acc6 is justified by the occurrence of liquefaction. Figure 3.43 shows clearly that the reduction of the amplitude and frequency of the signal in acc6 occurred in correspondence of a large excess pore pressure build-up.

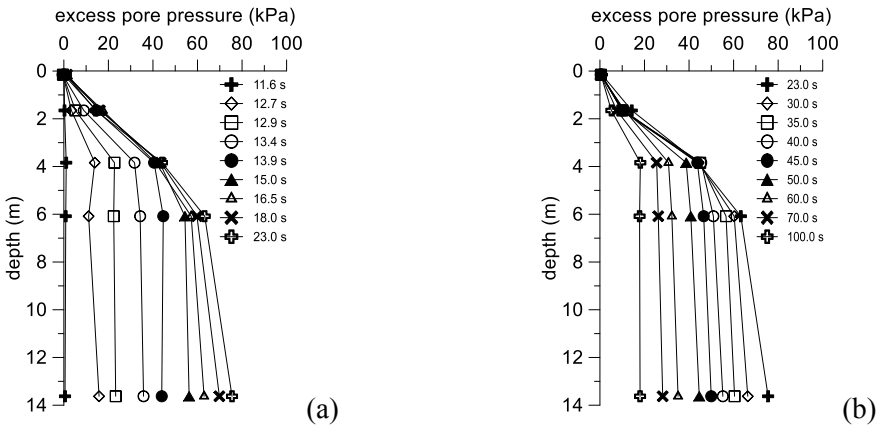

Figure 3.44. M2_S1_GM31: vertical profiles of excess pore water pressure time histories for build-up phase (a) and dissipation phase (b).

The vertical profiles in Figure 3.44a show a fast excess pore pressure build-up in the lower part of the model and the linear distribution of excess pore pressure suggests that the liquefaction occurred in upper part of the model. Figure 3.44b shows that in the dissipation phase there is an anomaly in the distribution immediately below the crust (around 2m depth): a fast dissipation was recorded in this area. As previously mentioned, this effect maybe due to either a break or uplift of the crust. However, the dissipation phase was slower than the model without crust, indicating an effect of the lower permeability of the upper crust soil.

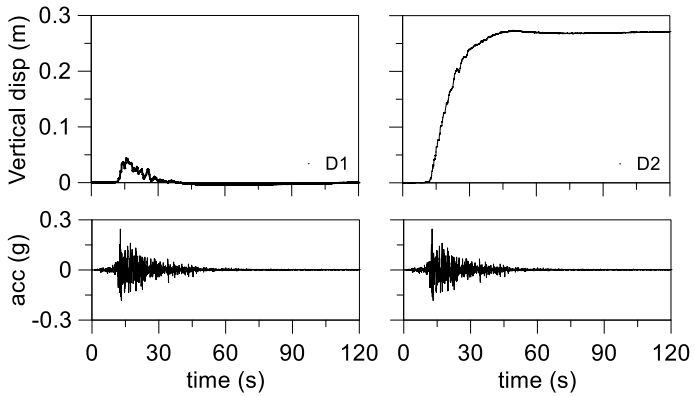

Figure 3.45. M2_S1_GM31: ground surface displacement time histories.

The displacement transducer D1 shows probably either a slight uplift of the clay crust after 45 seconds or a disruption. Displacement transducer D2 shows a large settlement that leads to a mean volumetric strain of the sand equal to about 6% evaluated on the liquefied soil thickness that is equal to about 4.5m. This value is higher than the upper boundary of the interval proposed by Lee and Albaisa (1974), but in this case the punching of the displacement transducers tip was not allowed by the presence of the crust, so the total value of the settlement was due to the reconsolidation process.

3.10.3 Building on single layer model (M1F_S1)

This test was performed aiming to study the effect of the pore pressure build-up on the interaction between a liquefiable soil and a simplified structure. The structure discussed in the section 3.9 was placed on the top of the soil profile with 1.5m of embedded of the foundation avoiding the contact between the soil and the transversal stiffening elements that link both foundation beams. Four accelerometers and four pore pressure transducers were deployed in the model during the sand deposition. Furthermore, an accelerometer was glued to the foundation and another one to the roof of the structure.

The accelerometers and pore pressure transducers in the soil created two vertical arrays to measure the accelerations and the pore pressures along the vertical section. The settlements of the ground surface were recorded by two displacement transducers (D1 and D2 in Figure 3.46), an aluminium plate was applied on their tip to avoid punching. Other three displacement transducers were deployed on the structure (D3, D4 and D5 in Figure 3.46) to measure settlements and rotation.

A schematic of the model is shown in Figure 3.46a and, at the prototype scale, in Figure 3.46b.

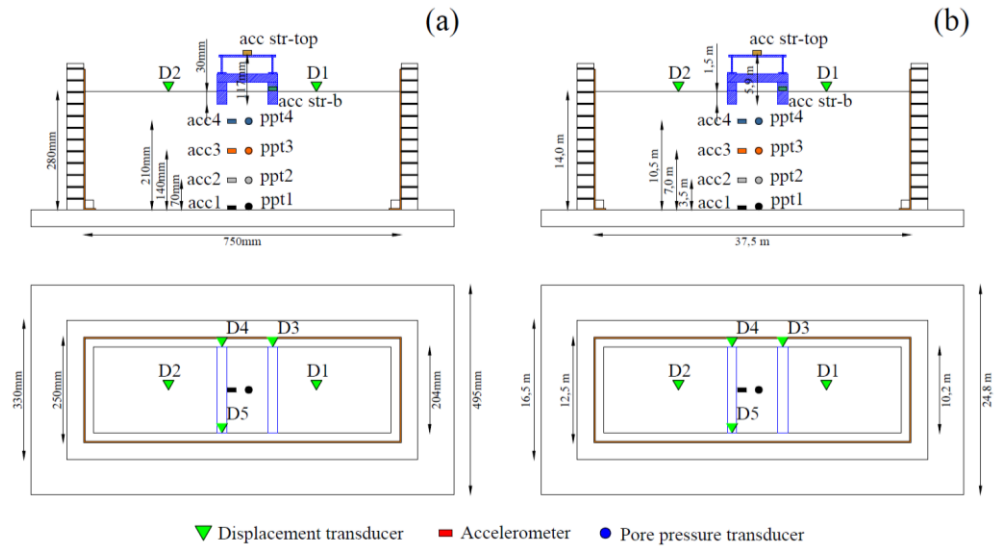

Figure 3.46. M1F_S1_GM31 and GM31+: model scale (a) and prototype scale (b).

The centrifuge model was tested twice. In the first test the standard input ground motion was applied (GM31) but no clear evidences of the liquefaction were observed. Therefore, a second ground shaking of higher intensity was modelled by applying at the base an amplified input motion (GM31+). In the following sections, the results of the two shakings are discussed separately.

3.10.3.1 Ground motion GM31

The relative density of the model after spin-up phase was equal to 49.0%. The acceleration time histories during the seismic signal are shown in Figure 3.47. The

accelerometers acc2 and acc3 are not present because they did not work. A small reduction of the amplitude and frequency of the signal is shown by shallowest accelerometer (acc4). The main time interval of the signal, valuated by intensity factor in the interval 5-95% (Arias, 1970), is shown on the right of the Figure 3.47.

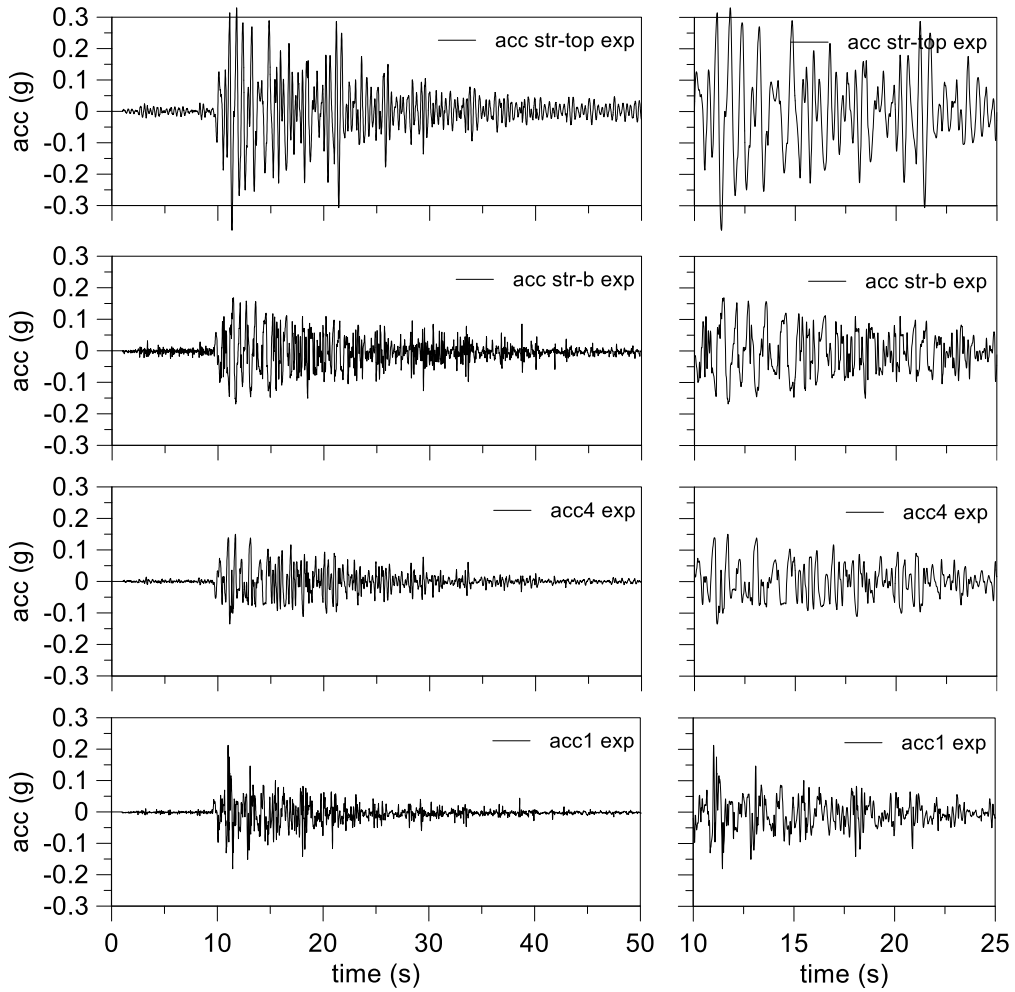

Figure 3.47. M1F_S1_GM31: main time interval of acceleration time histories.

Figure 3.48 shows that the significant frequency content of the input signal is in the first 10 Hz with largest peaks in 1 and 4 Hz. Noteworthy although this test has the same theoretical input motion of M1_S1_GM31 test, the maximum Fourier amplitude in this case is equal to about 0.10, that is lower than the amplitude reported in Figure 3.32 (equal to about 0.14). This difference may be due to the using of the same transfer function for two models with slightly different weight and geometry.

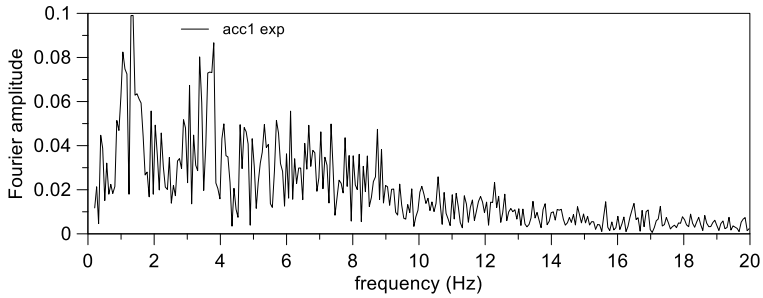

Figure 3.48. M1F_S1_GM31: Fourier spectrum of the input signal.

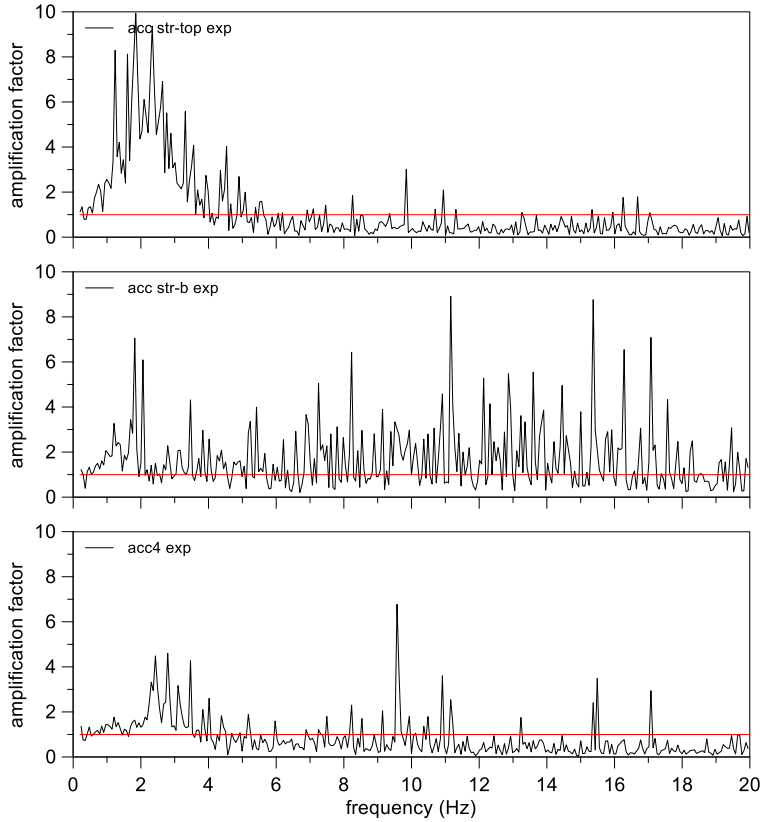

Figure 3.49. M1F_S1_GM31: amplification functions.

The amplification functions (Figure 3.49) show a light amplification in acc4 up to 4Hz and a subsequent de-amplification. A very strong amplification was recorded on the top of the structure (acc. str-top). Peaks of Fourier amplitude are located at 1 Hz, the frequency more energized by the input motion, and at about 3 Hz, the fundamental frequency of the structure. In acceleration term, the amplification factor between the input motion and the roof of the structure is equal to about 2.

The progressive build-up of excess pore water pressure is shown in Figure 3.50. Low excess water pressures were recorded and, as previously mentioned, liquefaction

manifestations were not observed. The excess pore pressure build-up was been grown faster on the bottom of the model up to achieving an almost constant distribution with depth (Figure 3.51a).

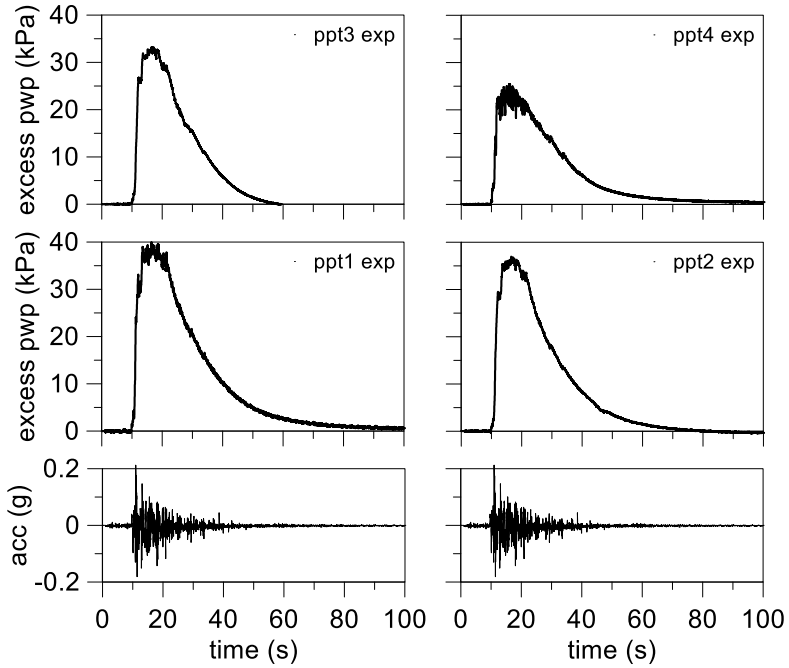

Figure 3.50. M1F_S1_GM31: excess pore water pressure time histories.

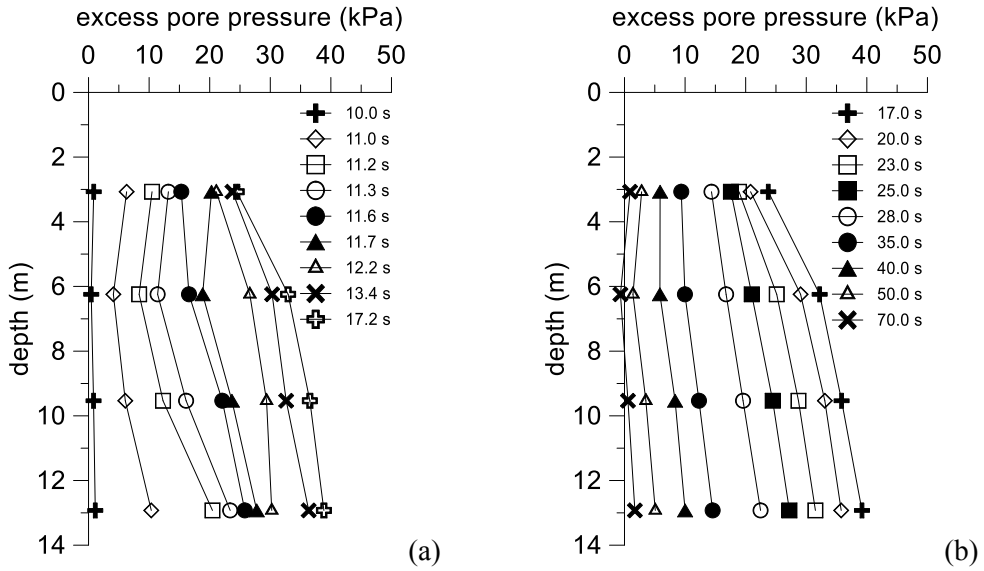

Figure 3.51. M1F_S1_GM31: vertical profiles of excess pore water pressure time histories for build-up phase (a) and dissipation phase (b).

The displacement transducers show that the amount of the settlement is larger on the lateral sides of the structure, where in "free-field" conditions can be assumed, than beneath the structure (Figure 3.52). In fact, below the foundation beam the increase of mean effective stress produced by the applied loads increases the liquefaction resistance, while laterally the prevailing increase of static shear stress tends to reduce it. Hence, larger amount of excess water pressure ratio at the sides of the foundation led to larger volumetric strains and, consequently, to larger settlements (Bray and Dashti, 2010; Karimi and Dashti, 2016).

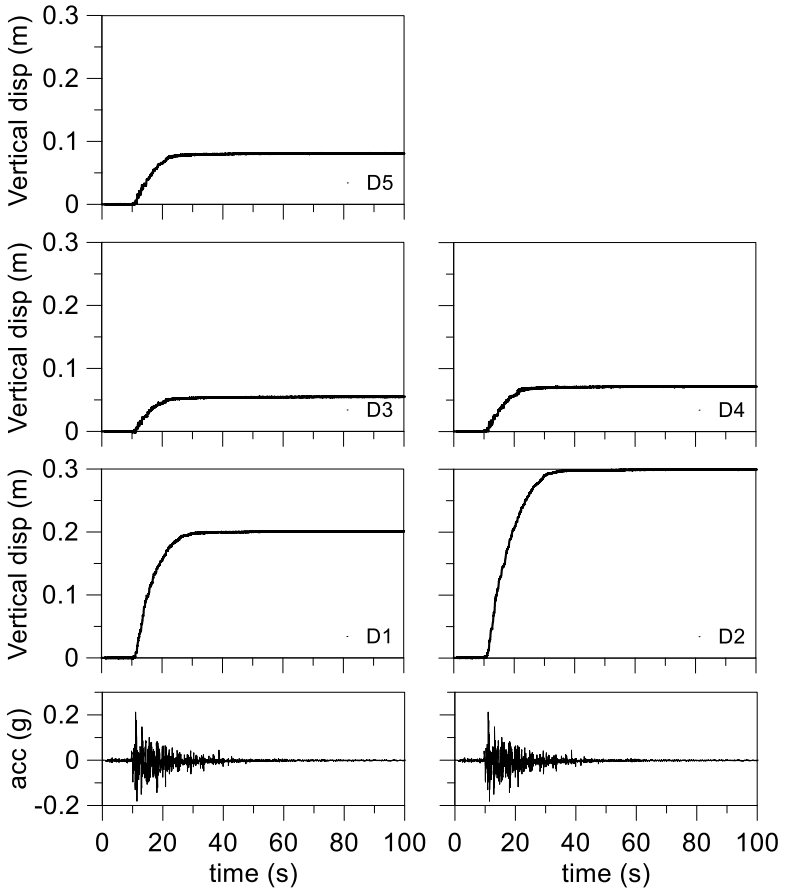

Figure 3.52. M1F_S1_GM31: ground surface and structure displacement time histories.

The difference of the settlements measured by D3-D4 and D3-D5 produced a small tilt of the structure. The mean tilt at the end of the shaking was equal to 0.2°.

3.10.3.2 Ground motion GM31+

The relative density of the model after the spin-up phase was equal to 52.6%. The acceleration time histories recorded during the seismic signal are shown in Figure 3.53. The accelerometers acc2 and acc3 are not present because did not work. Differently from previous test, a significant reduction of the amplitude and frequency of the signal is shown by shallowest accelerometer (acc4). The main time interval of the signal, valuated by intensity factor in the interval 5-95% (Arias, 1970), is shown on the right of the Figure 3.53.

Figure 3.54 shows that the significant frequency content of the input signal is in the first 8 Hz with largest peak in 1 Hz. This peak was higher than the peak of M1_S1_GM31 input motion, indeed a Fourier amplitude of 0.27 was achieved by GM31+.

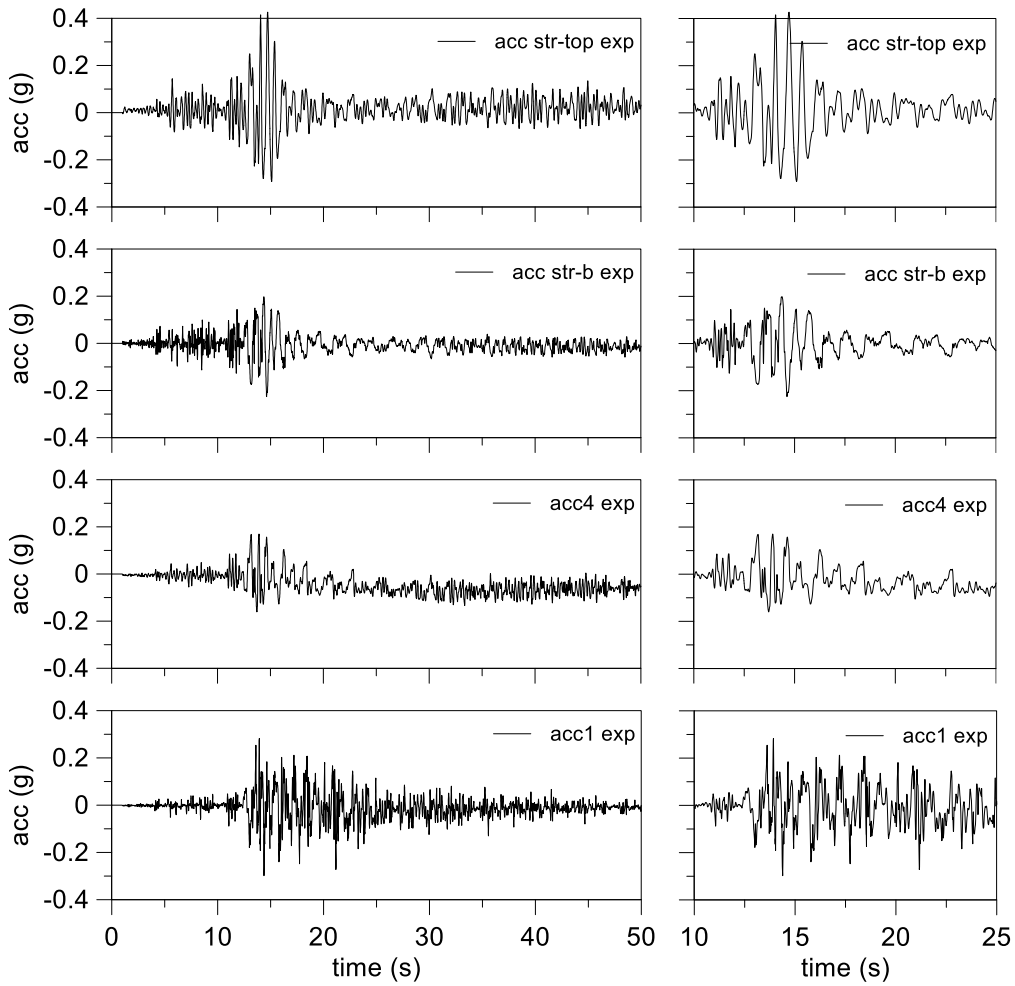

Figure 3.53. M1F_S1_GM31+: main time interval of acceleration time histories.

The amplification functions (Figure 3.55) show a peak at about 1 Hz that corresponds to0 the more energized frequency of the input signal. Significant amplification was also recorded on the structure roof in the interval between 2 and 3 Hz. The fundamental frequency of the

structure falls within this interval. In terms of acceleration, the amplification factor between the input motion and the roof of the structure is equal to about 1.33.

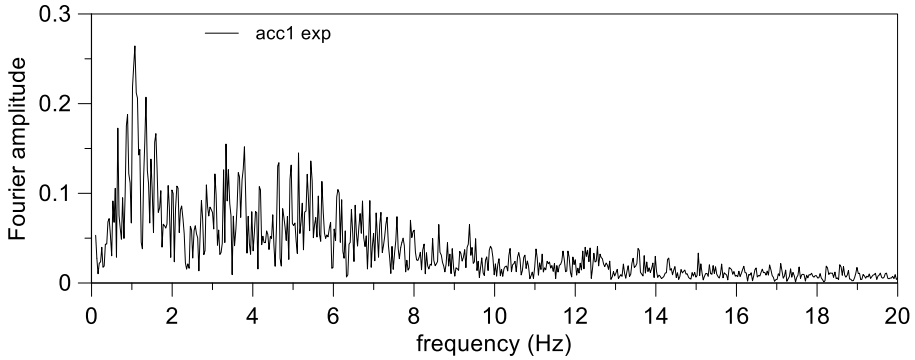

Figure 3.54. M1F_S1_GM31+: Fourier spectrum of the input signal.

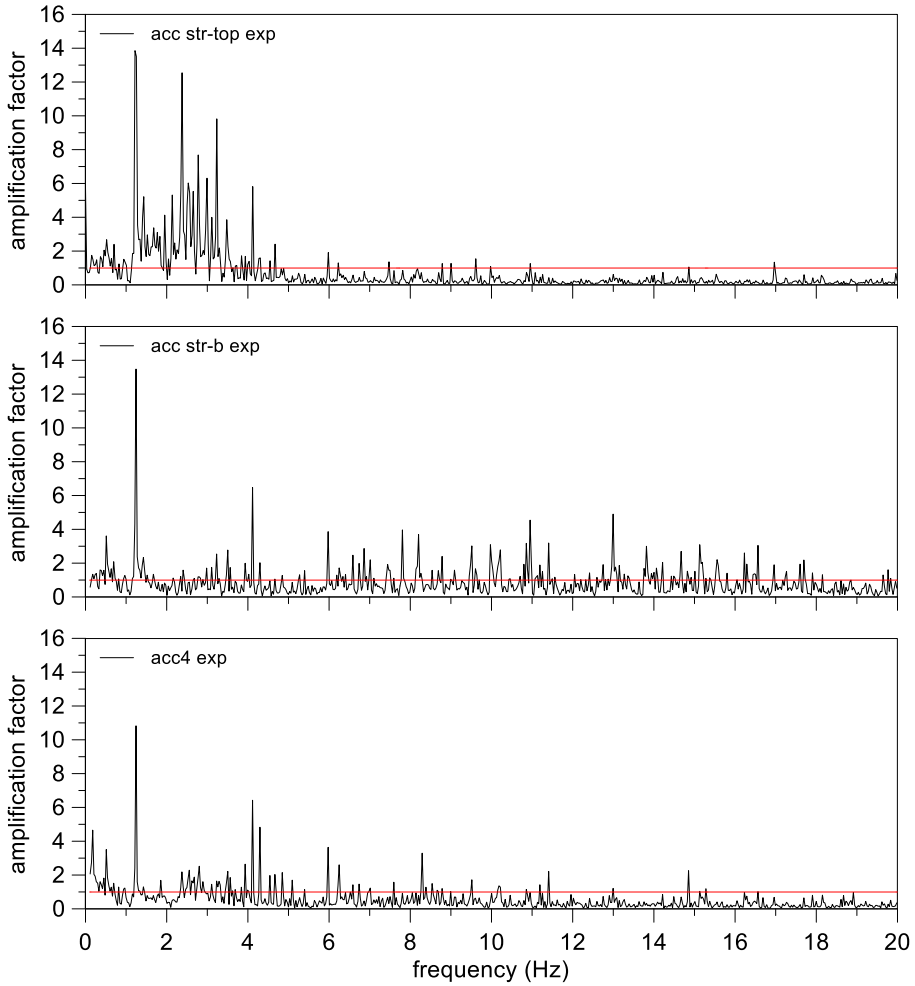

Figure 3.55. M1F_S1_GM31+: amplification functions.

The progressive build-up of excess pore water pressure is shown in Figure 3.56. In this case the stronger input motion led to higher levels of excess pore pressures. The transducers ppt3 and ppt4 seem to reach a threshold revealing the liquefaction triggering. The same value of maximum excess pore pressure was achieved by ppt1 and ppt2.

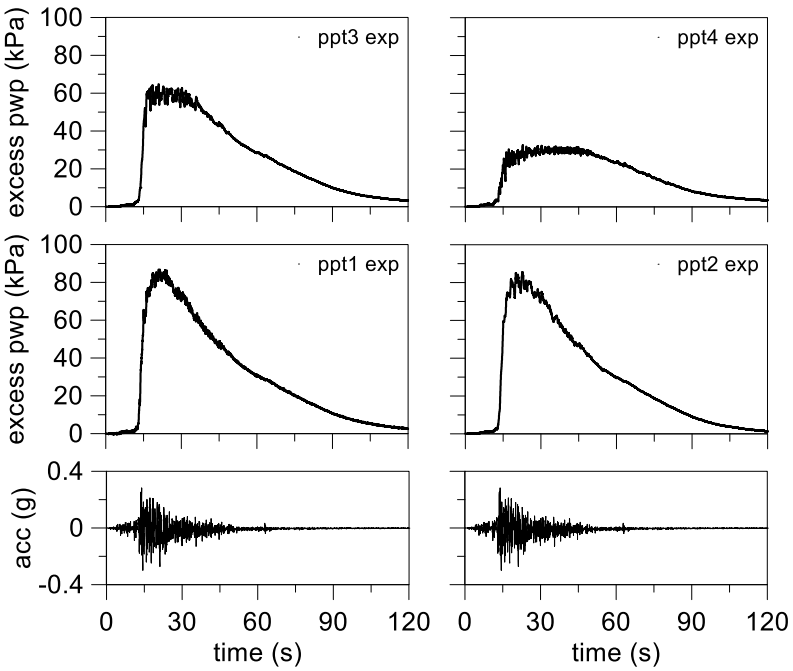

Figure 3.56. M1F_S1_GM31+: excess pore water pressure time histories.

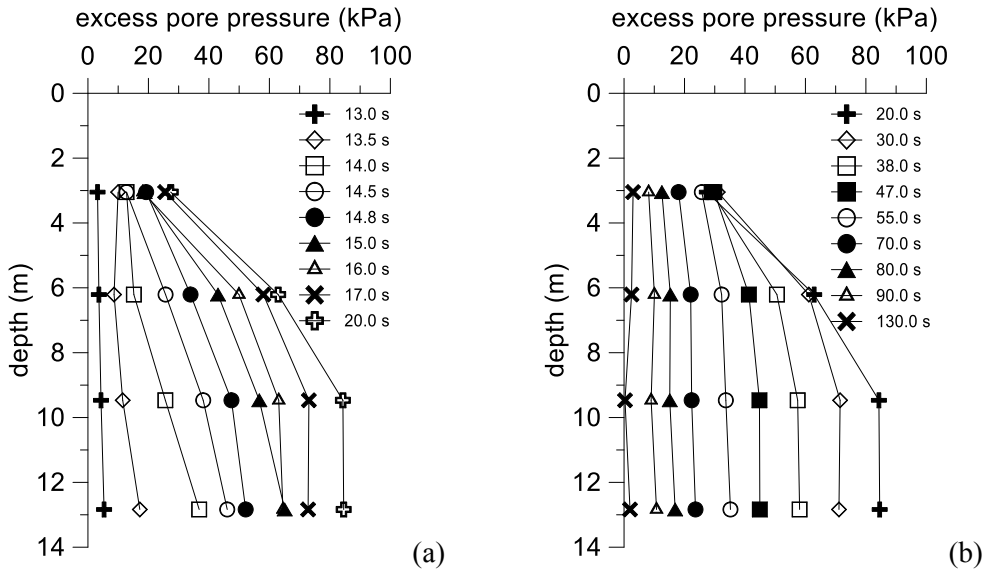

Figure 3.57. M1F_S1_GM31+: vertical profiles of excess pore water pressure time histories for build-up phase (a) and dissipation phase (b).

The threshold achievement by ppt4 persisted after the stronger part of the input motion for long time. This effect was due to the flow of the water from the bottom of the model to the upper seepage surface. The onset of water flow towards the top of the model is suggested by the distribution of the excess pore pressure with depth (Figure 3.57). The pressure build-up Figure 3.57a increased with a quasi-linear distribution until it reached an equilibrium between build-up and water flow that led to a constant excess pore pressure distribution in the lower part of the model.

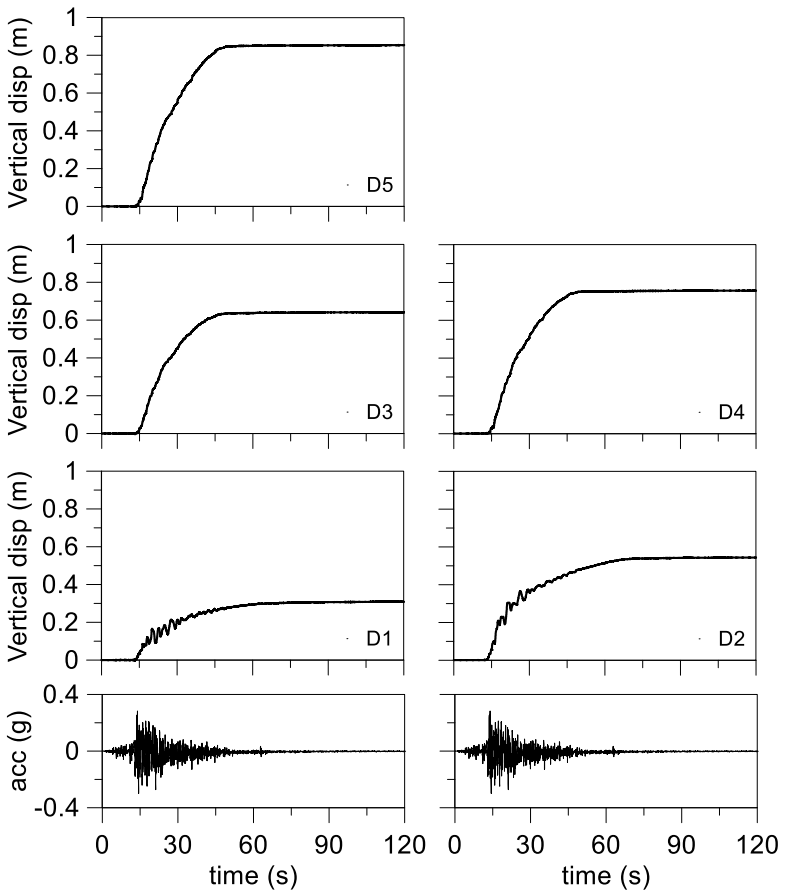

Figure 3.58. M1F_S1_GM31+: ground surface displacement time histories.

Conversely from previous test with input motion GM31, in this case the displacement transducers show that the amount of settlement below the structure is larger than laterally (Figure 3.58). This phenomenon could be due to the overall larger reduction of the shear stiffness and shear strength caused by triggering of liquefaction. Indeed, the deviatoric stresses imposed by the structure foundation beams may induce large soil flow below the foundation beams and consequent large settlements. While a reconsolidation settlement occurred laterally, that led to 4.5% of mean volumetric strain, value slightly higher than upper boundary of the Lee and Albaisa (1974) interval. A larger tilt of the structure than the previous test is shown between the difference of the settlements measured by D3-D4 and

D3-D5. The mean tilt at the end of the shaking was equal to 1.56°. Furthermore, a significant tilt equal to 0.9° happened in the transversal direction computed by the difference of the settlement measure by D4-D5.

3.10.4 Building on double layer model (M2F_S1_GM31+)

This test was performed aiming to study the effect of the water pressure build-up on the interaction between soil and a simplified structure in presence of a clay crust (Pontida clay). The structure discussed in the section 3.9 was placed on the top of the ground profile with 1.5m of embedment, thus reaching the sand layer below the crust. The contact between the soil and the transversal stiffening elements that link both foundation beams was prevented. Four accelerometers and six water pressure transducers were deployed during the sand deposition. Furthermore, an accelerometer was glued on the foundation and another one on the roof of the structure.

The accelerometers and water pressure transducers in the soil created two vertical arrays to measure the accelerations and the pore pressures along the vertical section. The settlements of the ground surface were recorded by two displacement transducers, a plate was applied on at their tip to avoid punching. Other three displacement transducers were deployed on the structure in triangular disposition to measure settlements and rotation.

In the Figure 3.59 the dimensions for centrifuge model (a) are shown, also at the prototype scale (b). The relative density of the model after the spin-up phase was equal to 52.5%

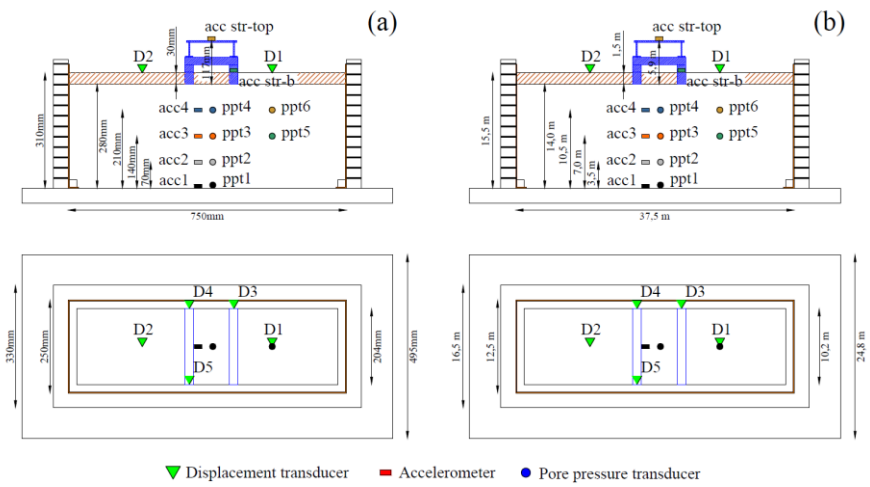

Figure 3.59. M2F_S1_GM31+: model scale (a) and prototype scale (b).

The acceleration time histories during the seismic signal are shown in Figure 3.60. The accelerometer acc3 shows a large reduction of the amplitude and frequency while the upper accelerometer acc4 shows a slight reduction of the amplitude and frequency. This effect may be due to the large contrast of impedance between soil and structure that generated descending shear waves from the foundation down to the soil.

The main time interval of the signal, valuated by an intensity factor in the interval 5-95% (Arias, 1970), is shown on the right of the Figure 3.60.

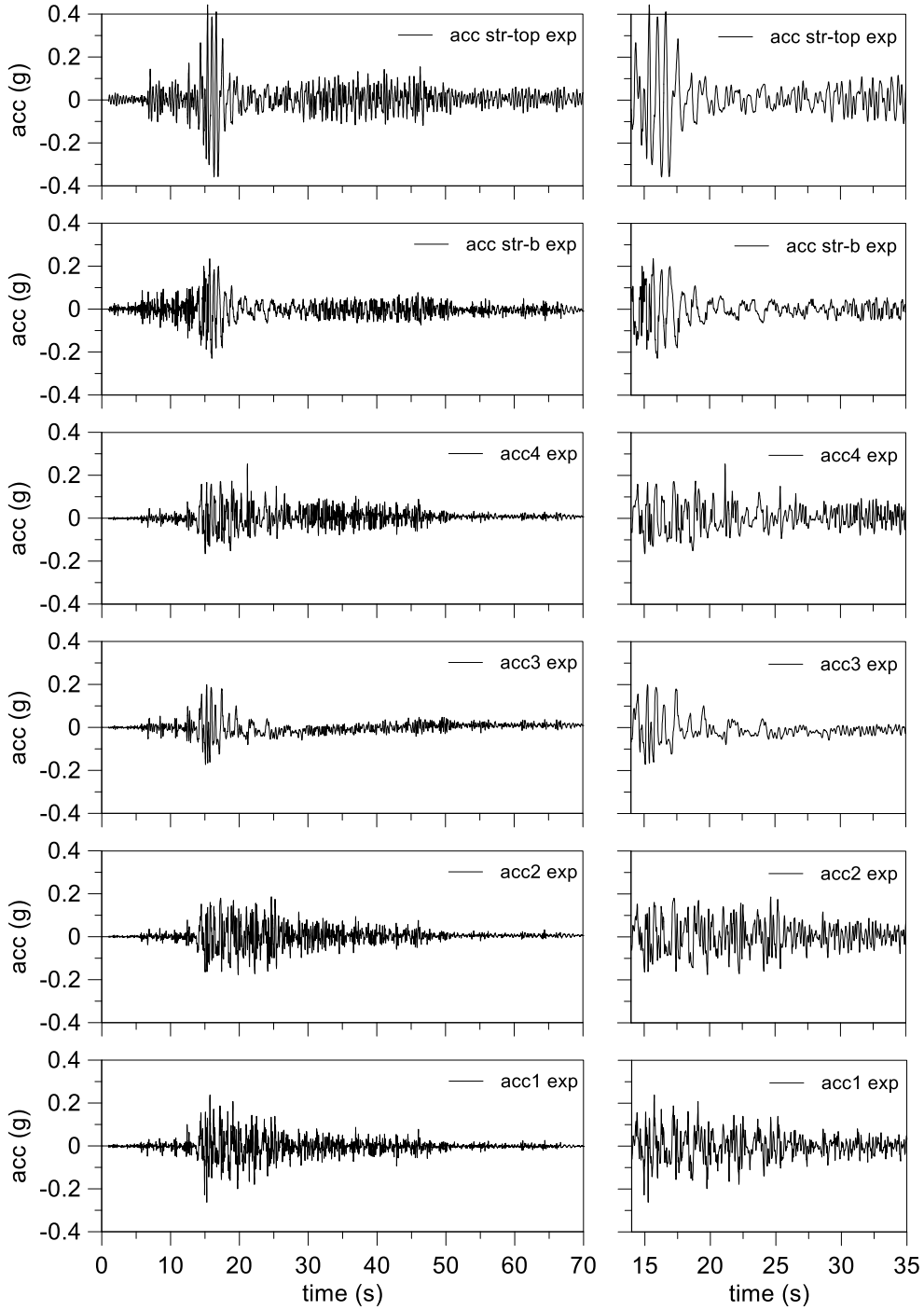

Figure 3.60. M2F_S1_GM31+: main time interval of acceleration time histories.

Figure 3.61 shows that the significant frequency content of the input signal is below 8 Hz with largest peak at 1 Hz. This peak is slightly lower than the peak of M1F_S1_GM31+ input motion.

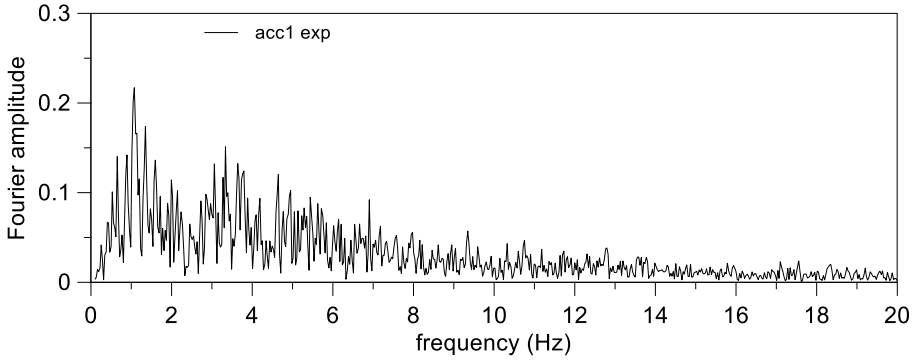

Figure 3.61. M2F_S1_GM31+: Fourier spectrum of the input signal.

The amplification functions (Figure 3.62) show that the signal was not amplified by the soil. A slightly amplification of the signal was recorded on the structure foundation. A larger amplification was recorded on the roof of the structure at frequency slightly lower than the fundamental frequency of the structure deducted in fixed base condition. This effect may be due to soil-structure resonance achieved at a decreased fundamental frequency of the structure with compliant foundation.

The progressive build-up of excess pore water pressure is shown in Figure 3.63 for each pore water pressure transducer. The transducers ppt1 and ppt2 reached the same value of excess water pressure. Noteworthy, ppt3 and ppt5 were at the same depth as ppt4 and ppt6. The transducer ppt6 reached the equilibrium threshold and preserved this condition for long time. Indeed, in the surrounding soil liquefaction occurred. However, ppt4, located at the same depth but below the structure, did not achieve clearly the triggering threshold and the excess water pressure decreased quickly. A similar behaviour was shown by ppt3 and ppt5. Probably, this effect was due to the presence of the structure that induced an increase of mean stress in the underlying soil, that increased the liquefaction strength.

The vertical profiles of excess water pressure in the time show the typical behaviour of the excess water pressure build-up (Figure 3.64a) and dissipation (Figure 3.64b). The quasi-linear distribution at maximum profile of excess water pressure suggests that liquefaction occurred between 4 and 11 m depths. Observing the maximum values and the threshold achievement in Figure 3.63, it is possible to assume that such a condition was achieved up to the clay layer, except locally below the structure.

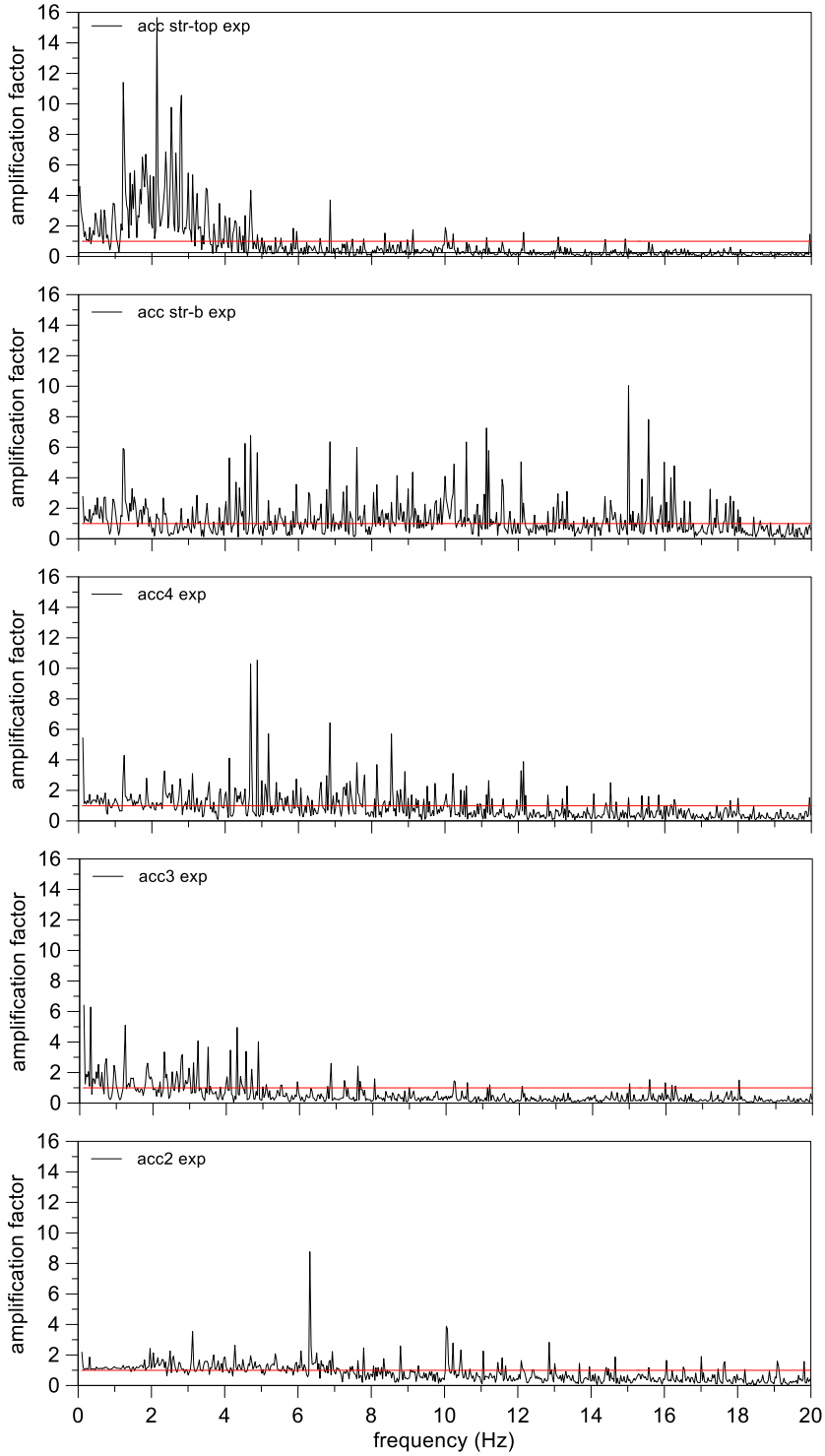

Figure 3.62. M2F_S1_GM31+: amplification functions.

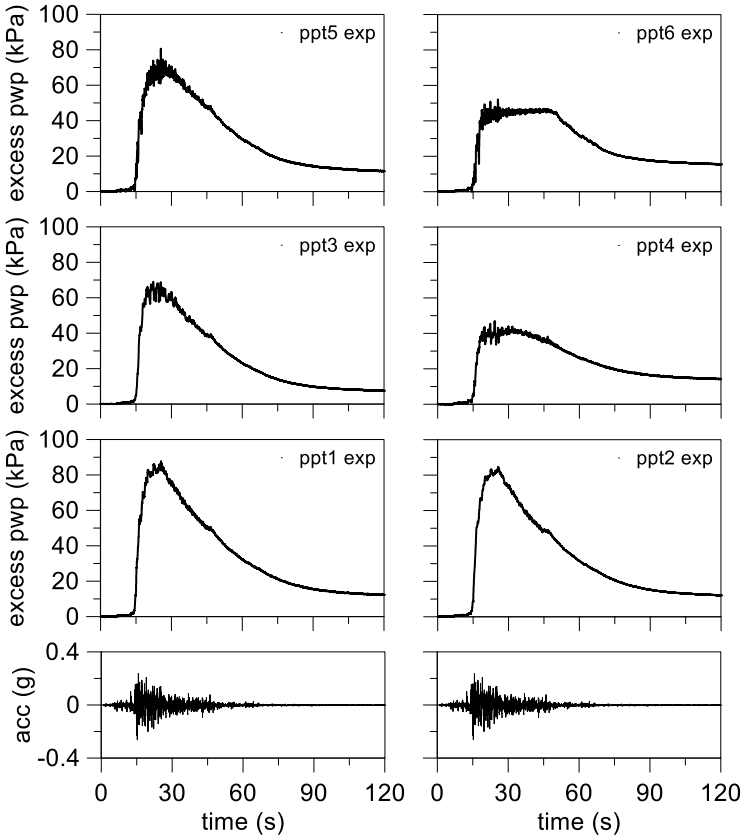

Figure 3.63. M2F_S1_GM31+: excess pore water pressure time histories.

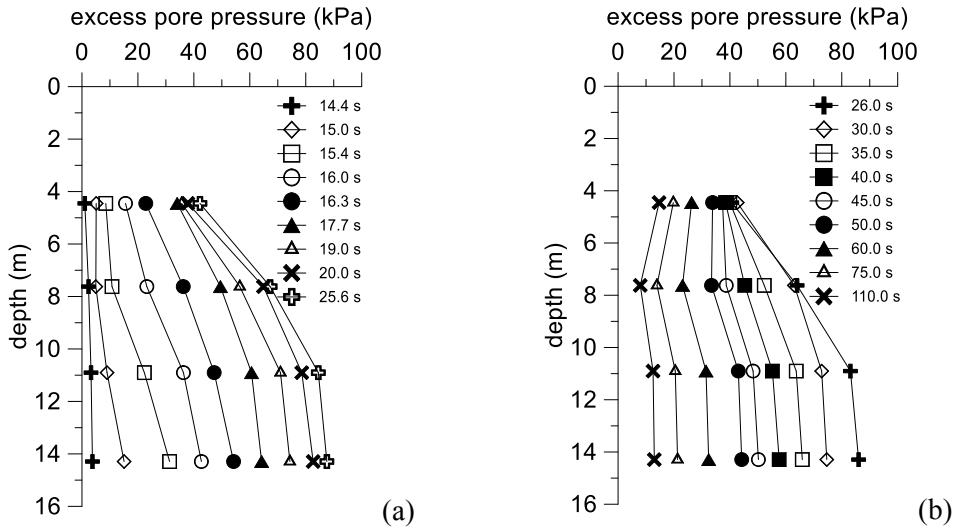

Figure 3.64. M2F_S1_GM31+: vertical profiles of excess pore water pressure time histories for build-up phase (a) and dissipation phase (b).

Conversely from previous test, the presence of the crust homogenized the settlement of the structure foundation with free field (Figure 3.65). The presence of the crust increased the excess water pressure near the ground surface, preventing a water flow from the liquefiable soil to the ground surface. At the same time, it avoided large volumetric strain, preventing the punching of the foundation and increased the bearing capacity of the foundation thanks to the adhesion at the lateral sides of the beams.

Reconsolidation settlements in free field condition leaded to a mean volumetric strain equal to 2.1%, value included in the Lee and Albaisa (1974) interval.

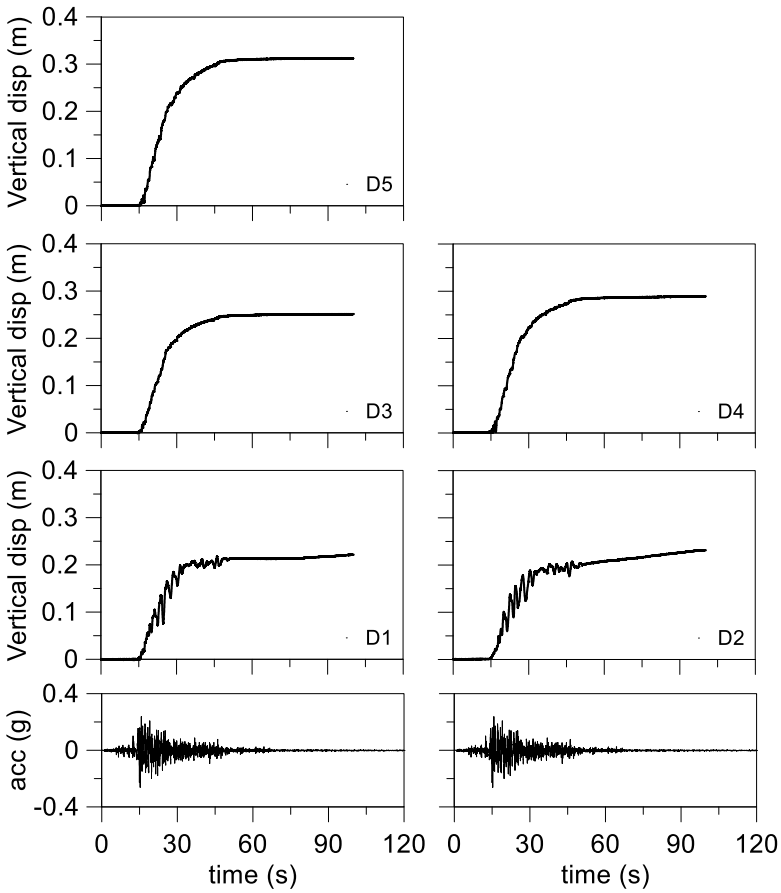

Figure 3.65. M2F_S1_GM31+: ground surface displacement time histories.

A small tilt of the structure was measured through the difference of the settlements measured by D3-D4 and D3-D5. The mean tilt at the end of the shaking was equal to 0.47°. Furthermore, a significant tilt equal to 0.22° occurred in the transverse direction, that could be computed by the difference of the settlement measurements from D4-D5.

3.11 Response with horizontal drains

In this section the results of the centrifuge tests with horizontal drains as mitigation techniques which were carried out by ISMGEO, are reported at the prototype scale in terms of records of accelerations, excess water pressure and vertical displacement of the ground surface.

The models were created with the procedure shown in the section 3.8. The drains and transducers were deployed during the pluviation phase. The drains were arranged in two different layouts, with spacing-diameter ratio (s/d) equal to 5 and 10, keeping the drains diameter equal to 300 mm (at prototype scale). This allowed to study the effects of the presence of drains and the influence of drains arrangement on the reduction and distribution of the excess water pressure in the soil.

An acceleration time history was applied on the bottom of the ESB through the shaking table installed in the centrifuge.

3.11.1 Single layer model (M1_S1_HD1&2_GM31)

The first model with horizontal drains was realised by a homogeneous soil profile of liquefiable sand (Ticino sand). Seven accelerometers and five pore pressure transducers were deployed in the sand during the deposition. The accelerometers were deployed in two vertical arrays. Two pore water pressure transducers were placed among the drains to measure the maximum excess water pressure reached in this area during the motion. Three more pore pressure transducers were located beneath, as shown in Figure 3.66. Unfortunately, no pore pressure transducer was in free field condition; therefore, the effect of the drain have to be studied in numerical way.

The settlements of the ground surface were recorded by two displacement transducers; a small plate was applied on their tip to avoid the punching. In the Figure 3.66 the dimensions of the model are shown (Figure 3.66a) also at the prototype scale (Figure 3.66b). The relative density of the sand layer after spin-up was assessed as equal to 54.5%.

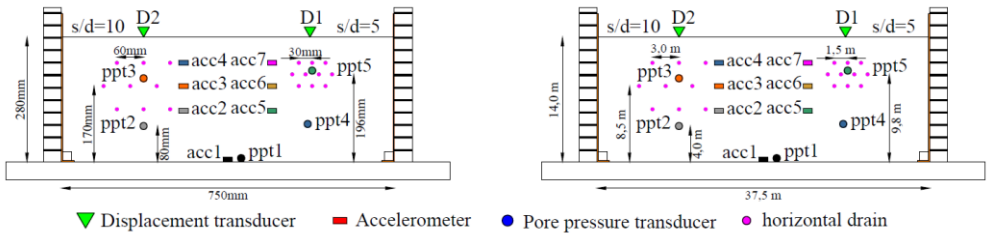

Figure 3.66. M1_S1_HD1&2_GM31: model scale (a) and prototype scale (b).

The acceleration time histories are reported in Figure 3.67 and the main time interval of the signal, evaluated as the interval when the intensity factor ranges between 5% and 95% (Arias, 1970), is shown on the right. The accelerometer acc3 did not work. The figure shows that the acceleration time histories did not exhibited significant reduction in frequencies and amplitude. This indicates that due the presence of the drains liquefaction did not occur.

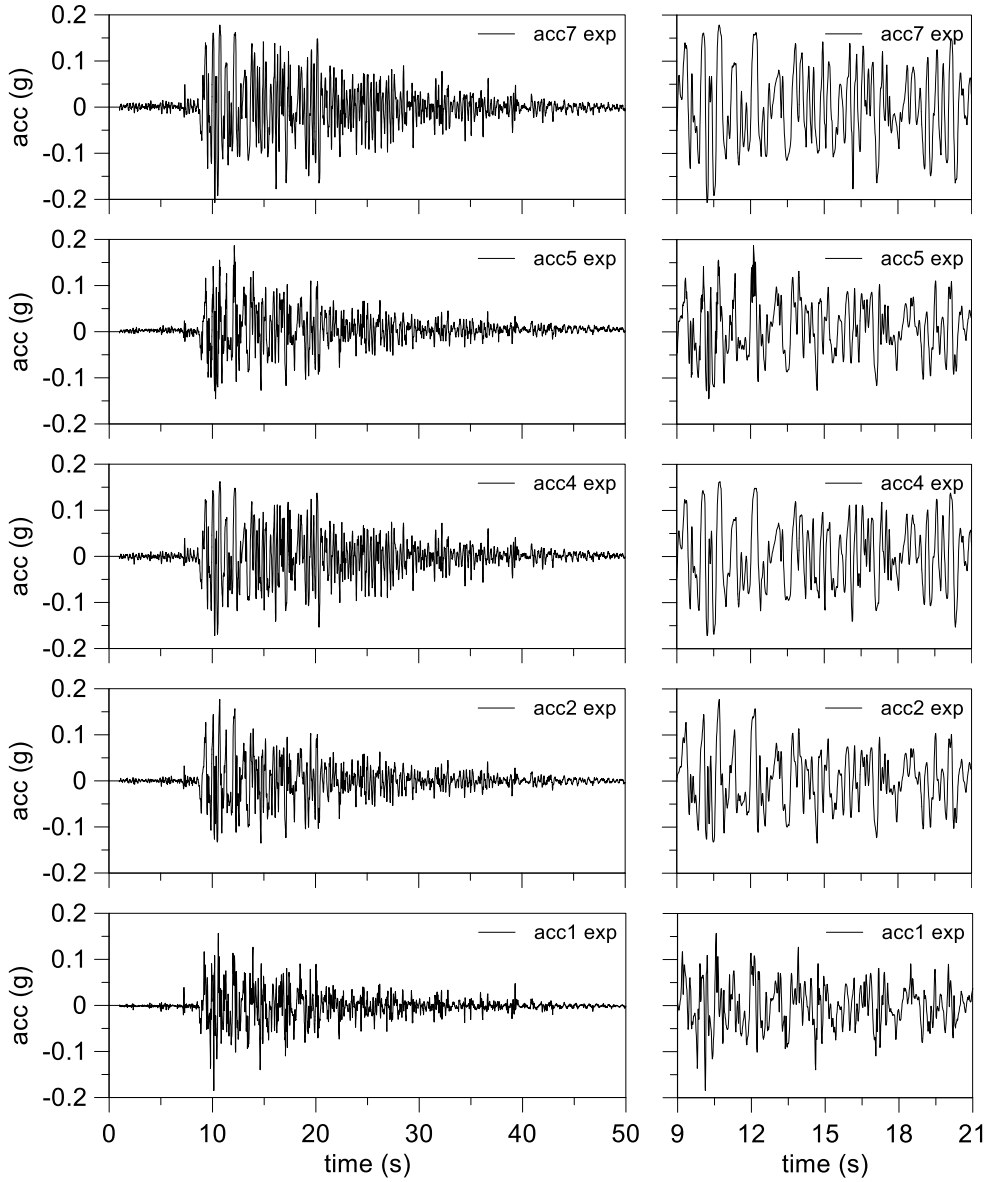

Figure 3.67. M1_S1_HD1&2_GM31: main time interval of acceleration time histories.

Figure 3.68 shows that the significant frequency content of the input signal falls beneath 10 Hz with the largest peak at about 1 Hz. Several isolated peak appear at higher frequencies, showing that the soil stiffness did not reduce significantly during the motion.

The amplification functions (Figure 3.69) show an amplification in all accelerometers. The shallower accelerometers (acc4 and acc7) exhibit the larger amplification around 2 and 3 Hz.

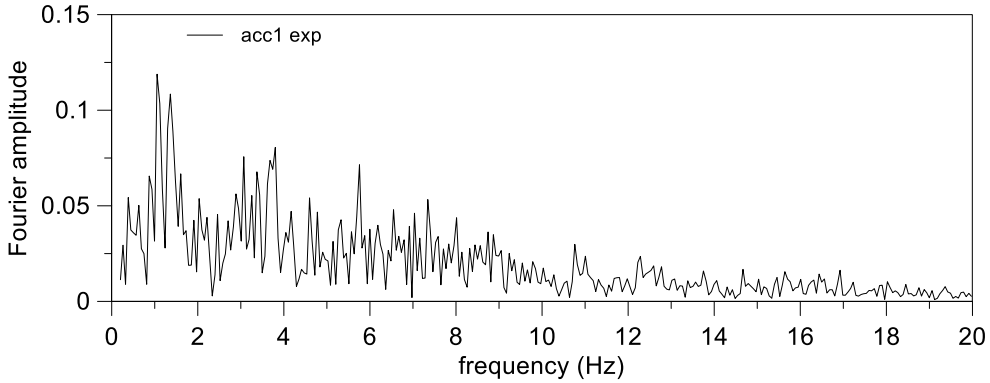

Figure 3.68. M1_S1_HD1&2_GM31: Fourier spectrum of the input signal.

The progressive build-up of excess pore water pressure is shown in Figure 3.70. The ppt4 did not work and all other transducers measured a small value of the excess water pressure compared to their depth.

The ppt5, positioned among the horizontal drains with s/d equal to 5, recorded a maximum excess pore pressure lower than ppt3 located among the drains with s/d=10. This result is consistent with the physic process of the consolidation. Indeed, the drains represent a seepage surface that reduce the drainage length accelerating the consolidation process. This effect can be observed also in the dissipation phase after the stronger part of the motion.

The profiles of excess pore pressure with depth show a larger accumulation at the bottom of the soil profile (Figure 3.71a) and a very fast dissipation at the drains level (i.e. at 4 m depth) after the stronger part of the motion (Figure 3.71b).

Smaller settlement (Figure 3.72) was recorded at the ground level above the drains with s/d = 5 (D1) than above the drains with s/d = 10 (D2). This result was due to the lower level of excess pore pressure reached in the soil near the drains arrangement with s/d equal to 5 that led to smaller reconsolidation volumetric strains. However, the amount of settlement was smaller than in the previous tests (M1_S1_GM31) and it developed faster. This effect shown the efficiency of the horizontal drains to reduce the excess pore pressure and, consequently, the amount of settlement.

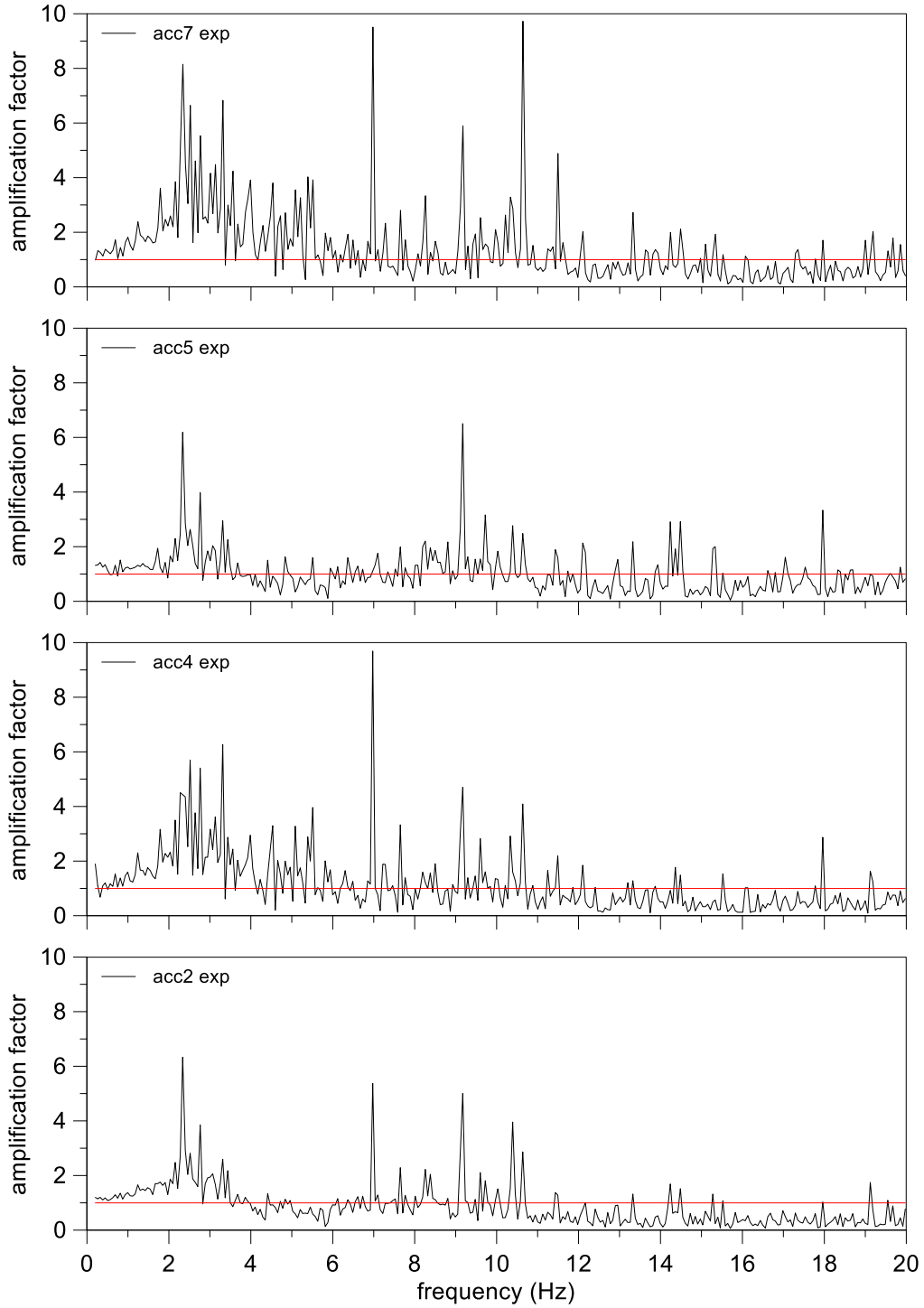

Figure 3.69. M1_S1_HD1&2_GM31: amplification functions.

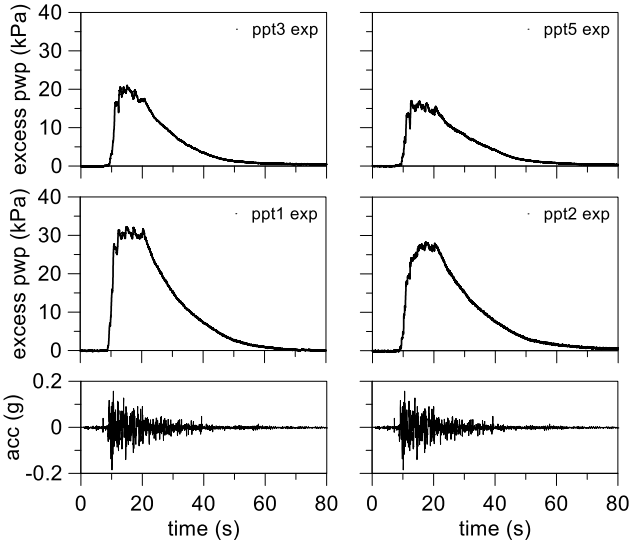

Figure 3.70. M1_S1_HD1&2_GM31: excess pore water pressure time histories.

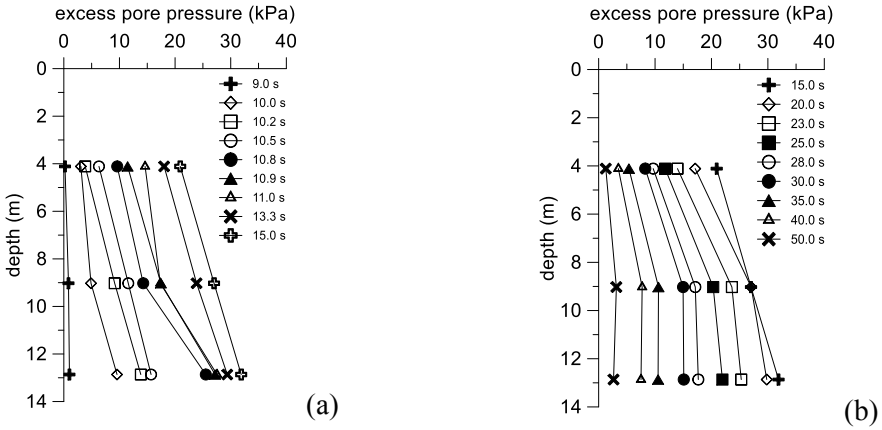

Figure 3.71. M1_S1_HD1&2_GM31: vertical profiles of excess pore water pressure time histories for build-up phase (a) and dissipation phase (b).

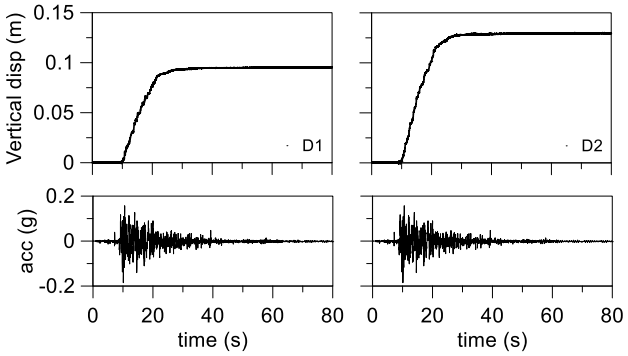

Figure 3.72. M1_S1_HD1&2_GM31: ground surface displacement time histories.

3.11.2 Double layer model (M2_S1_HD1&2_GM31)

Horizontal drains were deployed in the homogeneous soil profile of liquefiable sand (Ticino sand) with a clay crust (Pontida clay). The same layout of transducers of M1_S1_HD1&2_GM31 was employed.

In Figure 3.73 the dimensions of centrifuge model are shown (Figure 3.73a), also at the corresponding prototype scale (Figure 3.73b). The relative density of sand after spin-up was equal to 52.5%.

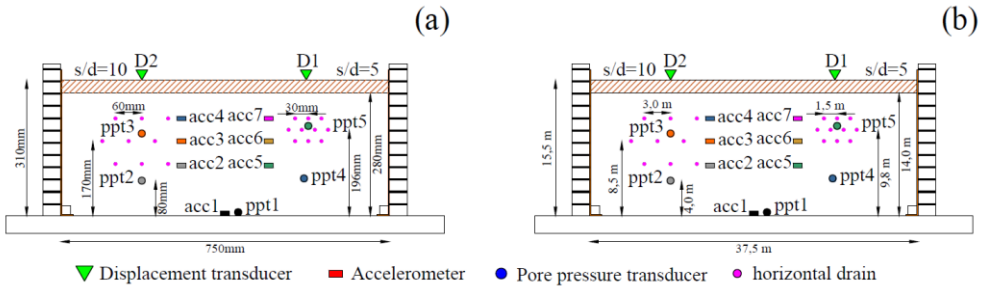

Figure 3.73. M2_S1_HD1&2_GM31: model scale (a) and prototype scale (b).

The acceleration time histories are reported in Figure 3.74 and the main time interval of the signal, evaluated as the interval when the intensity factor ranges between 5% and 95% (Arias, 1970), is shown on the right. The accelerometer acc3 did not work. An acceleration amplification from the bottom to the top of the model was recorded except for the accelerometer acc2 that showed a significant reduction of the amplitude. No evidence of liquefaction was observed in this test.

Figure 3.75 shows that the significant frequency content of the input signal falls under 13 Hz with the largest peaks around 1 and 4 Hz. The input motion had different frequency content and lower Fourier amplitude than in the test without cap. This does not permit a direct comparison between tests results, hence numerical analyses were complemented to compare the results of the experiments.

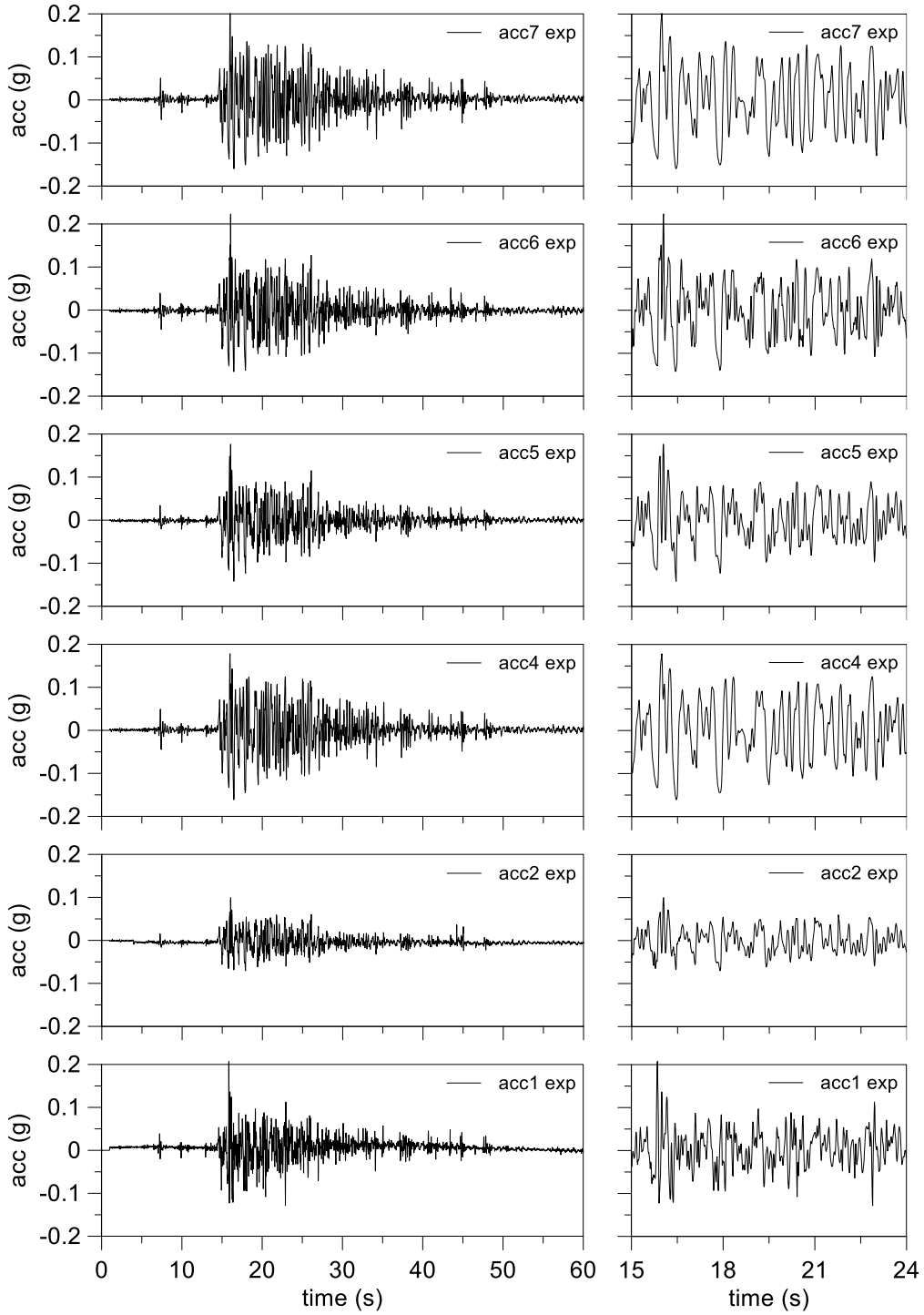

Figure 3.74. M2_S1_HD1&2_GM31: main time interval of acceleration time histories.

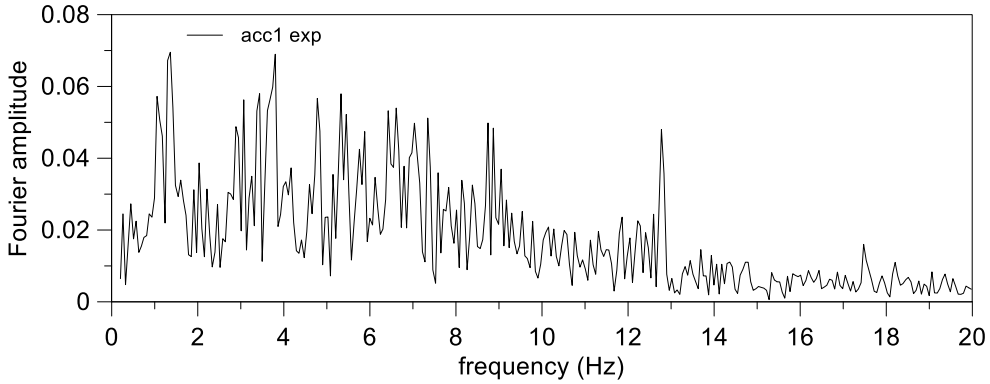

Figure 3.75. M2_S1_HD1&2_GM31: Fourier spectrum of the input signal.

The amplification functions (Figure 3.76) show an amplification in all acceleration records in the range 1-4 Hz except acc2 that shows a slight attenuation. The shallower accelerometers (acc4 and acc7) exhibit the largest amplification around 2 and 3 Hz.

The excess pore water pressure time histories are shown in Figure 3.77. The ppt2 did not work and all other transducers measured a small value of the excess pore pressure compared to their depth. The maximum excess pore pressure was recorded at the bottom of the model (ppt1). Ppt4 shows an abnormal dissipation velocity probably due to a malfunctioning of the transducer.

All the transducers show a slower dissipation phase compared to the test with horizontal drain without clay crust on top. This highlights the existence of a substantial water flow induced by the presence of the upper seepage surface.

The ppt5, positioned among the horizontal drains with s/d = 5, recorded a maximum excess pore pressure lower than ppt3 located among the drains with s/d=10.

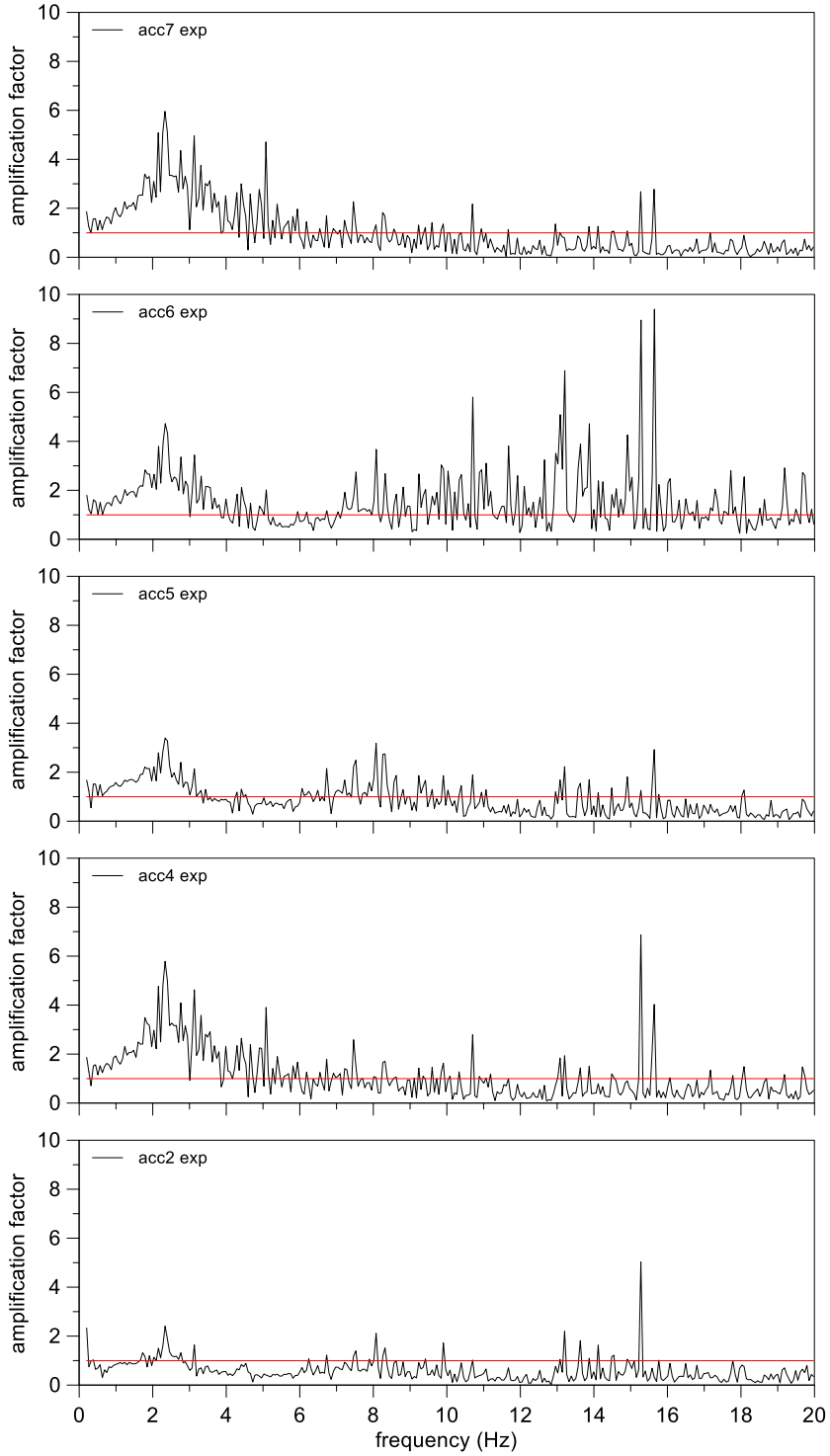

Figure 3.76. M2_S1_HD1&2_GM31: amplification functions.

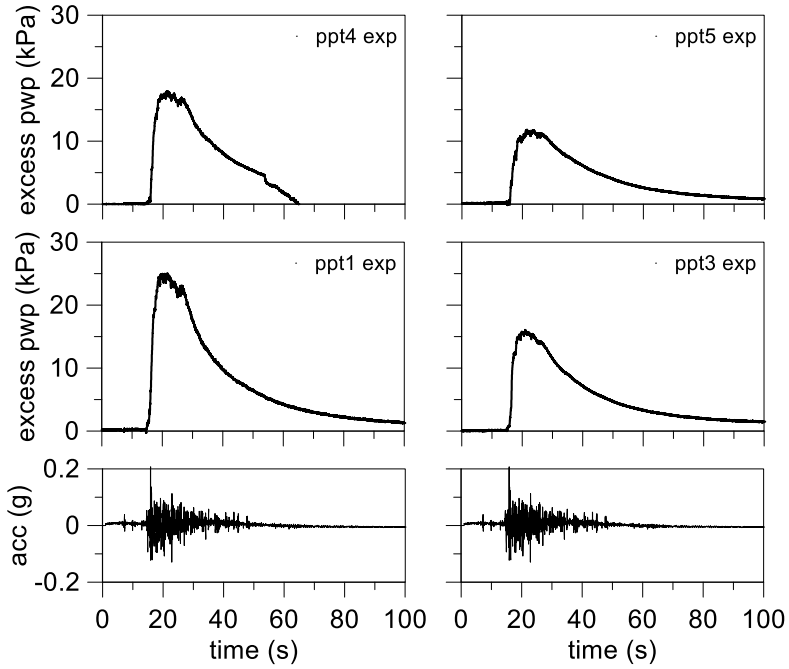

Figure 3.77. M2_S1_HD1&2_GM31: excess pore water pressure time histories.

The excess pore pressure profiles with depth show a larger build-up at the bottom of the model (Figure 3.78a) that decreases progressively up to horizontal drains located around 4 m depth. In the dissipation phase (Figure 3.78b) the excess pore pressure profiles show an anomalous concavity that may be due to the malfunctioning of the transducer located at 10 m depth (ppt4).

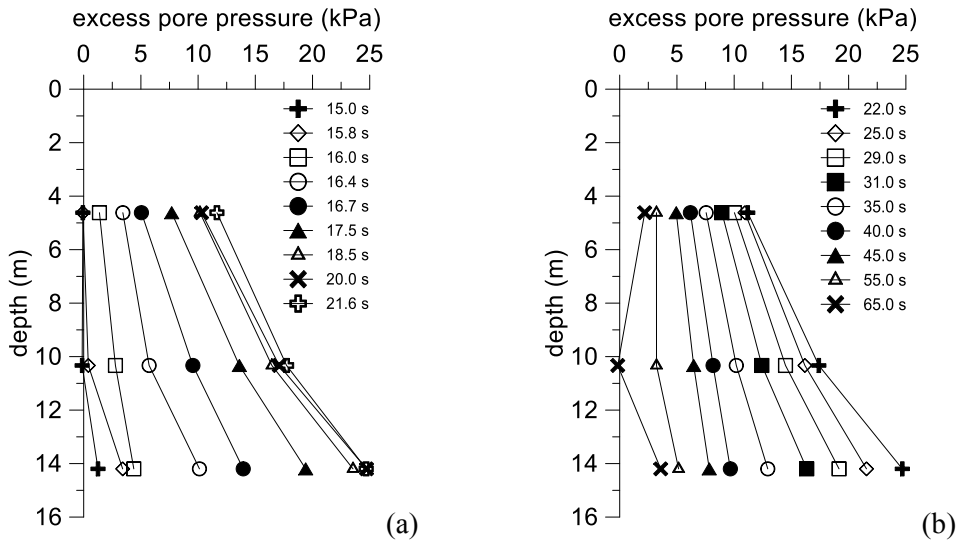

Figure 3.78. M2_S1_HD1&2_GM31: vertical profiles of excess pore water pressure time histories for build-up phase (a) and dissipation phase (b).

Differently from the previous test, the settlement of the ground surface upon the two different drains arrangements was very similar (Figure 3.79), due to the distributing effect of the upper crust. However, smaller settlements were measured than the test without crust. Most part of settlement occurred during the strong part of the motion and the amount of post shaking settlement was negligible.

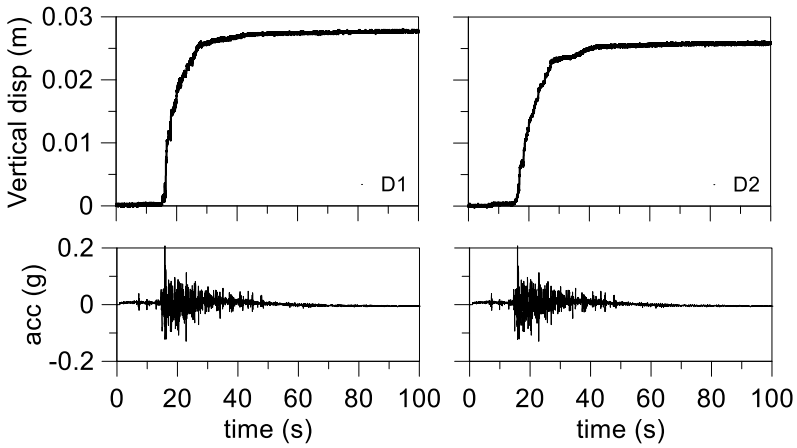

Figure 3.79. M1_S1_HD1&2_GM31: ground surface displacement time histories.

3.11.3 Building on single layer model (M1F_S1_HD1_GM31+)

This test was performed aiming to study the effect of the water pressure build-up on the interaction between soil and a simplified structure in presence of horizontal drains below the structure foundation. The structure discussed in the section 3.9 was founded in the ground profile with 1.5m of embedment. The contact between the soil and the transversal stiffening elements that link both foundation beams. Four accelerometers, six pore pressure transducers and ten pierced plastic tubes, acting as drains, with a spacing-diameter ratio equal to 5 below the structure were deployed during the sand deposition. Furthermore, an accelerometer was glued on the foundation and another one on the roof of the structure.

The accelerometers and pore pressure transducers from ppt1 to ppt4 created two vertical arrays to measure the accelerations and the pore pressures along the vertical section. While ppt5 and ppt6 allowed to know the water pressure in "free field" conditions.

The settlements of the ground surface were recorded by two displacement transducers, a plate was applied at their tip to avoid soil punching. Other three displacement transducers were deployed on the structure to measure settlements and rotation.

In the Figure 3.80 the dimensions of the centrifuge model and prototype are shown (Figure 3.80a) also at the prototype scale (Figure 3.80b). The relative density of sand after spin-up was equal to 51.2%.

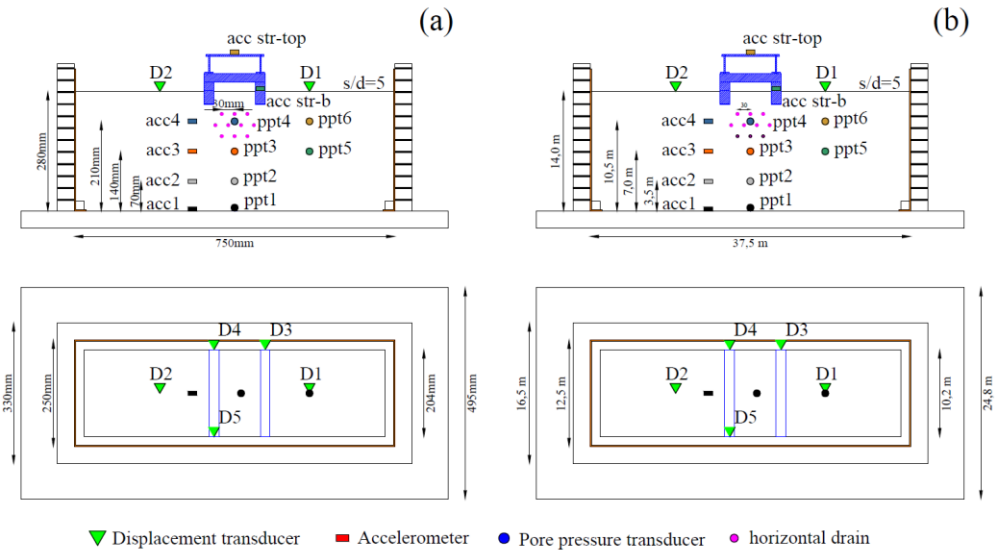

Figure 3.80. M1F_S1_HD1_GM31+: model scale (a) and prototype scale (b).

A reduction of amplitude and frequency is shown by the acceleration time histories starting from the bottom of the model to the ground surface (Figure 3.81). Whereas a substantial amplification was recorded at the structure roof. The main portion of input motion was included in the frequency interval between 1 and 8 Hz (Figure 3.82). The peak is slightly lower than in the test with structure without horizontal drains (M1F_S1_GM31+).

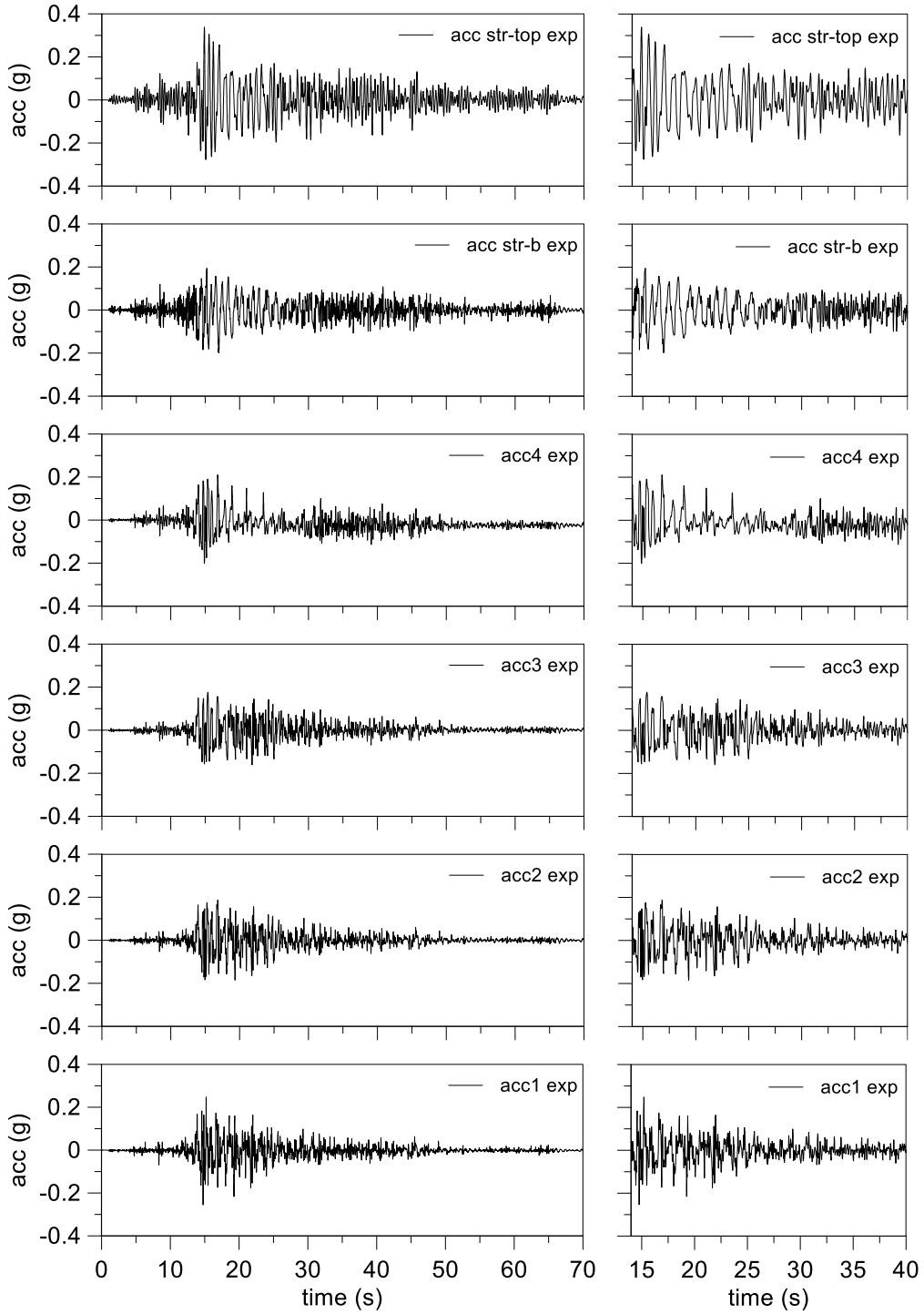

Figure 3.81. M1F_S1_HD1_GM31+: main time interval of acceleration time histories.

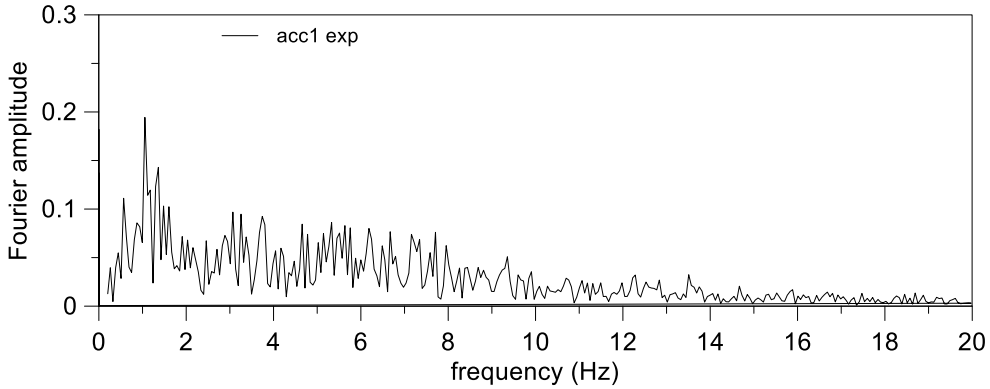

Figure 3.82. M1F_S1_HD1_GM31+: Fourier spectrum of the input signal.

As previously seen in the acceleration time histories, the amplification functions show the same results. Indeed, the accelerometers from acc2 to acc4 exhibit a progressive amplification of the signal in the first 4 Hz. Furthermore, the structure was subjected to a strong amplification of the signal around its fundamental frequency that was included in 2-3 Hz interval.

The excess pore pressure build-up into the model recorded by transducers are shown in Figure 3.84. The transducer ppt1 did not work. The transducer ppt4 deployed among the horizontal drains shows a strong reduction of excess pore pressure compared to ppt6 located to the same depth but far from the drains. Abnormal excess pore pressure path was read by ppt3 that read negative values at the end of the dissipation phase. However, this transducer read a smaller excess pore pressure than ppt5 that is maybe due to the proximity to the drains. The excess water pressure reached at the depth (ppt2) is lower than the value achieved in the test with the structure but without drains (M1F_S1_GM31+). The faster dissipation velocity is to be attributed to the drains effect.

The profile of excess pore pressure along a vertical section of the model beneath the structure shows a fast build-up in the deeper part (Figure 3.85a). In the dissipation phase the transducer at around 6m depth (ppt3) shows a faster excess water pressure dissipation (Figure 3.85b) than the transducer among the drains (ppt4). This result is inconsistent with the consolidation process. It may indicate that, the ppt4 transducer did not work well. As previously seen, the influence of the drains achieved also the deeper part of the model, indeed the ppt2 shows a very high dissipation velocity. Neglecting the transducer at 6m depth, the excess pore pressure on the bottom reached the pressure between the drains during the consolidation process. This result highlights that the water flow due to the presence of the drains keeps the excess pore pressure constant among the drains and this accelerated the dissipation process in the deeper part of the model up to reaching a quasi-constant distribution of the excess pore pressure.

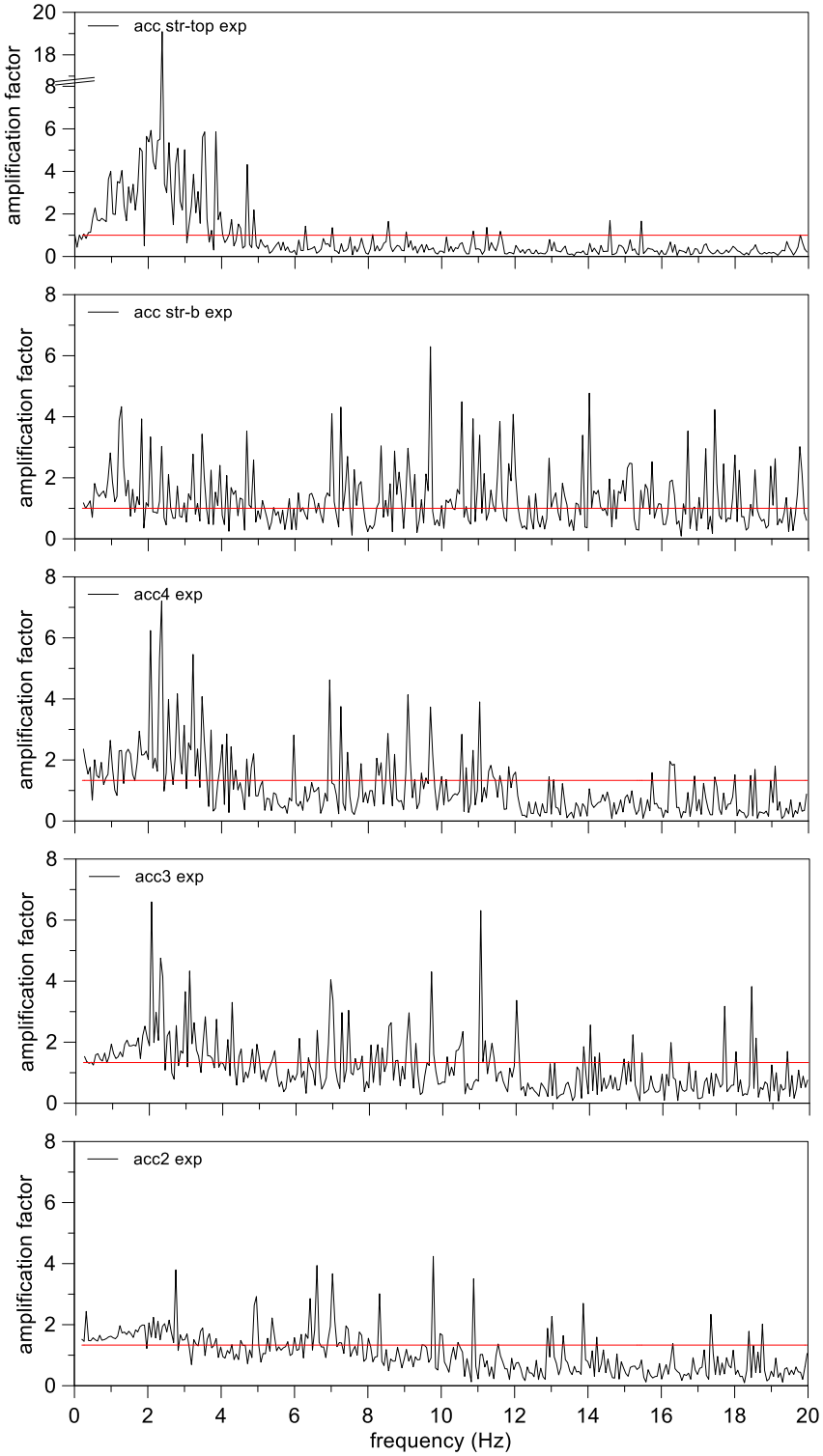

Figure 3.83. M1F_S1_HD1_GM31+: amplification functions.

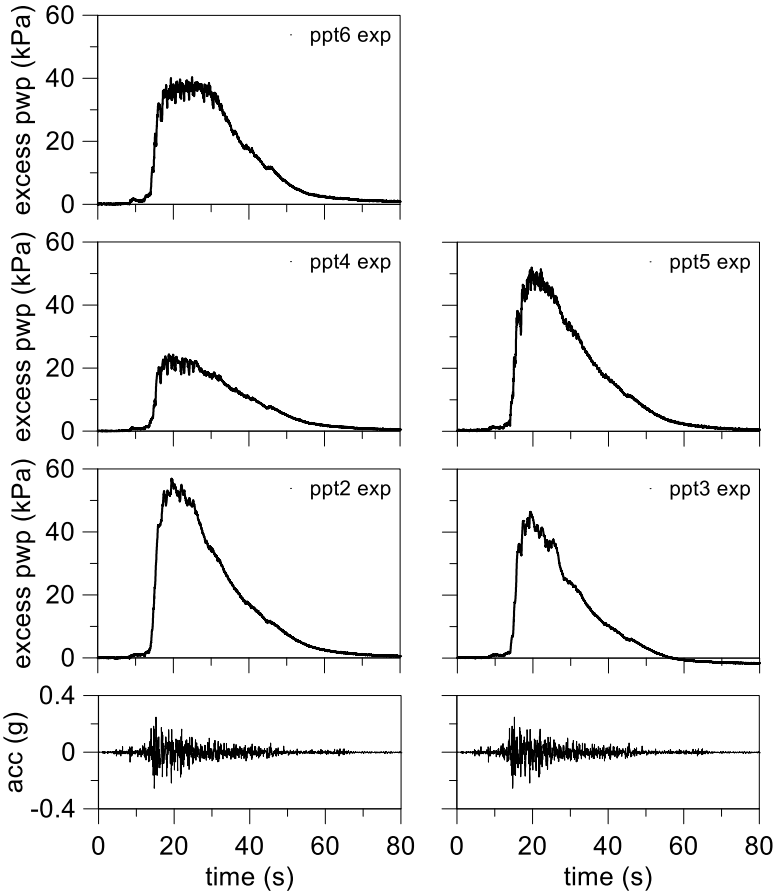

Figure 3.84. M1F_S1_HD1_GM31+: excess pore water pressure time histories.

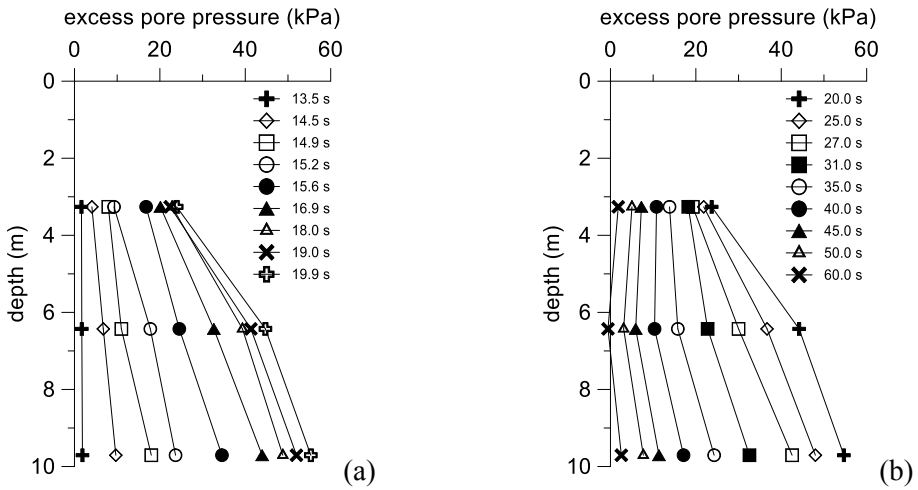

Figure 3.85. M1F_S1_HD1_GM31+: vertical profiles of excess pore water pressure time histories below the structure for build-up phase (a) and dissipation phase (b).

The amount of settlements in "free field" condition (Figure 3.86, D1 and D2) was the same as in the test without horizontal drains (Figure 3.58), whereas the structure exhibited significant smaller settlements in presence of horizontal drains. Indeed, the absolute settlements were reduced from about 0.8m to about 0.33m. Moreover, the tilt of the structure, computed from the settlements measured on D3-D4 and D3-D5, was largely reduced. The mean tilt at the end of the shaking was equal to 0.3°, whereas a tilt equal to 0.12°, as computed by the difference of the settlement measure by D4-D5, occurred in the transverse direction. This result highlights the efficiency of the horizontal drains as liquefaction mitigation technique, since they avoid large reduction of shear stiffness and shear strength during the earthquake. Reconsolidation settlement in free field condition led to 3.3% of mean volumetric strain, computed on 10m of the soil, value included in Lee and Albaisa (1974) range.

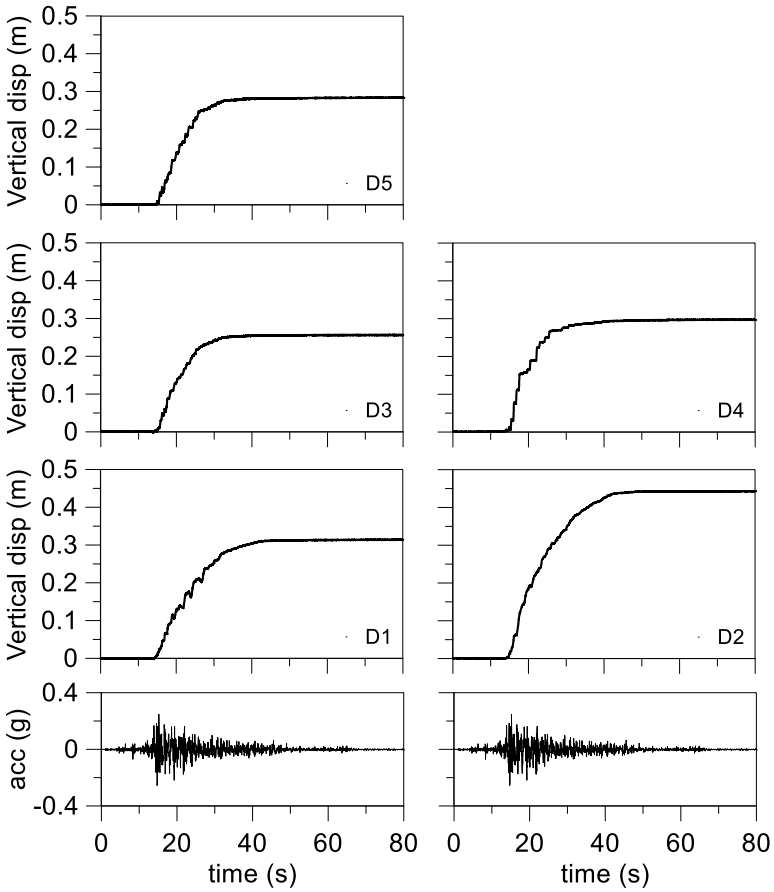

Figure 3.86. M1F_S1_HD1_GM31+: ground surface displacement time histories.

3.11.4 Building on double layer model (M2F_S1_HD1_GM31+)

The difference between this test and the previous one is the presence of a 1.5m of clay crust (Pontida clay) on the top of the model. The structure discussed in the section 3.9 was embedded in the soil profile for 1.5m, reaching the underlying sand. Four accelerometers, six pore pressure transducers and ten drains with a spacing-diameter ratio equal to 5 below the structure were deployed during the sand deposition. Furthermore, an accelerometer was glued on the foundation and another one on the roof of the structure.

The accelerometers and pore pressure transducers from ppt1 to ppt4 created two vertical arrays to measure the accelerations and the pore pressures along the vertical section. The remaining ppt5 and ppt6 allowed to know the pore pressure in "free field" conditions.

The settlements of the ground surface were recorded by two displacement transducers, a plate was applied on their tip to avoid soil punching. Other three displacement transducers were deployed on the structure to measure settlements and rotation.

In the Figure 3.87 the dimensions of the centrifuge model are shown (Figure 3.87a), also at the corresponding prototype scale (Figure 3.87b). The relative density of sand after spin-up was equal to 52.6%.

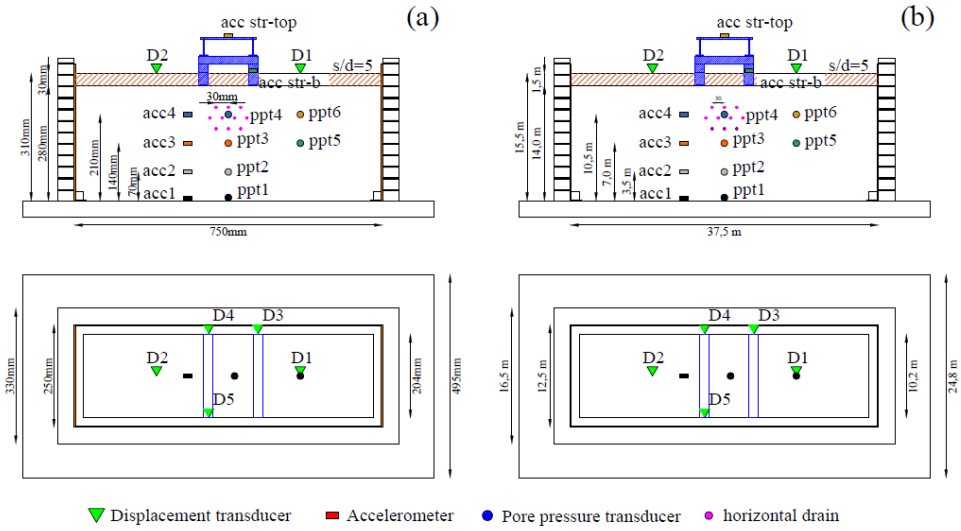

Figure 3.87. M2F_S1_HD1_GM31+: model scale (a) and prototype scale (b).

The accelerometers show a negligible reduction of amplitude and frequency in the singal propagating form the bottom up to the ground surface (Figure 3.88), whereas a substantial amplification was recorded at the structure roof with an amplification factor equal to about 2. The main part of input motion was included in the frequencies range between 1 and 8 Hz (Figure 3.89) and shows a high frequency content with a peak at 1 Hz.

The same result of the amplification is shown by the amplification functions (Figure 3.90) with a mean amplification factor on the structure roof equal to about 3.

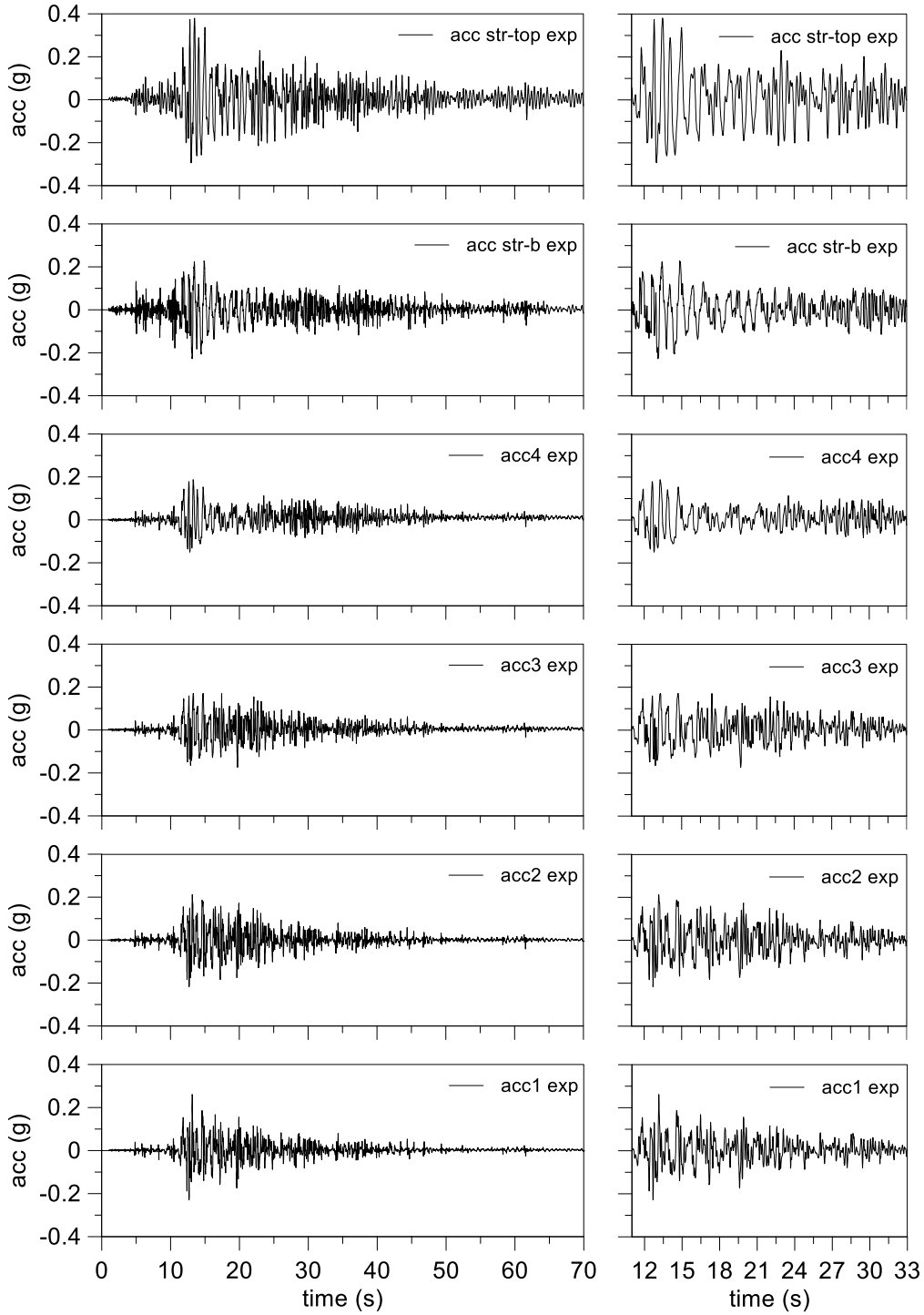

Figure 3.88. M2F_S1_HD1_GM31+: main time interval of acceleration time histories.

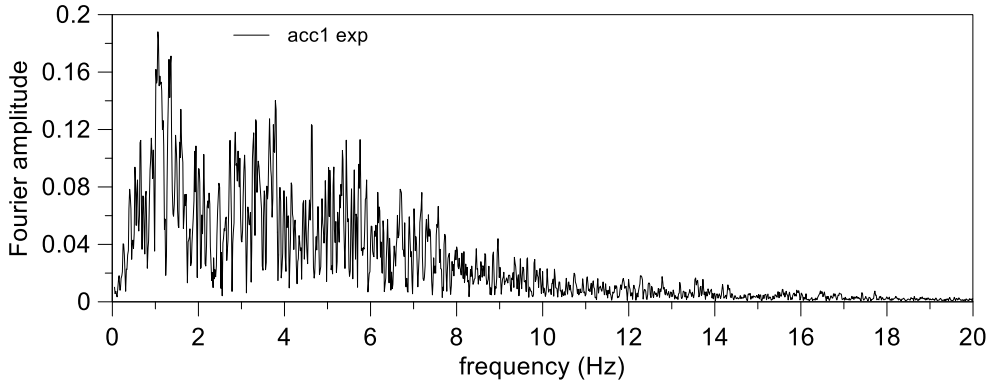

Figure 3.89. M2F_S1_HD1_GM31+: Fourier spectrum of the input signal.

The motion led to the excess pore pressure build-up (Figure 3.91) with higher value at the bottom of the model (ppt1 and ppt2). The transducer between the drains recorded lower excess pore pressure than ppt6 highlighting the efficiency of the drains. The ppt6 achieved a threshold exhibiting the occurrence of liquefaction in the surrounding soil. A very slow dissipation process was recorded from all the pore pressure transducers; this effect could be due to the presence of the clay crust that prevented the water flow through the upper surface. The vertical profiles (Figure 3.91a) show a fast excess pore pressure build-up in the deeper part of the model. The strong slope of the profile between 5 and 9 meters indicates a large hydraulic gradient imposed by the presence of the horizontal drains. During the dissipation phase (Figure 3.91b) the concavity of the vertical profile of the excess pore pressure indicates the presence of a water flow from the bottom to the drains. The quasi-vertical profiles in the dissipation phase indicates that the influence of the drains reached also the deepest part of the soil domain.

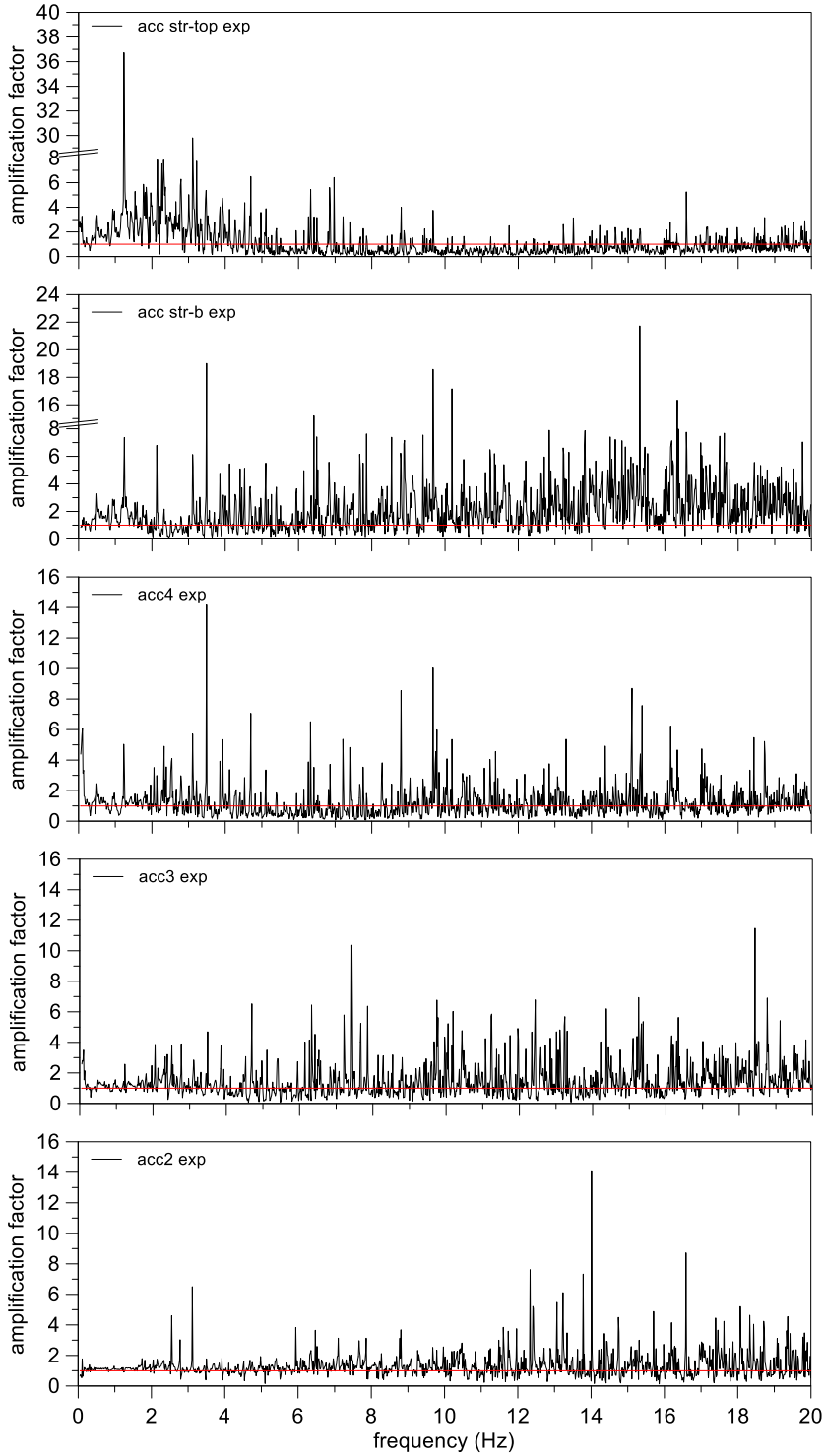

Figure 3.90. M2F_S1_HD1_GM31+: amplification functions.

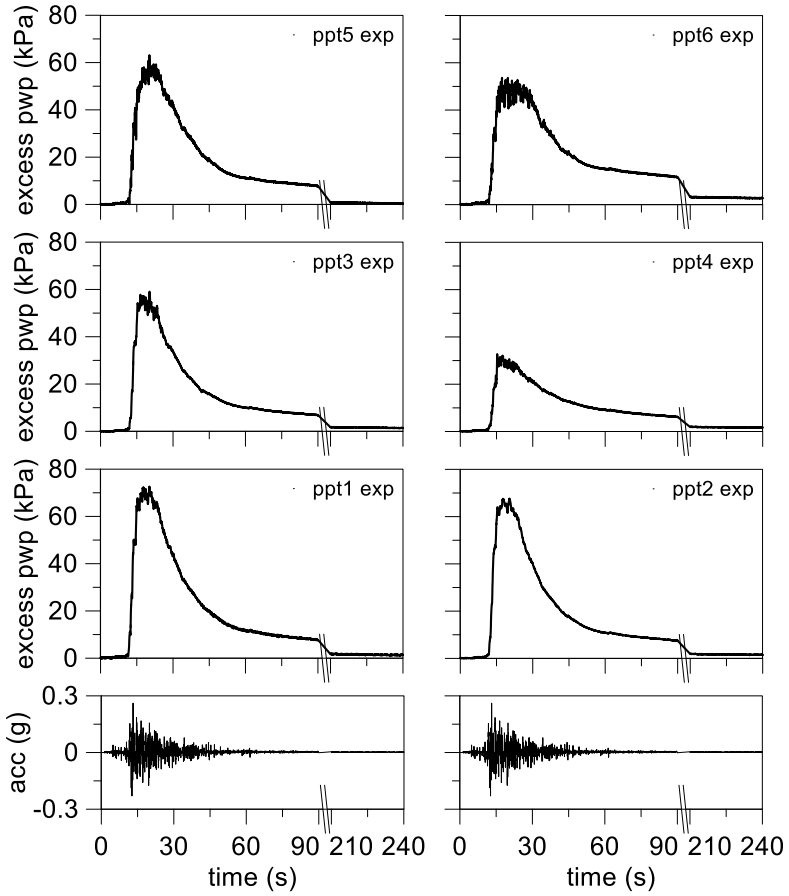

Figure 3.91. M2F_S1_HD1_GM31+: excess pore water pressure time histories.

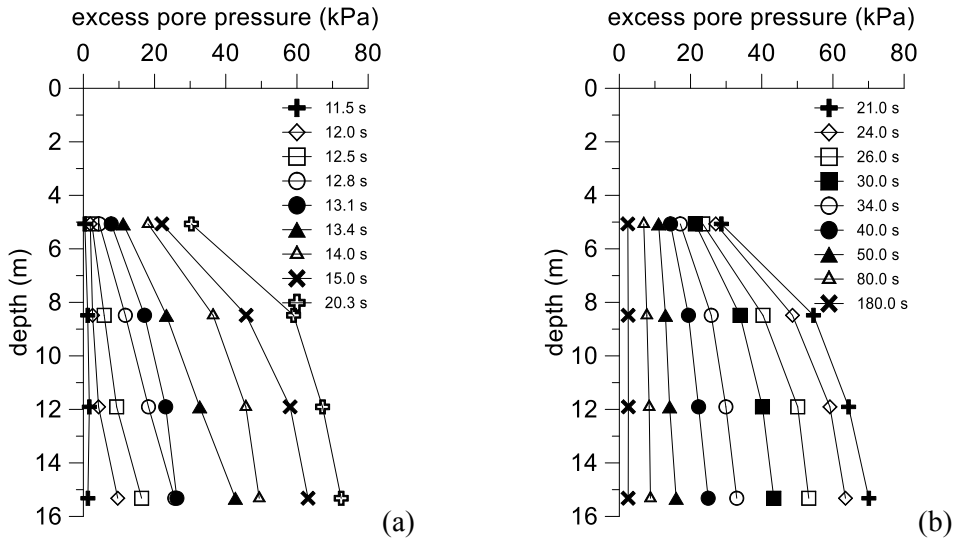

Figure 3.92. M2F_S1_HD1_GM31+: vertical profiles of excess pore water pressure time histories for build-up phase (a) and dissipation phase (b).

The amount of settlements in “free field” condition (Figure 3.93, D1 and D2) was been the same of the test without horizontal drains (Figure 3.65), whereas the structure exhibited half settlements in presence of horizontal drains. Absolute settlements were reduced from about 0.3m to about 0.15m. Moreover, the tilt of the structure from the settlements measured on D3-D4 and D3-D5 were largely reduced. The mean tilt at the end of shaking was equal to 0.7°, whereas a tilt equal to 0.1° occurred in the transversal direction computed by the difference of the settlement measurements by D4-D5. This result highlights the efficiency of the horizontal drains as liquefaction mitigation technique also in the presence of a lower permeably crust. Reconsolidation settlement in free field condition leaded to 2.3% of mean volumetric strain value, fully included in Lee and Albaisa (1974) interval.

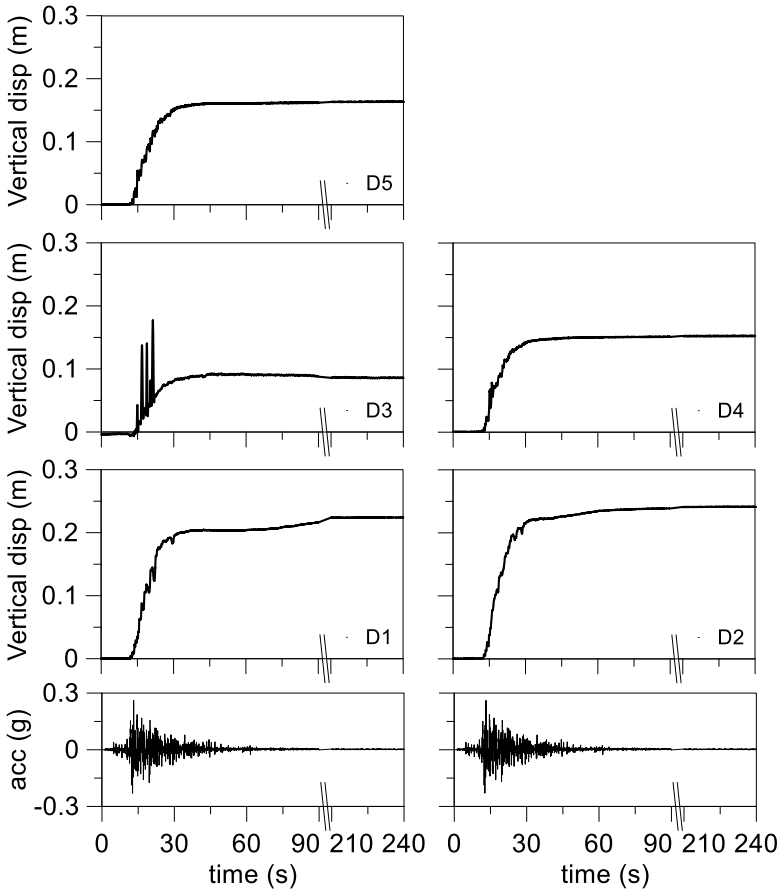

Figure 3.93. M2F_S1_HD1_GM31+: ground surface displacement time histories.

3.12 Response with induced partial saturation

In this section the results of the centrifuge tests with induced partial saturation (IPS) as mitigation techniques, which were carried out by ISMGEO, are reported in terms of records of accelerations, excess pore pressure and displacements of the ground surface, at the prototype scale.

The models were created with the procedure shown in section 3.8. Four nozzles were employed on the bottom of the model injecting air to desaturate the soil. This allowed to study the effects of the reduction of pore fluid bulk stiffness on the excess water pressure build-up. Indeed, the induced partial saturation creates a pore fluid composed by disperse air bubbles and water that has a very smaller bulk stiffness than pure water. For this mitigation technique, small desaturation degree is necessary and the suction in these conditions is generally negligible. The nozzles for air injection and transducers for measuring acceleration and pore pressure were deployed during the pluviation phase.

The settlements of the ground surface were recorded by two displacement transducers.

3.12.1 Single layer model (M1_S1_IPS4)

The layout of the model is shown in Figure 3.94, four accelerometers and five pressure transducers were deployed in the soil during deposition forming two vertical arrays, except ppt2 that was located in the centre of the model above the nozzles.

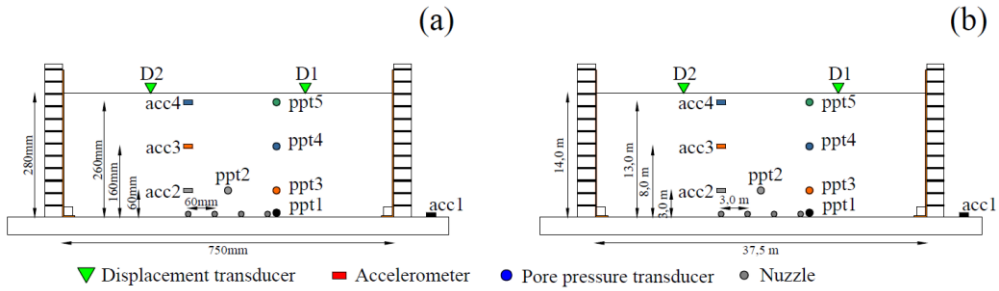

Figure 3.94. M1_S1_IPS4_GM31: model scale (a) and prototype scale (b).

The centrifuge model was tested twice. In the first test the standard input ground motion was applied (GM31) but no clear evidences of the liquefaction were observed. Therefore, a further amplified input motion was applied (GM31+).

3.12.1.1 Ground motion GM31

The acceleration time histories measured during shaking are shown in Figure 3.95. The accelerometers acc2 is not shown because it did not work. An amplification of the amplitude of the signal is shown by shallowest accelerometer (acc4). The signal was subjected to an elongation during the travel through the soil. Indeed the significant duration, evaluated as the period of time when the intensity factor is comprised in the range from 5% to 95% (Arias, 1970), is equal to 13s for the acc1 whereas it is 18s for the acc4, with an increment of the 40%. The main time interval of the signal is shown on the right of the Figure 3.95.

Figure 3.96 shows that the significant frequency content of the input signal is in the first 10 Hz with largest peaks in 1 and 4 Hz. Noteworthy that also this test has the same theoretical input motion of M1_S1_GM31 test, but the maximum Fourier amplitude in this case is equal to around 0.06, so largely lower than the amplitude reported in Figure 3.32, equal to around 0.14. Moreover, the relative density of the model after spin-up phase was equal to 52.4% higher than the free field test equal to 45.5%. Therefore, a direct comparison between these tests is not possible.

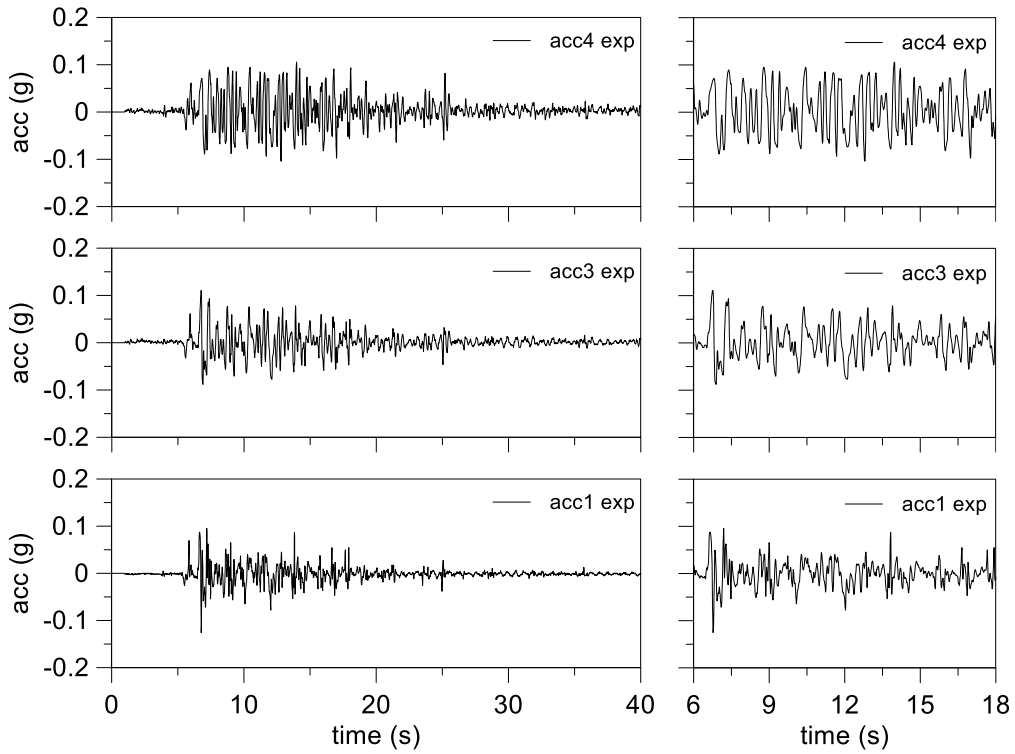

Figure 3.95. M1_S1_IPS4_GM31: main time interval of acceleration time histories.

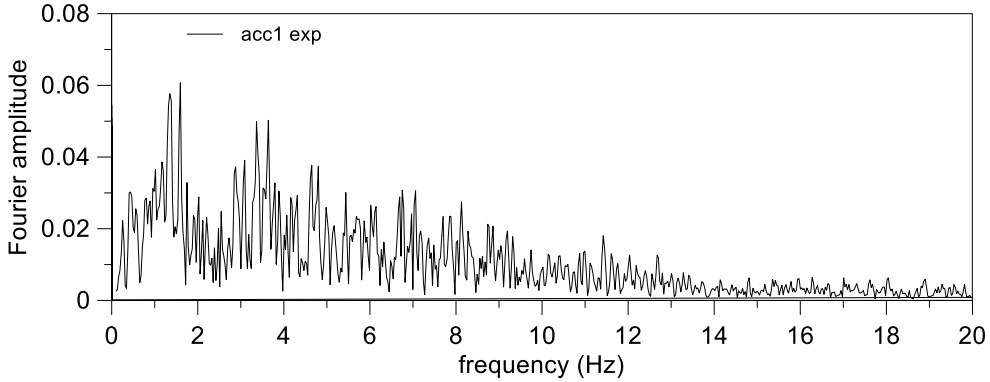

Figure 3.96. M1_S1_ IPS4_GM31: Fourier spectrum of the input signal.

The amplification functions show a progressive amplification from the base of the model up to the ground surface (Figure 3.97). The amplification interval is included between 1-4 Hz with isolated peaks at high frequency that indicate smaller stiffness loss during the motion, compared to the corresponding untreated model (M1_S1_GM31), that may be due to a lower amount of excess pore pressure build-up.

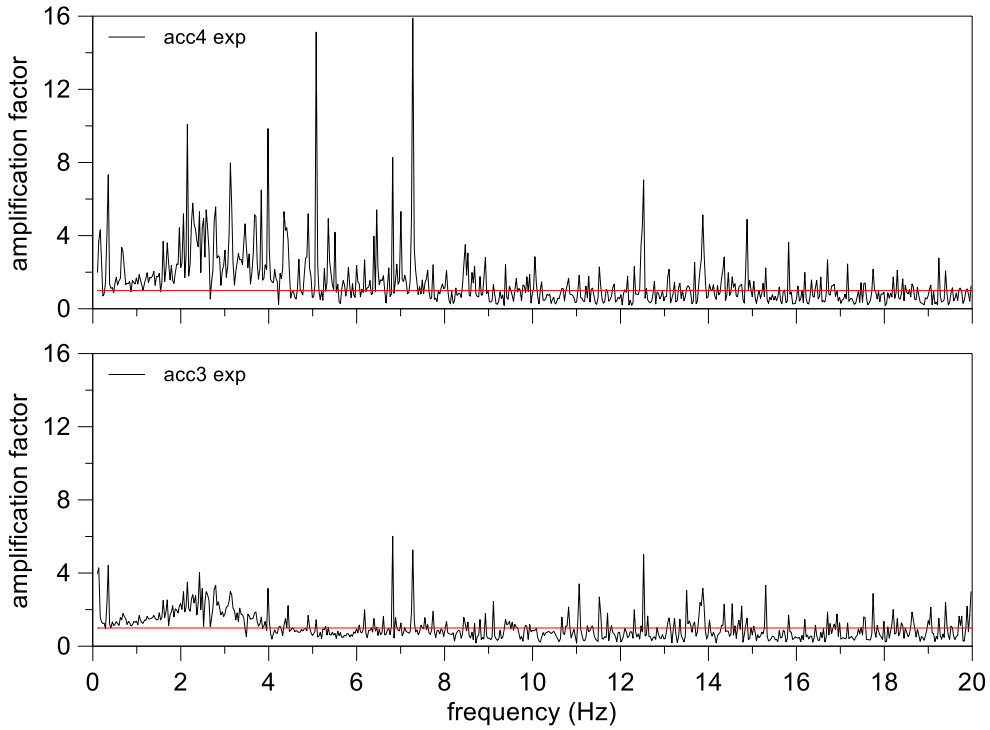

Figure 3.97. M1_S1_ IPS4_GM31: amplification functions.

Indeed, the time histories of excess pore pressure (Figure 3.98) show small peaks for each transducer except for shallowest ppt5 that likely reached liquefaction. The ppt3 recorded larger values of excess pore pressure than ppt2, although they are at the same depth. Indeed ppt3, as well as ppt1, may be not strongly affected by the air injection, due to its position, while ppt2, located just above the nozzles, is largely subjected to the desaturation of the surrounding soil. The transducer ppt2 placed on the nuzzles and surrounding soil is largely subjected to the air injection. This transducer presents a lower peak than ppt3 that proves the efficiency of the IPS to reduce the excess pore pressure build-up.

The vertical profiles of excess water pressure show a typical behaviour in the build-up phase (Figure 3.99a) with larger excess water pressure on the bottom that indicate a water flow directed to upper seepage surface. The vertical profiles of excess pore pressure show that all the pore pressure transducer, except ppt6, reached an excess pore pressure value below the straight line that joins the zero value at the ground surface and the excess pore pressure in ppt6. This proves that the liquefaction did not occur in the deeper soil layers.

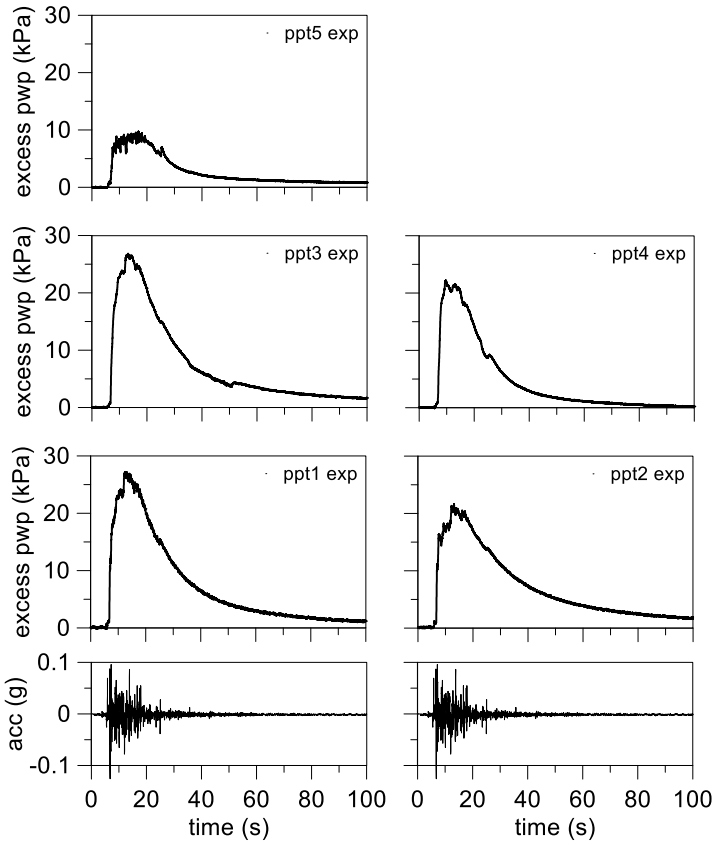

Figure 3.98. M1_S1_ IPS4_GM31: excess pore water pressure time histories.

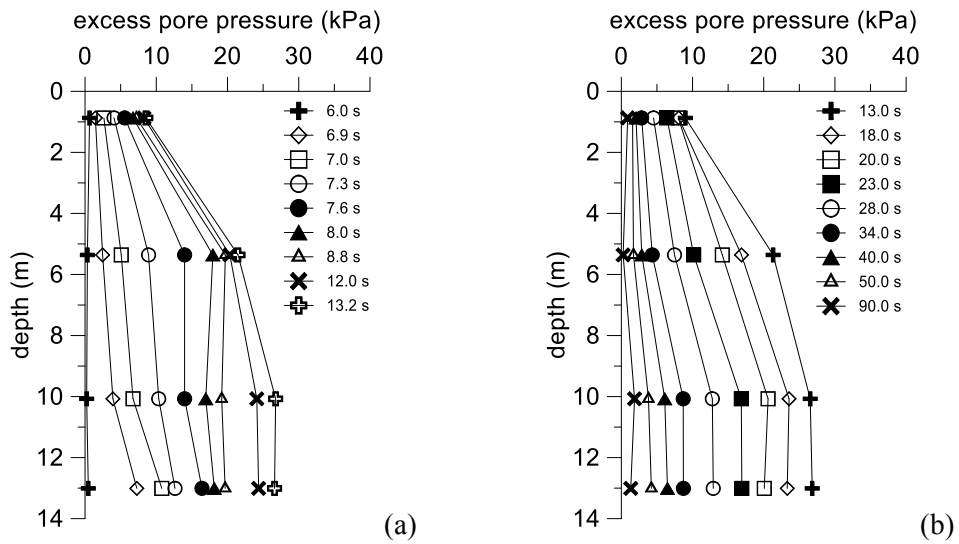

Figure 3.99. M1_S1_ IPS4_GM31: vertical profiles of excess pore water pressure time histories for build-up phase (a) and dissipation phase (b).

As previously mentioned, the time history of settlement was recorded through the two displacement transducers deployed on the ground surface. The development of the settlement is shown in Figure 3.100. It is possible to note a slight difference between the two transducer records. Large settlements were observed during the strong part of the input signal. This result could be due to two likely mechanisms: partial drainage behaviour of the soil during the strong motion; punching of the plates located on the tip of the displacement transducers.

If the punching is assumed negligible, the settlement is due to the reconsolidation of the soil. Considering the thickness of liquefied soil equal to about 13 m, the mean volumetric strain in the soil would be equal to 0.9%. This value is below the lower boundary of the interval suggested by Lee and Albaisa (1974). The amount of the displacement measured after strong motion, in this case, is almost equal to the total settlement.

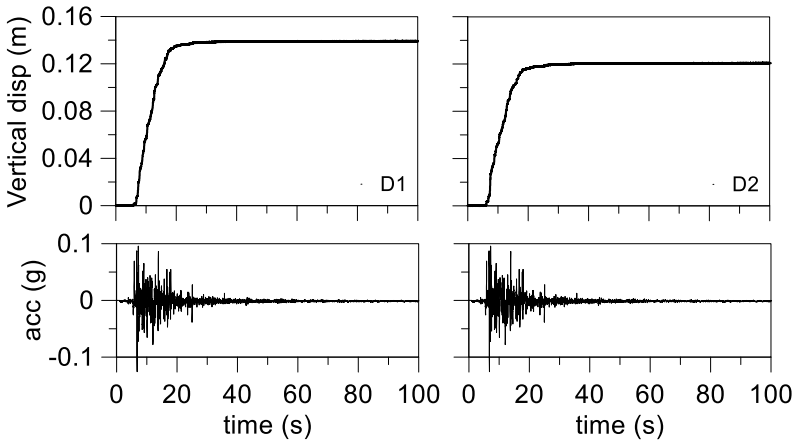

Figure 3.100. M1_S1_ IPS4_GM31: ground surface displacement time histories.

3.12.1.2 Ground motion GM31+

The acceleration time histories during the seismic signal are shown in Figure 3.101. The accelerometers acc2 is not shown because it did not work. A slight reduction of the amplitude and frequencies content of the signal is shown by acc3 and acc4. This last accelerometer showed an abnormal offset after about 15 seconds. The signal was subjected to an elongation during the travel through the soil, indeed the significant duration, evaluated by intensity factor in the for the acc1 is equal to 21s whereas for the acc4 is equal to 34s with an increment of the 62%. The main time interval of the signal, determined as 5-95% intensity factor (Arias, 1970), is shown on the right of the Figure 3.101.

Figure 3.102 shows that the significant frequency content of the input signal is in the first 10 Hz with largest peaks in 1 and 4 Hz. It is worth noting that the input motion shows a Fourier amplitude peak and frequencies content significantly different from the input motion measured for M1_S1_GM31 test. Moreover, the initial relative density after spin-up phase was equal to 57.2%, that is higher than in the free-field test, where it was equal to 45.5%. Therefore, a direct comparison between the results of these tests is not possible.

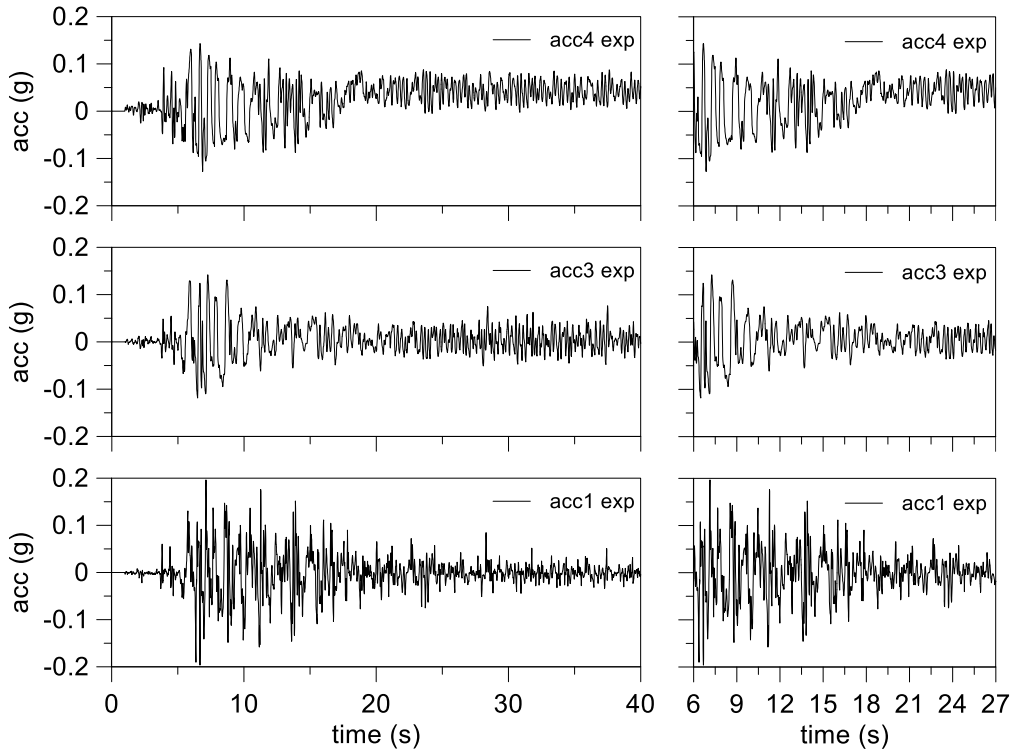

Figure 3.101. M1_S1_IPS4_GM31+: main time interval of acceleration time histories.

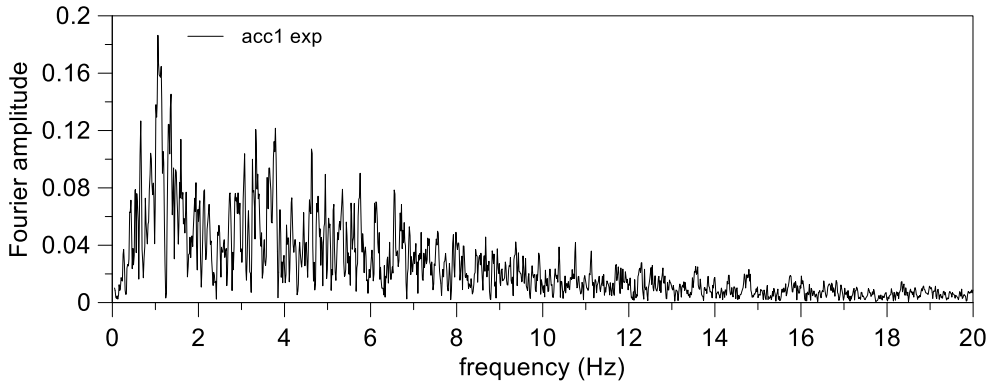

Figure 3.102. M1_S1_ IPS4_GM31+: Fourier spectrum of the input signal.

The amplification functions do not show significant amplification or deamplification (Figure 3.103). The accelerometer acc4 shows some isolated peaks with a mean value near the unity and a large peak at very low frequencies due to the offset previously mentioned.

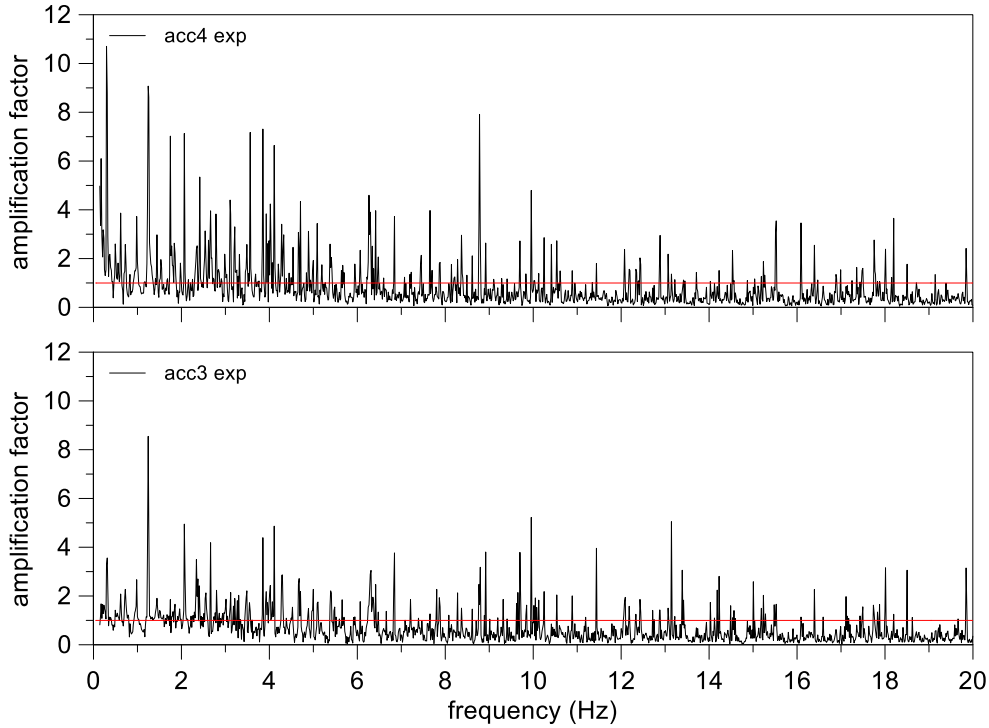

Figure 3.103. M1_S1_ IPS4_GM31+: amplification functions.

Large excess water pressure builds-up was read by transducers (Figure 3.104). Peak values of excess water pressure were recorded by ppt1 and ppt3, that were not strongly affected by the air injection. The transducer ppt2 located at the same depth of ppt3 read a lower peak, proving that the IPS mitigation technique had reduced the excess water pressure build-up. Moreover, ppt2 shows a slight slower dissipation velocity that could be an effect of the partial saturation.

The shallower transducers ppt4 and ppt5 show the achievement of a stable value of excess pore pressure, proving the liquefaction occurrence in the surrounding soil. The ppt4 shows an abnormal drop near 10s and a negative excess water pressure at 90s, that may be due to a malfunctioning. The transducer ppt5 preserved the excess pore pressure for long time since in this area it was maintained by the water flow toward the upper seepage surface.

The vertical profiles show a large excess pore pressure build-up in the upper and middle part of the model (Figure 3.105a). The liquefaction occurrence in ppt5 and the linear distribution of excess water pressure at the end of the stronger part of the motion prove that the liquefaction was extended up to 10m depth. The malfunctioning of ppt4, located at 5m depth, can be noted in the vertical profile during the dissipation phase (Figure 3.105b). However, the vertical profiles exhibit the existence of a water flow direct from the model bottom to the upper seepage surface.

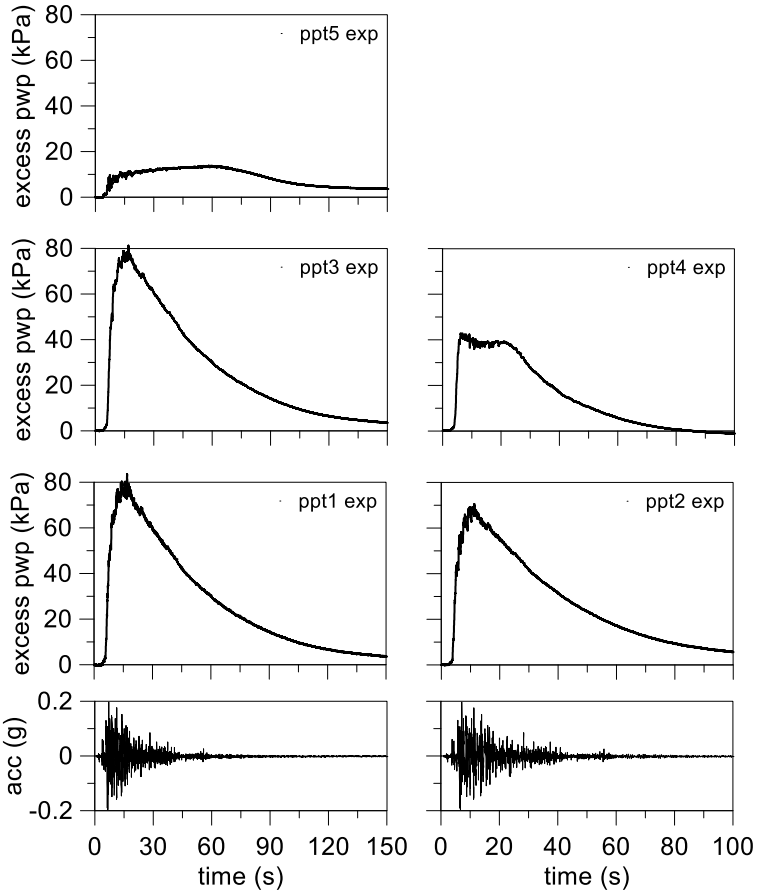

Figure 3.104. M1_S1_ IPS4_GM31+: excess pore water pressure time histories.

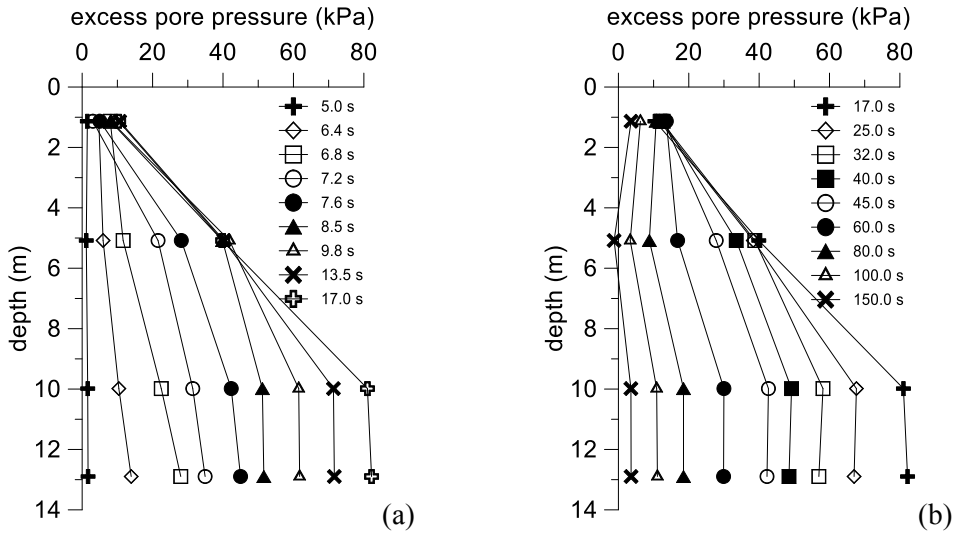

Figure 3.105. M1_S1_ IPS4_GM31+: vertical profiles of excess pore water pressure time histories for build-up phase (a) and dissipation phase (b).

The settlements of the ground surface are shown in Figure 3.106. A gradual development of settlement was recorded and after the stronger part of the input motion, it was still significant increasing. This result was due to a slower reconsolidation process.

Considering the thickness of liquefied soil equal to about 10m, the mean volumetric strain in the soil is equal to 3.9%. This value is in the interval suggested by Lee and Albaisa (1974).

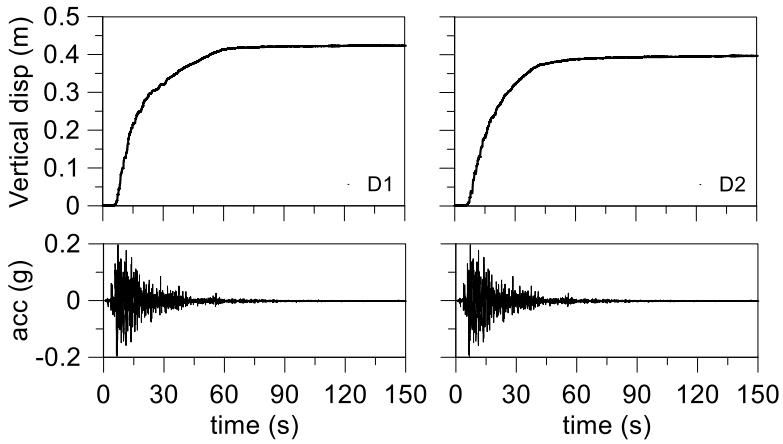

Figure 3.106. M1_S1_ IPS4_GM31+: ground surface displacement time histories.

3.12.2 Double layer model (M2_S1_IPS4)

In this section are shown the results of the centrifuge tests with induced partial saturation (IPS) as mitigation techniques in presence of a low permeable clay crust (Pontida clay) with a 1.5 thickness. In the following the acceleration, excess water pressure and displacements of ground surface records are shown in prototype scale.

The models were realised with the procedure showed in the section 3.8. The nozzles and transducers were placed during the pluviation phase. Four nozzles were employed on the bottom of the model injecting air to desaturate the soil. This test allowed to study the behaviour of IPS in presence of a low permeable crust that could modify the distribution and the saturation degree in the soil.

The settlements of the ground surface were recorded by two displacement transducers.

Figure 3.107 shows the transducers position and model dimensions (Figure 3.107a) and their correspondent prototype scale (Figure 3.107b).

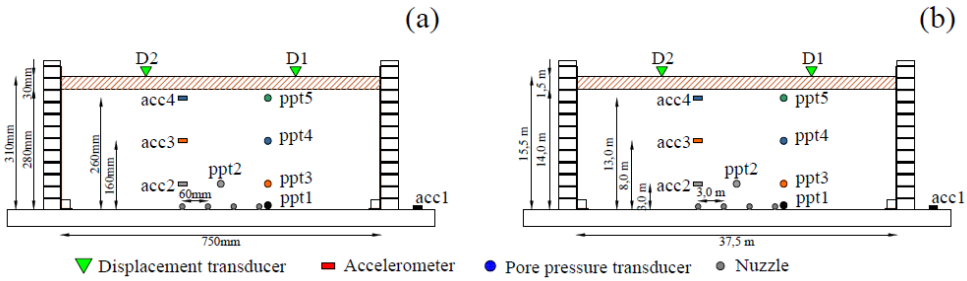

Figure 3.107. M2_S1_IPS4_GM31and GM31+: model scale (a) and prototype scale (b).

3.12.2.1 Ground motion GM31

The acceleration time histories during the seismic signal are shown in Figure 3.108. The mean amplitude of signals increases from the bottom up to ground surface. on the right of the Figure 3.108 is shown the main portion of the signal evaluated by the intensity factor in the interval 5-95% (Arias, 1970).

Figure 3.109 shows that the significant frequency content of the input signal is beneath 10 Hz with two larger peaks in 1 and 3 Hz. It is worthy note that also this test has the same theoretical input motion of M2_S1_GM31 test, but the maximum Fourier amplitude in this case is equal to around 0.10, slightly higher than the peak shown in Figure 3.40, equal to around 0.09. Moreover, the relative density of the soil after spin-up was equal to 47.2% almost the same of the test without mitigation technique that has a relative density of the soil equal to 50.5%. Therefore, a direct comparison between these tests is possible.

The amplification functions show a progressive amplification starting from the bottom of the model up to the ground surface (Figure 3.110). The maximum amplification factor is included between 2-3 Hz where reached a value equal to about 4. The absence of a significant changing of frequencies content highlights that probably the liquefaction did not occur.

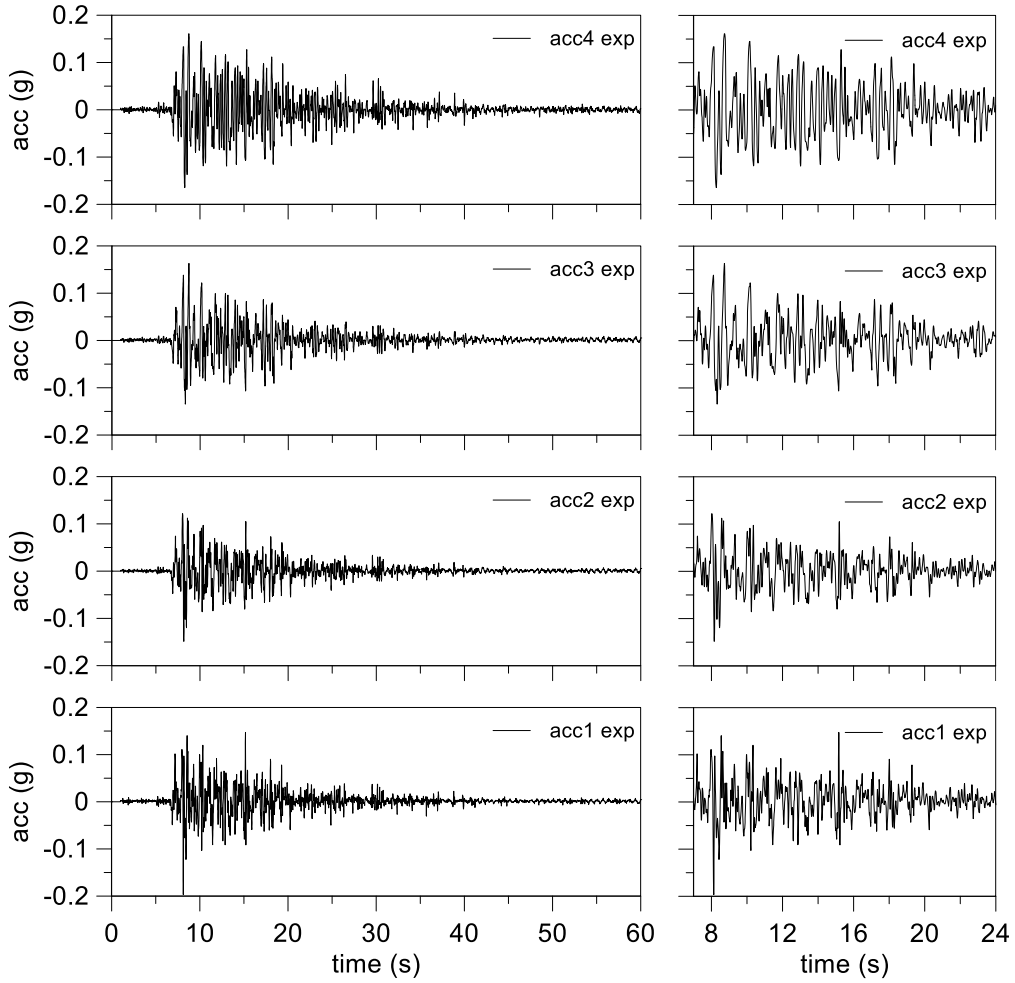

Figure 3.108. M2_S1_ IPS4_GM31: main time interval of acceleration time histories.

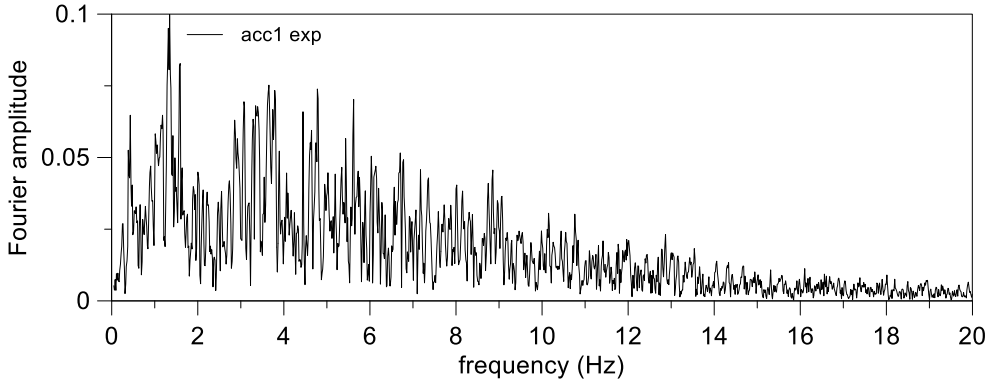

Figure 3.109. M2_S1_ IPS4_GM31: Fourier spectrum of the input signal.

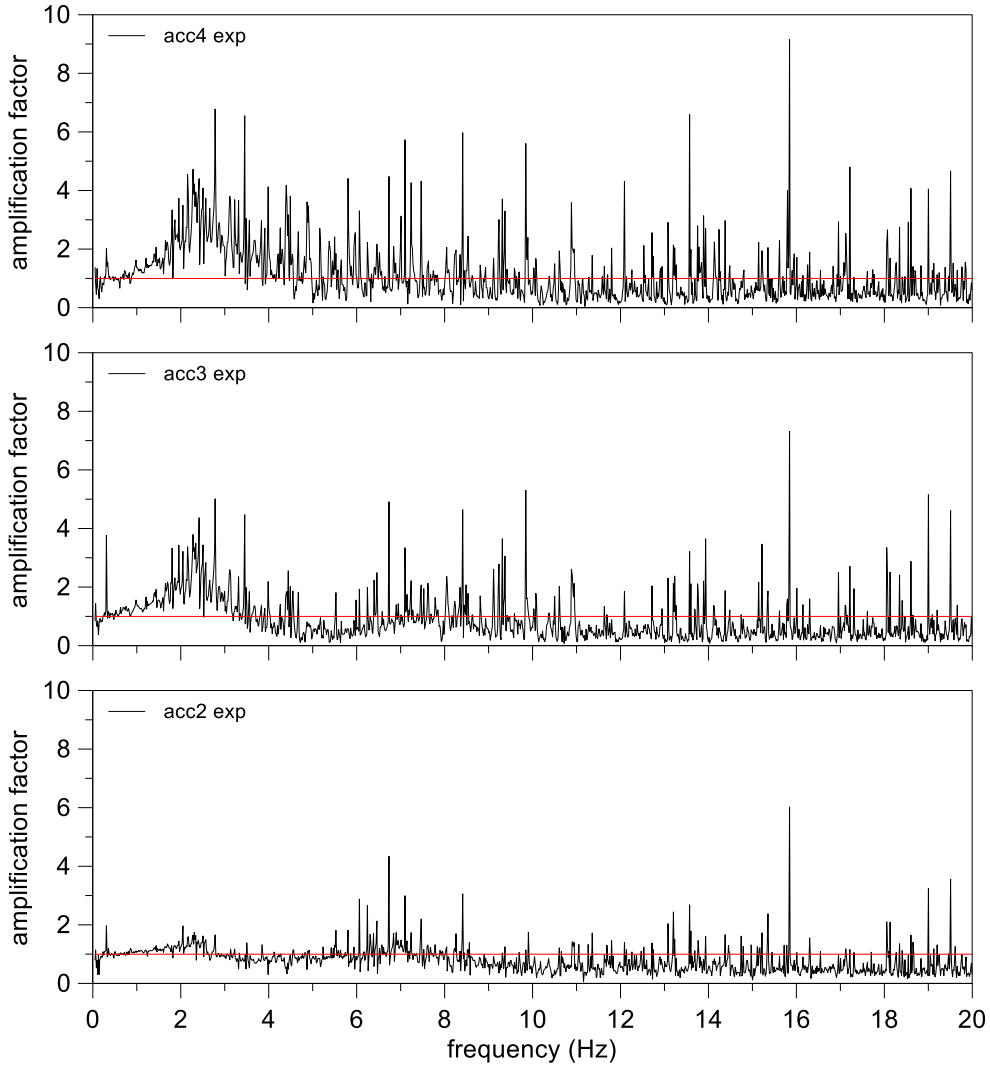

Figure 3.110. M2_S1_ IPS4_GM31: amplification functions.

Indeed, the amount of excess pore pressures in the time histories (Figure 3.111) do not show an achievement of the liquefaction. The presence of clay cap slowed down the dissipation of the excess water pressures in the time proving that the clay crust reduced the dissipation capability of the system.

The peak values of excess water pressure are significantly lower than the values recorded in the test without mitigation technique (Figure 3.42), this proves the efficiency of the IPS in the reducing the excess water pressure build-up. Furthermore, the same peak value reached by transducers ppt2 and ppt3 proves a higher homogeneity of the mitigation treatment.

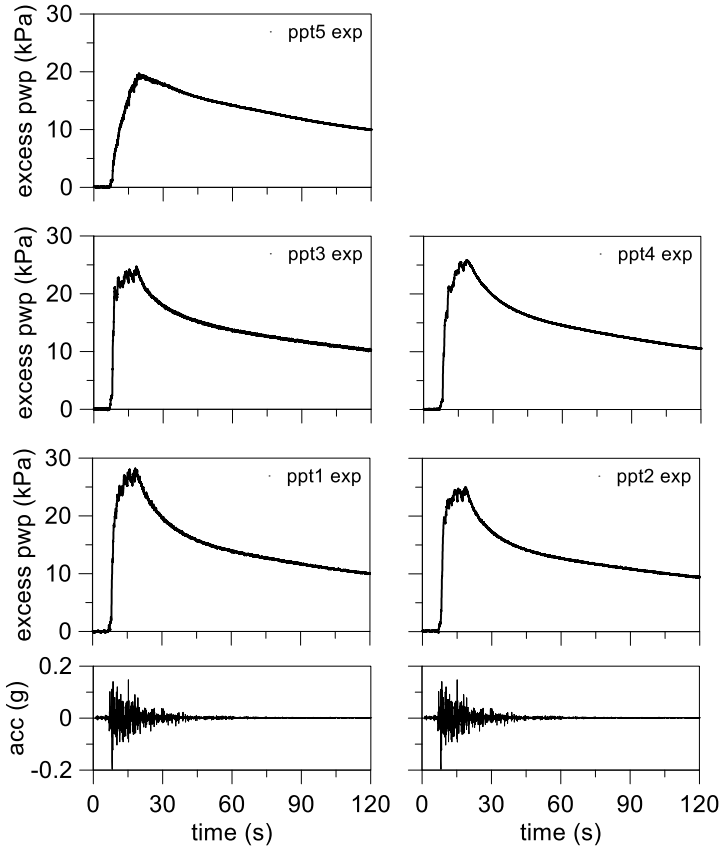

Figure 3.111. M2_S1_ IPS4_GM31: excess pore water pressure time histories.

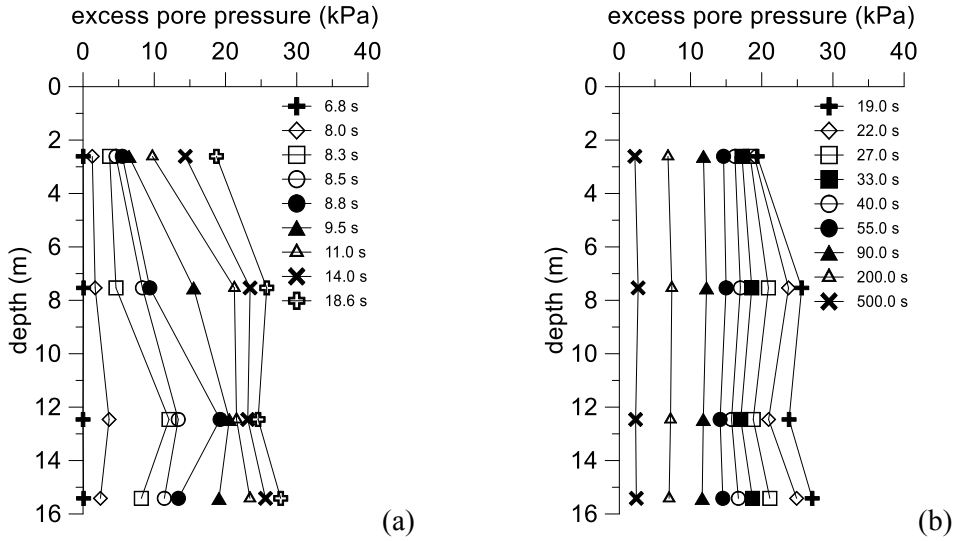

Figure 3.112. M2_S1_ IPS4_GM31: vertical profiles of excess pore water pressure time histories for build-up phase (a) and dissipation phase (b).

The vertical profiles show abnormal excess water pressure build-up (Figure 3.112a) with at 12m depth. This anomaly is present in the first part of the dissipation (Figure 3.112b) until reaching of a constant distribution with depth (after the 55s). Hence, the distribution did not lead to a vertical flow, impeded by clay crust, but probably an internal redistribution from the soil regions with higher excess water pressure to lower ones was happened.

Figure 3.113 shows the settlement of the ground surface. The larger part of the settlements was developed during the strong part of the motion. The difference between the two maximum values of settlements is smaller than in the tests without clay crust.

Considering the maximum settlement and whole the height of the model, the mean volumetric strain in the soil is equal about to 0.3%. This value is significant smaller than the lower boundary of the range suggested by Lee and Albaisa (1974) proving that the liquefaction did not occur.

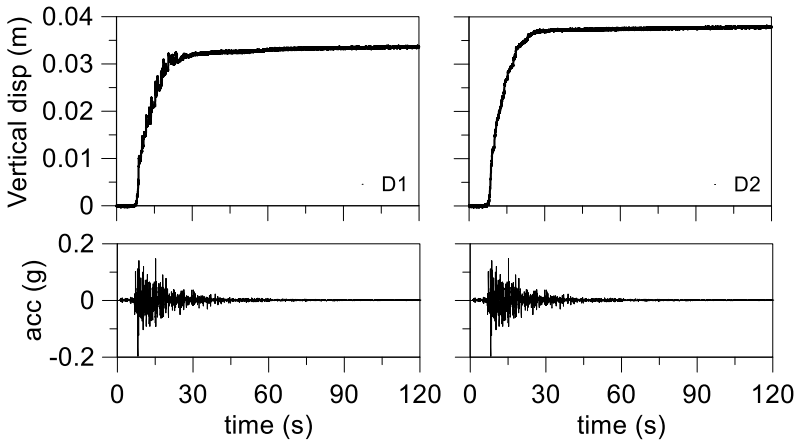

Figure 3.113. M2_S1_ IPS4_GM31: ground surface displacement time histories.

3.12.2.2 Ground motion GM31+

The acceleration time histories during the seismic signal are shown in Figure 3.114. The mean amplitude of signals decreases from the bottom up to ground surface. The significant duration of the signal evaluated by intensity factor in the interval 5-95% (Arias, 1970) is shown on the right of Figure 3.114. The accelerometer acc4 shows a strong reduction of the amplitude after about 25 seconds, probably due to the liquefaction occurrence in the surrounding soil.

Figure 3.115 shows that the significant frequency content of the input signal is beneath 10 Hz with large peaks in 1 and 3 Hz. The relative density of the soil model after spin-up was equal to 48.5%.

The amplification functions (Figure 3.116) show an almost constant amplification factor with depth with a slight deamplification in correspondence of the shallowest accelerometer (acc4).

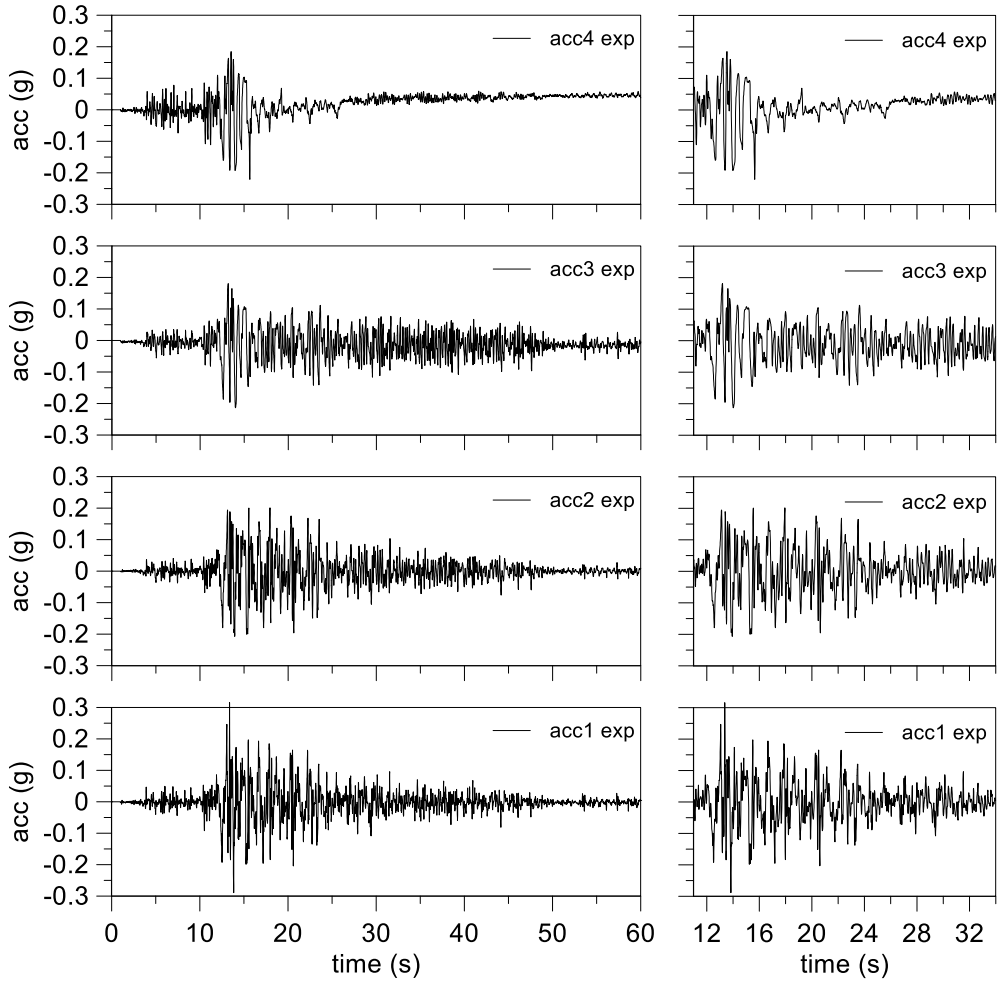

Figure 3.114. M2_S1_ IPS4_GM31+: main time interval of acceleration time histories.

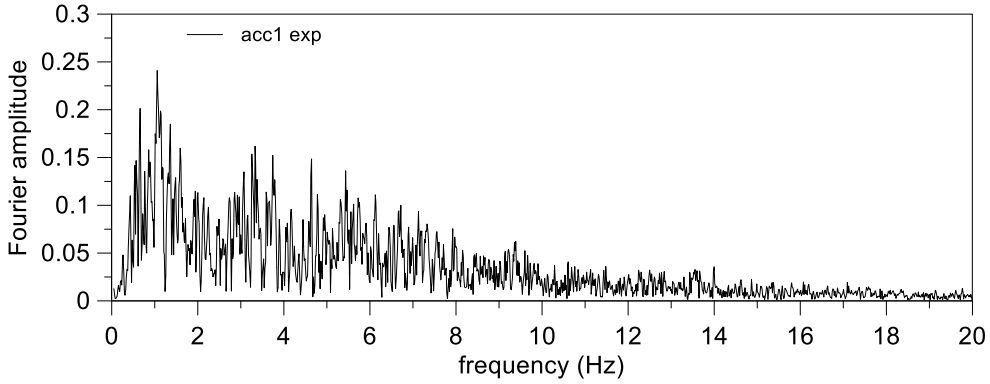

Figure 3.115. M2_S1_ IPS4_GM31+: Fourier spectrum of the input signal.

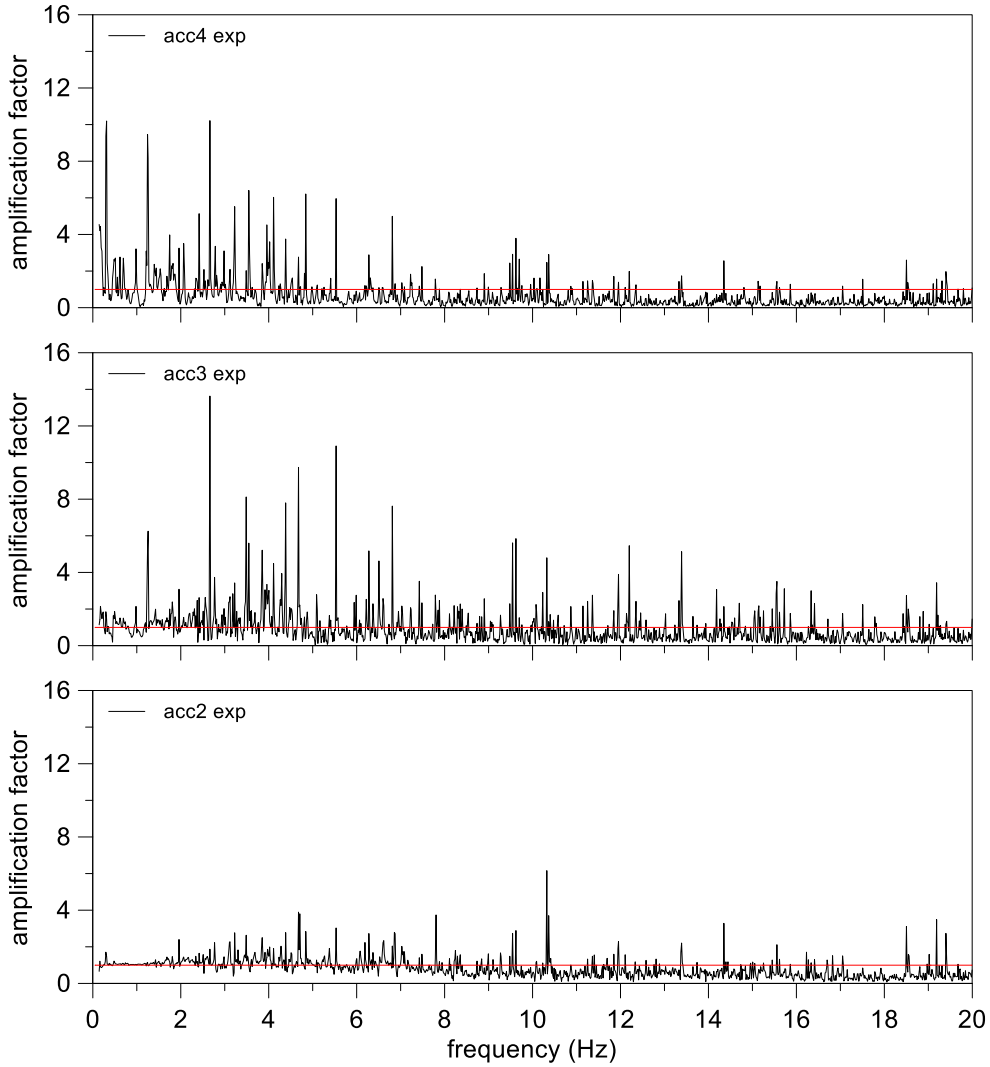

Figure 3.116. M2_S1_ IPS4_GM31+: amplification functions.

High levels of the excess pore pressure were reached in shallowest part of the model (Figure 3.117) in correspondence with ppt4 and ppt5, achieving liquefaction identified by a threshold. Liquefaction lasted for long time after the stronger portion of the shaking. The presence of the clay crust led to a very slow dissipation of the excess pore pressures.

The highest peak value of the excess pore pressure was recorded in lower part of the model (ppt1 to ppt3). The transducer ppt2 positioned above the nozzles did not show a significant reduction of the peak excess pore pressure compared to the ppt3 placed at the same depth. This effect may be due either to a homogeneous distribution of the induced partial saturation or to a negligible effect of the mitigation technique on the excess pore pressure build-up.

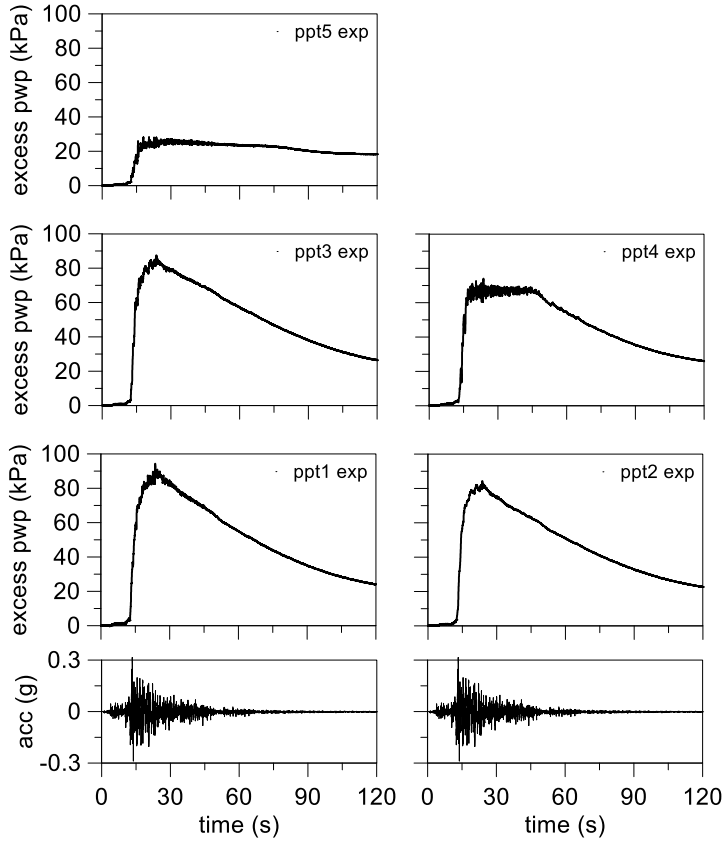

Figure 3.117. M2_S1_ IPS4_GM31+: excess pore water pressure time histories.

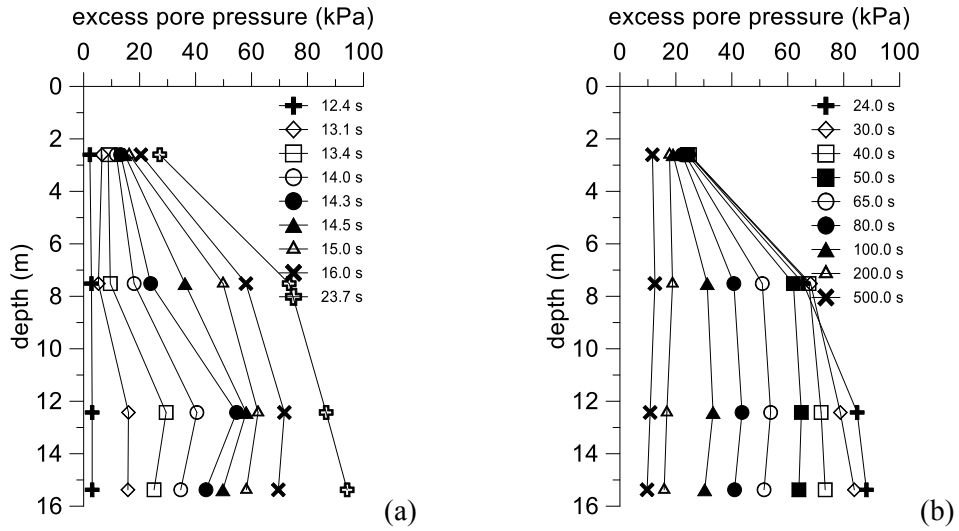

Figure 3.118. M2_S1_ IPS4_GM31+: vertical profiles of excess pore water pressure time histories for build-up phase (a) and dissipation phase (b).

A large excess pore pressure build-up was recorded at about 12 m depth (Figure 3.118a). The liquefaction occurred in the upper part of the model (ppt4 and ppt5). The distributions of the excess pore pressure prove the existence of an initial significant water flow direct towards the upper surface during the dissipation (Figure 3.118b). After about 50 seconds the lower part of the vertical profiles shows a slope that indicates the presence of a water flow from 12m depth towards the bottom of the model.

The settlements of the ground surface are shown in Figure 3.119. A significant part of the settlement development after strong part of the motion for the presence of the clay crust that reduced the dissipation capability of the system.

Considering the maximum settlement and the thickness of the liquefied soil equal to about 8m, the mean volumetric strain in the soil is equal about to 2.8%. This value is in the range suggested by Lee and Albaisa (1974) proving that the liquefaction occurred.

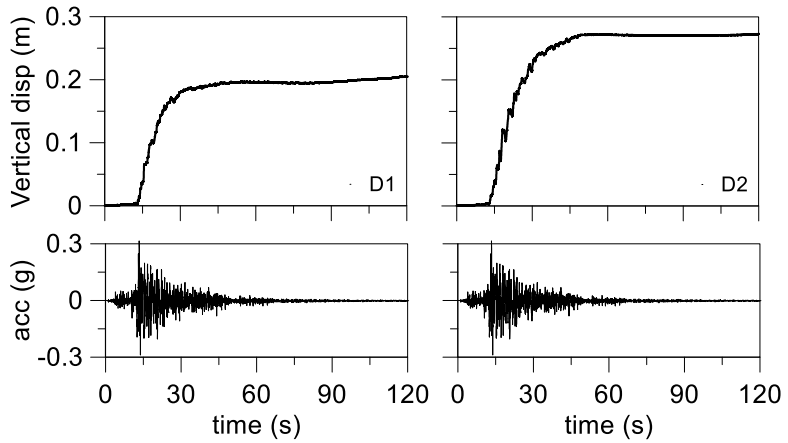

Figure 3.119. M2_S1_ IPS4_GM31+: ground surface displacement time histories.

3.12.3 Building on single layer model (M1F_S1_IPS4)

This test was performed aiming to study the effect of the induced partial saturation (IPS) on the water pressure build-up in presence of a simplified structure. The structure discussed in the section 3.9 was placed at the top of the soil profile with 1.5m of embedment avoiding the contact between the soil and the transversal stiffening elements.

Four nozzles for air injection were deployed at the bottom of the model. Four accelerometers and six pore pressure transducers were placed at different depth during the sand deposition. Furthermore, an accelerometer was glued on the foundation and another one on the roof of the structure (Figure 3.120Figure 2.1). The accelerometers and water pressure transducers from ppt1 to ppt4 formed two vertical arrays to measure the accelerations and the pore pressures along the vertical section. While ppt5 and ppt6 allowed to know the water pressure in the "free field" conditions. The settlement of the ground surface was recorded by two displacement transducers, a plate was fixed on their extremity to avoid punching. Other three displacement transducers were deployed to measure settlements and rotation of the structure. Figure 3.120 shows the model with its monitoring arrangement in model scale (Figure 3.120a) and also in prototype scale (Figure 3.120b).

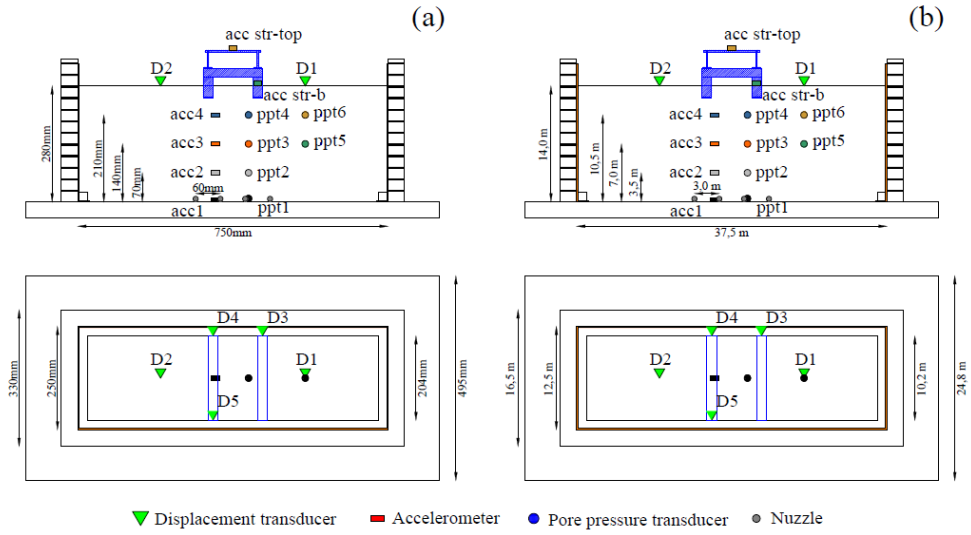

Figure 3.120. M1F_S1_IPS4_GM31+and GM31++: model scale (a) and prototype scale (b).

3.12.3.1 Ground motion GM31+

A clear liquefaction occurrence was not recorded in the previous tests with the structure, for this reason an amplified input motion (GM31+) was applied in this test aiming to achieve the soil liquefaction. The acceleration time histories during the seismic signal are shown in Figure 3.121. The mean amplitude of signals in the soil profile did not increase significantly up to ground surface, whereas a large amplification of the acceleration was recorded at the structure roof.

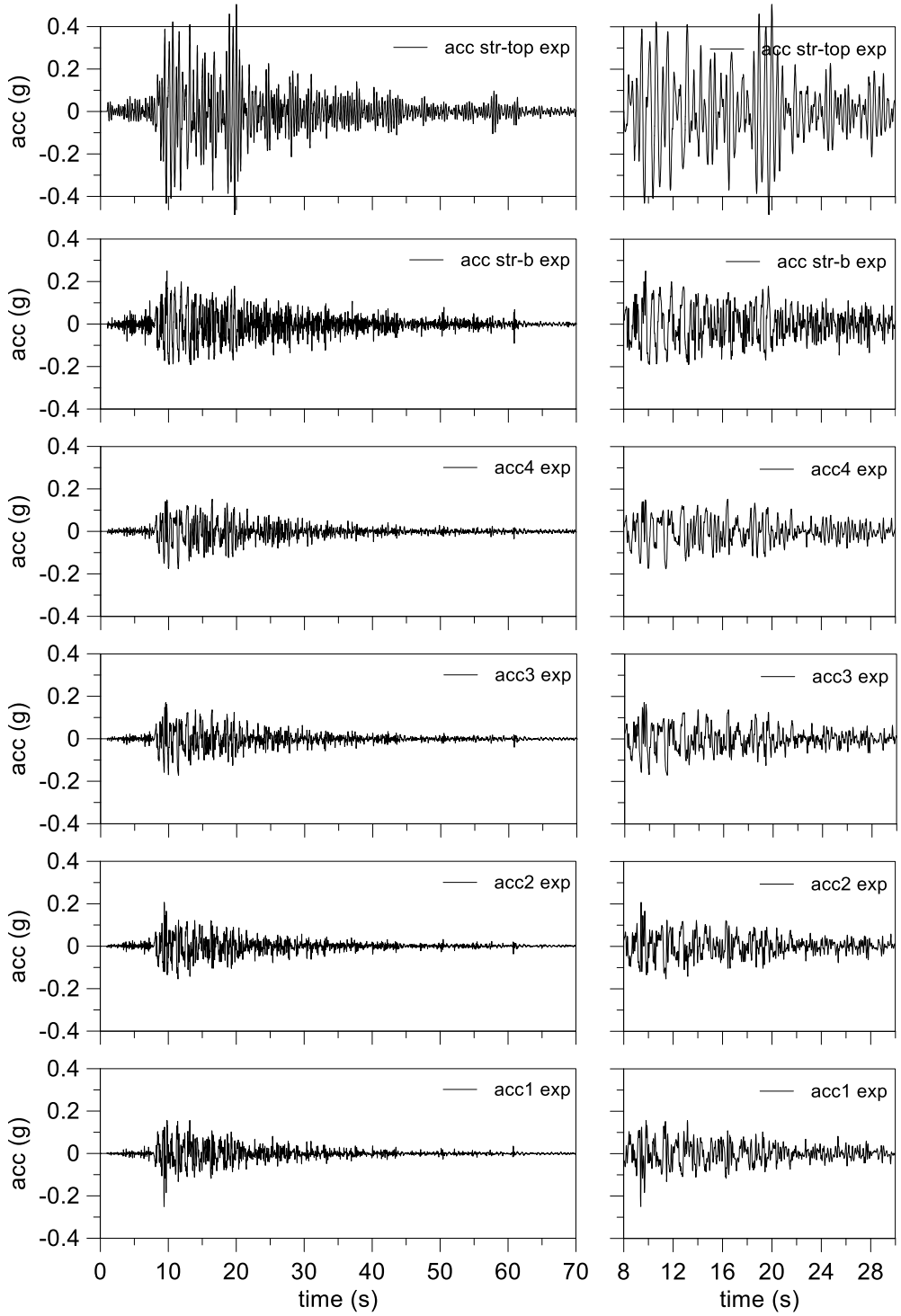

Figure 3.121. M1F_S1_IPS4_GM31+: main time interval of acceleration time histories.

Figure 3.122 shows that the significant frequency content of the input signal is within 10 Hz with larger peaks in 1 and 3 Hz. The relative density of the soil model after spin-up phase was equal to 55.8%.

The amplification functions show a slight amplification of the signal from the bottom of the model towards the ground surface (Figure 3.123). A larger amplification was recorded on the structure foundation and roof within 1-3 Hz.

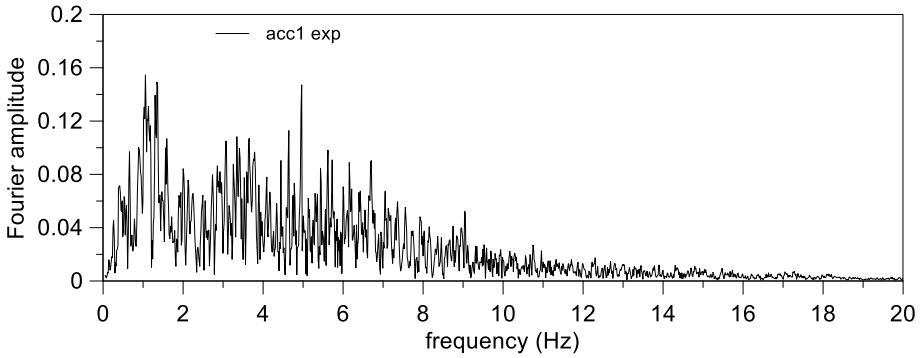

Figure 3.122. M1F_S1_IPS4_GM31+: Fourier spectrum of the input signal.

Very small levels of excess pore pressures in the lower part of the model (Figure 3.124) were recorded by transducers ppt1 and ppt2. The shallowest transducers ppt3 and ppt4 below the structure show a very low levels of excess pore pressure, probably due to a large desaturation of surrounding soil. The liquefaction occurrence was not recorded by transducers, but in ppt5 and ppt6, deployed in "free-field" condition, recorded large excess pore pressure. Transducer ppt2 shows a lower excess pore pressure compared ppt5 and ppt6 proving the effect of mitigation technique in the soil surrounding ppt2.

The vertical profiles show that the excess water pressure build-up was inhibited in the soil surrounding ppt3 and ppt4 while it increased in the lower part of the model (Figure 3.125a). A progressive water flow direct towards the upper surface increased the excess water pressure in ppt3 and ppt4 (Figure 3.125b) proving the presence of an internal redistribution process of excess pore pressures. After about 26 seconds the vertical profiles reached a usual distribution of excess water pressure in the dissipation phase. Hence, the excess pore pressure in shallowest portion of the model increases after the input motion. This could lead to a significant drop of the shear stiffness and strength of the soil below the structure inducing large settlement and tilting.

The amount of settlements in "free-field" condition (Figure 3.126, D1 and D2) was largely reduced compared to the test without mitigation technique (Figure 3.58). However, the "free-field" condition and the structure exhibited not uniform settlements probably due to the smaller values of the absolute settlements measured. Tilt of the structure from the settlement measured on D3 and D4 was equal to 0.15°, whereas a tilt equal to 0.04° happened in the transversal direction computed by the difference of the settlement measure by D4 and D5. This result highlights the efficiency of the induced partial saturation as liquefaction mitigation technique avoiding significant reduction of shear stiffness and shear strength during the earthquake. Reconsolidation settlement in free-field condition led to 0.8% of

mean volumetric strain, computed on 7m of the soil from the bottom to 6m depth, value smaller than the lower boundary of Lee and Albaisa (1974) range.

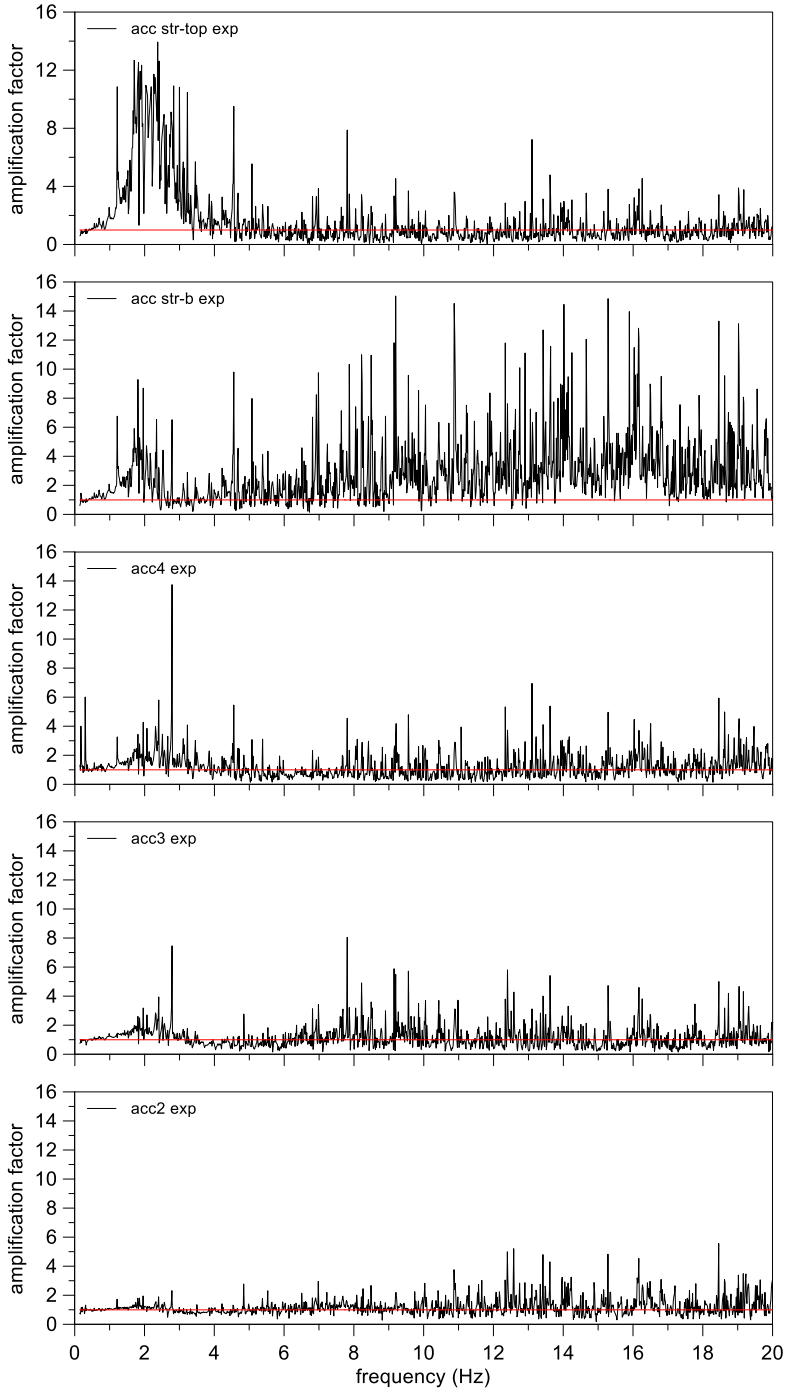

Figure 3.123. M1F_S1_IPS4_GM31+: amplification functions.

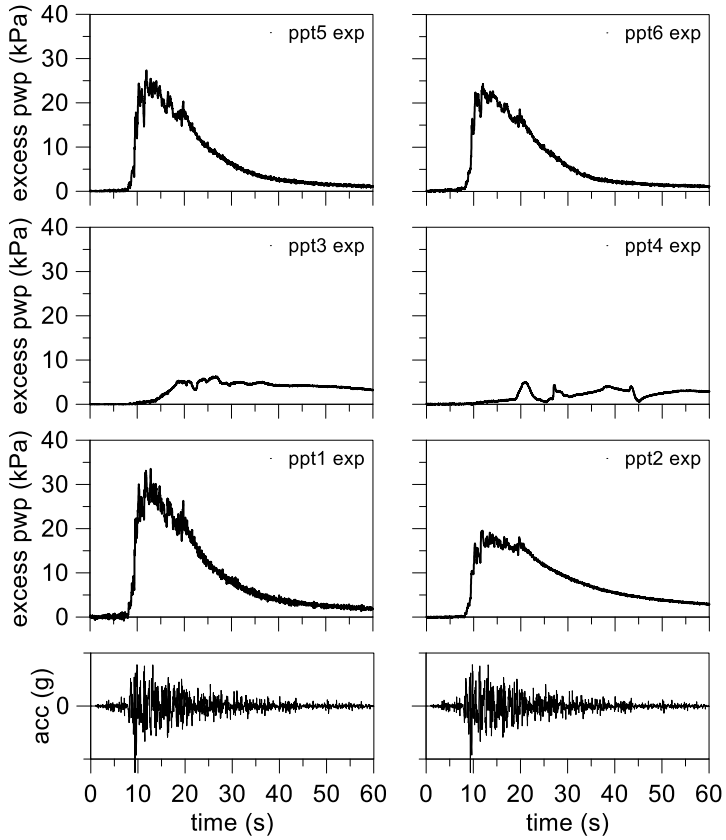

Figure 3.124. M1F_S1_IPS4_GM31+: excess pore water pressure time histories.

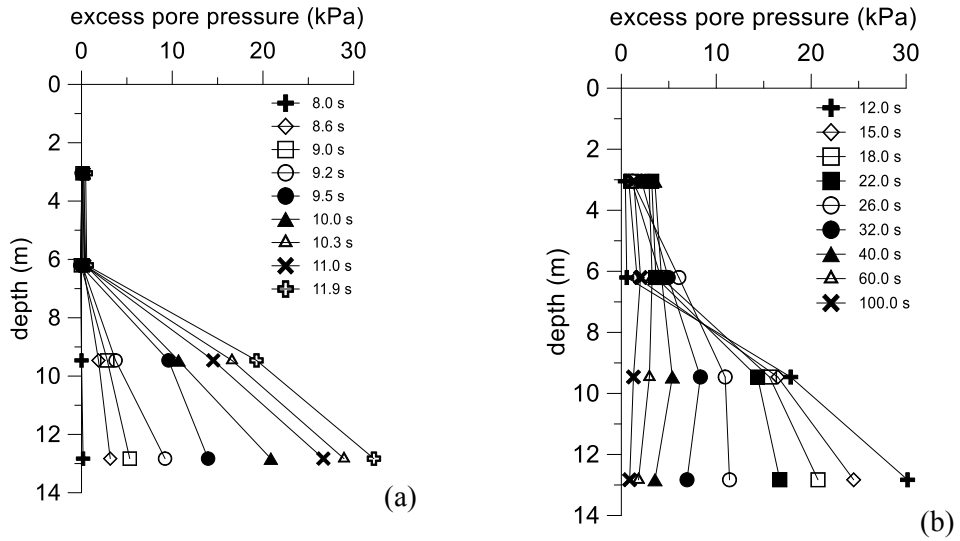

Figure 3.125. M1F_S1_IPS4_GM31+: vertical profiles of excess pore water pressure time histories for build-up phase (a) and dissipation phase (b).

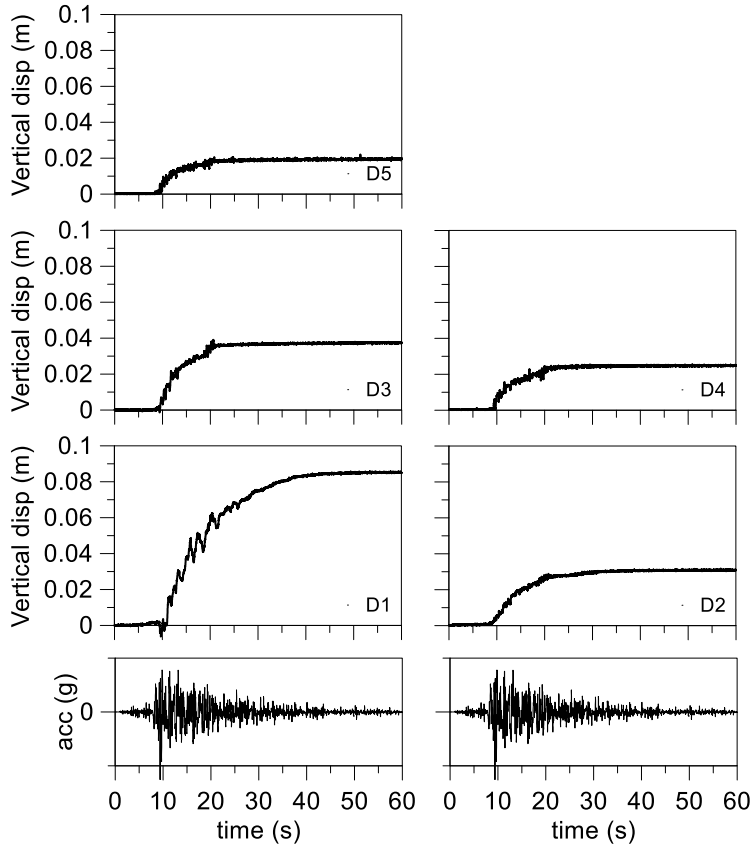

Figure 3.126. M1F_S1_IPS4_GM31+: ground surface displacement time histories.

3.12.3.2 Ground motion GM31++

As previously seen, the liquefaction was not reached using the input motion GM31+. For this reason, in following test a further amplified input motion was applied (GM31++).

The acceleration time histories during the motion are shown in Figure 3.127. A slight decrease of the mean amplitude and frequencies content of the signal was recorded from the bottom of the model towards the ground surface, whereas a large amplification of the acceleration was recorded in correspondence of the structure roof. The significant duration of the signal is evaluated by intensity factor in the interval 5-95% (Arias, 1970) and it is shown on the right of the Figure 3.127.

Figure 3.128 shows that the significant frequency content of the input signal is within 10 Hz with two larger peaks in 1 and 3 Hz. The relative density of the model soil after spin-up phase was equal to 57.3%.

The amplification functions show a slight deamplification of the signal from the bottom of the model towards the ground surface (Figure 3.129). An amplification of acceleration was recorded at basement and roof of the structure within 1-3 Hz frequencies range. High frequencies were largely energized by this amplified input motion.

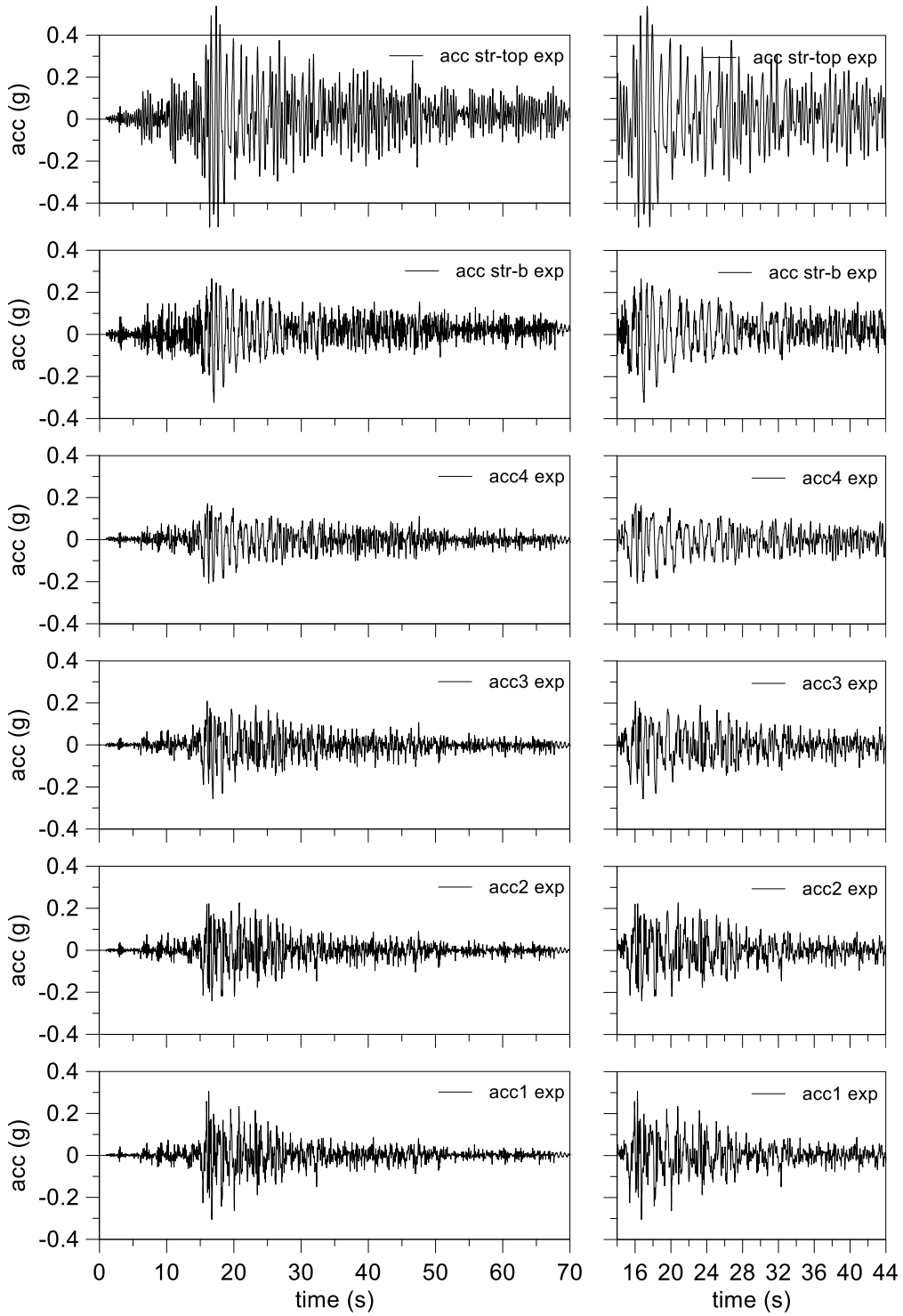

Figure 3.127. M1F_S1_IPS4_GM31++: main time interval of acceleration time histories.

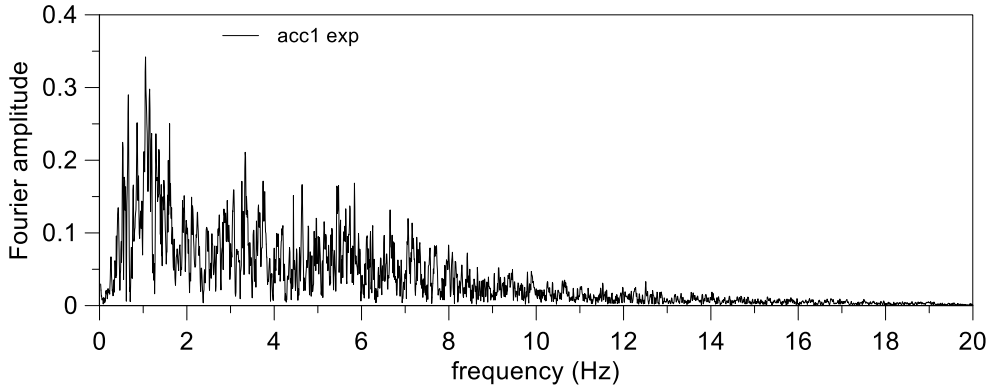

Figure 3.128. M1F_S1_IPS4_GM31++: Fourier spectrum of the input signal.

Small amount of excess pore pressures was recorded by transducers (Figure 3.130) at the lower part of the model (ppt1 and ppt2). The shallowest transducers ppt3 and ppt4 deployed beneath the structure reached a small excess water pressure with a smooth evolution due to the more compressible pore fluid. The shallow transducers ppt5 and ppt6, placed in "free-field" condition, show high peak values of excess pore pressure achieving a threshold in the ppt6, this proves that the liquefaction occurred in the surrounding soil.

The efficiency of the treatment in the soil near the transducer ppt3 and ppt4 was proved by the smaller excess pore pressure reached compared to ppt5 and ppt6 deployed at the same depth.

Like for the previous test, the vertical profiles show that the excess pore pressure build-up was strongly reduced in the soil near ppt3 and ppt4 while it increased in the lower part of the model (Figure 3.131a). The vertical profiles during the dissipation phase (Figure 3.131b) show that a progressive water flow direct towards the upper surface increased the excess pore pressure in ppt3 and ppt4 by an internal redistribution process of pore pressures. The vertical profiles reached a typical distribution of excess pore pressure after about 35 seconds with a large value of excess pore pressure beneath the structure (ppt4). This can lead to large settlement and tilting after the shaking. An inverse slope at 50 seconds suggesting the presence of a water flow from the central part of the model towards bottom, effect probably due to the presence of pore pressure redistribution from the saturated soil to the desaturated one.

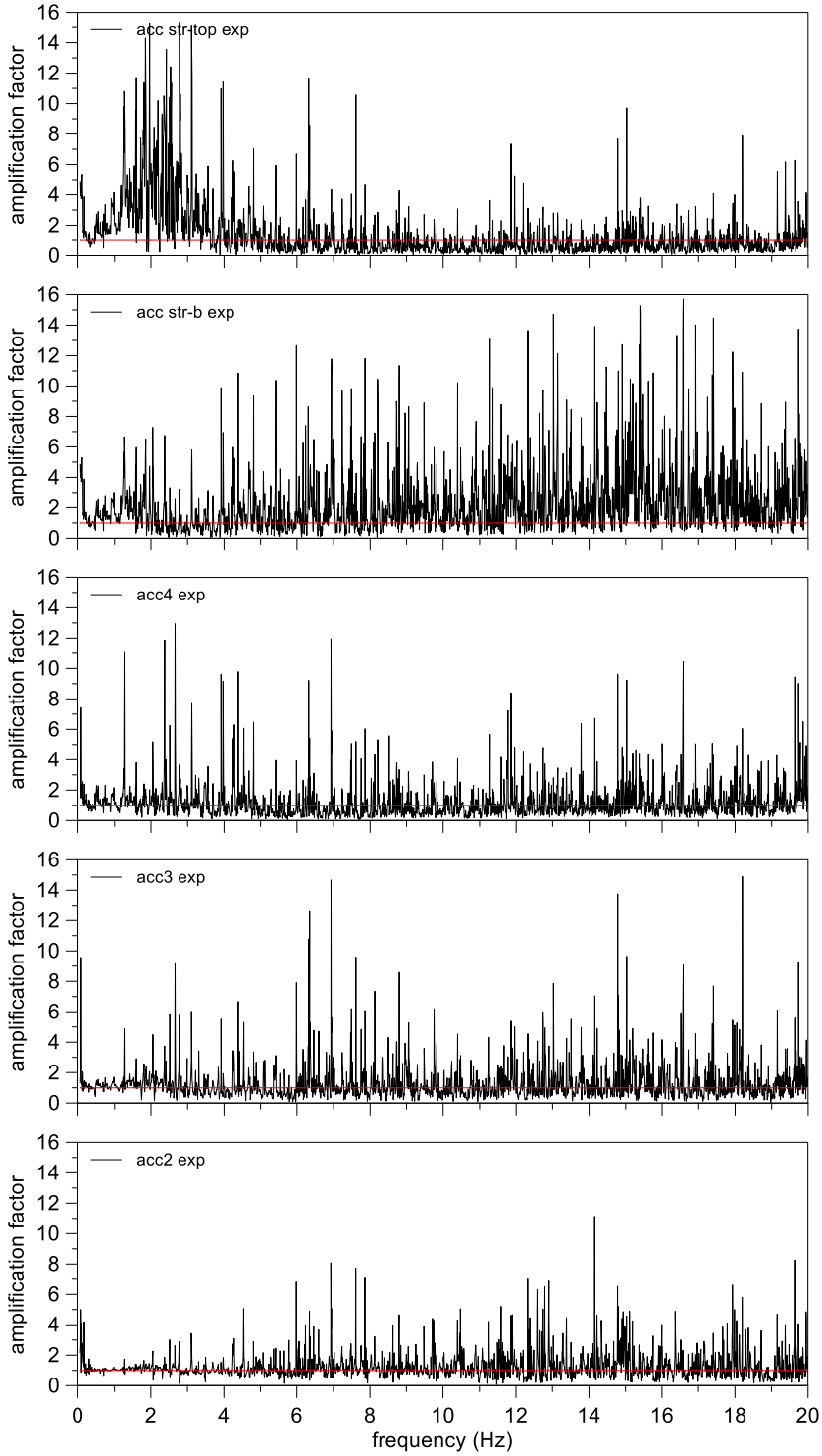

Figure 3.129. M1F_S1_IPS4_GM31++: amplification functions.

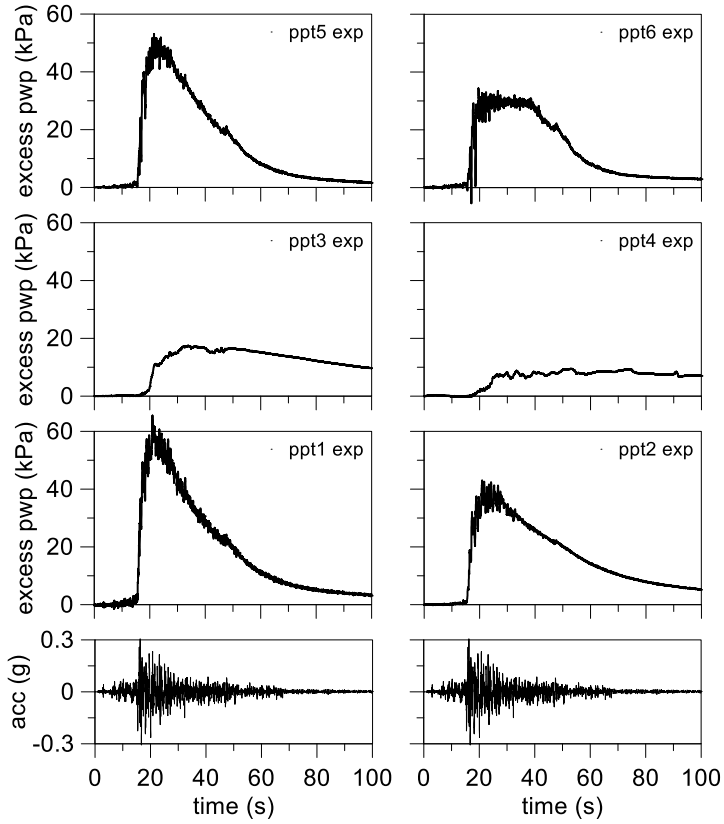

Figure 3.130. M1F_S1_IPS4_GM31++: excess pore water pressure time histories.

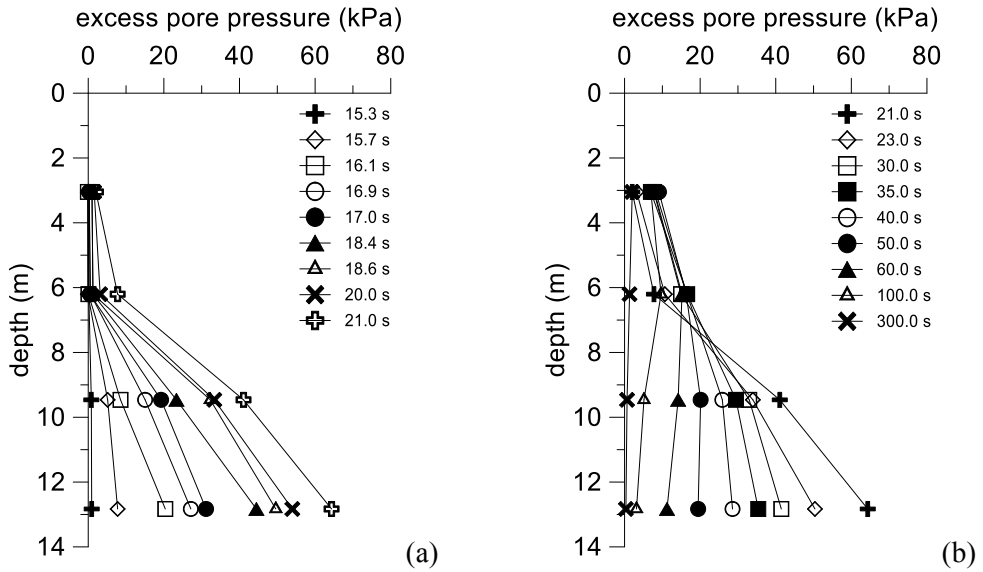

Figure 3.131. M1F_S1_IPS4_GM31++: vertical profiles of excess pore water pressure time histories for build-up phase (a) and dissipation phase (b).

The amount of settlements in "free-field" condition (Figure 3.132, D1 and D2) was significantly reduced compared to the test without mitigation technique (Figure 3.58) and with weaker input motion (GM31+). However, the structure was subjected to an abnormal large tilt equal to 2.0° measured by settlements of D3 and D4, whereas a tilt equal to 0.14° was measured in the transversal direction by D4 and D5. Reconsolidation settlement in free field condition leaded to 1.45% of mean volumetric strain, computed on 7m of the soil from the bottom to 6m depth, value included in the Lee and Albaisa (1974) range.

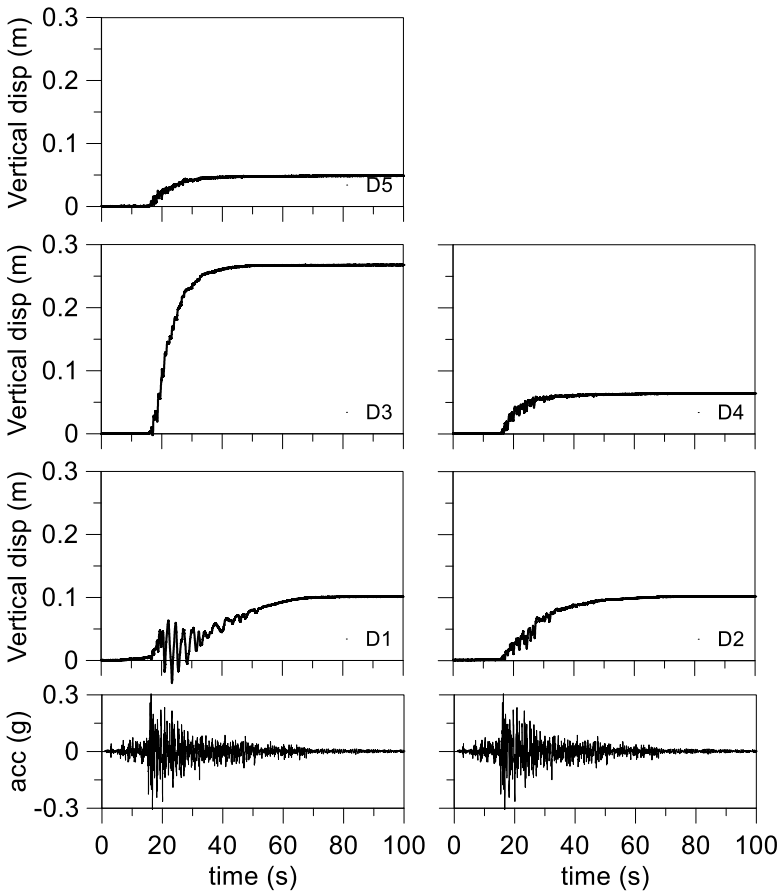

Figure 3.132. M1F_S1_IPS4_GM31++: ground surface displacement time histories.

4 NUMERICAL SIMULATION OF CENTRIFUGE TESTS

As previously mentioned, centrifuge tests are a useful tool to study complex phenomena in geotechnical engineering. However, they are affected by some important limitations as:

- physic quantities can be measured only in a finite number of discrete points within the model;
- limited geometrical configurations can be tested;
- tests are much expensive.

Numerical simulations allow to overcome – at least in part - these limitations. A reliable numerical simulation is based on the use of an appropriate constitutive model, to calibrate on experimental data. The model must be capable to reproduce the main aspects of the problem as the behaviour of the soil under different stress paths, and the analysis of real tests represents them.

In this section, numerical analyses were performed using two different constitutive soil models: PM4sand (Boulanger and Ziotopoulou, 2015) and UBC3D-PML (Petalas and Galavi, 2013). Both models are conceived to model the behaviour of the soil under undrained cyclic stress paths and are thus able to predict the excess water pressure build-up of liquefiable soils till a zero effective stress state (soil-fluid transition). A brief explanation of the theoretical bases of the models is reported in APPENDIX B.

4.1 Boundary conditions

Numerical simulations require the definition of boundary conditions, that largely affect the reliability of numerical results. Obviously, boundary conditions must reproduce the real kinematic and hydraulic conditions of the physical problem under analysis, as for instance laboratory tests. As previously mentioned in the section 3.5, an equivalent shear beam box (ESB) was used in the centrifuge tests studied in this work to reproduce a horizontal indefinite extension of the soil model. The alternance between aluminium and rubber rings allows shear deformation of boundaries with a rigid link at the external sides between the portions of the soil at the same depth. An acceleration time history was applied to the bottom of the model by a shaking table installed in the geotechnical centrifuge.

Impervious hydraulic boundary conditions were realized by a latex membrane on the bottom and the lateral walls of the ESB box. The upper boundary was an unfixed surface.

The numerical model adopted in 2D conditions has been built using the software platform Plaxis 2D (Brinkgreve et al., 2011). The lateral boundaries were realized by using *tied degree of freedom* (Zienkiewicz et al., 1989) which represent a rigid link between nodes on the two sides of the 2D model at the same depth. The bottom boundary was fixed in the vertical direction and an acceleration time history was applied in the horizontal one. This last condition leads to a high impedance ratio on the bottom that represents the contact between the steel bottom and soil realised in the centrifuge. Impervious hydraulic condition was

imposed to the bottom and to the lateral boundaries, the upper boundary was modelled as unfixed and pervious.

4.2 Calibration procedure for the constitutive soil models

The calibration procedures adopted for both constitutive soil models used for the numerical analyses are shown in this section. The calibration of some parameters is a function of relative density of soil for both procedures. Whereas, the calibration for other parameters requires cyclic resistance curves of the adopted soil material. The physical meaning of parameters is explained in the APPENDIX B.

4.2.1 UBC3D-PML

The calibration procedure suggested by Beaty and Byrne (2011) was used in this work for UBC3D-PML constitutive soil model. This procedure uses the blows number of SPT field test $(N_{1,60})$ to determine some parameters using the following relationships:

$$K_G^e = 21.7 \cdot 20 \cdot \left(N_{1,60}^2\right)^{0.333} \quad (4\text{-}1)$$

$$K_B^e = \frac{2(1+\nu)}{3(1-2\nu)} \cdot K_G^e \quad (4\text{-}2)$$

$$K_G^p = 0.003 \cdot K_G^e \cdot N_{1,60}^2 + 100 \quad (4\text{-}3)$$

$$R_f = 1.1 \cdot \left(N_{1,60}\right)^{-0.15} \quad (4\text{-}4)$$

$$\varphi_p = \left(\varphi_{cv} + \frac{N_{1,60}}{10}\right) + \max\left(0; \frac{N_{1,60} - 15}{5}\right) \quad (4\text{-}5)$$

This blows number can be calculate referring to the relative density (RD) though the following relationship:

$$N_{1,60} = 46 \cdot RD^2 \quad (4\text{-}6)$$

The parameters f_{dens} has to be calibrated on the best fit of cyclic resistance curve. For the sand used in this work the calibration led to a value of f_{dens} equal to 7. The cyclic resistance curve produced in numerical way is compared to the experimental one, obtained from Fioravante and Giretti (2016) in Figure 4.1. This parameter influences the slope of the cyclic resistence curve.

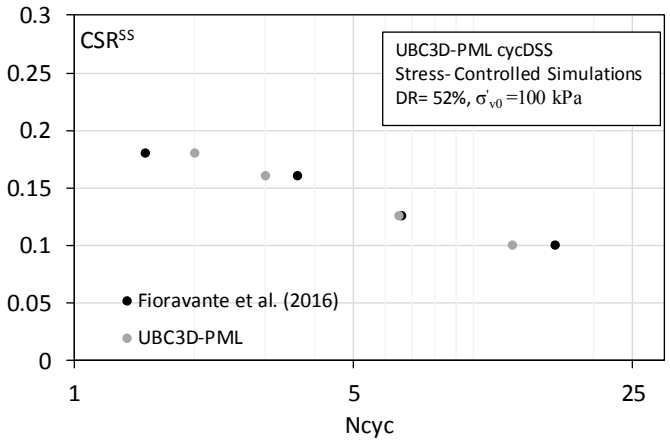

Figure 4.1. Calibration of f_{dens} on the liquefaction cyclic resistance curve of Ticino sand (Fioravante and Giretti, 2016).

$f_{E,post}$ parameter was set equal to 1 and the rest of parameters were set in their default value. The permeability of the sand was determined via laboratory tests at RD=40%.

4.2.2 PM4SAND

The calibration of PM4SAND constitutive soil model was performed through the advises proposed by Xavier Nuques Luque (2017) that uses the shear waves velocity in the soil and the coefficient of earth pressure at rest (Jaky, 1944) to determine the shear stiffness coefficient (G_0) by the relationship:

$$G_0 = \frac{\rho \cdot V_s^2}{p_a \left(\frac{1+K_0}{2}\right)^{\frac{1}{2}}} \qquad (4\text{-}7)$$

V_s is the shear wave velocity in the soil computed in function of relative density as:

$$V_s = 125 \cdot (RD + 1)^{0.1} \qquad (4\text{-}8)$$

All other parameters were setted on the default value except h_{p0} that was calibrated by a best fitting porecedure on cyclic resistance curve of Ticino sand (Figure 4.2) obtained by Fioravante and Giretti (2016). The calibration procedure led a value of h_{p0} equal to 0.08. This parameter influences the slope of the numerical cyclic resistence curve.

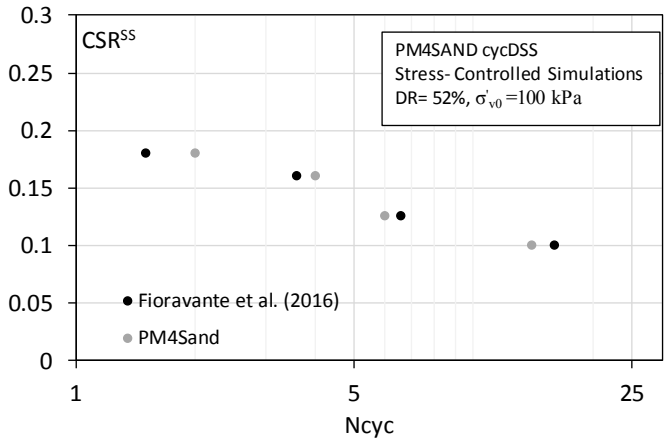

Figure 4.2. Calibration of h_{p0} on the liquefaction cyclic resistance curve of Ticino sand (Fioravante and Giretti, 2016).

4.3 Response without mitigation technique

The analyses without mitigation techniques aim to check the reliability of calibration of constitutive model and the accuracy of boundary conditions. The check consists in the verification of the capability of the model to follow the excess water pressure build-up path and the corresponding degradation of soil stiffness during the decrease of the effective stresses. In order to verify the reliability of the calibration, analyses were carried out with different geometrical configurations and boundary conditions.

4.3.1 Single layer model (M1_S1_GM31)

The calibration of the constitutive models started from the simplest centrifuge model realised by a homogeneous single layer of liquefiable soil (Ticino sand) in free-field conditions. This allows to check the reliability of the adopted calibration procedure.

4.3.1.1 UBC3D-PLM

The following numerical prediction of the centrifuge test was performed by UBC3D-PML following the calibration procedure shown in the section 4.2.1. The parameters adopted are shown in Table 4.1.

Table 4.1. Parameters for the constitutive soil model.

γ_{unsat}	γ_{sat}	RD	$N_{1,60}$	e_{max}	e_{min}	K_B^e	K_G^e	K_G^p	m_e	n_e	n_p	φ_{cv}	φ_p	f_{dens}	$f_{E,post}$	R_f	k
(kN/m^3)	(kN/m^3)	(%)	(-)	(-)	(-)	(-)	(-)		(-)	(-)		(°)	(-)	(-)	(m/s)	(-)	(m/s)
14.95	19.20	47.5	10.0	0.923	0.574	1577.0	946.0	407.0	0.5	0.5	0.4	33.0	34.0	7.0	1.0	0.77	$1.66 \cdot 10^{-3}$

The numerical analysis of the centrifuge tests led to the acceleration time histories shown in Figure 4.3, a good agreement with experimental records was found in the lower part of the domain (acc2), where liquefaction did not occur, whereas high frequencies and amplitude were recorded in the portion of ground that was subjected to liquefaction (acc3 and acc4).

Although the accelerations amplitude after liquefaction (acc3 and acc4 after 15 seconds) was almost the same as the experimental measured one, the presence of some numerical spikes can be noticed, that may be the consequence of the large stiffness reduction induced by the excess pore pressure build-up.

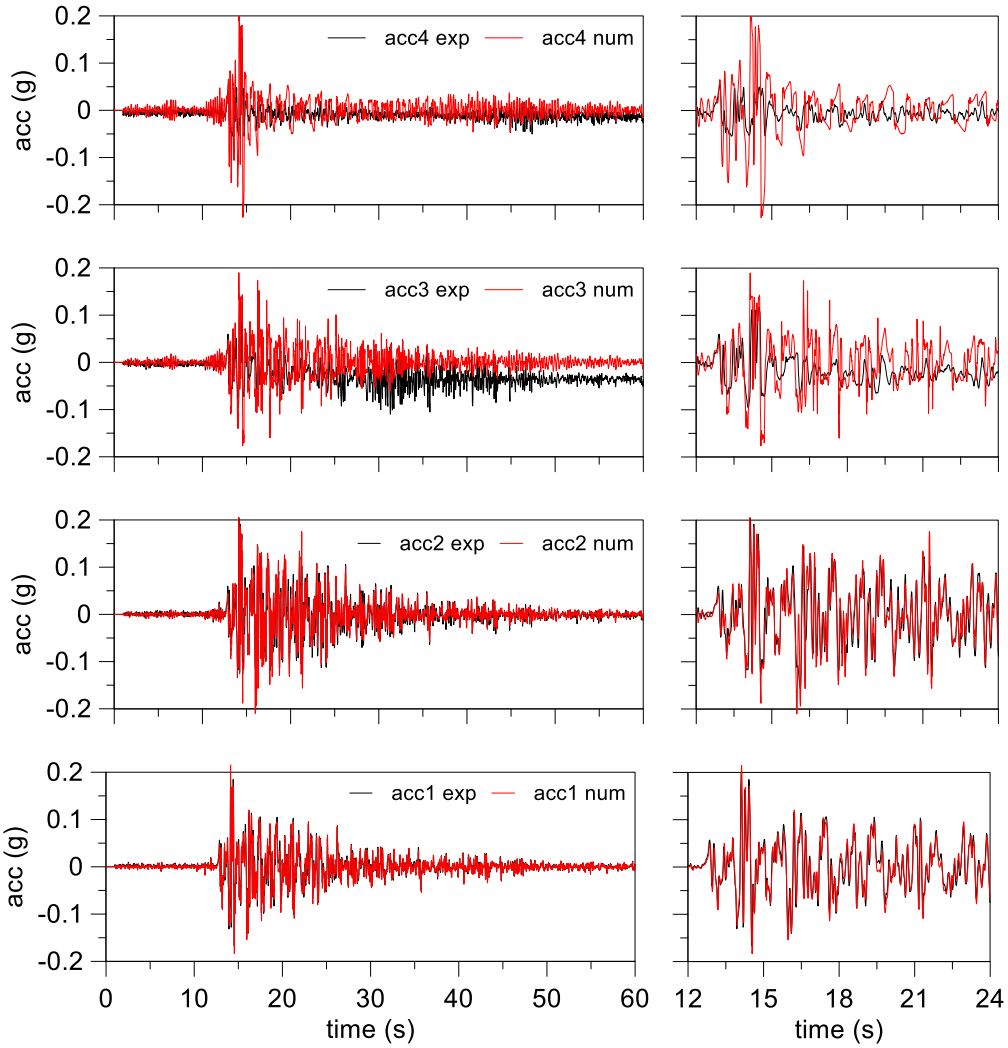

Figure 4.3. M1_S1_GM31: main time interval of acceleration time histories.

In Figure 4.4 the time histories of excess pore pressure ratio calculated by the numerical analysis are shown and compared to the experimental values. A good agreement was reached on the maximum value and path in the time except for the last portion of shallowest transducers ppt4 and ppt6, where a faster dissipation of the excess pore pressure was calculated from 40 seconds on. A possible reason for this difference may be the desaturation of the soil above the water table, that could have reduced the permeability in the experiments.

However, since no evidence of this was reported from testing, such reduction of permeability was not introduced in the numerical analyses.

Liquefaction was clearly achieved in the soil surrounding the transducers ppt3, ppt4, ppt5 and ppt6, because the experimental results show the "saturation" of r_u to an upper bound. The reason why this upper bound is not unity may be likely slight overestimation of the effective stresses deduced from the numerical model, ascribable to a slightly different position of the transducers compared to the numerical points.

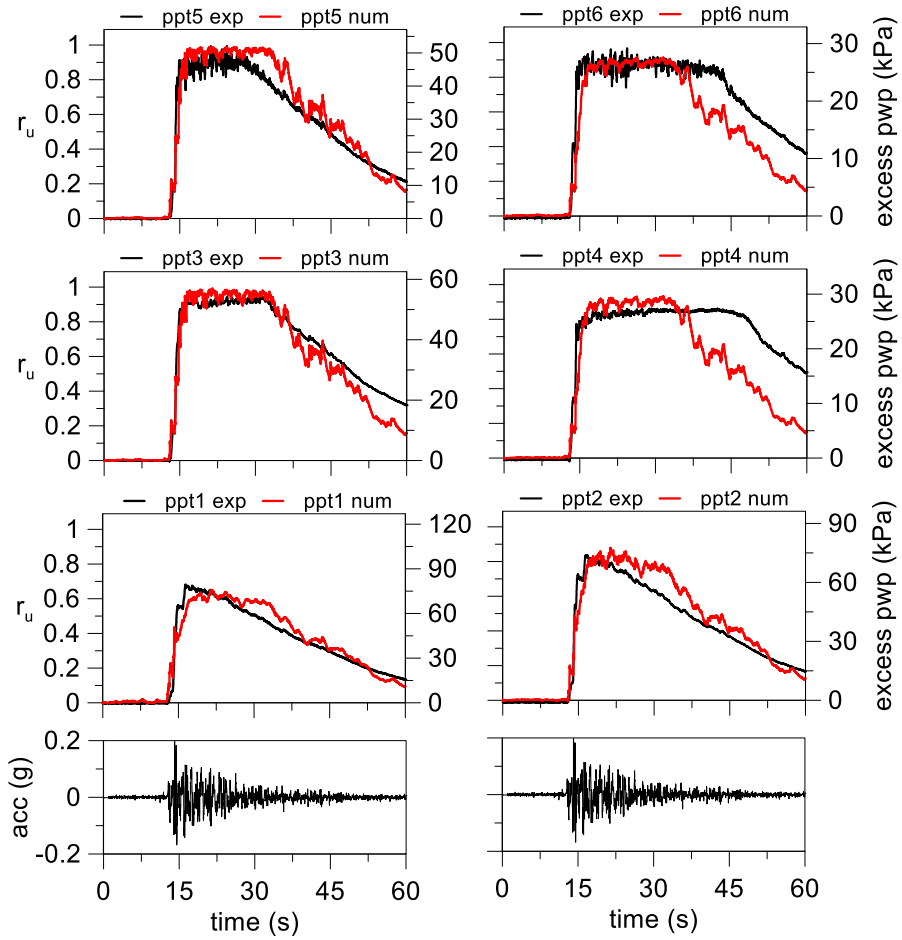

Figure 4.4. M1_S1_GM31: excess pore water pressure time histories.

Smaller ground surface settlements were computed than actually measured in the test (Figure 4.5). Indeed, since the horizontal strains were inhibited in the model container, the settlement of ground surface is due to volumetric strains only. Hence, despite being able to model the excess pore pressure build-up, the constitutive model seems unable to reproduce the large volumetric strains developed during liquefaction in free field condition.

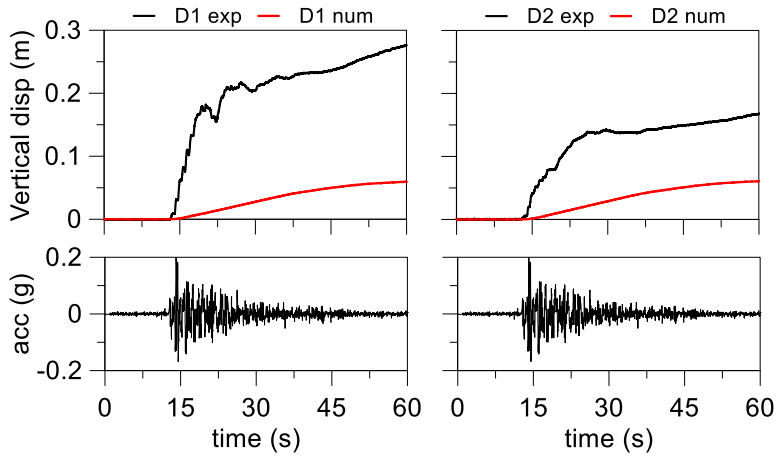

Figure 4.5. M1_S1_GM31: ground surface displacement time histories.

4.3.1.2 PM4SAND

The same centrifuge test was analysed using PM4SAND as constitutive model. The parameters used for the constitutive soil model are shown in Table 4.2.

Table 4.2. Parameters for the constitutive soil model.

γ_{unsat}	γ_{sat}	RD	G_0	h_{p0}	e_{max}	e_{min}	n_b	n_d	φ	ν	Q	R	k
(kN/m^3)	(kN/m^3)	(%)	(-)	(-)	(-)	(-)	(-)	(-)	(°)	(-)	(-)	(-)	(m/s)
14.95	19.20	47.5	376.6	0.08	0.923	0.574	0.50	0.10	33	0.3	10.0	1.5	$1.66 \cdot 10^{-3}$

The calculated time histories of acceleration (Figure 4.6) show a good agreement with experimental records except for the ppt4 where after the peak an abnormal behaviour probably due to the strong drop of the stiffness due to the excess pore pressure build-up.

PM4SAND gives a better simulation of the acceleration amplitude than UBC3D-PML: this result is due to the different behaviour of these models at first load cycles, indeed PM4SAND accumulates higher excess pore pressure in the firs load cycles than UBC3D-PML. Hence, the initial excess pore pressure is better predicted by PM4SAND.

Figure 4.7 shows the time histories of excess pore pressure that were well simulated by numerical analysis. Like in the analysis with UBC3D-PML, the shallowest transducers ppt4 and ppt6 show a higher dissipation rate of the excess pore pressure: this result proves that this effect is not ascribable to the constitutive model or to its calibration and the hypothesis of a lower permeability in the centrifuge model, above the groundwater table, seems to be more likely.

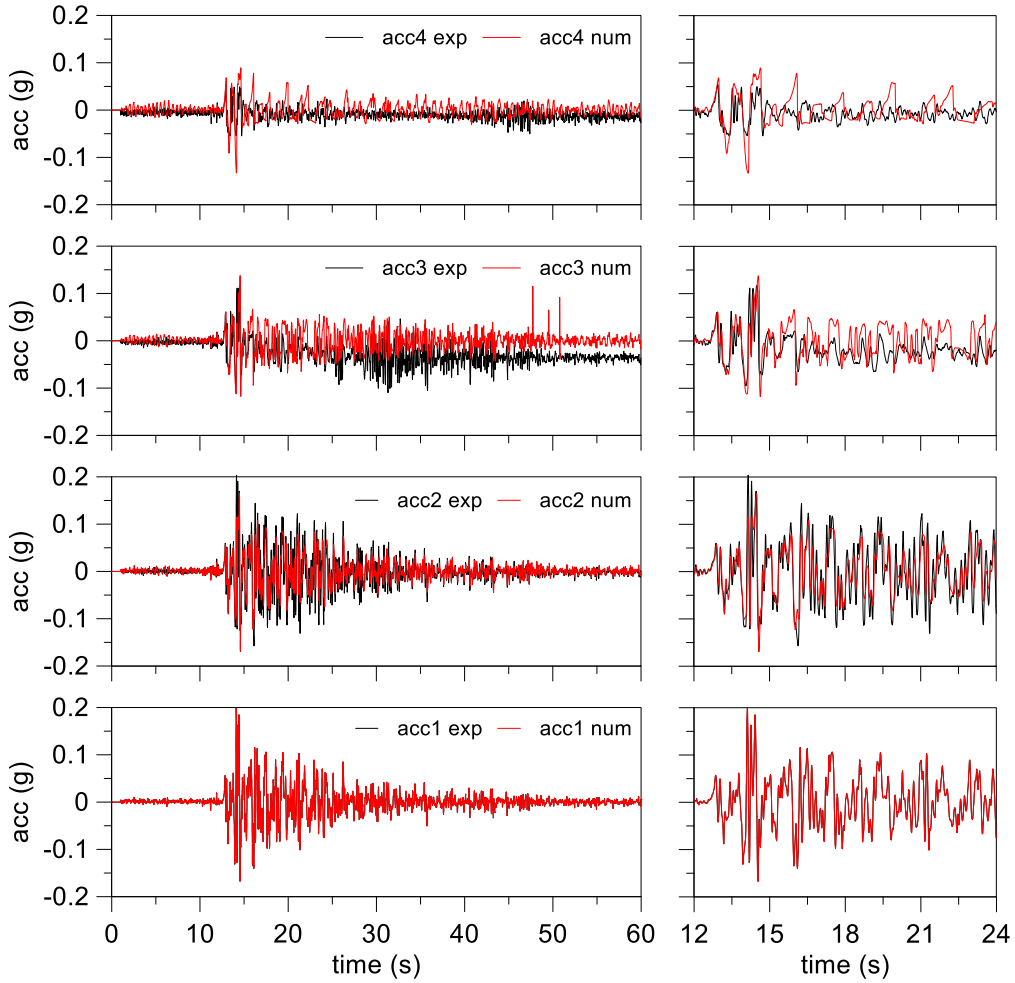

Figure 4.6. M1_S1_GM31: main time interval of acceleration time histories.

As for UBC3D-PML, the computed settlements at ground surface are smaller than the experimental ones (Figure 4.8), likely for the same reason. However, it is worth noting that in PM4SAND this issue is partially addressed by a switch that reduces the shear and bulk stiffness of the soil after liquefaction, through a sedimentation factor (F_{sed}). Indeed, during the soil liquefaction a large portion of the settlements in free-field condition is due to a sedimentation effect. This numerical solution is activated after the main part of the shaking; therefore, it requires to determine the significant duration of the strong motion (i.e. by an intensity factor). In other to compare the two constitutive models this approach was not applied in the analyses with PM4SAND.

The inability of the constitutive models to reproduce the volumetric strains can be proven also in the static condition. Figure 4.9 shows numerical simulations of an isotropic compression test using both constitutive models and the bulk stiffness of numerical simulations is significantly larger than experimental one.

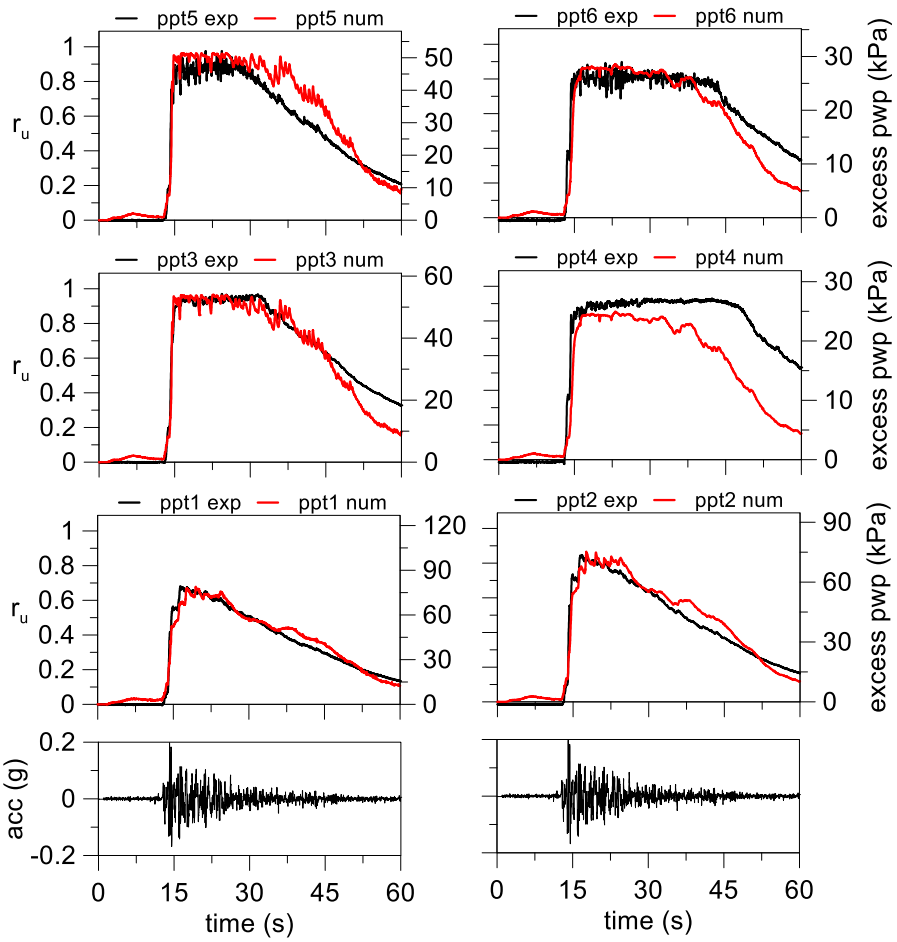

Figure 4.7. M1_S1_GM31: excess pore water pressure time histories.

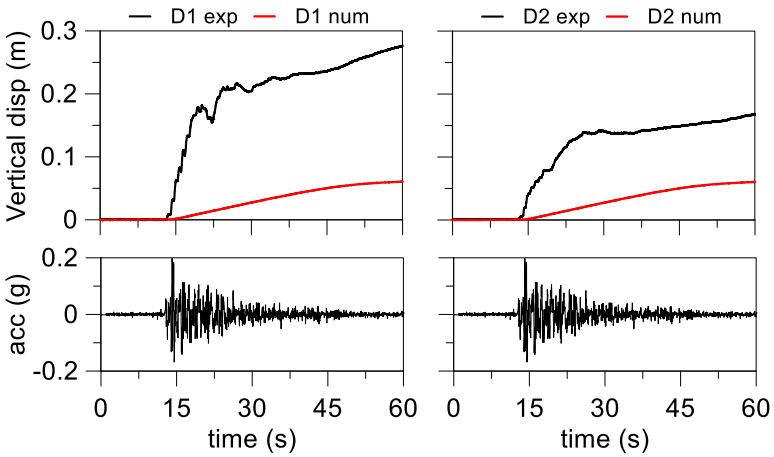

Figure 4.8. M1_S1_GM31: ground surface displacement time histories.

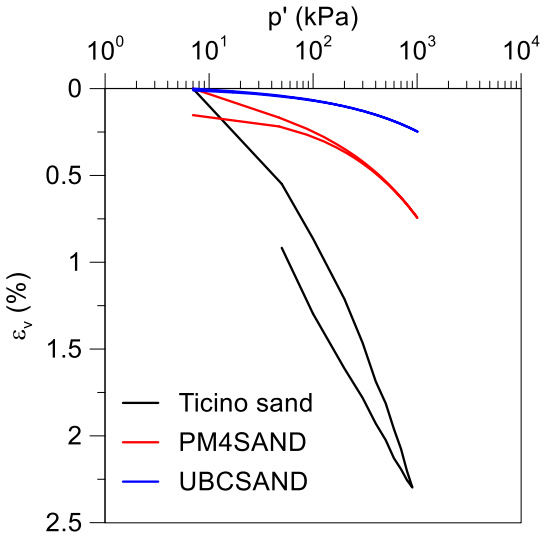

Figure 4.9. Numerical simulations of an isotropic compression test.

4.3.2 Double layer model (M2_S1_GM31)

The reliability of the model calibration was checked also against the results of the test with an upper non-liquefiable crust.

4.3.2.1 UBC3D-PML

The calibration of constitutive model was performed following the previous calibration procedure and the adopted parameters are shown in Table 4.3.

Table 4.3. Parameters for the constitutive soil model.

γ_{unsat}	γ_{sat}	RD	$N_{1,60}$	e_{max}	e_{min}	K_B^e	K_G^e	K_G^p	m_e	n_e	n_p	φ_{cv}	φ_p	f_{dens}	$f_{E,post}$	R_f	k
(kN/m^3)	(kN/m^3)	(%)	(-)	(-)	(-)	(-)	(-)	(-)	(-)	(-)	(-)	(°)	(°)	(-)	(m/s)	(-)	(m/s)
15.05	19.25	50.5	11.7	0.923	0.574	1643.0	985.9	508.3	0.5	0.5	0.4	33	34.2	7.0	1.0	0.76	$1.66 \cdot 10^{-3}$

Figure 4.10 shows a good agreement between numerical acceleration time histories and experimental ones except for the presence of same spikes in acc4 and acc6.

The numerical acceleration amplitude in acc6 is slightly higher than the experimental one and it presents a strange behaviour after the strong portion of the shaking due to the large drop of the stiffness that destabilised the numerical solution. Some spikes are in the numerical acceleration time history for acc4.

In Figure 4.11 the numerical excess pore pressure ratios are compared with experimental data. A good agreement was found but with a slight advance of pore pressure build-up. The transducer ppt2 did not work.

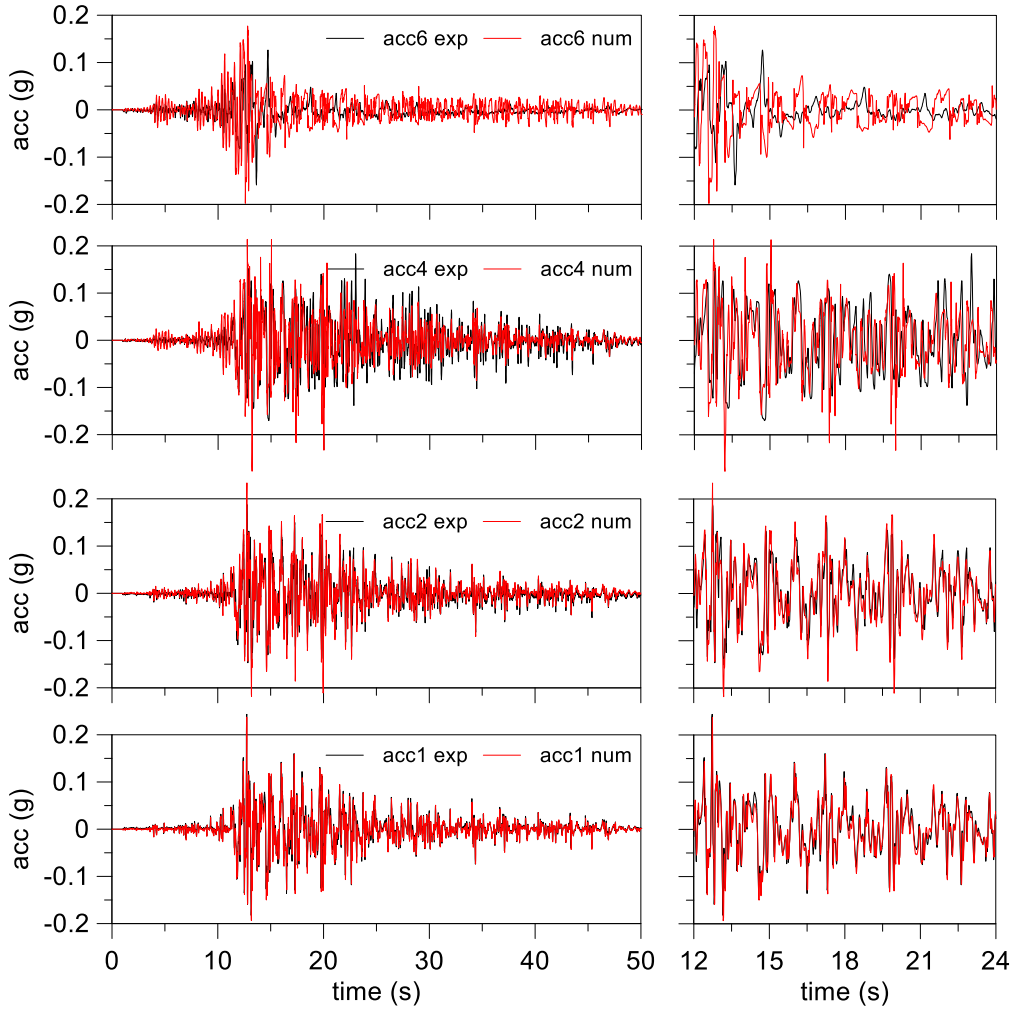

Figure 4.10. M2_S1_GM31: main time interval of acceleration time histories.

The transducer ppt5 shows an abnormal path probably due to either a clay crust cracking or uplift occurred during the experimental test. This caused a rapid drop of excess pore pressure that was not reproduced by the numerical calculation.

The experimental measurements are close to zero value at the transducer ppt6, this result is consistent with the nature of surrounding soil constituted by Pontida clay that is unable to accumulate excess pore pressure. However, numerical simulation led to a significant excess pore pressure in ppt6 but this did not produced a stiffness change, because the clay crust was modelled by Mohr-Coulomb constitutive soil model, with a Young's modulus independent from the effective stress.

Compared to the experiment, a faster dissipation of excess pore pressure was computed from about 35 seconds on.

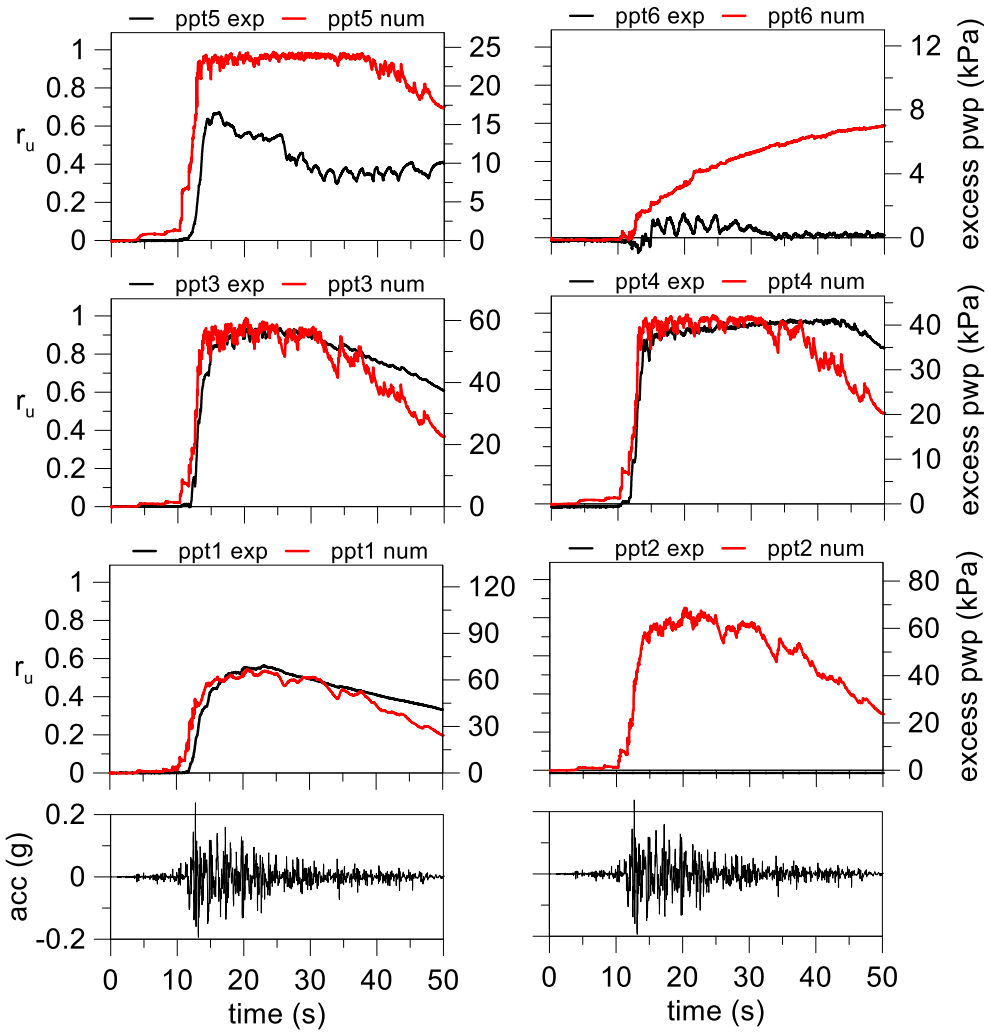

Figure 4.11. M2_S1_GM31: excess pore water pressure time histories.

The presence of the clay crust inhibited the excess pore pressure decrease avoiding a vertical water flow towards the ground surface. This effect reduces the development of the vertical settlements, induced by the volumetric strains due to the dissipation of excess pore pressure, as it is possible to see in Figure 4.12 from numerical results. An abnormal rotation of the ground surface can be inferred from the experimental settlements. This rotation likely led to the development of some cracks in the clay crust, as it was observed in the test that explains the readings of the pore pressure transducer ppt5, deployed just below the clay crust.

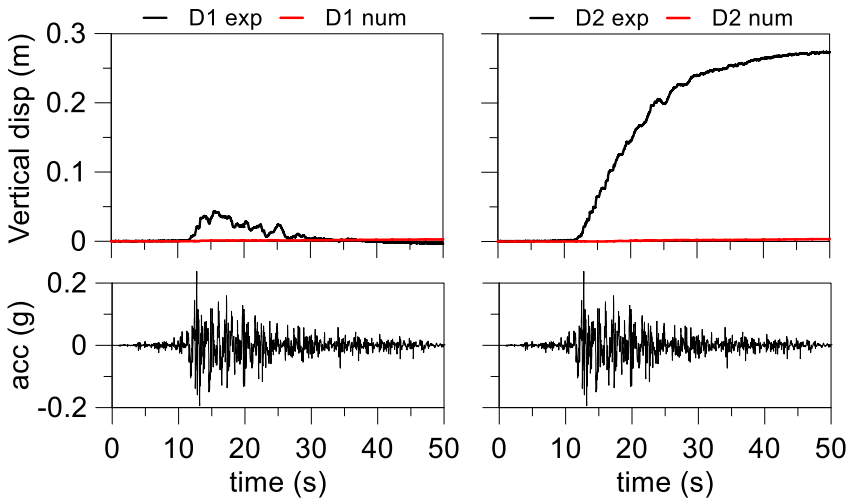

Figure 4.12. M2_S1_GM31: ground surface displacement time histories.

4.3.2.2 PM4SAND

Table 4.4 shows the model parameters adopted in this calculation according to the calibration procedure shown in section 4.2.2.

Table 4.4. Parameters for the constitutive soil model.

γ_{unsat}	γ_{sat}	RD	G_0	h_{p0}	e_{max}	e_{min}	n_b	n_d	φ	ν	Q	R	k
(kN/m^3)	(kN/m^3)	(%)	(-)	(-)	(-)	(-)	(-)	(-)	(°)	(-)	(-)	(-)	(m/s)
15.05	19.25	50.5	379.2	0.08	0.923	0.574	0.5	0.1	33.0	0.3	10.0	1.5	$1.66 \cdot 10^{-3}$

The numerical acceleration time histories for the shallower transducers show a slight smaller amplitude than the experimental one (Figure 4.13) with the presence of some spikes in the main part of the motion.

As seen in the previous analysis with UBC3D-PML, the shallowest accelerometer (acc6) shows some spikes and different frequency content due to the large drop of the stiffness induced by liquefaction occurrence.

The excess pore pressure ratios (Figure 4.14) show a faster build-up in the deeper part of the model (ppt1 and ppt2). The numerical time history for ppt3 and ppt4 exhibits a higher dissipation rate than the experimental one as seen for the previous analysis. The numerical excess pore pressure path in ppt5 is very similar to the previous numerical analysis, this result confirms that the behaviour observed from the experimental readings of the transducers ppt5 must be associated to a cracking of clay crust, that caused a rapid drop of excess pore pressure.

Similar to what is observed in the results of the analysis with UBC3D-PLM, the numerical settlements of ground surface computed with PM4SAND were very small (Figure 4.15). Indeed, the settlement in free-field condition is due to a volume changing of the soil model that was partially impeded by the presence of the clay crust.

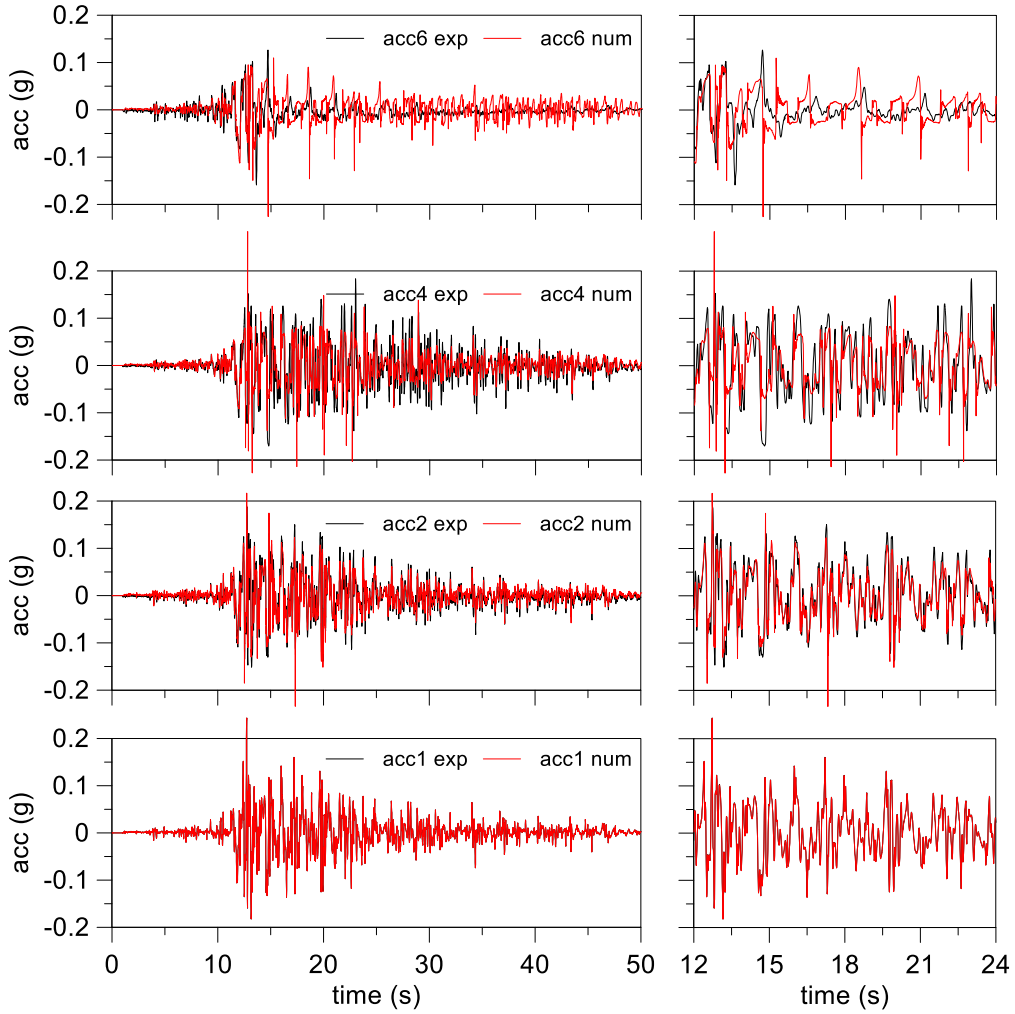

Figure 4.13. M2_S1_GM31: main time interval of acceleration time histories.

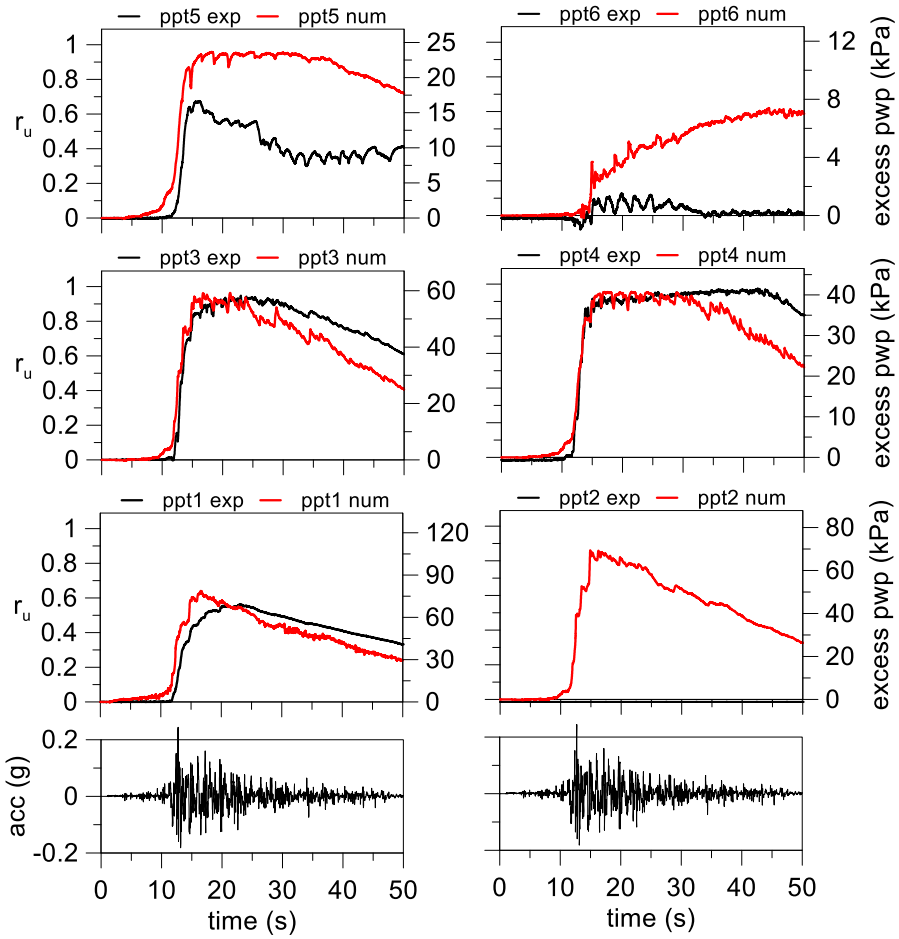

Figure 4.14. M2_S1_GM31: excess pore water pressure time histories.

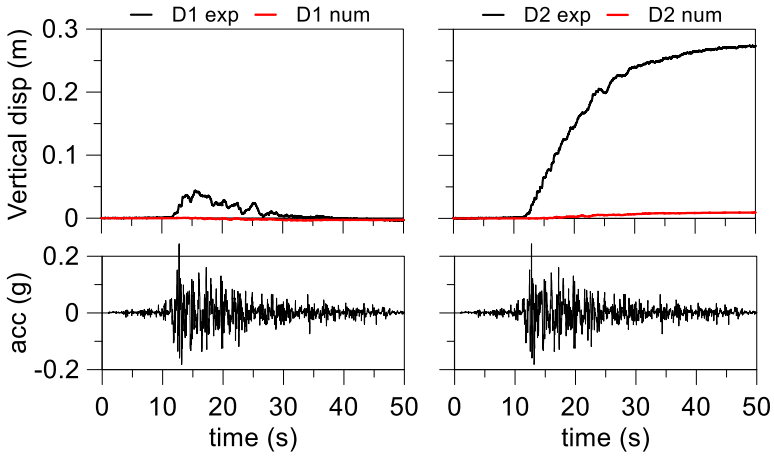

Figure 4.15. M2_S1_GM31: ground surface displacement time histories.

4.3.3 Building on single layer model (M1F_S1)

In this section geotechnical model of a single liquefiable layer with the simplified structure described in the section 3.10, was modelled by using both UBC3D-PML and PM4SAND. This analysis aimed to reproduce soil-structure interaction and to highlight the performance of the two different constitutive models.

The simplified structure, used in the centrifuge tests seen before, was modelled in the numerical model by plates having mass and stiffness comparable to the physical model. The conformity of dynamic properties between the physical model and numerical one was checked on the numerical model of the structure with fixed base, like as done in the experimental check of the fundamental period (section 3.9.2). The numerical model structure had a fundamental period equal to 0.3 seconds adopting the fixed base, this fundamental period is almost the same of the physical one.

4.3.3.1 UBC3D-PML (Ground motion GM31)

The analysis of the homogeneous liquefiable soil with the structure is shown in this section adopting the UBC3D-PML constitutive soil model.

The parameters defined by the calibration procedure on the relative density of the soil are shown in Table 4.5.

Table 4.5. Parameters for the constitutive soil model.

γ_{unsat}	γ_{sat}	RD	$N_{1,60}$	e_{max}	e_{min}	K_B^e	K_G^e	K_G^p	m_e	n_e	n_p	φ_{cv}	φ_p	f_{dens}	$f_{E,post}$	R_f	k
(kN/m^3)	(kN/m^3)	(%)	(-)	(-)	(-)	(-)	(-)		(-)	(-)		(°)	(-)	(-)	(m/s)	(-)	(m/s)
15.0	19.2	49.0	11.0	0.574	0.923	1000.0	965.7	453.4	0.5	0.5	0.4	33.0	34.1	7.0	1.0	0.77	$1.66 \cdot 10^{-3}$

The comparison between the numerical and experimental acceleration time histories are shown in Figure 4.16. A good agreement was found in general with a slight amplification of the acceleration at the top of the structure in the more energized portion of the shaking. Furthermore, a slight acceleration reduction was recorded by the transducers in the soil and on the structure from 15 seconds on. This effect is due to a larger drop of soil stiffness in the numerical analysis that led to a larger isolation effect. Indeed, the numerical time histories of excess pore pressure (Figure 4.17) show a higher level of excess pore pressure ratio than the experimental ones that may have produced a large drop of the effective stresses and stiffness.

Moreover, the higher values of the excess pore pressure ratio led to larger numerical settlements of the structure compared to the experimental ones (Figure 4.18). This proves that a strong decrease of soil shear stiffness occurred in the numerical analysis. Indeed, the settlements of the structure were due to the deviatoric stress imposed by its weight and dynamic interaction between soil and structure that increase the deviatoric stress by the overturn moment. The numerical model showed its incapability to reproduce volumetric strains induced by the dissipation of excess pore pressure. Indeed, an uplift of the ground surface was recorded in the numerical simulation in correspondence of the displacement transducers D1 and D2 deployed in free-field condition. Conversely, the constitutive model led to a large reduction of shear stiffness with the excess water pressure build-up that led to larger settlements for the structure than the experimental ones.

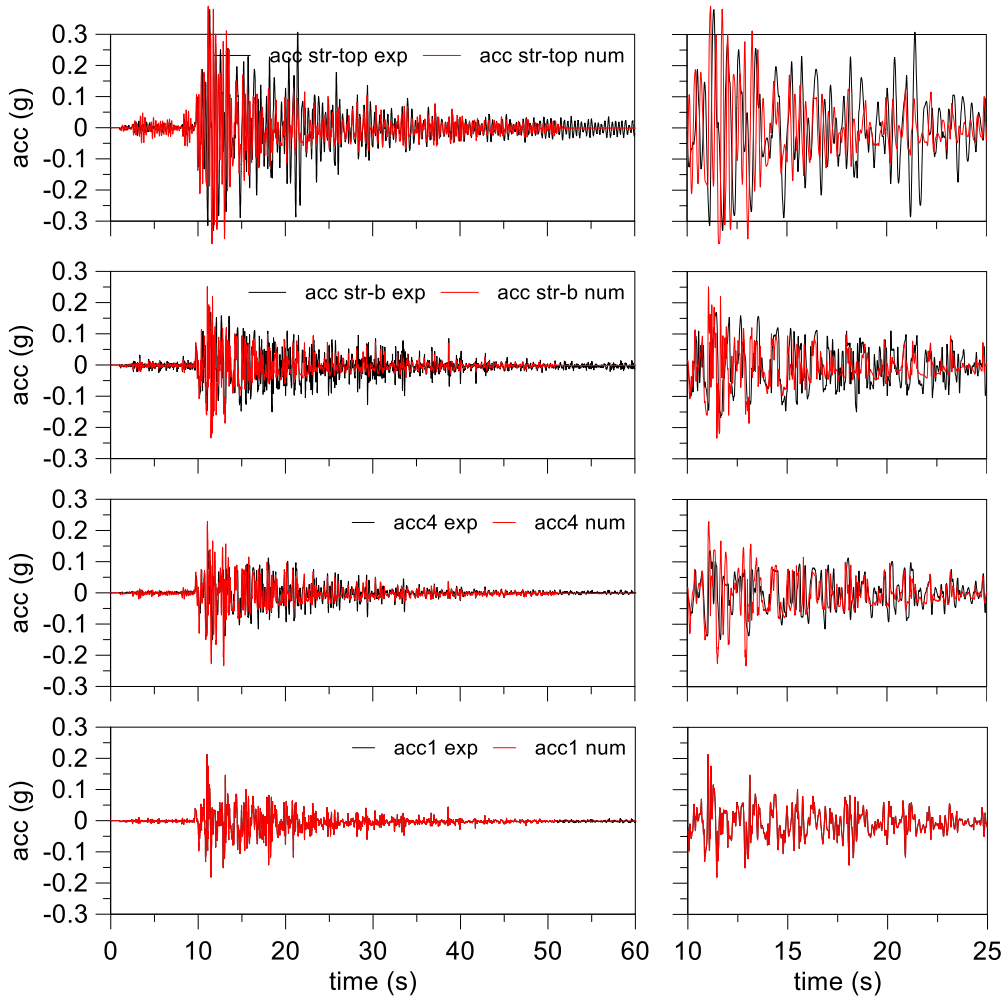

Figure 4.16. M1F_S1_GM31: main time interval of acceleration time histories.

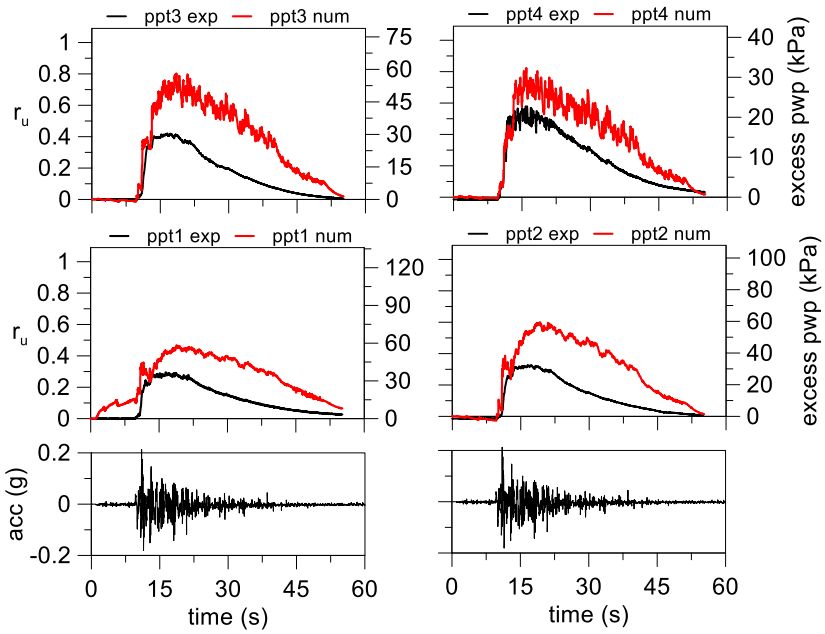

Figure 4.17. M1F_S1_GM31: excess pore water pressure time histories.

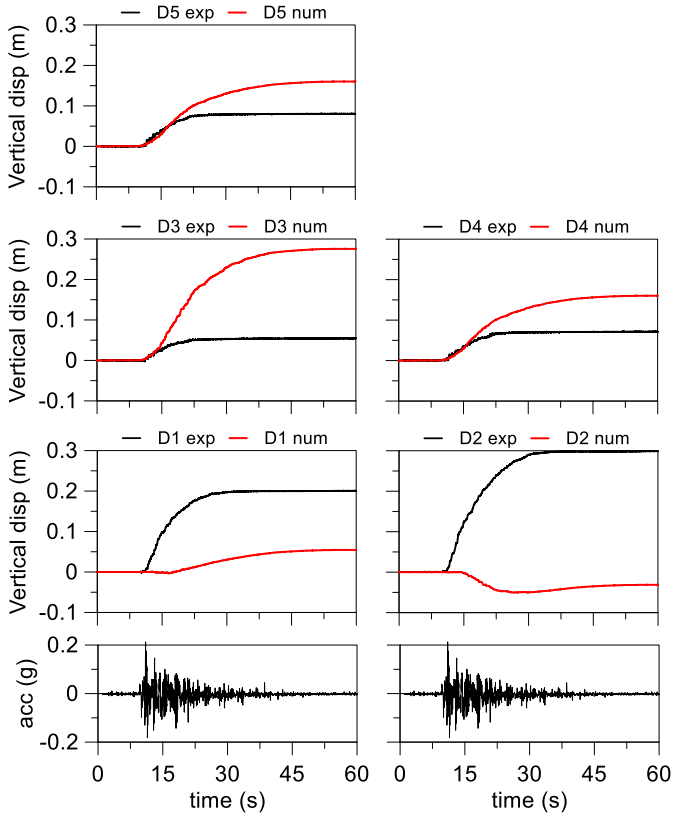

Figure 4.18. M1F_S1_GM31: ground surface displacement time histories.

4.3.3.2 PM4SAND (Ground motion GM31)

As done for the previous analyses, the following analysis was performed by the PM4SAND constitutive model. The parameters used for the soil constitutive model are shown in Table 4.6.

Table 4.6. Parameters for the constitutive soil model.

γ_{unsat}	γ_{sat}	RD	G_0	h_{p0}	e_{min}	e_{max}	n_b	n_d	φ	ν	Q	R	k
(kN/m^3)	(kN/m^3)	(%)	(-)	(-)	(-)	(-)	(-)	(-)	(°)	(-)	(-)	(-)	(m/s)
15	19.2	49.0	377.8	0.08	0.574	0.923	0.5	0.1	33	0.3	10	1.5	$1.66 \cdot 10^{-3}$

The numerical time histories of acceleration show a smaller amplitude at each transducer in the soil than the analysis with UBC3D-PLM.

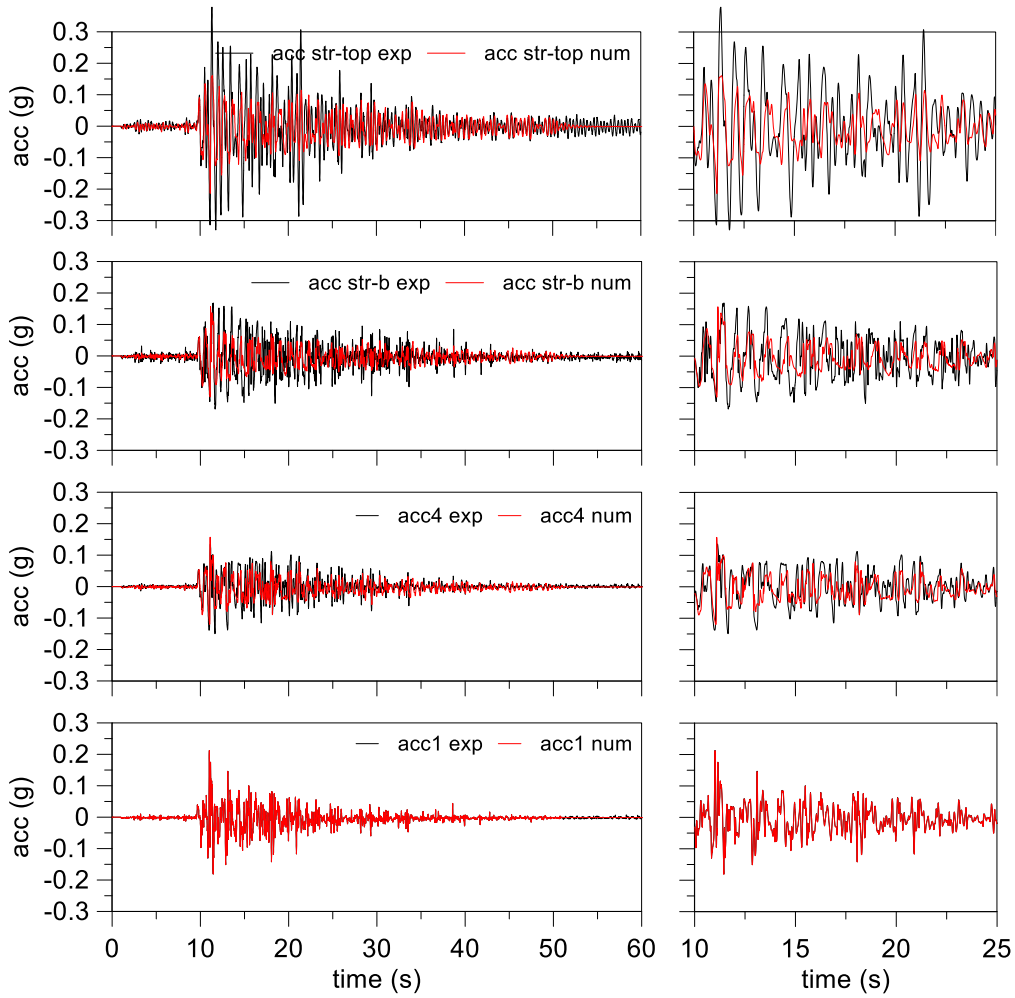

Figure 4.19. M1F_S1_GM31: main time interval of acceleration time histories.

This effect was due to a fast excess pore pressure build-up recorded in the numerical analysis (Figure 4.20) in the initial portion of the strong motion that reduced significantly

the shear stiffness of the deeper soil layer. This created an isolation effect for the upper part of the domain, including the structure, leading to lower acceleration.

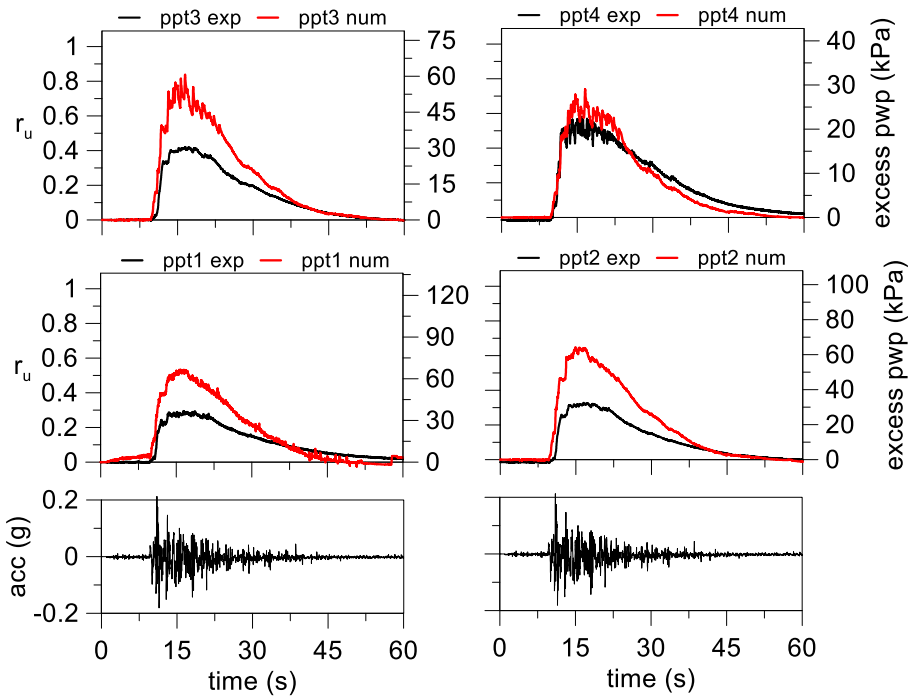

Figure 4.20. M1F_S1_GM31: excess pore water pressure time histories.

The numerical excess pore pressures were overestimated except at the pore pressure transducer ppt4 that is deployed directly beneath the structure. A faster dissipation was calculated in the deeper part of the domain.

Numerical settlements were underestimated in the "free-field" conditions also in this analysis for the same reason previously seen. A good agreement of numerical settlements with experimental ones was found for the structure (Figure 4.21). This result was due to the better numerical prediction of the excess pore pressure in the soil directly below the structure (ppt4). However, the tilt of the structure, calculated by the difference between settlements in D3 and D4 (or D5), was not good predicted by the numerical analysis that led to a larger tilt than the experimental one.

Hence, this constitutive soil model is able to predict the caused by deviatoric stress induced by the structure, and the accuracy of numerical settlements is strongly influenced by the amount of the excess pore pressure in the soil.

It is worth noting that although liquefaction was not achieved both in numerical analysis and in the experiment, large settlements of the structure were recorded. This result highlights the importance of excess water pressure ratio prediction also when liquefaction does not occur.

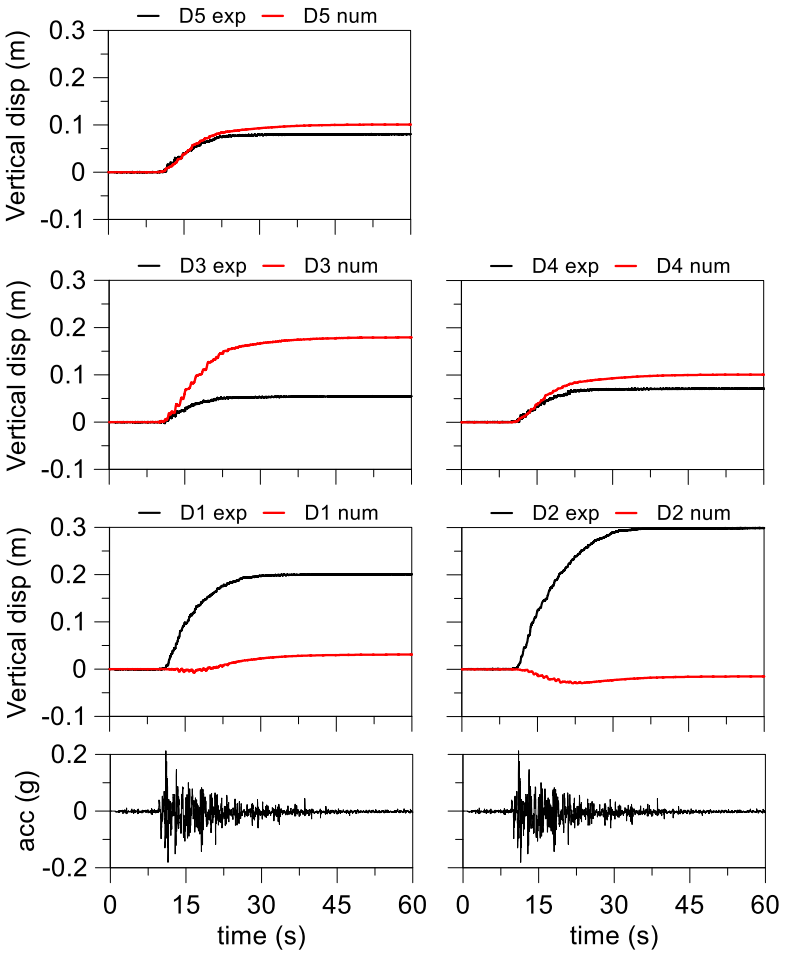

Figure 4.21. M1F_S1_GM31: ground surface displacement time histories.

4.3.3.3 UBC3D-PML (Ground motion GM31+)

In the previous test the liquefaction was not achieved, for this reason a more energized input motion was applied to the model to reach the soil liquefaction. Since the first shaking modified the initial state of the soil in the centrifuge model, a different initial relative density of the soil was assumed, as calculated by the settlements measured in the "free-field" condition. The corresponding parameters are shown in Table 4.7.

Table 4.7. Parameters for the constitutive soil model.

γ_{unsat}	γ_{sat}	RD	$N_{1,60}$	e_{min}	e_{max}	K_B^e	K_G^e	K_G^p	m_e	n_e	n_p	φ_{cv}	φ_p	f_{dens}	$f_{E,post}$	R_f	k
(kN/m^3)	(kN/m^3)	(%)	(-)	(-)	(-)	(-)	(-)		(-)	(-)		(°)	(-)	(-)	(m/s)	(-)	(m/s)
15.1	19.3	52.6	12.7	0.574	0.923	1687.0	1012.0	592.0	0.5	0.5	0.4	33	34.3	7.0	1.0	0.75	$1.66 \cdot 10^{-3}$

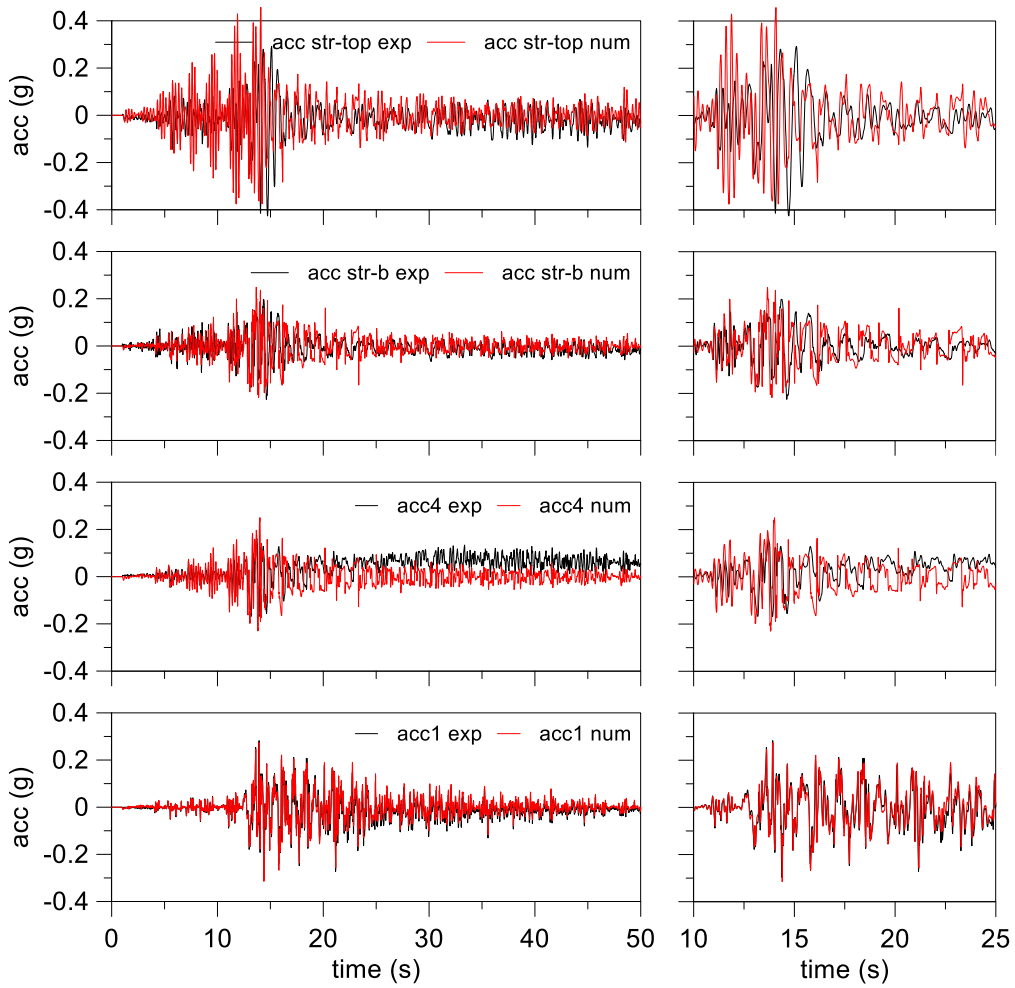

Figure 4.22. M1F_S1_GM31+: main time interval of acceleration time histories.

The numerical acceleration time histories are close to the experimental ones for all transducers in the soil and on the base of the structure (Figure 4.22). The computed accelerations diverge form the experimental ones from 17 seconds onwards, probably due

to a numerical instability induced by the large drop of soil stiffness. Finally, a larger numerical acceleration amplitude on the roof of the structure (acc str-top) was recorded until 15 seconds.

The numerical excess pore pressures are much closer to the experimental ones (Figure 4.23) than in the previous analysis (Figure 4.20). A slightly higher numerical excess pore pressure was predicted in the deeper soil layers (ppt1 and ppt2), while a good agreement was found in the shallowest ones (ppt3 and ppt4).

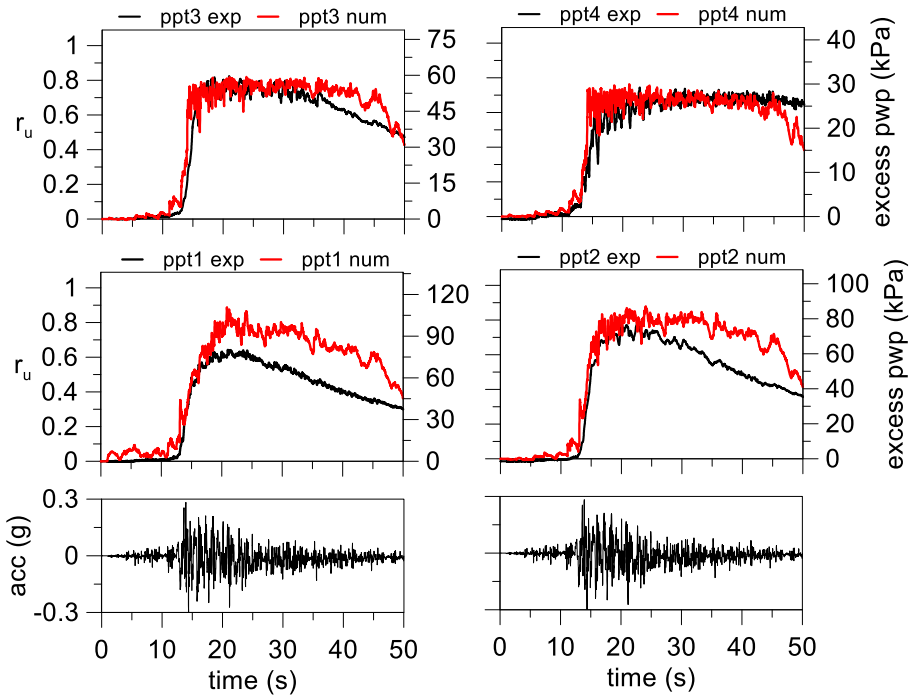

Figure 4.23. M1F_S1_GM31+: excess pore water pressure time histories.

Figure 4.24 shows the settlements of the structure and in "free-field" conditions. Computed settlements highlight an up-lift of the ground surface in free-field conditions (D1 and D2) due to the same reasons explained in the previous analyses. The numerical settlements of the structure are smaller than the experimental ones, this effect may be due to the incapability of the model to reproduce:

- large volumetric strains, recorded when the soil liquefaction is reached;
- the large drop of shear stiffness once liquefaction occur.

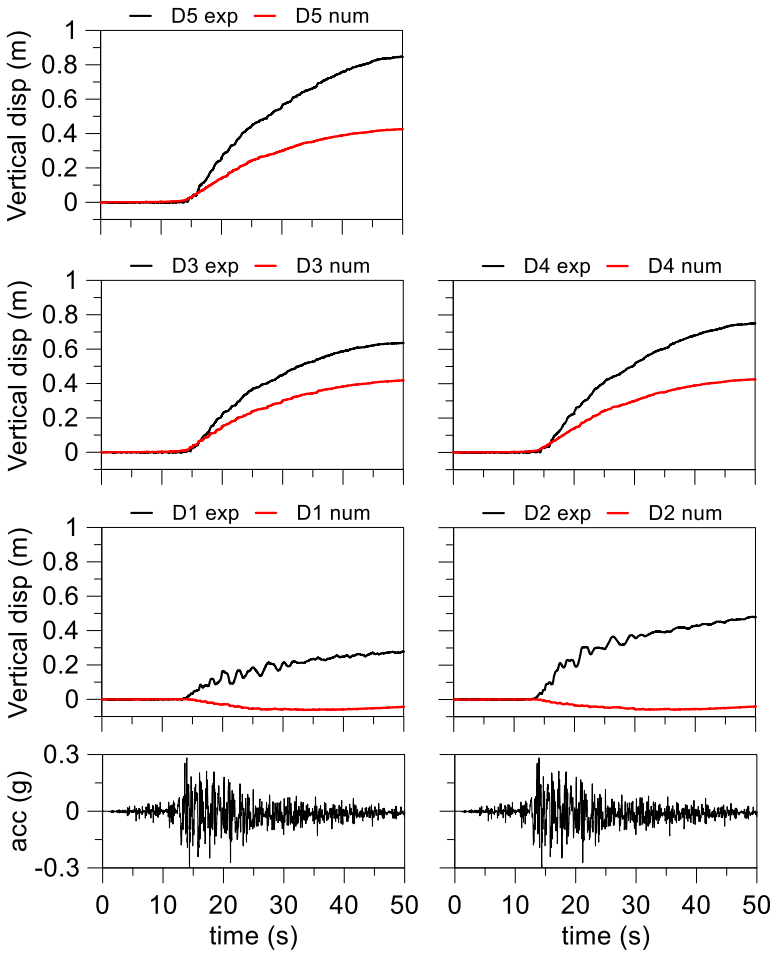

Figure 4.24. M1F_S1_GM31+: ground surface displacement time histories.

4.3.3.4 PM4SAND (Ground motion GM31+)

The same centrifuge test was analysed in numerical way using PM4SAND constitutive soil model. the parameters used in this analysis are shown in Table 4.8.

Table 4.8. Parameters for the constitutive soil model.

γ_{unsat}	γ_{sat}	RD	G_0	h_{p0}	e_{min}	e_{max}	n_b	n_d	φ	ν	Q	R	k
(kN/m^3)	(kN/m^3)	(%)	(-)	(-)	(-)	(-)	(-)	(-)	(°)	(-)	(-)	(-)	(m/s)
15.1	19.3	52.6	381	0.08	0.574	0.923	0.5	0.1	33	0.3	10	1.5	$1.66 \cdot 10^{-3}$

The amplitude of computed acceleration in the soil (acc1 and acc4) was close to the experimental ones except for the acceleration on the top of the structure (acc str-top) where a smaller amplitude was computed at the beginning of the stronger part of the signal.

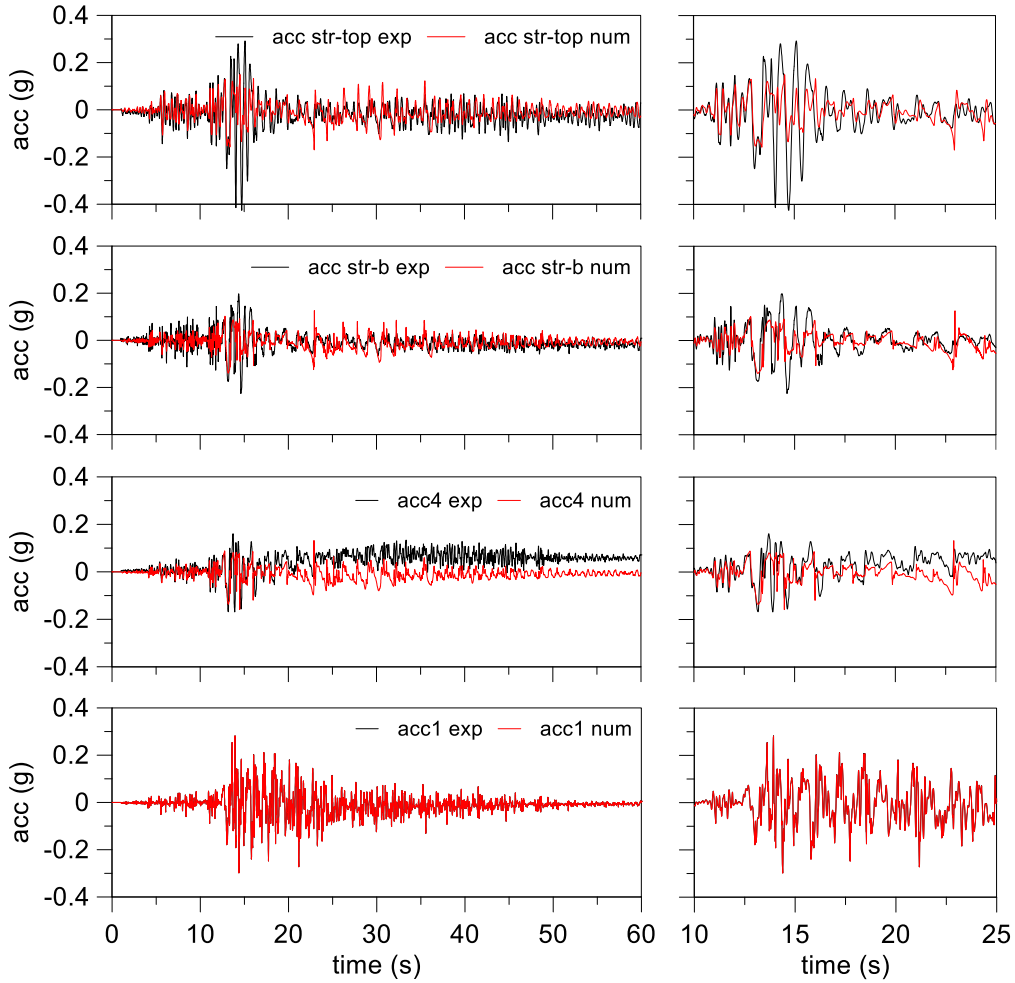

Figure 4.25. M1F_S1_GM31+: main time interval of acceleration time histories.

This small acceleration amplitude in the numerical analysis is due to the faster excess pore pressure build-up recorded at the transducers ppt1 and ppt2 (Figure 4.26). This decreased significantly the shear stiffness of the soil creating an isolation mechanism that reduced the transmission of the shear wave from the bottom of the model to the above soil layer.

The excess pore pressure in the ppt3 was well predicted, whereas at the transducer ppt4 a faster dissipation started from 25 seconds on. The numerical peaks of excess pore pressure are very close to the experimental ones in the shallower part of the domain (ppt3 and ppt4). However, in ppt4 a faster dissipation rate was computed in the numerical simulation.

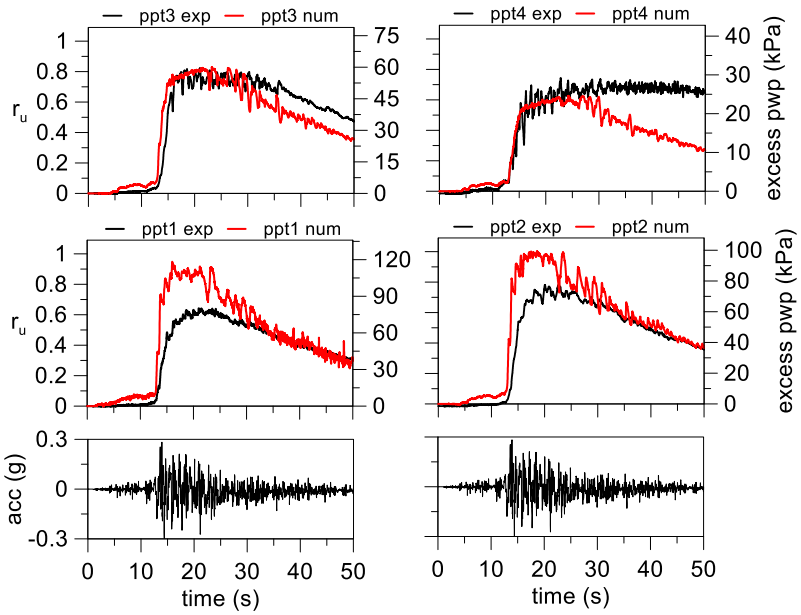

Figure 4.26. M1F_S1_GM31+: excess pore water pressure time histories.

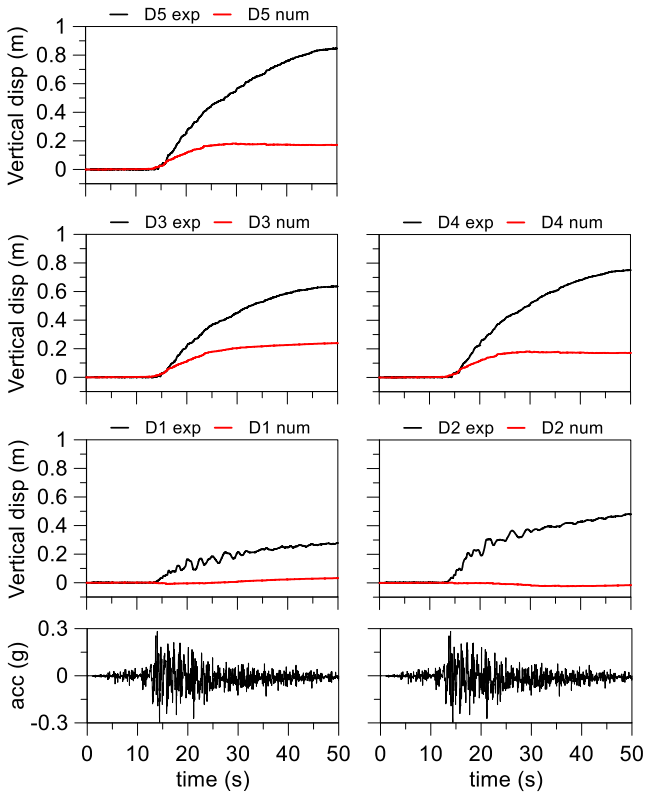

Figure 4.27. M1F_S1_GM31+: ground surface displacement time histories.

Figure 4.27 shows the settlements of the structure (D3, D4 and D5) and in free-field condition (D1 and D2). A slight up-lift was shown by the numerical simulation in free-field condition. The structure was subject to larger settlements in experimental test than in numerical analysis where the settlements showed also a slower increasing in the time.

Probably the constitutive model is not able to reproduce the very low shear stiffness of the soil reached in the experimental test. The experimental measurement at D1 and D2 suggest that the structure settlements are due also to significant volumetric strains, hence the large difference between numerical and experimental settlements can be attributed to the inability of the model to reproduce this strains type. Indeed, comparing the settlements recorded in D1 with D3 and D2 with D4 and D5 it is possible to ascertain that the difference between the numerical and experimental settlements of the structure are almost equal to the difference between the numerical and experimental settlements in the free-field condition.

4.3.4 Building on double layer model (M2F_S1_GM31+)

The numerical analysis was performed also for the model with the structure in presence of a clay crust. The structure was embedded in the soil for 1.5 meters and the base of the foundation were placed at the depth of the interface between the liquefiable soil (Ticino sand) and the clay crust (Pontida clay). It is worth noting that while in the numerical model the presence of the foundation beams of the structure presents water flow from the sand towards the ground surface, this is non-guaranteed in the experiment, where the development of cracks is possible.

4.3.4.1 UBC3D-PML

The following section the analysis was performed by the UBC3D-PML constitutive soil model. The model parameters deduced by the relationships calibrated on the relative density of the soil are shown in Table 4.9.

Table 4.9. Parameters for the constitutive soil model.

γ_{unsat}	γ_{sat}	RD	$N_{1,60}$	e_{min}	e_{max}	K_B^e	K_G^e	K_G^p	m_e	n_e	n_p	φ_{cv}	φ_p	f_{dens}	$f_{E,post}$	R_f	k
(kN/m^3)	(kN/m^3)	(%)	(-)	(-)	(-)	(-)	(-)		(-)	(-)		(°)	(-)	(-)	(m/s)	(-)	(m/s)
15.1	19.3	52.5	12.4	0.574	0.923	1675.0	1005.0	566.0	0.5	0.5	0.4	33	34.2	7.0	1.0	0.75	$1.66 \cdot 10^{-3}$

A good agreement of numerical accelerations with experimental ones was found (Figure 4.28). However, a higher frequency content was recorded in the numerical acceleration at transducer acc3 and a slightly smaller amplitude of numerical acceleration in the main part of the signal was shown at accelerometers at the base and top of the structure.

The experimental peak distribution of excess pore pressure was well predicted by numerical analysis (Figure 4.29), a faster pore pressure build-up was computed at all pore pressure transducers that probably led to the smaller amplitude of numerical acceleration recorded at the structure during the main portion of the shaking. High amount of excess water pressures persists for longer time in the numerical simulation.

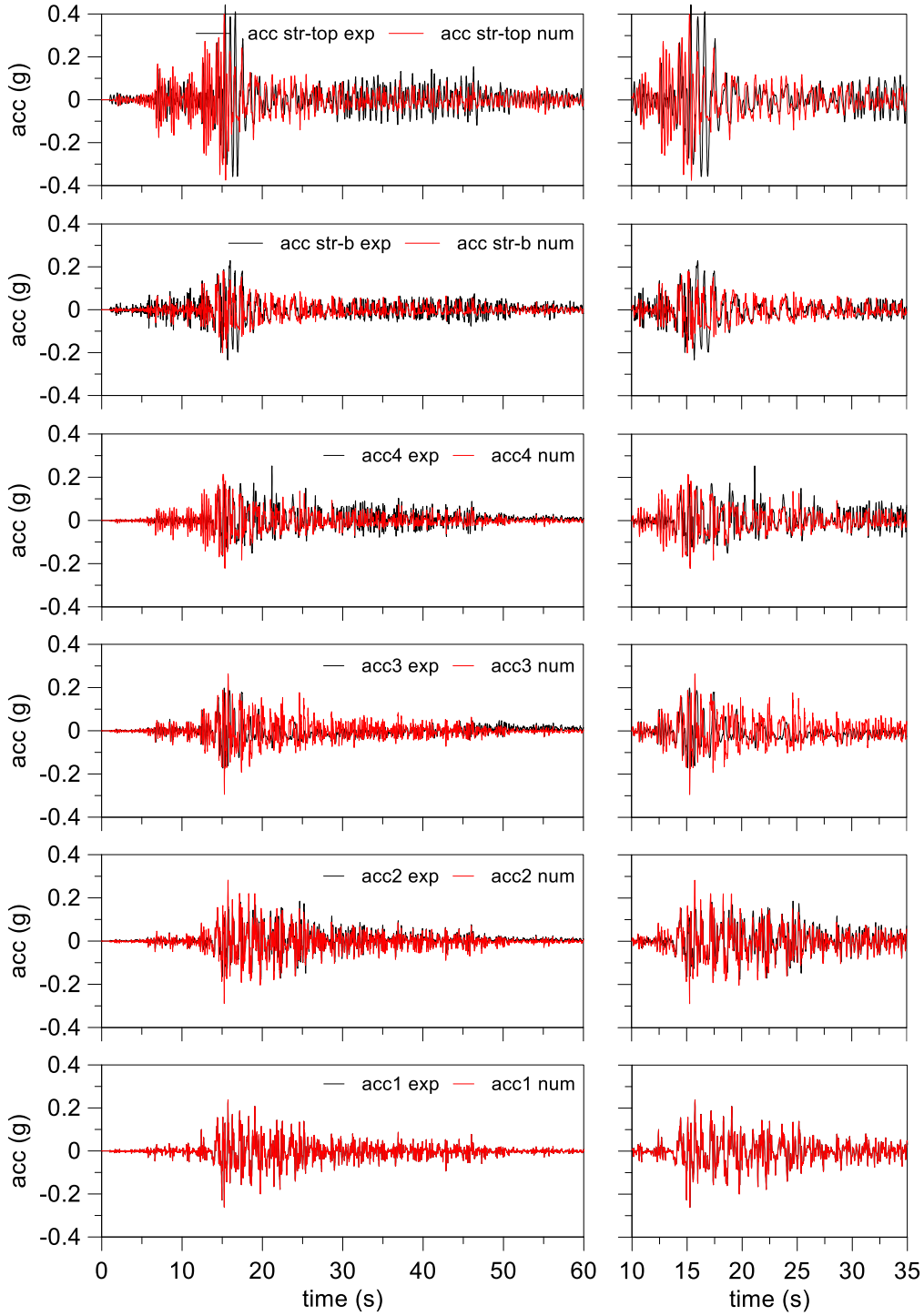

Figure 4.28. M2F_S1_GM31+: main time interval of acceleration time histories.

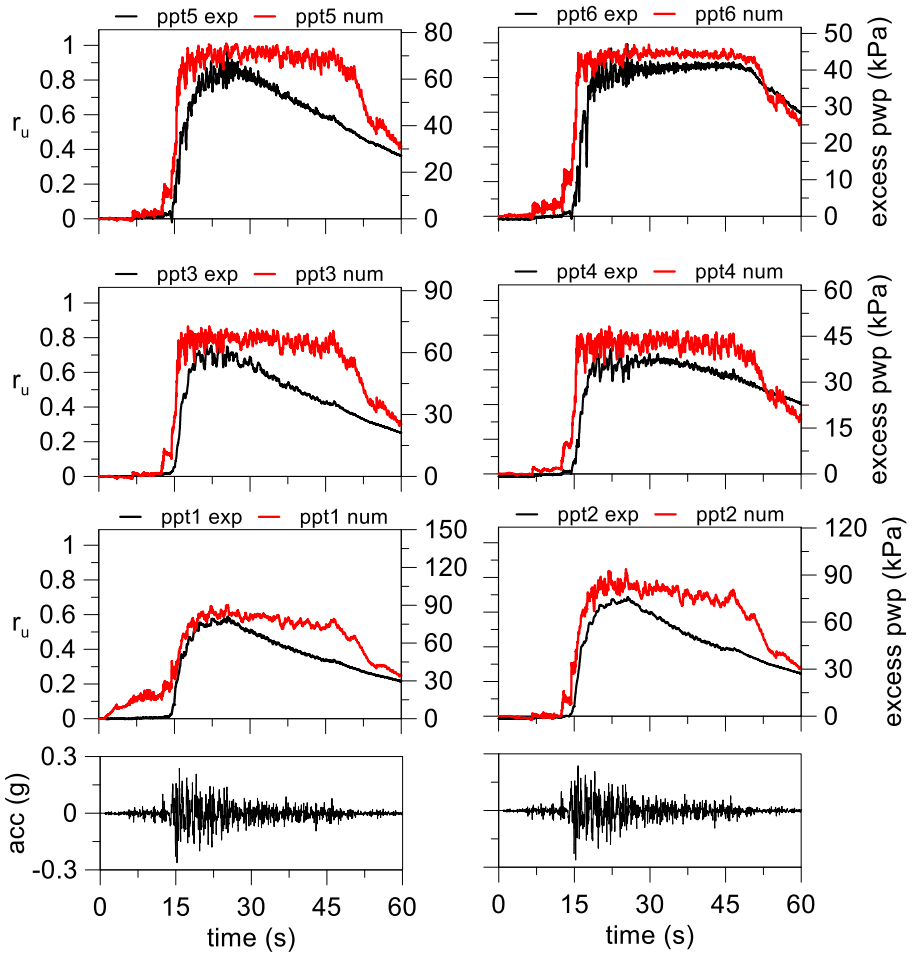

Figure 4.29. M2F_S1_GM31+: excess pore water pressure time histories.

The longer duration of numerical high excess pore pressure than the experimental led to larger structure settlements than the experimental ones (Figure 4.30). The presence of the clay crust avoided a water flow from the soil towards the ground surface leading to large level and duration of excess pore pressure. This prevented the development of volumetric strains, thus prevailing the deviatoric settlements, as it is possible to deduce by the transducers D1 and D2. That the volumetric strains were negligible can be deduced also from the experiments by comparing the settlements at transducers D1 and D2 in this test and in the previous one. The presence of the clay crust reduced the settlement from almost 0.3 meters (Figure 4.27) to 0.2 meters. (Figure 4.30).

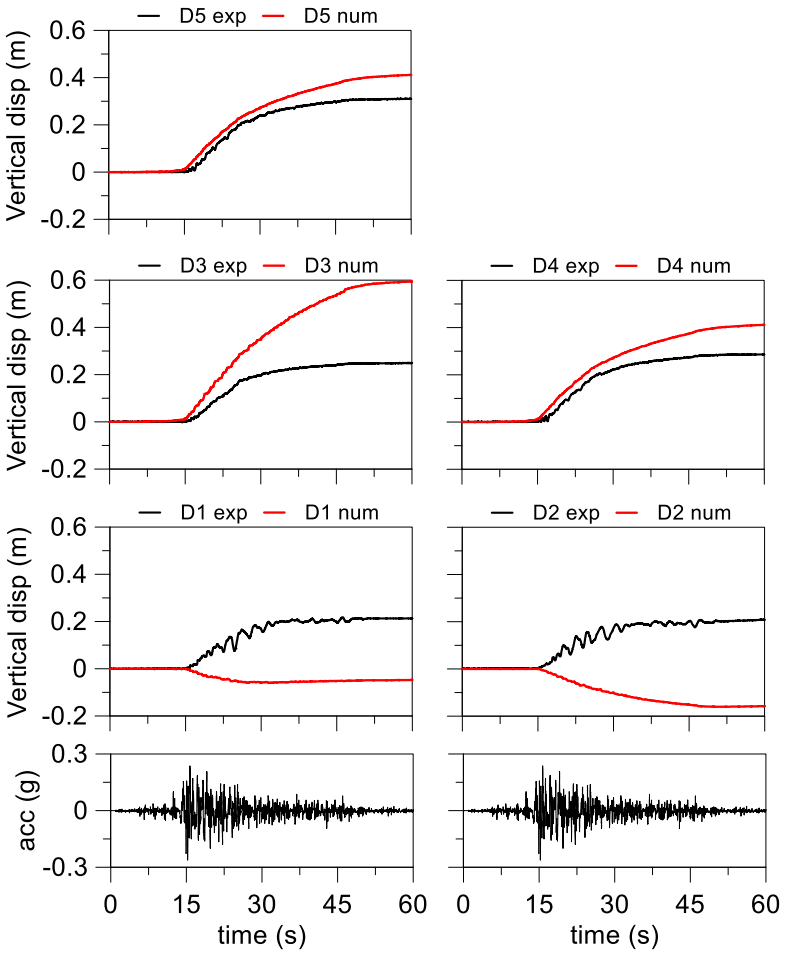

Figure 4.30. M2F_S1_GM31+: ground surface displacement time histories.

4.3.4.2 PM4SAND

In this section the analysis of the same experimental test seen in previous section was performed using the PM4SAND constitutive soil model. The parameter used for the constitutive model are shown in Table 4.10.

Table 4.10. Parameters for the constitutive soil model.

γ_{unsat}	γ_{sat}	RD	G_0	h_{p0}	e_{min}	e_{max}	n_b	n_d	φ	ν	Q	R	k
(kN/m^3)	(kN/m^3)	(%)	(-)	(-)	(-)	(-)	(-)	(-)	(°)	(-)	(-)	(-)	(m/s)
15.1	19.3	52.5	381	0.08	0.574	0.923	0.5	0.1	33	0.3	10	1.5	$1.66 \cdot 10^{-3}$

A large decrease of the acceleration amplitude was calculated in the numerical analysis especially in the vicinity of the ground surface and on the structure.

However, the peak values of the excess water pressure (Figure 4.32) are the same of the previous numerical analysis performed by UBC3D-PML, so this constitutive model shows a stronger dependence of stiffness from the effective stresses than UBC3D-PML.

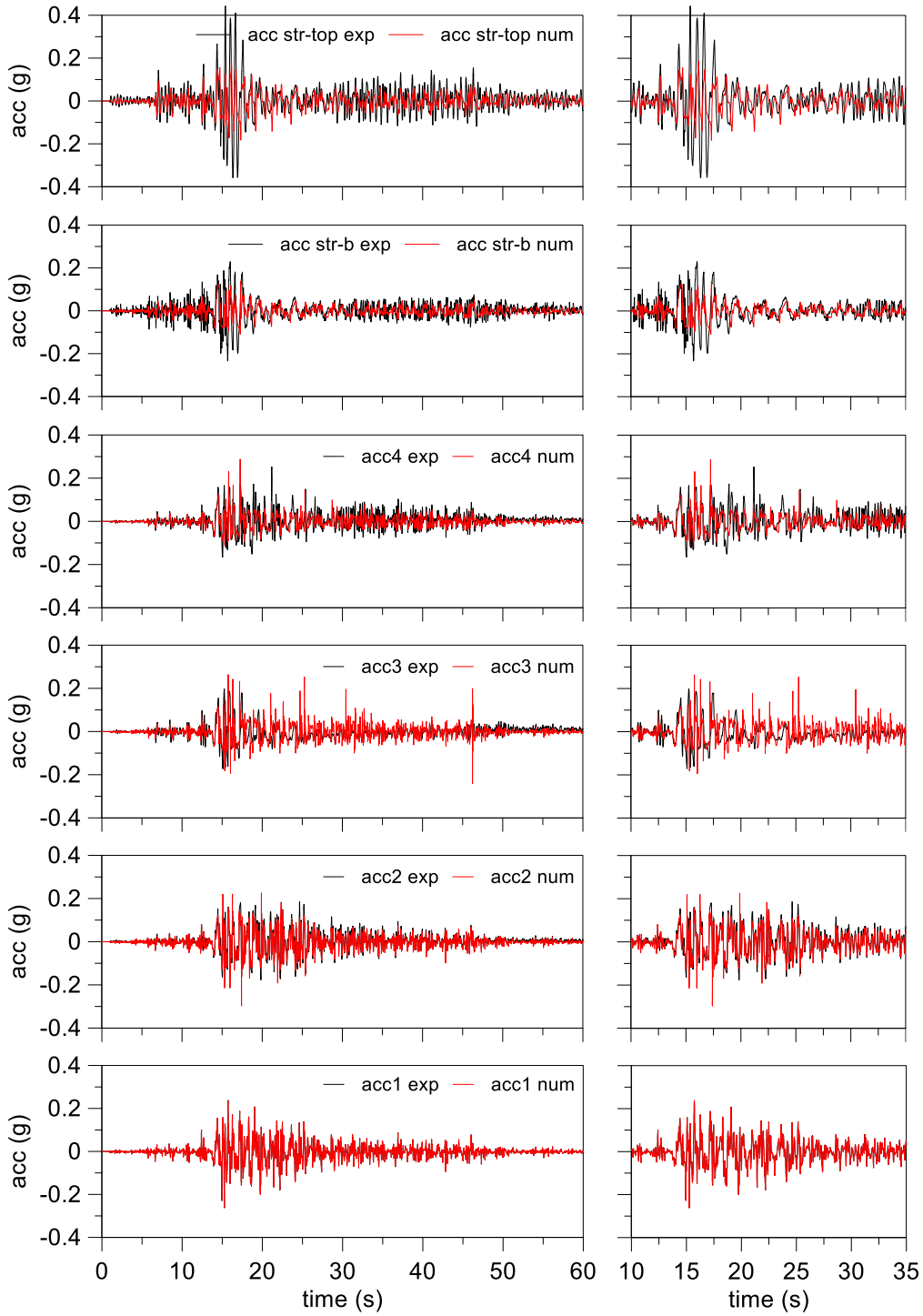

Figure 4.31. M2F_S1_GM31+: main time interval of acceleration time histories.

Conversely from the previous analysis the high levels of excess pore pressure had a shorter duration, with a dissipation rate similar to the experimental one (Figure 4.32).

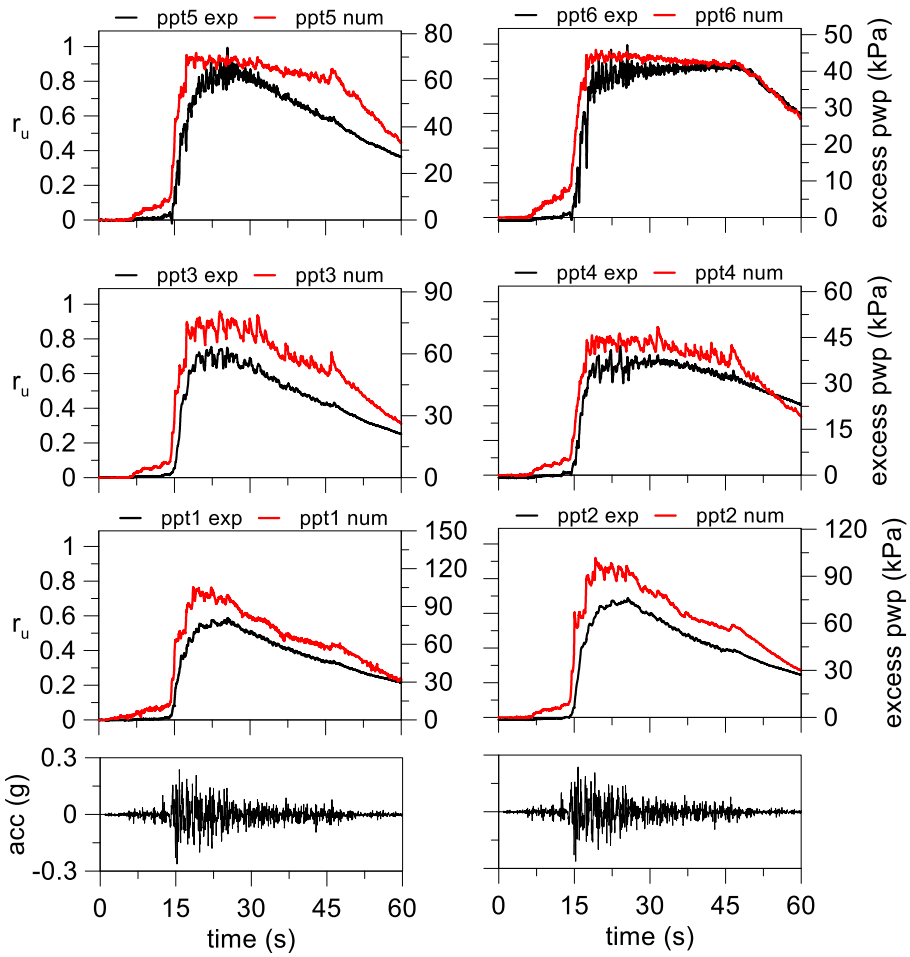

Figure 4.32. M2F_S1_GM31+: excess pore water pressure time histories.

This last effect led to a faster recovery of the shear stiffness in this analysis inducing smaller computed settlements of the structure than the previous one. Therefore, the settlements of the structure in this numerical analysis are closer to the experimental ones than in the previous analysis. However, an up-lift was calculated at the transducers placed in “free-field” conditions (D1 and D2), that was not observed experimentally.

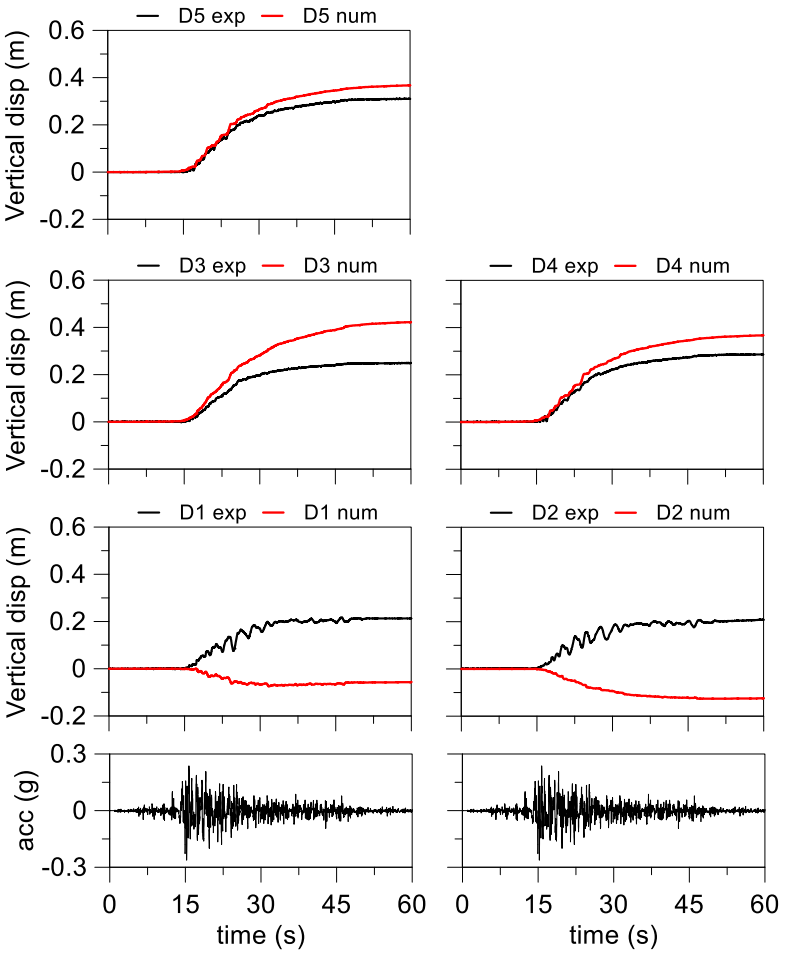

Figure 4.33. M2F_S1_GM31+: ground surface displacement time histories.

4.4 Horizontal drains numerical model

In this section the capability of the constitutive models and the reliability of the calibration procedure were tested reproducing some experimental tests with horizontal drains as liquefaction mitigation technique.

Horizontal drains were created in the numerical model through two coaxial circles that delimited a region in which a material with an equivalent permeability was modelled to reproduce the permeability of the drains deployed in the centrifuge model as explained in section 3.8. A time constant water head equal to the hydrostatic one was applied to the inner diameter of the drains in the numerical analysis.

4.4.1 Single layer model (M1_S1_HD1&2_GM31)

The model with a single liquefiable layer with horizontal drains, seen in the section 3.11, was reproduced numerically. The simple geometrical scheme allowed to check the capability and reliability of the model to reproduce the effects induced by the presence of horizontal drains.

4.4.1.1 UBC3D-PML

The calibration procedure for UBC3D-PML constitutive soil model led to the parameters shown in Table 4.11.

Table 4.11. Parameters for the constitutive soil model.

γ_{unsat}	γ_{sat}	RD	$N_{1,60}$	e_{min}	e_{max}	K_B^e	K_G^e	K_G^p	m_e	n_e	n_p	φ_{cv}	φ_p	f_{dens}	$f_{E,post}$	R_f	k
(kN/m^3)	(kN/m^3)	(%)	(-)	(-)	(-)	(-)	(-)	(-)	(-)	(-)	(-)	(°)	(-)	(-)	(m/s)	(-)	(m/s)
15.2	19.3	54.5	13.7	0.574	0.923	1728.0	1036.0	680.6	0.5	0.5	0.4	33	34.4	7.0	1.0	0.74	$1.66 \cdot 10^{-3}$

The computed acceleration time histories are very close to the experimental ones (Figure 4.34). However, the shallowest computed accelerometers (acc4 and acc7) show a slight deamplification after the strong part of the shaking.

The computed excess pore pressure ratios shown in Figure 4.34 exhibit an irregular behaviour with the mean value close to the experimental one. Only the pore pressure transducer ppt1 shows an excess pore pressure higher than the experimental one.

Horizontal drains dissipate the excess pore pressure in the surrounding soil during and after the earthquake. The effect of the horizontal drains on the distribution of excess pore pressure ratio in the soil is shown in Figure 4.36. The distribution of r_u highlights that within the arrangement of the drains with ratio s/D = 10 (on the right of the Figure 4.36) higher values of excess pore pressure ratio were achieved than within the disposition with s/D = 5, but a larger decrease of r_u was recorded in the soil below the horizontal drains with s/D = 10.

This result influences the distribution of the settlements that in these conditions (free-field) are due to the volumetric strains. The inability of the constitutive model to reproduce large volumetric strains led to an underestimation of numerical settlements (Figure 4.37). However, computed and experimental settlements show an inconsistency on the maximum values. Indeed, numerical settlements above horizontal drains s/d=5 (D1) are larger than settlements above horizontal drains with s/d=10 (D2). Opposite result is shown in the experiment.

Figure 4.36 shows that the horizontal drain with s/d=10 produces a more homogeneous decrease of the excess pore pressure in the soil profile than the arrangement with s/d=5 leading to a smaller loss of soil stiffness, so smaller settlements. The incongruence of the experimental settlements probably is due to a slight punching of the displacement transducer tip in the soil above horizontal drains with s/d=10 justified by the presence of higher excess water pressure nearby the ground surface.

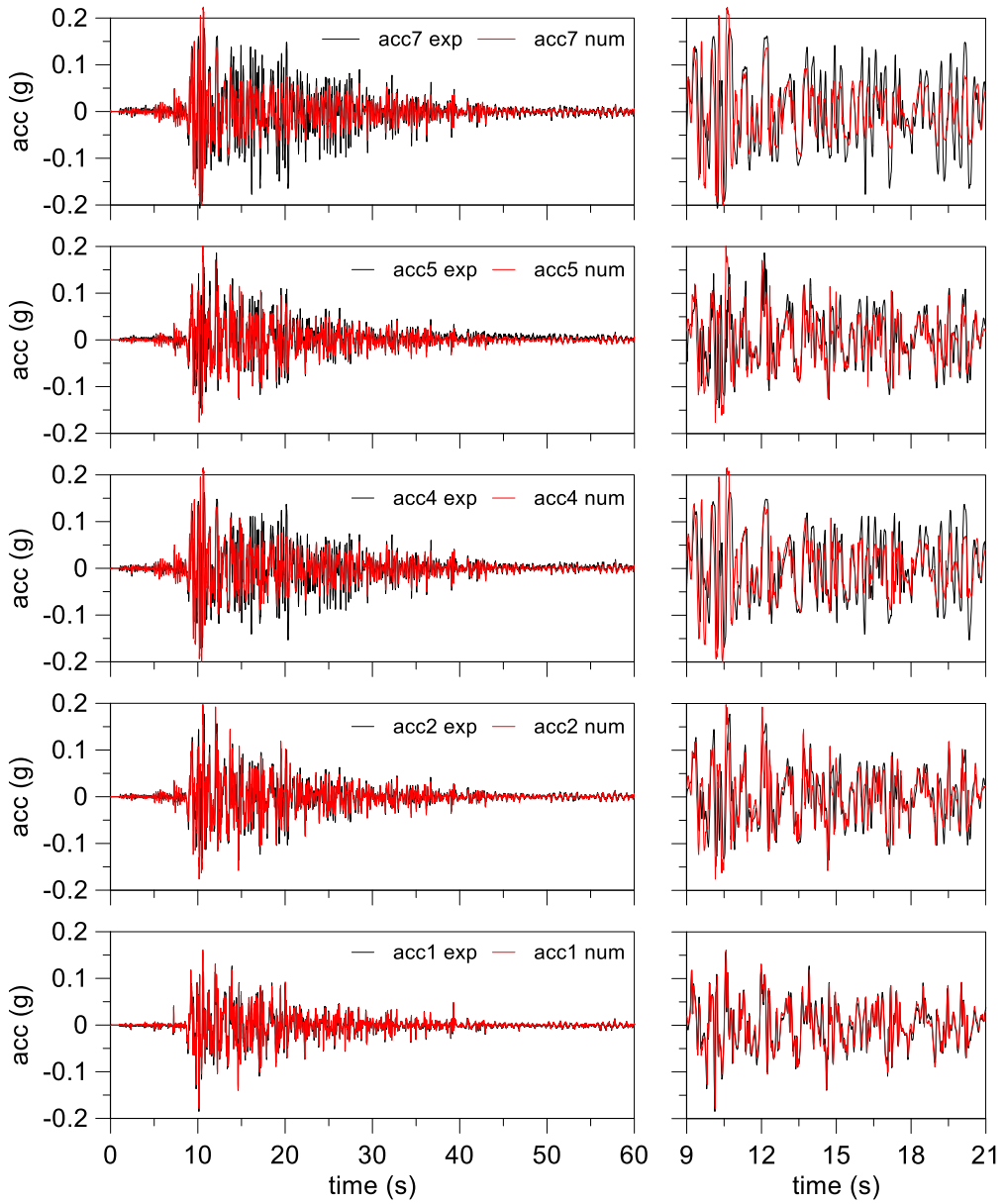

Figure 4.34. M1_S1_HD1&2_GM31: main time interval of acceleration time histories.

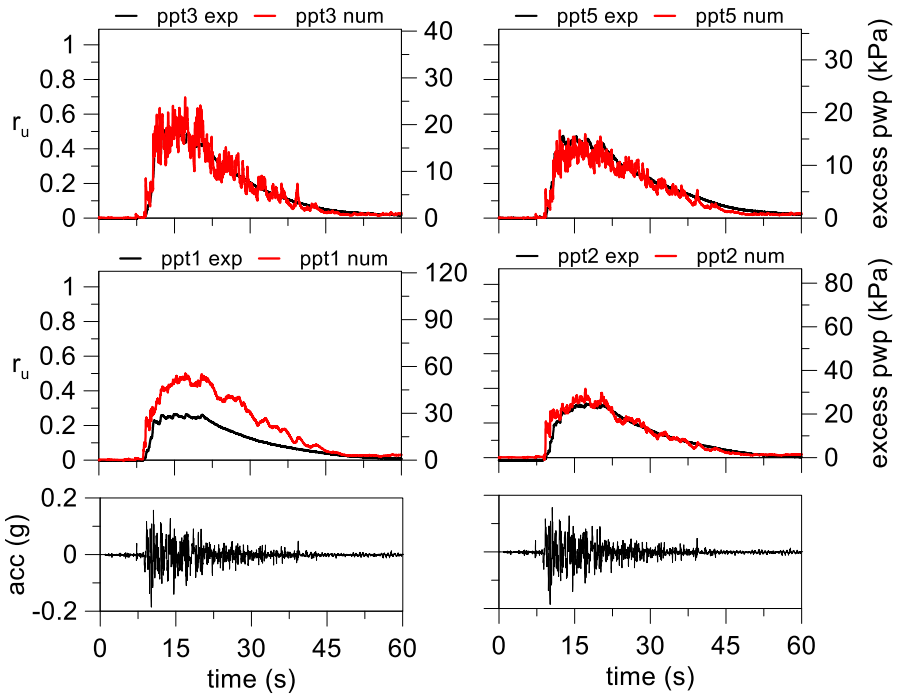

Figure 4.35. M1_S1_ HD1&2_GM31: excess pore water pressure time histories.

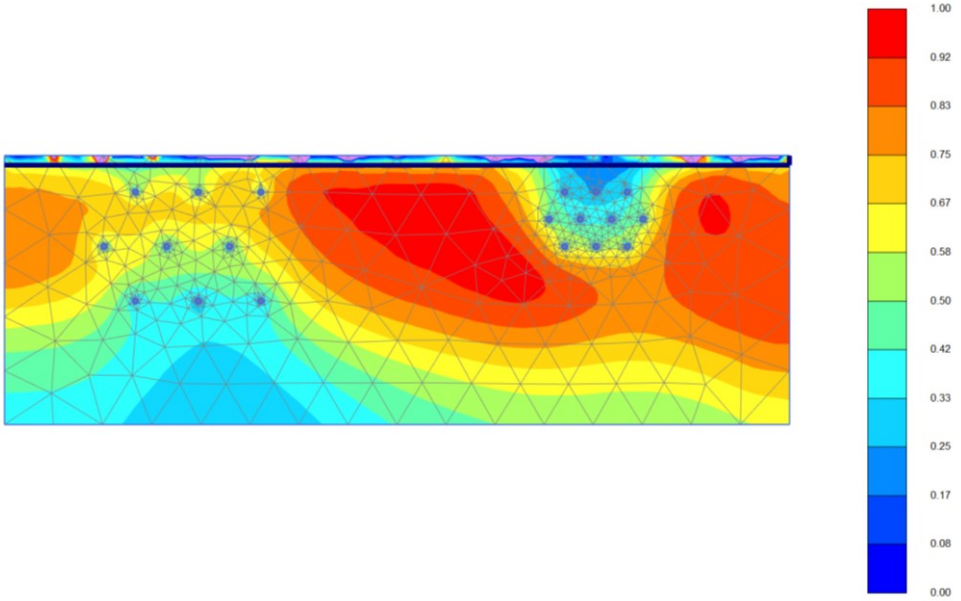

Figure 4.36. M1_S1_ HD1&2_GM31: effect of horizontal drains on the distribution of excess pore pressure ratio at 16 seconds.

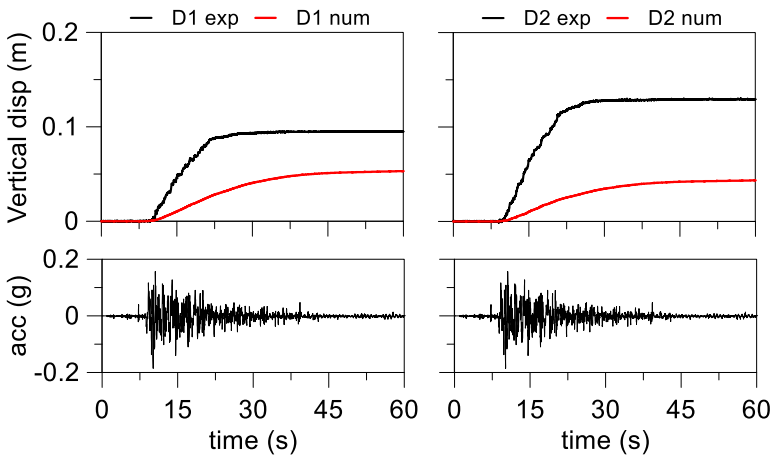

Figure 4.37. M1_S1_ HD1&2_GM31: ground surface displacement time histories.

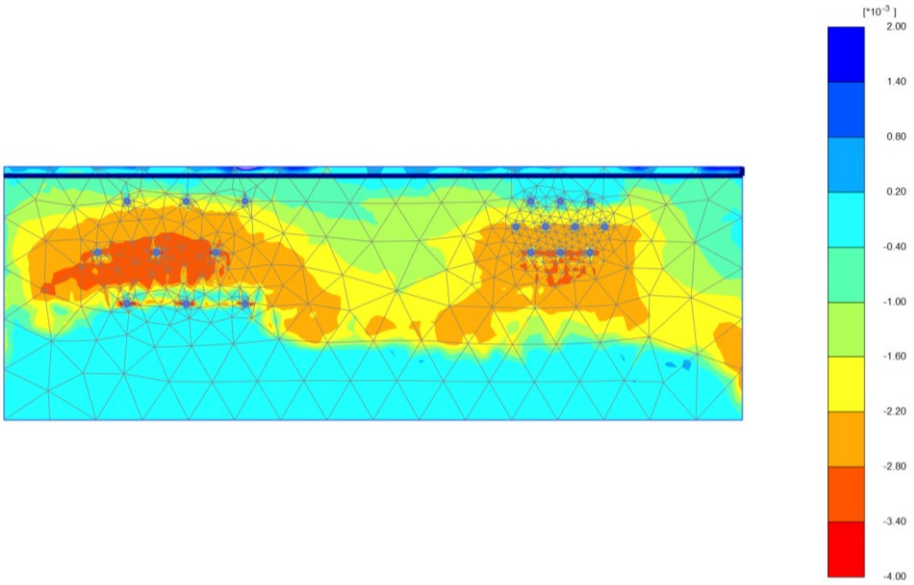

Figure 4.38. M1_S1_ HD1&2_GM31: effect of horizontal drains on the distribution of volumetric strain at 16 seconds (ε_v<0 compression).

Figure 4.38 shows that the presence of the horizontal drains induces larger volumetric strains in the surrounding soil. This effect is more evident between the drains with s/d = 10 arrangement. The drains dissipate larger incremental amount of excess pore pressure in the time in presence of a low bulk stiffness induced by the high excess pore pressure.

4.4.1.2 PM4SAND

The same centrifuge model was analysed by PM4SAND constitutive soil model. The calibration procedure led to determine the parameters shown in Table 4.12.

Table 4.12. Parameters for the constitutive soil model.

γ_{unsat} (kN/m^3)	γ_{sat} (kN/m^3)	RD (%)	G_0 (-)	h_{p0} (-)	e_{min} (-)	e_{max} (-)	n_b (-)	n_d (-)	φ (°)	ν (-)	Q (-)	R (-)	k (m/s)
15.2	19.3	54.5	382.7	0.08	0.574	0.923	0.5	0.1	33	0.3	10	1.5	$1.66 \cdot 10^{-3}$

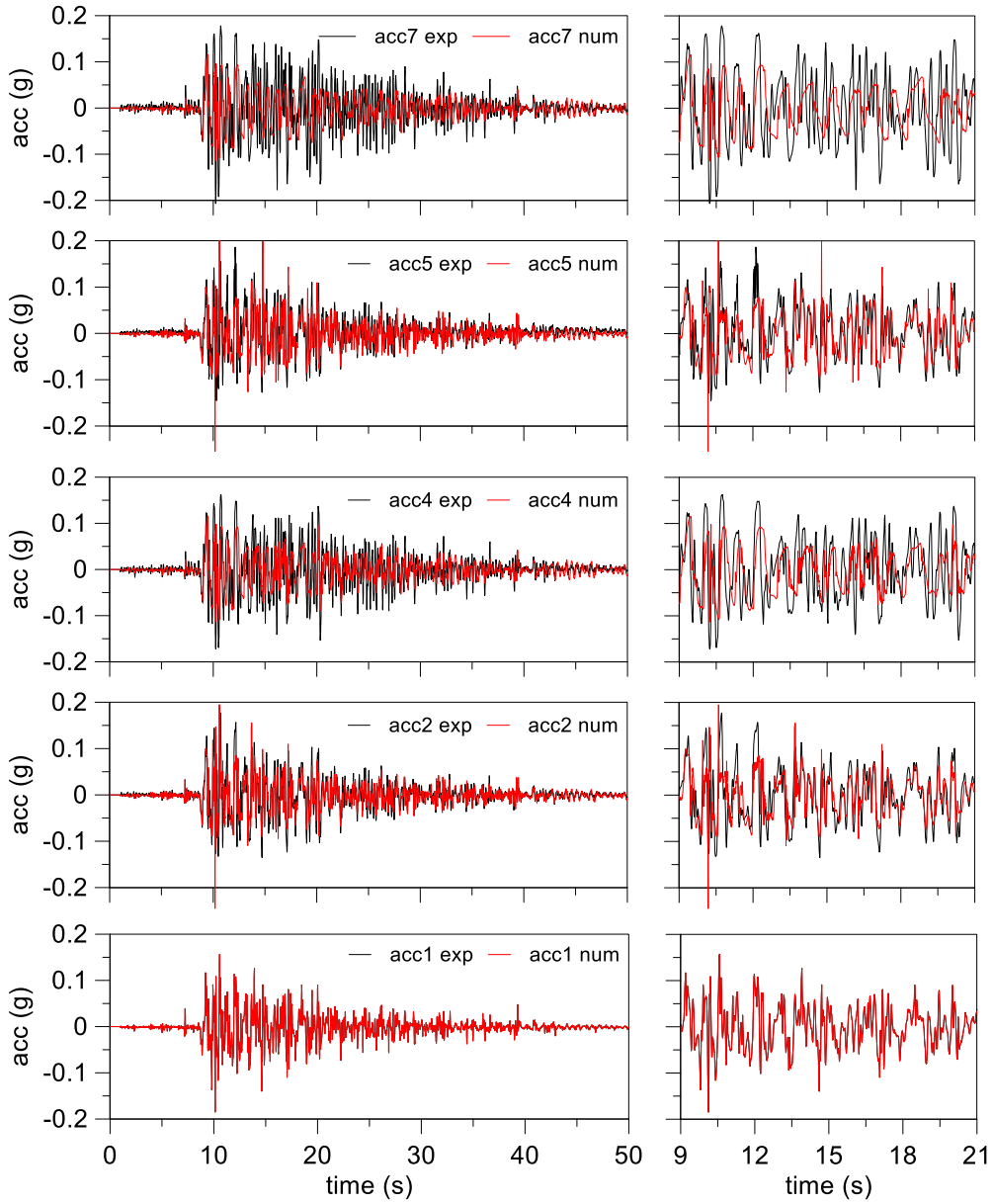

Figure 4.39. M1_S1_HD1&2_GM31: main time interval of acceleration time histories.

A larger decrease of the computed acceleration amplitude was recorded in the shallowest acceleration transducers acc4 and acc7 (Figure 4.39) compared to the previous analysis. This result is due to a higher level of numerical excess pore pressures (Figure 4.40) than the experimental ones in the deeper part of the model (ppt1 and ppt2).

The excess pore pressure peaks between the drains were well predicted by numerical analysis, but a higher dissipation rate was computed.

Numerical settlements had the same behaviour of the previous analysis. This result reinforces the hypothesis of punching of the displacement transducer tip in the experiment.

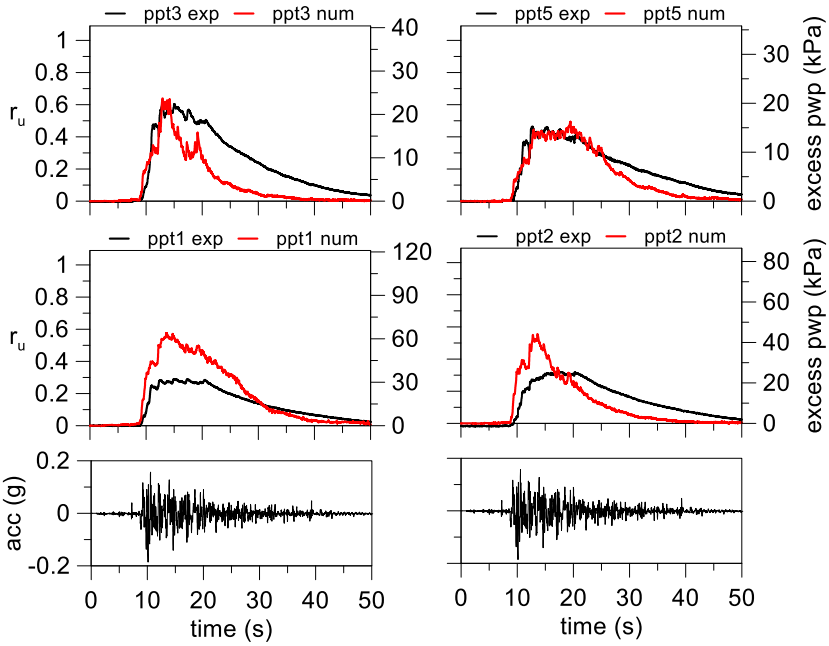

Figure 4.40. M1_S1_HD1&2_GM31: excess pore water pressure time histories.

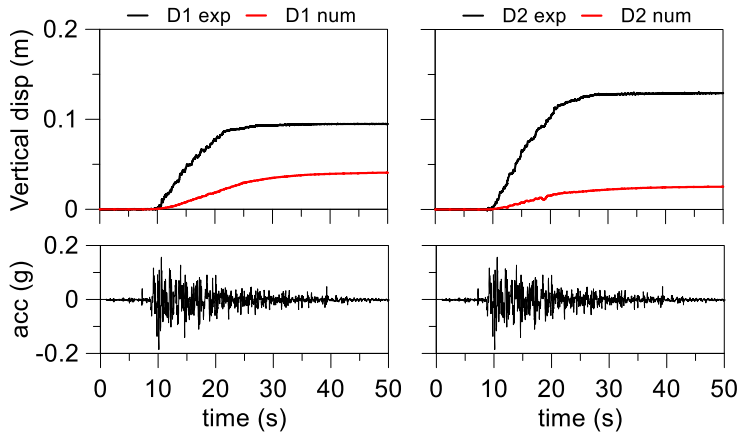

Figure 4.41. M1_S1_HD1&2_GM31: ground surface displacement time histories.

As seen before, horizontal drains lead to an increment of volumetric strains in the surrounding soil during the shaking thanks to their drainage effect. In the following this effect has been studied by some numerical cyclic simple shear stress tests introducing two seepage surfaces on the top and bottom of the sample with one meter high (Figure 4.42). A 1 Hz frequency was fixed as shear stress input.

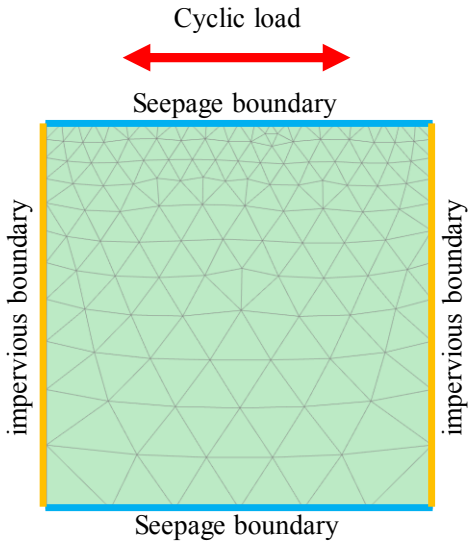

Figure 4.42. Numerical model used for the cyclic simple shear stress tests.

Figure 4.43a shows that the volumetric strain increases with the soil permeability. The amount of volumetric strain begins to decrease when the permeability prevents the soil liquefaction occurrence.

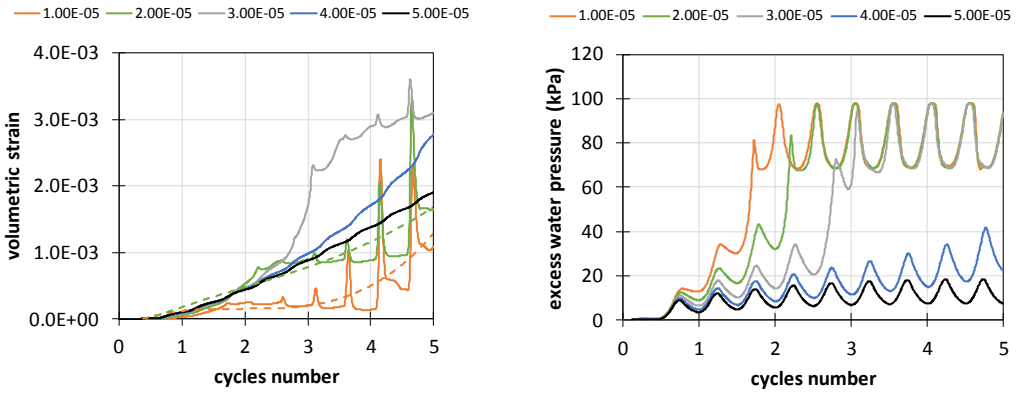

Figure 4.43. Paths of cyclic simple shear stress tests for different permeability coefficients expressed in m/s.

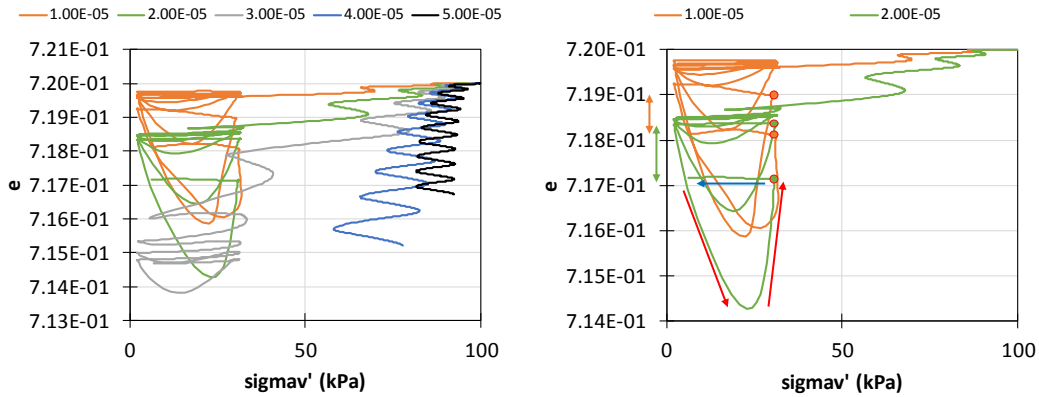

Figure 4.44. Paths in (p'-e) plane.

The behaviour of the soil in term of void ratio and mean effective stress is significantly different in the cases where the liquefaction occurs (Figure 4.44). It is worth noting that the sample with lowest permeability shows a smaller volumetric strain, whereas in the cases where the liquefaction does not occur show a volumetric strain comparable to the green and grey lines. This effect is due to the progressive dissipation of a large amount of excess pore pressure in the time.

Hence, the volumetric strain is the result of the balance between the excess water pressure build-up of the soil and the capability excess water pressure dissipation of the soil system. This effect is clearly shown in the Figure 4.44b where the higher dissipation capability of the system in green line leads to a larger volumetric strain than the system in orange line (see the green and orange arrows). However, the excess pore pressure build-up in a single cycle happens with high velocity and so in quasi-undrained condition (blue arrow), whereas the upswing of the effective stress (red arrows) happens in partial drained conditions. This effect leads to a progressive increase of volumetric strains.

Hence, some drainage conditions and horizontal drains arrangements can produce larger volumetric strains than the soil without mitigation technique with a consequent larger settlement in free-field condition.

4.4.2 Double layer model (M2_S1_HD1&2_GM31)

In this section the centrifuge test with a clay crust in presence of horizontal drains was performed numerically. The presence of the clay crust decreases the capability of the soil system to dissipate the excess pore pressure by a water flow from the soil towards the upper seepage surface.

4.4.2.1 UBC3D-PML

The numerical simulation of the centrifuge test was performed by UBC3D-PML constitutive soil model in this section. The soil parameters employed in the numerical analysis are shown in Table 4.13.

Table 4.13. Parameters for the constitutive soil model.

γ_{unsat} (kN/m³)	γ_{sat} (kN/m³)	RD (%)	$N_{1,60}$ (-)	e_{min} (-)	e_{max} (-)	K_B^e (-)	K_G^e (-)	K_G^p	m_e (-)	n_e (-)	n_p	φ_{cv} (°)	φ_p (-)	f_{dens} (-)	$f_{E,post}$ (m/s)	R_f (-)	k (m/s)
15.1	19.3	52.5	12.7	0.574	0.923	1685.0	1011.0	588.0	0.5	0.5	0.4	33	34.4	7.0	1.0	0.75	$1.66 \cdot 10^{-3}$

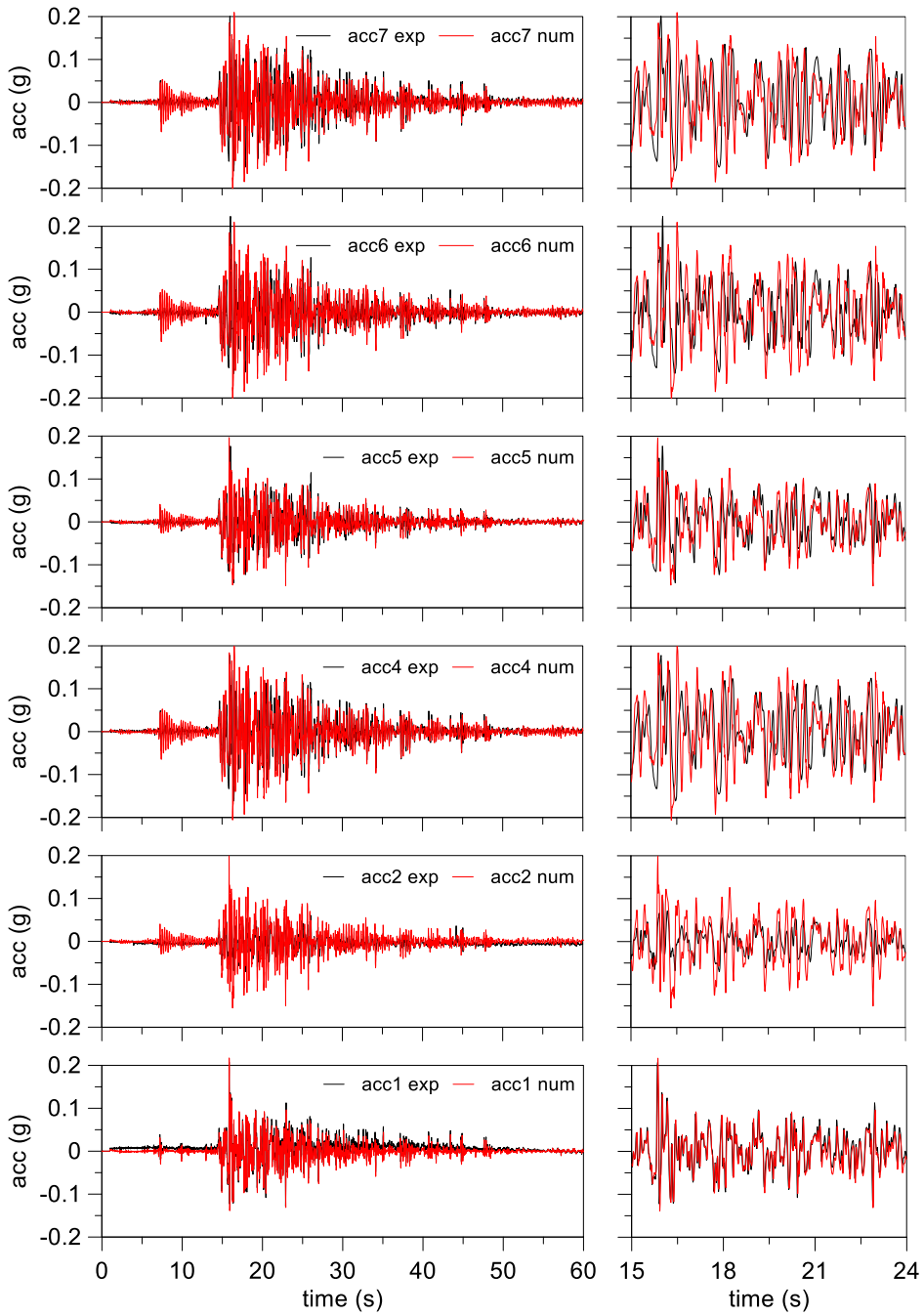

Figure 4.45. M2_S1_HD1&2_GM31: main time interval of acceleration time histories.

Computed acceleration time histories (Figure 4.45) show a slight amplification at each acceleration transducer especially for acc2. However, a good agreement was found.

Figure 4.46 shows the excess pore pressure time histories that present an abnormal peak in each pore pressure transducer at about 15 seconds, in correspondence of the highest acceleration peak (Figure 4.45). The transducers deployed among the drains (ppt3 and ppt5) predicted an excess pore pressure slightly lower than the experimental one. However, numerical results and experimental ones show a good agreement. The presence of the clay crust led to a progressive increase of the excess pore pressure in correspondence of the interface between liquefiable soil and crust (Figure 4.47).

Furthermore, the clay crust reduced the amount of volumetric strains induced by the dissipation of excess pore pressure during the shaking through the seepage ground surface. This effect reduced the gap between the computed settlements and experimental ones (Figure 4.48). A large dilatation of the soil was computed in the thin layer near the interface (Figure 4.49).

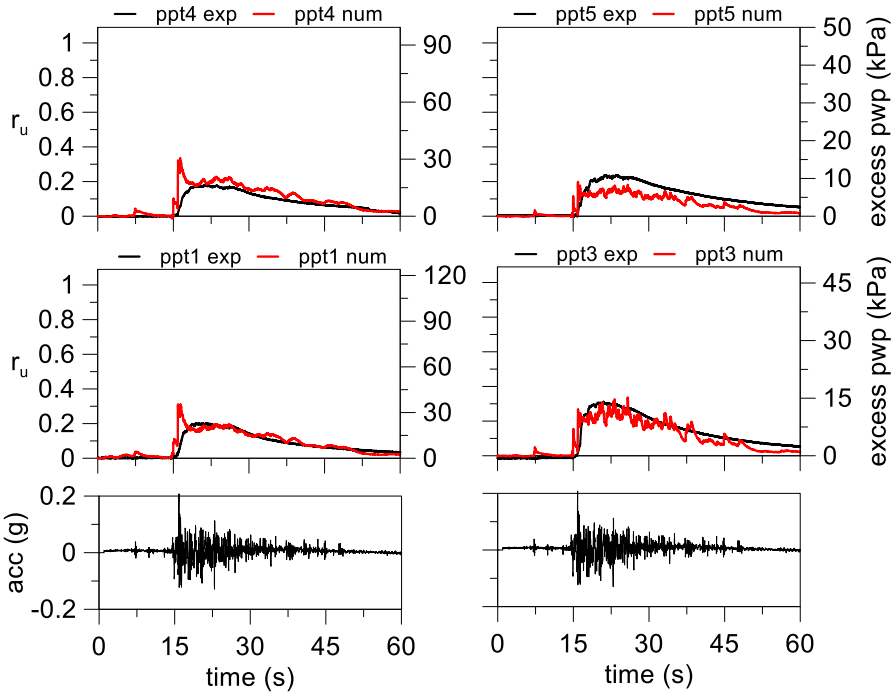

Figure 4.46. M2_S1_ HD1&2_GM31: excess pore water pressure time histories.

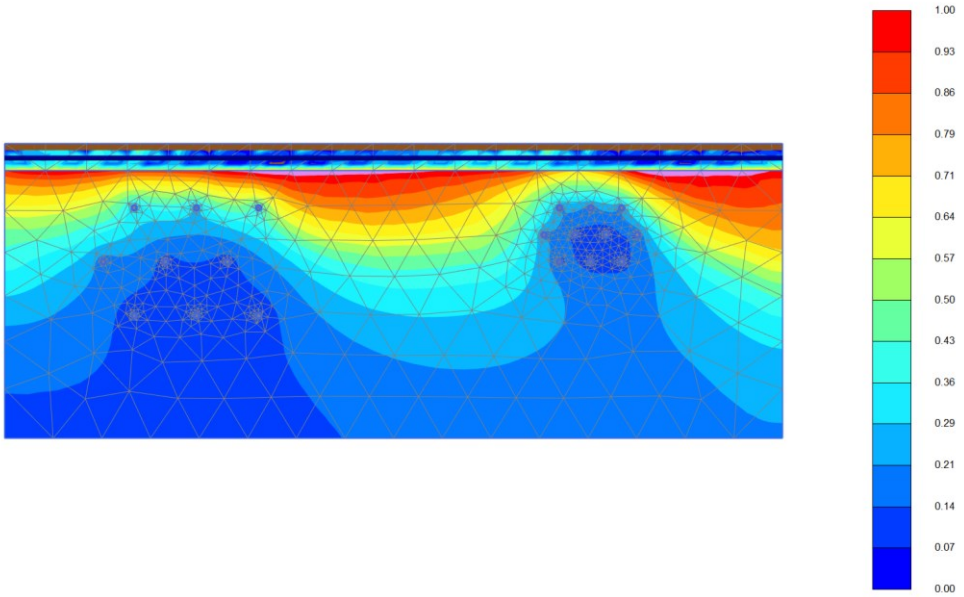

Figure 4.47. M2_S1_ HD1&2_GM31: effect of horizontal drains on the distribution of excess pore pressure ratio at 18 seconds.

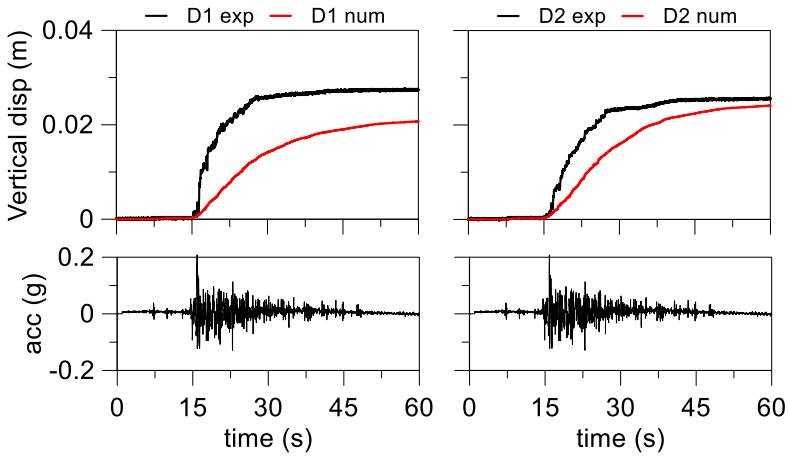

Figure 4.48. M2_S1_ HD1&2_GM31: ground surface displacement time histories.

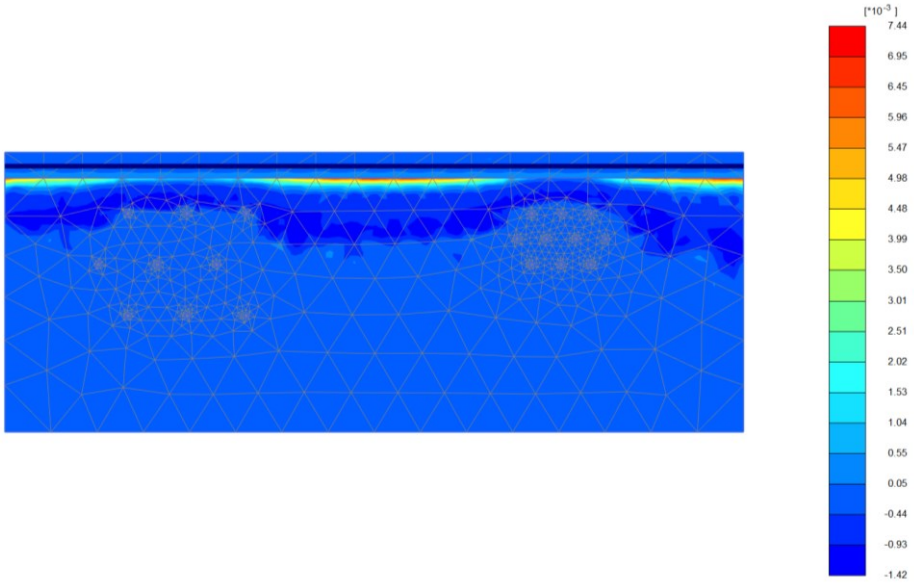

Figure 4.49. M2_S1_ HD1&2_GM31: effect of horizontal drains on the distribution of volumetric strain at 18 seconds (ε_v<0 compression).

4.4.2.2 PM4SAND

The same centrifuge test was simulated using the PM4SAND constitutive soil model. The parameters used in the numerical analysis are shown in Table 4.14.

Table 4.14. Parameters for the constitutive soil model.

γ_{unsat}	γ_{sat}	RD	G_0	h_{p0}	e_{min}	e_{max}	n_b	n_d	φ	ν	Q	R	k
(kN/m^3)	(kN/m^3)	(%)	(-)	(-)	(-)	(-)	(-)	(-)	(°)	(-)	(-)	(-)	(m/s)
15.1	19.3	52.5	381	0.08	0.574	0.923	0.5	0.1	33	0.3	10.0	1.5	$1.66 \cdot 10^{-3}$

The computed acceleration time histories (Figure 4.50) show a conversely behaviour of the previous analysis showing a smaller acceleration amplitude than the experimental one. This effect was due to a faster excess pore pressure build-up in this numerical simulation (Figure 4.51) that led to an initial excess pore pressure higher than the experimental one. However, the numerical prediction gives values near to the experimental ones especially among the drains (ppt3 and ppt5). The simulation shows a higher dissipation rate than the experimental one.

Figure 4.52 shows the comparison between the computed and experimental ground surface settlements. Numerical results were significantly smaller than the experimental ones and lower than the simulation with UBC3D-PML. This result may be due to the fast dissipation of the excess pore pressure that led to a fast upswing of shear stiffness avoiding the accumulation of significant volumetric strains in the time.

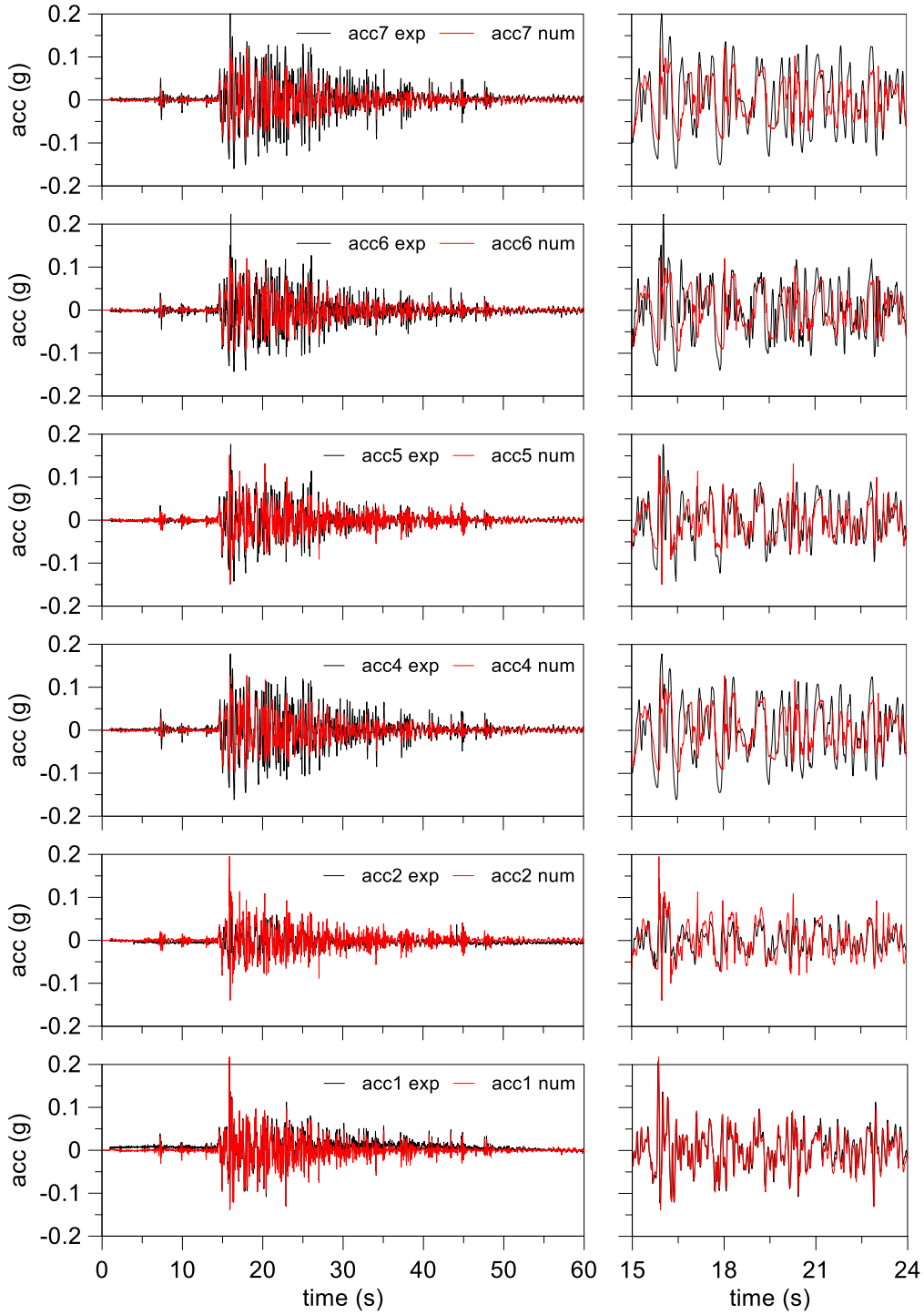

Figure 4.50. M2_S1_HD1&2_GM31: main time interval of acceleration time histories.

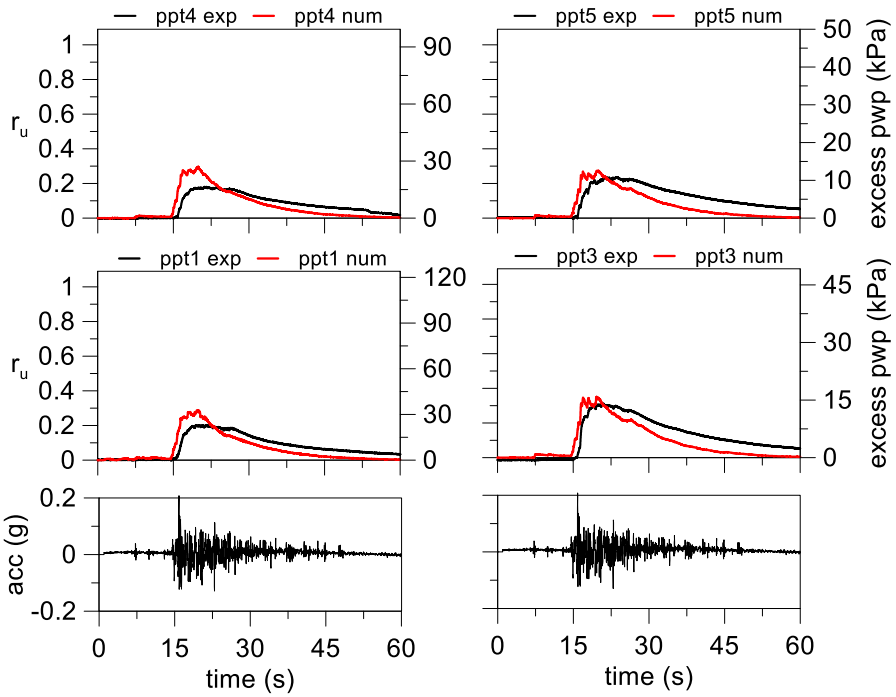

Figure 4.51. M2_S1_HD1&2_GM31: excess pore water pressure time histories.

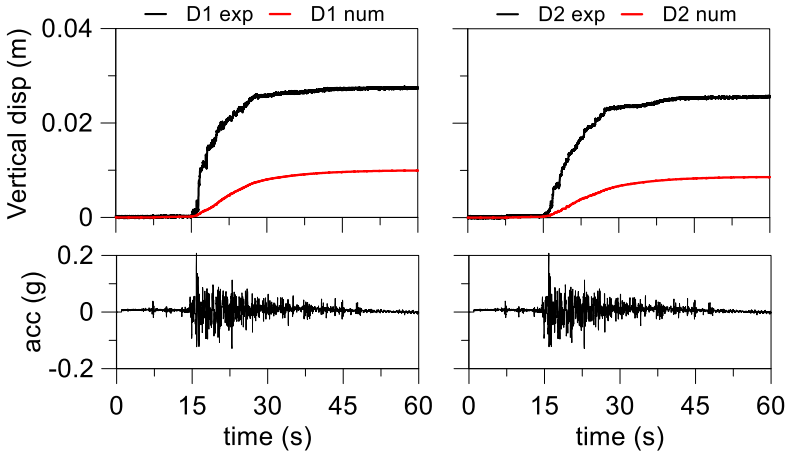

Figure 4.52. M2_S1_HD1&2_GM31: ground surface displacement time histories.

4.4.3 Building on single layer model (M1F_S1_HD1_GM31+)

In this section the numerical investigation of the horizontal drains effect below the structure is shown. These analyses are helpful to understand how the drains modify the distribution of the excess water pressure below the structure and their effect on the absolute and differential settlements.

4.4.3.1 UBC3D-PML

As for the previous numerical analyses, the constitutive model UBC3D-PML was calibrated on the relative density. The parameters used for the analysis are shown in Table 4.15.

Table 4.15. Parameters for the constitutive soil model.

γ_{unsat}	γ_{sat}	RD	$N_{1,60}$	e_{min}	e_{max}	K_B^e	K_G^e	K_G^p	m_e	n_e	n_p	φ_{cv}	φ_p	f_{dens}	$f_{E,post}$	R_f	k
(kN/m^3)	(kN/m^3)	(%)	(-)	(-)	(-)	(-)	(-)		(-)	(-)		(°)	(-)	(-)	(m/s)	(-)	(m/s)
15.1	19.25	51.2	12.1	0.574	0.923	1657.0	994.0	533.0	0.5	0.5	0.4	33	34.2	7.0	1.0	0.76	$1.66 \cdot 10^{-3}$

The numerical analysis led to a good agreement with experimental results in terms of accelerations (Figure 4.53) except for the numerical higher frequency recorded before the stronger part of the input motion at the roof of the structure.

Figure 4.54 shows that the numerical peaks of excess pore pressures are close to the experimental ones except between the horizontal drains (ppt4) where a smaller amount was recorded. The numerical excess water pressures exhibited a slower dissipation rate and an irregular behaviour.

The ground surface settlements are smaller than the experimental ones (Figure 4.56) with an uplift in D2 due to the incapability of the model to reproduce the large volumetric strains occurred in the experiment. However, deviatoric strains below the foundation of the structure permitted to reach the experimental settlements recorded in D3.

It is worth noting that the settlements below the structure are smaller than the structure without horizontal drains (Figure 4.24).

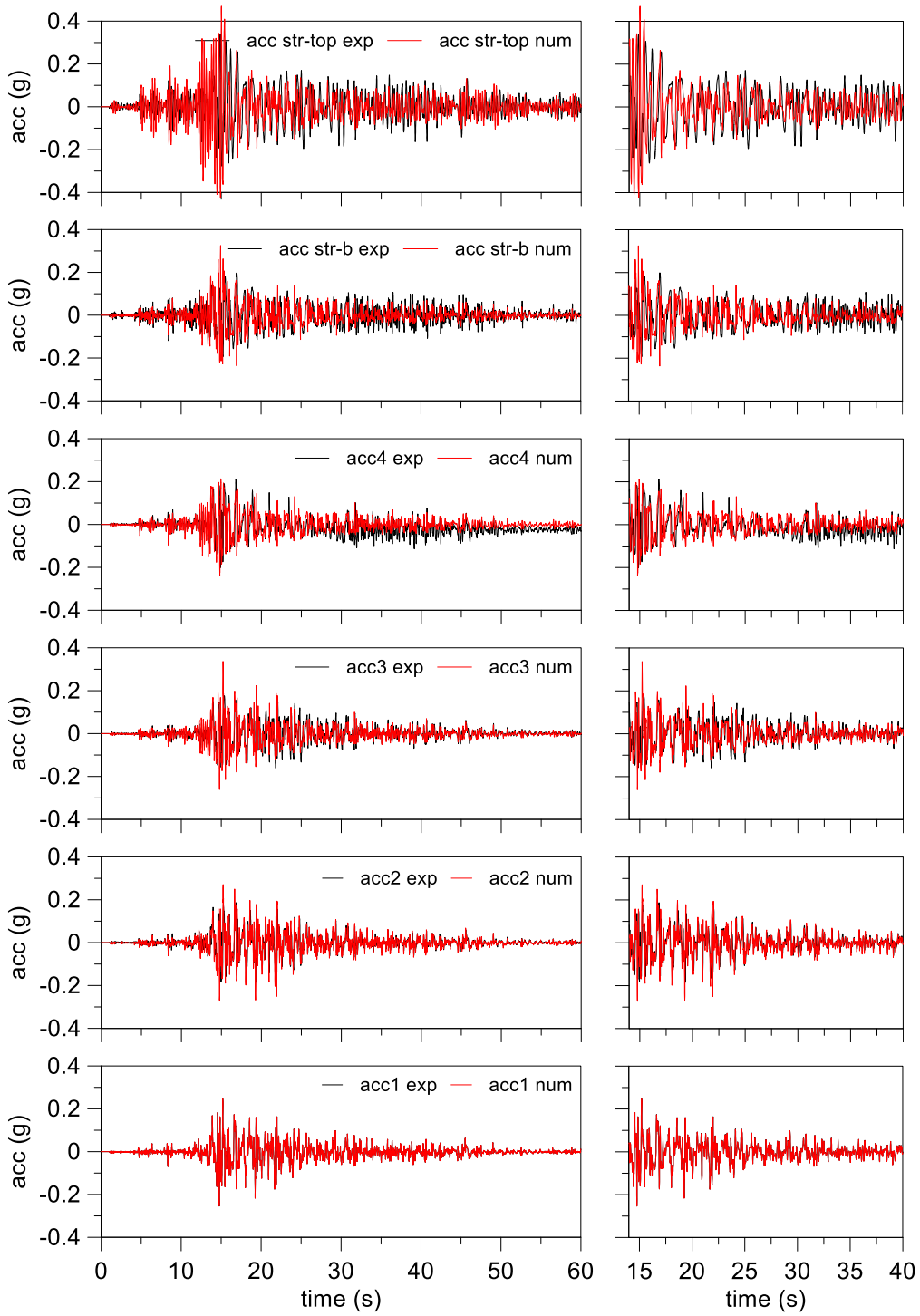

Figure 4.53. M1F_S1_HD1_GM31+: main time interval of acceleration time histories.

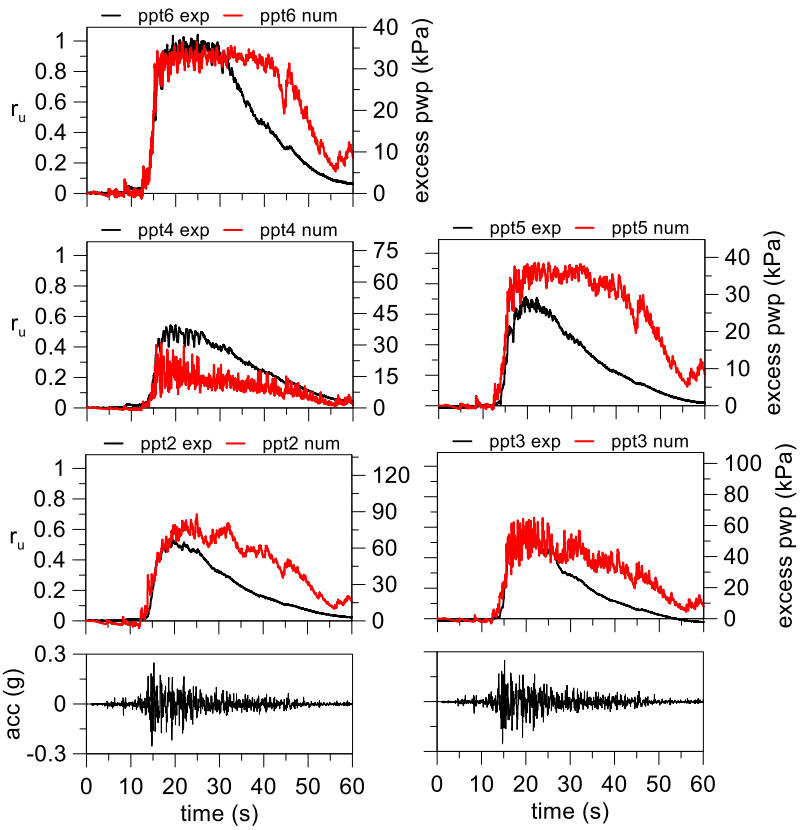

Figure 4.54. M1F_S1_HD1_GM31+: excess pore water pressure time histories.

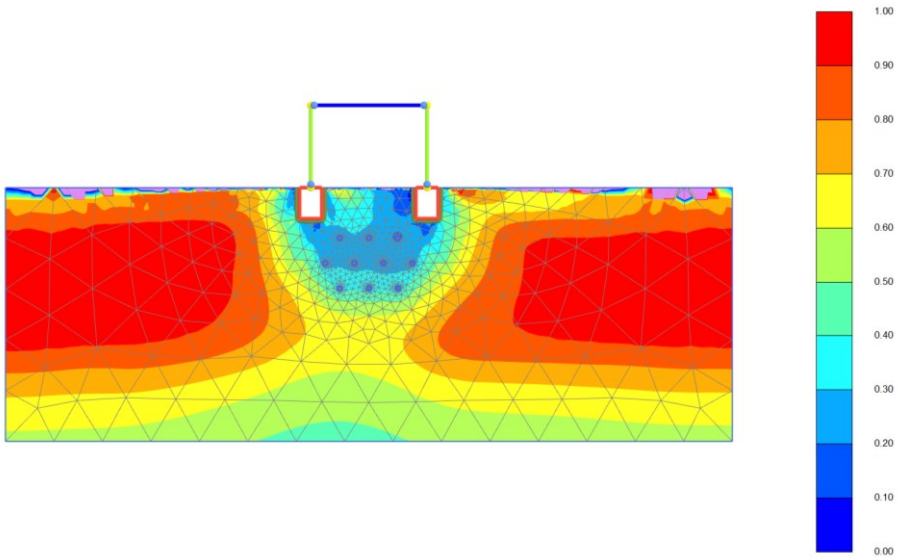

Figure 4.55. M1F_S1_HD1_GM31+: effect of horizontal drains on the distribution of excess pore pressure ratio at 20 seconds.

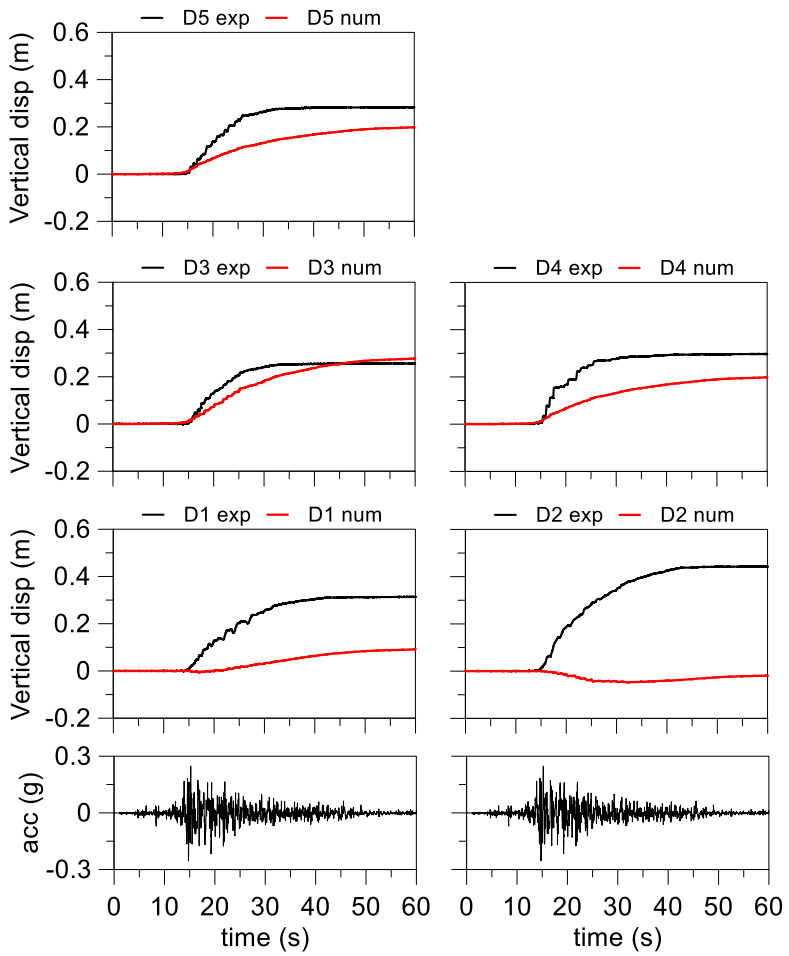

Figure 4.56. M1F_S1_HD1_GM31+: ground surface displacement time histories.

4.4.3.2 PM4SAND

The same centrifuge test was analysed numerically using PM4SAND constitutive soil model adopting the parameters in Table 4.16.

Table 4.16. Parameters for the constitutive soil model.

γ_{unsat}	γ_{sat}	RD	G_0	h_{p0}	e_{min}	e_{max}	n_b	n_d	φ	ν	Q	R	k
(kN/m^3)	(kN/m^3)	(%)	(-)	(-)	(-)	(-)	(-)	(-)	(°)	(-)	(-)	(-)	(m/s)
15.1	19.25	51.2	379.8	0.08	0.574	0.923	0.5	0.1	33	0.3	10.0	1.5	$1.66 \cdot 10^{-3}$

A significant decrease of computed acceleration amplitude was recorded in the accelerometers into the soil and on the structure after the beginning of the more energized portion of the shaking (Figure 4.57). This effect was the consequence of the large drop of the soil shear stiffness due to the high numerical excess pore pressure computed in the deeper part of the domain (ppt1) that realised a sort of the isolation effect (Figure 4.58). The

computed excess pore pressure among the horizontal was lower tanh experimental one. The time histories show a slower numerical dissipation rate in all pore pressure transducers.

Figure 4.59 shows the computed settlements that were slightly smaller than the experimental ones for the structure foundation.

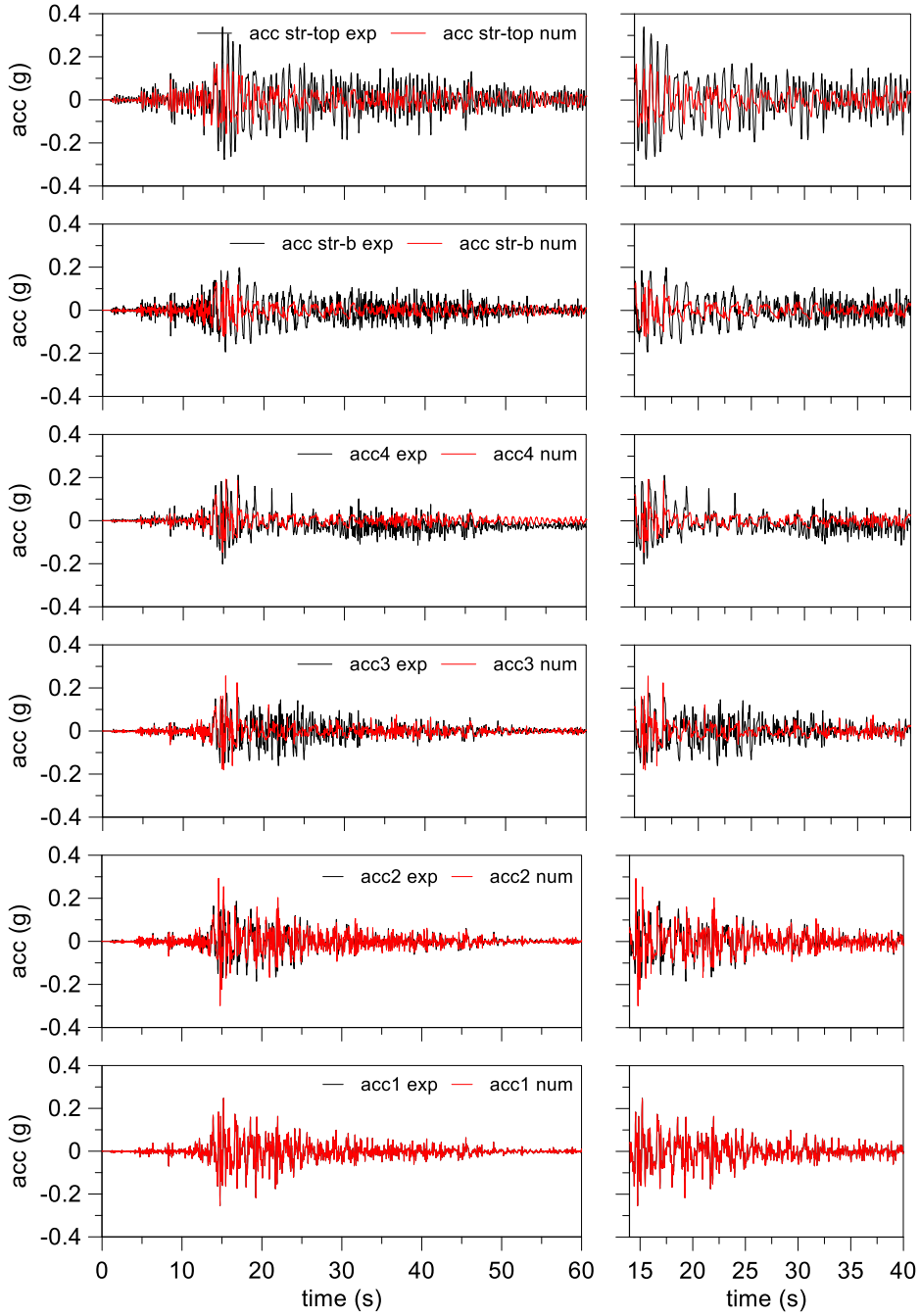

Figure 4.57. M1F_S1_HD1_GM31+: main time interval of acceleration time histories.

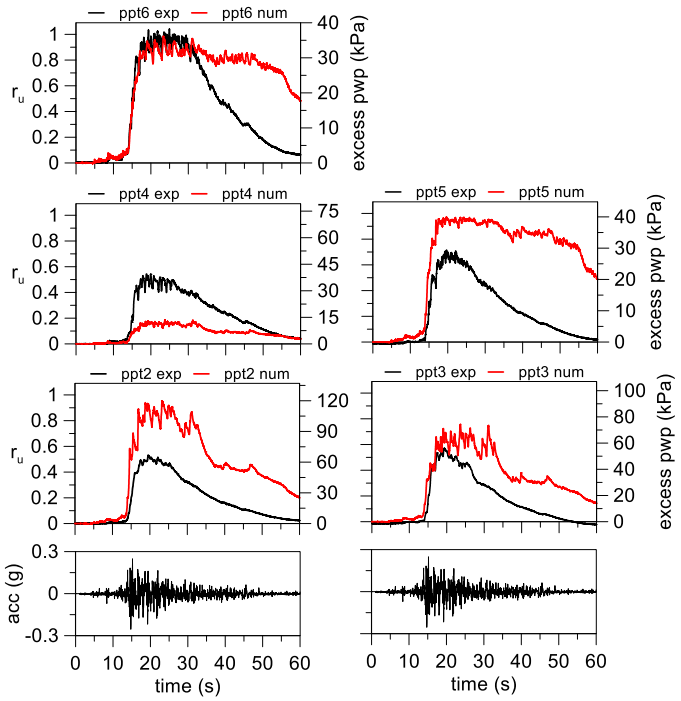

Figure 4.58. M1F_S1_HD1_GM31+: excess pore water pressure time histories.

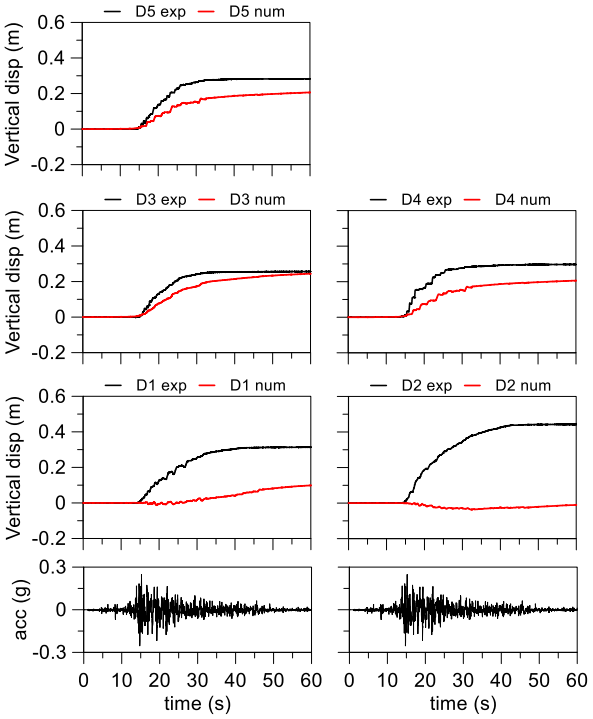

Figure 4.59. M1F_S1_HD1_GM31+: ground surface displacement time histories.

4.4.4 Building on double layer model (M2F_S1_HD1_GM31+)

As previous made for the free-field conditions, in this section the effect of the horizontal drains in presence of clay crust and structure is shown. As previously mentioned, the clay crust decreases the capability of the system to dissipate the excess pore pressure during the shaking and it modifies the distribution of the pressure in the soil. The numerical analyses were performed using both the constitutive models.

4.4.4.1 UBC3D-PML

The calibration procedure for UBC3D-PML constitutive soil model led to define the parameters shown in Table 4.17.

Table 4.17. Parameters for the constitutive soil model.

γ_{unsat}	γ_{sat}	RD	$N_{1,60}$	e_{min}	e_{max}	K_B^e	K_G^e	K_G^p	m_e	n_e	n_p	φ_{cv}	φ_p	f_{dens}	$f_{E,post}$	R_f	k
(kN/m^3)	(kN/m^3)	(%)	(-)	(-)	(-)	(-)	(-)		(-)	(-)		(°)	(-)	(-)	(m/s)	(-)	(m/s)
15.1	19.3	52.6	12.7	0.574	0.923	1687.4	1012.4	592.0	0.5	0.5	0.4	33	34.3	7.0	1.0	0.75	$1.66 \cdot 10^{-3}$

The computed acceleration time histories shown a good agreement with the experimental ones except for the high frequency computed at the roof of the structure until the beginning of the stronger portion of the shaking (Figure 4.60).

The computed excess pore pressures reached almost the same peak values recorded in the experiment (Figure 4.61) showing an irregular behaviour, but the dissipation rate in the numerical analysis was slower than experimental one. Only the computed excess pore pressure among the drains was smaller than experimental one.

The persisting of high levels of numerical excess pore pressure beyond the excess pore pressure peaks led to larger settlements for the structure induced by a progressive accumulation of strains during the input motion in presence of low stiffness (Figure 4.63).

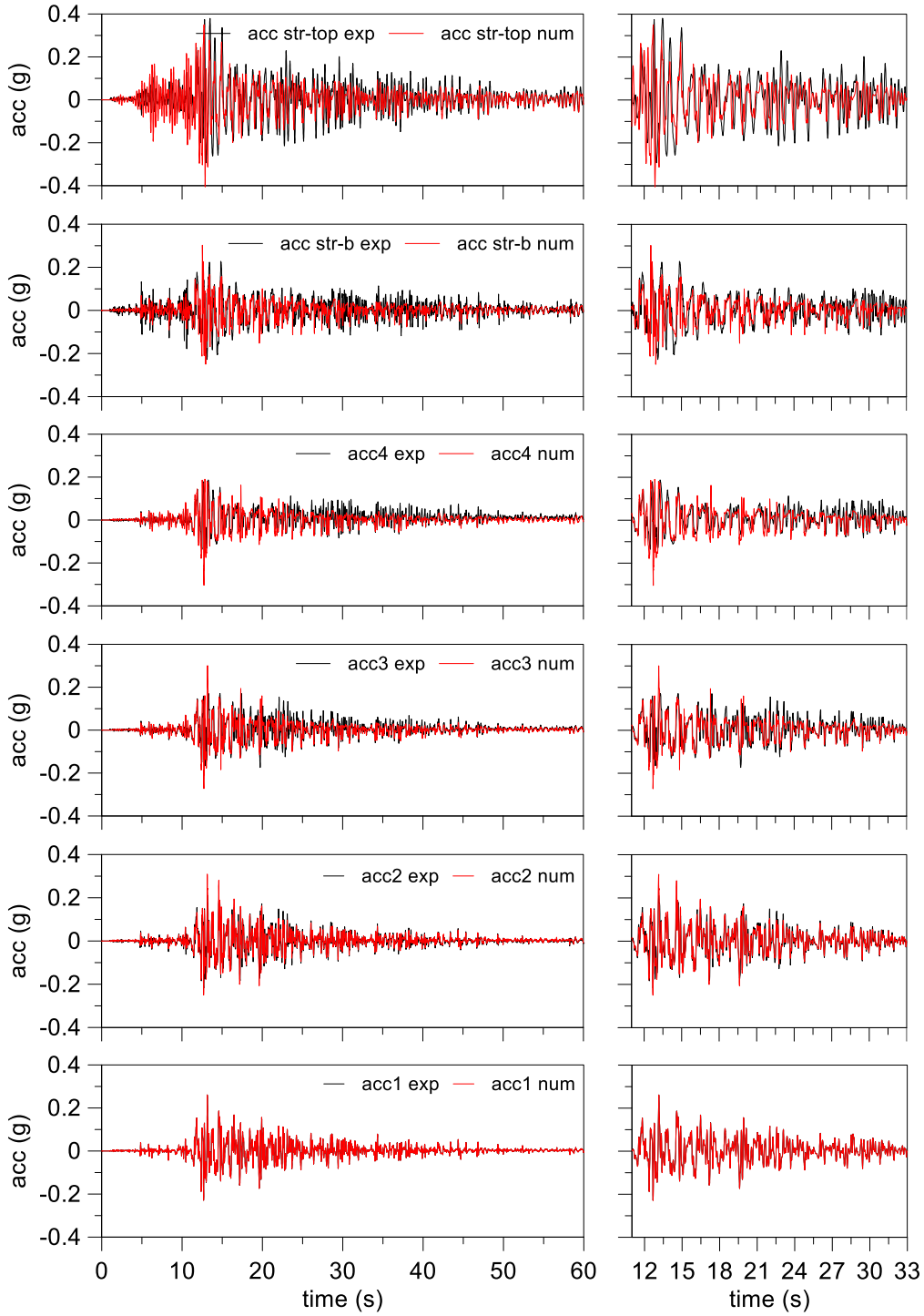

Figure 4.60. M2F_S1_HD1_GM31+: main time interval of acceleration time histories.

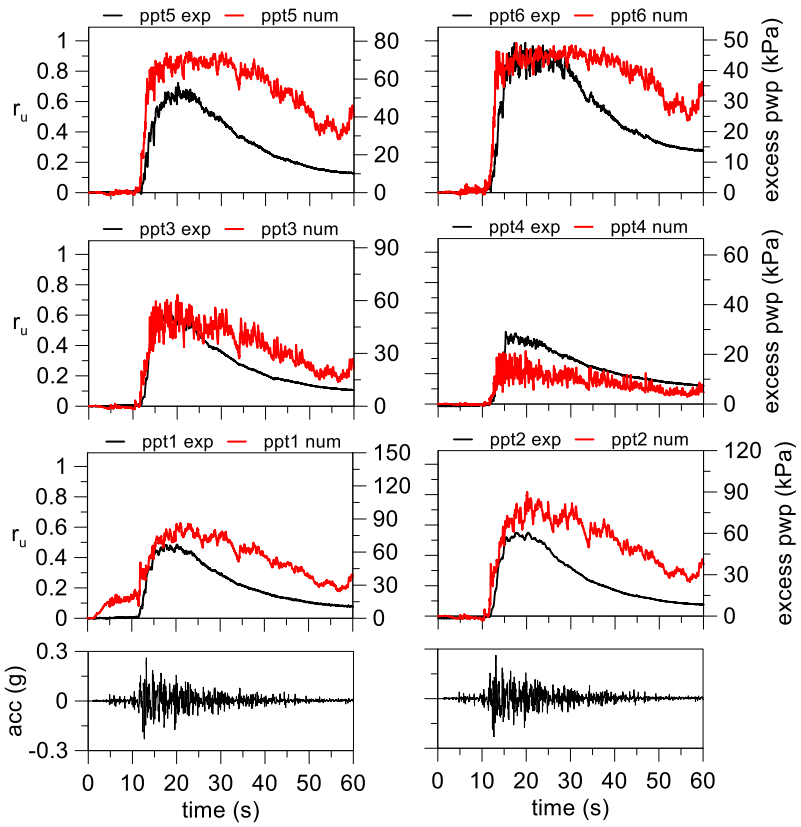

Figure 4.61. M2F_S1_HD1_GM31+: excess pore water pressure time histories.

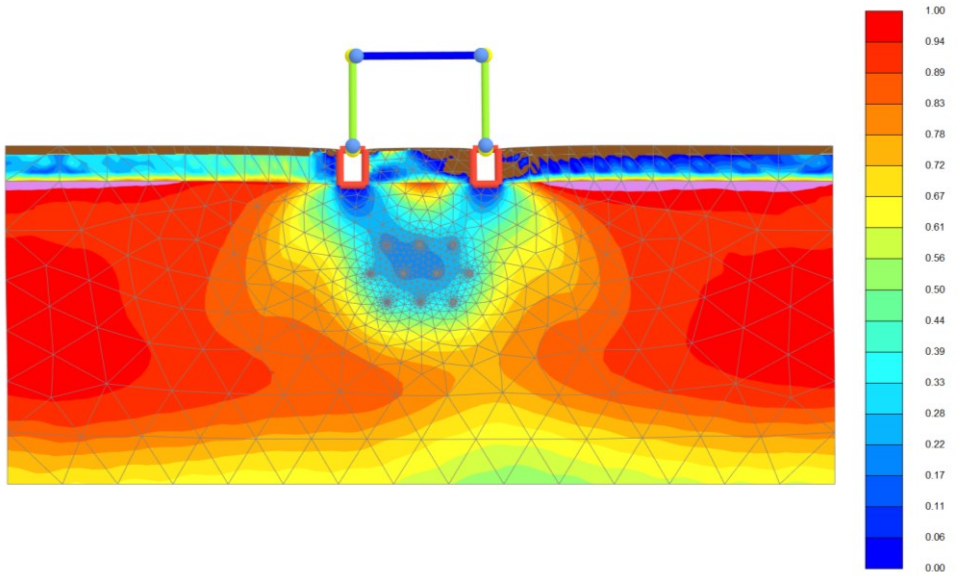

Figure 4.62. M2F_S1_HD1_GM31+: effect of horizontal drains on the distribution of excess pore pressure ratio at 18 seconds.

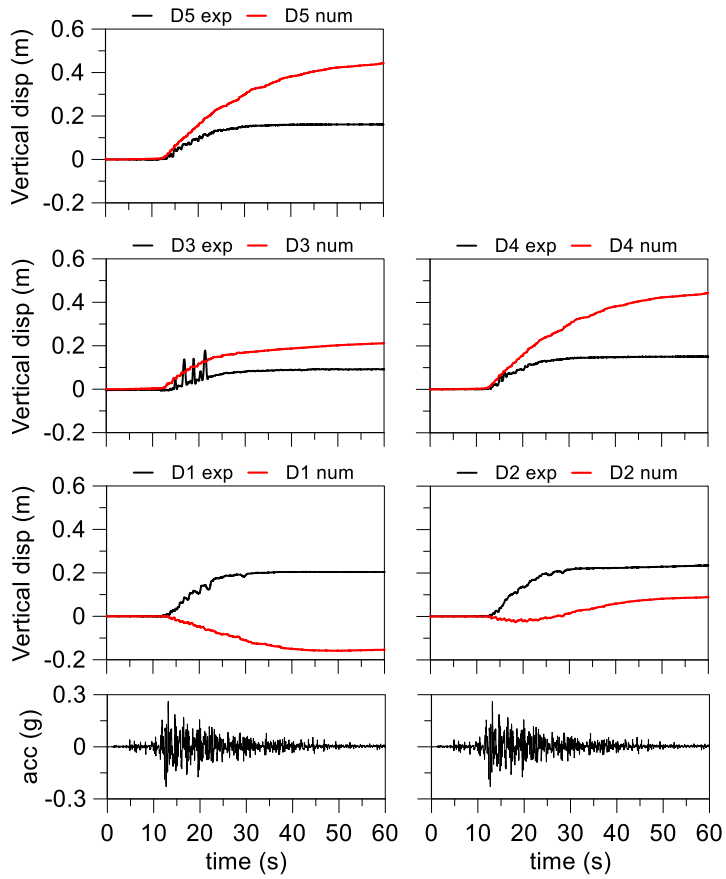

Figure 4.63. M2F_S1_HD1_GM31+: ground surface displacement time histories.

4.4.4.2 PM4SAND

In this section the analysis was carried out by using PM4SAND constitutive soil model. The parameters adopted for the soil are reported in Table 4.18.

Table 4.18. Parameters for the constitutive soil model.

γ_{unsat}	γ_{sat}	RD	G_0	h_{p0}	e_{min}	e_{max}	n_b	n_d	φ	ν	Q	R	k
(kN/m^3)	(kN/m^3)	(%)	(-)	(-)	(-)	(-)	(-)	(-)	(°)	(-)	(-)	(-)	(m/s)
15.1	19.3	52.6	381	0.08	0.574	0.923	0.5	0.1	33	0.3	10.0	1.5	$1.66 \cdot 10^{-3}$

This constitutive model produced a worse prediction of experimental data compared to UBC3D-PML. Indeed, a significant deamplification of the acceleration was computed by numerical analysis (Figure 4.64). This result was due to the large drop of the shear stiffness of the deeper soil layer consequent to the reaching of numerical excess pore pressures higher than the experimental ones in ppt1 and ppt2 (Figure 4.65). Moreover, the transducer ppt5 indicates that in the numerical analysis the surrounding soil achieved the liquefaction unlike as seen in the experimental test.

The development of higher numerical excess pore pressure that persisted for long time led to larger numerical incremental settlements of the structure that exceeded the experimental ones (Figure 4.66). Furthermore, a ground surface rotation was highlighted by the numerical settlement in D1 and D2.

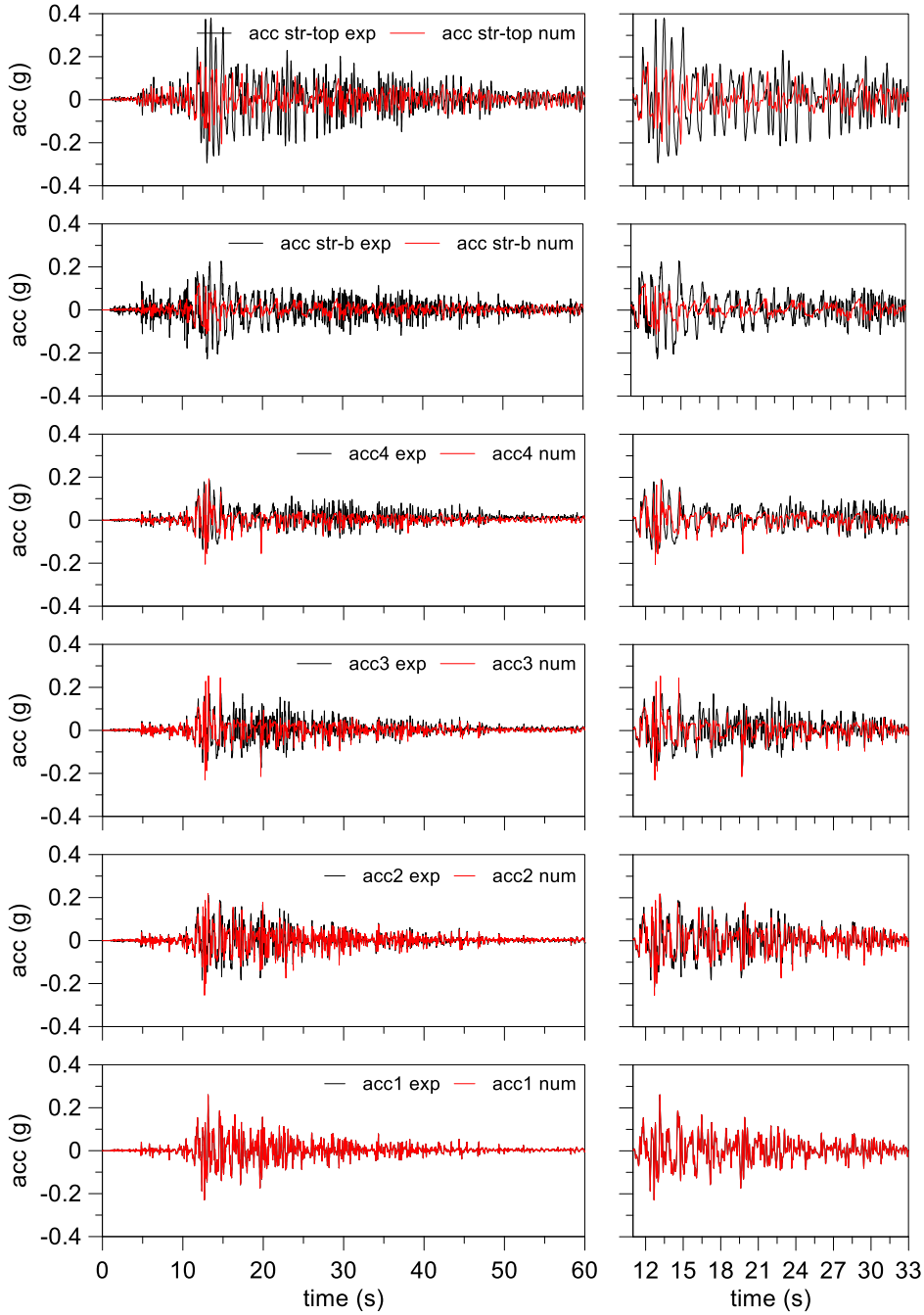

Figure 4.64. M2F_S1_HD1_GM31+: main time interval of acceleration time histories.

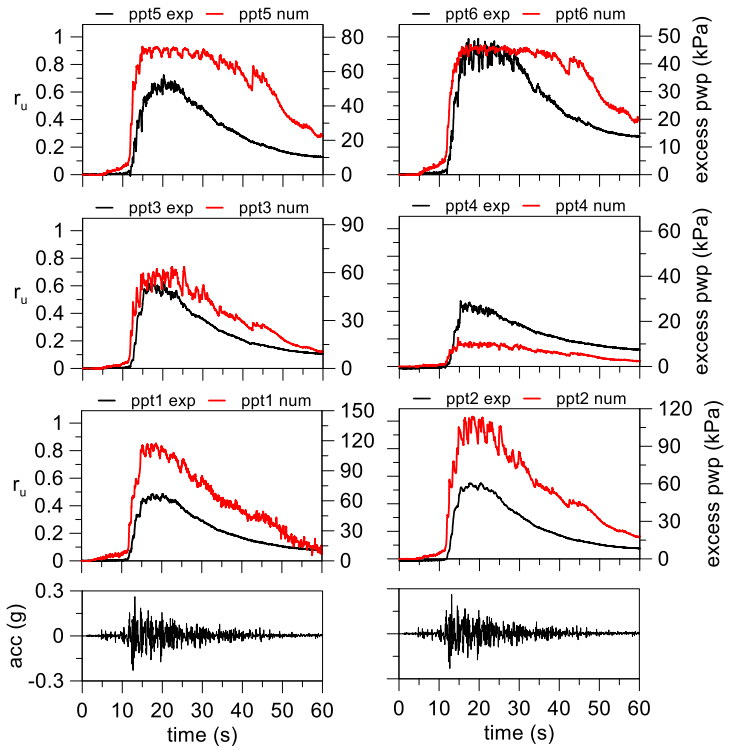

Figure 4.65. M2F_S1_HD1_GM31+: excess pore water pressure time histories.

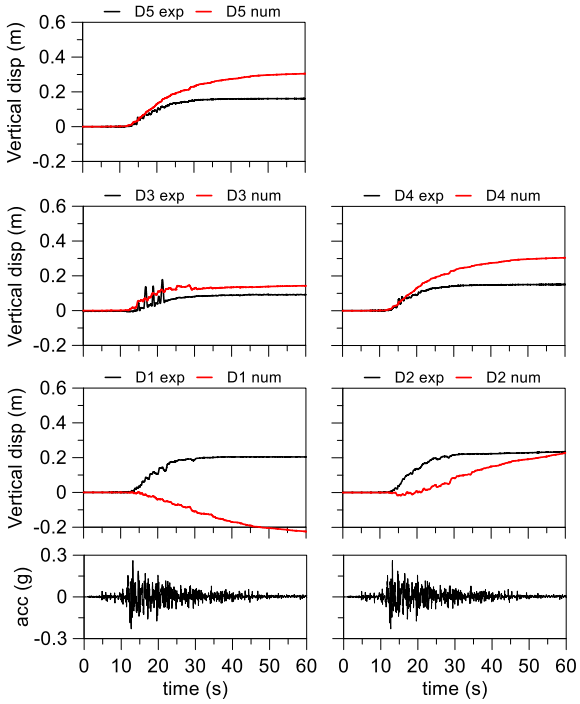

Figure 4.66. M2F_S1_HD1_GM31+: ground surface displacement time histories.

4.5 Induced partial saturation numerical model

In this section a procedure to model and calibrate the induced partial saturation (IPS) in the numerical analyses is shown. Different laboratory and field tests showed that a low degree of desaturation increases significatively the liquefaction strength, so the induced partial saturation represents an effective liquefaction mitigation technique. High levels of saturation were analysed in the following and the effects of suction can be neglected in these conditions. The application modality of the induced partial saturation in centrifuge tests was previously shown in section 3.8.

The analyses shown in the following aim to check the reliability of the implementation method and calibration procedure for the IPS.

4.5.1 Single layer model (M1_S1_IPS4)

The numerical analyses started from the simplest centrifuge soil model with induced partial saturation realised by a homogeneous liquefiable soil profile. The air injection was applied when the centrifuge reached the steady-state conditions at 50g of centrifugal acceleration. An estimate of mean saturation degree of soil after injection can be made by a procedure based on the changing of the pore pressure near the ground surface during the air injection (c). This procedure was applied to this centrifuge test on the time history of pore pressure at transducer ppt5 (Figure 4.67).

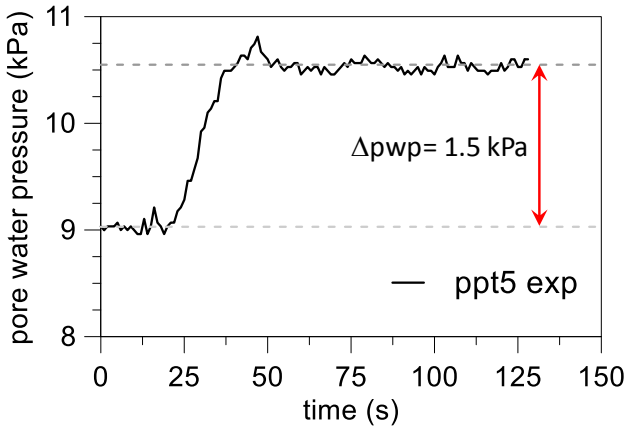

Figure 4.67. Increasing of pore water pressure during air injection.

An increment equal to 1.5 kPa was recorded, this was induced by an uplift of the water table due to an emission of pore fluid, substituted by injected air, from the soil. Hence, the mean saturation degree of the model can be calculated through the relationship (4-9) in the hypothesis of the equality between the expelled water and the injected air volume.

$$S_r(t) = S_{r0} - \frac{\Delta h(t)}{h_s \cdot n} \qquad (4\text{-}9)$$

In the relationship (4-9) S_{r0} is the initial degree of saturation; $\Delta h(t)$ is the increment of the height of the water level during the air injection; h_s is the height of the model at the end of the consolidation and n is the porosity of the soil.

Considering a fully saturated model, confirmed by measurement in preparation phase, before the air injection, a height of the model equal to 0.26 m and a soil porosity equal to 0.43; using the increment of the pore pressure after injection (Figure 4.67) the saturation degree of soil reached a value equal about 97%.

The effect of the desaturation was implemented in the numerical model by a reduction of bulk stiffness of pore fluid emulating a mixture of water and air. The bulk stiffness of fluid was calculated following the relationship proposed by Rebata-Landa and Santamarina, (2012):

$$K_f = \frac{1}{S_r \frac{1}{K_w} + (1 - S_r) \frac{3r}{2T_s}} \qquad (4\text{-}10)$$

where K_w is the bulk stiffness of the water (~2.2 GPa); r is the mean radius of air bubbles and T_s is the surface tension for the water (0.072 N/m).

The measurement of air bubbles radius is very hard in experimentally, for this reason critical radius was used in the calculation of K_f for the following numerical models. Critical radius was calculated by the following relationship:

$$r_{critical} = \frac{2\,T_s}{\sigma \cdot u} \qquad (4\text{-}11)$$

where σ is the supersaturation and u is the absolute pressure at which bubbles nucleate.

In the following analyses the supersaturation was imposed equal to 80 (mean value for nitrogen) and u was fixed equal to the absolute pore pressure at the depth of bubble nucleation.

Fixed the supersaturation and calculated the water pressure surrounding the bubble, the evolution of the bulk stiffness of the pore fluid is a function only of saturation degree and its evolution is shown in Figure 4.68.

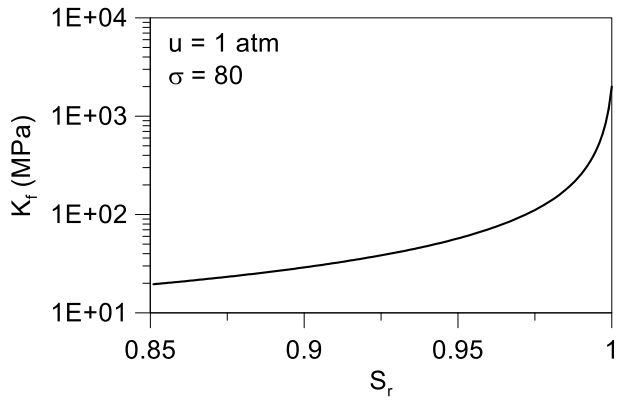

Figure 4.68. Evolution of pore fluid bulk stiffness with saturation degree.

Numerical model was realised by different overlapping soil layers giving a different fluid bulk stiffness to each of them to consider the variability of the critical radius with the depth induced by different pore pressure. The model used for the analyses of free-field conditions was realised by seven layers each of them about 2 meters thick.

Considering a constant value of saturation degree with depth, this method leaded to a linear distribution of K_f with depth (Figure 4.69).

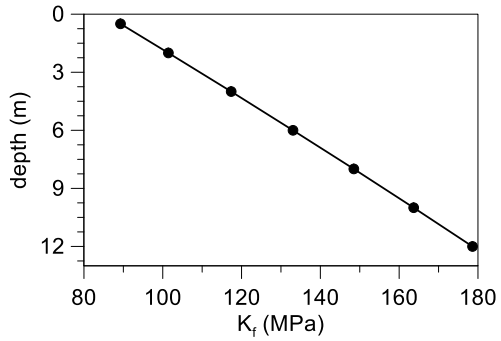

Figure 4.69. Values of pore fluid bulk stiffness in the barycentre of the layers.

4.5.1.1 PM4SAND (Ground motion GM31)

In this section PM4SAND constitutive soil model was used to analyse the centrifuge test with homogeneous profile of liquefiable soil (Ticino sand). The parameters of the model were defined by the calibration procedure used for the previous analyses and they are reported in Table 4.19.

Table 4.19. Parameters for the constitutive soil model.

γ_{unsat}	γ_{sat}	RD	G_0	h_{p0}	e_{min}	e_{max}	n_b	n_d	φ	ν	Q	R	k
(kN/m^3)	(kN/m^3)	(%)	(-)	(-)	(-)	(-)	(-)	(-)	(°)	(-)	(-)	(-)	(m/s)
15.1	19.3	52.4	381	0.08	0.574	0.923	0.5	0.1	33	0.3	10.0	1.5	$1.66 \cdot 10^{-3}$

The capability of the model to reproduce the behaviour of the soil in presence of a pore fluid with a low bulk stiffness is verified through the numerical simulation of some liquefaction strength curves in partial saturation conditions (Figure 4.70) compared with the theoretical curves deduced by Mele et al. (2018). Numerical points and theoretical curves calibrated on the cyclic simple shear test show a good agreement confirming the reliability of the modelling and calibration procedure for induced partial saturation.

Three different numerical models were performed to understand the effect of the induced partial saturation on the acceleration and excess pore pressure. The results of the analyses are reported for:

1. Fully saturated numerical model;
2. Partial saturated numerical model reproduced by bulk modulus of pore fluid distribution reported in Figure 4.69;

3. Partial saturated numerical model with reduced permeability, indeed the presence of air babbles can reduce the permeability coefficient of the soil.

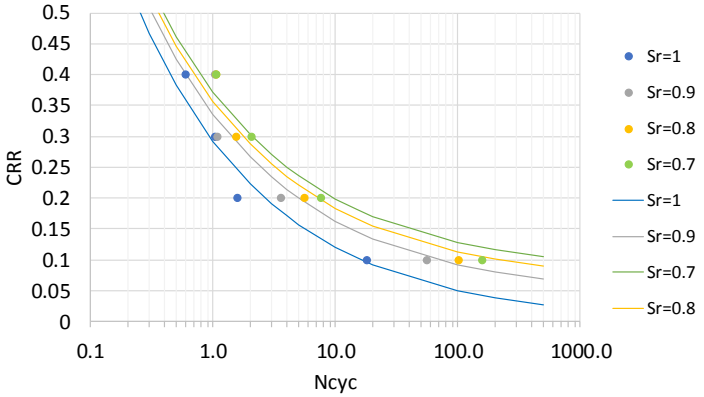

Figure 4.70. Numerical simulation of liquefaction strength curves.

Figure 4.71, Figure 4.72 and Figure 4.73 show the numerical results in terms of acceleration. It is worth noting that the computed amplitude was slightly lower than the experimental one for all three numerical analyses. However, a good agreement was found.

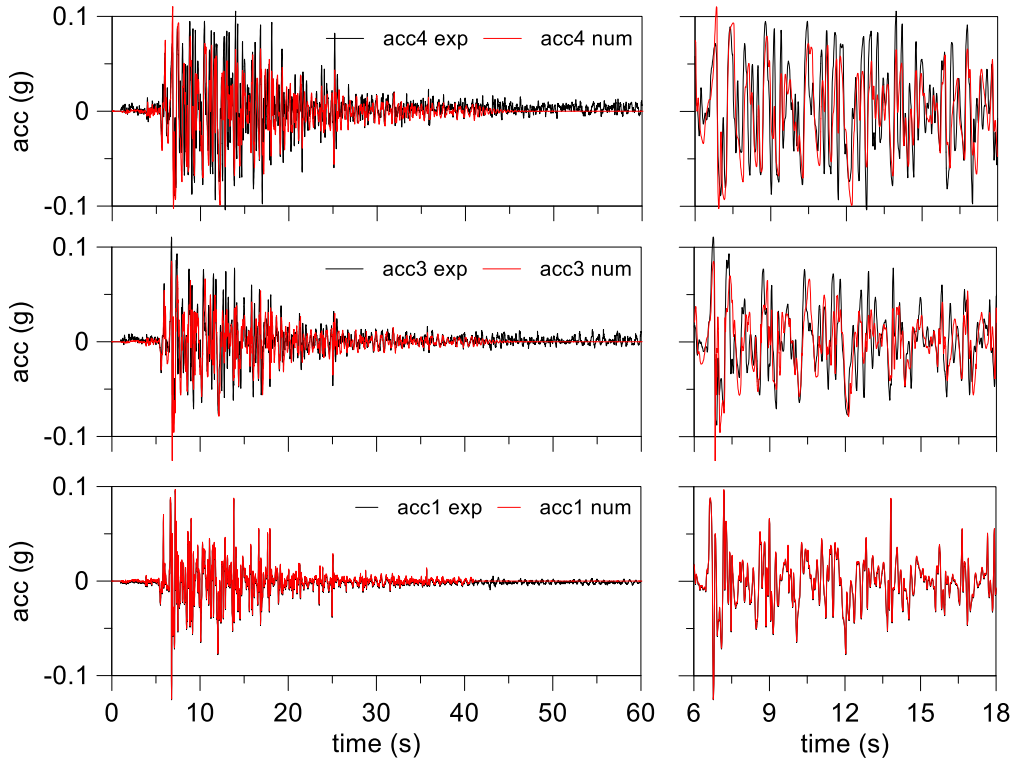

Figure 4.71. M1_S1_IPS4_GM31: main time interval of acceleration time histories for saturated model.

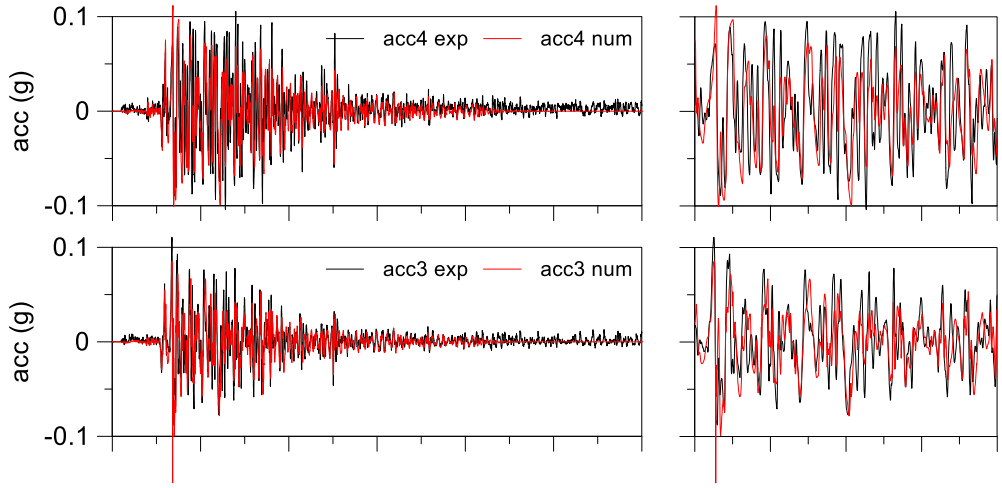

Figure 4.72. M1_S1_IPS4_GM31: main time interval of acceleration time histories for desaturated model with permeability in saturated condition.

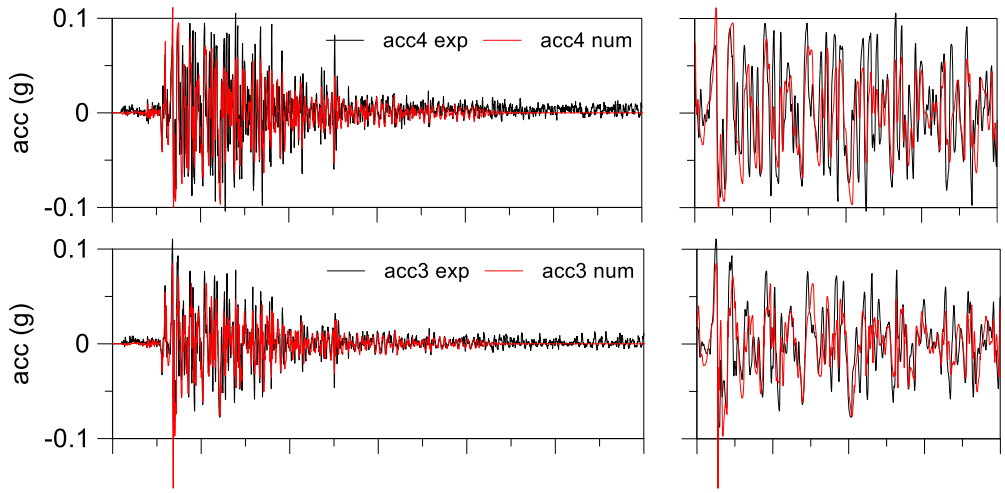

Figure 4.73. M1_S1_IPS4_GM31: main time interval of acceleration time histories for desaturated model with reduced permeability.

The computed excess water pressure ratio (Figure 4.74) show that the saturated model achieved peaks equal to experimental ones except for the shallowest transducer ppt5, but with a larger dissipation rate. Moreover, the excess water pressure build-up in the saturated condition was faster than the experimental one.

The introduction of the smaller bulk stiffness for the soil layers, simulating the application of IPS, reduced the amount of the maximum excess water pressure but the dissipation rate is still high. This result suggested to introduce a lower permeability coefficient. Therefore, the calibration procedure for the analysis of centrifuge test with IPS can be made following two steps:

1. Introduction of reduced bulk stiffness of pore fluid by the measurements of pore pressure (Figure 4.67);
2. Calibration of the soil permeability on the dissipation velocity after the main part of the shaking.

This procedure led to a permeability coefficient equal to $7 \cdot 10^{-4}$ m/s and the results in terms of excess pore pressure ratio are reported in the Figure 4.74 (green lines). A good agreement was found with the experiment except for the shallowest transducer (ppt5) where the experimental excess pore pressure was larger than the numerical one. This result may be due to the presence of a saturated soil surrounding the pressure transducer ppt5 in the experiment.

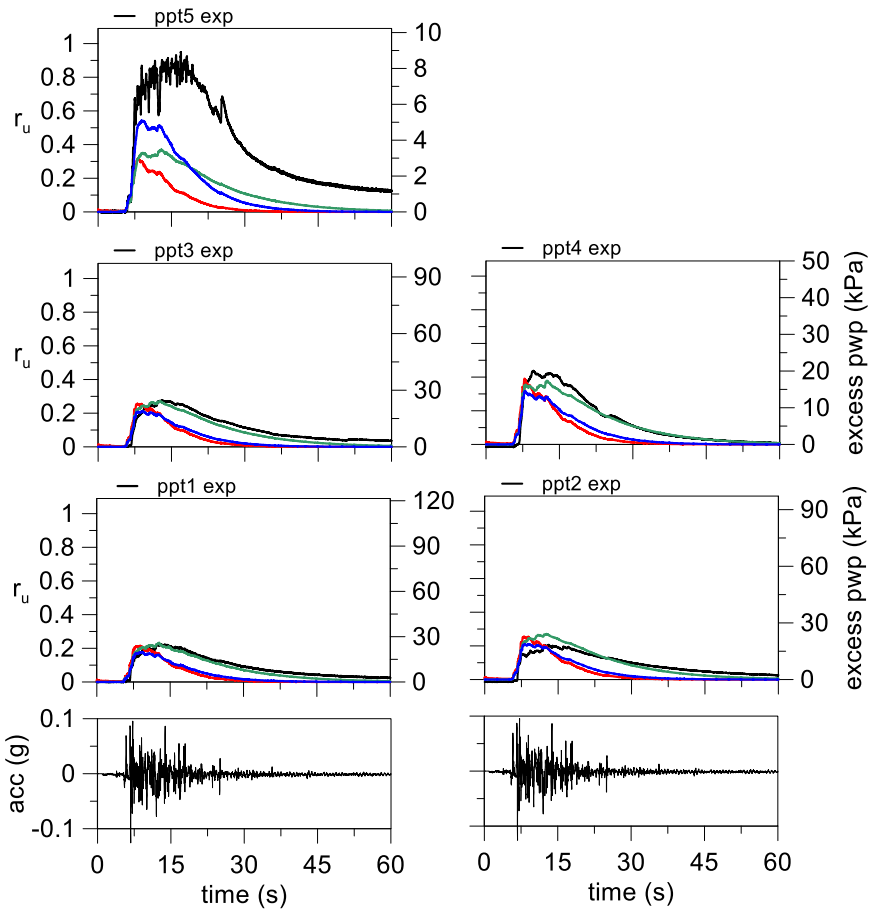

Figure 4.74. M1_S1_IPS4_GM31: excess pore water pressure time histories for saturated model (red lines), desaturated model with permeability in saturated condition (blue lines) and desaturated model (green lines).

The computed settlements were largely smaller than the experimental ones (Figure 4.75). This result may be due to the punching of the tip of the displacement transducers in the test.

It is worth noting that the introduction of the induced partial saturation in this case led to a worse condition compared to the saturated one. Indeed, high levels of excess pore pressure

in the desaturated model persist for longer time than in the model with permeability in saturated condition.

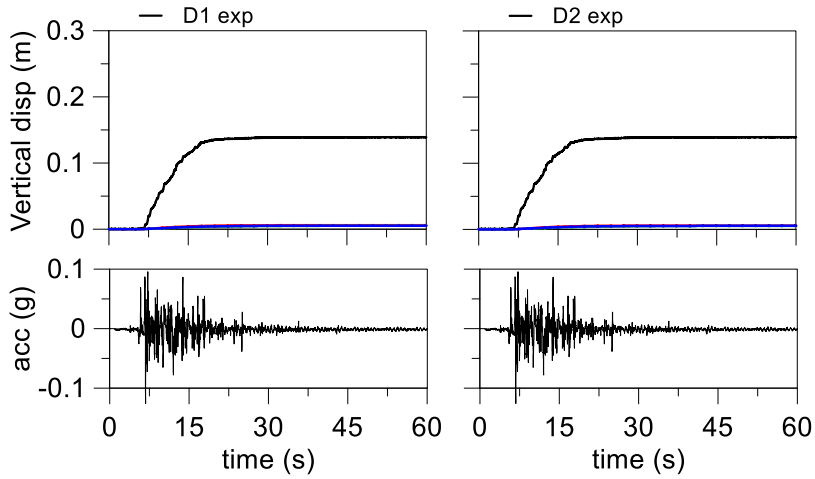

Figure 4.75. M1_S1_IPS4_GM31: ground surface displacement time histories for saturated model (red lines), desaturated model with permeability in saturated condition (blue lines) and desaturated model (green lines).

4.5.1.2 PM4SAND (Ground motion GM31+)

In this section the results of the analysis for the same centrifuge model configuration with a more energized ground motion (GM31+) are shown. However, the model had a different relative density so different parameters were used (Table 4.20).

Table 4.20. Parameters for the constitutive soil model.

γ_{unsat}	γ_{sat}	RD	G_0	h_{p0}	e_{min}	e_{max}	n_b	n_d	φ	ν	Q	R	k
(kN/m^3)	(kN/m^3)	(%)	(-)	(-)	(-)	(-)	(-)	(-)	(°)	(-)	(-)	(-)	(m/s)
15.2	19.35	55.8	383.8	0.08	0.574	0.923	0.5	0.1	33	0.3	10.0	1.5	$1.66 \cdot 10^{-3}$

The same degree of saturation of previous analysis (S_r = 97%) was used in the calculation of the bulk stiffness of the pore fluid.

The calculated accelerations for the analyses are close to the experimental ones (Figure 4.76, Figure 4.77 and Figure 4.78) except for the shallowest transducer where a slight decrease of the amplitude was recorded. Furthermore, the numerical acceleration time histories show some spikes due to the large drop of the stiffness occurred for the high values of excess pore pressure reached during the shaking.

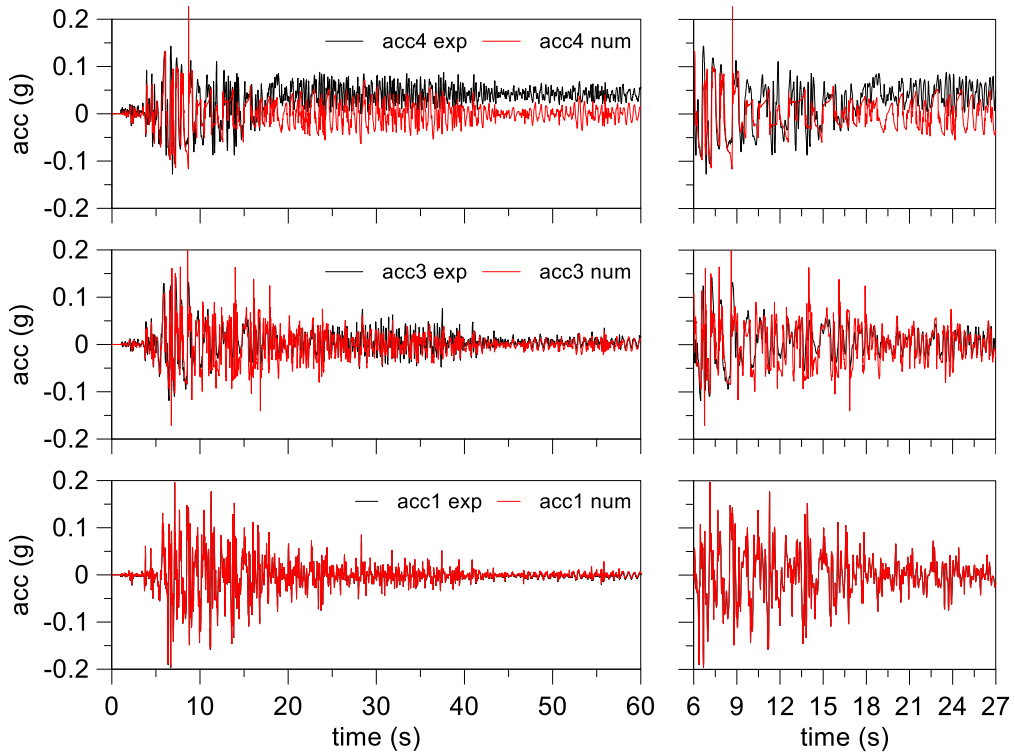

Figure 4.76. M1_S1_IPS4_GM31+: main time interval of acceleration time histories for saturated model.

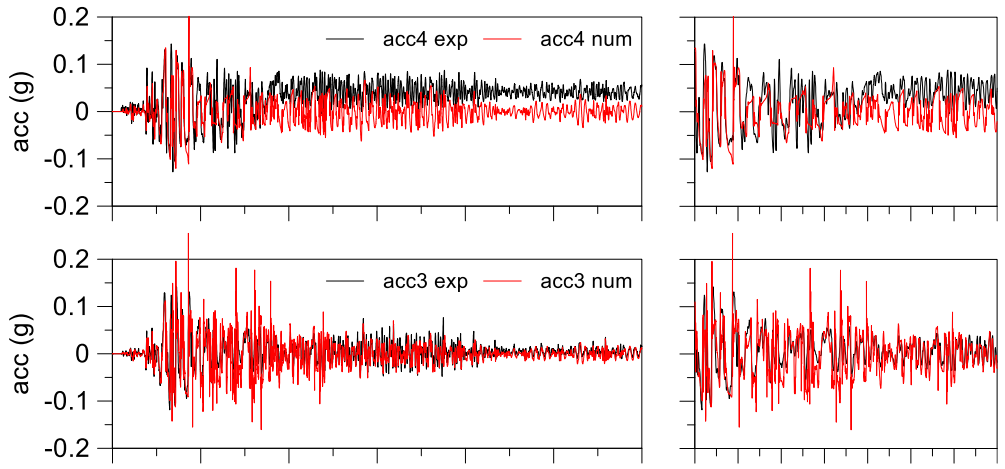

Figure 4.77. M1_S1_IPS4_GM31+: main time interval of acceleration time histories for desaturated model with permeability in saturated condition.

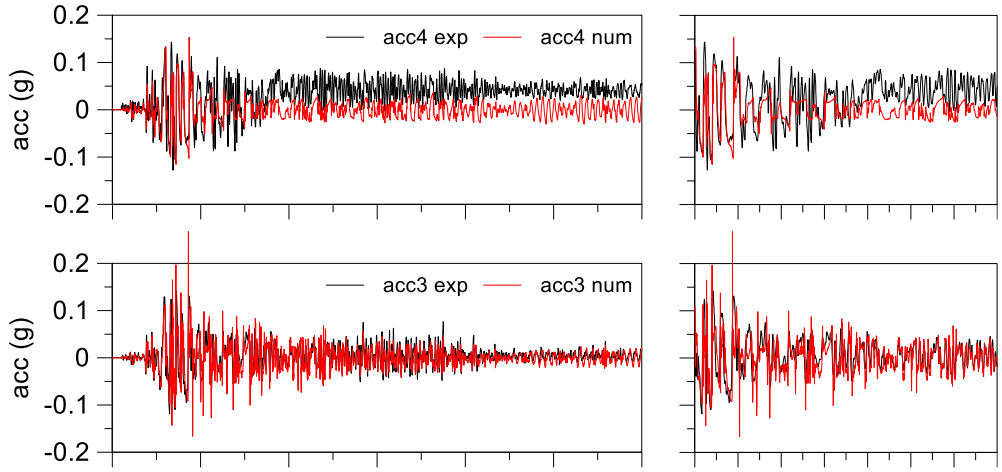

Figure 4.78. M1_S1_IPS4_GM31+: main time interval of acceleration time histories for desaturated model.

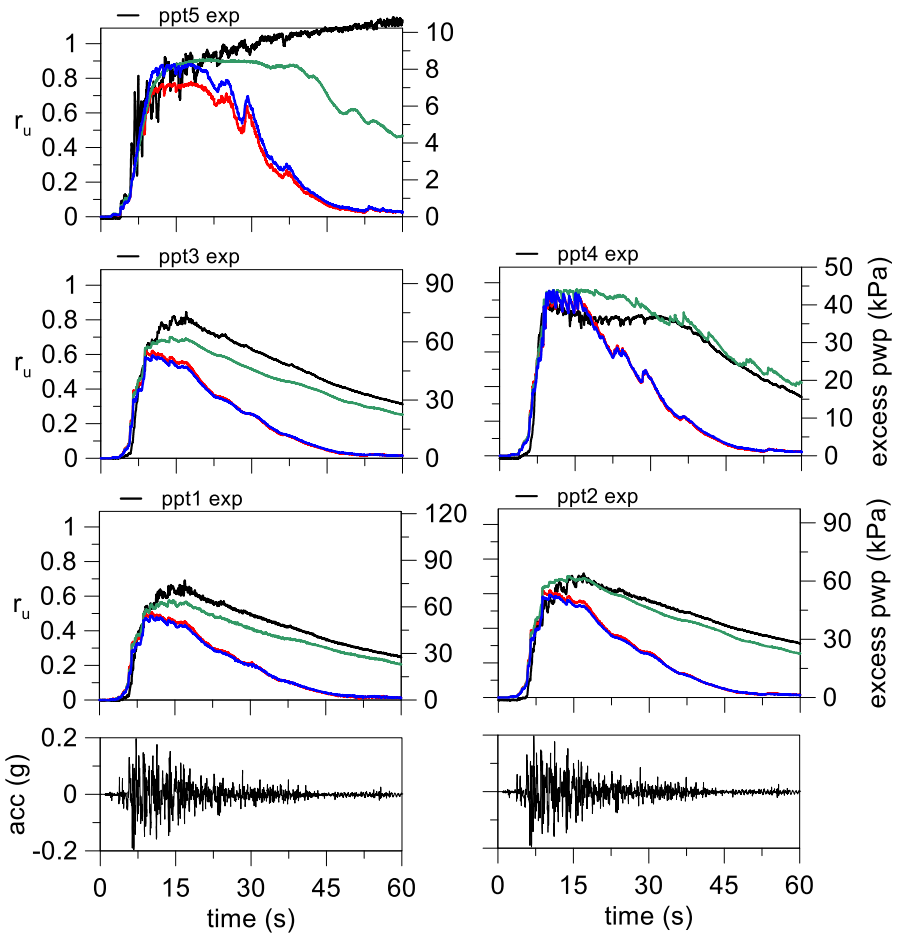

Figure 4.79. M1_S1_IPS4_GM31+: excess pore water pressure time histories for saturated model (red lines), desaturated model with permeability in saturated condition (blue lines) and desaturated model (green lines).

Figure 4.79 shows the evolution of the excess water pressure ratios for all transducers deployed in the model. Saturated model (red line) and partial saturated model with permeability in saturated conditions (blue line) are close and both analyses show peaks values lower than experimental ones with a higher dissipation rate after the main part of the signal. The results obtained by the numerical partial saturated model with reduced permeability (green line) are closer to the experimental ones and show a dissipation rate almost equal to the experimental one.

It is worth noting that the desaturated model with reduced permeability (green lines) reached excess pore pressure ratios larger than saturated model. This effect was due to the lower permeability induced by the partial saturation that reduced the capability of the model to dissipate the excess water pressures. Hence, as seen in the previous analysis, the IPS could lead to unexpected results, indeed the desaturation, reducing the permeability coefficient, can increase the liquefaction susceptibility. Therefore, a great attention must be applied to the design of induced partial saturation as soil liquefaction mitigation technique.

The computed settlements are largely smaller than the experimental ones (Figure 4.80).

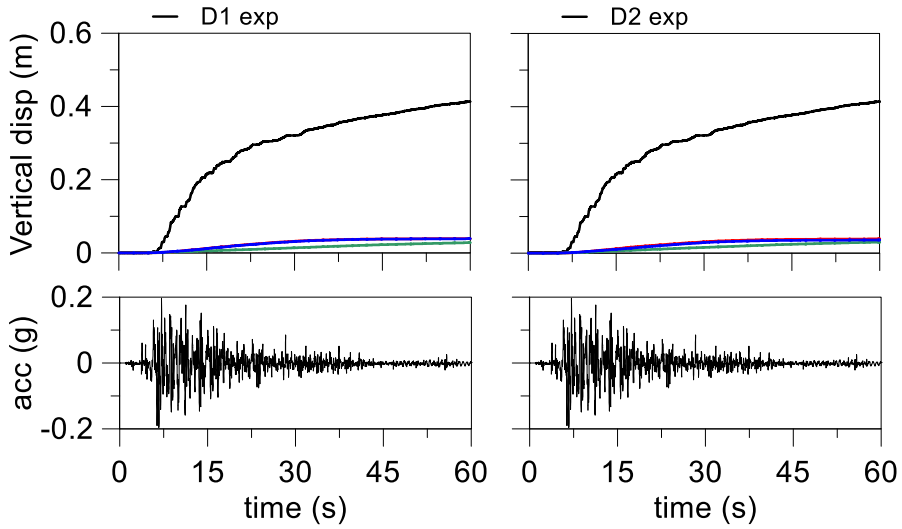

Figure 4.80. M1_S1_IPS4_GM31+: ground surface displacement time histories for saturated model (red lines) desaturated model with permeability in saturated condition (blue lines) and desaturated model (green lines).

4.5.2 Double layer model (M2_S1_IPS4)

In this section double layer numerical model with induced partial saturation is shown. The presence of the clay crust reduces the capability of the model to dissipate the excess pore pressure during the shaking by a water flow from the soil through the upper surface.

As done for the previous centrifuge test, an estimate of mean saturation degree in the centrifuge model was performed through the data of pore water pressure recorded at ppt5 during the air injection (Figure 4.81).

The increment of the pore pressure shown in Figure 4.81 was due to the emission of pore fluid from the soil caused by the substitution of the water with the injected air. A mean degree of saturation equal to 99.4% was determined using the relationship (4-9). The path of the pore water pressure during the air injection was strongly irregular, and this decreases the reliability of the of the calculated saturation degree.

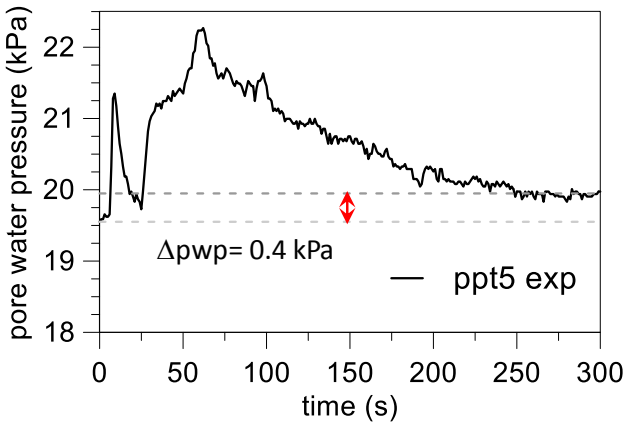

Figure 4.81. Increasing of pore water pressure during air injection.

4.5.2.1 PM4SAND (Ground motion GM31)

In the following the centrifuge model was analysed using PM4SAND constitutive soil model. The parameters inferred by the calibration are shown in Table 4.21.

Table 4.21. Parameters for the constitutive soil model.

γ_{unsat}	γ_{sat}	RD	G_0	h_{p0}	e_{min}	e_{max}	n_b	n_d	φ	ν	Q	R	k
(kN/m^3)	(kN/m^3)	(%)	(-)	(-)	(-)	(-)	(-)	(-)	(°)	(-)	(-)	(-)	(m/s)
15.0	19.2	47.2	376.3	0.08	0.574	0.923	0.5	0.1	33	0.3	10.0	1.5	$1.66 \cdot 10^{-3}$

The computed acceleration time histories (Figure 4.82, Figure 4.83 and Figure 4.84) show a good agreement with experimental ones. A slight decrease of the numerical amplitude was computed in the shallowest transducer (acc4) in the saturated model (Figure 4.82) and partial saturated one at 99.4% of saturation degree (Figure 4.83). The saturation degree calibrated by a back analysis equal to 52% led to better results (Figure 4.84).

The excess water pressure ratio evolution is shown in Figure 4.85 for all the three analyses. The fully saturated soil model (red lines) and partial saturated one with saturation degree equal to 99.4% (blue lines) show a faster pore pressure build-up and higher peaks than experimental ones. The computed excess pore pressure of back analysis of the saturation degree (green lines) are close to the experimental ones, however the analysis gives a slower dissipation rate.

The significant low degree of saturation predicted by the analysis (S_r=52%) led to a large increase of the ground surface settlements (Figure 4.86) due to a large volumetric deformability of the soil induced by strong desaturation.

Conversely as seen in the previous analyses with IPS, the effect of the induced partial saturation is clearly shown by the excess pore pressure time histories. Indeed, the partial saturated model with S_r=52% (green line) show a significant decrease of excess pore pressure compared to the saturated model.

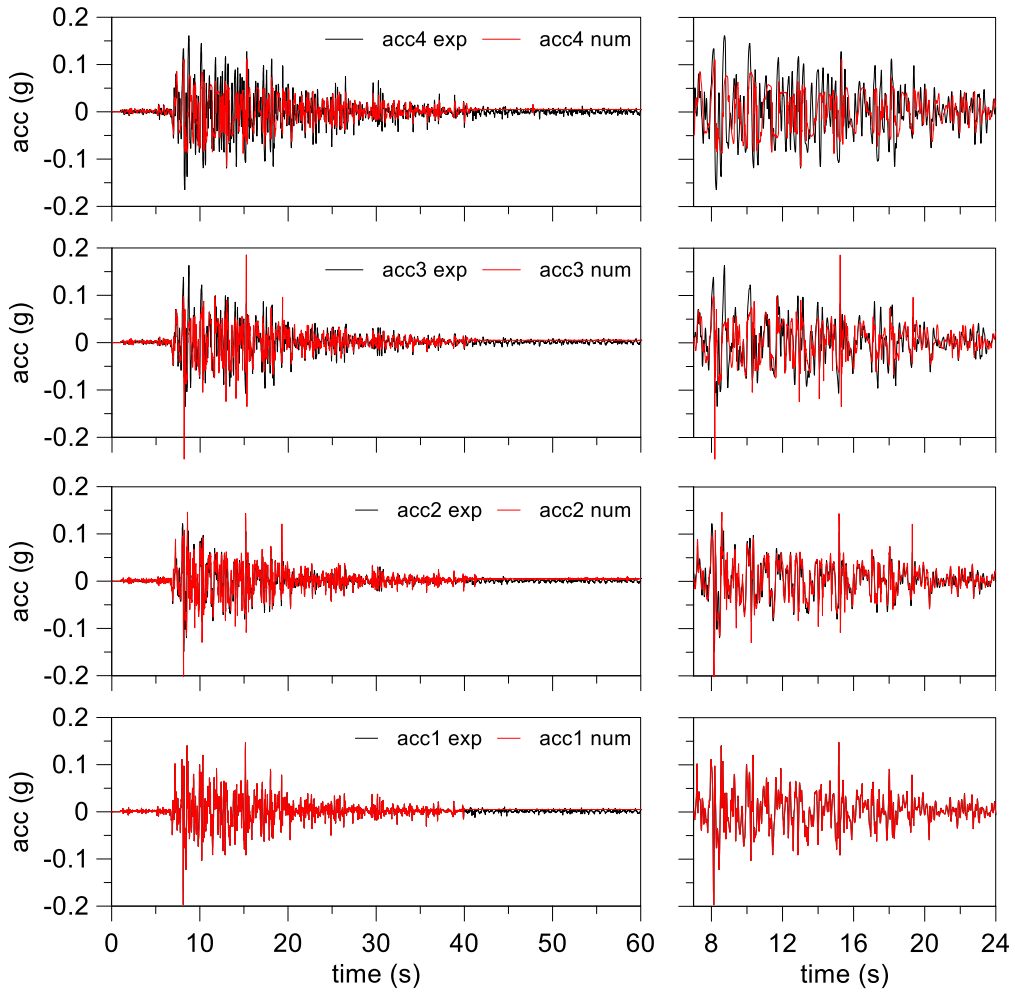

Figure 4.82. M2_S1_IPS4_GM31: main time interval of acceleration time histories for saturated model.

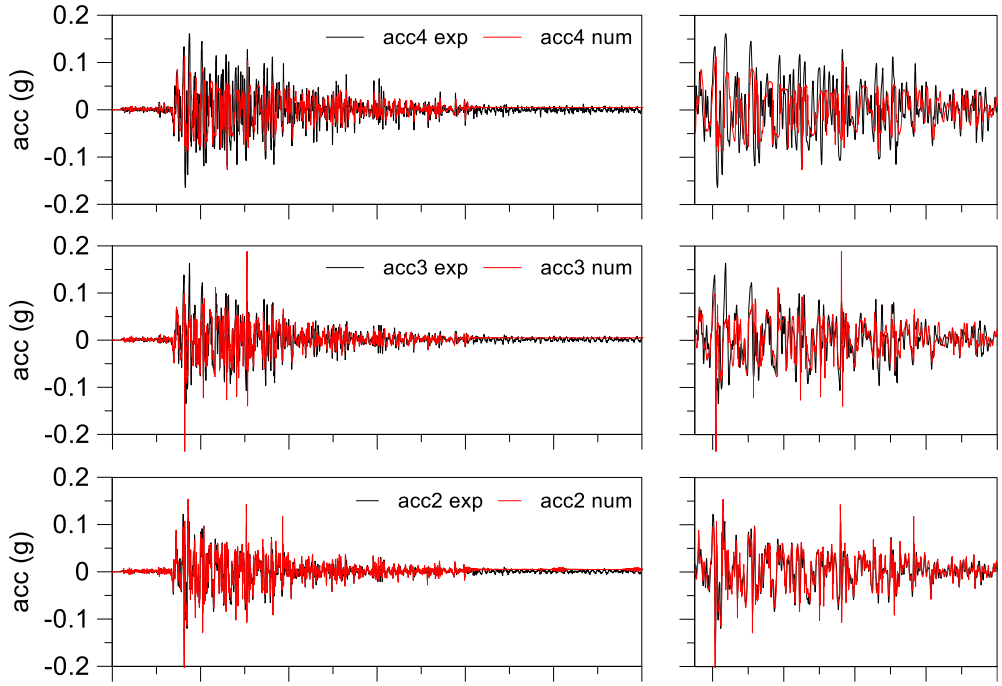

Figure 4.83. M2_S1_IPS4_GM31: main time interval of acceleration time histories for desaturated model with permeability in saturated condition.

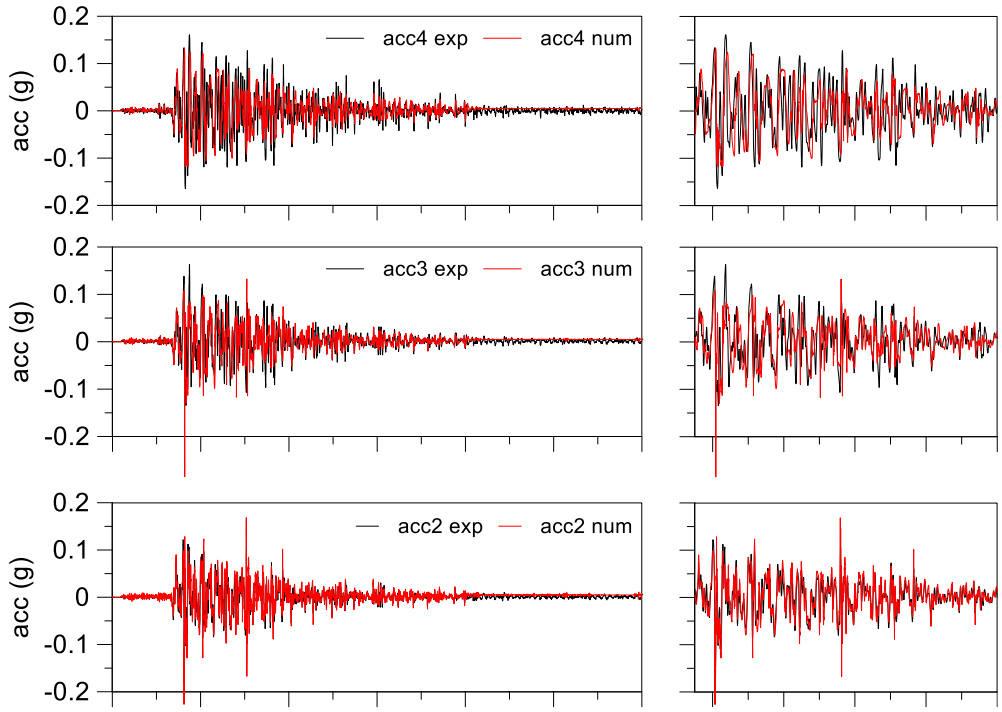

Figure 4.84. M2_S1_IPS4_GM31: main time interval of acceleration time histories for desaturated model at Sr=52% with permeability in saturated condition.

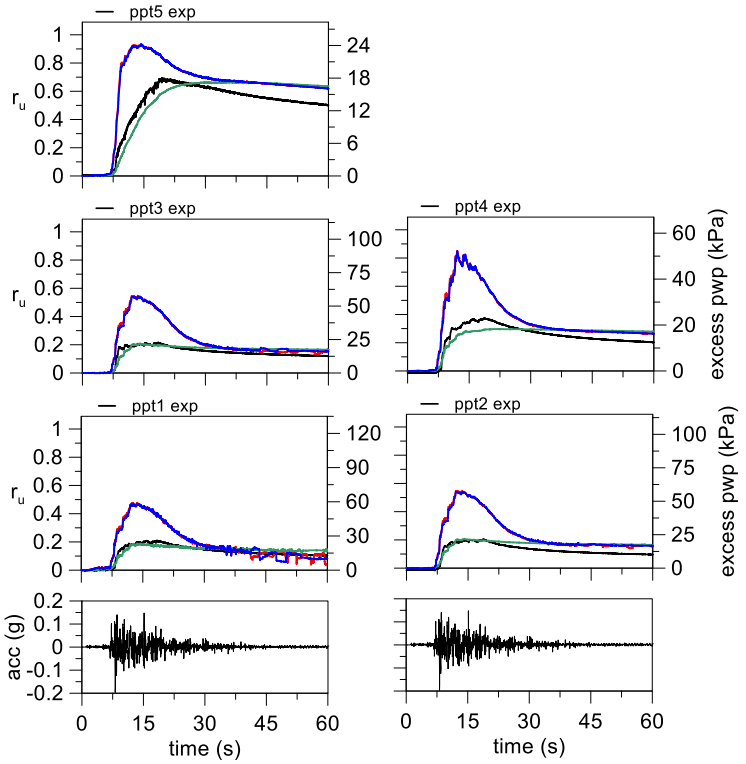

Figure 4.85. M2_S1_IPS4_GM31: excess pore water pressure time histories for saturated model (red lines), desaturated model with permeability in saturated condition (blue lines) and desaturated model at Sr=52% (grey line).

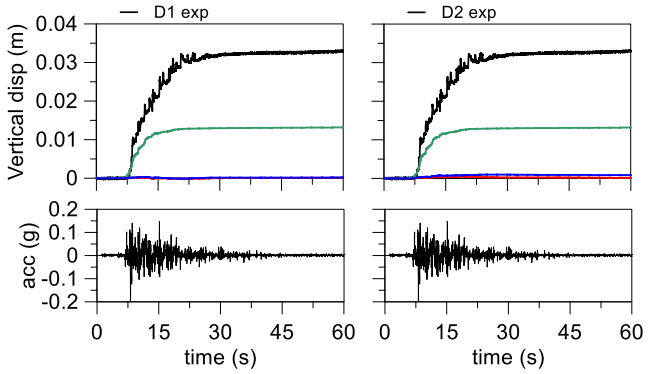

Figure 4.86. M2_S1_IPS4_GM31: ground surface displacement time histories for saturated model (red lines), desaturated model with permeability in saturated condition (blue lines) and desaturated model at Sr=52% (grey line).

4.5.2.2 PM4SAND (Ground motion GM31+)

Another test on the same centrifuge model was performed using a more energized input motion (GM31+) to trigger the liquefaction that was not achieved in the previous centrifuge

test. The same calibration procedure was adopted for the constitutive soil model and the used parameters are show in Table 4.22.

Table 4.22. Parameters for the constitutive soil model.

γ_{unsat} (kN/m^3)	γ_{sat} (kN/m^3)	RD (%)	G_0 (-)	h_{p0} (-)	e_{min} (-)	e_{max} (-)	n_b (-)	n_d (-)	φ (°)	ν (-)	Q (-)	R (-)	k (m/s)
15.0	19.2	48.5	377.4	0.08	0.574	0.923	0.5	0.1	33	0.3	10.0	1.5	$1.66 \cdot 10^{-3}$

Figure 4.87, Figure 4.88 and Figure 4.89 show the comparison in terms of acceleration time history between numerical analyses and experiment. The numerical analysis with saturated model led to amplitude accelerations smaller than the experimental ones especially for the shallowest transducers acc3 and acc4 (Figure 4.87). Similar results were achieved by the numerical partial saturated model (Figure 4.88). The better results were found by the back analysis of the saturation degree that led to a saturation degree equal to 45% (Figure 4.89).

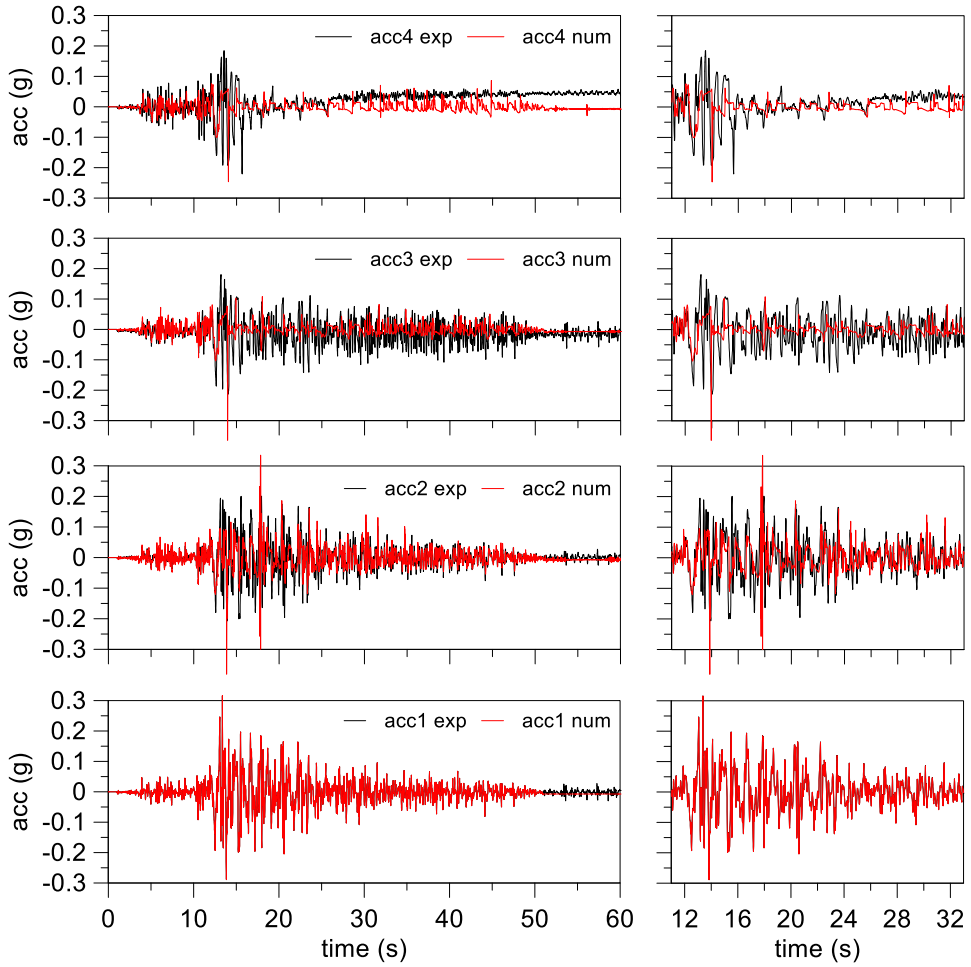

Figure 4.87. M2_S1_IPS4_GM31+: main time interval of acceleration time histories for saturated model.

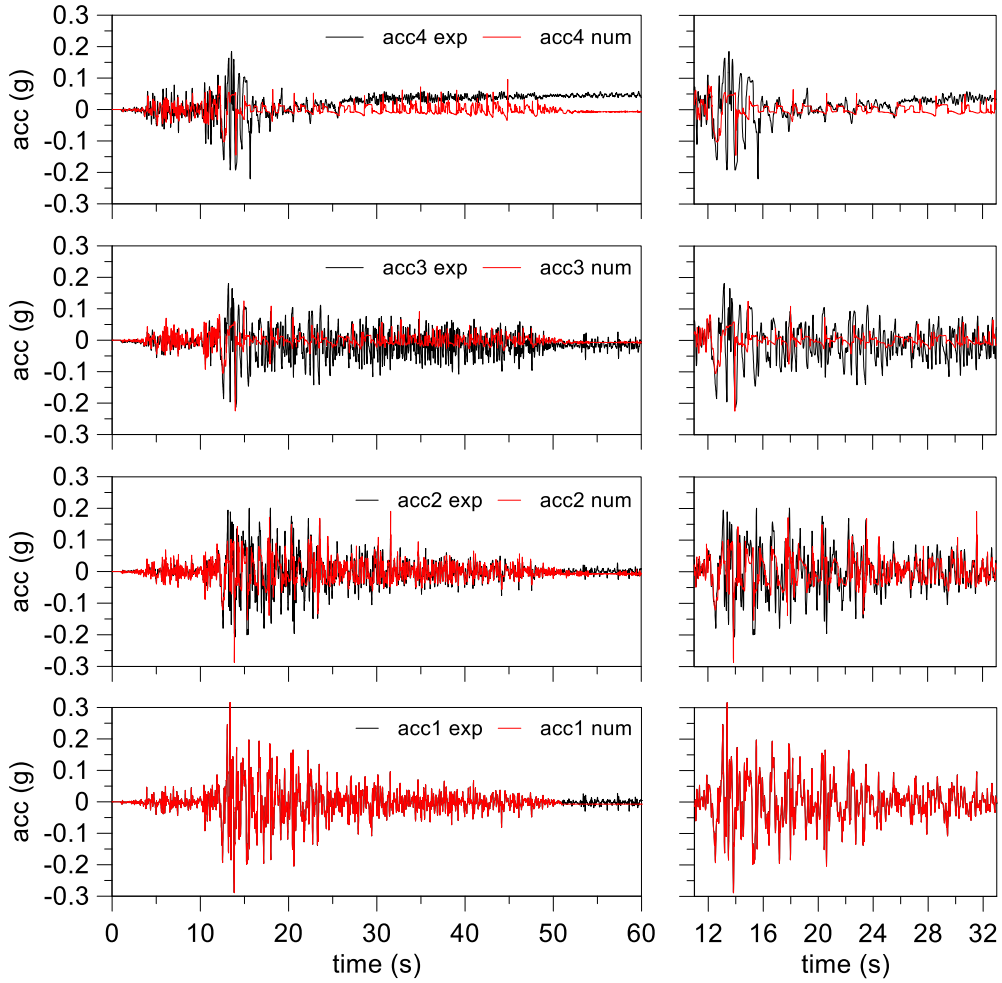

Figure 4.88. M2_S1_IPS4_GM31+: main time interval of acceleration time histories for desaturated model with permeability in saturated condition.

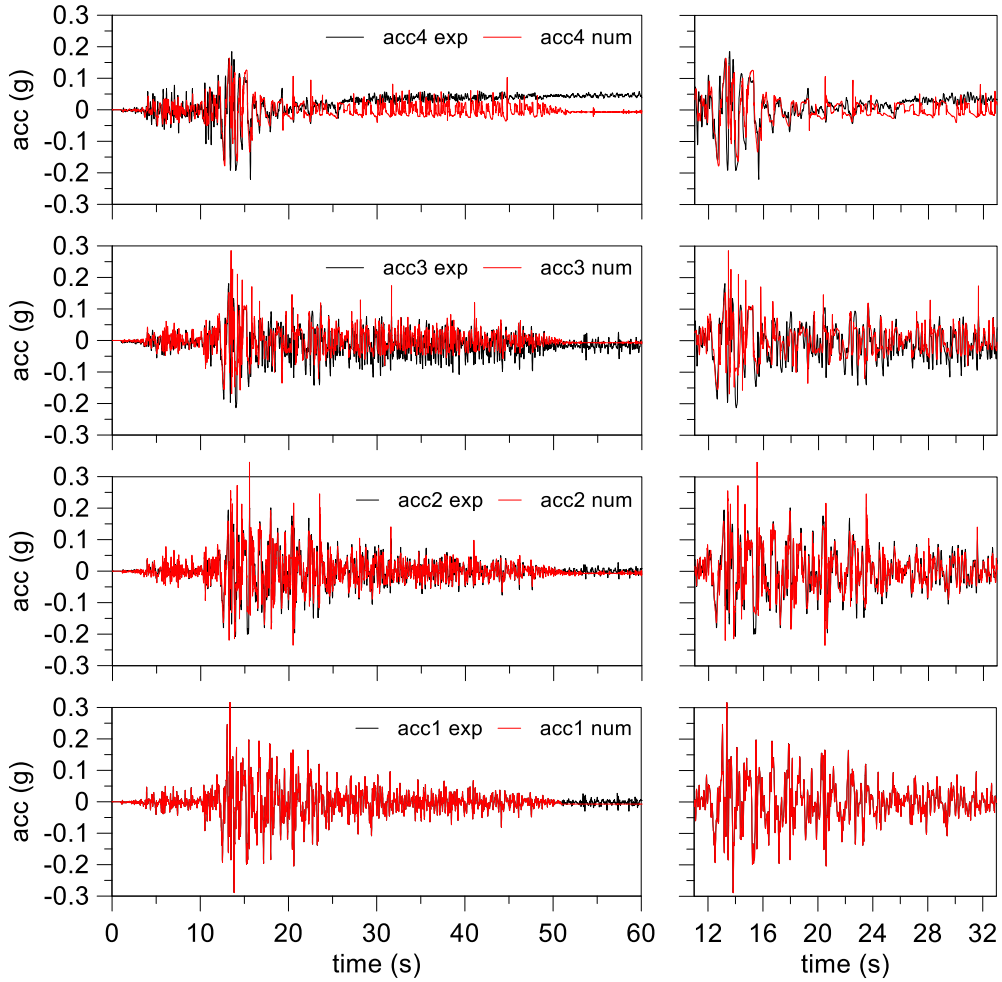

Figure 4.89. M2_S1_IPS4_GM31+: main time interval of acceleration time histories for desaturated model at Sr=45%.

Figure 4.90 show the time histories of excess pore pressure ratio of numerical analyses compared with the experimental ones. The analysis with saturated model (red lines) and analysis with desaturate model with 99.4% of saturation degree (blue lines) predicted larger levels of excess pore pressure ratios than the experimental ones. Moreover, these analyses show a faster pore pressure build-up. These led to the large decrease of the numerical acceleration at the shallowest transducers for both analyses. The better agreement with experimental data was achieved by the model with 45% of saturation degree defined by a back analysis (green lines).

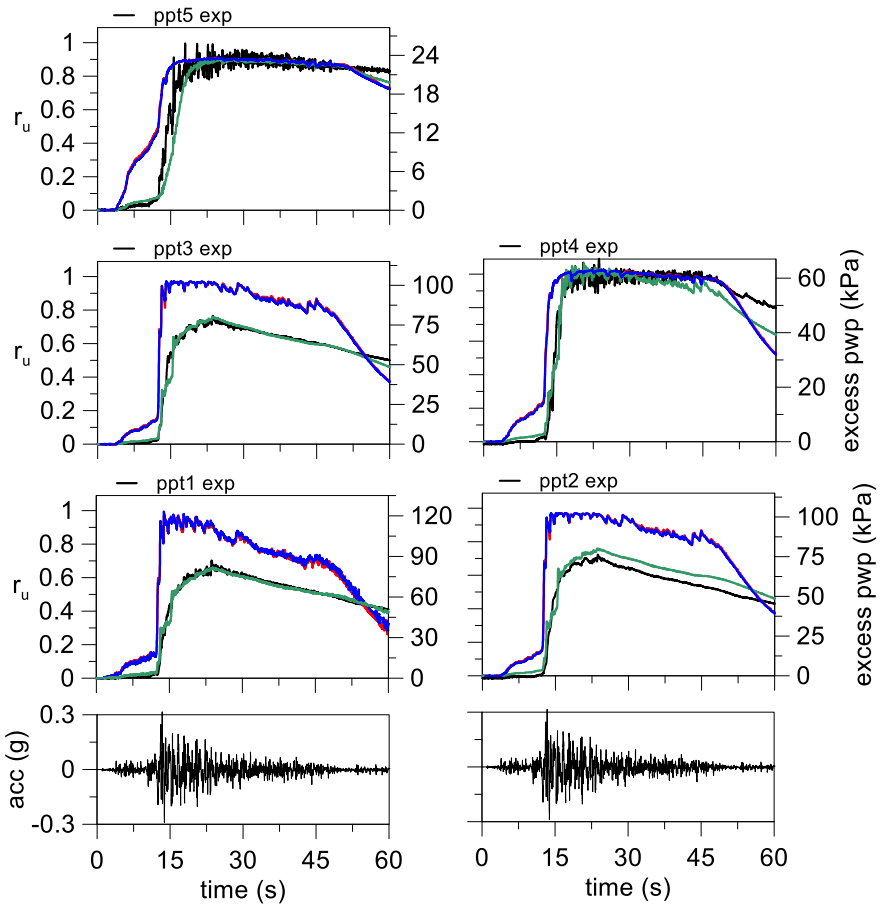

Figure 4.90. M2_S1_IPS4_GM31+: excess pore water pressure time histories for saturated model (red lines), desaturated model with permeability in saturated condition (blue lines) and desaturated model at Sr=45% (green line).

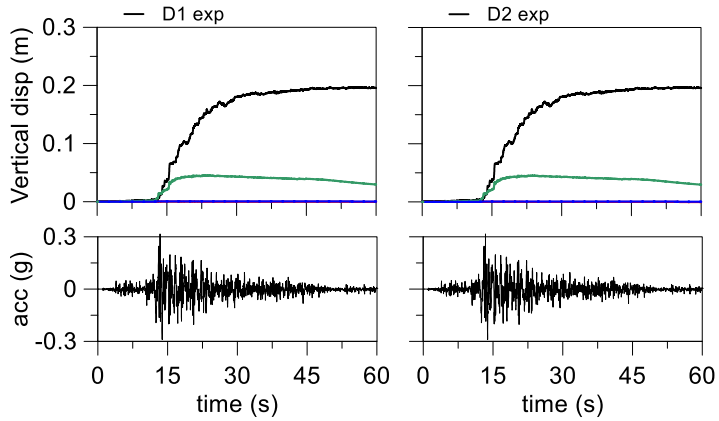

Figure 4.91. M2_S1_IPS4_GM31+: ground surface displacement time histories for saturated model (red lines), desaturated model with permeability in saturated condition (blue lines) and desaturated model at Sr=45% (green line).

As seen for the previous analysis, the ground surface settlements increased for the back analysis with lower saturation degree equal to 45% (green lines, Figure 4.91). It is worth noting that the settlements show a progressive decrease in the time, this effect is due to the small bulk stiffness of the pore fluid that was strongly deformed by the excess pore pressure. The progressive dissipation of the excess pore pressure induced to an expansion of the pore fluid, in particular the air present in the fluid, with an expansion of the soil.

4.5.3 Building on single layer model (M1F_S1)

The initial degree of saturation of soil after the application of IPS for the centrifuge model with the structure was determined in the same way as done for the previous analyses. A saturation degree equal to about 94% was defined considering the height of the model equal to 0.23 meters, the porosity equal to 0.42 and the uplift of the water table height deduced by the pore pressure increment shown in Figure 4.92.

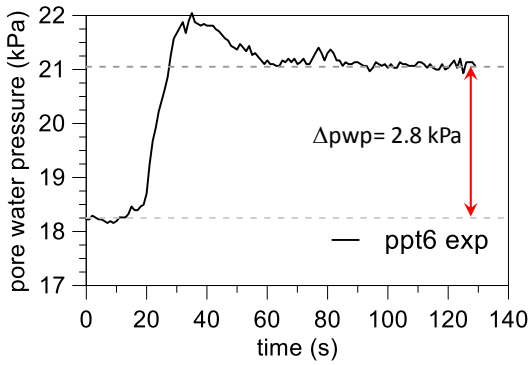

Figure 4.92. Increasing of pore water pressure during air injection.

4.5.3.1 PM4SAND (Ground motion GM31+)

The numerical analysis was performed using PM4SAND constitutive soil model. This was calibrated in function of the relative density of the soil and the used parameters are shown in Table 4.23.

Table 4.23. Parameters for the constitutive soil model.

γ_{unsat} (kN/m^3)	γ_{sat} (kN/m^3)	RD (%)	G_0 (-)	h_{p0} (-)	e_{min} (-)	e_{max} (-)	n_b (-)	n_d (-)	φ (°)	ν (-)	Q (-)	R (-)	k (m/s)
15.2	19.35	55.8	383.8	0.08	0.574	0.923	0.5	0.1	33	0.3	10.0	1.5	$1.66 \cdot 10^{-3}$

The comparison between the computed acceleration time histories and experimental ones are shown in Figure 4.93, Figure 4.94 and Figure 4.95. The saturated model and the partial saturated model with 94% of saturation degree show a progressive deamplification of the acceleration from the bottom to the roof of the structure compared to the experimental measurements. The better results were reached by the model realised with 50% of saturation degree defined by a back analysis (Figure 4.95). however, this analysis led to a slight deamplification of the acceleration on the roof of the structure.

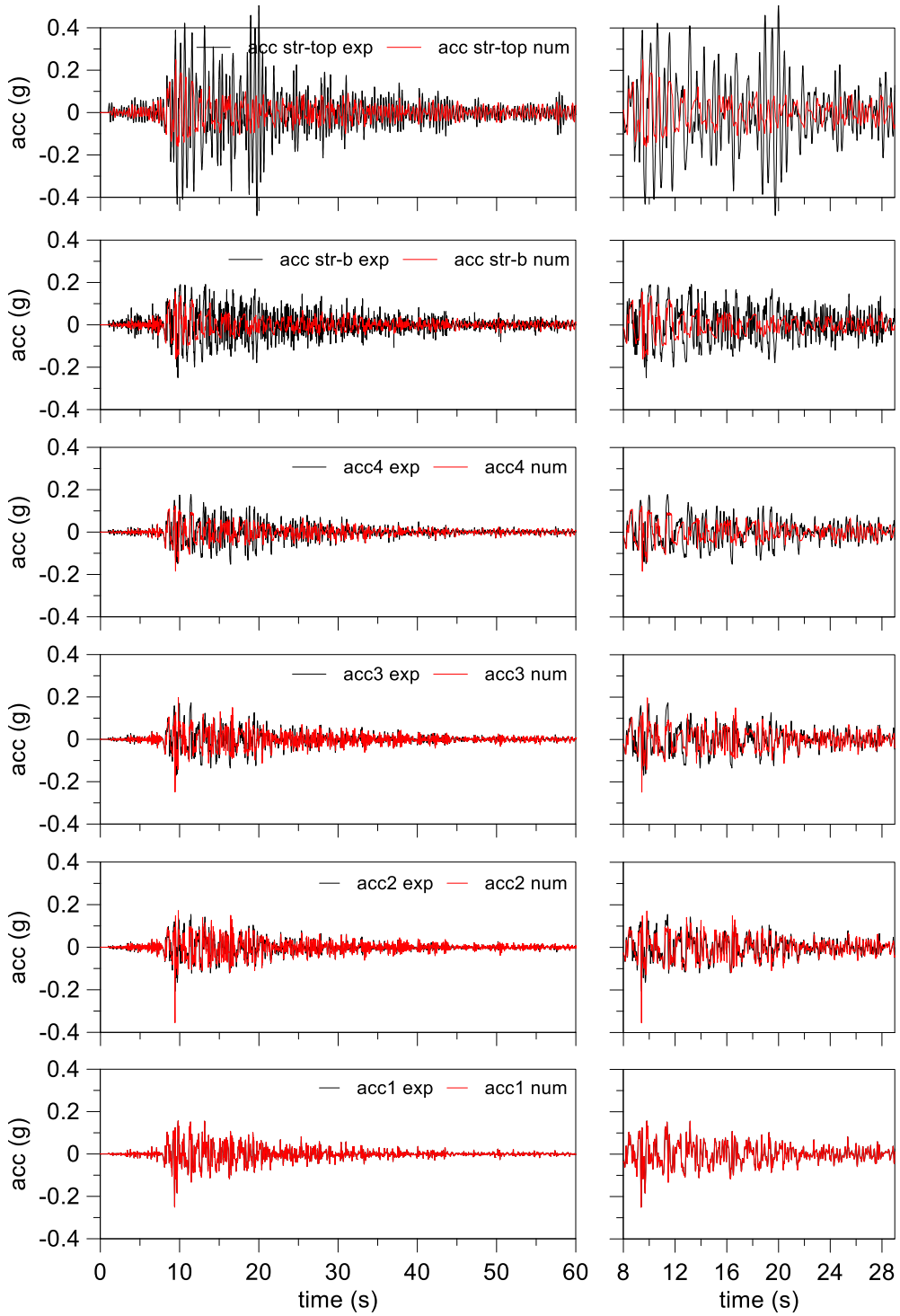

Figure 4.93. M1F_S1_IPS4_GM31+: main time interval of acceleration time histories for saturated model.

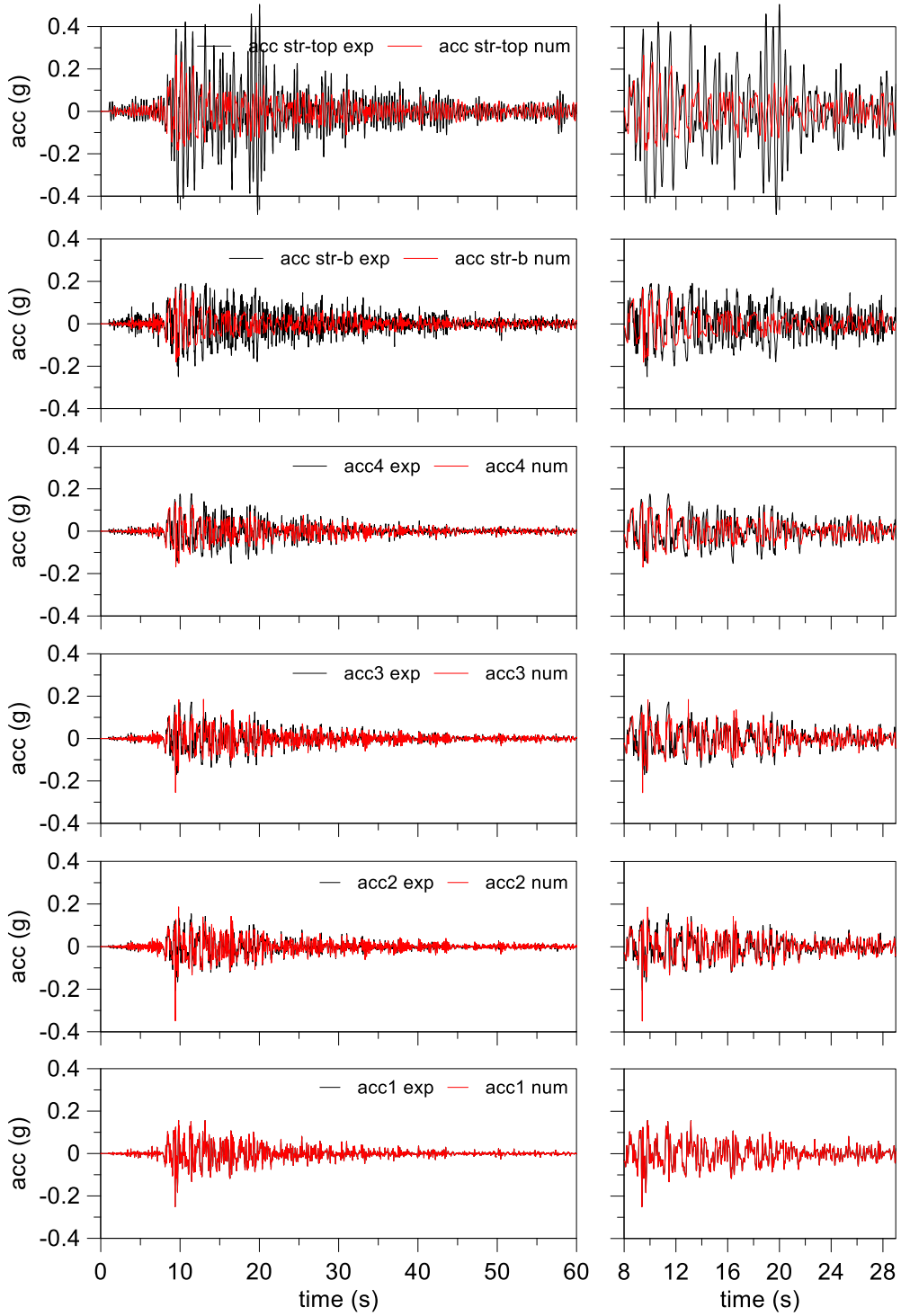

Figure 4.94. M1F_S1_IPS4_GM31+: main time interval of acceleration time histories for desaturated model with permeability in saturated condition.

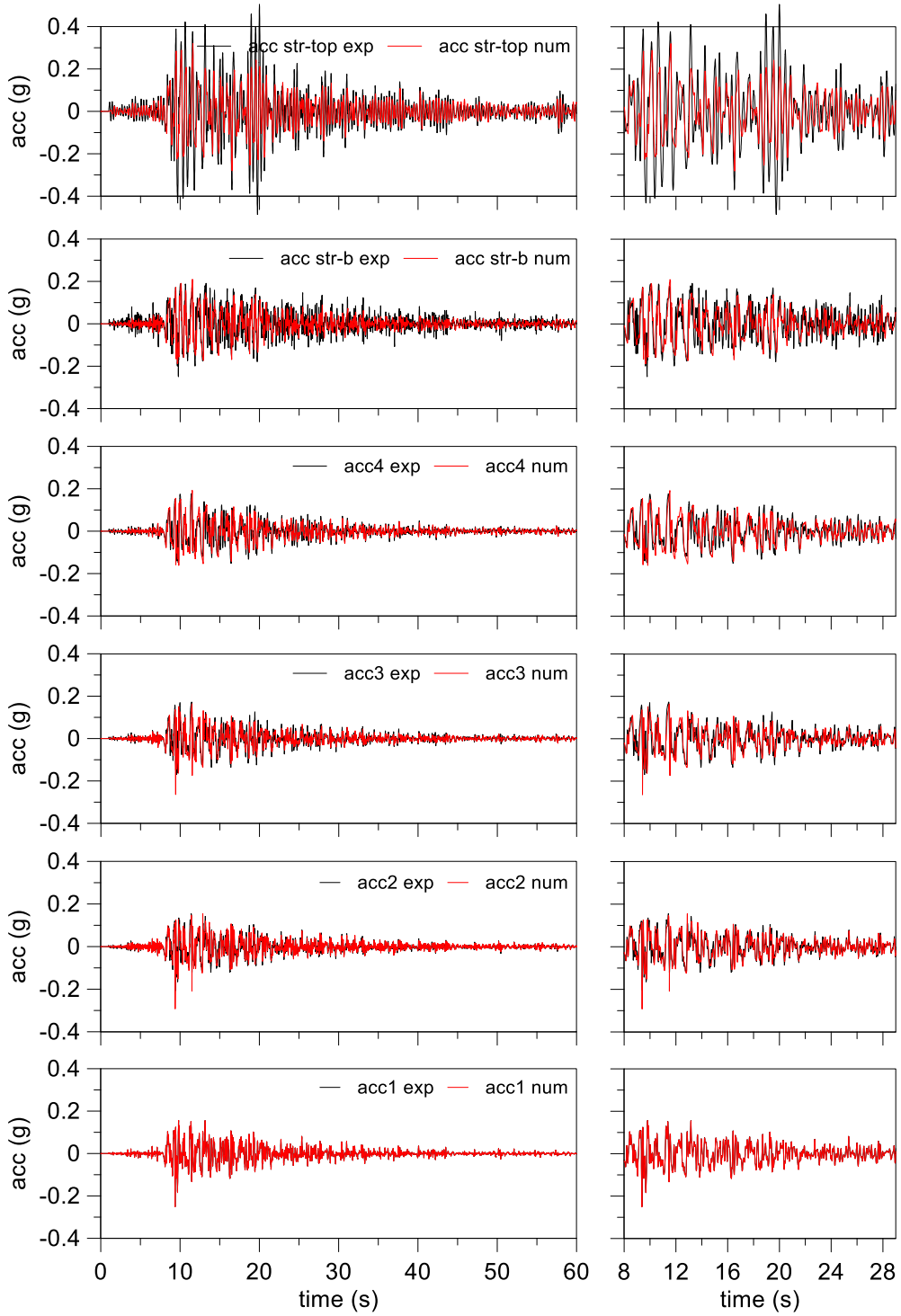

Figure 4.95. M1F_S1_IPS4_GM31+: main time interval of acceleration time histories for desaturated model at Sr=50%.

Figure 4.96 shows the time histories of excess pore pressure ratio for numerical analyses compared to experimental measurements. The computed excess pore pressure ratios for the saturated model and desaturated one with 94% of saturation degree are largely higher than the experimental ones, whereas a better prediction was obtained by the model with 50% of saturation degree.

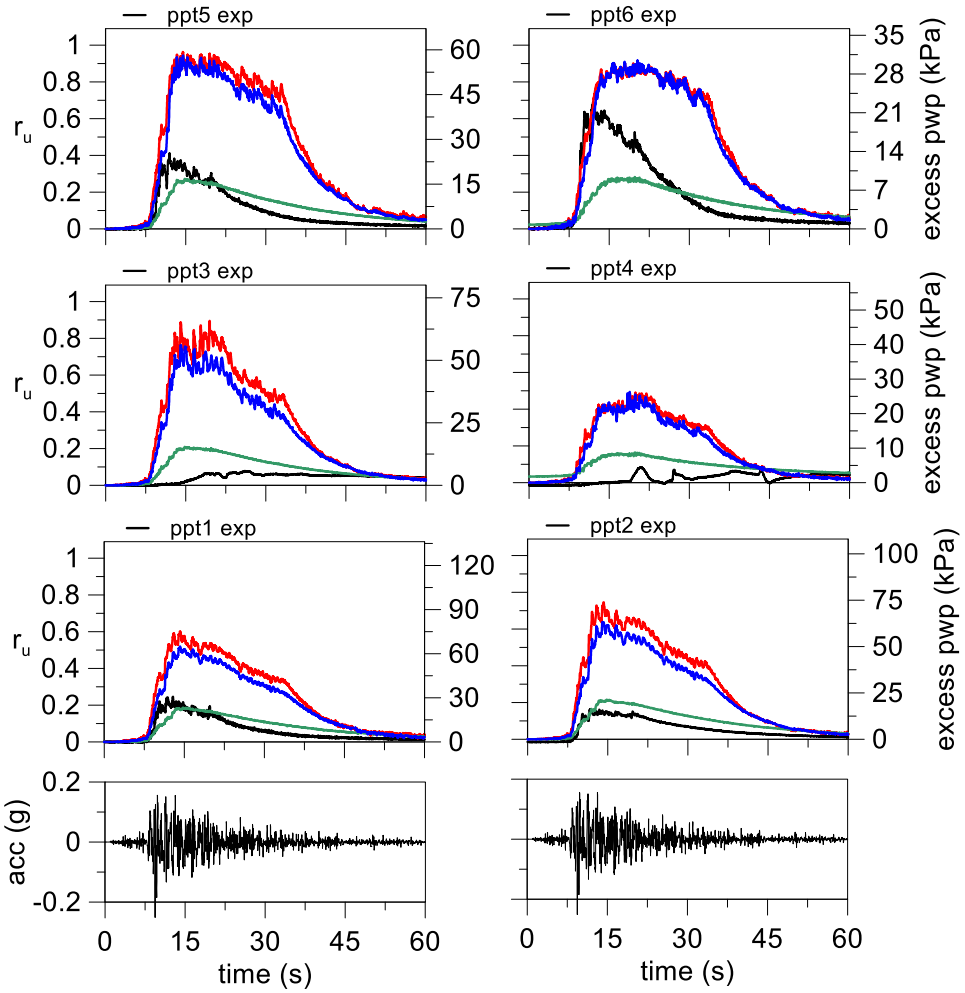

Figure 4.96. M1F_S1_IPS4_GM31+: excess pore water pressure time histories for saturated model (red lines), desaturated model with permeability in saturated condition (blue lines) and desaturated model at Sr=50% (green line).

Figure 4.97 shows as the induced partial saturation increased the volumetric deformability producing larger volumetric strains as possible to see by the settlement in "free-field" conditions (D1 and D2). However, the large decrease of excess pore pressures led by the IPS avoided a large drop of soil shear stiffness preventing large settlements of the structure. This effect was not achieved in the two other numerical analyses in which the settlements were significantly larger.

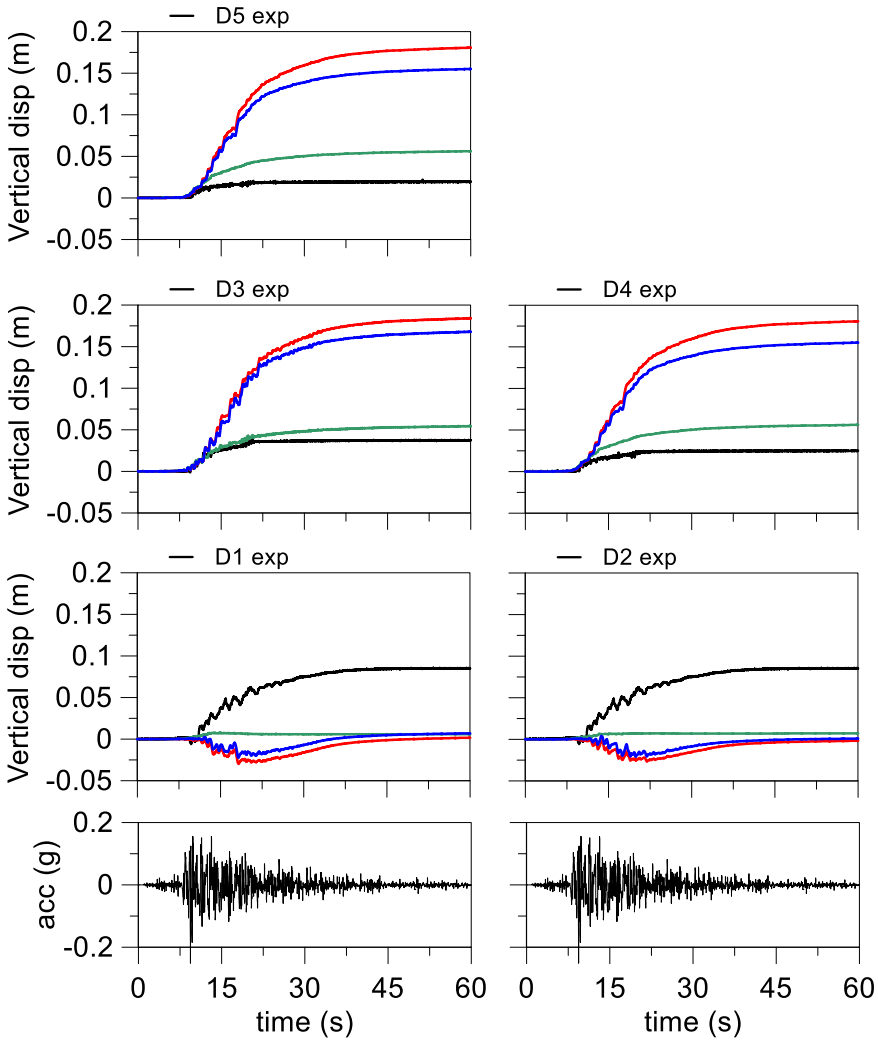

Figure 4.97. M1F_S1_IPS4_GM31+: ground surface displacement time histories for saturated model (red lines), desaturated model with permeability in saturated condition (blue lines) and desaturated model at Sr=50% (green line).

5 PARAMETRIC ANALYSES

Calibration and check of numerical models on different centrifuge test configurations allow to study, in a parametric way, the effects of geometrical configuration and soil profile with a good reliability. In this section the effect of different geometrical configurations of mitigation techniques was studied. The results are reported in terms of pore water pressure distribution in the soil profile, acceleration and settlements at ground surface, at the base and roof of the simple structure. As suggested by different approach, liquefaction susceptibility of a site has to define in within 20 meters depth, hence in the following analyses a 20 meters thick soil profile was considered with a water table placed at ground surface.

In all the following analyses was used the input motion of the centrifuge test with the horizontal drains without clay crust and the respectively soil relative density (RD = 54.5%).

5.1 Effects of the horizontal drains in soil profile with upper seepage surface

In this section the results for the parametrical analyses with horizontal drains in homogeneous soil profile in presence of an upper seepage surface are shown. Parametric analyses were performed changing the depth of first row of horizontal drains (H/d) and the spacing among them (s/d). Three different values equal to 5 10 and 15 were considered for H/d and s/d.

Figure 5.1 shows that the presence of horizontal drains induces an increase of maximum acceleration within period equal to 1.2 seconds with higher amplifications at about 0.15 and 0.35 seconds. The input acceleration spectrum shows than these periods are already more energized.

Figure 5.2 and Figure 5.3 show that an increase of the efficiency of the horizontal drains system on the pore pressure distribution increases acceleration at the ground surface compared to the case without drains (no-drains).

Lower levels of excess pore pressure lead to a smaller drop of the shear stiffness that reduces strongly the isolation effect due to the liquefied soil layers.

Moreover, horizontal drains reduce the amount of ground surface settlements due to volumetric strains (Figure 5.4) except for the case H/d=5 and s/d=5 for the same reason seen in Figure 4.44. Indeed, this arrangement of the horizontal drains led to higher level of excess pore pressure in the soil portion below the drains with a larger incremental dissipation of excess pore pressure with larger amount of final volumetric strains.

Hence, the use of horizontal drains to mitigate the liquefaction susceptibility decreases significatively the amount of excess pore pressure in the soil but it leads to an increase of the acceleration at ground surface and at the eventually structure founded on this.

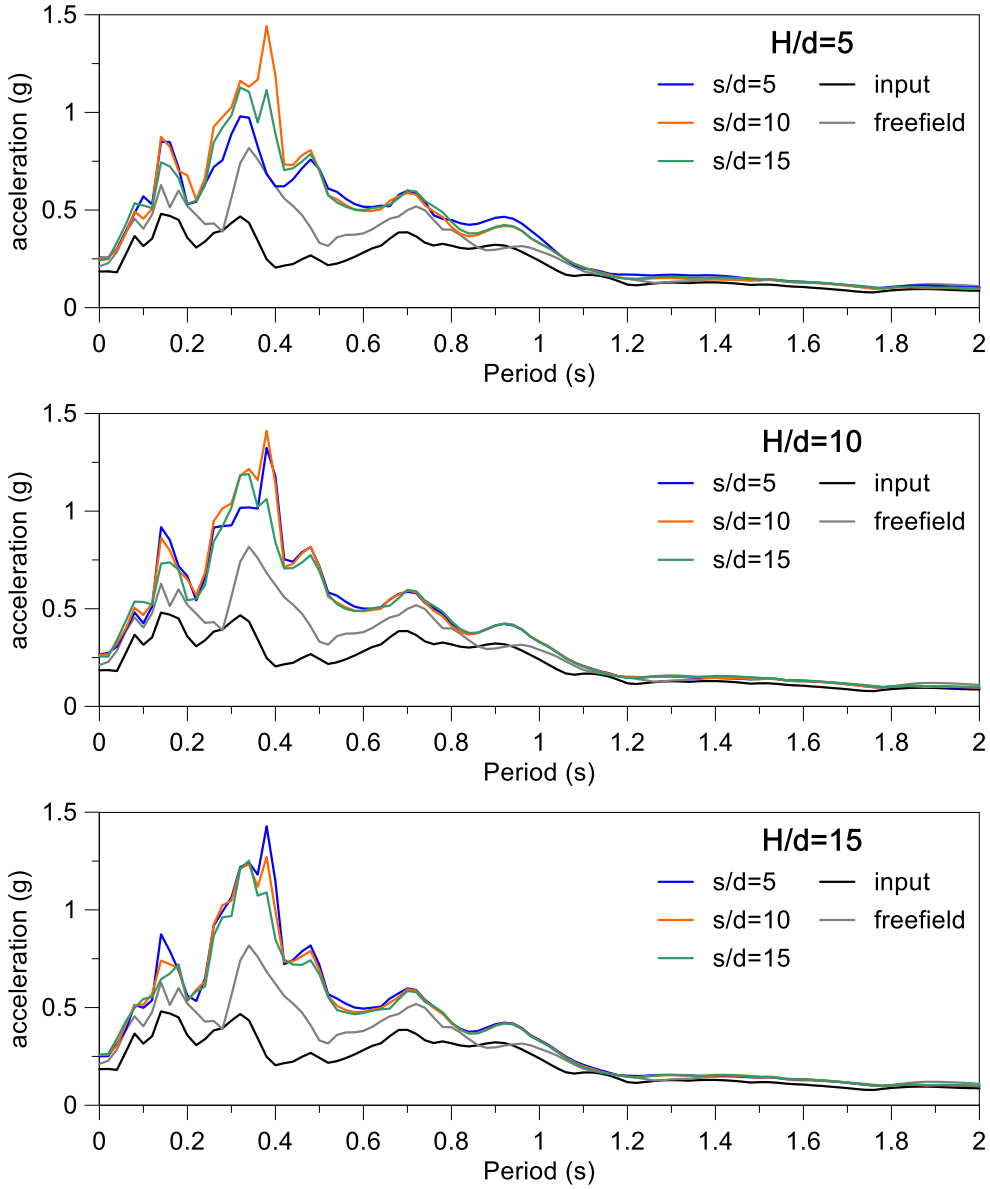

Figure 5.1. Response spectra on the ground surface for different horizontal drains dispositions.

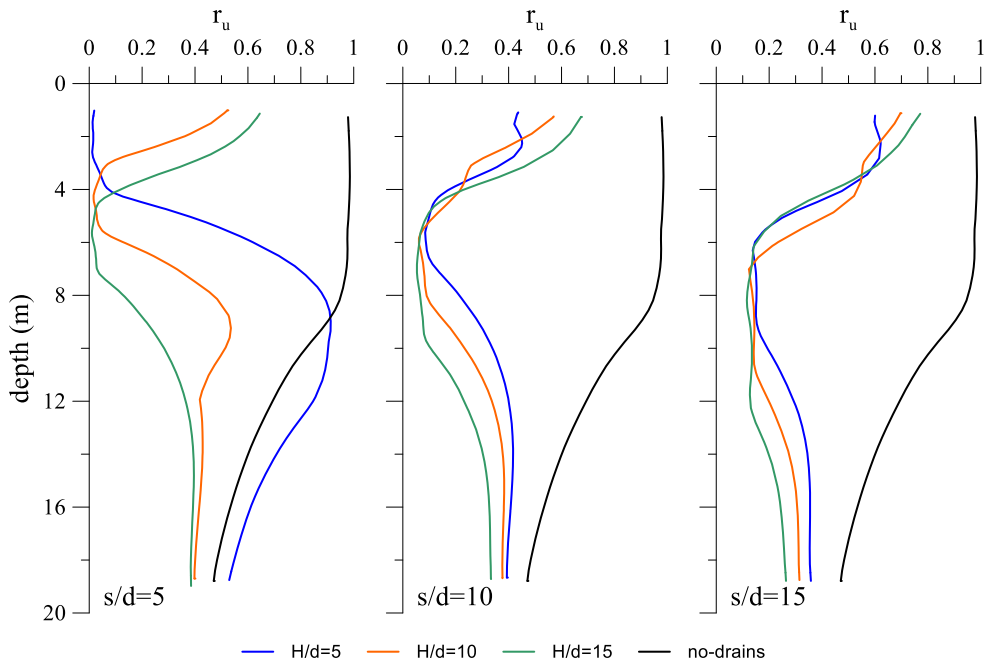

Figure 5.2. Distributions of the excess water pressure ratio in function of the first-row depth (H/d).

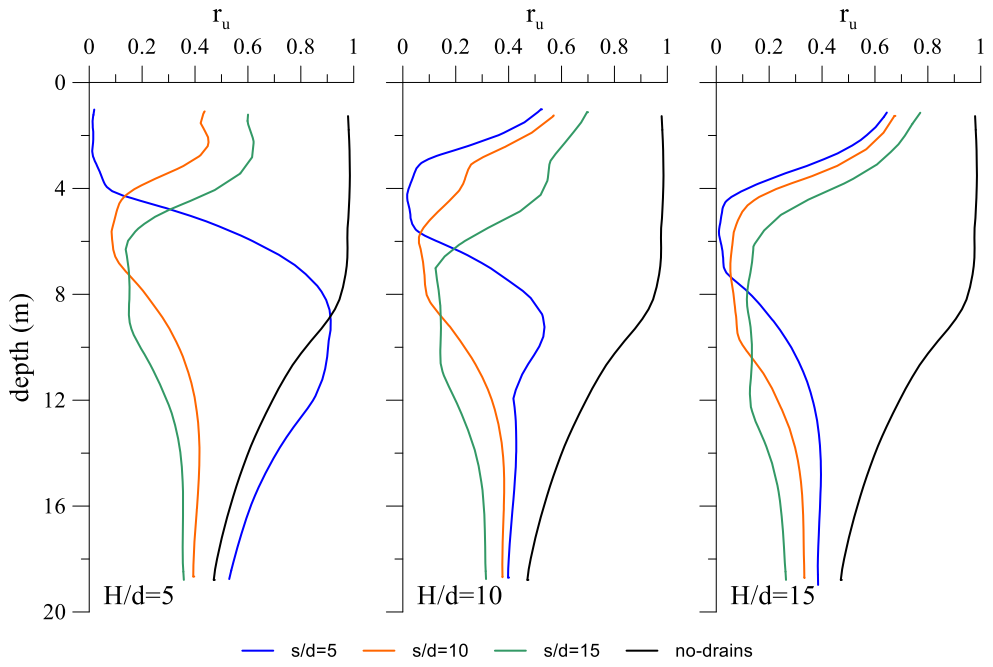

Figure 5.3. Distributions of the excess water pressure ratio in function of the spacings between drains (s/d).

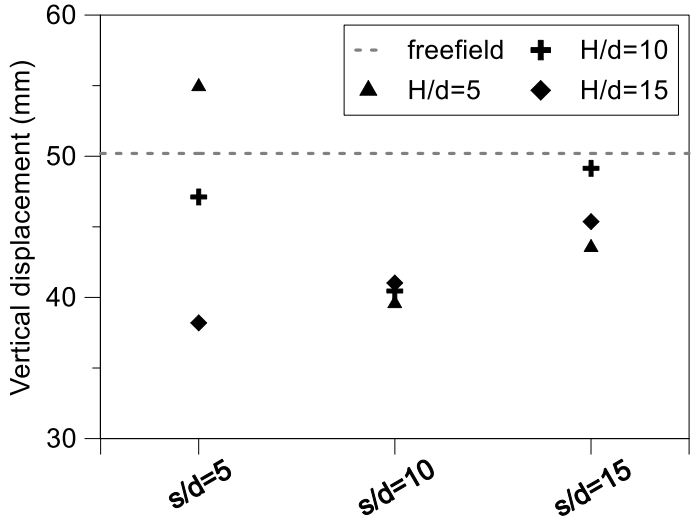

Figure 5.4. Settlements of the ground surface in function of the geometry of the horizontal drains.

5.2 Effects of the horizontal drains in soil profile with impervious upper surface.

In this section were studied the same arrangements studied in the previous one. However, an impervious surface was realised on the top of the soil profile through a soil layer with low permeability (Pontida clay) with 1 meter thick.

Figure 5.5 shows the results of parametric analyses in term of acceleration spectra. Larger values of acceleration were recorded within period equal to 1.2 seconds with higher amplifications at about 0.15 and 0.35 seconds. The input acceleration spectrum shows than these periods are already more energized.

Acceleration spectra show a lower variability compared to the previous back analyses with pervious upper surface. This effect is due to the distribution of excess pore pressure profile (Figure 5.6 and Figure 5.7) below the drains that in these analyses are closer than in the previous ones. Higher excess pore pressures were recorded between the drains than in the previous analyses. This led to a more deformable soil layer that decreased the shear stress in the deeper soil layers reducing the pore pressure build-up in this soil portion.

In this case the settlements without horizontal drains are very small, this is due to the presence of impervious upper surface that induced a quasi-undrained condition to the system and consequentially very small volumetric strains. This condition was not true in presence of horizontal drains, indeed larger settlements were recorded for all horizontal drain arrangements than the case without drains.

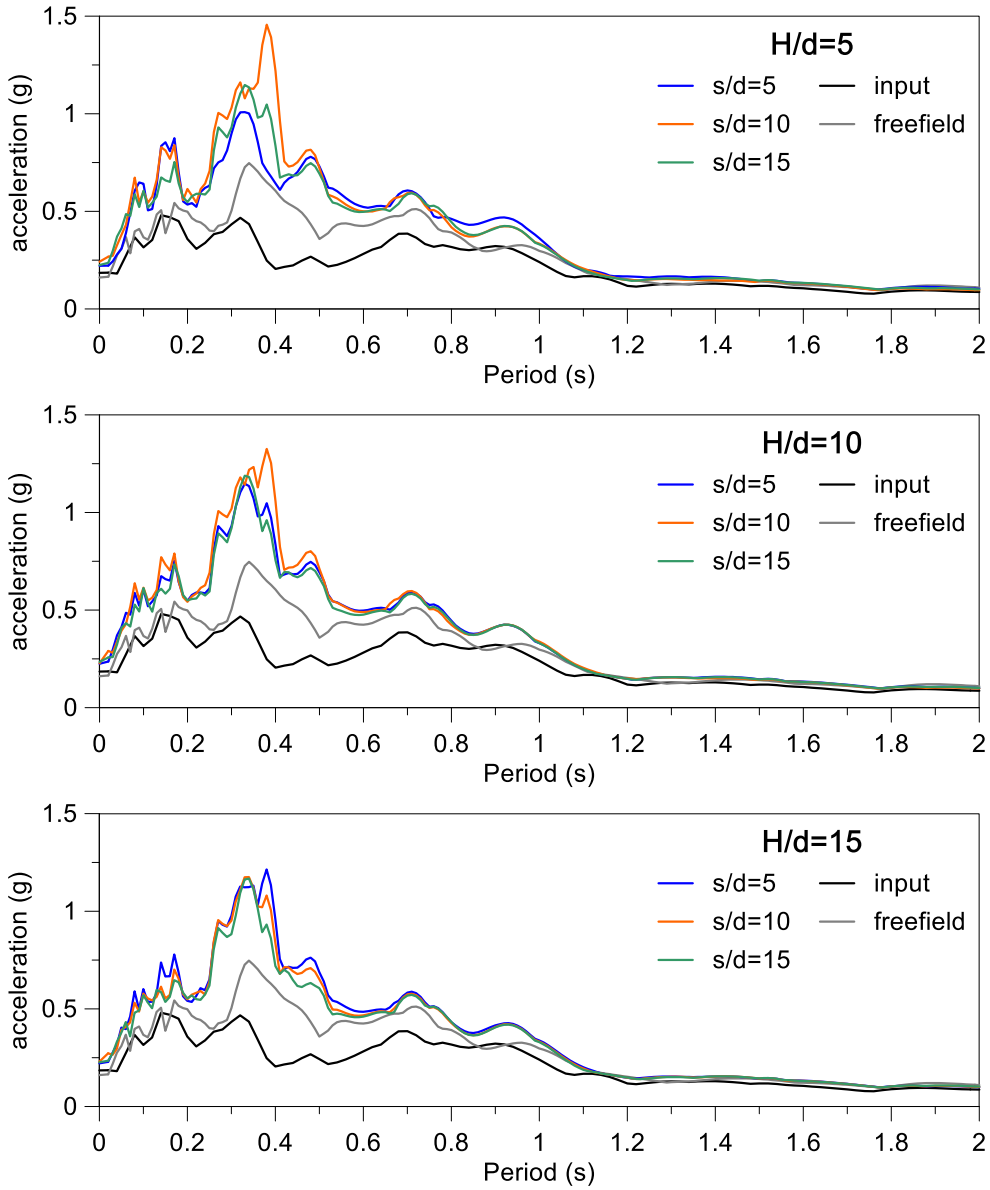

Figure 5.5. Response spectra on the ground surface for different horizontal drains dispositions.

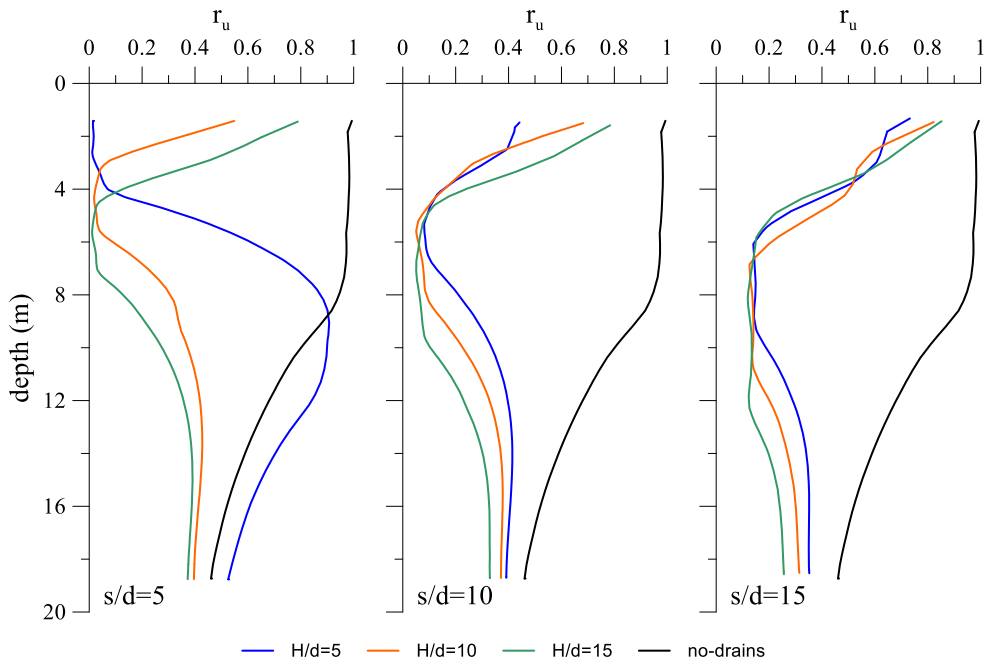

Figure 5.6. Distributions of the excess water pressure ratio in function of the first-row depth (H/d).

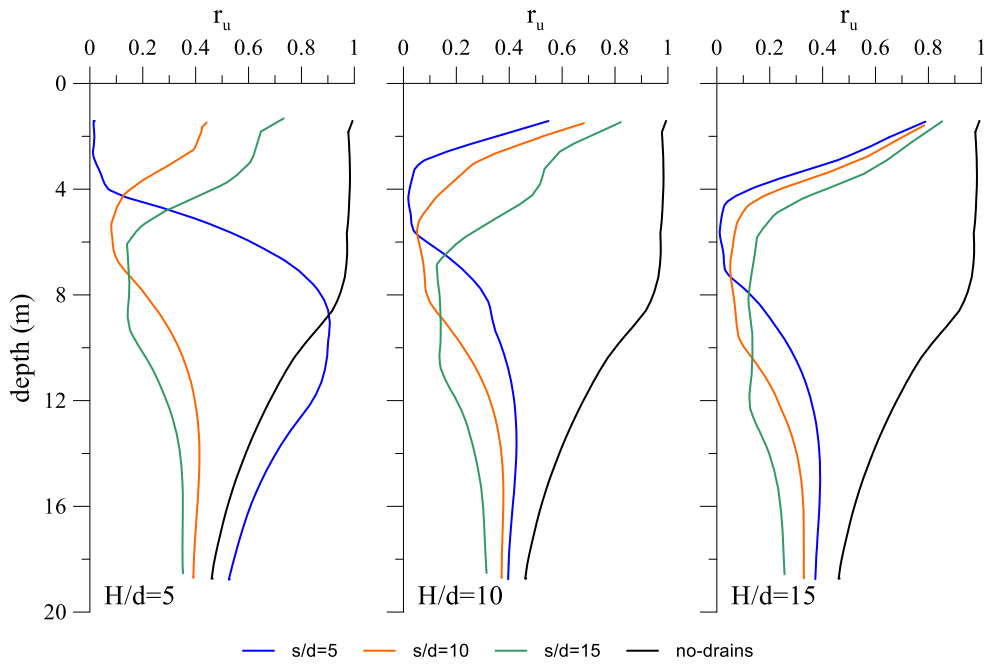

Figure 5.7. Distributions of the excess water pressure ratio in function of the spacings between drains (s/d).

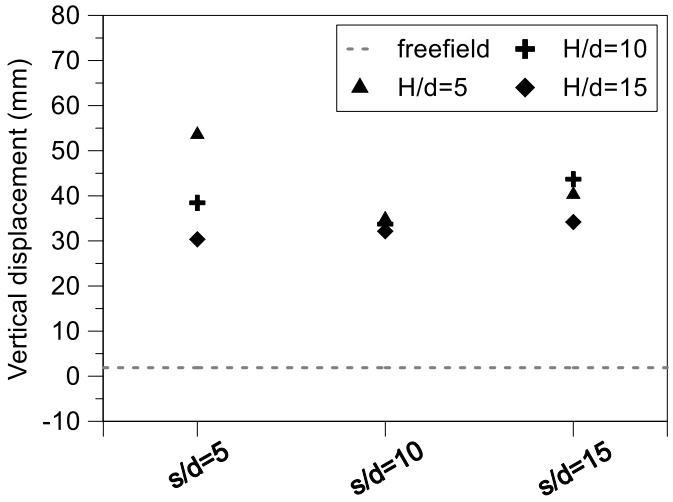

Figure 5.8. Settlements of the ground surface in function of the geometry of the horizontal drains.

5.3 Effects on the building of horizontal drains extension in soil profile with upper seepage surface

In this section the effects of different arrangements of horizontal drains in presence of the simple structure were studied. The horizontal drains were deployed below the structure with the central axis in correspondence of the centre of the foundation of the structure. The drains were arranged in the schemes with the depth of the first row (H/d) equal to 10 and 15 and the dimensionless spacing (s/d) equal to 10 and 15.

The presence of the structure introduced a new geometrical variable that consists in the horizontal extension of the drains system. In the following were considered different horizontal extensions (Figure 5.9):

- Indefinite horizontal disposition of horizontal drains (indefinite)
- Horizontal drains included in the track of the structure foundation (B);
- Horizontal drains extended for two spacings outside the track of structure foundation (2s)

This parametric analysis aims to find the optimized horizontal extension of the drains system evaluated on the excess pore pressure reduction below the structure. The section below the foundation beam was taken to account to evaluate the excess pore pressure ratio with depth (section A-A in Figure 5.9).

The results in terms of acceleration are shown in terms of acceleration spectra evaluated on the base of the structure (Figure 5.10) and on its roof (Figure 5.11Figure 5.10).

The adoption of the horizontal drains led to an amplification of the acceleration in all cases especially for the indefinite arrangement. The same results were found at the roof of the structure with a largest amplification in correspondence of the fundamental period of the structure (~ 0.3 seconds).

A progressive reduction of acceleration was recorded for smaller extension. This result is ascribable to the effect of the lateral nontreated soil that was subjected to a large excess pore pressure during the shaking that led to a larger isolation effect for the structure (Figure 5.12).

Figure 5.13 and Figure 5.14 show that the structure influenced the distribution of the excess pore pressure ratio with depth. The condition with structure and without drains (no-drains) the vertical profile below the foundation beam shows a lower level of excess pore pressure ratio than the free-field condition. This effect is due to the increment of vertical effective stress in the soil induced by the weight of the structure that reduce the excess pore pressure ratio. Indeed, in the numerical analyses the presence of the structure modifies the distribution of the effective stresses in the soil but it does not change the distribution of excess pore pressure, so below the structure the reduction of the r_u was induced only by an increment of effective vertical stress.

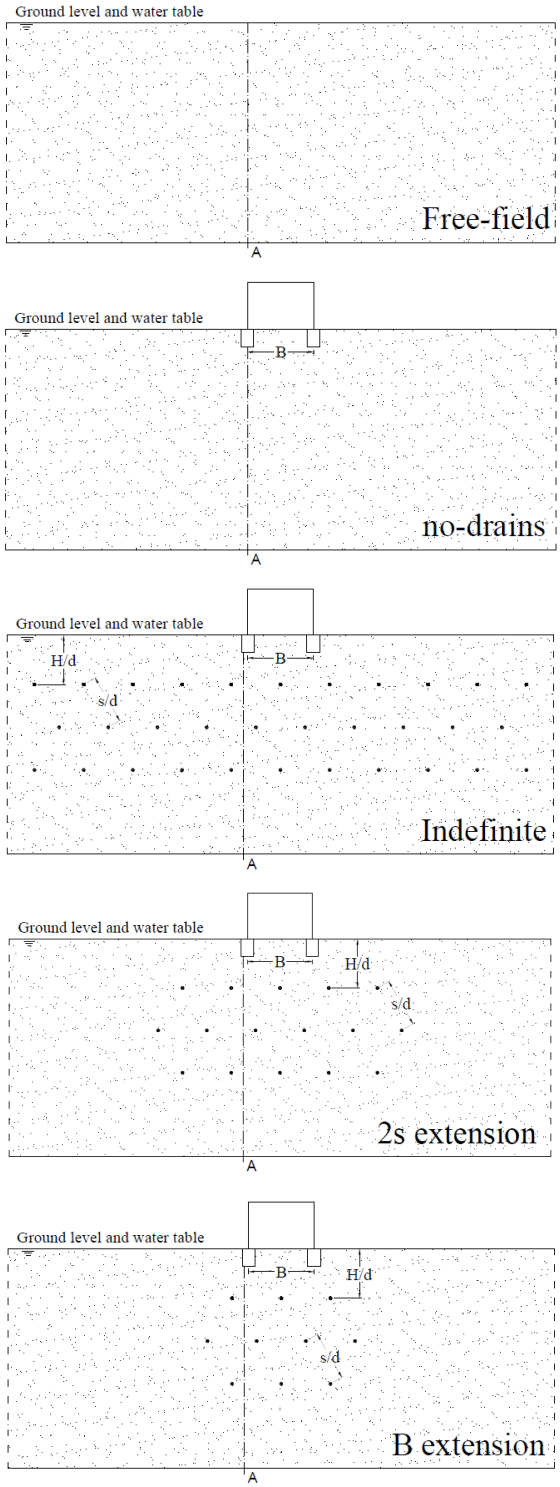

Figure 5.9. Geometry of the horizontal drains below the structure.

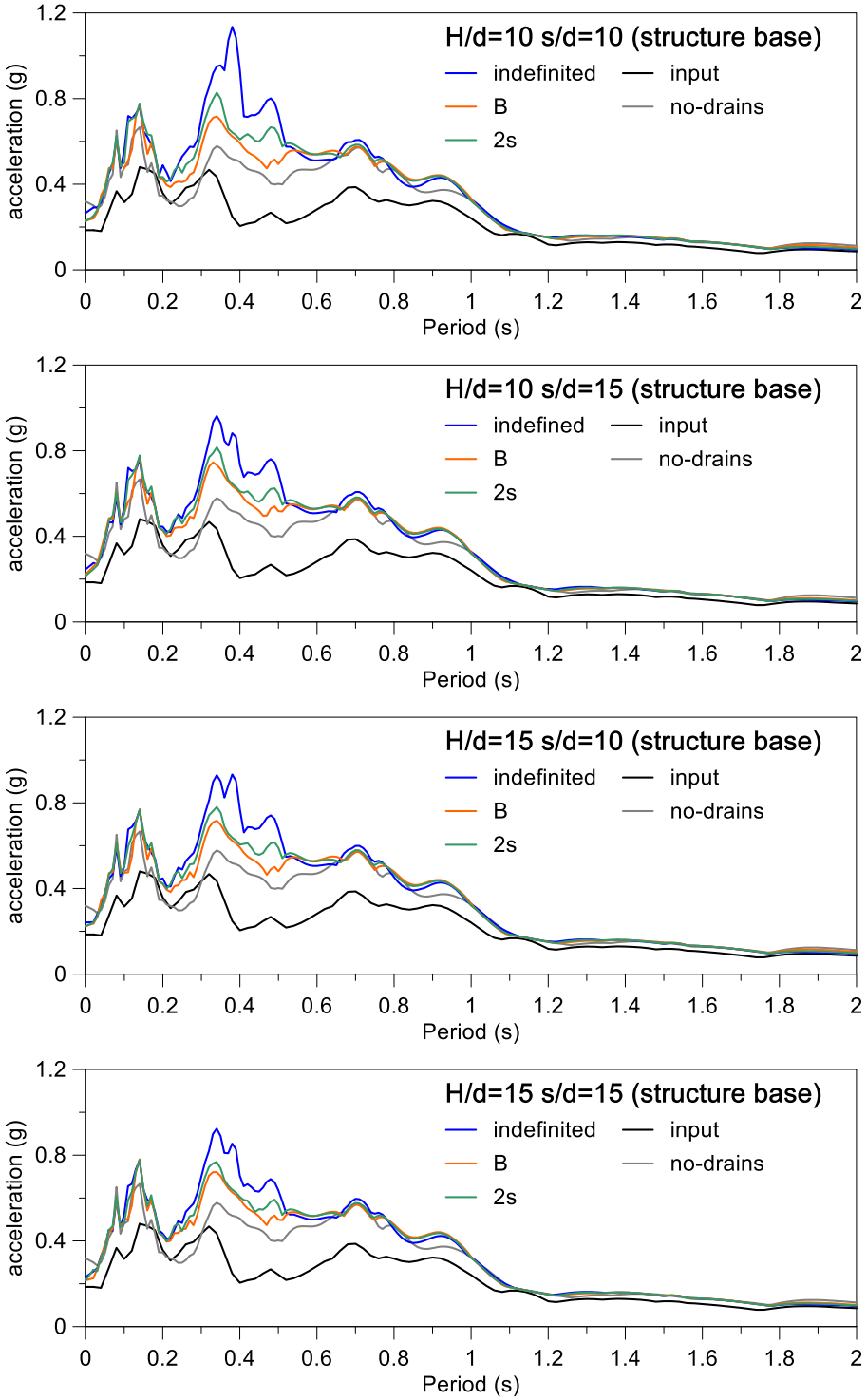

Figure 5.10. Response spectra on the structure base for different horizontal drains dispositions.

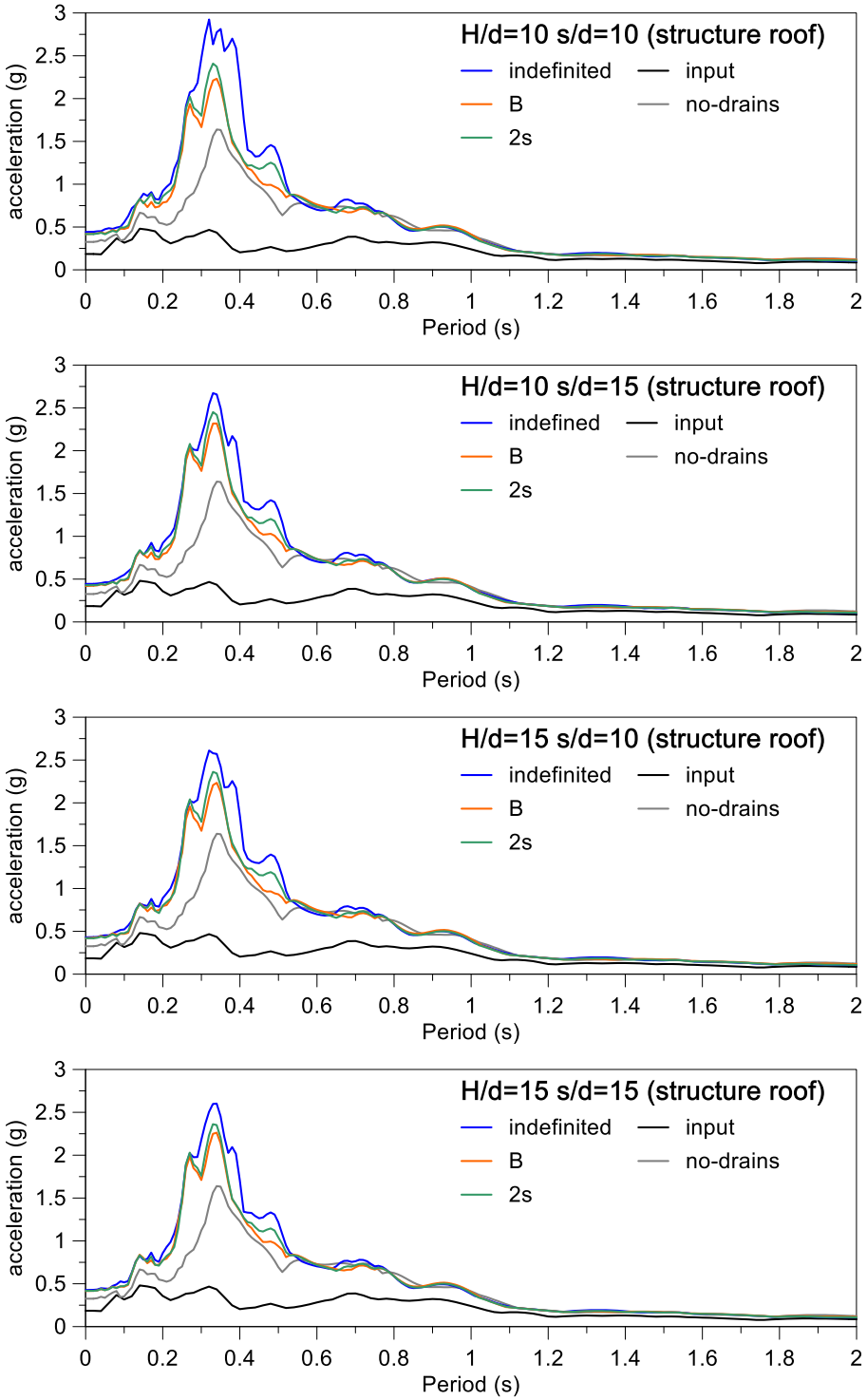

Figure 5.11. Response spectra on the structure roof for different horizontal drains dispositions.

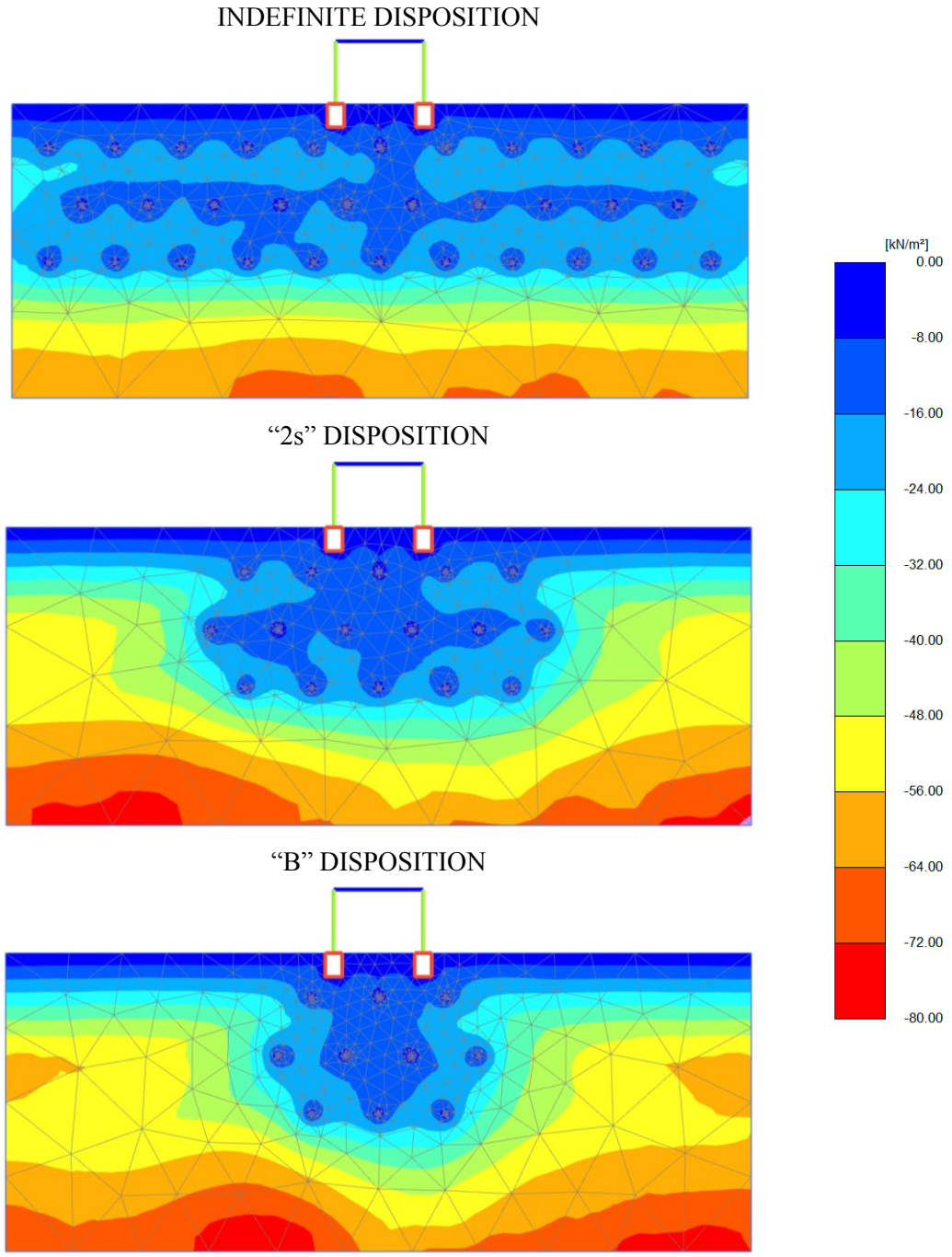

Figure 5.12. Effects of the horizontal extension of drains system on the lateral soil in terms of maximum excess pore pressure (compression is negative).

The presence of horizontal drains reduces significatively the excess pore pressure ratio and the scheme more efficient is represented by the drains with 2s extension. Indeed, this scheme led to lower excess pore pressure ratio in correspondence of the shallower soil layers

than the scheme with indefinite extension of horizontal drains. This reduction was due to the same effect that reduces the acceleration for the structure.

Hence, the soil volume subjected to an excess pore pressure reduction by the horizontal drains and the structure represent a partial isolated system its extension can identifiable by in the Figure 5.12.

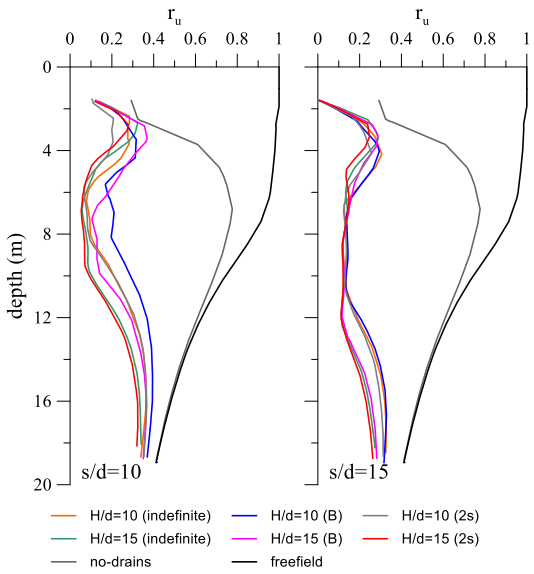

Figure 5.13. Distributions of the excess water pressure ratio in function of the first-row depth (H/d).

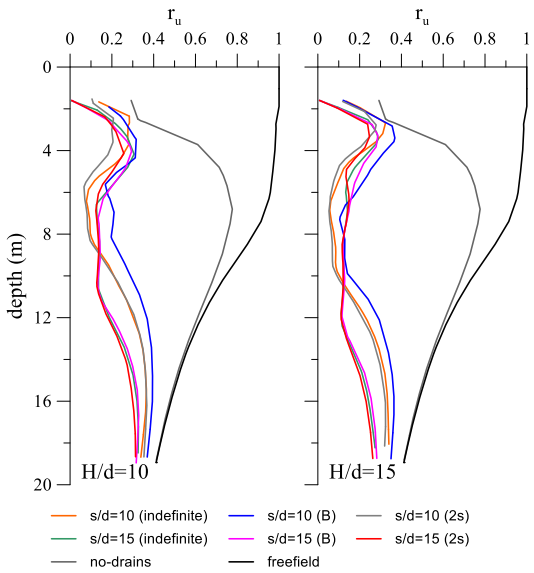

Figure 5.14. Distributions of the excess water pressure ratio in function of the spacings between drains (s/d).

The settlements in presence of horizontal drains show a very small variability in function of the drains arrangement and they were largely reduced compared to the no-drains system (Figure 5.15).

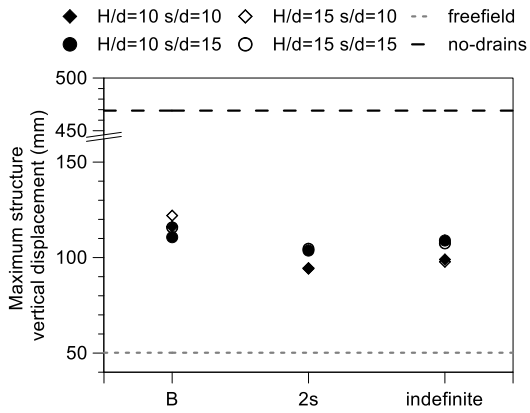

Figure 5.15. Maximum settlements of the structure in function of the geometry of the horizontal drains.

Moreover, the presence of drains reduced the tilt of the structure increasing the volume subjected to the drains influence.

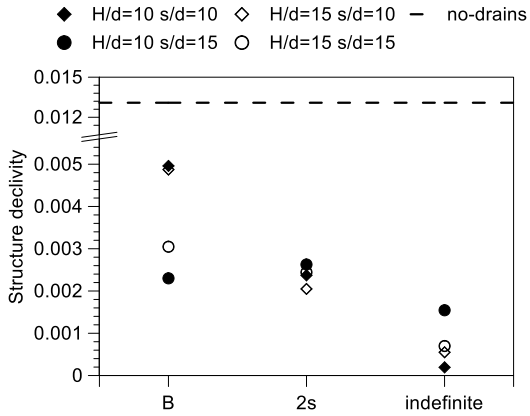

Figure 5.16. Declivity of the structure in function of the geometry of the horizontal drains.

5.4 Effects of induced partial saturation with different geometry of treated soil volume and saturation degrees.

In this section the effect of induced partial saturation (IPS) was studied changing the saturation degree and the geometry of the treated soil volume. Geometries were realised changing the ratio between the height and width of the treated volume in the cases with structure. The effects of the partial saturation were implemented in the numerical analyses by the method explained in the section 4.5.1.

5.4.1 Analyses with permeability in saturated conditions

In this section some parametric analyses are shown to evaluate the effect of the saturation degree and geometry of the induced partial saturation on the acceleration at ground surface and on the distribution of the excess water pressure ratio with depth. The reduction of the permeability coefficient induced by the induced partial saturation was not considered in these analyses, so the permeability in saturated conditions was used.

The analyses were performed for three different thickness of the treated soil equal to 4, 8, 12 meters respectively. Moreover, three saturation degrees were considered: 95%, 90% and 85%.

For all these analyses the acceleration response spectra (Figure 5.17) show a slight reduction of the acceleration at low periods within 0.3 seconds, whereas the acceleration at higher periods show a large increment especially in correspondence of 0.7 seconds, the same result was found for the system without IPS (no-IPS, grey lines).

The increment of the acceleration increases with the thickness of the treated soil, indeed for the IPS with 4 meters thick the spectra are very close to the no-IPS one, increasing the thickness the spectra mitigated systems are above the no-IPS one. The same effect was recorded reducing the saturation degree.

Figure 5.18 show the distributions of the excess water pressure ratio with depth. The distributions were slightly influenced by the presence of desaturated soil, moreover some desaturated model led to profile with larger values of r_u than no-IPS condition. This effect is ascribable to the presence of shallower soil layers with smaller drop of the shear stiffness that induced larger shear strains in the lower soil layers. This effect was due to different excess pore pressure build-ups recorded in the treated system and in the system without IPS. As shown in Figure 5.20 the system with IPS shows a slower excess pore pressure build-up compared to the system without IPS. The same results are shown by the vertical profiles of excess pore pressure ratio in Figure 5.21.

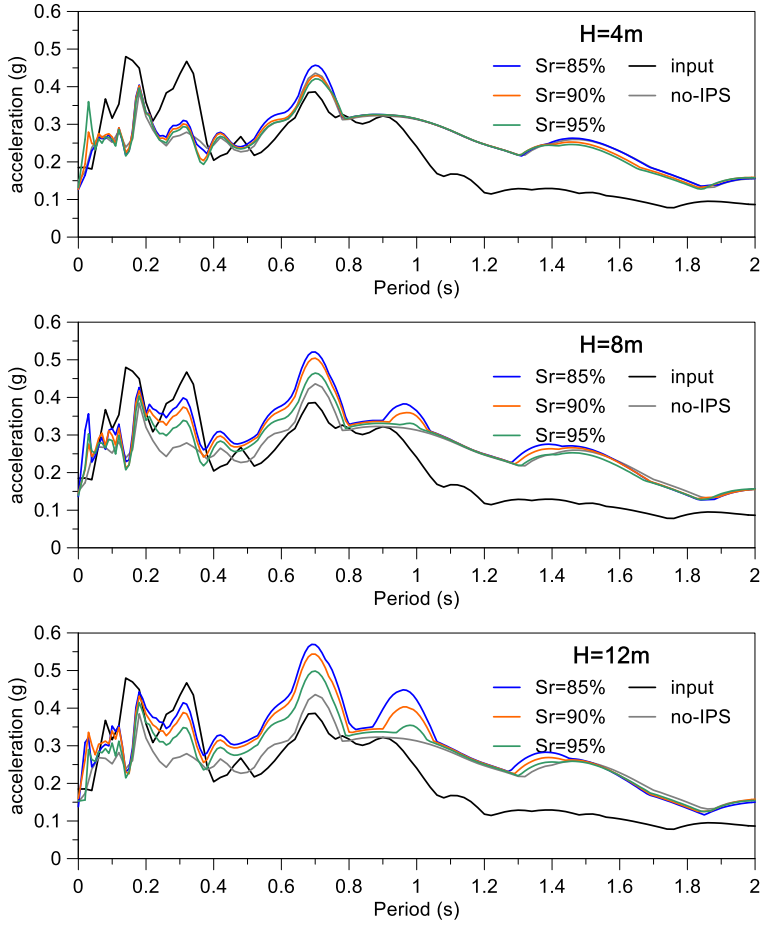

Figure 5.17. Response spectra on the ground surface for different thickness of induced partial saturation.

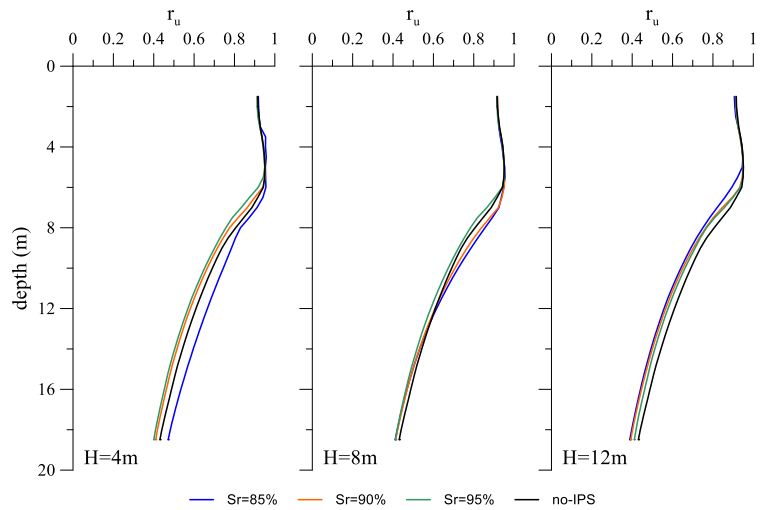

Figure 5.18. Distributions of the maximum excess water pressure ratio in function of saturation degrees.

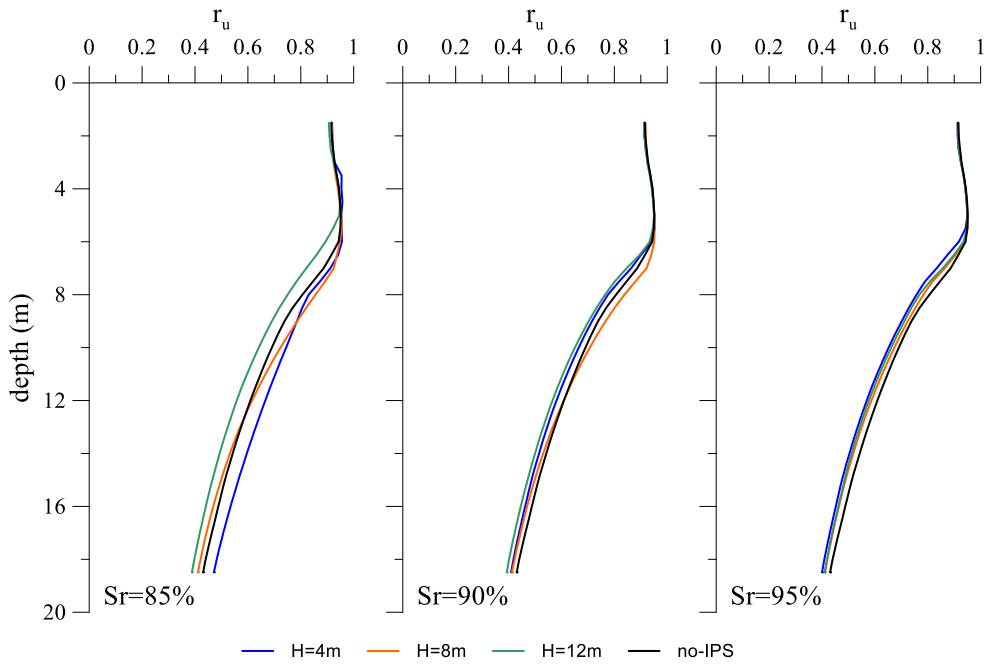

Figure 5.19. Distributions of the maximum excess water pressure ratio in function of desaturated soil thickness.

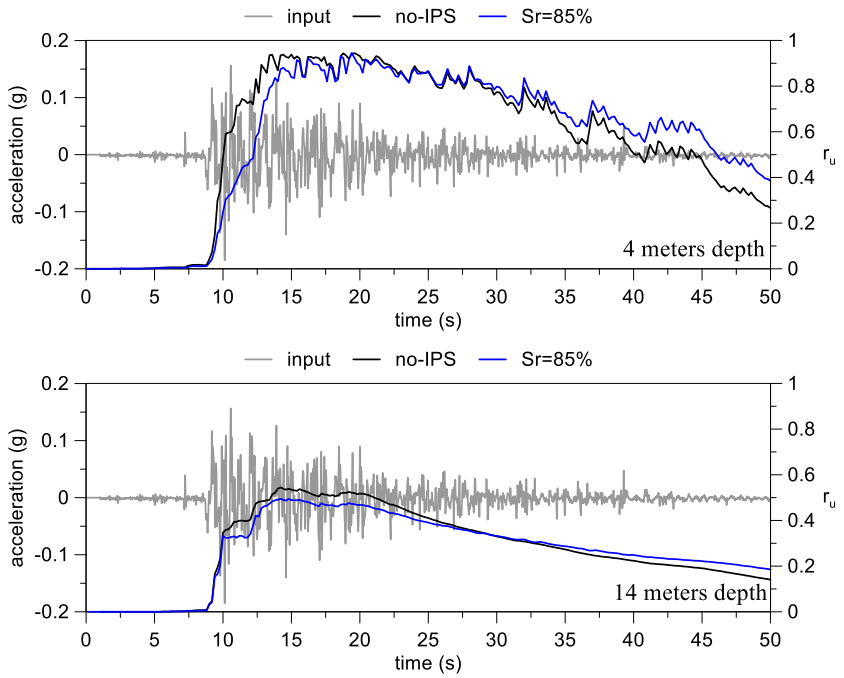

Figure 5.20. Time history of r_u in the point to 4 meters depth and 14 meters depth for the model with 12 meters thick of desaturated soil.

The ground surface settlements show slight differences with the values found for the free-field condition. However, smaller settlements were recorded for the system with IPS with 12 meters thick.

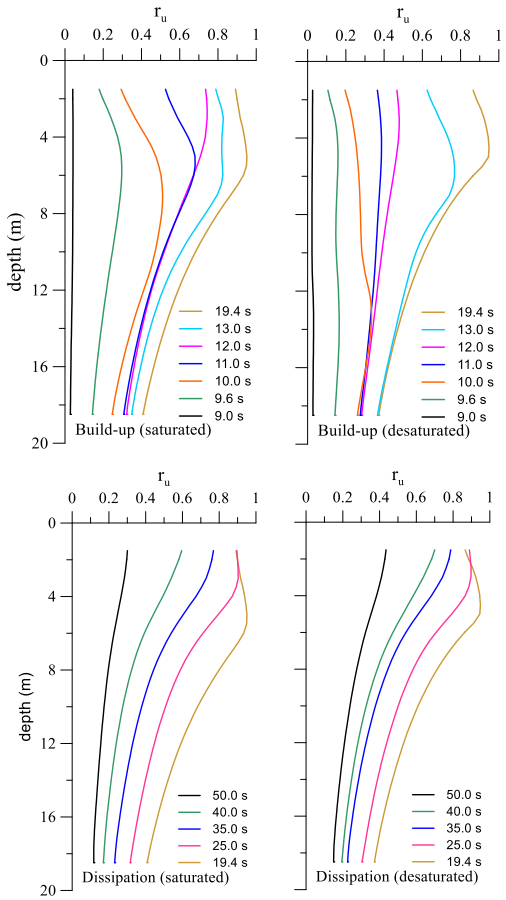

Figure 5.21. Vertical profiles of r_u for different time steps in the saturated model and desaturated one (Sr=0.85% - H=12).

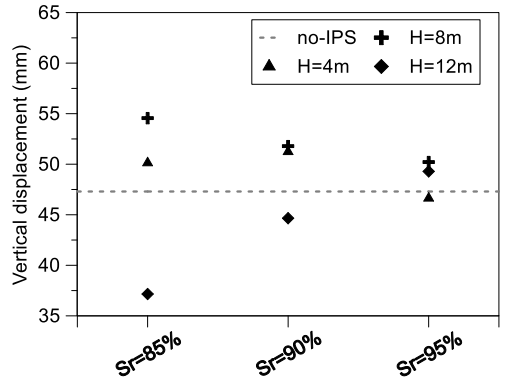

Figure 5.22. Settlements of the ground surface in function of thickness and desaturation degree of soil.

5.4.2 Analyses with permeability reduction in function of saturation degree

As seen in the previous section, in the following a parametric analysis was performed considering the effect that has the induced partial saturation on the permeability coefficient. Indeed, the presence of air babbles in the soil reduces the permeability so the excess pore pressure dissipation capability of soil system.

The relationship proposed by Van Genuchten (1980) was used to determine the permeability coefficient in function of saturation degree. This relationship was calibrated by the relative permeability coefficient obtained by the numerical back analysis of the M1_S1_IPS4_GM31 centrifuge test (Figure 5.23, red dot) and the parameters used are shown in Table 5.1.

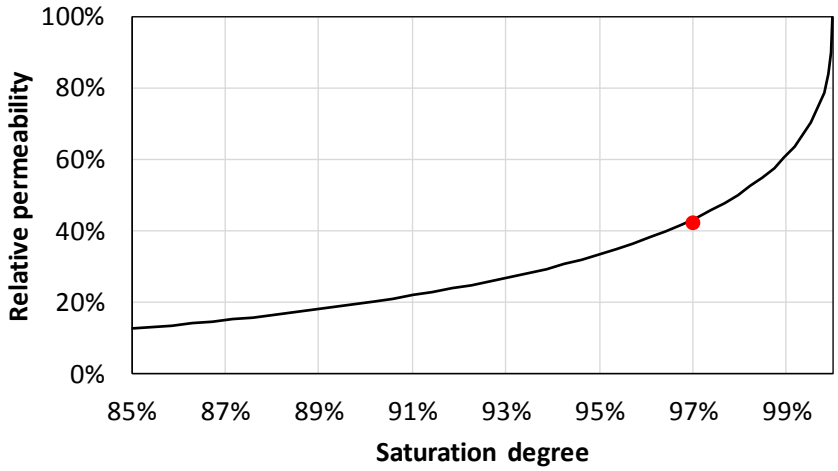

Figure 5.23. Settlements of the ground surface in function of thickness and desaturation degree of soil.

Table 5.1. Parameters for the relative permeability coefficient and saturation degree relationship (Van Genuchten, 1980).

ϑ_r	ϑ_s	g_a	g_n	g_c	g_l	k_{sat}
(-)	(-)	(1/m)	(-)	(-)	(-)	(m/s)
0.045	0.43	14.5	1.7	-0.41176	0.5	1.66E-03

Conversely to the previous parametric analysis, this analysis shows a significant increment of acceleration compared with no-IPS (Figure 5.24) only for the system with 12 meters treated soil thick.

This smaller amplification of the acceleration is ascribable to higher levels of maximum excess pore pressure reached in the soil profiles (Figure 5.25 and Figure 5.26) compared to the free-field condition (black line). This increment was due to the incapability of the soil system to dissipate the excess pore pressure during the shaking.

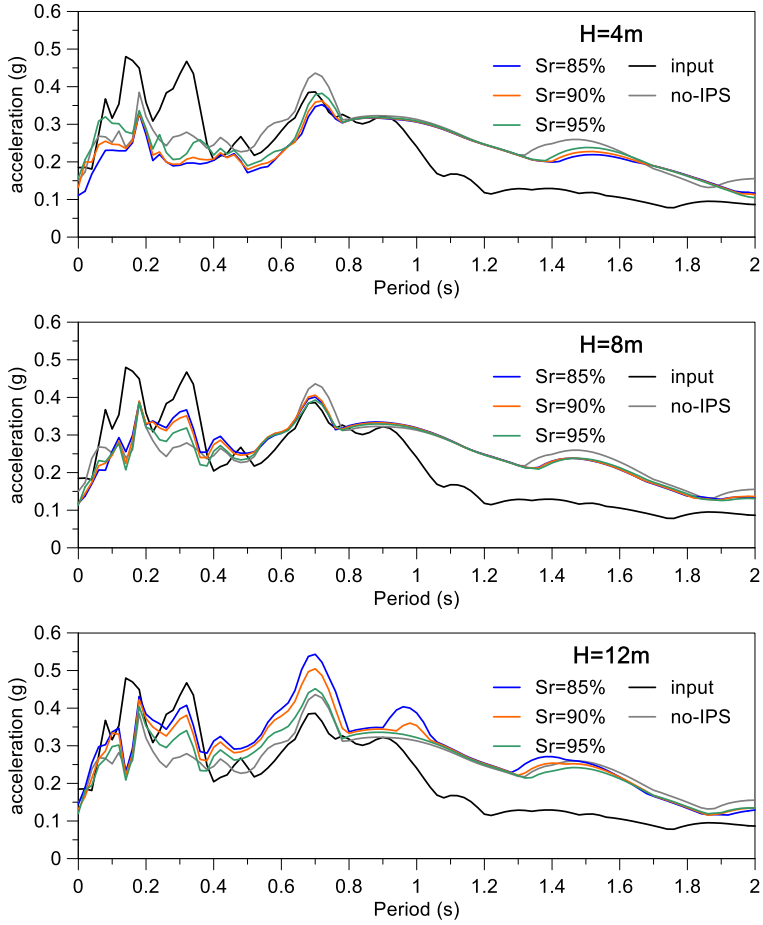

Figure 5.24. Response spectra on the ground surface for different thickness of induced partial saturation.

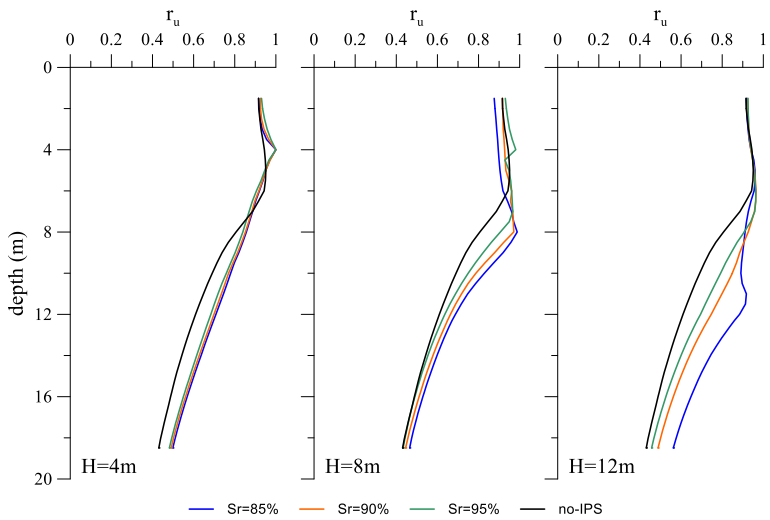

Figure 5.25. Distributions of the maximum excess water pressure ratio in function of saturation degrees.

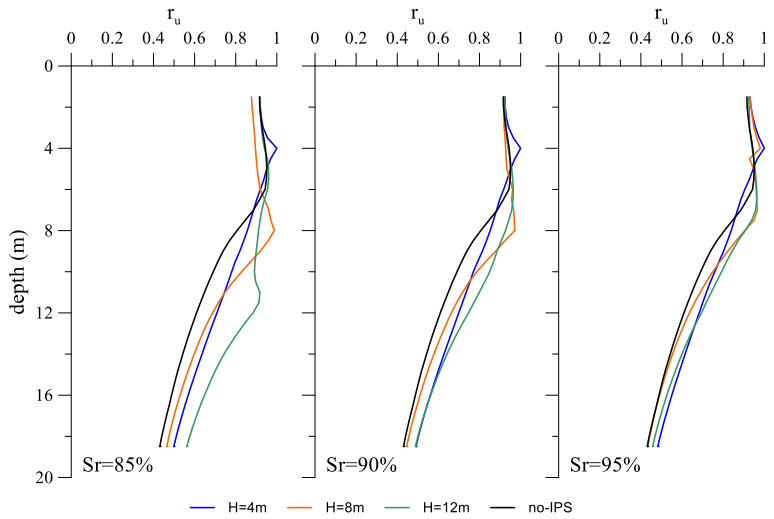

Figure 5.26. Distributions of the maximum excess water pressure ratio in function of desaturated soil thickness.

Figure 5.27 shows that all the IPS configurations reached a smaller ground surface settlement compared to the settlement measured without IPS (dashed line). This result was due to a lower capability of the soil system to dissipate the excess pore pressure during the shaking that led to smaller volumetric strains induced by the consolidation.

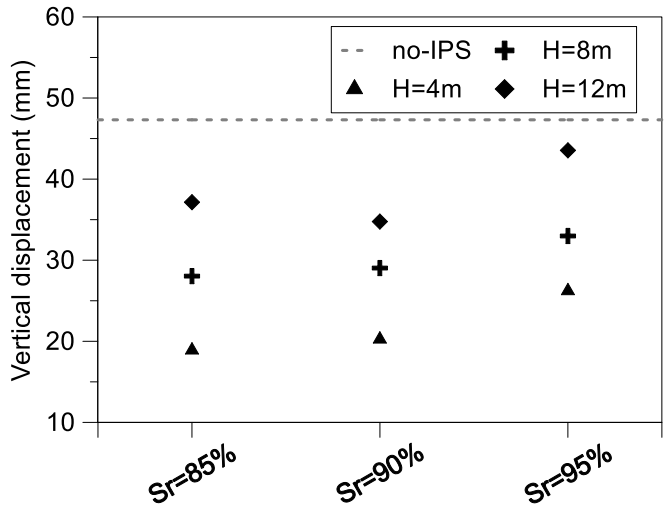

Figure 5.27. Settlements of the ground surface in function of the geometry of the horizontal drains.

5.5 Effects of saturation degree on the excess water pressure build-up

The previous parametric analyses prove that the IPS mitigation technique is not always useful for the liquefaction mitigation, but an accurate design of saturation degree is required.

The induced partial saturation (IPS) decreases bulk stiffness of the pore fluid reducing the pore water pressure build-up with an increase of liquefaction strength, so to understand the effect of IPS in practice way it is possible define some cyclic resistance curve in numerical way (Figure 5.28) changing the bulk stiffness of the pore fluid (K_f).

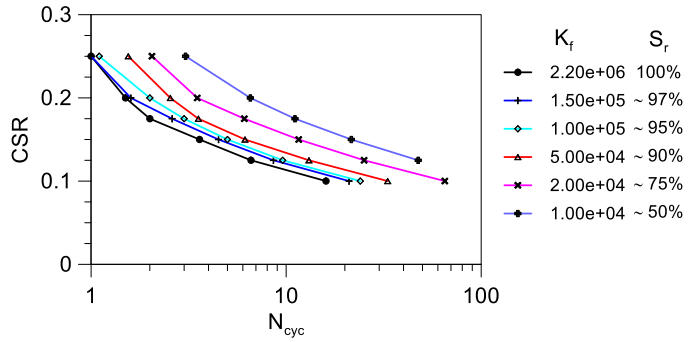

Figure 5.28. Cyclic strength curves for IPS.

In Figure 5.28 are reported six curves and the lower boundary is represented by the curve in saturated condition (black line). As suggested by Rebata-Landa and Santamarina (2012), each value of K_f corresponds to a degree of saturation as function of the absolute water pressure surrounding the bubble (so it is a function of the depth from the water table). In the following table are shown the value of saturation degree for the values of K_f used for the cyclic strength curves:

Table 5.2. Mean degree of saturation corresponding to K_f at 5 meters below the water table.

z_w [m]	u_{abs} [Pa]	r_c [m]	K_f [kPa]	Sr [-]
5.00	150000	1.2E-08	150000.00	0.98
5.00	150000	1.2E-08	100000.00	0.96
5.00	150000	1.2E-08	50000.00	0.92
5.00	150000	1.2E-08	20000.00	0.80
5.00	150000	1.2E-08	10000.00	0.60

Table 5.3. Mean degree of saturation corresponding to K_f at 10 meters below the water table.

z_w [m]	u_{abs} [Pa]	r_c [m]	K_f [kPa]	Sr [-]
10.00	200000	9E-09	150000.00	0.97
10.00	200000	9E-09	100000.00	0.95
10.00	200000	9E-09	50000.00	0.90
10.00	200000	9E-09	20000.00	0.74
10.00	200000	9E-09	10000.00	0.47

Table 5.4. Mean degree of saturation corresponding to K_f at 15 meters below the water table.

z_w [m]	u_{abs} [Pa]	r_c [m]	K_f [kPa]	Sr [-]
15.00	250000	7.2E-09	150000.00	0.96
15.00	250000	7.2E-09	100000.00	0.94
15.00	250000	7.2E-09	50000.00	0.87
15.00	250000	7.2E-09	20000.00	0.67
15.00	250000	7.2E-09	10000.00	0.33

It is worth note that a lower saturation degree is required to achieve the same value of K_f with depth. The saturation degrees corresponding to the same K_f defer largely with pore water pressure for lower saturation degree. This aspect highlights that an optimised design of a treatment with induced partial saturation requires a variable saturation degree with depth.

Evaluating the effect of the input motion in terms of CSR (Seed and Idriss, 1971) the original input motion is represented in the Figure 5.29 with a blue dot and its vertical profile is shown in Figure 5.30. The position of this point is very high in the chart N_{cyc} - *CSR* and far from the resistance curves. Therefore, an application of IPS in this case could be require very low saturation degree that is beyond the aim of this mitigation technique.

A scaled input motion was used to prove the correspondence between the simplified approach used in the evaluation of liquefaction susceptibility, proposed in the literature, and the fully coupled numerical analyses. This input was created scaling the original input motion of the centrifuge test with horizontal drains (M1_S1_HD1&2_GM31) by a factor equal to 2.

The CSR evaluate at the ground surface and its vertical profile are shown in Figure 5.29 (red point) and Figure 5.30 (green line) respectively.

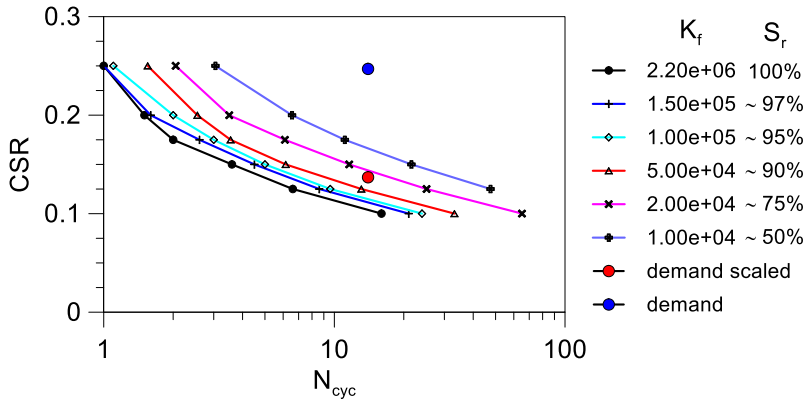

Figure 5.29. Cyclic strength curves for IPS with CSR points for original input and scaled one.

Noteworthy that the point is between two curves with reduced K_f, so the liquefaction mitigation adopting the IPS is possible. The vertical profiles show that the liquefaction was achieved within 10 meters from the ground surface. A fully coupled numerical analysis was

performed in undrained condition congruently with the condition in which cyclic strength lines were realised.

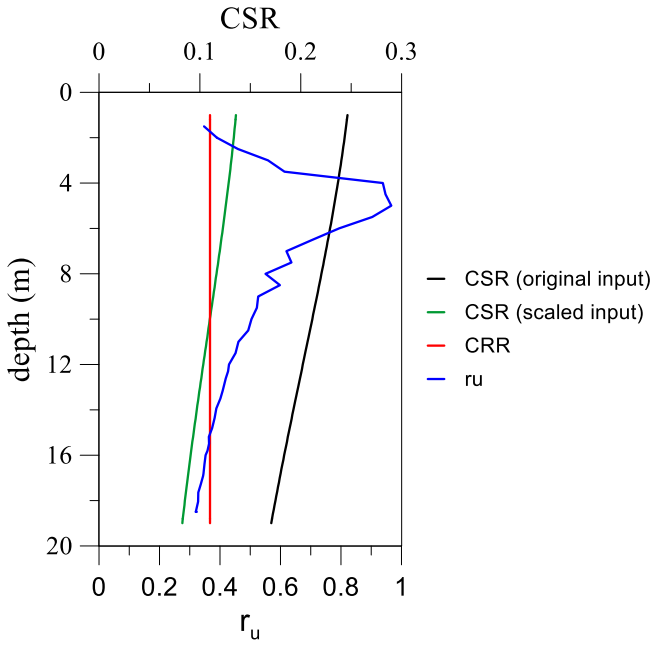

Figure 5.30. Vertical profiles of CSR.

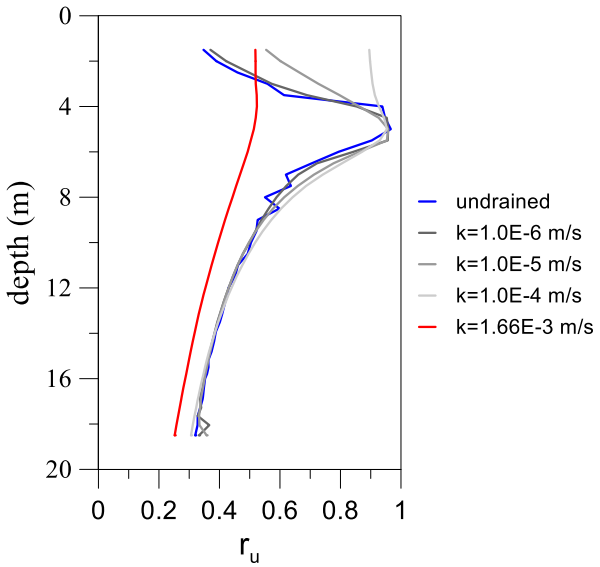

Figure 5.31. Vertical profiles of r_u comparison between undrained model and seepage models.

The vertical profile of r_u for the numerical analysis (Figure 5.30, blue line) shows that the liquefaction happens between 4 and 6 meters depth and high values were reached in the range where safety factor (FS=CRR/CSR) is lower than 1.

The assumption of an undrained condition in the simplified approach can be led to an inaccurate determination of the soil layers subjected to the liquefaction. Generally, this approach is largely conservative. This depends on the capability of the system to dissipate the excess water pressure during the earthquake, so it is a function of consolidation coefficient. A comparison between different vertical profiles of r_u for different permeability coefficients are shown in Figure 5.31.

The increment of the permeability coefficient modifies significantly the profiles of r_u. Indeed, a high permeability coefficient could avoid the liquefaction triggering (Figure 5.31, red line), whereas for low permeability coefficients , in this case equal to 1.0E-6 m/s (deeper grey line), the profile could be equal to the undrained one (black line) , whereas an increase of permeability induces higher value of r_u in the shallowest part of the soil profiles. This effect is ascribable to a redistribution of the excess water pressure in the soil and the soil layers that reach the liquefaction first represents a source of excess water pressure for the shallower soil layers that could reach the liquefaction by an upward water flow. Hence, the hypothesis of undrained condition considered in the simplified approach is conservative in presence of soils with high permeability coefficient. Obviously, this result is dependent on the amplitude and frequency of the input motion.

The effect of the redistribution of excess water pressure is highlighted in Figure 5.32 where the soil at 5 meters depth reach the liquefaction and holds this status for a long time inducing an upward water flow that leads the above layers to liquefy (red arrow). The presence of a water flow from the liquefied soil to the surrounding soil is highlighted by the vertical profiles of groundwater head (Figure 5.32). In the soil layer placed at 6 meters depth in correspondence of 16.2 seconds a water flow had an upward and downward vertical component. This prove the existence of a redistribution of excess water pressure in the soil domain.

Vertical profiles of r_u for different permeability coefficient in presence of a low permeable soil crust are shown in Figure 5.33. This upper layer modifies the distribution of the r_u in the layers included between the top surface and the liquefied soil leading to higher value of excess water pressure than the profile without “impervious” crust. The presence of upper impervious soil realises an undrained system, however an internal redistribution of excess water pressure avoids the liquefaction of the soil except for a very thin soil layer at the interface between liquefiable soil and crust. So, the hypotheses of simplified approach are correct only for systems either with low permeability coefficient ($k \leq$ 1E-6 m/s, in this case) or for soil system largely interlayered by low permeable soils.

The redistribution of the excess water pressure in the soil is very evident in this case. A flow with upward and downward component is shown in Figure 5.34 starting from 13.8 seconds at about 6 meters depth.

Following the simplified approach, the mitigation technique has to be applied in the first 10m of the soil profile where the safety factor is lower than 1. The position of red point in Figure 5.29 suggests for the treatment of soil with IPS a degree of saturation such to achieve a K_f included between 5.0E4 and 2.0E4 kPa.

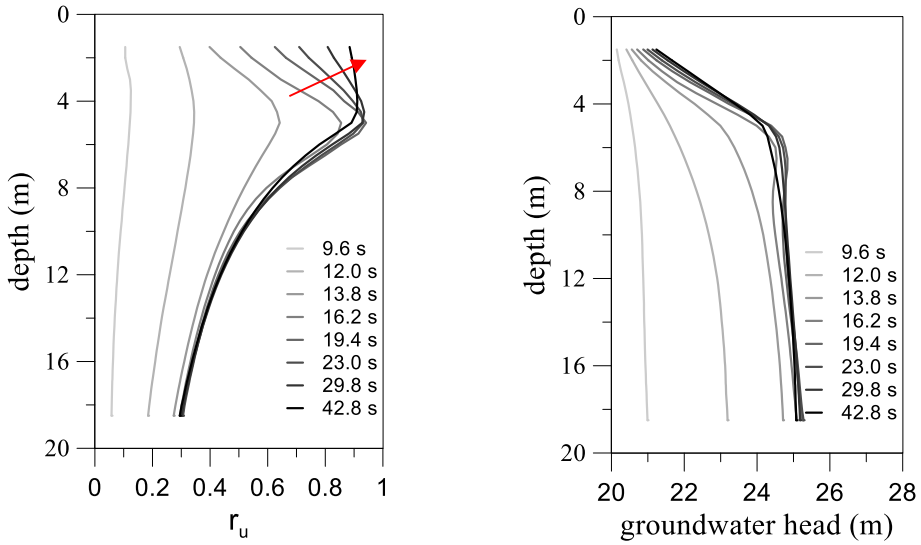

Figure 5.32. Vertical profiles of r_u and groundwater head in the time for the model with permeability coefficient equal to 1.0E-4 m/s.

The results of numerical analyses with K_f equal to 5.0E4 and 2.0E4 kPa, respectively, are shown in Figure 5.35. Liquefaction conditions were not achieved in the desaturated layer for both desaturated models indicating that the desaturation has an effectiveness as liquefaction mitigation technique. Moreover, the use of liquefaction resistance curves represents a conservative design approach.

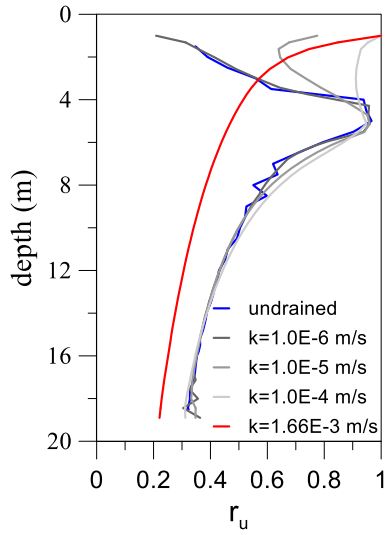

Figure 5.33. Vertical profiles of r_u with impervious upper surface for different permeability coefficient.

It is worth noting that the presence of the treated soil layer induces higher level of r_u in the deeper untreated soil layers than in the untreated soil profile. This effect follows from a

smaller loss of the stiffness and strength of the treated layers during the shaking that induces a dynamic overload on the underlying soil.

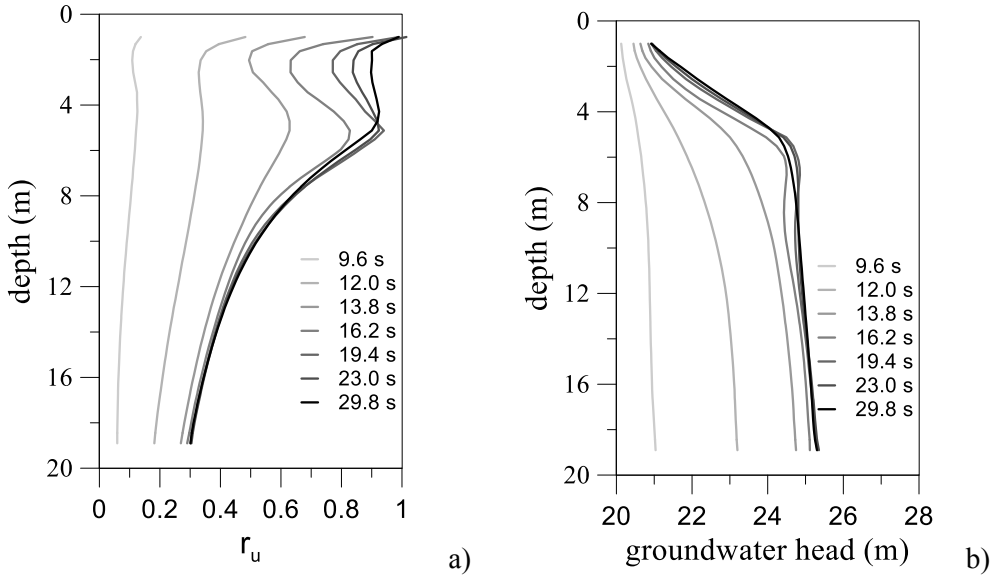

Figure 5.34. Vertical profiles of r_u and groundwater head in the time for the model with impervious upper surface and the permeability coefficient equal to 1.0E-4 m/s.

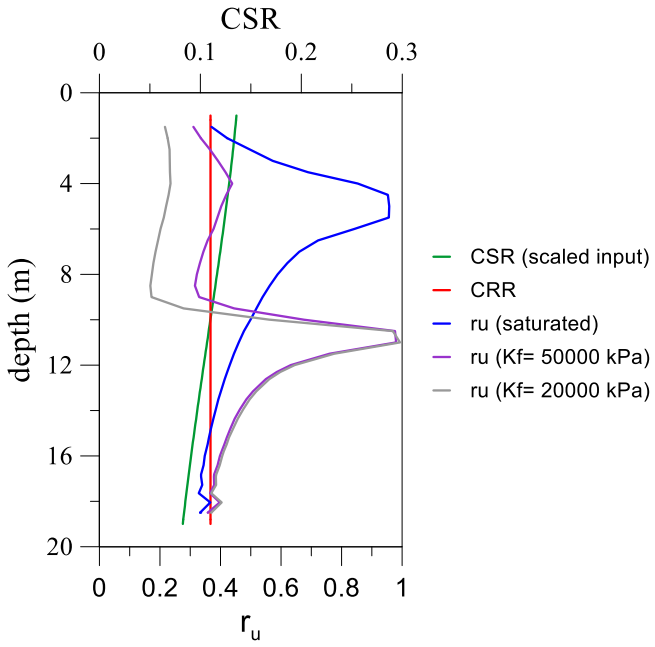

Figure 5.35. Vertical profiles of r_u comparison between fully saturated model and desaturated models.

5.6 Effects on the building of induced partial saturation extension

In the following section the effects of induced partial saturation on the simple structure seen before were computed by a parametric analysis. The effects on the structure and soil are shown in terms of acceleration spectra, vertical profiles of excess pore pressure ratio, displacements and tilts of the structure.

The structure introduced the horizontal extension of treated soil as a new geometric variable. In the following parametric analysis three different horizontal extensions were considered:

- Indefinite extension, where the treated soil was extended for whole width of the model;
- "3B" extension, in which the treated soil was extended on both outsides of the structure for a dimension equal to the track of the structure (B);
- "B" extension, in which the treated soil was only below the structure for whole its track.

Two different thicknesses of the treated soil equal to "B" and "2B" were assumed, where B is equal to 6 meters to define the absolute dimensions of the system (Figure 5.36).

The chosen dimensions are able to define the following aspect ratios of the treatment (B/H): 0.5; 1.0; 1.5; 3.0.

Two different bulk stiffness of the pore fluid were considered:

- K_f = 50000 kPa that represents a mean saturation degree equal to 90% within 20 meters depth;
- K_f = 20000 kPa that represents a mean saturation degree equal to 75% within 20 meters depth.

The results of the parametric analysis in terms of acceleration spectra are shown in Figure 5.37. All the geometry of the treated soil and both saturation degree led to a substantial constancy of acceleration spectra except for the indefinite extension with H equal to 2B. The same result was recorded on the roof of the structure (Figure 5.38).

The effects in terms of excess pore pressure ratio are shown in Figure 5.39 in correspondence of the section A-A placed below the foundation beam of the structure. The profile in free-field condition show than the liquefaction was achieved, but only the presence of the structure reduced significantly the amount of r_u (no-IPS, grey line). The presence of desaturated soil layer reduced further the excess pore pressure ratio but with an increment in correspondence of the interface between the treated soil and natural one. This effect, as seen in the previous cases, is due to the increase of the shear loads induced by the presence of the treated soil that showed a smaller drop of stiffness and strength producing a change of impedance that induced larger shear stresses in the underlying untreated soil. This effect is more evident for the thin treatment (H = B).

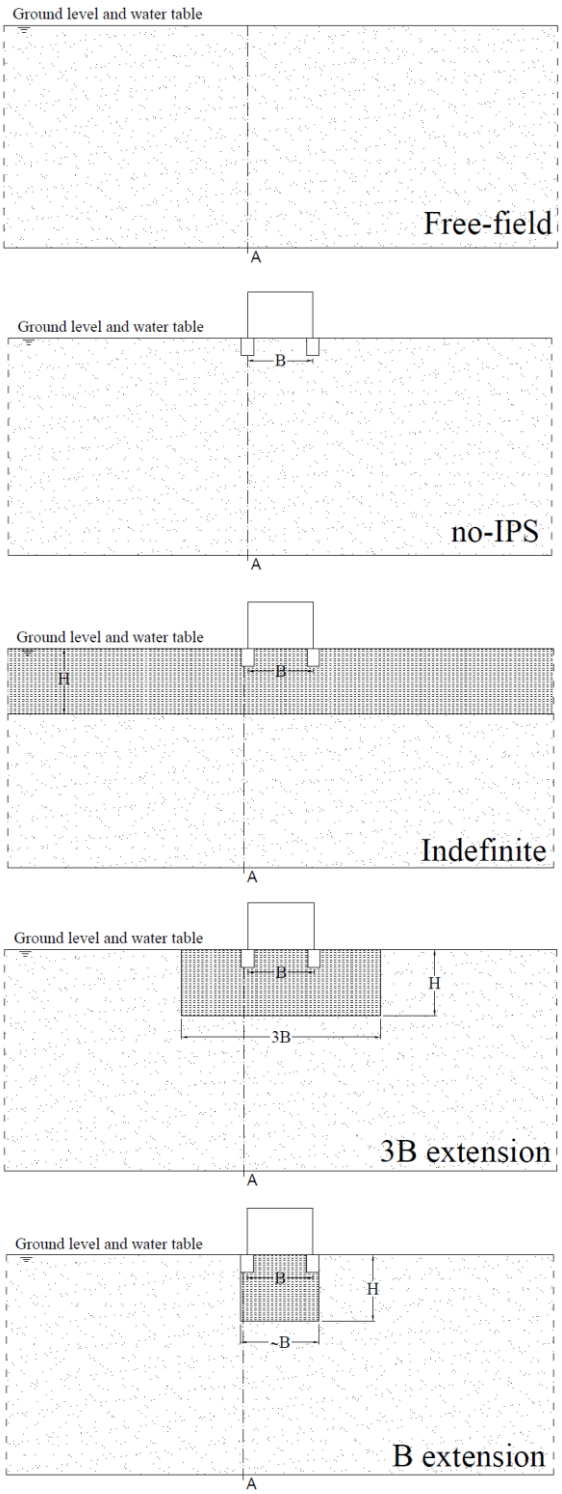

Figure 5.36. Geometry of induced partial saturation (IPS) below the structure.

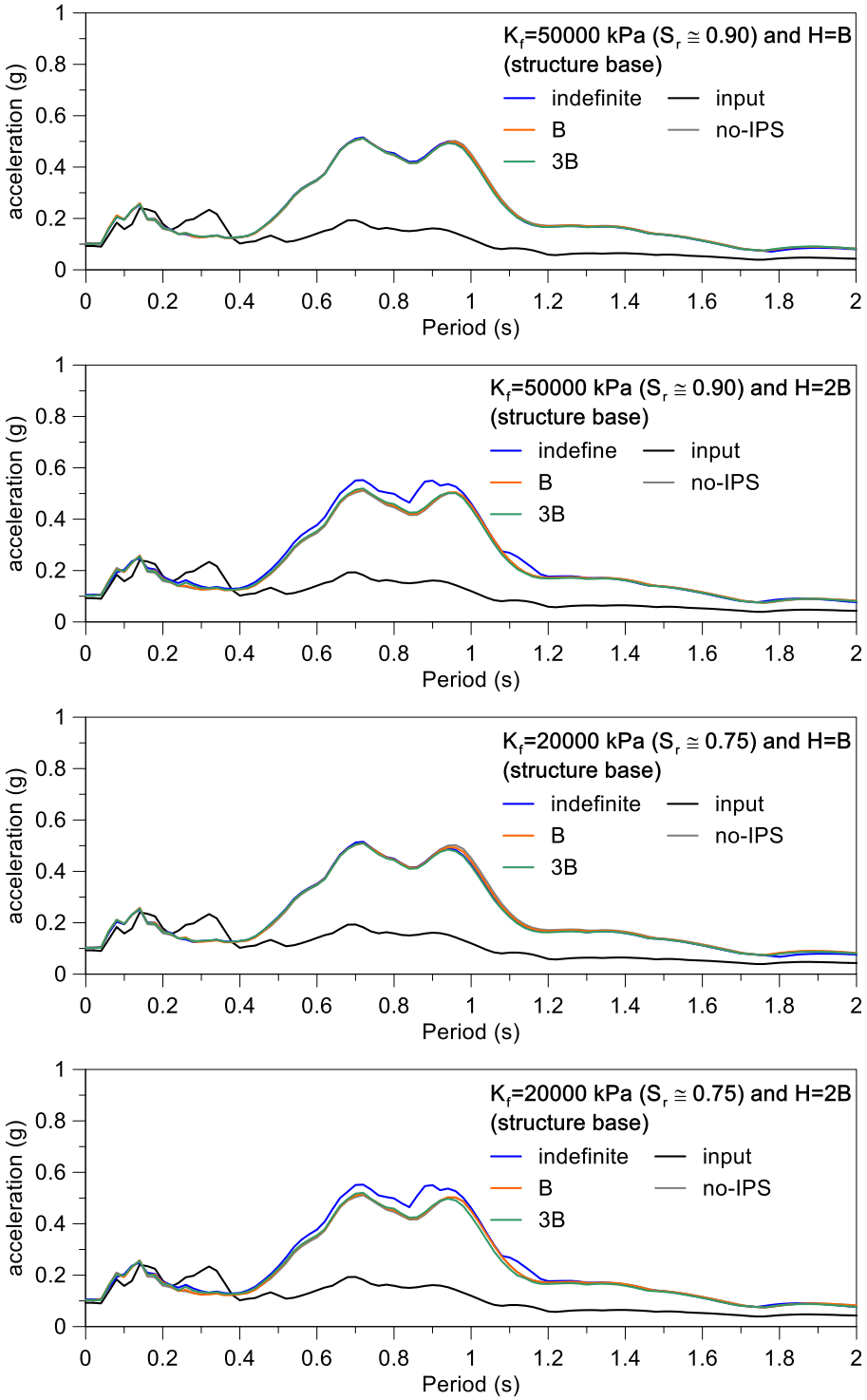

Figure 5.37. Response spectra on the structure base for different IPS extensions.

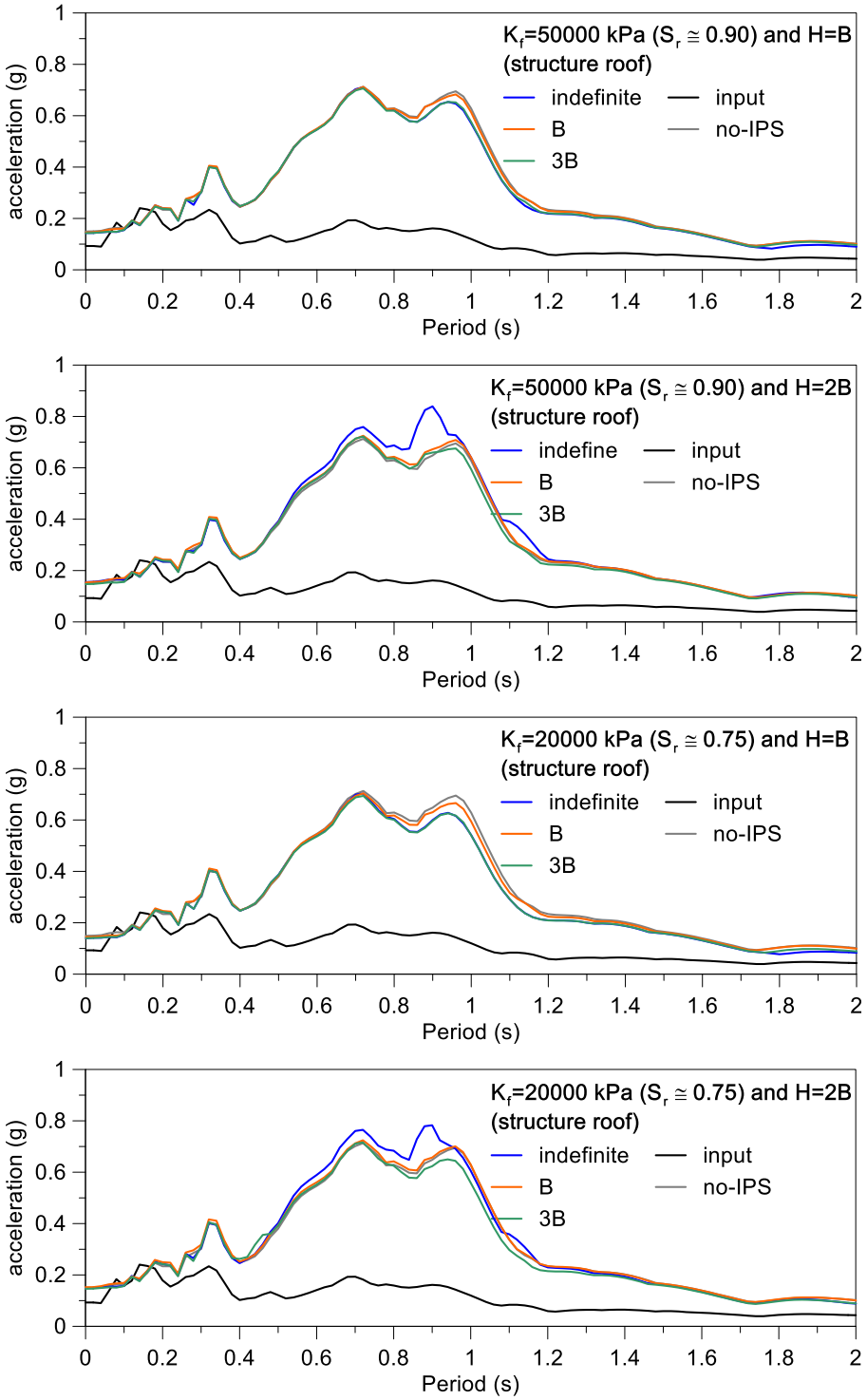

Figure 5.38. Response spectra on the structure roof for different IPS extensions.

The effect of the fluid bulk stiffness reduction is less evident in thin treatment than in the thicker one, indeed, the difference between K_f equal to 50000 kPa and 20000 kPa is evident in the IPS with H equal to 2B. The latter thick led to a larger reduction of excess pore pressure ratio in the treated soil.

The profiles show that the treatment with extension equal to 3B led to a distribution of excess pore pressure close to the indefinite extension one, whereas the extension equal to B led to a higher r_u immediately below the foundation beam.

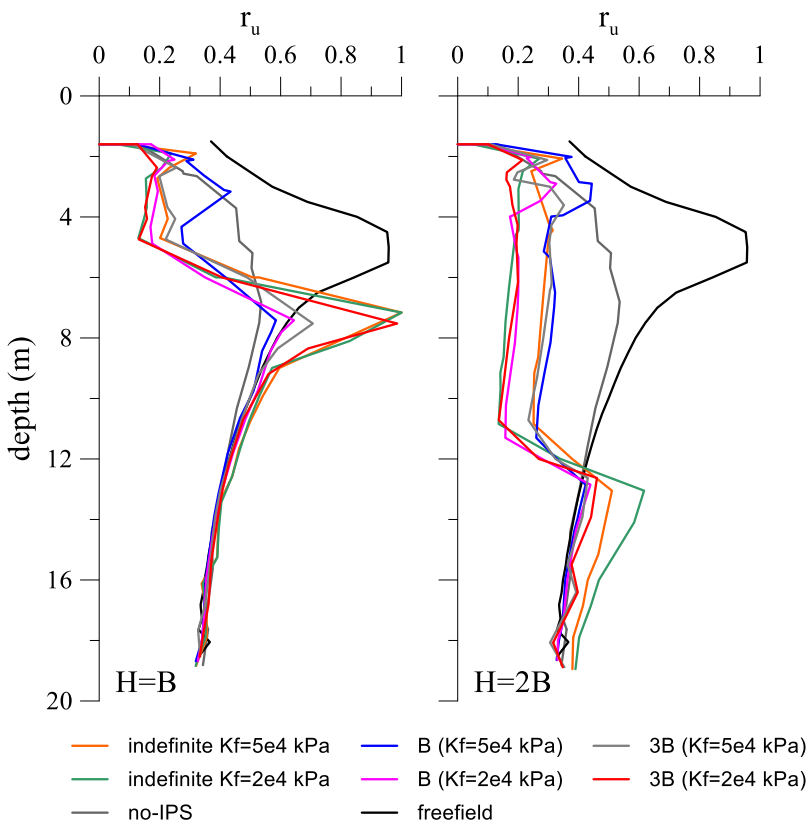

Figure 5.39. Distributions of the excess water pressure ratio in function of different geometry of IPS.

Figure 5.40 show the maximum settlements of the structure after the total dissipation of the pore pressure that have been developed during the shaking. The introduction of the induced partial saturation, with the geometries analysed, led to a decrease of the settlement compared with structure but without treatment (no-IPS, dashed black line). The same results were recorded for the tilt of the structure (Figure 5.41).

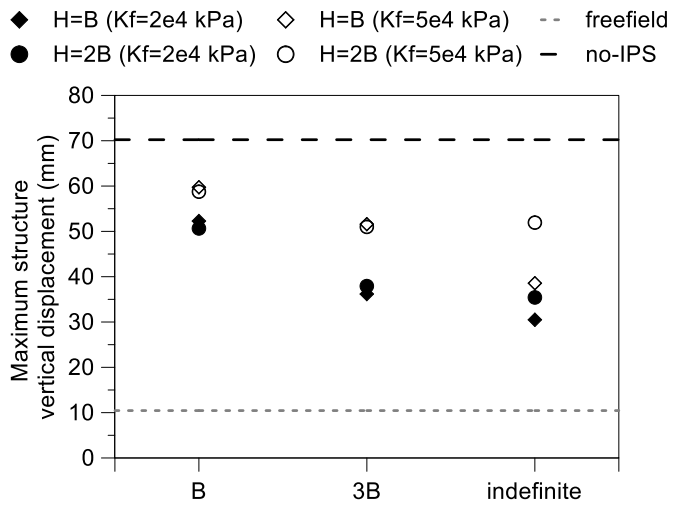

Figure 5.40. Maximum settlements of the structure in function of different geometry of IPS.

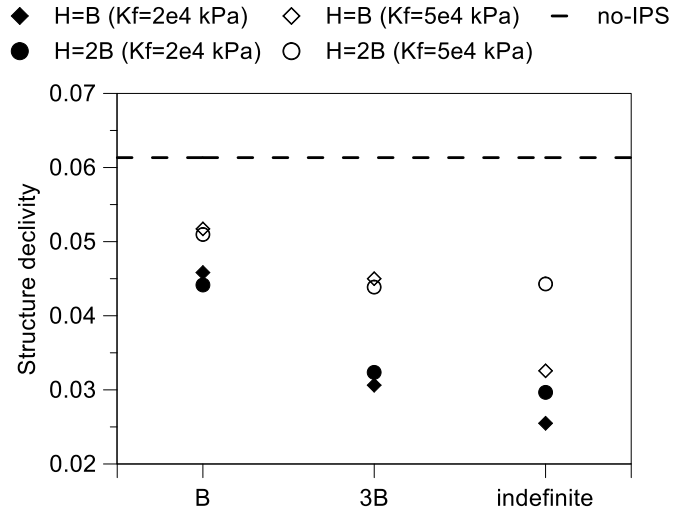

Figure 5.41. Declivity of the structure in function of the geometry of different geometry of IPS.

6 DESIGN OF MITIGATION TECHNIQUES

6.1 Horizontal drains

As previously seen, horizontal drains are extremely efficient to mitigate liquefaction risk. This technique can be used where conventional vertical drains cannot be applied, like beneath existing structures. The design goal in this case is an appropriate spacing among drains, the depth of the drains and the number of layers. The usual assumptions of radial consolidation around drains, stemming from the original assumption of an infinite number of vertical drains, may not be appropriate for the horizontal ones, since the latter are generally arranged in few rows at a shallow depth.

The insertion of drains into the liquefiable soil modifies the hydraulic boundary conditions accelerating the consolidation process during seismic shaking, with a beneficial reduction of soil susceptibility to liquefaction. Some design methods based on the solution of radial consolidation are already available in literature to assign drains spacing for vertical drains (Bouckovalas et al., 2009). Following the same approach, in this section a design method for horizontal drains is proposed. This type of drains can be installed by directional drilling (Allouche et al., 2000) directly underneath existing structures where there is no alternative ground improvement technology available to tackle liquefaction risk. This is a very promising evolution, whose use should not pose critical installation problems, at least as long as the horizontal drains are shallow (not deeper than 10 m), and their diameter is not very large (not more than 30 cm). The design of seismic horizontal drains is similar but not identical to that of the vertical one. Two main differences exit:

- being the drains horizontal, radial consolidation around each drain occurs in the vertical plane and may be influenced by the presence of a free-drainage ground horizontal surface or layer at a close distance.
- the hypothesis of an infinite number of drains implicitly assumed in the design of vertical drains is completely unrealistic because only two, or at the most three, lines of drains may be placed on site.

Starting from these considerations, a design approach is herein proposed for the case of three rows of horizontal drains placed in a shallow liquefiable layer for both the cases of free drainage at ground level or impermeable crust.

6.1.1 Analytical solution

The pore pressure increments due to seismic excitation are caused by the volumetric – distortional coupling of soil constitutive behaviour. Advanced constitutive models, like UBCSAND and PM4SAND, should be used to simulate the complex coupled hydro-mechanical consolidation process. The complexity of these constitutive models (or, better, the difficulty of calibrating them in usual class A prediction problems) precludes their use in common practice and simplifications are introduced to evaluate the seismically induced pore pressure increments. A simple uncoupled approach can be adopted to design a drainage

system if the aim it is the reduction of excess water pressures (Fasano et al., 2019). The consolidation process is then usually solved in the hypothesis of Terzaghi-Rendulic who consider the invariance of the total stress and the incompressibility of the pore fluid (Rendulic, 1936). In plane strain conditions, it reads:

$$\frac{k}{\gamma_w}\left(\frac{\partial^2 u}{\partial x^2}+\frac{\partial^2 u}{\partial y^2}\right)=m_v\frac{\partial u}{\partial t} \qquad (6\text{-}1)$$

where x and y are the spatial coordinates in the plane, k is the hydraulic conductivity (assumed isotropic), u is the excess pore pressure and m_v is the volumetric compressibility coefficient. The hypothesis of isotropic permeability is reasonable in the case of sandy soils, interested by liquefaction issues. As previously mentioned, in the case of ongoing cyclic loading, the quantification of u is a very complex problem, being it the resultant of concurrent dissipation (due to consolidation) and increment (due to cyclic shaking). A fundamental contribution to the solution was given by Seed et al. (1975), who proposed to write eq. (6-2(6-1) modifying its right-hand term as the algebraic sum of the change ∂u taking place in the time interval, ∂t, because of the consolidation process, plus an accumulation term related to the ongoing seismic shaking. By so doing, eq. (6-1) becomes

$$\frac{k}{\gamma_w}\left(\frac{\partial^2 u}{\partial x^2}+\frac{\partial^2 u}{\partial y^2}\right)=m_v\left(\frac{\partial u}{\partial t}-\frac{\partial u_g}{\partial N}\frac{\partial N}{\partial t}\right) \qquad (6\text{-}2)$$

where u_g is the pore pressure increment generated during shaking and ∂N is the number of cycles taking place in the time interval, ∂t. Within this framework, that is by far the most popular one adopted to study the dynamic consolidation of soils, different choices can be done to quantify the cyclic pore pressure build up $(\partial u_g/\partial N)$. Seed et al. (1975) proposed to this aim a function of the ratio N_{eq}/N_l between the seismic action, quantified through the number of equivalent cycles, N_{eq}, and the number of cycles required to cause liquefaction, N_l. Analysing the experimental results on shaking table by Harada et al. (2006), however, Bouckovalas et al. (2009) observed that, for very small values of the ration N/N_l, the tangent the pore water pressure build-up curve is basically constant for a given soil, varying only as a function of soil fabric. In order to cope with this experimental evidence, they proposed a different equation for $\partial u_g/\partial N$:

$$\frac{\partial u_g}{\partial N}=\frac{\sigma_0'}{\pi A N_l}\frac{1}{\left(\frac{t}{t_d}\frac{N_{eq}}{N_l}\right)^{1-\frac{1}{2A}}\cos\left(\frac{\pi}{2}r_u\right)} \qquad (6\text{-}3)$$

where σ_0' is the initial vertical effective stress, A is an empirical parameter affecting the shape of the accumulation curve, t is the time variable, t_d is the significant duration of seismic shaking, r_u is the excess pore pressure ratio (u_g/σ_0'). In the hypothesis of a linear dependency of the number of cycles on time, it can be written that:

$$\frac{\partial N}{\partial t}=\frac{N_{eq}}{t_d} \qquad (6\text{-}4)$$

Hence, by substituting (6-3) and (6-4) in (6-2), and using dimensionless variables, the following form of the equation of consolidation is obtained:

$$T_{ad}\left(\frac{\partial^2 r_u}{\partial\left(\frac{x}{d}\right)^2}+\frac{\partial^2 r_u}{\partial\left(\frac{y}{d}\right)^2}\right)=\frac{\partial r_u}{\partial\left(\frac{t}{t_d}\right)}-\frac{N_{eq}}{\pi A N_l}\frac{1}{\left(\frac{N_{eq}}{N_l}\frac{t}{t_d}\right)^{1-\frac{1}{2A}}\cos\left(\frac{\pi}{2}r_u\right)} \qquad (6\text{-}5)$$

where d is the drain diameter and T_{ad} is a dimensionless time factor defined as:

$$T_{ad}=\frac{t_d k}{d^2 m_v \gamma_w} \qquad (6\text{-}6)$$

in which γ_w is the specific weight of water. T_{ad} is a non-dimensional time, expressed as a function of a given drain diameter (d) and of a specific site seismic hazard through the significant seismic duration (t_d).

6.1.2 Numerical model

Eq. (6-5) has been used to solve the dynamic consolidation process considering the existence of horizontal drains, with the final goal to draw simple design charts to assign the spacing among them.

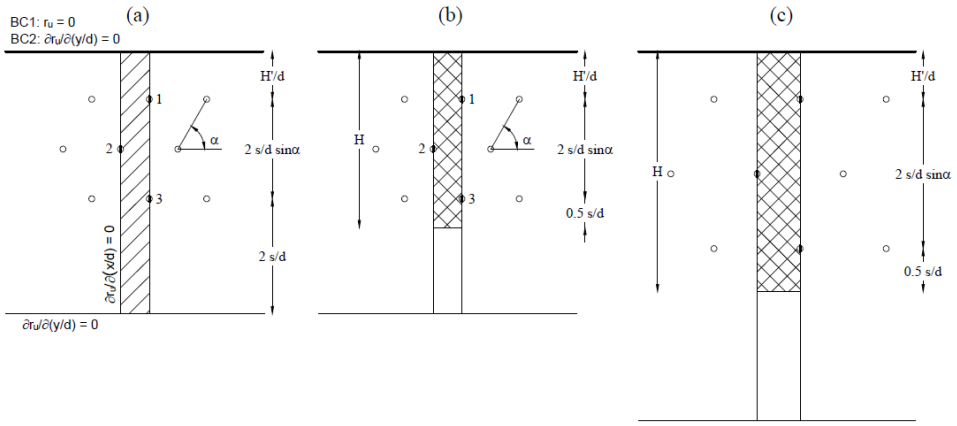

Figure 6.1. (a) Numerical model domain, (b) numerical solution domain, and (c) numerical solution domain with increased s/d.

The geometrical layout of the problem considered in this work is shown in Figure 6.1. The model is representative of a homogeneous layer of liquefiable soil. In the domain, three rows of drains (each one made of an infinite number of constantly spaced drains) are deployed in a staggered arrangement ('*quincunces*'). H' is the distance from the upper boundary to the upper row of drains. As shown in Figure 6.1, the layout is defined by the spacing between the drains, s, and the angle α (assumed equal to 60°, as typical in this configuration). The numerical analyses have been carried out considering all the dimensions

normalized to the inner diameter of the drains *d* (Figure 6.1a). The lower boundary, assumed impervious, is located at a depth of *2s/d* from the lower row of drains. Its position has been chosen far enough from the drains not to affect the solution. Taking advantage of symmetry, the analyses have been carried out with reference to a numerical domain of reduced area (Figure 6.1a). The left and right boundaries of such a domain are defined by two impervious planes of symmetry (Figure 6.1a).

The numerical solution of the problem was performed with a free seepage upper boundary (BC1) at atmospheric pressure and also with an impervious one (BC2), the latter representing the presence of a less permeable layer (made of silt or clay) upon the liquefiable one. Along the impervious vertical sides of the model, the drains are modelled as segments with zero excess pore water pressure. Rigorously, this hydraulic boundary condition should be applied on the inner surface of the drain and some authors showed that drain hydraulic resistivity is not negligible in calculations, since it can affect the consolidation process (Onoue, 1988). However, horizontal drains are likely made of microperforated pipes, and thus their longitudinal hydraulic resistivity is negligible compared to the cross-sectional permeability of the pipe, which is higher than that of the soil. In the limiting case of drain permeability equal to that of the soil, the circular ring of the pipe behaves (hydraulically) as a soil layer, and the hypothesis of zero excess pore water pressure applied on the inner surface of drain holds true. If drain equivalent permeability is higher than that of soil, then the hypothesis is obviously conservative.

Even though the solution of the consolidation process is obtained in the whole numerical model domain, the effect of excess pore water pressure dissipation due to the drains is evaluated only in the part of it having thickness *H* from the upper boundary, being $H=(H'/d+2s/d\cdot\sin\alpha+0.5\cdot s/d)$ (Figure 6.1b). This assumption stems from the observation that, at a depth equal or higher than *0.5 s/d* below the lower drains ($z>H$), the pore pressure increments are not affected by the presence of the drains, as shown in the following. These assumptions infer that by changing the normalized spacing *s/d* among the drains the geometrical features of both the numerical model and the solution domains are modified (Figure 6.1c).

The problem was solved with an implicit finite difference method (Crank and Nicolson, 1947; D'Acunto, 2011) discretizing the domain with a rectangular grid. Spatial variables were related to drain diameter to simplify the design approach; as already pointed out, drain diameter is limited by technology, thus it is easy to assign, and, by consequence, H'/d can be determined. Each drain segment was discretized by six nodes. By solving the consolidation problem, it is possible to know the excess pore pressure ratio in each point of the model grid, at a dimensionless time, t/t_d. The problem has been solved in a parametric way by varying the geometrical layout (spacing *s/d* and distance of the upper surface, H'/d), the soil properties (i.e. the volumetric compressibility coefficient, m_v, and the coefficient of hydraulic conductivity, k) and the parameters defining the seismic action (T_{ad}, N_{eq}/N_l).

6.1.3 Numerical results

Once the numerical problem is solved, it is possible to know the excess pore water pressure ratio in each point of the domain. The effect of the horizontal drains on the

distribution of r_u in the domain is shown by contours in Figure 6.2 with BC1 upper boundary condition. It can be observed a high gradient of r_u around drains that is independent on *H'/d* for the two deeper rows. The effect of the first row of drains is instead dependent on the distance from the upper boundary.

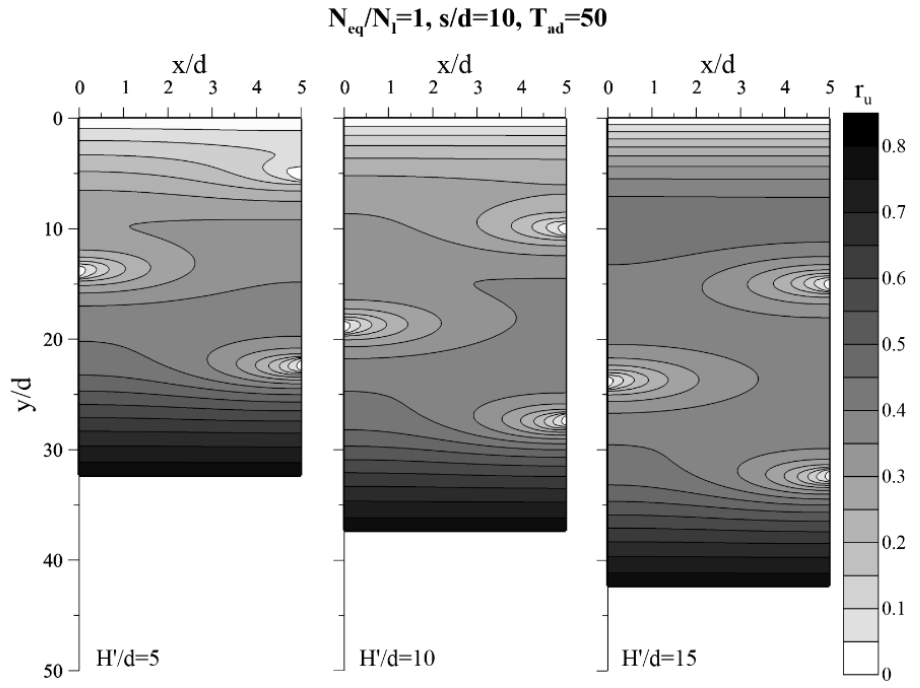

Figure 6.2. Contours of excess pore pressure ratio in the solution domain at the end of shaking with N_{eq}/N_l = 1, s/d = 10, and T_{ad} = 50.

When *H'/d* is lower than *s/d*, the effect of the upper boundary is predominant on the effect of the drain, lowering its efficiency. When *H'/d* is equal to *s/d*, there is almost no overlap between the upper boundary and the first row of drains, and its efficiency is enhanced; this is evident in the contour for *H'/d=5*, where the distribution of r_u in the upper part of the domain is similar to the distribution of *H'/d=10*. Finally, if *H'/d* is higher than *s/d*, the drains act almost as a boundary condition, with a lower excess pore pressure ratio, on the upper part of the domain at a distance from the first row almost equal to half of the spacing. In the last case, three areas can be distinguished: an upper part, where the gradients of excess pore pressure ratio are almost vertical, and the behaviour is almost one-dimensional; a middle part, between drains, where r_u is almost constant except for the area surrounding the drains, where the gradients are much higher; the lower part, where the effect of drains vanishes and again the gradients become vertical. When *H'/d* is lower or equal to *s/d*, the first two areas are partially overlapped. The contours also show that the excess pore water pressure ratio on a horizontal plane is almost constant except for the depths corresponding to the rows of drains, as already pointed out.

The average and maximum excess pore pressure ratios, respectively $r_{u,mean}$ *(t, y/d)* and $r_{u,max}$ *(t, y/d)*, were calculated for each depth to quantify the effect of drains. The vertical profiles of these quantities at the end of the analysis are presented in Figure 6.3, Figure 6.4, Figure 6.5 and Figure 6.6.

In Figure 6.3 the effect of drain spacing with $T_{ad}=50$ and $N_{eq}/N_l=1$, is shown for two different values of *H'/d*. The mean and maximum profiles of $r_u(y/d)$ at the end of shaking are similar, differing more around the depths of drains, with such a difference being a function of drains' spacing: obviously, for closer spacing the effectiveness of drains increases. It is worth noting that when *s/d* is much smaller than *H'/d*, the maximum value of r_u is attained in the upper part of the domain, where there is the largest drainage distance. When spacing increases and becomes higher than *H'/d*, the maximum value is attained in the lower part of the domain.

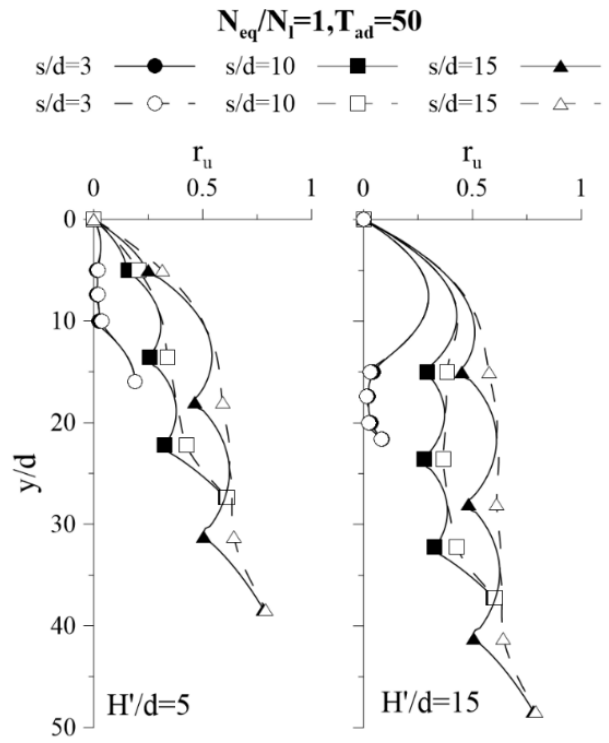

Figure 6.3. Vertical profiles of $r_{u\ mean}$ (continuous grey lines) and $r_{u\ max}$ (dashed black lines) at the end of shaking with $N_{eq}/N_l = 1$ and $T_{ad} = 50$.

In Figure 6.4 the vertical profiles of r_u with $T_{ad}=50$, *s/d=10*, *H'/d=10* and different values of N_{eq}/N_l are plotted. There is a slight difference between $N_{eq}/N_l=0.75$ and $N_{eq}/N_l=1$ and in both cases the excess pore pressure ratio is below 0.6 along the whole vertical. However, when $N_{eq}/N_l=2$, the excess pore pressure ratio is equal to 1 everywhere except for the area above the upper row of drains and around the drains themselves.

It must be noted that a value of N_{eq}/N_l lower than 1 implies that during the seismic shaking, no liquefaction occurs (r_u is lower than 1), either with or without drains. Although in these cases liquefaction does not occur, the excess pore pressure build-up reduces both shear stiffness and strength of the soil. This induces non-negligible settlements and deformations under existing structures. Therefore, drains are useful also for $N_{eq}/N_l \leq 1$, to reduce pore pressure build-up (or r_u) during shaking.

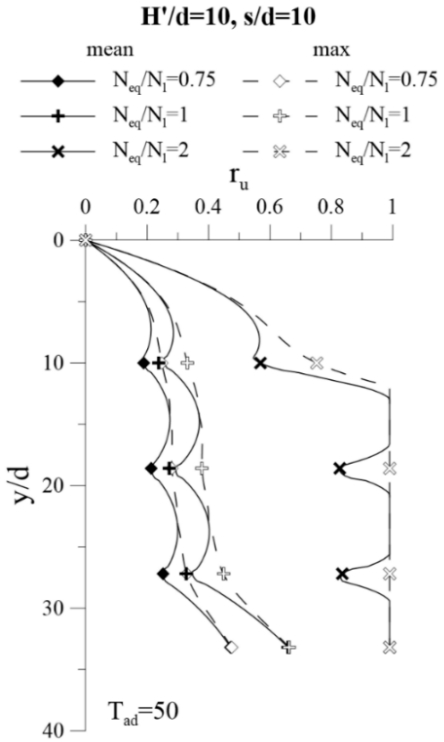

Figure 6.4. Vertical profiles of $r_{u\ mean}$ (continuous grey lines) and $r_{u\ max}$ (dashed black lines) with H'/d = 10 and s/d = 10 at the end of shaking: effect of N_{eq}/N_l with T_{ad} = 50.

In Figure 6.5a and Figure 6.5b the effect of T_{ad} is shown. When N_{eq}/N_l is equal to 1, because of the drains, liquefaction is not triggered even if T_{ad} is as low as 25, their beneficial effect being enhanced significantly as T_{ad} increases. When $N_{eq}/N_l=2$, however, the effect of T_{ad} is much more significant. As a matter of fact, with *s/d=10* and *H'/d=10*, drains are not able to prevent liquefaction when T_{ad} is low and as a consequence a smaller spacing is needed.

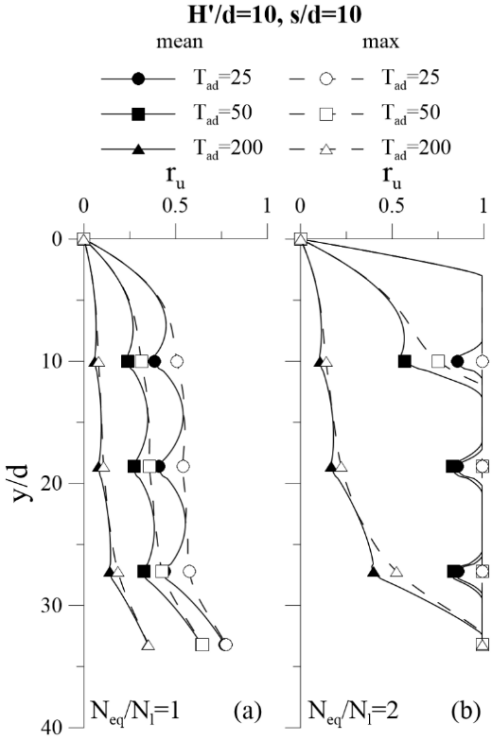

Figure 6.5. Vertical profiles of $r_{u\ mean}$ (continuous grey lines) and $r_{u\ max}$ (dashed black lines) with H'/d = 10 and s/d = 10 at the end of shaking: effect of T_{ad} for N_{eq}/N_l = 1 and 2.

When increasing *H'/d*, the efficiency of drains on the upper part of the domain rises up while the effect of the upper boundary surface decreases. The combination of both effects gives a similar profile of r_u above the first row of the drains for different values of *H'/d* (< *s/d*). When *H'/d* exceeds the value of *s/d*, the negative effect of the increased distance between the upper boundary and the first row of drains exceeds the positive combined effect of the two boundaries, and thus a higher excess pore pressure ratio is calculated.

A comparison between the vertical profiles of the mean, $r_{u,mean}$ (y/d, t/td) and maximum, $r_{u,max}$ (y/d, t/t_d), values of r_u on the horizontal plane (at the end of earthquake significant duration, t/t_d=1) for the boundary condition BC1 and BC2 are presented in Figure 6.7. Results refer to H'/d=10, N_{eq}/N_l=1 and T_{ad}=50, with varying spacing and upper boundary condition. At increasing spacing, the excess pore water pressure increases as well in each point of the domain, regardless of upper boundary condition, along with an expansion of the thickness influenced by drains. Maximum and mean excess pore water pressure slightly differ only at drain depths.

The effect of the upper boundary condition is significant especially above the first row of drains, as it can be observed in Figure 6.7. An impervious boundary (BC2) leads to higher pore water pressures in the upper part of the domain compared to pervious boundary case (BC1). However, the difference becomes negligible with depth; in the comparison proposed in Figure 6.7, the difference extinguishes below the second row of drains.

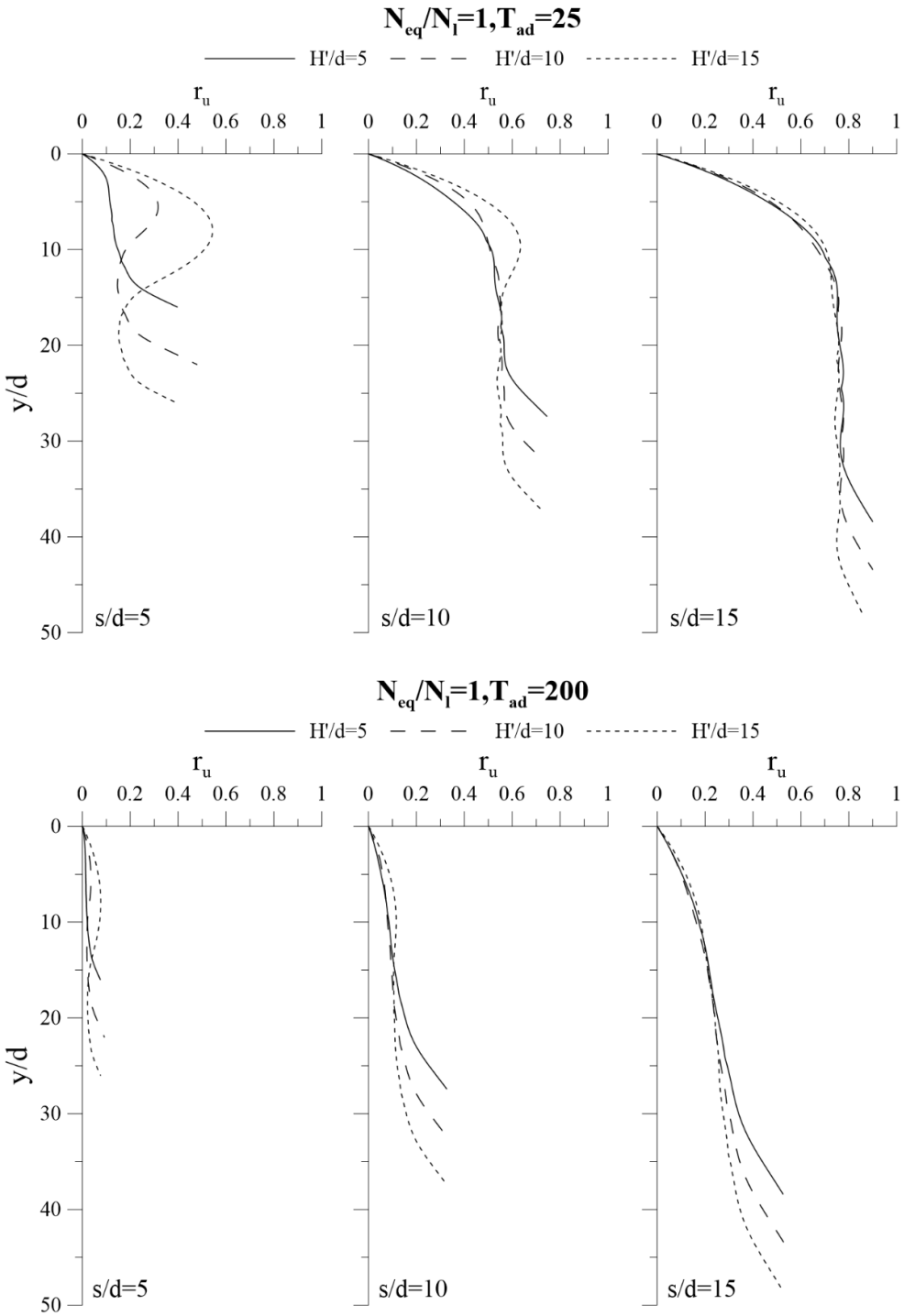

Figure 6.6. Vertical profiles of $r_{u\,max}$ at the end of shaking with N_{eq}/N_l = 1 and T_{ad} = 25 (above) and T_{ad} = 200 (below).

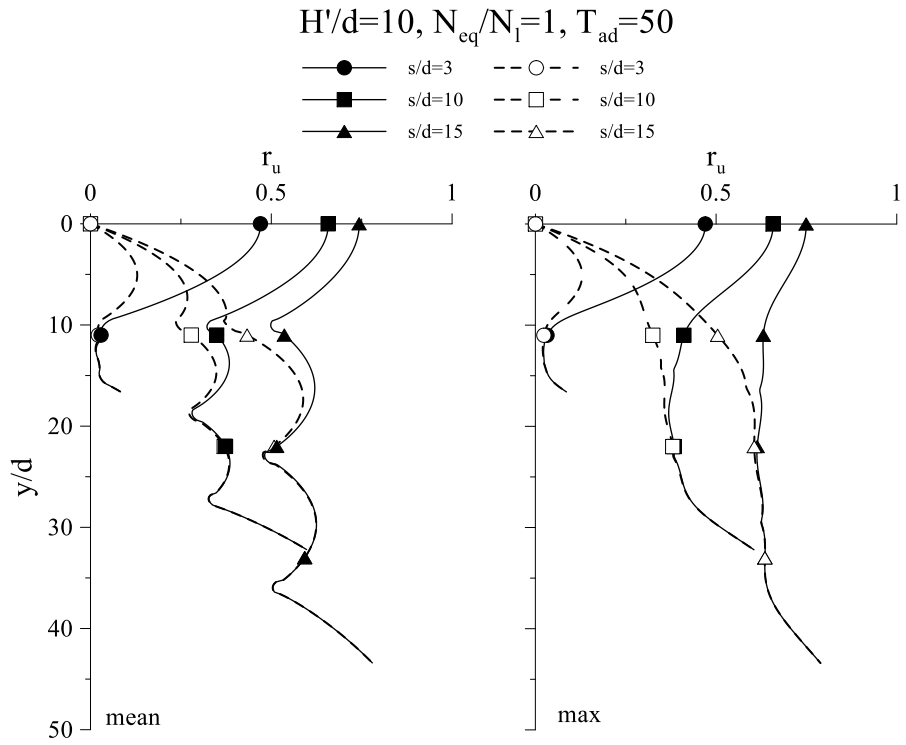

Figure 6.7. Vertical profiles of $r_{u,mean}$ (left) and $r_{u,max}$ (right) for H'/d=10, T_{ad}=50 and N_{eq}/N_l=1.

6.1.4 Validation of results

The results obtained with the presented numerical model were validated via some FEM simulations presented in section 4.4.3.1 using UBC3D-PML model.

As previously seen, a good agreement was found between the fully-coupled numerical analysis and the centrifuge test in terms of excess pore pressure and acceleration (Figure 4.34 and Figure 4.35) for both the spacings of drains adopted in the centrifuge test.

In order to carry out the validation of the numerical model proposed, a further step had to be done: once the FEM analyses were proven to be reliable and well calibrated, a further Plaxis2D analysis with the same coupled model was carried out by modelling drains by a zero excess pore pressure surface. In so doing, the results of FEM analyses can be compared to those obtained with the approach proposed, for which the drains are modelled as surfaces with infinite permeability (being characterized by zero excess pressure). In this comparison, the FEM analyses will be assumed as the "true" results.

In order to carry out the comparison, the volumetric compressibility coefficient (m_v) required to determine T_{ad}, was derived from an isotropic compression curve at an isotropic compressive stress equal to 50 kPa; the number of equivalent cycles, N_{eq} was calculated based on the procedure suggested by Biondi et al. (2012). The number of cycles required to cause liquefaction was derived by the cyclic resistance curve; the Cyclic Stress Ratio (*CSR*)

was calculated based on the approach proposed by Seed et al. (1975) with the maximum acceleration at ground surface derived by a dynamic total stress analysis. *CSR* is a function of the depth and by consequence, also N_l is a function of *z*; thus, a representative depth has to be assumed to assign N_{eq}/N_l. In a design procedure, the depth would be set at the middle of the layer that has to be treated. Hence, the depth was set at the middle of numerical solution domain (Figure 6.1b), that is equal to 2.3 m and 4 m for *s/d = 5* and *s/d = 10*, respectively. The upper boundary with zero excess pore pressure is represented by the water table, thus *H'/d* (dimensionless distance between upper boundary and first row of drains) is equal to 4.33.

Table 6.1. Earthquake characteristics; T_r is the return period, M_w is the moment magnitude, R_{ep} is the epicentral distance, t_d is the significant duration, a_{max} refers to maximum acceleration at the bottom of centrifuge model.

Source file	T_r	M_w	R_{ep}	t_d	a_{max}
(-)	(years)	(-)	(km)	(s)	(g)
ESM EU.HRZ..HNE.D.19790415.061941.C.ACC.ASC	2475	6.9	62.9	18.67	0.18

Fig. 10 shows excess pore pressure ratio vertical profiles related to three vertical sections (left boundary, right boundary and middle section of simplified model). The curves are very similar and show an almost constant distribution of excess pore pressure ratio on the horizontal direction.

Table 6.2. Parameters for numerical model; r_d is the shear stress reduction factor that accounts for dynamic response of the soil profile (Idriss, 1999), CSR is the cyclic stress ratio at depth z; a_{max} refers to the acceleration at the top of centrifuge model, k, and m_v are permeability and volumetric compressibility coefficient of soil.

s/d	a_{max}	z	r_d	CSR	N_l	N_{eq}/N_l	k	m_v	T_{ad}
(-)	(g)	(m)	(-)	(-)	(-)	(-)	(m/s)	(1/MPa)	(-)
5	0.159	2.3	0.98	0.214	1.2	14	1.66E-03	0.05	689
10		4	0.96	0.209	1.6	11			

The profiles are reported for two instants, related to the time at which maximum excess pore pressure ratio was observed in FE analysis, and at the end of earthquake significant duration. The dashed lines represent the bottom of the solution domain that is used to produce the design charts. A very good agreement can be observed on *s/d=5* at both times along all the vertical profile. The vertical profiles at *s/d=10* are quite similar from the top surface to the central row of drains, but numerical analysis overestimates significantly excess pore pressure ratio in the lower part of the domain, that is deeper compared to the case *s/d=5*; this is due to the assumption that *CSR* is constant with depth, while it should decrease with depth. Thus, the proposed numerical approach overestimates the pore pressure build up in depth compared to the reference FE dynamic analysis. Furthermore, once excess pore pressure ratio achieves unity, the build-up of pore water pressure, $\partial u_g/\partial t$, given by eq. (6-3) is much higher than the dissipation due to drains, $\partial u/\partial t$, and thus the reduction of r_u calculated in the coupled dynamic analysis performed in Plaxis is not well captured in the numerical analysis.

However, the simplification considered in the proposed method leads to a conservative design approach, and the procedure can be thus considered validated.

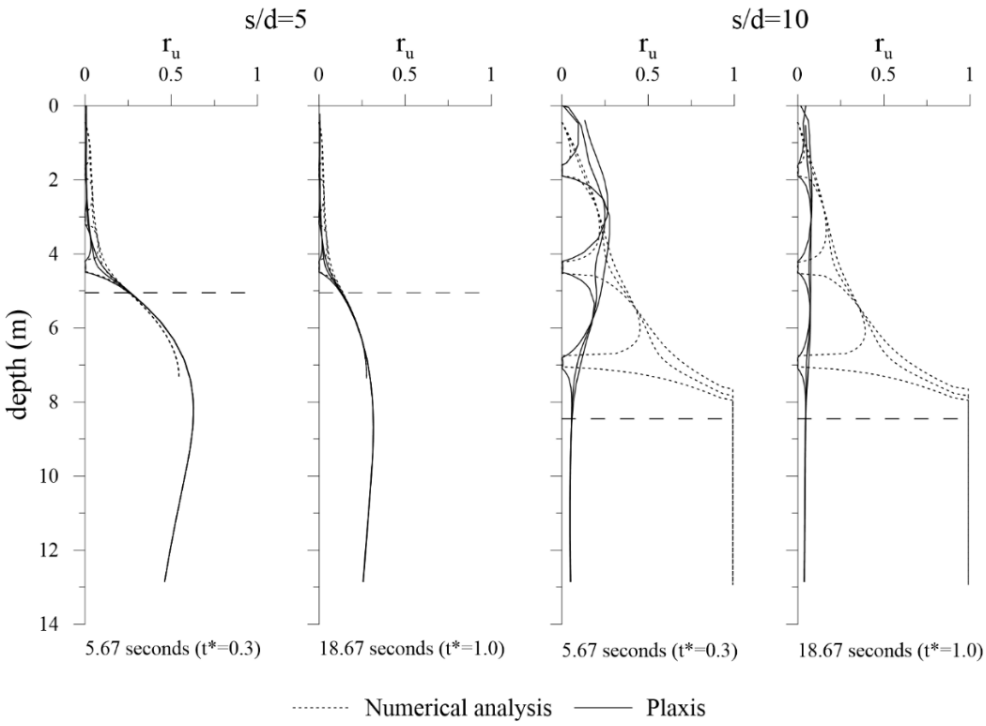

Figure 6.8. Vertical profiles of excess pore pressure ratio for s/d = 5 and 10 at two times ($t^* = t/t_d$). Dashed and continuous lines refer to the numerical and Plaxis analyses, respectively.

6.1.5 Design method

The purpose is to define a simple and straightforward method to design a set of horizontal drains for the mitigation of soil liquefaction. Thus, the results of the previously commented analyses (referred to the case of three lines of horizontal drains) are herein summarised in design charts. An example is shown in Figure 6.9, the other charts are collected below for the seepage upper boundary (Figure 6.10, Figure 6.11 and Figure 6.12) and impervious one (Figure 6.13, Figure 6.14 and Figure 6.15). The charts represent the excess pore pressure ratio in the solution domain for different sets of parameters. For each instant t, the mean and maximum excess pore pressure ratios in the solution domain have been evaluated. Because of the seepage induced by the hydraulic gradients around drains, the worst conditions are not necessarily attained at the end of the shaking, being possible to observe them during the shaking. Therefore, the maximum values in time of the mean and maximum excess pore pressure ratios calculated over the whole domain, $r_{u,mean}$ and $r_{u,max}$, were considered in the design charts. Each one of them is related to specific values of the ratios H'/d and N_{eq}/N_l; each curve refers to a value of T_{ad} and represents the excess pore pressure ratio for different values of s/d. The use of the charts requires the definition of N_{eq} and t_d. Both these parameters are related to the seismic hazard of the site, and in literature different ways to quantify them are available (e.g. Green and Terri, 2005; Trifunac and Brady, 1975a). To quantify T_{ad}, the

hydraulic and mechanical properties of the liquefiable soil (in terms of volumetric compressibility m_v and hydraulic conductivity coefficient k) and the drain diameter must be defined. Finally, it is necessary to know soil resistance to liquefaction in terms of the number of equivalent constant amplitude cycles that lead to liquefaction, N_l. Hence the ratio N_{eq}/N_l may be calculated. Once the depth of the first row of drains, H', is chosen, the ratio H'/d can be calculated and the related chart (for a given value of N_{eq}/N_l) can be selected, while the curve to be used is defined by T_{ad}.

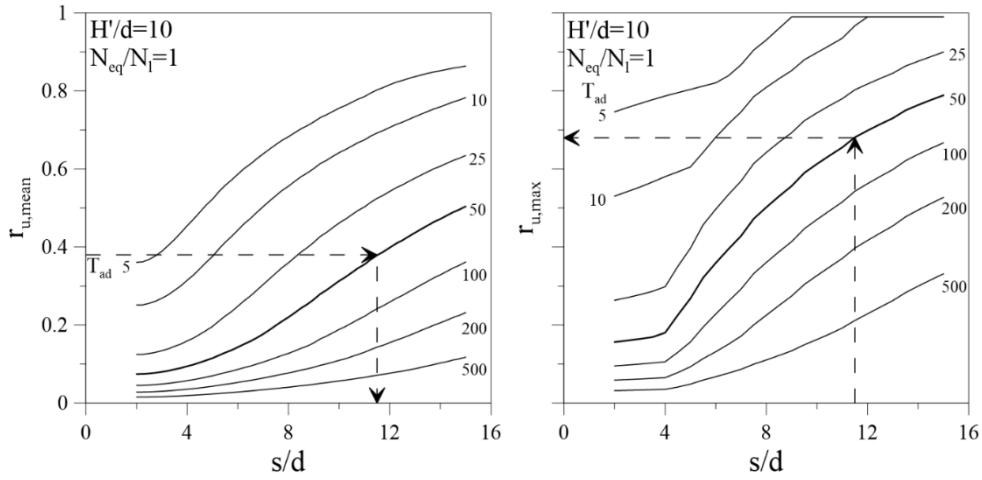

Figure 6.9. Design charts for $H'/d = 10$ and $N_{eq}/N_l = 1$ (for seepage upper boundary condition).

The last step is the definition of the design target for the mean (or maximum) r_u. Its value can be decided based on a reference limit state. Generally, r_u is chosen referring to the allowable settlements or to the bearing capacity of shallow foundations.

Finally, once the target excess pore pressure ratio r_u is defined, a dimensionless spacing s/d can be obtained from the relevant chart.

An application can be carried out using the chart shown in Figure 6.9, for $H'/d=10$, $T_{ad}=50$ and $N_{eq}/N_l=1$. Supposing that the design mean excess pore pressure ratio $r_{u,mean}$ is equal to 0.4, from the chart the design spacing s/d is around 11.5. Given the spacing, it is possible to verify that the value of $r_{u,max}$ is acceptable: in this case it is equal to 0.69. It is worth noting that the s/d obtained from the design chart is almost equal to H'/d, which means that in this case the maximum excess pore pressure ratio is likely to be achieved in the lower part of the domain (less critical from an engineering point of view), as discussed before.

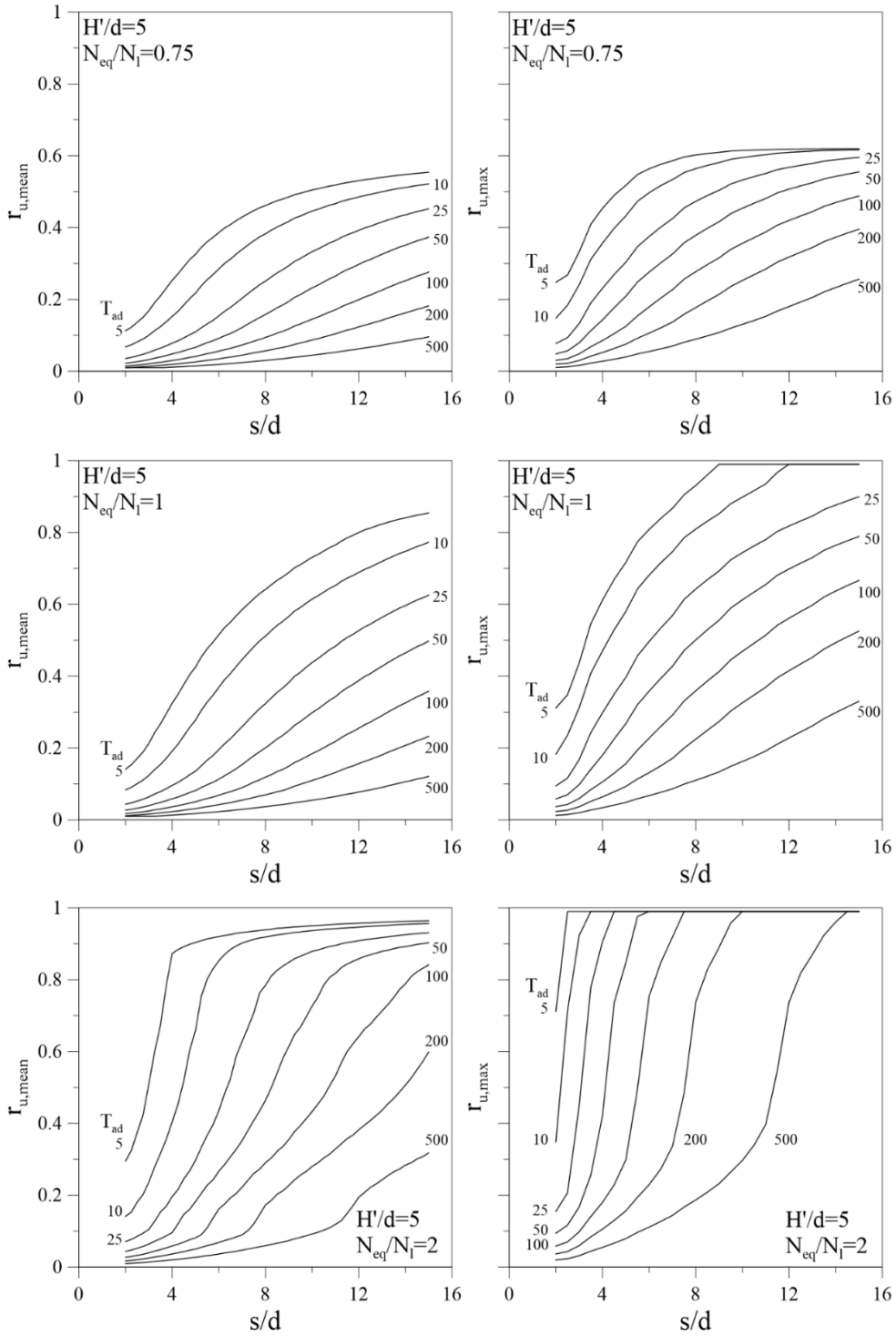

Figure 6.10. Design charts for H0/d = 5 (for seepage upper boundary condition).

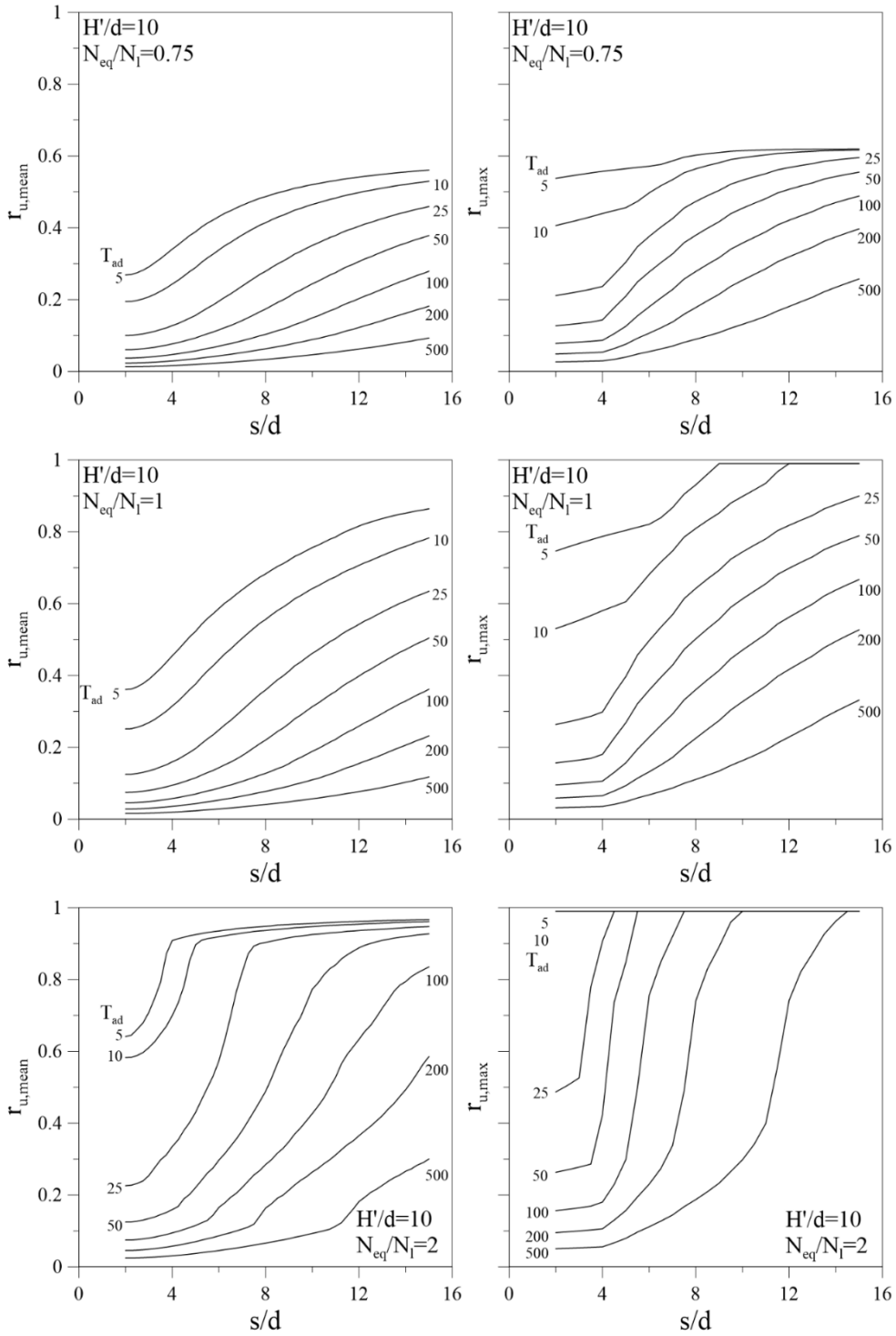

Figure 6.11. Design charts for H'/d = 10 (for seepage upper boundary condition).

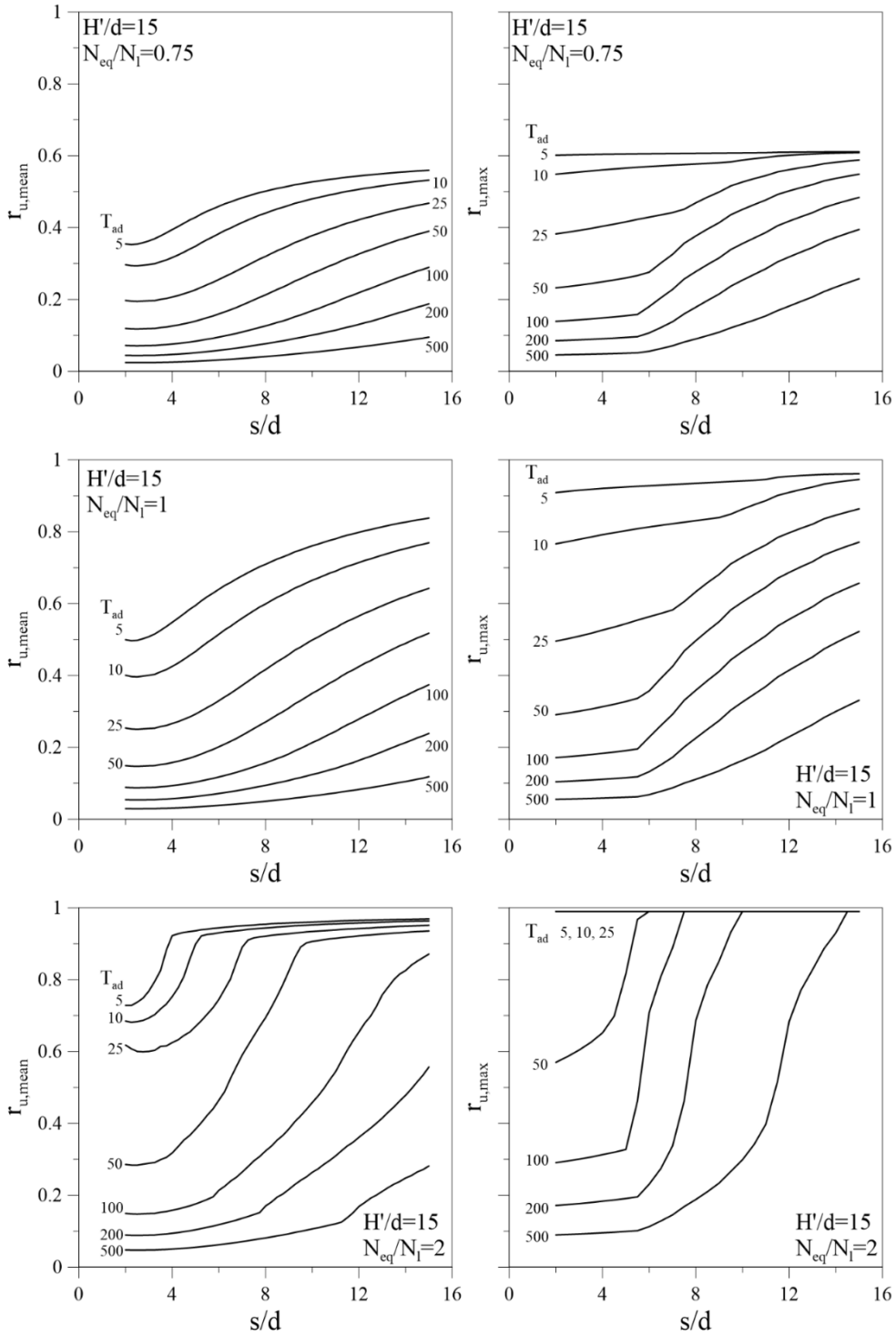

Figure 6.12. Design charts for H'/d = 15 (for seepage upper boundary condition).

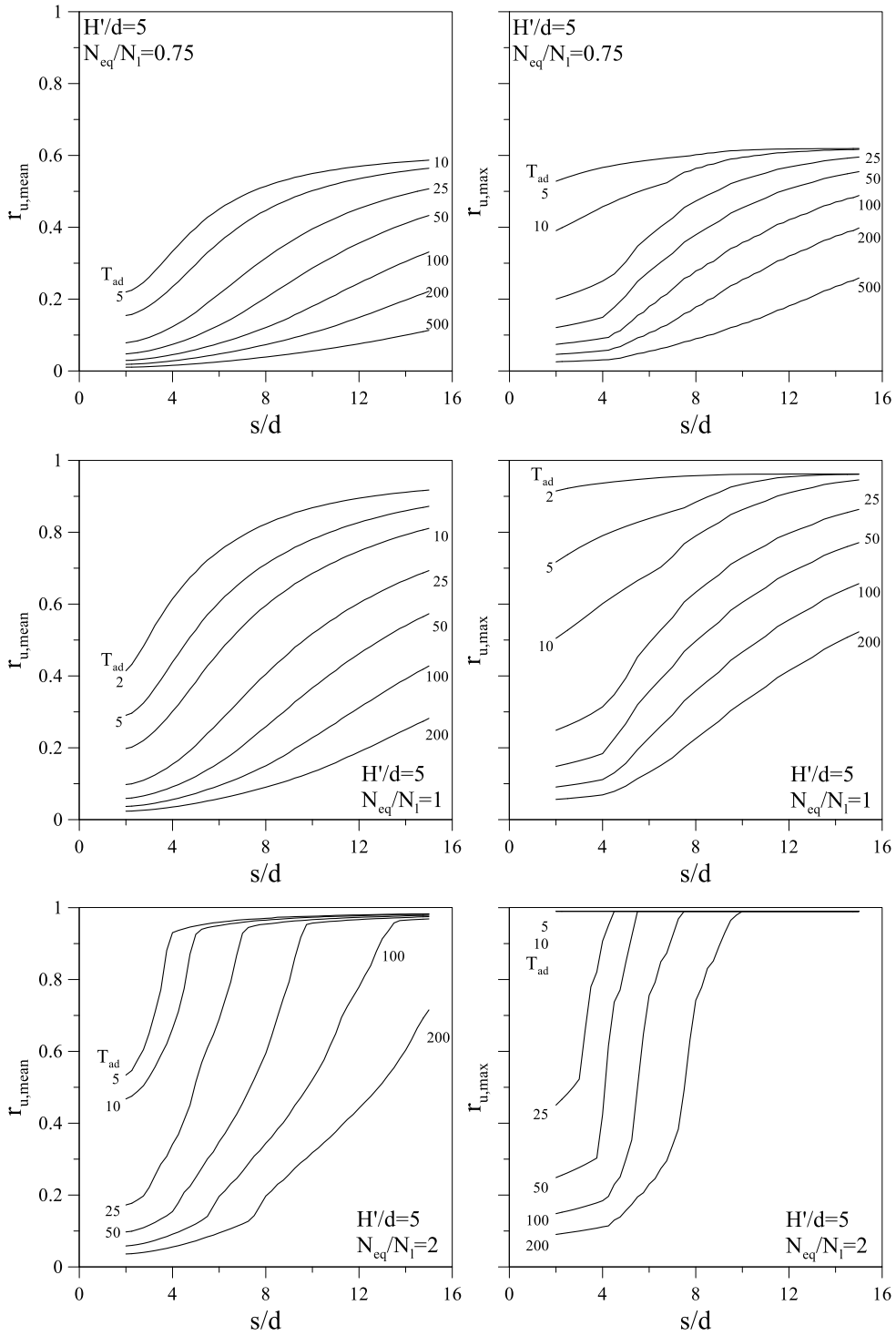

Figure 6.13. Design charts for H'/d = 5 (for impervious upper boundary condition).

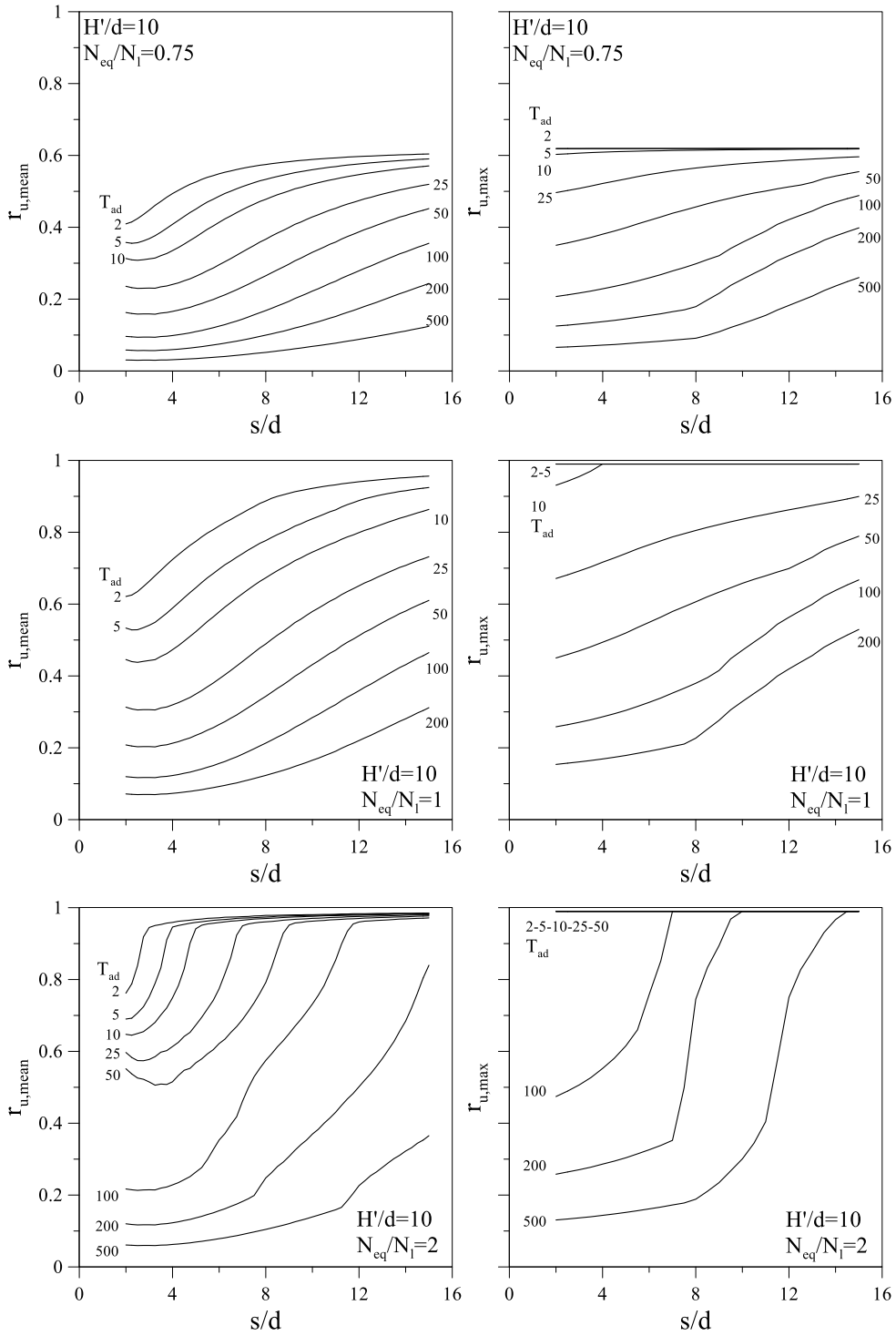

Figure 6.14. Design charts for H'/d = 10 (for impervious upper boundary condition).

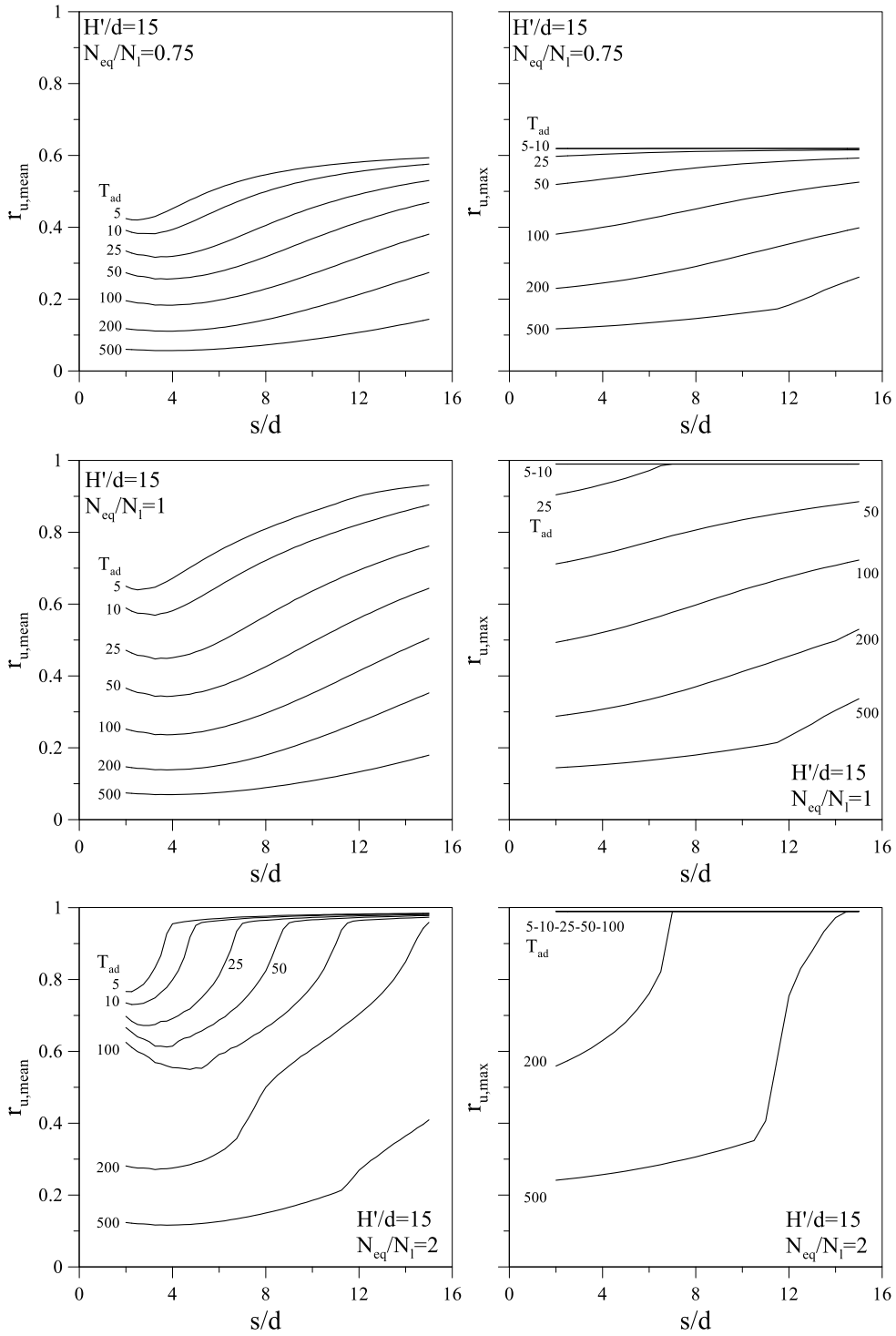

Figure 6.15. Design charts for H'/d = 15 (for impervious upper boundary condition).

6.1.5.1 Comparison of solution

The effect of upper boundary drainage conditions (pervious or impervious) can be noticed in the design charts; in Figure 6.16, a comparison between the two boundary conditions, for both maximum and mean excess pore water pressure ratio, is presented for different values of T_{ad}. Obviously, the curves referring to pervious boundary conditions (BC1, dashed lines) are always below the curves (corresponding to the same T_{ad}) with impervious boundary conditions (BC2, solid lines) due to the beneficial effect of the free draining surface. This effect is enhanced at low spacings and time factors (T_{ad}). The difference in terms of $r_{u,max}$ between the two boundary conditions goes to zero at increasing s/d. The same trend cannot be observed on $r_{u,mean}$. Both these evidences depend on the fact that, for high values of s/d, the maximum pore pressure increment value tends to be attained below the drains, far from the influence of upper boundary condition.

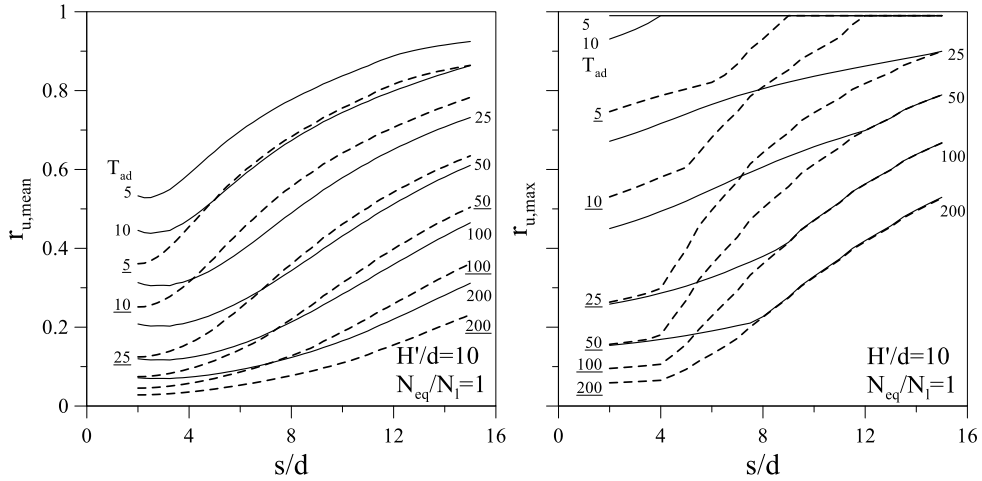

Figure 6.16. Comparison between design charts with pervious upper boundary condition (dashed lines) and impervious one (solid lines).

As previously mentioned, the design of horizontal drains in dynamic condition for mitigation of liquefaction risk is generally carried out in the hypothesis of radial consolidation, so that the solution proposed for vertical drains by Seed and Booker (1976) and revised by Bouckovalas et al. (2009) can be applied. They solved an axial-symmetrical flow problem in the hypothesis of indefinite vertical drains system with regular grid. By using these solutions, the contribution of vertical drainage induced by top pervious surface is neglected. Moreover, the hypotheses of radial flow and indefinite drainage system can be far from the case of horizontal drains even if top surface is impervious; indeed, as already pointed out, there can hardly be more than 3 rows of drains. Thus, a comparison between axial-symmetrical solutions after Bouckovalas et al. (2009) and bidimensional solution, in the case of impervious upper boundary condition, was also carried out.

Figure 6.17 shows the comparison between Bouckovalas solution (dashed lines) and the solution herein proposed in the previous sections (solid lines), for H'/d equal to 5 and 10.

Solutions substantially differ in all the range of values of T_{ad} and s/d, for both maximum and mean r_u. It can be concluded that the design charts for vertical drains are not trustworthy for horizontal drains, despite the impervious upper surface that should make the drainage mechanism similar. The excess pore pressure ratio calculated by the approach for the vertical drains (Bouckovalas et al., 2009) lead to higher values of r_u for larger s/d ration, this effect is due to the lower efficiency calculated by the solution for the vertical drains respect to the solution for horizontal drains in the volume of soil between the first row of horizontal drains and upper boundary of the domain.

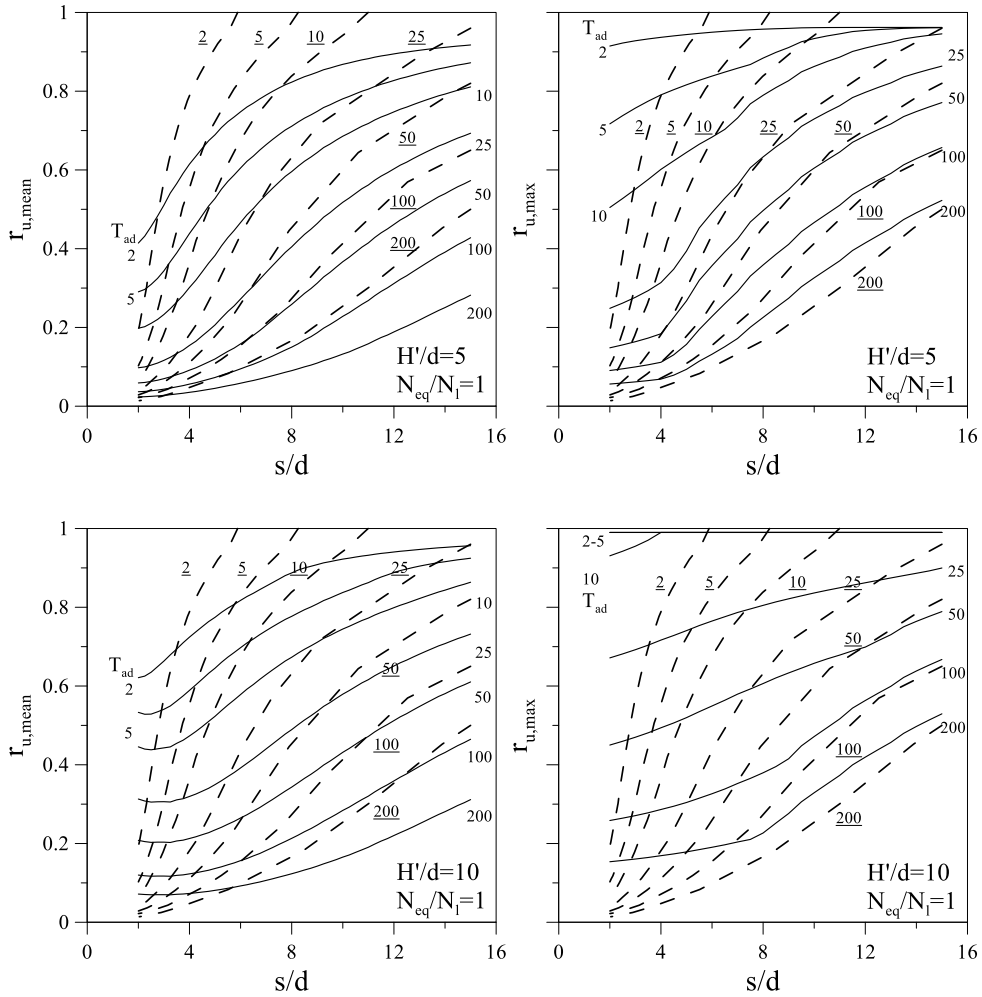

Figure 6.17. Comparison between design charts of Bouckovalas et al. 2009 (dashed lines) and model with hypothesis BC2 (solid line).

6.2 Induced partial saturation (IPS)

In this section a design method for the induced partial saturation (IPS) technique to mitigate the liquefaction susceptibility is shown. The design strategy follows the approach proposed in §5.5. The design method is related to so called stress-based approach which reference to the liquefaction strength curve in the CSR-N plane and to the value of CSR analytically computed (Seed and Idriss, 1967). The limitations of this simplified approach have been explained in section 5.5. Generally, this approach leads to conservative results, which is the reason of its popularity. In this section, a procedure to make a somehow more reliable numerical calculation under the same hypothesis is introduced.

The design starts from the calculation of the action in terms of shear stress (CSR) and equivalent number of cycles (N_{eq}), that allow to identify the action point (demand) on the plane CSR-N_{cyc} (e.g. red dot in Figure 6.18). If the action point is above the cyclic resistance curve for the saturated soil (capacity), liquefaction is considered to take place.

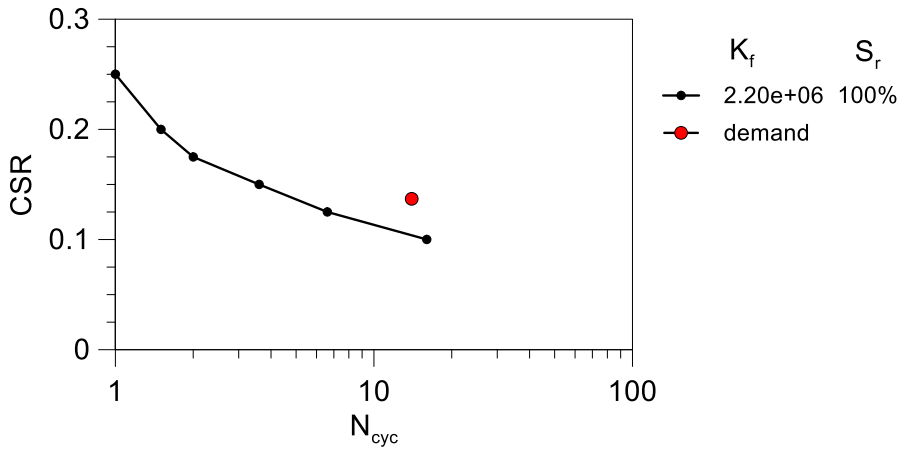

Figure 6.18. Cyclic strength curve for saturated soil and action point.

The thickness of potentially liquefiable soil is defined by the profile of safety factor with depth. In the case of a homogeneous soil profile, the capacity CRR is almost constant with depth (Figure 6.19). As a consequence, the thickness of soil subjected to liquefaction is individuated by the safety factor lower than 1. Hence, at least this portion of soil has to be treated.

In principle, the saturation degree necessary to mitigate the liquefaction susceptibility with the desired margins of safety should be chosen, once the effect of different degree of saturation on the $CRR_{(Sr)}$-N curve is known. The desired safety factor in the soil treated with IPS can be applied for the assumed demand, identifying the capacity needed for the number of equivalent cycles of interest. Thus, the value of S_r to be assigned to the soil at that depth is evaluated. With reference to Figure 6.19, however, this is only an analytical procedure that would lead to different degrees of saturation at different depths (because of the different initial values of the safety factor). Obviously, from an engineering point of view this has no sense (a single possible, reasonable engineering solution would in this case be the adoption

of the most conservative value (i.e. the lowest possible value of $S_r(z)$). However, this design conclusion stems from the analytical application of the stress-based approach, which does not consider the system response and assumes no hydraulic connections between different parts of the same soil, having different values of FS and thus of the water head. As a matter of fact, because of these unbalanced values of water head, transient filtration process is triggered, with an internal redistribution of pore pressure continuously taking place (Cubrinovski et al., 2019).

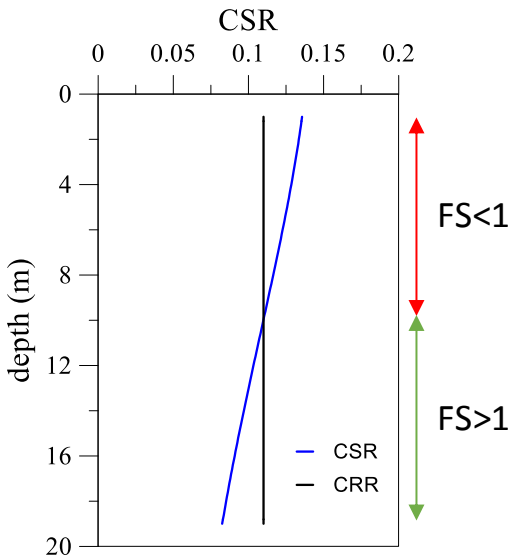

Figure 6.19. Vertical profiles of CSR and CRR.

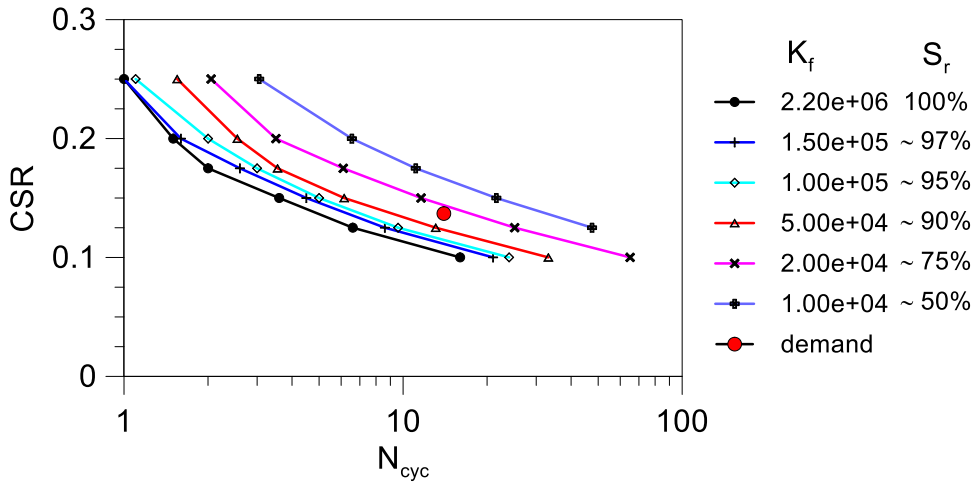

Figure 6.20. Cyclic strength curves for IPS with CSR points at ground surface.

As a matter of fact, in §5.5 it was shown that, from a computational point of view, in order to simplify FEM analyses, as long as the effect of desaturation is the existence of

disperse bubbles into a continuous water phase (i.e. high degrees of saturation, and no matric suction), there is no real need to consider unsaturated soil mechanics, and an equivalent compressible fluid can be introduce to take into account the existence of air bubbles, with an equivalent fluid bulk stiffness K_f decreasing as S_r decreases. Figure 6.20 reports the different cyclic resistance curves for different values of K_f (and hence of S_r). This chart can be used for a preliminary design of the saturation degree to apply in the numerical computation.

Then, an alternative way to compute the desired degree of saturation is the adoption of a FEM calculation as follows: the problem under investigation is taken into consideration (building, pipeline, or whatever case) and geometrically modelled. Then, the constitutive models suited for the different soils are adopted, calibrating the mechanical properties of all materials on the basis of all the available in situ and laboratory results. For the liquefiable layers, constitutive models able to take into account the phase transformation from solid to liquid state are adopted (see APPENDIX B), and the parameters related to fully saturated conditions are introduced. Then, the results of the numerical analysis are analysed in terms of structural response, that is looking at the performance of the structure to protect. The performance criterion may be related to the bearing capacity safety factor, to the absolute or differential settlement, etc.. Then, in case the performance of the structure is not satisfactory, the bulk stiffness of the fluid within the liquefiable soils is progressively reduced, till the value Kf for which the performance is satisfactory (whatever the target). Finally, the calibration curves reported in Figure 6.20 are used to find what is the degree of saturation to be reached on site by IPS, using the correspondence there reported between Kf and Sr.

This “performance based” approach is certainly sound, in the sense that allows whatever system interaction has to take place within the soil mass because of unbalanced water heads, thus overcoming one of the most critical drawbacks of the analytical stress-based approach.

7 CONCLUSIONS

A series of geotechnical centrifuge test was performed in the LIQUEFACT project to evaluate soil liquefaction triggering and the effects of two innovative liquefaction mitigation techniques (horizontal drains and induced partial saturation). Two soil profiles were adopted (section 3.6) to study the effect of simple stratified soil: homogeneous liquefiable layer (M1) and double layers profile with a low permeable crust (M2). The centrifuge tests highlighted that the input motion chosen for the test was able to induce liquefaction in the soil. Moreover, the achievement of the liquefaction induced a significative ground motion attenuation at the ground surface that represents a typical effect of the liquefaction. Tests confirmed that the soil liquefaction induces significant large settlement of the ground surface.

A simple structure, having one degree of freedom founded on shallow beams, was designed (section 3.9) and used to evaluate the effect of liquefaction and mitigation techniques on the soil-structure system response. The structure represents a two stories masonry building. The structure, in the tests where the liquefaction was achieved, showed large settlements induced by the low shear stiffness and strength of the liquefied soil in proximity of the foundation beams (section 3.10).

Two arrangements of horizontal drains (HD) were employed to study the drainage effectiveness of the technique to reduce the liquefaction susceptibility of soil. Two different arrangement of drains have been disposed to evaluate the effect of the geometry on the distribution of excess pore pressure during the shaking in the soil profile. The results of centrifuge test showed that the horizontal drains decrease the excess pore pressure and the settlements respect the model without mitigation technique. However, the reduction of excess pore pressure induced by horizontal drains induced an increase of the acceleration in correspondence of the ground surface. The effects of horizontal drains were also investigated in presence of the structure where the drains were deployed directly below the structure to evaluate the response of the soil-structure system (section 3.11).

Induced partial saturation (IPS) was adopted in some centrifuge models, it was induced by air injection from the bottom of soil profile using four nozzles. Single and double soil layer were tested using different ground motions and saturation degrees to evaluate the effectiveness of the mitigation technique. Moreover, the effect of the soil-structure interaction was studied in presence of the induced partial saturation. The effectiveness of the IPS can be deduced by the excess pore pressure records that proved that the liquefaction was not achieved also for the stronger input motion GM31++ (section 3.12).

In this work, the main experimental results have been presented and interpreted, also by the means of numerical analyses. A first series of numerical analyses was performed to individuate the more reliability calibration procedure for two constitutive soil models (UBC3D-PML and PM4SAND) able to reproduce the excess pore pressure build-up that leads to the achievement of liquefaction (section 4.2). The calibration of the constitutive soil models used in the analyses was achieved by established procedures presented in the literature, mainly based on the best fit of the cyclic resistance curve (CRR, N_{cyc}).

The best calibration procedure for both constitutive soil models was chosen by the comparison between the numerical results and the experimental data for the centrifuge tests without mitigation techniques focusing on the excess pore pressure comparison (section 4.3).

Later, the reliability of the numerical model with mitigation (horizontal drains and induced partial saturation) was checked against the relevant experiments (section 4.4 and section 4.5).

As a general statement, the numerical results showed a large effectiveness of both the horizontal drains and the induced partial saturation to reduce the excess pore pressure in the soil. The contours reported in the section 4.4 show clearer than the experimental results that the presence of horizontal drains reduce significantly the excess pore pressure ratio so the technique is very efficient in the reduction of liquefaction susceptibility.

Some exceptions were registered, such as in the case of the homogeneous model with IPS (single layer model: M1_S1_IPS4) where in the partial saturated models higher peak values of excess pore pressure than in the saturated ones were achieved this effect is ascribable to the reduction of the permeability coefficient induced by the partial saturation that reduces the capability of the soil to dissipate the excess pore pressure during the earthquake. The use of induced partial saturation in presence of energized input motion may lead only to a delay excess pore pressure build-up but that achieves in any case the same peak value. The induced partial saturation was reproduced by a numerical procedure that considers the decrease of the pore fluid bulk stiffness allowing to contemplate the presence of air bubbles in the pores. This reduces the excess pore pressure build-up.

The effect of the arrangement of horizontal drains on the distribution of excess pore pressure was further investigated by a parametric numerical analysis where spacing and depth of the first row of horizontal drains were changed (section 5.1 and 5.2). The results show an increase of acceleration spectra for all periods. This highlights that the presence of horizontal drains increases the inertial forces on an eventual structure embedded on the soil profile. A large decrease of the excess pore pressure was recorded between the drains with small spacing, but a more efficient in whole soil profile was recorded for more homogeneous arrangement of the drains. The presence of horizontal drains reduces the amount of the ground surface settlements for the soil profile with upper seepage surface, whereas it increases the settlements in presence of an upper impervious surface.

Moreover, the effect of the horizontal drains layout on the soil-structure interaction was studied to define a minimum extension of the volume of ground to be drained in order to maximize the mitigation (section 5.3). As for the free-field conditions, the acceleration spectra show a significant increase of the acceleration on the structure roof. However, the disposition 2s results a good compromise in terms of excess pore pressure decreasing and structure settlements, moreover this disposition led to a lower acceleration amplification. Furthermore, the presence of horizontal drains reduces significantly the amount of settlements of the structure.

A parametric analysis was also performed to study the effect of the induced partial saturation (IPS) by changing the treated soil thickness and the target saturation degree. The stronger ground motion (GM31 for M1_S1_HD1&2_GM31) used for the parametric analysis highlighted that the induced partial saturation might have detrimental effects on the liquefaction mitigation, hence it has to been designed carefully in function of seismic and

soil characteristics of the site (section 5.4). This result is due to the reduction of the drainage capability of the soil for the reduction of the permeability of the soil induced by the partial saturation.

A further parametric analysis with IPS was performed by adopting a scaled-up input motion that allowed to evaluate the effect of the induced partial saturation on the distribution of excess pore pressure and acceleration attained at the ground surface (section 5.5). The analyses performed with the scaled-up input, compatible with the cyclic resistance of the partial saturation soil, showed that the mitigation technique reduces significantly the excess pore pressure build-up avoiding the soil liquefaction. Furthermore, the parametric analyses allowed to evaluate the effect of redistribution of the excess pore pressure into the soil profile that has a significant influence on the maximum value of the excess pore pressure achieved during the earthquake and on its position.

The parametric analyses with induced partial saturation are also performed in presence of the structure. As made for the horizontal drains, attention was given to the horizontal extension of the treated soil region below the structure (section 5.6) to identify the more efficient geometry of the mitigation technique in terms of excess pore pressure decrease. The geometry with 3B extension gave better results in terms of excess pore pressure. The acceleration at ground surface in terms of spectra may be not significantly modified by the presence of the induced partial saturation. The settlements were reduced by the presence of IPS.

Finally, a design approach was proposed for horizontal drains and induced partial saturation, respectively (section 6). Design charts were provided for the technique of horizontal drains taking to account three rows of drains in staggered arrangement. The charts allow to know the amount of mean and maximum excess pore pressure ratio in the soil for a typical range of spacing and diameter ratio in function of the depth of first row of drains and the ratio between equivalent cycles number (N_{eq}) and the cycles number that leads to liquefaction (N_l).

The design procedure for the induced partial saturation allows to determine the possibility of IPS use for the liquefaction mitigation for a specific site and to identify the degree of saturation necessary to a significant reduction of the excess pore pressure. However, a numerical analysis is required to know the distribution of excess pore pressure ratio in the soil.

REFERENCES

Airoldi, S., Fioravante, V., Giretti, D., 2018a. Soil Liquefaction Tests in the ISMGEO Geotechnical Centrifuge, in: Proceedings of China-Europe Conference on Geotechnical Engineering. Springer, pp. 469–472.

Airoldi, S., Fioravante, V., Giretti, D., 2016. The ISMGEO seismic geotechnical Centrifuge., in: EUROFUGE 2016. Thorel, Bretschneider, Blanc and Escoffier eds, pp. 67–72.

Airoldi, S., Fioravante, V., Giretti, D., Moglie, J., 2018b. Validation of liquefaction retrofitting techniques from geotechnical centrifuge small scale models [WWW Document]. https://doi.org/10.5281/ZENODO.1281598

Alba, P. De, Baldwin, K., Janoo, V., Roe, G., Celikkol, B., 1984. Elastic-wave velocities and liquefaction potential. Geotech. Test. J. 7, 77–88.

Alessio, G., Alfonsi, L., Brunori, C.A., Burrato, P., Casula, G., Cinti, F.R., Civico, R., Colini, L., Cucci, L., De Martini, P.M., Falcucci, E., Galadini, F., Gaudiosi, G., Gori, S., Mariucci, M.T., Montone, P., Moro, M., Nappi, R., Nardi, A., Nave, R., Pantosti, D., Patera, A., Pesci, A., Pezzo, G., Pignone, M., Pinzi, S., Pucci, S., Salvi, S., Tolomei, C., Vannoli, P., Venuti, A., Villani, F., 2013. Liquefaction phenomena associated with the Emilia earthquake sequence of May-June 2012 (Northern Italy). Nat. Hazards Earth Syst. Sci. 13, 935–947. https://doi.org/10.5194/nhess-13-935-2013

Allard, M.A., Schenkeveld, F.M., 1994. The Delft Geotechnics model pore fluid for centrifuge test, in: International Conference on Centrifuge Modelling, Centrifuge ’94. pp. 133–138.

Allouche, E.N., Ariaratnam, S.T., Lueke, J.S., 2000. Horizontal directional drilling: profile of an emerging industry. J. Constr. Eng. Manag. 126, 68–76. https://doi.org/10.1061/(ASCE)0733-9364(2000)126:1(68)

ARIAS A, 1969. Measure of Earthquake Intensity. Massachusetts Inst. of Tech., Cambridge. Univ. of Chile, Santiago de Chile.

Asgari, A., Oliaei, M., Bagheri, M., 2013. Numerical simulation of improvement of a liquefiable soil layer using stone column and pile-pinning techniques. Soil Dyn. Earthq. Eng. 51, 77–96. https://doi.org/10.1016/j.soildyn.2013.04.006

Baldi, G., 1988. The ISMES geotechnical centrifuge. Centrifuge’88.

Bardet, J.P., Oka, F., Sugito, M., Yashima, A., 1995. The great Hanshin earthquake disaster. The January 17, 1995.

Barksdale, R.D., Bachus, R.C., 1983. Design and construction of stone columns, vol. I. Turner-Fairbank Highway Research Center.

Beaty, M.H., Byrne, P.M., 2011a. UBCSAND Constitutive Model, Version 904aR, Itasca UDM Web Site.

Beaty, M.H., Byrne, P.M., 2011b. UBCSAND CONSTITUTIVE MODEL Version 904aR, Itasca UDM Web Site.

Bertalot, D., 2013. Seismic behaviour of shallow foundations on layered liquefiable soils.

Bian, H., Jia, Y., Shahrour, I., 2008. A potential cost effective liquefaction mitigation countermeasure: induced partial saturation, in: AIP Conference Proceedings. AIP, pp. 427–433.

Biondi, G., Cascone, E., Di Filippo, G., 2012. Affidabilità di alcune correlazioni empiriche per la stima del numero di cicli di carico equivalente. Riv. Ital. di Geotec. 2012, 11–41.

Bolt, B.A., 1973. Duration of strong ground motion, in: 5th World Conference on Earthquake Engineering. pp. 1304–1313.

Bouckovalas, G., Papadimitriou, A., Niarchos, D., 2009. Gravel drains for the remediation of liquefiable sites: The Seed & Booker (1977) approach revisited. pp. 61–75. https://doi.org/10.1201/NOE0415556149.ch4

Boulanger, R.W., 2003. Relating Kα to Relative State Parameter Index. J. Geotech. Geoenvironmental Eng. 129, 770–773. https://doi.org/10.1061/(ASCE)1090-0241(2003)129:8(770)

Boulanger, R.W., Idriss, I.M., 2016. CPT-based liquefaction triggering procedure. J. Geotech. Geoenvironmental Eng. 142, 04015065. https://doi.org/10.1061/(ASCE)GT.1943-5606.0001388

Boulanger, R.W., Ziotopoulou, K., 2015. A Sand Plasticity Model for Earthquake Engineering Applications PM4SAND (Version 3): Cent. Geotech. Model. Rep. No. UCD/CGM-15/01, Dep. Civ. Environ. Eng. Univ. California, Davis, Calif 108.

Bradley, B.A., Araki, K., Ishii, T., Saitoh, K., 2013. Effect of lattice-shaped ground improvement geometry on seismic response of liquefiable soil deposits via 3-D seismic effective stress analysis. Soil Dyn. Earthq. Eng. 48, 35–47. https://doi.org/10.1016/j.soildyn.2013.01.027

Bradley, B.A., Cubrinovski, M., 2011. Near-source strong ground motions observed in the 22 February 2011 Christchurch earthquake. Bull. New Zeal. Soc. Earthq. Eng. 44, 181–194. https://doi.org/10.5459/bnzsee.44.4.181-194

Bray, J.D., Dashti, S., 2014. Liquefaction-induced building movements. Bull. Earthq. Eng. 12, 1129–1156. https://doi.org/10.1007/s10518-014-9619-8

Bray, J.D., Dashti, S., 2010. Liquefaction-induced movements of buildings with shallow foundations, in: Fifth International Conference on Recent Advances in Geotechnical Earthquake Engineering and Soil Dynamics. Missouri University of Science and Technology.

Brennan, A.J., Madabhushi, S.P.G., 2006. Liquefaction remediation by vertical drains with varying penetration depths. Soil Dyn. Earthq. Eng. 26, 469–475.

Brennan, A.J., Madabhushi, S.P.G., 2002. Effectiveness of vertical drains in mitigation of liquefaction 22, 1059–1065.

Brennan, A.J., Madabhushi, S.P.G., Houghton, N.E., 2006. Comparing laminar and equivalent shear beam (ESB) containers for dynamic centrifuge modelling, in: Physical Modelling in Geotechnics, 6th ICPMG'06 - Proceedings of the 6th International Conference on Physical Modelling in Geotechnics. pp. 171–176. https://doi.org/10.1201/noe0415415866.ch17

Brinkgreve, R.B.J., Swolfs, W.M., Engin, E., Waterman, D., Chesaru, A., Bonnier, P., Galavi, V., 2011. PLAXIS 2D Reference manual. Delft Univ. Technol. PLAXIS bv Netherlands.

Burland, J.B., Symes, M., 1982. A simple axial displacement gauge for use in the triaxial apparatus. Geotechnique 32, 62–65. https://doi.org/10.1680/geot.1982.32.1.62

Butler, C.S., Mason, J.R., 1997. Structure-function analysis of the bacterial aromatic ring-hydroxylating dioxygenases, in: Advances in Microbial Physiology. Elsevier, pp. 75–84. https://doi.org/10.1016/s0065-2911(08)60155-1

Butler, D.K., Skoglund, G.R., Landers, G.B., 1978. CROSSHOLE: An interpretive computer code for crosshole seismic test results, documentation, and examples. [Defense Department, Department of the Army], Corps. of Engineers, Waterways ….

Casagrande, A., 1936. Characteristics of cohesionless soils affecting the stability of slopes and earth fills. J. Bost. Soc. Civ. Eng. 23, 13–32.

Cascone, E., Bouckovalas, G.D., 1998. Seismic bearing capacity of footings on saturated sand with a clay cap. Engineering 1–12.

Castro, G., 1975. Liquefaction and Cyclic Mobility of Saturated Sands. J. Geotech. Eng. Div. https://doi.org/10.1098/rspb.2008.1131

Castro, G., 1969. Liquefaction of sands, Harvard soil mechanics series. Harvard Univ. 81.

Castro, G., Poulos, S.J., 1977. Factors affecting liquefaction and cyclic mobility. J. Geotech. Geoenvironmental Eng. 103.

Chang, F.K., Krinitzsky, E.L., 1977. Duration, spectral content and predominant period of strong motion earthquake records from Western United States, Miscellaneous paper 5-73-1. US Army Corps Eng. Waterw. Exp. Stn. Vicksburg, Missipppi.

Chiaradonna, A., Özcebe, A.G., Bozzoni, F., Fama, A., Zuccolo, E., Lai, C.G., Flora, A., Cosentini, R.M., D'Onofrio, A., Bilotta, E., 2018. Numerical simulation of soil liquefaction during the 20 May 2012 M6. 1 Emilia Earthquake in Northern Italy: the case study of Pieve di Cento, in: Proceedings, 16th European Conference on Earthquake Engineering, 16ECEE, Thessaloniki, Greece. pp. 18–21.

Constantz, J., Herkelrath, W.N., Murphy, F., 1988. Air encapsulation during infiltration. Soil Sci. Soc. Am. J. 52, 10–16.

Cox, B.R., Griffiths, S.C., 2010. Practical recommendations for evaluation and mitigation of soil liquefaction in Arkansas.

Craig, W.H., 1989. Edouard Phillips (1821-89) and the idea of centrifuge modelling. Géotechnique 39, 697–700.

Crank, J., Nicolson, P., 1947. A practical method for numerical evaluation of solutions of partial differential equations of the heat-conduction type. Math. Proc. Cambridge Philos. Soc. 43, 50–67. https://doi.org/10.1017/S0305004100023197

Cubrinovski, M., Rhodes, A., Ntritsos, N., Van Ballegooy, S., 2019. System response of liquefiable deposits. Soil Dyn. Earthq. Eng. 124, 212–229. https://doi.org/10.1016/j.soildyn.2018.05.013

D'Acunto, B., 2011. Computational partial differential equations for engineering science, Computational Partial Differential Equations for Engineering Science. Nova Science Publishers, New York.

Dafalias, Y.F., Manzari, M.T., 2004. Simple Plasticity Sand Model Accounting for Fabric Change Effects. ASCE, J. Geotech. Eng. Div. 130, 622–634.

Daily, W., Ramirez, A., 1995. Environmental process tomography in the United States. Chem. Eng. J. Biochem. Eng. J. 56, 159–165.

Dashti, S., Bray, J.D., Pestana, J.M., Riemer, M., Wilson, D., 2009. Centrifuge testing to evaluate and mitigate liquefaction-induced building settlement mechanisms. J. Geotech. geoenvironmental Eng. 136, 918–929. https://doi.org/10.1061/(ASCE)GT.1943-5606.0000306

Derkx, F., Thorel, L., Chazelas, J.L., Escoffier, S., Rault, G., Buttigieg, S., Cottineau, L.M., Garnier, J., 2006. Dynamic tests and simulation of earthquakes in the LCPC's centrifuge, in: Physical Modelling in Geotechnics, 6th ICPMG'06 - Proceedings of the 6th International Conference on Physical Modelling in Geotechnics. pp. 181–186. https://doi.org/10.1201/noe0415415866.ch19

Dobry, R., Ladd, R.S., Yokel, F.Y., Chung, R.M., Powell, D., 1982. Prediction of pore water pressure buildup and liquefaction of sands during earthquakes by the cyclic strain

method. National Bureau of Standards Gaithersburg, MD.
Drnevich, V.P., 1972. Undrained Cyclic Shear of Saturated Sand. ASCE J Soil Mech Found Div 98, 807–825.
Drnevich, V.P., 1967. Effect of Strain History on the Dynamic Properties of Sand 151.
Dyvik, R., Madshus, C., 1985. Lab Measurements of G m a x Using Bender Elements, in: Advances in the Art of Testing Soils under Cyclic Conditions. ASCE, pp. 186–196.
Elias, V., Welsh, J., Warren, J., Lukas, R., Collin, J.G., Berg, R.R., 2008. Ground Improvement Methods. Struct. Found. Des. Man. 124–139. https://doi.org/10.1002/9780470775066.ch8
Erdik, M., 2000. Report on 1999 Kocaeli and Düzce (Turkey) earthquakes. Boğaziçi Üniversitesi, Kandilli Rasathanesi ve Deprem Araştirma Enstitüsü.
Ewing, W.M., Jardetzky, W.S., Press, F., Beiser, A., 1957. Elastic waves in layered media. Phys. Today 10, 27.
Fasano, G., De Sarno, D., Bilotta, E., Flora, A., 2019. Design of horizontal drains for the mitigation of liquefaction risk. Soils Found.
Fayer, M.J., Hillel, D., 1986. Air encapsulation: I. Measurement in a field soil. Soil Sci. Soc. Am. J. 50, 568–572. https://doi.org/10.2136/sssaj1986.03615995005000030005x
Finn, W.D.L., Emery, J.J., Gupta, Y.P., 1971. Liquefaction of large samples of saturated sand on a shaking table, in: Proc. 1st Can. Conf. Earthquake Eng. Vancouver. pp. 97–110.
Fioravante, V., 2000. Anisotropy of Small Strain Stiffness of Ticino and Kenya Sands from Seismic Wave Propagation Measured in Triaxial Testing. Soils Found. 40, 129–142. https://doi.org/10.3208/sandf.40.4_129
Fioravante, V., Giretti, D., 2016. Unidirectional cyclic resistance of Ticino and Toyoura sands from centrifuge cone penetration tests. Acta Geotech. 11, 953–968. https://doi.org/10.1007/s11440-015-0419-3
Fioravante, V., Giretti, D., Jamiolkowski, M.B., 2008. Physical modelling of piled rafts. Deep Found. bored auger piles 241–248.
Fourie, A.B., Blight, G.E., Papageorgiou, G., 2001. Static liquefaction as a possible explanation for the Merriespruit tailings dam failure. Can. Geotech. J. 38, 707–719.
Garnier, H., Gilson, M., Young, P.C., Huselstein, E., 2007. An optimal IV technique for identifying continuous-time transfer function model of multiple input systems. Control Eng. Pract. 15, 471–486.
Goto, S., Tatsuoka, F., Shibuya, S., Kim, Y., Sato, T., 1991. A simple gauge for local small strain measurements in the laboratory. Soils Found. 31, 169–180.
Green, R., Terri, G., 2005. Number of Equivalent Cycles Concept for Liquefaction Evaluations—Revisited. J. Geotech. Geoenvironmental Eng. 131, 477–488. https://doi.org/10.1061/(ASCE)1090-0241(2005)131:4(477)
Griffiths, D.H., King, R.F., 1965. Applied geophysics for engineers and geologists. Pergamon Press.
Gutenberg, B., Richter, C.F., 1936. On seismic waves (third paper). Gerlands Beitr. Geophys 47, 73–131.
Hanks, T.C., Kanamori, H., 1979. A moment magnitude scale. J. Geophys. Res. Solid Earth 84, 2348–2350.
Hanks, T.C., McGuire, R.K., 1981. The character of high-frequency strong ground motion. Bull. Seismol. Soc. Am. 71, 2071–2095.
Harada, N., Towhata, I., Takatsu, T., Tsunoda, S., Sesov, V., 2006. Development of new

drain method for protection of existing pile foundations from liquefaction effects. Soil Dyn. Earthq. Eng. 26, 297–312. https://doi.org/10.1016/j.soildyn.2005.02.019

Hardin, B.O., Drnevich, V.P., 1972. Shear modulus and damping in soils: measurement and parameter effects. J. Soil Mech. Found. Div 98.

Haskell, N.A., 1953. The dispersion of surface waves on multilayered media. Bull. Seismol. Soc. Am. 43, 17–34.

He, J., Chu, J., Ivanov, V., 2013. Mitigation of liquefaction of saturated sand using biogas, in: Bio- and Chemo- Mechanical Processes in Geotechnical Engineering - Geotechnique Symposium in Print 2013. ICE Publishing, pp. 116–124. https://doi.org/10.1680/bcmpge.60531.011

Hoar, R.J., Stokoe, K.H., 1978. Generation and measurement of shear waves in situ, in: Dynamic Geotechnical Testing. ASTM International.

Howell, R., Rathje, E.M., Kamai, R., Boulanger, R., 2012. Centrifuge modeling of prefabricated vertical drains for liquefaction remediation. J. Geotech. geoenvironmental Eng. 138, 262–271.

Hushmand, B., Scott, R.F., Crouse, C.B., 1988. Centrifuge liquefaction tests in a laminar box. Géotechnique 38, 253–262. https://doi.org/10.1680/geot.1988.38.2.253

Idriss, I.M., Boulanger, R.W., 2008. Soil liquefaction during earthquakes. Earthquake Engineering Research Institute.

Imamura, S., 1998. Nishimatsu dynamic geotechnical centrifuge facility. Proc. Centrifuge 98 19–24.

Ishihara, K., 1993. Liquefaction and flow failure during earthquakes. Geotechnique 43, 351–451.

Ishihara, K., 1985. STABILITY OF NATURAL DEPOSITS DURING EARTHQUAKES. PROCEEDINGS OF THE ELEVENTH INTERNATIONAL CONFERENCE ON SOIL MECHANICS AND FOUNDATION ENGINEERING, SAN FRANCISCO, 12-16 AUGUST 1985. Publ. Balkema.

Ishihara, K., 1984. Post-earthquake failure of a tailings dam due to liquefaction of pond deposit.

Ishihara, K., Koga, Y., 1981. Case studies of liquefaction in the 1964 Niigata earthquake. Soils Found. 21, 35–52.

Ishihara, K., Li, S.-I., 1972. Liquefaction of saturated sand in triaxial torsion shear test. Soils Found. 12, 19–39.

Ishihara, K., SHIMIZU, K., YAMADA, Y., 1981. Pore water pressures measured in sand deposits during an earthquake. Soils Found. 21, 85–100.

Ishihara, K., Yoshimine, M., 1992. Evaluation of settlements in sand deposits following liquefaction during earthquakes. Soils Found. 32, 173–188.

Ishihara, M., Okamura, M., Oshita, T., 2003. Desaturating sand deposit by air injection for reducing liquefaction potential. Pacific Conf. Earthq. Eng.

Jaky, J., 1944. The coefficient of earth pressure at rest. J. Soc. Hungarian Archit. Eng. 355–358.

Kaiser, A., Holden, C., Beavan, J., Beetham, D., Benites, R., Celentano, A., Collett, D., Cousins, J., Cubrinovski, M., Dellow, G., 2012. The Mw 6.2 Christchurch earthquake of February 2011: preliminary report. New Zeal. J. Geol. Geophys. 55, 67–90.

Kanamori, H., 1977. The energy release in great earthquakes. J. Geophys. Res. 82, 2981–2987.

Karimi, Z., Dashti, S., 2016. Seismic performance of shallow founded structures on

liquefiable ground: validation of numerical simulations using centrifuge experiments. J. Geotech. Geoenvironmental Eng. 142, 4016011.
Kitazume, M., Terashi, M., 2013. The deep mixing method. CRC press.
Kleyn, A.H., 1982. Seismic reflection interpretation. Springer.
Kovacs, W.D., Leo, E., 1981. Cyclic simple shear of large scale sand samples: effects of diameter to height ratio.
Kramer, S., 1996. Geotechnical Earthquake Engineering. Prentice-Hall, Inc. New Jersey 348–422.
Kramer, S.L., Seed, H.B., 1988. Initiation of soil liquefaction under static loading conditions. J. Geotech. Eng. 114, 412–430.
Ladd, R.S., Dutko, P., 1985. Small Strain Measurements Using Triaxial Apparatus, in: Advances in the Art of Testing Soils Under Cyclic Conditions. ASCE, pp. 148–165.
Lai, C.G., Bozzoni, F., Mangriotis, M.-D., Martinelli, M., 2015. Soil liquefaction during the 20 may 2012 M5. 9 Emilia earthquake, northern Italy: field reconnaissance and post-event assessment. Earthq. Spectra 31, 2351–2373.
Lambe, P.C., 1981. Dynamic centrifuge modelling of a horizontal sand stratum. Civ. Eng. Massachusetts Inst. Technol. Cambridge, USA.
Langhaar, H.L., 1951. Dimensional analysis and theory of models. Wiley New York.
Lawrence, F. V, 1963. Propagation velocity of ultrasonic waves through sand. MIT Res. Rep. R63-8.
Lee, K.L., Albaisa, A., 1974. Earthquake induced settlements in saturated sands. J. Geotech. Geoenvironmental Eng. 100.
Lee, M.K.W., Finn, W.D.L., 1975. DESRA-1, Program for the dynamic effective stress response analysis of soil deposits including liquefaction evaluation. Soil Mech. Ser. No 36.
Lombardi, D., Bhattacharya, S., 2014. Liquefaction of soil in the Emilia-Romagna region after the 2012 Northern Italy earthquake sequence. Nat. hazards 73, 1749–1770.
Lukas, R.G., 1995. Dynamic compaction. Federal Highway Administration, Office of Engineering, Office of Technology ….
Lundegard, P.D., Andersen, G., 1996. Multiphase numerical simulation of air sparging performance. Groundwater 34, 451–460.
Ma, X.F., He, Z.M., Zhu, H.H., Lin, M., 2006. Development of a new geotechnical centrifuge at Tongji University in Shanghai, in: Proc. 6th Int. Conf. on Physical Modelling in Geotechnics. pp. 151–156.
Manzari, M.T., Dafalias, Y.F., 1997. A critical state two-surface plasticity model for sands. Géotechnique 47, 255–272. https://doi.org/10.1680/geot.1997.47.2.255
Marcuson, W.F., Hynes, M.E., Franklin, A.G., 1990. Evaluation and use of residual strength in seismic safety analysis of embankments. Earthq. Spectra 6, 529–572.
Matsuo, O., 1998. The dynamic geotechnical centrifuge at PWRI, in: Proc. Intl. Conf. CENTRIFUGE'98. pp. 25–30.
McCray, J.E., 2000. Mathematical modeling of air sparging for subsurface remediation: state of the art. J. Hazard. Mater. 72, 237–263.
Mele, L., Tian, J.T., Lirer, S., Flora, A., Koseki, J., 2018. Liquefaction resistance of unsaturated sands: experimental evidence and theoretical interpretation. Géotechnique 69, 541–553.
Miller, G.F., Pursey, H., Bullard, E.C., 1955. On the partition of energy between elastic waves in a semi-infinite solid. Proc. R. Soc. London. Ser. A. Math. Phys. Sci. 233, 55–

69.
Minarelli, L., Amoroso, S., Tarabusi, G., Stefani, M., Pulelli, G., 2016. Down-hole geophysical characterization of middle-upper Quaternary sequences in the Apennine Foredeep, Mirabello, Italy. Ann. Geophys. 59, 543.
Mogami, T., 1953. The behavior of sand during vibration, in: Proc. 3rd ICSMFE. pp. 152–155.
Nacci, V.A., 1967. Influence of clay structure on elastic wave velocities. Proc. Int. Sympo. Wave Propag. Dyn. Prop. Earth Mater. 491–502.
Naesgaard, E., 2011. A hybrid effective stress–total stress procedure for analyzing soil embankments subjected to potential liquefaction and flow.
Nguyen, T. V, Rayamajhi, D., Boulanger, R.W., Ashford, S.A., Lu, J., Elgamal, A., Shao, L., 2012. Effect of DSM grids on shear stress distribution in liquefiable soil, in: GeoCongress 2012: State of the Art and Practice in Geotechnical Engineering. pp. 1948–1957.
O'Rourke, T.D., 1995. Geotechnical effects. Preliminary Report from the Hyogoken-Nanbu Earthquake of January 17, 1995. Natl. Cent. Earthq. Eng. Res. Bull. Suny, Buffalo 9.
Okamura, M., Ishihara, M., Oshita, T., 2003. Liquefaction resistance of sand deposit improved with sand compaction piles. Soils Found. 43, 175–187.
Okamura, M., Soga, Y., 2006. Effects of pore fluid compressibility on liquefaction resistance of partially saturated sand. Soils Found. 46, 695–700.
Okamura, M., Takebayashi, M., Nishida, K., Fujii, N., Jinguji, M., Imasato, T., Yasuhara, H., Nakagawa, E., 2011. In-Situ Desaturation Test by Air Injection and Its Evaluation through Field Monitoring and Multiphase Flow Simulation. J. Geotech. Geoenvironmental Eng. 137, 643–652. https://doi.org/10.1061/(ASCE)GT.1943-5606.0000483
Onoue, A., 1988. Diagrams considering well resistance for designing spacing. Soils Found. 2091. https://doi.org/10.1248/cpb.37.3229
Paolucci, E., Albarello, D., D'Amico, S., Lunedei, E., Martelli, L., Mucciarelli, M., Pileggi, D., 2015. A large scale ambient vibration survey in the area damaged by May–June 2012 seismic sequence in Emilia Romagna, Italy. Bull. Earthq. Eng. 13, 3187–3206.
Petalas, A., 2012. PLAXIS LIQUEFACTION MODEL UBC3D-PLM.
Petalas, A., Galavi, V., 2013. Plaxis Liquefaction Model UBC3DPLM. PLAXIS Rep.
Phillips, E., 1869a. De l'équilibre des solides élastiques semblables., in: C.R. Acad. Sct., Paris 68. pp. 75–79.
Phillips, E., 1869b. Du mouvement des corps solides élastiques semblables., in: C.R. Acad. Sct., Paris 69. pp. 911–912.
Phillips, E., 1868. Calcul de l'inluence de l'elasticité de l'anneau bimétallique du balancier compensateur des chronomètres sur l'isochronisme, indépendament des variations de température., in: C.R. Acad. Sct., Paris 67. pp. 508–515.
Poulos, S.J., 1981. The steady state of deformation. J. Geotech. Geoenvironmental Eng. 107.
Poulos, S.J., Castro, G., France, J.W., 1985. Liquefaction evaluation procedure. J. Geotech. Eng. 111, 772–792.
Puebla, H., Byrne, P.M., Phillips, R., 1997. Analysis of CANLEX liquefaction embankments: prototype and centrifuge models. Can. Geotech. J. 34, 641–657. https://doi.org/10.1139/t97-034
Rayamajhi, D., Nguyen, T. V, Ashford, S.A., Boulanger, R.W., Lu, J., Elgamal, A., Shao, L., 2013. Numerical study of shear stress distribution for discrete columns in

liquefiable soils. J. Geotech. Geoenvironmental Eng. 140, 4013034.
Rebata-Landa, V., Santamarina, J.C., 2012a. Mechanical Effects of Biogenic Nitrogen Gas Bubbles in Soils. J. Geotech. Geoenvironmental Eng. 138, 128–137. https://doi.org/10.1061/(ASCE)GT.1943-5606.0000571
Rebata-Landa, V., Santamarina, J.C., 2012b. Mechanical effects of biogenic nitrogen gas bubbles in soils. J. Geotech. Geoenvironmental Eng. 138, 128–137.
Rendulic, L., 1936. Porenziffer und porenwasserdruck in tonen. Der Bauingenieur 17, 559–564.
Richter, C.F., 1935. An instrumental earthquake magnitude scale. Bull. Seismol. Soc. Am. 25, 1–32.
Robertson, P.K., Campanella, R.G., 1985. Liquefaction potential of sands using the CPT. J. Geotech. Eng. 111, 384–403.
Rollins, K.M., Quimby, M., Johnson, S.R., Price, B., 2009. Effectiveness of stone columns for liquefaction mitigation of silty sands with and without wick drains, in: Advances in Ground Improvement: Research to Practice in the United States and China. pp. 160–169.
Rowe, P.W., 1962. The Stress-Dilatancy Relation for Static Equilibrium of an Assembly of Particles in Contact. Proc. R. Soc. A Math. Phys. Eng. Sci. 269, 500–527. https://doi.org/10.1098/rspa.1962.0193
Sabetta, F., Pugliese, A., 1987. Attenuation of peak horizontal acceleration and velocity from Italian strong-motion records. Bull. Seismol. Soc. Am. 77, 1491–1513.
Schima, S., LaBrecque, D.J., Lundegard, P.D., 1996. Monitoring air sparging using resistivity tomography. Groundw. Monit. Remediat. 16, 131–138.
Schofield, A.N., 1980. Cambridge geotechnical centrifuge operations. Geotechnique 30, 227–268.
Sciarra, A., Cantucci, B., Buttinelli, M., Galli, G., Nazzari, M., Pizzino, L., Quattrocchi, F., 2012. Soil-gas survey of liquefaction and collapsed caves during the Emilia seismic sequence. Ann. Geophys. 55.
Seed, H., Idriss, I., 1971. Simplified Procedure for Evaluating Soil Liquefaction Potential. J. Soil Mech. Found. Div. https://doi.org/10.1017/S1431927610093359
Seed, H.B., Booker, J.R., 1976. Stabilization of potentially liquefiable sand deposits using gravel drains. ASCE, J. Geotech. Eng. Div. https://doi.org/10.1017/CBO9781107415324.004
Seed, H.B., Idriss, I.M., Arango, I., 1983. Evaluation of liquefaction potential using field performance data. J. Geotech. Eng. 109, 458–482.
Seed, H.B., Idriss, I.M., Makdisi, F., Banerjee, N., 1975. Representation of irregular stress time histories by equivalent uniform stress series in liquefaction analyses. EERC 75-29. Earthq. Eng. Res. Center, Univ. California, Berkeley.
Seed, R.B., Harder Jr, L.F., 1990. SPT-based analysis of cyclic pore pressure generation and undrained residual strength. Bolton Seed Memorial Symposium.
Severi, P., Staffilani, F., 2012. Geologia ed Idrogeologia della pianura Ferrarese, in: WARB Conference, Copparo Ferrara, Italy.
Shen, C.K., 1998. Development of a geotechnical centrifuge in Hong Kong, in: Proc. Int. Conf. Centrifuge 98.
Shirley, D.J., Anderson, A.L., 1975. In situ measurement of marine sediment acoustical properties during coring in deep water. IEEE Trans. Geosci. Electron. 13, 163–169.
Siddharthan, R., Finn, W.D.L., 1982. TARA-2, two-dimensional non-linear static and

dynamic response analysis. Soil Dyn. Gr.
Silver, M.L., Seed, H.B., 1971. Volume changes in sands during cyclic loading. J. Soil Mech. Found. Div.
Sondermann, W., Wehr, W., 2004. Deep vibro techniques. Gr. Improv. 2, 57–92.
Stark, T.D., Mesri, G., 1992. Undrained shear strength of liquefied sands for stability analysis. J. Geotech. Eng. 118, 1727–1747.
Steedman, R.S., Sharp, M., 2001. Liquefaction of deep saturated sands under high effective confining stress.
Stokoe, K.H., Wright, S.G., Bay, J.A., Roesset, J.M., 1994. Characterization of geotechical sites by SASW method. Unkn. J. 15–25.
Taylor, M.L., Cubrinovski, M., Bradley, B.A., 2012. Characterisation of ground conditions in the Christchurch Central Business District.
Thevanayagam, S., Martin, G.R., Nashed, R., Shenthan, T., Kanagalingam, T., Ecemis, N., 2006. Liquefaction remediation in silty soils using dynamic compaction and stone columns.
Thomson, W.T., 1950. Transmission of elastic waves through a stratified solid medium. J. Appl. Phys. 21, 89–93.
Tokimatsu, K., Seed, H.B., 1987. Evaluation of settlements in sands due to earthquake shaking. J. Geotech. Eng. 113, 861–878.
Tokimatsu, K., Yoshimi, Y., Ariizumi, K., 1990. Evaluation of liquefaction resistance of sand improved by deep vibratory compaction. Soils Found. 30, 153–158.
Traylen, N., 2017. Resin Injection Ground Improvement Research Trials. Res. Rep.
Trifunac, M.D., Brady, A.G., 1975a. On the correlation of seismic intensity scales with the peaks of recorded strong ground motion. Bull. Seismol. Soc. Am. 65, 139–162.
Trifunac, M.D., Brady, A.G., 1975b. A study on the duration of strong earthquake ground motion. Bull. Seismol. Soc. Am. 65, 581–626. https://doi.org/10.1016/0148-9062(76)90487-3
Tsegaye, A., 2010. Plaxis liquefaction model. Extern. report. PLAXIS Knowl. base www. plaxis. nl.
Tsukamoto, Y., Ishihara, K., Nakazawa, H., Kamada, K., Huang, Y., 2002. Resistance of partly saturated sand to liquefaction with reference to longitudinal and shear wave velocities. Soils Found. 42, 93–104.
Ueno, K., 1998. Methods for preparation of sand samples, in: Proceedings of 1998 Int. Conf. of Centrifuge. pp. 1047–1056.
Vaid, Y.P., Chern, J.C., 1985. Cyclic and monotonic undrained response of saturated sands, in: Advances in the Art of Testing Soils under Cyclic Conditions. ASCE, pp. 120–147.
Van Genuchten, M.T., 1980. A closed-form equation for predicting the hydraulic conductivity of unsaturated soils 1. Soil Sci. Soc. Am. J. 44, 892–898.
Van Laak, P.A., Adalier, K., Dobry, R., Elgamal, A.-W., 1998. Design of RPI's large servohydraulic centrifuge shaker, in: Centrifuge 98. pp. 105–110.
Vannucchi, G., Crespellani, T., Facciorusso, J., Ghinelli, A., Madiai, C., Puliti, A., Renzi, S., 2012. Soil liquefaction phenomena observed in recent seismic events in Emilia-Romagna Region, Italy. Int. J. Earthq. Eng. 2.
Vasquez-Herrera, A., Dobry, R., Ng, T.-T., 1988. Pore pressure buildup and liquefaction failure of anisotropically consolidated sand due to cyclic straining, in: Hydraulic Fill Structures. ASCE, pp. 346–366.
Xavier Nuques Luque, R., 2017. Numerical Analyses of Liquefaction-Induced Building

Settlement. University of California, Berkeley.
Yasuda, S., 2007. Remediation methods against liquefaction which can be applied to existing structures, in: Earthquake Geotechnical Engineering. Springer, pp. 385–406.
Yasuhara, H., Okamura, M., Kochi, Y., 2008. Experiments and Predictions of Soil Desaturation By Air-Injection Technique and the Implications Mediated By Multiphase Flow Simulation. Soils Found. 48, 791–804. https://doi.org/10.3208/sandf.48.791
Yegian, M.K., Eseller-Bayat, E., Alshawabkeh, A.A., Ali, S., 2007. Induced-partial saturation for liquefaction mitigation: experimental investigation. J. Geotech. Geoenvironmental Eng. 133, 372–380. https://doi.org/10.1061/(ASCE)1090-0241(2007)133
Yokota, K., Imai, T., Konno, M., 1981. Dynamic deformation characteristics of soils determined by laboratory tests. OYO Tec. Rep 3, 13–37.
Youd, T.L., 2018. Application of MLR Procedure for Prediction of Liquefaction-Induced Lateral Spread Displacement. J. Geotech. Geoenvironmental Eng. 144, 4018033.
Youd, T.L., 1995. Liquefaction-induced lateral ground displacement.
Youd, T.L., 1984. Recurrence of liquefaction at the same site, in: Proc. 8th World Conf. Earthq. Engng. Prentice-Hall Inc, pp. 231–238.
Youd, T.L., 1972. Compaction of sands by repeated shear straining. J. Soil Mech. Found. Div 98.
Youd, T.L., Hoose, S.N., 1977. Liquefaction susceptibility and geologic setting, in: Proc., 6th World Conf. on Earthquake Engineering. Indian Society of Earthquake Technology Roorkee, India, pp. 37–42.
Zeng, X., Schofield, A.N., 1996. Design and performance of an equivalent-shear-beam container for earthquake centrifuge modelling. Geotechnique 46, 83–102.
Zeybek, A., Madabhushi, S.P.G., 2017. Centrifuge testing to evaluate the liquefaction response of air-injected partially saturated soils beneath shallow foundations. Bull. Earthq. Eng. 15, 339–356.
Zienkiewicz, O.C., Bicanic, N., Shen, F.Q., 1989. Earthquake input definition and the trasmitting boundary conditions, in: Advances in Computational Nonlinear Mechanics. Springer, pp. 109–138.

A APPENDIX A

A.1 Seismology hints

Many places in the world are affected by medium and high earthquake hazard and seismic events represent a great risk for anthropic environment. Earthquake is the result of energy propagation in the ground due, principally, to the fault rupture or volcanic activities. Fault is the opening of a fracture in the rock, which could be some kilometres length, due to tectonic actions. Usually in engineer practice, the fault is gathered in a point called *hypocentre*, his projection on the ground surface is called *epicentre*.

Effects of the earthquake depend on the location of the fault. Generally, a deep fault has a greater energy than shallow one, this is a consequence of stress condition. Effects at the ground surface, due to the fault rupture, are strongly depending on the distance of the site from the hypocentre. Indeed, the soil has a high nonlinear behaviour and the propagation of the earthquake waves leads to a great dissipation of energy along the way from the fault to the ground surface. For this reason, a shallow earthquake could lead to more damages on the buildings than a deep one with higher energy.

Fault rupture leads to an impulse which is modified in frequency and duration by the propagation in the ground. Indeed, an acceleration time history can be registered at the ground surface (Figure A. 1). The energy propagation takes place through different wave types. Ground is not a homogeneous medium and its layering modifies direction and wave type. Generally, it is possible to divide waves in two different groups: body waves and surface waves.

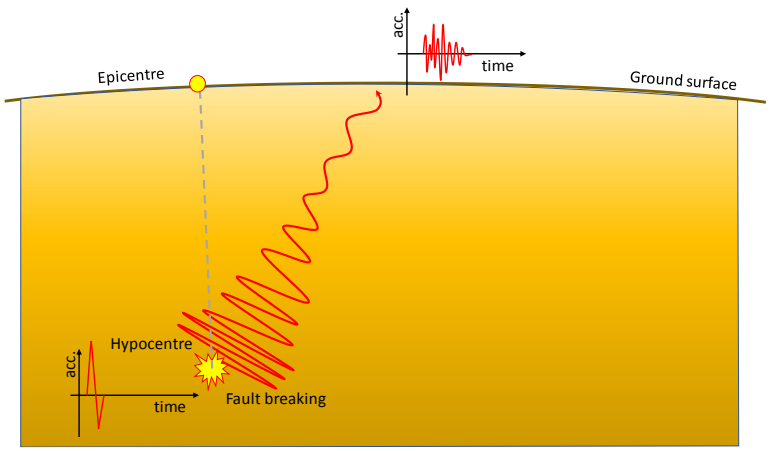

Figure A. 1. Propagation of energy through soil system.

Body waves travel in the internal part of the earth and are divided in two types: primary waves (p-waves) that have the oscillation in the propagation direction and they can travel also in the fluid; secondary waves (s-waves) that have the oscillation perpendicular to their

propagation direction, they cannot travel in fluids. The primary waves are faster than secondary ones.

Secondary waves are further divided in two types: vertical secondary waves (SV) whose particles movement occurs in the vertical plane; horizontal secondary waves (SH) whose particles movement occurs in the horizontal plane.

Surface waves rise from the interaction between body waves and the earth surface. These waves travel along the earth surface and their amplitude decrease exponentially with the depth (Gutenberg and Richter, 1936). It has been shown that surface waves have a not negligible effect on the peak ground motion at great distance from the epicentre (Kramer, 1996).

Two types of surface waves have relevance in engineering practice: Rayleigh waves which stem from the interaction of P and SV waves with the earth surface; Love waves which arise from the interaction of SH waves with soft surficial soil.

A.1.1 Magnitude

Amount of energy released by fault rupture represents an important aspect to valuate effects of earthquake on the environment. Magnitude represents the most significant quantity to evaluate the energy. Different kinds of magnitude are available in the literature:

Richter Local Magnitude (M_L) is defined as the logarithm (base 10) of the maximum trace amplitude (in micrometres) recorded on a Wood-Anderson seismometer located at 100 km (62 miles) from the epicentre of the earthquake (Richter, 1935);

Surface Waves Magnitude (M_S) appropriated for very large distance from the epicentre where the motion is dominate from the surface waves. the expression for M_S is shown in the following equation:

$$M_S = \log A + 1.66 \log \Delta + 2.0 \qquad (A\text{-}1)$$

where A is the maximum ground displacement in micrometres and Δ is the distance from the epicentre valuated in degrees (360° correspond to the earth circumference). This magnitude is suitable to evaluate the size of shallow medium and large earthquakes;

Body Waves Magnitude (m_b) is based on the amplitude and period of firs few cycles of primary waves and it is defined as:

$$m_b = \log A - \log T + 0.01\Delta + 5.9 \qquad (A\text{-}2)$$

where A is the amplitude of primary waves and T is the period of primary waves;

Conversely from the other magnitudes, **Moment Magnitude (M_w)** does not represent an empirical correlation between the energy of the earthquake and his effect and it does not present a scale saturation (Figure A. 2) for strong earthquakes (Hanks and Kanamori, 1979; Kanamori, 1977).

M_w represents a direct calculation of the energy released by fault rupture:

$$M_w = \frac{\log M_0}{1.5} - 10.7 \; ; \; M_0 = \mu A \overline{D} \qquad (A\text{-}3)$$

where M_0 is the seismic moment in dyne-cm; μ is the strength of fault material; A is the rupture area; $\overline{D}$ is the average fault slip.

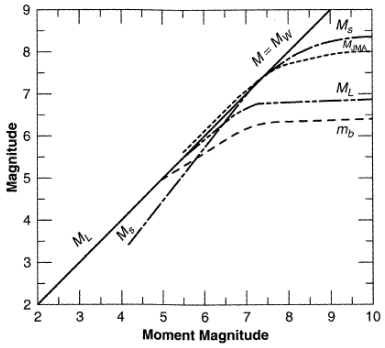

Figure A. 2. Saturation of magnitude scales.

A.1.2 Signal analysis

As previously mentioned, system of soil layers modifies the impulsive nature of fault rupture until producing a periodic signal (Figure A. 1). Generally, time histories of three different component of velocity, acceleration or displacement (one vertical and two orthogonal horizontal ones) are recorded to characterise an earthquake. The rotational components are neglect given their small amplitude.

Records are realised by velocimeters and/or accelerometers that allow to define some significative characteristics of the earthquake like: amplitude, frequency content and significant duration.

The acceleration **amplitude** is frequently used and it is directly correlated to the inertial forces that arise in structures on ground surface. The peak horizontal acceleration (PHA) is the maximum absolute value of horizontal acceleration in time. The peak vertical acceleration (PVA) reaches significant amplitude only in proximity of the epicentre. Furthermore, the vertical component of acceleration has low interest since the structures have great safety factor for vertical loads.

The peak of acceleration could be a significant parameter to evaluate earthquake power and his destructive capacity. However, many earthquakes with a great peak acceleration led to negligible damages due to the small duration of the peak conditions.

In the same way, the peak is defined also for time history of velocity (PHV). This physical quantity is more sensible to moderate frequencies that are strongly correlated to structure damages (Trifunac and Brady, 1975a).

Finally, the peak displacement is often calculated by integration of acceleration or velocity time history. Displacement time history is more sensible to low frequency and it can be affected by significative errors due to environmental noise.

Frequency is another important parameter to define the characteristic of seismic signal. Dynamic response of the structure is strongly influenced by frequency content and by the amplitude associated to each frequency. Dynamic coupling between soil and structure is governed by frequency content and it represents an important aspect to determine the characteristic of the motion.

Fourier amplitude spectrum is one of many useful instruments to analyse periodic signal. This spectrum allows to determine the amplitude associated to each frequency (Figure A. 3).

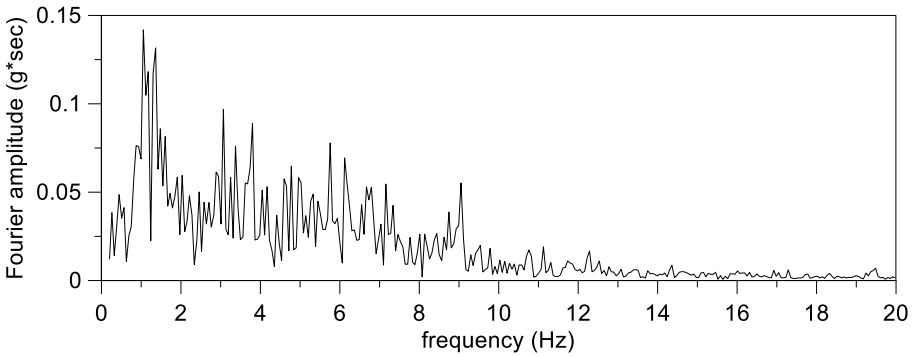

Figure A. 3. Fourier amplitude spectrum.

The **total intensity** of ground motion in the time domain is another important parameter to estimate the statistical properties of signal. The total intensity is defined as integer of squared acceleration time history ((A-4).

$$I_0 = \int_0^{T_d} [a(t)]^2 \, dt \qquad (A\text{-}4)$$

where T_d is the duration of the ground motion.

Response spectrum is frequently used in the engineering practice, this spectrum determines the response of a single degree freedom system (SDOF) under the action due to the earthquake. An elastic behaviour is assumed for the SDOF, but the real behaviour of the common structures is nonlinear under earthquake actions. For this last reason, inelastic response spectra are made by using of the nonlinear relationship between forces and displacements. The response spectrum is not able to characterize strong ground motion, but it allows to evaluate potential effects of earthquake on structures.

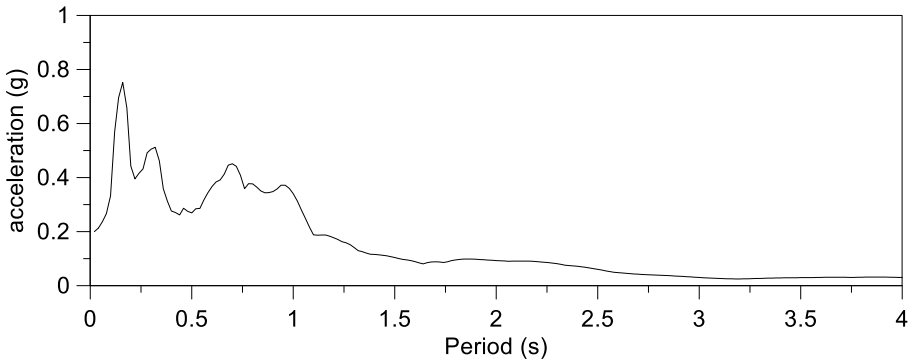

Figure A. 4. Response acceleration spectrum.

Duration of strong motion has a significant influence on the amount of damage on the structure. Indeed, high number of load reversals induces an incremental damage. For this reason, a motion with high amplitude and short duration could lead to lower level of damage than a motion with moderate amplitude and long duration. The duration of earthquake is directly correlated to the amount of energy released from the fault rupture. Indeed, the earthquakes with higher magnitude have a longer duration (Hanks and McGuire, 1981).

A method to evaluate earthquake duration is the *bracketed duration* (Bolt, 1973). This method is based on the assumption of a threshold of a motion parameter. The earthquake duration is defined as time interval between the first and last exceedance.

The total intensity allows to define the significant duration of a ground motion that represents the time interval where the main earthquake actions are. One of the common approaches to determine the significant duration of earthquake is due to (ARIAS A, 1969). The Arias intensity is defined as shown in equation (A-5) and the significant duration is individuated through the choice of a low and high values of the ratio between Arias intensity at a generic time and the maximum value of intensity.

$$I_a = \frac{\pi}{2g}\int_0^{\infty} [a(t)]^2\, dt \qquad (A\text{-}5)$$

The duration of the earthquake could be defined also as an equivalent number of cycles (Seed et al., 1975). In this case, earthquake signal is summarised in a regular harmonic stress function with an amplitude equal to 65% of the maximum amplitude of real shear stress. The equivalent number of cycles is strongly correlated to earthquake magnitude (Table 0.1). In soil liquefaction problems this parameter is very helpful to determine the level of excess pore pressure reached during a seismic event.

Table 0.1. Equivalent number of cycles (Seed et al., 1975).

Earthquake magnitude	*Equivalent number of cycles*
5.25	*2-3*
6	*5*
6.75	*10*
7.5	*15*
8.5	*26*

A.1.3 Magnitude and distance effects

The motion characteristics of the earthquake are strongly correlated to the energy released in the fault failure, so they are dependent from the magnitude. This energy travels through the soil as stress waves and the energy per unit volume decreasing quickly with the distance from the hypocentre. In the years, a large number of earthquakes events were recorded by several measurement stations. This database allowed to study the effect of the waves propagation in the soil as a function of different parameters.

Through regression analyses of data, it was possible to define some predictive relationships that give ground motion parameters in function of characteristic of earthquake source, site conditions, etc. Predictive relationships are functions of different parameters, but they are strongly correlated to earthquake magnitude and distance of site. Generally, these relationships are defined as follow:

$$Y = f(M, R, P_i) \qquad (A\text{-}6)$$

where M is the magnitude, R is the distance from source and P_i is a generic parameter.

Noteworthy that regression analyses highlighted that body waves amplitude decreases according to $1/R$ whereas surface waves amplitude decreases according $1/\sqrt{R}$.

Predictive relationships are dependent on seismology of region and they do not take into account the directionality of fault rupture.

Different seismological parameters present a statistical distribution and predictive relationship can be written as:

$$\log Y = a + bM - c\log(R + C) + F + S \pm \sigma_{\log Y} \qquad (A\text{-}7)$$

where C is an attenuation correction factor, F and S are site and source factors and $\sigma_{\log Y}$ is the standard deviation.

Predictive relationships for parameters that decrease with the distance are named *attenuation relationships*. Acceleration, velocity and displacement belong to this type of relationships.

Some attenuation relationships for different motion parameters are shown in the following:

- Peak acceleration (Sabetta and Pugliese, 1987)

$$\log(PHA) = 0.306\, M_w - \log\sqrt{(D^2 + 5.8^2)} - 0.169\, S_1 - 1.56 \pm 0.19 \qquad (A\text{-}8)$$

Where S_1 is equal to 0 for stiff and deep deposits and equal to 1 for soft and shallow ones.

- Peak velocity (Sabetta and Pugliese, 1987)

$$\log(PHV) = 0.455\, M_w - \log\sqrt{(D^2 + 3.6^2)} - 0.133\, S_3 - 0.71 \pm 0.22 \qquad (A\text{-}9)$$

Where S_3 is equal to 0 for stiff and deep deposits and equal to 1 for soft and shallow ones.

- Earthquake duration (Chang and Krinitzsky, 1977)

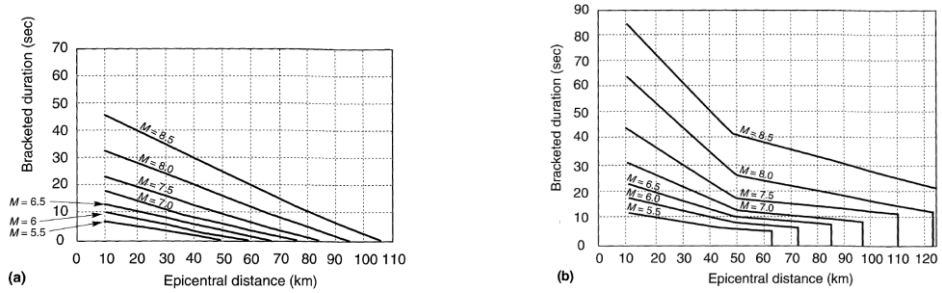

Figure A. 5. Earthquake duration with distance from epicentre: a) rock site; b) soil site.

The amount of earthquake duration depends on its definition. The duration decreases with distance from the source if absolute acceleration levels is taken to account (Chang and Krinitzsky, 1977), whereas duration increases with the distance from the source if relative acceleration levels is taken to account (Trifunac and Brady, 1975b).

- Equivalent number of cycles (Biondi et al., 2012)

$$\ln(N_{eq}) = \alpha + \beta \ln PHA + \gamma \ln I_a + \delta \ln \nu_0 + \varepsilon \ln D_{5-95} \qquad (A\text{-}10)$$

where α, β, γ, δ and ε are parameters that depend by seismic category of soil; I_a is the Arias intensity; D_{5-95} is the significant earthquake duration (Trifunac and Brady, 1975a); ν_0 is the frequency of zero acceleration value in D_{5-95} time interval.

A.2 Dynamic soil properties

As previously mentioned, the energy released during fault rupture travels in the soil by a propagation of mechanical waves. Nature and characteristics of these waves depend on dynamic soil properties. In geotechnical engineering, dynamic problems require a different type of soil investigations as compared to static problems.

Generally, dynamic behaviour of soil is studied by cyclic loads that allow to measure dynamic soil properties in elastic region, inducing very small strain levels, and soil properties in higher strain levels, reaching the transition of soil behaviour from elastic region to elastoplastic one. These dynamic properties have an important role in the propagation and modification of earthquake waves.

A wide range of field and laboratory tests to define dynamic soil properties are available in engineering practice. Tests allow to measure various property and many of these are complementary in the study of soil dynamic behaviour.

Propagation of waves is function of density, stiffness, damping and Poisson's ratio. stiffness and damping have the more important role and these properties show a significative variability in the transition from small to large strain level.

A.2.1 Field tests

Several techniques and instruments are available for the dynamic field tests. Some of these require a drilling while other ones are performed by ground surface. Field tests show vary advantages, they do not require sampling and allow to test large volume of soil. On the other hand, field tests do not allow to control effects of conditions like: drainage, stress, etc.

Dynamic field tests consist in the measurement of induced wave propagation in the soil. Generally, in this tests kind shear strain level is very low (0.001%), this allows to apply the linear theory to evaluate the characteristics of waves propagation.

The type of waves propagated depends on the source kind. The source is represented by hammer, small explosive charges and machines with rotating eccentric mass. For the hammer the impact direction produces different kinds of waves: vertical impact mainly generates P-waves, whereas horizontal impact (using a small beam as support) mainly generates SH-waves.

P-waves are faster than S-waves, therefore their arrival time is easier to measure. However, P-waves could be affected by some interferences as the position of the water table. Indeed, P-waves reach a velocity equal almost to 1500 m/s in saturated soil independently from the nature of soil skeleton.

Arrival time of S-waves is much difficult to define. For this reason, the technique of polarity inversion is fundamental in the measurements of this type of waves. This technique is applied in SH-waves propagation striking on opposite end of beam. P-waves amplitude and environmental noises are reduced combining the records with opposite polarity. Thereby arrival time of S-wave is much clear. Shear waves are not affected by water presence in the soil.

Some dynamic field tests are based on the reflection and/or refraction of the waves. Measurements of the **Reflected Waves** are performed from ground surface and allow to determine dynamic soil properties in very large volume of soil and for very deep stratigraphy. Generally, P-waves are employed in this test. Waves travel through the soil from the source to the receiver where arrival time is measured. One wave propagates on the soil surface and it is the first wave that arrives to the receiver, another one is reflected in correspondence with the transition between two different soils with different stiffness and/or density (Ewing et al., 1957; Griffiths and King, 1965; Kleyn, 1982). An important limitation of this technique is represented by the using of first arrival time regardless of receiver position.

The seismic test with **Refracted Waves** has not this last limitation. This technique is performed using a source and receives (geophones) array that measures arrival time of different waves. Refraction test allows to define a stratigraphy with a great number of layers.

The detecting of wave arrivals and arrival time is avoided by using **Steady-State test**. A vibrating circular footing is used to propagate mainly surface Rayleigh waves (Miller et al., 1955). A receiver is placed on the source and another one is moved at different distances from the source. When the two receivers are in-phase the distance between receivers is equal to wavelength of Rayleigh. Therefore, the velocity of Rayleigh wave is:

$$v_R = \omega \frac{\lambda_R}{2\pi} = f\lambda_R \qquad (A\text{-}11)$$

Through this velocity is possible to calculate the velocity of S-waves by the following relationship:

$$v_S \approx 1.09\, v_R \qquad (A\text{-}12)$$

The Rayleigh wavelength changes when soil stiffness changes with depth, this effect is a function of frequency of source. Indeed, Rayleigh wave propagates up to $\lambda_R/3$ to $\lambda_R/2$ of depth. An estimate of waves velocity with depth is possible through this test varying the frequency of source signal. Consecutive soil layers with large dissimilar stiffness are not detected with this test.

The **Spectral Analysis of Surface Waves (SASW)** test represents an upgrade of steady-state test. Dispersion curve of wave velocity is used in this test. The same procedure of steady-state test is adopted to generate the dispersion curve. An impulsive or random noise can be used as waves source (Stokoe et al., 1994). Two receivers are employed in the test that record the waves in vertical direction. The signals are elaborated in frequency domain

by fast Fourier transform. Arrival time is calculated by the phase difference for each frequency (Eq. (A-13)

$$\Delta t(f) = \frac{\phi(f)}{2\pi f} \tag{A-13}$$

where ϕ is the phase of a wave with a frequency f.

Velocity and wavelength of Rayleigh waves can be calculated by the distance between the receivers and frequency of each wave (Eqs. (A-14(A-15). Thickness and shear waves velocity of each soil layer are defined by an iterative matching of theoretical dispersion curve with experimental one. The theoretical dispersion curve is evaluated by the Haskell-Thomson solution (Haskell, 1953; Thomson, 1950).

$$v_R(f) = \frac{\Delta d}{2\pi\, \Delta t(f)} \tag{A-14}$$

$$\lambda_R(f) = \frac{v_R(f)}{f} \tag{A-15}$$

From the equation (A-15 is deduced that the waves with lower frequencies reach deeper soil layers.

Multichannel Analysis of Superficial Waves (MASW) is a variant of SASW. This technique uses a sinusoidal signal source and more than two receivers placed in linear disposition with variable spacing. The combination two by two of the signals at receivers leads to different dispersion curves that allow to find more vibrational modes of soil stratigraphy. This aspect is important where an inversion of waves velocity with depth is. Indeed, in this case vibrational modes higher than one are activated.

Other field tests for study of dynamic soil properties require making of boreholes. This kind of test are more expensive than superficial ones, but they introduce lower number of uncertainties in the interpretation of the results.

Cross-Hole test is made realizing two or more boreholes. An impulsive source is placed in one borehole, whereas receivers are placed other ones. The source and receivers are fixed in boreholes at the same depth and arrival time of wave is recorded by each receiver. In this case the waves travel through the soil in horizontal direction and the wave velocity of the soil layer is determined knowing the horizontal distance between boreholes. The source impulse can be applied in different ways: explosive, SPT blows, torsional impact (Hoar and Stokoe, 1978), etc. Better results are achieved with reversible source. Cross-hole test allows to measure, with great reliability, waves velocity at large depth (≈60m), however in this case the monitoring of boreholes verticality is necessary. The reliability of this technique decreases when a very higher velocity layer is nearby and the refraction interpretation is required (Butler et al., 1978).

As previously mentioned, this technique requires at least two boreholes. Therefore, the cross-hole test is very expensive for large deep.

Down-Hole (or Up-Hole) is a cheaper test than Cross-hole since requires one borehole. The source (receiver for Up-Hole) is located on ground surface, close to the borehole, and

receiver or multi receivers are located (source for Up-Hole) in the borehole. An impulse is generated by source and receiver records arrival time of p-waves and/or s-waves. The test is performed in several phase where in each of them the receiver (source for Up-Hole) is moved at different depth and an impulse is generated. The interpretation of Down-Hole measurements could be affected by several issues: presence of water table, soil disturbance during drilling, energy of source, environmental noises.

The maximum depth of investigation for this technique is around 60 m, this limit is due to the damping that dissipates input energy during waves propagation.

Seismic Cone (Robertson and Campanella, 1985) allows to perform Down-Hole test without borehole. This technology consists in a standard CPT test adopting a tip with a geophone or accelerometer. Cross-Hole can be performed using two seismic cones stopping the tips at the same depth.

A.2.2 Laboratory tests

In this section will be shown some laboratory tests to valuate dynamic soil properties. Unlike dynamic field tests, laboratory tests allow to control drainage, stress and strain conditions of soil. However, these tests have some limitations like: specimen represents a small portion of soil domain and it could not be representative of the in-situ significant volume behaviour; soil sampling induces disturbance at the soil structure; stress paths are fixed by the type of test. Sampling in cohesive soils produces little disturbance, whereas causes significative disturbance in cohesionless soils. For this reason, dynamic field tests, without sampling, are adopted to evaluate mechanical property at very low strain level. While, the relative effect of stress and strain level on dynamic soil properties are evaluated by laboratory tests.

Resonant Column test (RC) allows to study dynamic soil behaviour at very small strains. Solid or hollow specimen is used in this test, a sinusoidal load is applied on the top through an electromagnetic apparatus. The frequency and amplitude of the load are controlled.

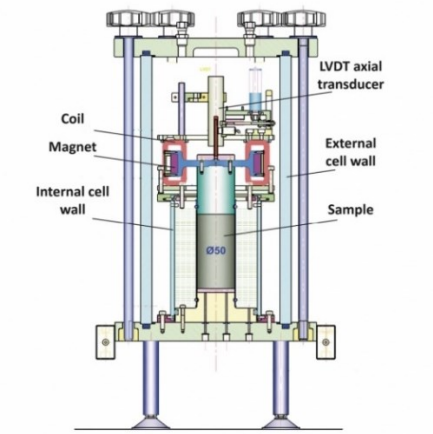

Figure A. 6. Resonant Column test apparatus.

The cyclic load is applied on consolidated specimen. Starting with smallest load amplitude, the frequency of load is gradually increased until the strain amplitude reaches a maximum associated value, in this case the resonance of specimen is achieved. The lowest resonant frequency individuates the fundamental one that is a function of the test apparatus, soil dynamic properties and geometry of specimen.

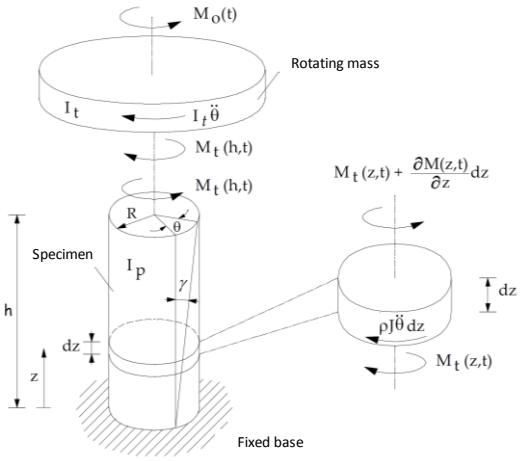

Figure A. 7. Equilibrium of Resonant Column test.

Shear modulus is found by dynamic equilibrium between applied torsional force and inertial forces of application force apparatus and specimen (Figure A. 7).

The applied torsional force at the top of the specimen is equal to:

$$M_0(t) = M_t(h,t) + I_t \frac{\partial^2 \theta}{\partial t^2} \tag{A-16}$$

where I_t is the axial moment of inertia of load apparatus.

The equilibrium of generic soil element leads to the following relationship:

$$\frac{\partial M_t(z,t)}{\partial z} = \rho \cdot J \frac{\partial^2 \theta}{\partial t^2} \tag{A-17}$$

where ρ is the density of material and J is the polar moment of inertia of the soil element section.

In elastic condition the equilibrium solution gives:

$$G(n) = \rho \left(\frac{2\pi f_n h}{\beta} \right)^2 \tag{A-18}$$

where f_n is the natural frequency of the n vibration mode, h is the height of the specimen and β is equal to:

$$\beta = \frac{\omega_n \, h}{V_s} \qquad V_s = \sqrt{\frac{G}{\rho}} \qquad \omega_n = 2\pi \, f_n \qquad \text{(A-19)}$$

G modulus is taken in correspondence of the first vibration mode (fundamental mode).

In solid specimens the shear strain is not uniform along the radius of a generic section of the specimen. For this reason, a conventional value of shear strain is considered. Hardin and Drnevich (1972) suggested to take the value of shear strain at $2/3R$.

Resonant Column allows to calculate damping ratio at different levels of shear strains. Two different methods are available for the damping ratio: Amplitude Decay method and Steady State method.

Amplitude Decay method analyses the deamplification of signal in free dynamic system condition that can be represented by a logarithmic function as:

$$\delta = \frac{1}{(n-1)} \ln \left[\frac{A(t_i)}{A(t_{i+n})} \right] \qquad \text{(A-20)}$$

where n is the number of peaks between the two peaks taken into account (Figure A. 8).

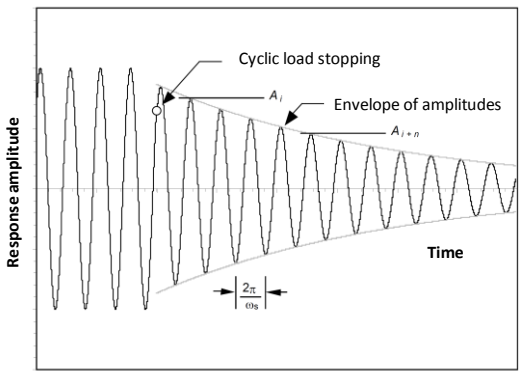

Figure A. 8. Amplitude Decay method.

The damping ratio is evaluable by the following relationship:

$$\xi = \sqrt{\frac{\delta^2}{4\pi^2 + \delta^2}} \qquad \text{(A-21)}$$

Steady State method is applicable also in presence of applied torsional force. The common procedure is the *half power method*. This method is applied changing the frequency of the external forces until reaching steady state for each frequency (Figure A. 9). Found two frequencies that lead to the same system response, the damping can be calculated as:

$$\xi \approx \frac{\beta_2 - \beta_1}{2} \quad or \quad \xi \approx \frac{f_2 - f_1}{f_2 + f_1} \qquad \text{(A-22)}$$

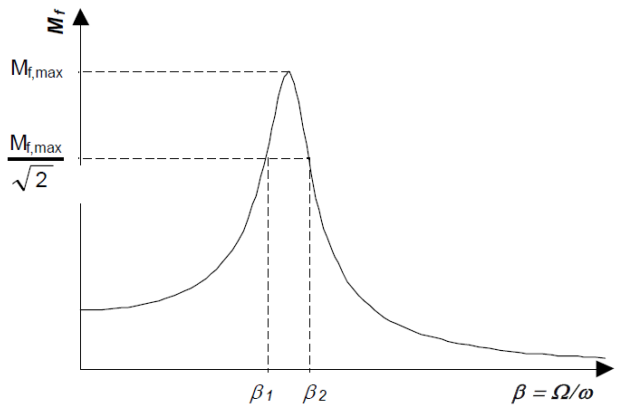

Figure A. 9. Amplification factor curves for Steady State method.

Torsional Cyclic Shear test allows to apply larger shear strains than Resonant Column. The deformation path is the same of RC test. The interpretation of the results is made by static relationships considering that the dynamic influence on the results is negligible. This test allows to study the evolution of shear modulus and damping with number of load cycles. *Degradation indices* can be defined to consider this effect and they are defined as:

$$\delta_G = \frac{G(N)}{G(1)} \qquad \delta_D = \frac{D(N)}{D(1)} \tag{A-23}$$

these indices are function of soil nature, drainage condition, consolidation degree, shear strains amplitude and velocity.

The results of Resonant Column and Torsional Cyclic Shear test can be summarised by some analytical relationships. Yokota et al. (1981) proposed two relationships (A-24) for shear modulus (G) and damping ratio (D).

$$\frac{G}{G_0} = \frac{1}{1 + \alpha\,\gamma^{\beta}} \qquad \frac{D}{D_{max}} = e^{\lambda \frac{G}{G_0}} \tag{A-24}$$

where α and β are two parameters calibrated on linear regression of experimental data, λ is a calibration coefficient.

Ultrasonic Pulse test is a direct measurement test of shear waves that travel through the specimen (Lawrence, 1963; Nacci, 1967). This technique uses ultrasonic transmitters and receivers applied on both ends of the specimen. Transmitters are made by piezoelectric material that changes its dimensions when a voltage across its faces and vice versa it produces voltage when subjected to a deformation. High-frequency electrical signal is applied to transmitter and stress waves travel along specimen reaching the receiver. Waves velocity can be calculated by travel time record and height of specimen.

Piezoelectric Bender Element test is an upgrade of Ultrasonic Pulse test that allows to measure shear wave velocity using bender elements (Alba et al., 1984; Dyvik and Madshus, 1985; Shirley and Anderson, 1975). Bender elements are realised by two elements of piezoelectric material connected each other through insulation (Figure A. 10). Bender

element moves in transversal direction when two harmonic voltages flow in each piezoelectric material element with a phase difference of 180°. In this manner, one element contracts and the other one expands.

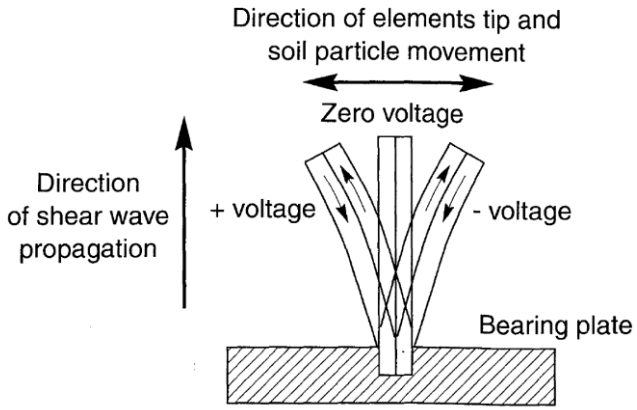

Figure A. 10. Piezoelectric bender element.

Bender elements can be used also as receivers reading the voltage signal that they produce when are subjected to a distortion. The time difference between the two voltage pulses, read by an oscilloscope, divided by specimen length allows to calculate shear waves velocity. Bender elements induce very small strains, so the specimen is still undisturbed.

The characterisation of soil behaviour at high level of shear strains is possible using **Cyclic Triaxial test**. The test apparatus is similar to the classic triaxial test, the difference consists in the possibility to apply a variable deviatoric stress. Generally, a sinusoidal load is applied on the vertical load axis with a frequency that depends on hydraulic and viscosity property of soil. The consolidation phase can be isotropic or anisotropic. Isotropic consolidation is commonly performed. In Cyclic Triaxial test principal stresses are vertical and horizontal, the rotation of them is instantaneous during the cyclic load application and equal to 90°. Stress path of Cyclic Triaxial test can be adapted to the stress path induces by the propagation of shear wave. However, a progressive rotation of principal stresses achieved during earthquake load is not possible.

The errors of measurement equipment and not uniform distribution of stresses and strains due to the presence of the cap and base allows to measure shear strains greater than 0.01%. however, local strain measurement can lead to more accurate measurements up to 0.0001% of shear strain (Burland and Symes, 1982; Goto et al., 1991; Ladd and Dutko, 1985).

Cyclic Direct Simple Shear test is able to apply to the soil a shear stress path similar to the earthquake one. This test is commonly used in the study of liquefaction phenomenon. Lateral confining stress to the cylindrical specimen can be applied by rigid vertical plates or by a vertical series of stiff rings. In this way, a K_0 condition is applied on the vertical boundaries that represents field condition. An upgrade of Cyclic Direct Simple Shear test allows to apply different horizontal confinement stresses by pneumatic way. In this case, the

specimen, already wrapped in a membrane, is in a cell filled with pressurized water. Vertical stress is applied by a rigid cap and shear stress is applied by a horizontal movement on the cap or bottom of the apparatus. However, this test is not able to apply perfectly the stress path produced by earthquake. Indeed, shear stress is guaranteed only on the horizontal specimen faces and not on the vertical ones. This effect generates a not uniform increment of vertical stress that can be reduced using specimens with high diameter-height ratio (Kovacs and Leo, 1981).

Cyclic Torsional Shear test allows to characterise the dynamic soil behaviour in wide range of strain. This test was developed by (Ishihara and Li, 1972) for solid cylindrical specimen. Shear stress is applied by a rotation of the cap that imposes a torsional deformation of the specimen with variable circumferential shear stress on the radius. Use of hollow cylindrical specimen (Drnevich, 1972, 1967) leads to a more uniform distribution of shear stress that avoids many theoretical interpretations of test result.

Generally, the interpretation of the results of these laboratory tests are summarised by an *equivalent linear model*. Hysteretic soil behaviour can be represented by a particular value of the shear modulus (G) and by specific dissipated energy (W_D).

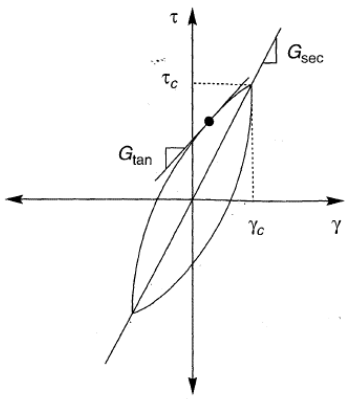

Figure A. 11. Hysteretic cycles in plane of shear stress (τ) and shear strain (γ).

These two parameters are function of strain level, shear modulus is represented by slope of each point of γ-τ curve and the area inside each cycle represents the specific dissipated energy (Figure A. 11).

Equation (A-25) shows the relationship for secant value of G, while W_D can allow to calculate the damping ratio (ξ) through equation (A-26.

$$G_{sec} = \frac{\tau_c}{\gamma_c} \qquad (A\text{-}25)$$

$$\xi = \frac{W_D}{4\pi W_s} = \frac{1}{2\pi}\frac{A_{loop}}{G_{sec}\gamma_s^2} \qquad (A\text{-}26)$$

where W_s is the area inside the triangle composed by τ_c, γ_c and the axes origin, A_{loop} is the area inside a hysteretic loop. Thus, a single loop due to cycling load can be summarised by secant shear modulus peak to peak and area inside the loop. The equivalent linear method approximates the nonlinear behaviour of the soil. Such an approach is not able to reproduce soil failure, but it leads to a very efficient computational process and to good results in dynamic analyses.

Calculation of secant shear modulus and damping for different levels of shear strain leads to define the curve for the modulus redaction (G/G_0) and the curve for the damping ratio. An example of these curve is shown in in Figure A. 12. Shape of these curves is influenced by void ratio, mean effective stress, plasticity index, overconsolidation ratio (OCR) and number of loading cycles. When the plasticity index and/or OCR increases the elastic range, located at very low shear strain levels, and the damping ratio is very small in this range. The maximum value of shear modulus is necessary to evaluate the absolute shear modulus at different value of shear strain. Generally, G_{max} is measured through field tests avoiding soil disturbances.

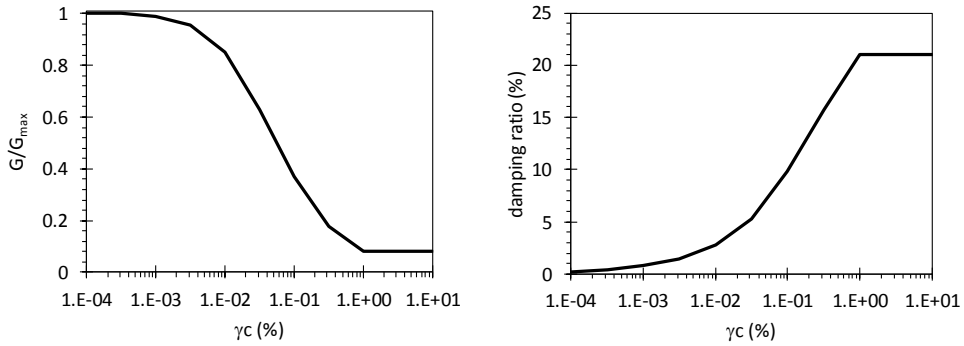

Figure A. 12. Evolution of secant shear modulus and damping ratio with shear strain.

A.2.3 Model tests

Unlike element test, model test reproduces a particular physical problem with real boundary conditions at small scale that represent a full-scale prototype problem. Model testing allows to verify the development of important phenomena and checks of predictive theories. Generally, the model can be subjected to a cyclic load through shaking table.

Stress level in the model test represent an important issue since soil is a stress dependent material. Small scale models can be tested at 1g gravity acceleration (shaking table) or at incremented gravity acceleration (centrifuge test). The increment of gravity acceleration by geotechnical centrifuge allows to reach the same stress level of the prototype scale and the interpretation of test results is made by some scaling laws (Langhaar, 1951) which are a function of the ratio between the centrifuge acceleration and the Earth's gravity N, also called scaling factor.

B APPENDIX B

Experimental tests have the objective to reproduce a physical phenomenon in monitored conditions. In each single test is possible to record some physical quantities which represent the results of the experimental test. Physical measurement records allow to define if the desired phenomenon is achieved. However, the discretization of the recorders does not permit to understand completely the development of phenomenon. Numerical simulation represents a helpful solution to reproduce the phenomenon and to observe the physical quantities in whole model. The using of suitable constitutive model for the materials and the calibration of the numerical model on experimental data increase strongly the reliability of the numerical results. Appropriate numerical models and constitutive models were used in this work to reproduce the different configuration of system realized in experimental centrifuge tests.

B.1 Constitutive models

The numerical simulation of the real mechanical behaviour of the liquefiable soil requires appropriate constitutive models. The excess pore pressure build-up of pore fluid represents the main feature in liquefaction problems. The build-up is governed by volumetric-distortional behaviour, this requires a link between plastic distortional strain and volumetric one. Some constitutive models reproduce this mechanical aspect through simplified approach that links the volumetric strains with the plastic distortional ones and the mobilized dilatancy angle. Furthermore, the shear stiffness evolution is a function of the number of cycles and the stiffness in liquefied status is assumed as a rate of the initial one.

More sophisticated constitutive models calculate the volumetric strain using the relative state parameter index defined as the vertical distance of the actual condition from the critical state in the plane D_R-p'.

B.1.1 UBC3D-PML

UBC3D-PML (Petalas, 2012) is a constitutive model based on the UBCSand model (Puebla et al., 1997) that uses two yield surfaces of the Mohr-Coulomb type, one related to isotropic hardening and the other to kinematic hardening.

It is an elastoplastic model with non-associated plastic flow rule and is based on the Drucker-Prager's low and Rowe's stress dilatancy hypothesis. The model parameters calibration can be performed by using empirical relationships based on sand relative density (Beaty and Byrne, 2011b).

This model has been developed for the prediction of liquefaction in sandy soils. Its formulation is based on classical plasticity theory with a hyperbolic strain hardening rule, based on the Duncan-Chang approach with modifications. The hardening rule relates the mobilized friction angle to the plastic shear strain at a given stress. The flow rule in the model is based on the stress-dilatancy theory developed by Rowe (1962), linearized and simplified according to energy considerations. The UBC3D model uses the Mohr-Coulomb yield condition in a 3-D principal stress space. Moreover, a modified non-associated plastic

potential function based on Drucker-Prager's criterion is used, in order to maintain the assumption of stress-strain coaxially in the deviatoric plane for a stress path beginning from the isotropic line (Tsegaye, 2010).

A soil densification rule is added in order to predict a more realistic evolution of excess pore pressures during cyclic loading. This allows the increase of the volumetric strains with a decreasing rate during shearing.

The elastic behaviour occurring within the yield surface is governed by a non-linear law. Two parameters control this non-linear behaviour: the elastic bulk modulus K and the elastic shear modulus G. K and G are non-linear functions of the mean stress:

$$K = K_B^e P_A \left(\frac{p}{P_{ref}}\right)^{me} \tag{B.1}$$

$$G = K_G^e P_A \left(\frac{p}{P_{ref}}\right)^{ne} \tag{B.2}$$

where K_B^e and K_G^e are the bulk and the shear modulus, respectively, at a reference stress level. The factors ne and me are parameters that define the rate of stress dependency of stiffness. The reference stress level (p_{ref}) is commonly taken as the atmospheric pressure (P_A=100 kPa). Pure elastic behaviour is predicted by the model during the unloading process. Once the stress state reaches the yield surface, plastic behaviour is predicted as long as the stress point is not going immediately back into the elastic zone. The hardening rule governs the amount of plastic strain as a result of mobilization of the shear strength ($\sin \varphi_{mob}$). The mobilized friction angle derived from the Mohr-Coulomb yield criterion is given as:

$$\sin \varphi_{mob} = \frac{\sigma_1' - \sigma_3'}{\sigma_1' + \sigma_3'} = \frac{t_{mob}}{s'} \tag{B.3}$$

where t_{mob} is the mobilized shear stress and s is the mean effective stress.

The hyperbolic hardening rule relates the increment of the sine of the mobilized friction angle to the plastic shear strain increment as follows:

$$\delta\gamma^p = \left(\frac{1}{G^*}\right) \delta \sin \varphi_{mob} \tag{B.4}$$

$$G^* = K_G^p \left(\frac{p'}{P_A}\right)^{np} \left\{1 - \left(\frac{\sin \varphi_{mob}}{\sin \varphi_{peak}}\right) R_F\right\}^2 \tag{B.5}$$

where K_G^p is the plastic shear modulus number; np is the plastic shear modulus exponent; φ_{mob} is the mobilized friction angle, which is defined by the stress ratio; φ_{peak} is the peak

friction angle; and R_F is the failure ratio $\frac{n_f}{n_{ult}}$, ranging from 0.5 to 1.0, where n_f is the stress ratio at failure and n_{ult} is the asymptotic stress ratio from the best fit hyperbola. The evolution of the plastic shear modulus with the plastic component γ^p of the shear strain is reported in Figure B. 1.

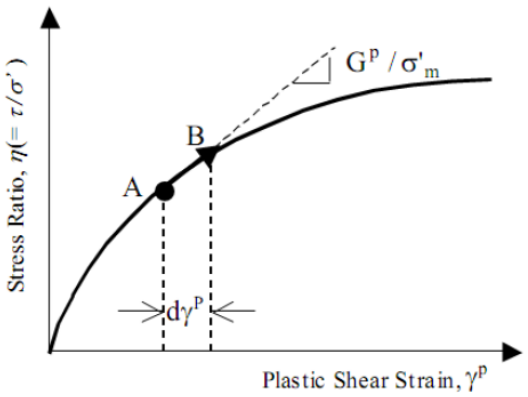

Figure B. 1. Evolution of the plastic shear modulus Gp as a function of the plastic component γp of the shear strain.

In the UBC3D-PLM model the flow rule of the original UBCSAND model is used, which was derived from energy considerations by Puebla et al. (1997). The flow rule used in UBCSAND is based on three observations:

1. there is a unique stress ratio, defined by the constant volume friction angle φ_{cv}, for which plastic shear strains do not cause plastic volumetric strains;

2. stress ratios which lie below $\sin\varphi_{cv}$ exhibit contractive behaviour, while stress ratios above it leads to a dilative response;

3. the amount of contraction or dilation depends on the difference between the current stress ratio and the stress ratio at $\sin\varphi_{cv}$.

The variation of the plastic volumetric strain is given by:

$$d\varepsilon_v^p = \sin\psi_m d\gamma^p \tag{B.6}$$

where:

$$\sin\psi_m = \sin\varphi_m - \sin\varphi_{cv} \tag{B.7}$$

The evolution of the volumetric soil behaviour is shown in Figure B. 2.

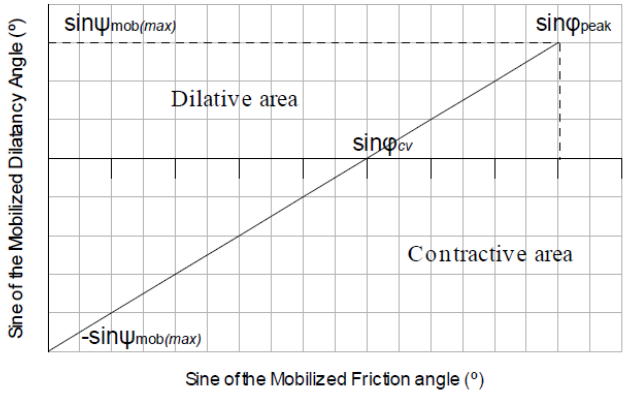

Figure B. 2. Mobilized dilatancy angle.

The densification rule is fully valid for symmetric loading cycles, for the case that shearing starts from the isotropic stress state. In a p' − q stress space when the mobilized friction angle is very small a half cycle is counted. The drained plastic shear modulus K_G^p becomes stiffer after the first full cycle in function of the follow equation:

$$K_G^p = K_{G,primary}^p \left(4 + \frac{n_{cross}}{2}\right) hard\ fac_{dens} \tag{B.8}$$

where n_{cross} is the number of half cycles generated from the beginning of the test, hard is a factor which is correcting the densification rule for loose soils and fac_{dens} is a multiplier which is a user input parameter to adjust the densification rule. A correction is made in the densification rule for loose sands $\left(5 \leq N_{1,60} \leq 9\right)$ according to the experimental observations and following the formulation of the UBCSAND for hard factor correlated to the SPT number and it follows the experimental observation proposed by Beaty and Byrne (2011) and reported by Naesgaard (2011):

$$hard = \min\left(1, \max(0.5; 0.1N_{1,60})\right) \tag{B.9}$$

the plastic shear modulus is limited by the maximum $N_{1,60}$ for a very dense soil that is defined as 60:

$$K_{G,max}^p = K_G^p \left(\max N_{1,60mox}^2\right) 0.003 + 100 \tag{B.10}$$

The new yield surfaces are schematically presented in Figure B. 3.

In Case a, primary loading occurs during the first half cycle in an arbitrary simple shear test starting from the p' axis. The initial input parameter for the plastic shear modulus K_G^p is used and both yield surfaces expand until the maximum stress state.

In Case b, elastic unloading occurs and the secondary yield surface shrinks until it reaches the isotropic axis where $\sin \varphi_{mob}$ is very small. A half cycle is counted. Since an isotropic

hardening rule is used for the primary yield surface, it remains at the maximum stress state reached since the beginning of the test.

In Case c, secondary loading occurs but with an identical plastic shear modulus as used in primary loading followed by elastic unloading. A full cycle is counted. After the full cycle the densification rule is activated.

In Case d, secondary loading occurs with a plastic shear modulus 4.5 times stiffer than used in primary loading. The secondary yield surface expands until it reaches the maximum stress state of the primary yield surface. Then primary loading is predicted again until the new maximum stress state.

Finally, *in Case e*, when the primary yield surface touches the peak stress state (governed by the peak friction angle) the secondary yield surface is deactivated. After the deactivation of the secondary yield surface the primary loading surface is used again.

A new input parameter is defined at this stage in order to include the post-liquefaction behaviour of the soil. If a non-zero multiplier fac_{post} is specified, from that stage in the primary yield surface a modified plastic shear modulus will be used based on the following equation:

$$K_G^p = K_{G,primary}^p \, fac_{post} \tag{B.11}$$

By setting the fac_{post} parameter to a value lower than one, the post-liquefaction behaviour of the soil is simulated. The post-liquefaction reduction of the plastic shear modulus given by eq. (3.18) is consistent with experimental observations. If the factor equals to 1 then a plastic modulus identical to that used in primary loading is taken. Both possibilities are depicted in case e.

The undrained behaviour of the soil is treated implicitly by the UBC3D- PLM constitutive model. Therefore, the increment of the pore water pressure is computed at each step of the analysis. Considering a saturated soil specimen, the increments in total stress during loading is given by the following equation:

$$dp = K_u d\varepsilon_v \tag{B.12}$$

where K_u is the bulk modulus of the undrained soil and $d\varepsilon_v$ is the increment of total volumetric strain. The effective stress increment can be computed as follows:

$$dp' = K' d\varepsilon_v \tag{B.13}$$

where K' is the bulk modulus of the soil skeleton.

The increment of the water pore pressure is computed by the following equation:

$$dp_w = \frac{K_w}{n} d\varepsilon_v \tag{B.14}$$

where K_w is the bulk modulus of the water and n is the soil porosity.

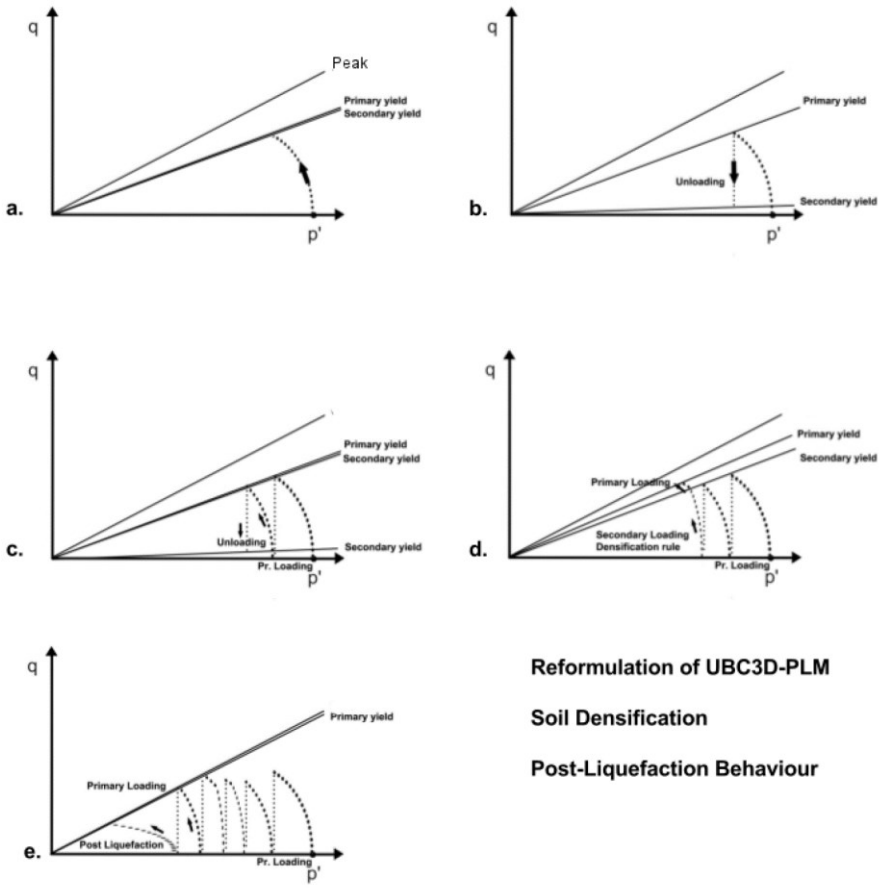

Figure B. 3. Representation of the soil densification effect in the p'-q plane.

The relationship between the total stresses, the effective stresses and the pore pressure is assumed according to Terzaghi's theory:

$$dp = dp' + dp_w \tag{B.15}$$

$$\frac{K_w}{n} = (K_u - K') \tag{B.16}$$

The value of K_u, the bulk modulus in undrained condition, is a function of the Poisson's ratio as follow:

$$K_u = \frac{2G^e(1 + \nu_u)}{3(1 - 2\nu_u)} \tag{B.17}$$

Where G^e is the elastic shear modulus and ν_u is the Poisson's ratio in undrained condition, it is equal to 0.495 value close to the limit equal 0.5.

For the unsaturated soil the fluid bulk modulus is calculated by the following equation:

$$K_{w,unsat} = \frac{K_w^{sat}\, K_{air}}{S\, K_{air} + (1 - S) K_w^{sat}} \quad (B.18)$$

where K_w^{sat} is the bulk modulus of the saturated water and K_{air} is the bulk modulus of air equal to 1kPa. Finally, S is the degree of the saturation.

The calibration of model parameters can be performed by using empirical relationships based on sand relative density (Beaty and Byrne, 2011b), which are based on the SPT number $N_{1,60}$. It is possible to relate this last parameter to the relative density (RD) using the relationship (Idriss and Boulanger, 2008):

$$N_{1,60} = 46\, RD^2 \quad (B.19)$$

B.1.2 PM4SAND

The PM4SAND (version 3) model follows the basic framework of the stress-ratio controlled, critical state compatible, bounding surface plasticity model for sands presented by Dafalias and Manzari (2004), who extended the previous work by Manzari and Dafalias (1997) by adding a fabric-dilatancy related tensor quantity to account for the effect of fabric changes during loading. The fabric-dilatancy related tensor was used to macroscopically model the effect that microscopically observed changes in sand fabric during plastic dilation have on the contractive response upon reversal of loading direction. The modifications were developed and implemented to improve the ability of the model to match existing engineering design relationships currently used to estimate liquefaction-induced ground deformations during earthquakes. These modifications are described in the manuals (version 1 in Boulanger 2010, version 2 in Boulanger and Ziotopoulou 2012, and version 3) and in the associated publications, as listed in the mentioned manuals.

The model is written in terms of effective stresses, with the conventional prime symbol dropped from the stress terms for convenience because all stresses are effective for the model. The stresses are represented by the tensor **r**, the principal effective stresses are σ_1, σ_2, and σ_3, the mean effective stress is p, the deviatoric stress tensor is s, and the deviatoric stress ratio tensor r. The current implementation was further simplified by casting the various equations and relationships in terms of the in-plane stresses only. This limits the implementation to plane-strain (2D) applications, having the further advantage in its simplified implementation to improve the computational speed. The relationships between the various stress terms can be summarized as follows:

$$\boldsymbol{\sigma} = \begin{pmatrix} \sigma_{xx} & \sigma_{xy} \\ \sigma_{xy} & \sigma_{yy} \end{pmatrix} \quad (B.20)$$

$$p = \frac{\sigma_{xx} + \sigma_{yy}}{2} \quad (B.21)$$

$$\boldsymbol{s} = \boldsymbol{\sigma} - p\boldsymbol{I} = \begin{pmatrix} s_{xx} & s_{xy} \\ s_{xy} & s_{yy} \end{pmatrix} = \begin{pmatrix} \sigma_{xx} - p & \sigma_{xy} \\ \sigma_{xy} & \sigma_{yy} - p \end{pmatrix} \tag{B.22}$$

$$\boldsymbol{r} = \frac{\boldsymbol{s}}{p} = \begin{pmatrix} r_{xx} & r_{xy} \\ r_{xy} & r_{yy} \end{pmatrix} = \begin{pmatrix} \dfrac{\sigma_{xx} - p}{p} & \dfrac{\sigma_{xy}}{p} \\ \dfrac{\sigma_{xy}}{p} & \dfrac{\sigma_{yy} - p}{p} \end{pmatrix} \tag{B.23}$$

In eq. (3.40), $\boldsymbol{I}$ is the identity matrix. The deviatoric stress and deviatoric stress ratio tensors are symmetric with $r_{xx} = -r_{yy}$ and $s_{xx} = -s_{yy}$ (meaning a zero trace).

The strains are represented by a tensor ε, expressed as the sum of the volumetric strain ε_v and of the deviatoric strain tensor e. The volumetric strain is,

$$\varepsilon_v = \varepsilon_{xx} + \varepsilon_{yy} \tag{B.24}$$

and the deviatoric strain tensor is,

$$\boldsymbol{e} = \boldsymbol{\varepsilon} - \frac{\varepsilon_v}{3}\boldsymbol{I} = \begin{pmatrix} \varepsilon_{xx} - \dfrac{\varepsilon_v}{3} & \varepsilon_{xy} \\ \varepsilon_{xy} & \varepsilon_{yy} - \dfrac{\varepsilon_v}{3} \end{pmatrix} \tag{B.25}$$

In incremental form, the deviatoric and volumetric strain terms are decomposed into an elastic and a plastic part,

$$d\boldsymbol{e} = d\boldsymbol{e}^{el} + d\boldsymbol{e}^{pl} \tag{B.26}$$

$$d\varepsilon_v = d\varepsilon_v^{el} + d\varepsilon_v^{pl} \tag{B.27}$$

where:

$d\boldsymbol{e}^{el}$ = elastic deviatoric strain increment tensor

$d\boldsymbol{e}^{pl}$ = plastic deviatoric strain increment tensor

$d\varepsilon_v^{el}$ = elastic volumetric strain increment tensor

$d\varepsilon_v^{pl}$ = plastic volumetric strain increment tensor

This constitutive model follows the critical state theory and uses the relative state parameter index (ξ_R) as defined by Boulanger (2003) and shown in Figure B. 4. This relative parameter is defined by an empirical relationship for the critical state line:

$$\xi_R = D_{R,cs} - D_R \tag{B.28}$$

$$D_{R,cs} = \frac{R}{Q - \ln\left(100\dfrac{p}{p_A}\right)} \tag{B.29}$$

where $D_{R,cs}$ is the relative density at critical state for the current mean effective stress, instead, Q and R are two parameters that define the shape of critical curve.

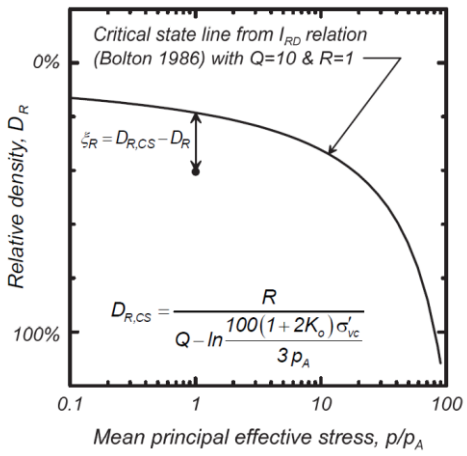

Figure B. 4. Relative state parameter index.

Bounding, dilatancy and critical surfaces are incorporated in PM4SAND following the form of Dafalias and Manzari (2004).

The bounding (M^b) and dilatancy (M^d) ratios can be related to the critical stress (M) ratio:

$$M^b = M \cdot \exp(-n^b \xi_R) \tag{B.30}$$

$$M^d = M \cdot \exp(-n^d \xi_R) \tag{B.31}$$

where n^b and n^d are model parameters. The relationship for M is:

$$M = 2 \cdot \sin(\phi_{cv}) \tag{B.32}$$

where ϕ_{cv} is critical state friction angle.

As the soil is sheared toward critical state $(\xi_R = 0)$, the values of M_b and M_d will both approach the value of M. Thus, the bounding and dilatancy surfaces move together during shearing until they coincide with the critical state surface when the soil has reached critical state.

The few experimental data for loose-of-critical sands (having no peak) show that the maximum friction angles (presumably determined at the limit of strains possible within the laboratory tests) were only slightly smaller than the critical state values, such that extending the above relationships to loose-of-critical sands may tend to underestimate the peak friction angles (in this case theoretically coinciding with the critical state one). Consequently, in the present formulation the model allows n_b and n_d to be different for loose-of-critical and dense-of-critical states for the same sand.

A large portion of the post-liquefaction reconsolidation strains are due to the sedimentation effects which are not easily incorporated into either the elastic or plastic components of behaviour. For this reason, in the PM4SAND a post-shaking function was implemented. In a strongly pragmatic way, this function reduces volumetric and shear moduli, thus increasing reconsolidation strains to somehow simulate the sedimentation ones (not included in the model).

The post-shaking elastic moduli are determined by multiplying the conventional elastic moduli by a reduction factor F_{sed} as,

$$G_{post-shaking} = F_{sed} \cdot G \tag{B.33}$$

$$K_{post-shaking} = F_{sed} \cdot K \tag{B.34}$$

for more information on the F_{sed} it is possible refer to Boulanger and Ziotopoulou (2015). For the calibration of the model it is possible to refer to Luque Nuques (2017), as also recalled in the relevant parts of §3.3.